Ion Beam Science

Solved and Unsolved Problems

Part I

Edited by Peter Sigmund

Matematisk-fysiske Meddelelser 52:1

Det Kongelige Danske Videnskabernes Selskab
The Royal Danish Academy of Sciences and Letters

DET KONGELIGE DANSKE VIDENSKABERNES SELSKAB
udgiver følgende publikationsrækker:

THE ROYAL DANISH ACADEMY OF SCIENCES AND LETTERS
issues the following series of publications:

	Authorized Abbreviations
Historisk-filosofiske Meddelelser, 8°	Hist.Fil.Medd.Dan.Vid.Selsk. (printed area 175 x 104mm, 2700 units)
Historisk-filosofiske Skrifter, 4° (History, Philosophy, Philology, Archaeology, Art History)	Hist.Filos.Skr.Dan.Vid.Selsk. (printed area 2 columns, each 199 x 77 mm, 2100 units)
Matematisk-fysiske Meddelelser, 8° (Mathematics, Physics, Chemistry, Astronomy, Geology)	Mat.Fys.Medd.Dan.Vid.Selsk. (printed area 180 x 126 mm, 3360 units)
Biologiske Skrifter, 4° (Botany, Zoology, Palaeontology, General Biology)	Biol.Skr.Dan.Vid.Selsk. (printed area 2 columns, each 199 x 77 mm, 2100 units)
Oversigt, Annual Report, 8°	Overs.Dan.Vid.Selsk.

General guidelines

The Academy invites original papers that contribute significantly to research carried on in Denmark. Foreign contributions are accepted from temporary residents in Denmark, participants in a joint project involving Danish researchers, or those in discussion with Danish contributors.

Instructions to authors

Manuscripts from contributors who are not members of the Academy will be refereed by two members of the Academy. Authors of papers accepted for publication will receive galley proofs and page proofs; these should be returned promptly to the editor. Corrections other than of printer's errors will be charged to the author(s) insofar as the costs exceed 15% of the cost of typesetting.

Authors receive a total of 50 free copies. An order form, quoting a special price for additional copies, will accompany the page proofs. Authors are invited to provide addresses of up to 20 journals to which review copies could profitably be sent.

Manuscripts can be returned, but only upon request made before publication of the paper. Original photos and artwork are returned upon request.

Ion Beam Science

Solved and Unsolved Problems

Invited lectures presented at a symposium arranged by the Royal Danish Academy of Sciences and Letters Copenhagen, 1-5 May 2006

Part I

Edited by Peter Sigmund

Matematisk-fysiske Meddelelser 52:1

Det Kongelige Danske Videnskabernes Selskab
The Royal Danish Academy of Sciences and Letters

Abstract

This book emerged from a discussion meeting held at the Royal Danish Academy of Sciences and Letters in May 2006. It covers a broad scope of applications and fundamentals in the area of ion beam science. Applications in astrophysics, magnetic and inertial fusion, particle therapy and radiation biology are followed up by topics in materials analysis and modification including radiation damage, particle tracks and phase transitions. Several contributions are devoted to particle-induced emission phenomena. The unusual placement of particle penetration and atomic collisions in the end reflects the structure of the meeting.

The book is neither a comprehensive review nor a tutorial. However, authors were asked to focus on essentials, both on unsolved problems in their general areas and on problems that have been around for a while but have come (close) to a satisfactory solution. The prime purpose of the book is to help those engaged in basic and applied research within ion-beam science to stay or become alert with respect to central problems in and around their area.

Figures were reproduced with the kind permission of the American Nuclear Society, the American Physical Society, Begell House Inc, Elsevier Science, the Institute of Physics, the International Atomic Energy Agency, ITER, the National Institute for Fusion Science, and Springer Verlag.

Prof. P. Sigmund
Department of Physics and Chemistry, University of Southern Denmark
DK-5230 Odense M, Denmark
sigmund@ifk.sdu.dk

Typeset by Karada Publishing Services (KPS), Slovenia. E-mail: kts@siol.net
Printed in Denmark by Special-Trykkeriet Viborg a-s
ISSN 0023-3323 ISBN10 87-7304-330-3 ISBN13 978-87-7304-330-1

Table of Contents

Volume 1

Preface 7

List of Contributors 9

Ion-Solid Interactions in Astrophysics 13
Raúl A. Baragiola

Hadron Therapy: Radiotherapy Using Fast Ion Beams 37
Oliver Jäkel

Spatial Distribution of DNA Double-Strand Breaks from Ion Tracks 59
A. Hauptner, W. Friedland, S. Dietzel, G.A. Drexler, C. Greubel, V. Hable, H. Strickfaden, T. Cremer, A.A. Friedl, R. Krücken, H.G. Paretzke and G. Dollinger

Magnetic Confinement Fusion: Ions in ITER – Beams and Surfaces 87
A.W. Kleyn

High Energy Density Matter Generated by Heavy-Ion Beams, and Application to Fusion Energy 109
A. Blazevic, B. Rethfeld and D.H.H. Hoffmann

Ion Beam Analysis of Lower Dimensional Structures 133
L.C. Feldman

Solved and Unsolved Problems in Ion-Beam Analysis: The Influence of Single Collisions 151
P.L. Grande, A. Hentz, R.P. Pezzi, I.J.R. Baumvol and G. Schiwietz

Nanoscale Morphology Control Using Ion Beams 187
M.J. Aziz

Ion-Induced Surface Evolution in the Linear Instability Regime: Continuum Theory and Kinetic Monte Carlo Simulation 207
Eric Chason and Wai Lun Chan

Some Ion-Beam Modification Issues: Ion-Induced Amorphisation and Crystallisation of Silicon 227
J.S. Williams, G. de M. Azevedo and A. Kinomura

Experimental Phenomena and Thermal Spike Model Description of Ion Tracks in Amorphisable Inorganic Insulators 263
M. Toulemonde, W. Assmann, C. Dufour, A. Meftah, F. Studer and C. Trautmann

Thermal-Spike Models for Ion Track Physics: A Critical Examination 293
S. Klaumünzer

Some Solved and Unsolved Problems in Transmission Electron Microscopy Studies of Radiation Damage in Solids 329
S.E. Donnelly

Radiation Damage in Carbon Nanotubes: What Is the Role of Electronic Effects? 357
K. Nordlund

Index 371

Volume 2

Ion Beam-Induced Amorphization: A Crystal-to-Glass Transition? 383
Harry Bernas

Sputtering: Experiment 405
Andreas Wucher

Sputter Theory 433
Herbert M. Urbassek

A Critical Review of the Electron-Tunnelling Model of Secondary Ion Formation 465
Klaus Wittmaack

Electron Emission from Solids Irradiated with Swift Ion Beams 497
Hermann Rothard and Benoit Gervais

Recent Advances in Slow Heavy Particle Induced Electron Emission 525
HP. Winter, F. Aumayr, H. Winter and S. Lederer

Stopping of Swift Ions: Solved and Unsolved Problems 557
Peter Sigmund

Charge States and Energy Loss of Ions in Solids 595
N.R. Arista

Charge Transfer in Atom-Surface Interactions 625
J.P. Gauyacq

Channeling and Blocking of Energetic Charged Particles in Crystals 655
Jens Ulrik Andersen

Penetration Phenomena at Relativistic Energies 699
U.I. Uggerhøj

Early History of Ion Beam Physics 731
John A. Davies

Index 751

Preface

The field of ion-beam science has a long history, starting with phenomena observed in gas discharges in the mid 19th century and followed up by the discovery of radioactivity and the development of atomic and nuclear physics. Experimental work was thriving long before modern accelerators and detectors became available, and basic theoretical tools were developed early in the 20th century. Applications in materials science and technology, micro electronics and micro mechanics, and radiomedicine and radio biology became of interest from the mid 20th century. Evidently, ion beams also play a key role in the more recent development of nano science and technology. As a result, conferences on fundamental and applied research in ion beam science attract hundreds of scientists and engineers, new facilities are being installed, and newcomers enter the field, not the least in applied research.

It is hard to enter a research field with such a longstanding tradition. While an attempt to overview the primary literature by a newcomer without the help of an experienced advisor is likely to fail, even review articles tend to abound of hundreds of references where it seems hard to see the forest amongst the trees.

The present book, focusing on *solved and unsolved problems*, is hoped to help the newcomer with some experience to get oriented in a broader area. It is not a tutorial, but authors were asked to focus on essentials, both on unsolved problems and on problems that have been around for a while but have come (close) to a satisfactory solution. It is notoriously difficult to make predictions concerning the future development of a research field. Nevertheless, this volume presents what some of our most experienced colleagues consider is important here and now.

All contributions are based on invited talks presented at a symposium with the same title, held at the Royal Academy of Sciences and Letters in Copenhagen from 1 to 5 May 2006. Papers were submitted, refereed and revised within a generous deadline after the meeting. Unfortunately, not all speakers were able to submit a written contribution within the given time limits.

The symposium was generously funded by the Royal Danish Academy of Sciences and Letters, the Danish Natural Science Research Council (FNU), and the Carlsberg Foundation who also funded the publication of this book. I like to

thank the members of the organizing committee as well as the speakers, authors and referees for their successful efforts. Special thanks are due to professors David Favrholdt and Ole Hindsgaul for their evening lectures on "The Academy and its building" and "The Carlsberg Academy", respectively. Finally I like to thank Pia Sigmund, Eva Bang Hansen, Bjarne Stavnshøj, as well as Uffe Møller and Erik Folven for practical assistance, and Dr. Flemming Lundgreen-Nielsen for his efficient handling of all issues concerning the publication of this volume.

Peter Sigmund
September 2006

List of Contributors

Andersen, J.U.
Department of Physics and Astronomy,
University of Aarhus, Denmark

Arista, N.R.,
División Colisiones Atómicas,
Centro Atómico Bariloche,
Instituto Balseiro, Argentina

Assmann, W.
Department of Physics,
University of Munich,
Garching, Germany

Aumayr, F.
Institut für Allgemeine Physik,
TU Wien, Austria

Azevedo, G. de M.
Research School of Physical Sciences
and Engineering,
Australian National University,
Canberra, Australia

Aziz, M.J.
Division of Engineering and Applied Sciences,
Harvard University,
Cambridge, U.S.A.

Baragiola, R.A.
Laboratory of Atomic and Surface Physics,
University of Virginia,
Charlottesville, U.S.A.

Baumvol, I.J.R.
Instituto de Física da Universidade Federal
do Rio Grande do Sul,
Porto Alegre, Brazil; and
Centro de Ciências Exatas e Technologia,
UCS, Brazil

Bernas, H.
CSNSM – CNRS,
Orsay, France

Blazevic, A.
Gesellschaft für Schwerionenforschung mbH,
GSI-Darmstadt, Germany

Chan, W.L.
Division of Engineering, Brown University,
Providence, U.S.A.

Chason, E.
Division of Engineering, Brown University,
Providence, U.S.A.

Cremer, T.
Department Biologie II,
LMU-München,
Martinsried, Germany

Davies, J.A.
Deep River, Ontario, Canada

Dietzel, S.
Department Biologie II,
LMU-München,
Martinsried, Germany

Dollinger, G.
Angewandte Physik und Messtechnik,
UniBw-München, Neubiberg, Germany

Donnelly, S.E.
Institute for Materials Research,
University of Salford,
Greater Manchester, U.K.

Drexler, G.A.
Strahlenbiologisches Institut,
LMU-München, Germany

Dufour, C.
SIFCOM, Laboratoire commun CNRS,
ENSICAEN, UCBN, Caen, France

Feldman, L.C.
Department of Physics and Astronomy,
Vanderbilt University,
Nashville, U.S.A.

Friedl, A.A.
Strahlenbiologisches Institut,
LMU-München, Germany

Friedland, W.
Institut für Strahlenschutz, GSF,
Neuherberg, Germany

Gauyacq, J.P.
Laboratoire des Collisions Atomiques
et Moléculaires,
Unité mixte de recherches CNRS,
Université Paris Sud,
Orsay, France

Gervais, B.
Centre Interdisciplinaire de Recherche
Ions Lasers,
CEA/CNRS/ENSICAEN/Université de Caen,
France

Grande, P.L.
Instituto de Física da Universidade Federal
do Rio Grande do Sul,
Porto Alegre, Brazil

Greubel, C.
Angewandte Physik und Messtechnik,
UniBw-München, Neubiberg, Germany

Hable, V.
Angewandte Physik und Messtechnik,
UniBw-München, Neubiberg, Germany

Hauptner, A.
Physik Department,
TU-München, Garching, Germany

Hentz, A.
Instituto de Física da Universidade Federal
do Rio Grande do Sul,
Porto Alegre, Brazil

Hoffmann, D.H.H.
Gesellschaft für Schwerionenforschung mbH,
GSI-Darmstadt, Germany; and
Institut für Kernphysik,
Technische Universität Darmstadt,
Germany

Jäkel, O.
Department for Medical Physics in
Radiation Oncology,
German Cancer Research Center,
Heidelberg, Germany

Kinomura, A.
Research School of Physical Sciences
and Engineering,
Australian National University,
Canberra, Australia

Klaumünzer, S.
Ionenstrahllabor, Hahn-Meitner-Institut,
Berlin, Germany

Kleyn, A.W.
FOM-Institute for Plasma Physics Rijnhuizen,
The Netherlands; and
Leiden Institute of Chemistry,
Leiden University, The Netherlands

Krücken, R.
Physik Department, TU-München,
Garching, Germany

Lederer, S.
Institut für Allgemeine Physik,
TU Wien, Austria

Meftah, A.
LRCPIS, Université de Skikda,
Algeria

Nordlund, K.
Accelerator Laboratory,
University of Helsinki,
Finland

Paretzke, H.G.
Institut für Strahlenschutz, GSF,
Neuherberg, Germany

Pezzi, R.P.
Instituto de Física da Universidade Federal
do Rio Grande do Sul,
Porto Alegre, Brazil; and
IBM Research Division,
T.J. Watson Research Center,
New York, U.S.A.

Rethfeld, B.
Gesellschaft für Schwerionenforschung mbH,
GSI-Darmstadt, Germany

Rothard, H.
Centre Interdisciplinaire de Recherche
Ions Lasers, CEA/CNRS/ENSICAEN,
Université de Caen, France

Schiwietz, G.
Abteilung SF4, Hahn-Meitner-Institut,
Berlin, Germany

Sigmund, P.
Department of Physics and Chemistry,
University of Southern Denmark,
Odense, Denmark

Strickfaden, H.
Department Biologie II,
LMU-München, Martinsried, Germany

Studer, F.
CRISMAT, Laboratoire commun CNRS,
ENSICAEN, UCBN, Caen, France

Toulemonde, M.
CIRIL, Laboratoir commun CEA,
CNRS, ENSICAEN, UCBN, Caen, France

Trautmann, C.
Materialforschung/GSI,
Darmstadt, Germany

Uggerhøj, U.I.
Department of Physics and Astronomy,
University of Aarhus, Denmark

Urbassek, H.M.
Fachbereich Physik,
Universität Kaiserslautern, Germany

Williams, J.S.
Research School of Physical Sciences
and Engineering,
Australian National University,
Canberra, Australia

Winter, H.
Institut für Allgemeine Physik,
Humboldt-Universität zu Berlin, Germany

Winter, HP.
Institut für Allgemeine Physik,
TU Wien, Austria

Wittmaack, K.
GSF – National Research Centre for
Environment and Health,
Neuherberg, Germany

Wucher, A.
Department of Physics,
University of Duisburg-Essen, Germany

Photo by S.E. Donnelly

Ion-Solid Interactions in Astrophysics

Raúl A. Baragiola*

Laboratory for Atomic and Surface Physics, University of Virginia
Charlottesville, VA 22904, USA

Abstract

This article gives an overview of the energetic ion spectra in different parts of the universe, the expected effects of ion interactions with airless celestial bodies, and some evidence for their occurrence. It is based mostly on research in a variety of topics at the author's laboratory but references are provided to the most current research elsewhere. The emphasis is on atomic collisions on molecular ices, which are both of greatest astrophysical interest and the subject of most past and current research. Many unsolved problems are stated or discussed, spanning from desorption of ices by thermal He^+ ions to the possible role of atomic collisions in the origin of life in the universe.

Contents

1 Energetic Ions in Space **14**
1.1 Solar Energetic Particles 15
1.2 Ions in Planetary Magnetospheres 17
1.3 Cosmic Rays 17

2 Astronomical Surfaces **17**
2.1 Planetary Regoliths 17
2.2 Remote Sensing of Surfaces in Space by Optical Reflectance Spectroscopy 19

3 Atomic Collision Topics and Questions **20**
3.1 Sputtering 20
3.1.1 Atomic Collisions on the Moon Surface 21
3.1.2 Sputtering of Regoliths – Effect of Porosity, Redeposition 21

* E-mail: rb9a@virginia.edu

3.1.3 Grain Destruction 21
3.1.4 Sputtering of Ices (Satellites, Rings, Comets, Outer Planets, Interstellar Grains) 22
3.1.5 Generation of Atmospheres by Sputtering 22
3.2 Amorphization of Crystalline Minerals and Ices 23
3.3 Electrostatic Charging of Surfaces 23
3.4 Radiation Chemistry 25
3.4.1 O_2 Synthesis from Water Ice 29
3.4.2 Ozone Synthesis 29
3.4.3 Synthesis of Hydrogen Peroxide 30
3.4.4 Other Ices 30

4 Was Ion Irradiation Needed for Primordial Life? 30
4.1 Energetic Ions as a Source of Biotic Energy 32

5 Summary and Outlook 33

Acknowledgements 33

References 33

1. Energetic Ions in Space

Living in our planet, protected by an atmosphere and a magnetic field, it is not apparent that most of the universe is violent, permeated with energetic radiation. But a glimpse of this violence can be had from beautiful polar auroras, from reports of the dangers of the ozone hole or the disruption of communications by solar storms, and by stunning astrophotographs of the surroundings of young and dying stars. Figure 1 shows an image of the Menzel 3 stellar object (Ant Nebula) taken by the Hubble Space Telescope. The gas outflow from the central dying star is quite visible. It moves at very high speeds, ~500 km/s in an intriguing, and yet unexplained, bipolar pattern. Given the high gas velocities (that can reach $v_{\mathrm{Bohr}} = 2188$ km/s near white dwarfs spawning other planetary nebulae), such stellar outflow can sputter surrounding objects, such as grains (typically of nm to μm size). In addition, there are more energetic particles, cosmic rays and ions in shock waves originating in supernovae, starburst regions and super massive black holes at active galactic centers. In our Solar system, the most common energetic particles are found in the escaping solar corona (solar wind, flares, and coronal mass ejection), ions in planetary magnetospheres, and galactic cosmic rays. Such ions impact the surface of objects that lack a protective atmosphere or magnetic field. The most affected are small unshielded bodies, such as comets,

Figure 1. Nebula Menzel 3 (Ant Nebula) STScI-PRC2001-05. Credit: NASA, Space Telescope Science Institute.

asteroids, grains, and most satellites, which also have a weak gravity needed to bind significant atmospheres.

The evidence for energetic ion impact on surfaces is indirect, with the exception of returned Moon rocks, which have been analyzed in detail, captured interplanetary and cometary grains that show ion tracks and, in the near future, samples implanted with solar wind ions returned by the Genesis mission (Burnett et al., 2003). The most common evidence of ion impacts is indirect, from spectroscopic analysis of reflected stellar light that sometimes reveals the presence of molecules synthesized by radiation and from the observation of atmospheres of non-thermal origin around Europa and Ganymede (two satellites of Jupiter), Saturn's rings, the Moon and Mercury. Such atmospheres can be explained to result from sputtering by either magnetospheric ions or the solar wind.

1.1. Solar Energetic Particles

The solar wind is expanding magnetized plasma emanating from the Sun, consisting of low energy electrons, energetic ions and a magnetic field. The ions are ~96% H^+, ~4% He^{++} and trace amounts of multiply-charged O, C, Si, Fe, and other species. On average, they move with a most probable velocity $v \sim 450$ km/s (~1 keV/amu) and a fast component at ~750 km/s . The flux of the solar wind at

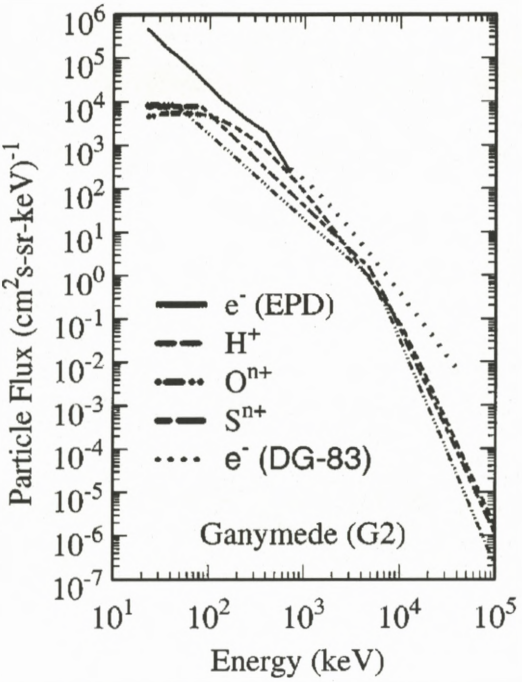

Figure 2. Flux spectra of particles near Ganymede. Compiled by Cooper et al. (2001).

the Earth ($R = 1$ AU) is $\sim 2 \times 10^8$ particles/cm^2-s and decays as $1/R^2$, where R is the distance to the Sun. The solar wind is not stable, variations in solar activity change its flux and velocity distribution constantly. Sporadically the Sun emits solar flares, which are bursts of ions of higher energy than the solar wind, reaching hundreds of MeV (Mewaldt et al., 2005). The most violent eruption from the sun is when a prominence in the corona becomes detached, this is called a coronal mass ejection and can attain very large velocities, 3000 km/s. When the coronal mass ejections reach the Earth they produce great perturbations in the geomagnetic field that induce large electric fields in electric power distribution systems (e.g., the Quebec Blackout of 1989). Strong efforts to understand space weather, i.e., the changing environment around the Earth due to the interaction of solar energetic particles with the magnetosphere, are motivated by the idea that one can predict the occurrence and magnitude of coronal mass ejections. Space research is also focused on radiation effects on spacecraft (e.g., communication satellites) such as in semiconductor devices which can malfunction due to single ion impacts: single event upsets, latchup and burnout (Messenger and Ash, 1997), and electrostatic charging that can produce arcs across spacecraft components (Baker, 2002).

1.2. Ions in Planetary Magnetospheres

The ion fluxes and energies in planetary magnetospheres are larger than in the solar wind, particularly around Jupiter ($R = 5.2$ AU) and Saturn ($R = 9.54$ AU). Figure 2 (taken from Cooper et al., 2001), is a compilation of energy distributions of high-energy ions and electrons near Ganymede, a satellite of Jupiter. One can see that the ions are mostly H^+, oxygen and sulfur with an energy distribution that has a broad peak at 10–100 keV. There is in addition a low energy (thermal) plasma component (not shown) that extends to eV energies. The ion distributions are measured in space, in the vicinity of the satellite. There are no measurements of the actual flux impinging on the surface, which should be different due to electrostatic charging of the surface and to the presence of magnetic fields. For instance, all of the electrons and most of the ions are thought to be excluded from the equatorial surface regions of Ganymede, due to its intrinsic magnetic field, a rare occurrence among satellites.

1.3. Cosmic Rays

The more energetic ions in space are the galactic cosmic rays, which are found over an enormous range of energies, extending up to more than 10^{20} eV. Figure 3 (Simpson, 1983) shows the energy distribution of different cosmic ray ions in the solar system. It falls at low energies, compared to the expected interstellar cosmic ray flux, due to the magnetic field of the solar wind. Cosmic rays can produce a multitude of effects, such as sputtering, amorphization, the single events in semiconductor devices mentioned above, and chemical alterations, either directly or through secondary particles resulting from nuclear reactions. Measurements of the density of etchable (amorphous) tracks in minerals produced by cosmic rays, coupled with estimates of the cosmic ray flux are used for dating rocks and man-made stone artifacts or pottery.

2. Astronomical Surfaces

2.1. Planetary Regoliths

The surfaces of airless bodies in space are not only subject to energetic ion and photon irradiation but are also impacted by meteorites, particularly by micron size particles. Micrometeorite impact pulverizes mineral and icy surfaces (comminution) and the local heat produced can melt the surface and even cause the thermionic emission of electrons and ions. Most of the debris ejected from the surface falls back on the surface (except in very small bodies of negligible gravity)

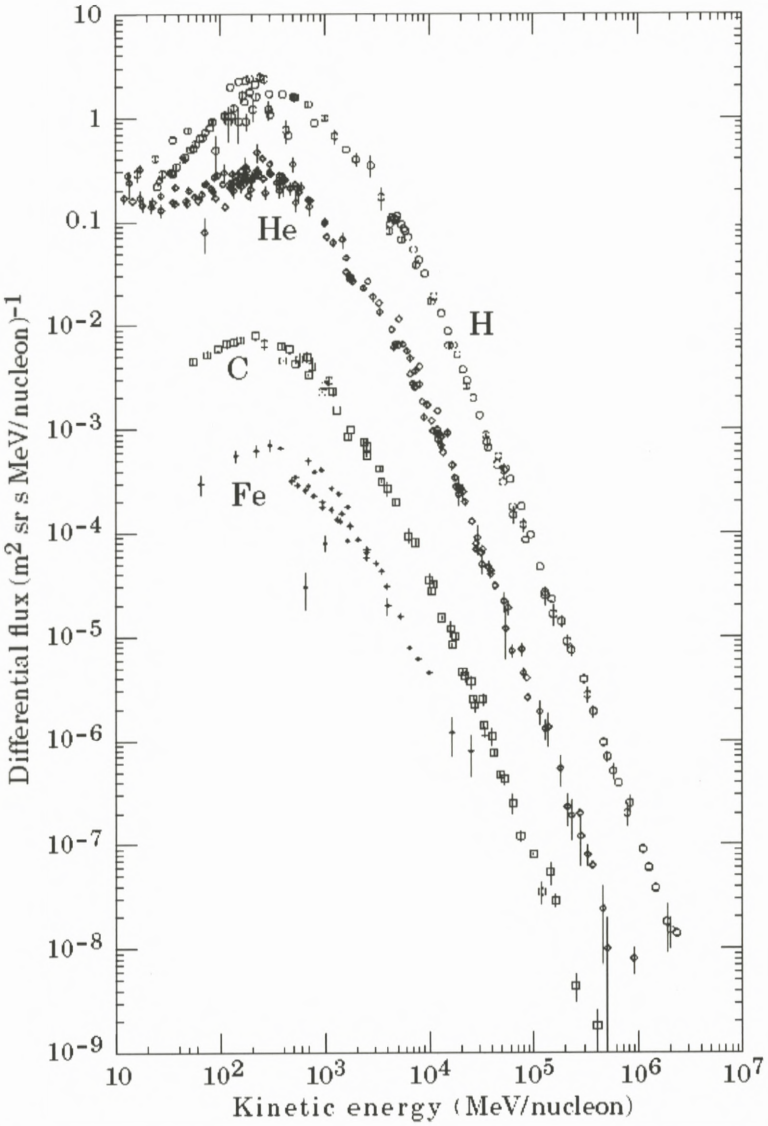

Figure 3. Flux spectra of the primary ions in cosmic rays. From Simpson (1983).

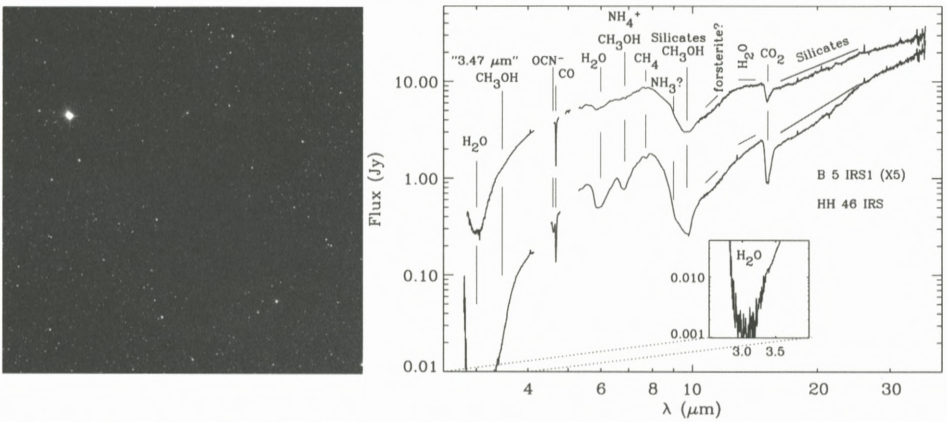

Figure 4. The Barnard 5 dark molecular cloud (left) associated with the constellation of Perseus and the infrared spectra obtained by the Spitzer telescope in the directions of embedded stars B5 IRS 1 (top, multiplied by 5) and HH 46 IRS (bottom). The labels identify absorbing molecules (Boogert et al., 2004).

and is impacted again by the continuing meteorite flux. These processes mix and redistribute the soil and bury ion irradiated material below the surface; this is called gardening or reworking. The gardening by micrometeorites, added to sputtering, re-deposition, and chemical alteration by energetic ion and photon impact is referred to as space weathering, and the highly porous and chemically altered surface layer is called the regolith (Hapke 2001; Chapman, 2004).

2.2. Remote Sensing of Surfaces in Space by Optical Reflectance Spectroscopy

Our knowledge of regolith processing comes from analysis of lunar rocks and simulations in the laboratory, inferences obtained from comparing scattering models to measurements of light reflected from the sun and of radar reflectance from ground based transmitters. The spectral analysis of reflected light in the infrared region can give information on surface composition from the absorption resulting from excitation of characteristic molecular vibrations and, in some cases, the temperature of the surface. However, infrared reflectance spectra may be distorted by scattering effects, by the fact that transitions in symmetric molecules are very weak ("forbidden"), and by the broadness and overlap of the absorption bands in solids. This last factor is particularly severe in large molecules (e.g., organics), making it difficult to identify them with confidence.

While radio astronomy gives abundances of gas-phase interstellar molecules, infrared spectroscopy gives most of the composition information of grains in in-

terstellar clouds. These grains, typically ~100 nm in size, are coated by a mantle of condensed gas (ice) in cold environments. Diffuse interstellar clouds having gas densities of the order of 100 atoms/cm^3 are at about 100 K, while in molecular clouds with gas densities of ~10^4 atoms/cm^3 temperatures are much lower, ~10 K. The composition of the grains and their mantles can be determined by aiming a telescope at a star embedded in or behind the cloud, such that the light is partially absorbed. An example is Figure 4 that shows absorption bands in the light from two young stars embedded in a dark molecular cloud (Barnard 5) associated with the constellation of Perseus (Boogert et al., 2004). The vibrational frequencies responsible for infrared absorption are specific to the molecules present and to their local (near-neighbor) environment, and are identified by comparison with laboratory spectra of pure and mixed ices grown by vapor deposition in vacuum and irradiated with UV photons or energetic particles (d'Hendecourt and Dartois, 2001; Strazzulla et al., 2001; Moore et al., 2001).

3. Atomic Collision Topics and Questions

We now turn into specific topics in atomic collisions in solids that have astrophysical applications: sputtering, amorphization, electron emission and electrostatic charging, and radiation chemistry.

3.1. Sputtering

Both elastic (knock-on) and electronic sputtering are important in astronomical environments. Elastic sputtering usually dominates at low projectile velocities, and is the primary mechanism for erosion of minerals and ices by the solar wind and low energy plasmas. The success of sputtering theories and computer simulations in describing elastic sputtering of elemental solids does not translate into the more complex natural solids such as molecular ices and silicates. In spite of their popularity with modelers, Monte Carlo codes like TRIM are not appropriate to simulate sputtering of minerals by low energy ions for two main reasons. First, simplified models of surface binding energies and the neglect of attractive potentials fail in multicomponent insulators, and second, radiation assisted diffusion and chemical reactions in the collision cascade cause compositional changes that currently cannot be predicted. Both these challenges are ripe for exploration with detailed quantum-mechanical molecular dynamics that can help identify the important physics and ways to improve Monte Carlo codes.

3.1.1. *Atomic Collisions on the Moon Surface*
The realization that energetic solar wind ions can sputter the Moon surface was realized from the beginning of the Apollo project. Lunar samples returned since 1969, and still being analyzed, showed evidence of erosion by sputtering, redeposition of sputtered ejecta in porous surfaces, preferential sputtering such as that leading to the formation of Fe nanoparticles by reduction of iron oxides (Dukes et al., 1999), ion implantation, and cosmic ray tracks. Many of these effects were anticipated by Wehner (1964) years before the first Apollo landing. Reviews of sputtering and chemical alteration processes on the Moon, asteroids, and Mercury, from different perspectives, can be found in Johnson and Baragiola (1991), Hapke (2001) and Chapman (2004).

3.1.2. *Sputtering of Regoliths – Effect of Porosity, Redeposition*
Even if laboratory data for sputtering of a mineral is known, its application to a porous regolith, such as the Moon's, is not straightforward. In a very rough or porous surface, an important part of the flux of sputtered species is intercepted by nearby surfaces. The effect is observed as a reduction of the sputtering yield over that of flat surfaces and in the appearance of surface coatings due to re-deposition of material (Hapke and Cassidy, 1978) and is a current topic for computer simulations (Cassidy and Johnson, 2005). The magnitude of the effect depends on several factors, such as the angular and energy distribution of sputtered particles, the topography of the surface, the sticking of ejected particles when they hit an adjacent surface, temperature, and the type of material. The sticking of sputtered particles depends in turn on their identity (and surface binding energy), kinetic energy, angle of impact and type of surface. One of the most important unknown in the calculations is the probability of sticking for ejected atoms or molecules with energies between a few tenths of eV and a few eV, which is a range where molecular dynamics simulations can be applied, once the non-trivial task of finding adequate interatomic potentials in silicates is done.

3.1.3. *Grain Destruction*
Cosmic rays impacting interstellar grains can sputter the grain and any existing ice mantle. The process can occur by atomic ejection at both ends of the ion track (Schutte, 1996). In addition, it has been proposed that grain destruction can occur by evaporation, if the energy absorbed by the grain is sufficient to cause a sufficient temperature increase. Modern molecular dynamics simulations have shown that the thermal sputtering yields are much smaller than anticipated (Bringa and Johnson, 2004).

On the opposite end of the energy scale, sputtering of ice mantles can occur by thermal ions if they carry high potential energy, e.g. He^+, He^{++} or other mul-

tiply charged ions. The mechanism, Auger desorption (Baragiola, 2005) is one in which the ion captures a valence electron from a condensed molecule, with the energy released exciting simultaneously another valence electron. Energetically, it is favored that the two final holes remain in different molecules. Their Coulomb repulsion energy, acting before the holes can drift away, can transform into kinetic energy and result in desorption. For this process to occur, the recombination energy of the incoming ion must exceed the energy of the two holes in the lattice. Such a condition will exist for He^+ impacting most condensed gases, and for H^+ on some ices with sufficiently small band gap. Less abundant multiply charged ions can be expected to produce Auger desorption with a higher probability per ion impact. There is a need for measurements and theory of Auger desorption from ices that that will allow predictions of desorption yields.

3.1.4. *Sputtering of Ices (Satellites, Rings, Comets, Outer Planets, Interstellar Grains)*

This topic has been reviewed from the point of collision physics by Johnson and Schou (1993) in general, and by Baragiola et al. (2003) for water ice, the most prevalent condensed gas in astrophysics. The reader is referred to those papers for details. Basically, the physical principles of electronic sputtering of ices are known, but the details are not and therefore predictions are not possible in general. What is known is that the electronic excitations produced by fast ions in insulators can result in the formation of repulsive states through several different pathways spanning times from roughly 10^{-16} to 10^{-11} s, depending on whether the states are formed promptly or through electron-ion recombination. What is not known, except for a handful of cases (i.e., the condensed rare gases), is the nature of the repulsive states and how they relax. Competing with the intermolecular repulsion is relaxation by decay through multiphonon, autoionization and radiative processes. As a result of the unknowns, most reliable quantities, such as sputter yields and distributions, come from experiments.

3.1.5. *Generation of Atmospheres by Sputtering*

Sputtering and desorption by solar ultraviolet photons and energetic charged particles from the solar wind and planetary magnetospheres can eject material from the surface of an astronomical body with a faint atmosphere. Depending on its velocity, the ejected material may escape the gravitational pull or may contribute to the formation of an atmosphere, adding to any existing contribution of sublimation (Shi et al., 1995; Cooper et al., 2001), volcanism or meteorite impact ejection. The effect of the incoming ions is more extensive, since they interact with the atmosphere dissociating molecules, adding to photodissociation by solar radiation (limited to daytime). The dissociation fragments can in turn scatter, react, and/or

be trapped in collisions with the surface. The generation of atmospheres by sputtering of ices is thought to be important in the icy satellites Ganymede and Europa of Jupiter, in most satellites of Saturn, Uranus, Neptune and trans-Neptunian objects. In addition, sputtering of Na from plagioclase feldspar minerals on Mercury and the Moon is thought to be an important source of the sodium exospheres that have been observed around those rocky bodies (Killen et al., 2004).

3.2. Amorphization of Crystalline Minerals and Ices

Crystalline silicates and ices are amorphized at relatively low doses by ion impact, not only at low energies as a result of elastic collisions (Brucato et al., 2004; Demyk et al., 2004) but also in ionization tracks produced by swift heavy ions (Meftah et al., 1994). In the latter case, if the energy deposition in the track is sufficiently dense, local melting occurs followed by an extremely fast re-solidification which leads to amorphization. Amorphous tracks are etched preferentially by chemical means and this enables easy visualization for measurements of ion fluxes or for dating. We note that amorphization of minerals by radiation damage is of great importance also in the encapsulation of radioactive waste in the nuclear energy. Most models of amorphization are empirical and the current view is that the problem is unsolved (Trachenko, 2004).

For water ice on icy satellites, the efficient amorphization by ions competes with thermal crystallization of amorphous ice. This gives the ratio of amorphous to crystalline ice obtained by infrared reflectance spectroscopy a valuable diagnostic value (Hansen and McCord, 2004). Figure 5 shows the drastic changes in the OH stretch vibration band of water during amorphization by ions (Baragiola et al., 2005) that demonstrate that the band shape is a sensitive indicator of the crystallinity of the ice. It is noteworthy and not yet understood that, while the shape of the infrared band evolves towards that of amorphous ice upon irradiation, significant differences remain. The temperature used in these experiments was 70 K to simulate amorphization of crystalline ice on Europa, a phase that may be produced by melting ice in tectonic processes or in meteorite impacts. The Ar^+ ions were used to simulate the S^+ ions that abound in the Jovian magnetosphere without the complication of chemical effects.

3.3. Electrostatic Charging of Surfaces

Astronomical surface materials (minerals or ices) are electrical insulators and, therefore, charge electrostatically when exposed to charged particles and ionizing photons. Surfaces charge positively by capturing a slow positive ion or by electron emission when hit by a sufficiently energetic ultraviolet photon or a fast ion. They

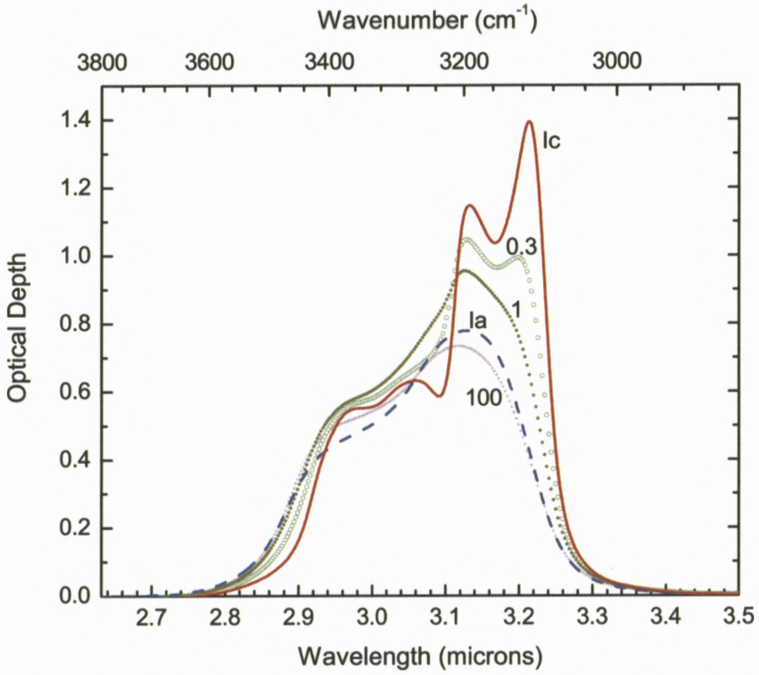

Figure 5. Optical depth of the infrared vibrational band due to the OH stretch in ice, measured at 70 K for a $\sim 10^{18}$ H_2O/cm^2 crystalline ice film grown at 150 K and irradiated at 70 K by 100 keV Ar^+ ions at normal incidence. Ic-unirradiated crystalline (cubic) ice. The spectra with symbols show Ic irradiated to different fluences indicated by the numbers adjacent to the curves, in units of 10^{13} ions/cm^2. The dashed curve labeled Ia is the spectrum of amorphous ice grown at 20 K and taken to 75 K. From Baragiola et al. (2005).

can charge negatively when impacted by either slow or high energy electrons with a secondary electron emission coefficient less than unity. It is difficult to predict the amount of charge accumulated on a surface because it depends on material properties, the balance between fluxes of incoming and ejected charges, their energy distribution, and the surface electrical potential. When the surface is inhomogeneous or when the particle flux and/or electromagnetic field is not uniform (for example part of the surface being in the shadow) the resulting differential charging will induce electric fields that can affect electron emission and may induce electrical breakdown. These conditions are relevant for electrically insulating surfaces in spacecraft, where the breakdown can produce malfunction by spurious electrical noise, and also permanent damage (Garrett and Whittlesey, 2000). Electrostatic charging can affect the dynamical behavior of small grains in regions of significant electromagnetic fields, such as planetary magnetospheres. A

most striking example is the presence of the spokes in Saturn's rings, thought to be caused by a competition of gravitational and electromagnetic forces (Mitchell et al., 2006). Analysis of the complex problem of electrostatic charging in dusty plasmas (e.g., Jurac et al., 1995; Weingartner and Draine, 2001) is still in its infancy and is hindered by the scarcity of data on electron emission from insulators by ions and electrons at energies below 100 eV and on surface charging with ion beams.

3.4. Radiation Chemistry

The similarity in the composition of volatiles in comets and the ice mantles of interstellar grains led early to the idea that interstellar ices are integrated into comets. However, the degree to which this occurs is still an unsolved problem. Icy grains can evaporate in the protoplanetary nebula and later condense into comets while being concurrently processed by the strong radiation environment. Alternatively, grains that have been exposed to energetic radiation in the interstellar medium may be incorporated with little alteration into comets in the outer regions of the protoplanetary disk. In both cases, energetic radiation will synthesize molecules and store radicals in the ice, but to a degree which is not fully understood. Figure 6 shows the results of radiation chemistry in a hydrogen peroxide film irradiated at 17 K with 50 keV protons that deposit their energy mainly by electronic processes. One can notice that irradiation produces new molecules: water, diatomic oxygen and ozone, which remain trapped in the sample at these low temperatures. Analysis of the infrared spectra, taking into account interference effects in the thin ice films, can be used to obtain quantitative fluence dependences, shown in Figure 7. A linear dependence of column density with fluence indicates that the product is formed in single collisions (case of water), in contrast with the case of di- and triatomic oxygen molecules. Other atoms and molecules are thought to be trapped as well but are very weakly sensitive to infrared light or, as in the case of OH radicals and HO_2 molecules, their absorption bands are hidden by the much stronger bands due to water and hydrogen peroxide.

We have used this type of radiolyzed material, obtained after high fluence irradiation, to study the evolution during heating using TDS (thermal desorption spectroscopy, also known as TPD: temperature programmed desorption). The material is thought to be a model system for cometary grains containing radiation processed ice and their behavior as the comet warms up on approach to the Sun and loses mass through sublimation of volatile gases. One needs to take into account in any thermal processing that the molecules desorbing may not be just the original trapped gas. Warming may allow chemical reactions involving frozen

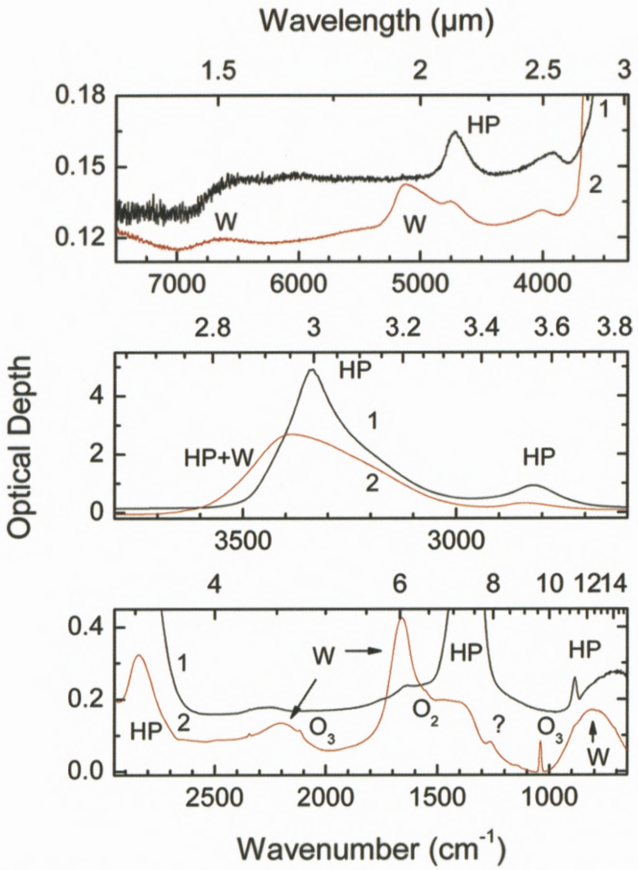

Figure 6. Infrared spectra of a solid H_2O_2 sample before (1) and after (2) irradiation at 17 K to a fluence of 1.8×10^{15} H^+ ions cm^{-2} at 50 keV. H_2O_2 is labeled as HP, H_2O as W. From Loeffler et al. (2006a).

radicals to overcome energy barriers and to alter the original composition of the ice by forming or destroying molecular species.

The absolute concentrations of the H_2O, O_2, H_2O_2 and O_3 molecules and their dependence on irradiation fluence was obtained by TDS using a combination of experimental techniques: UV-visible and infrared reflectance spectroscopy, quartz crystal microbalance microgravimetry and mass spectrometry (Loeffler et al., 2006b). The results of the last two techniques are shown in Figure 8 which suggest fractionation in the gas release from comets. The very high radiation yields for the decomposition of hydrogen peroxide can be explained by the occurrence of a chemical chain reaction.

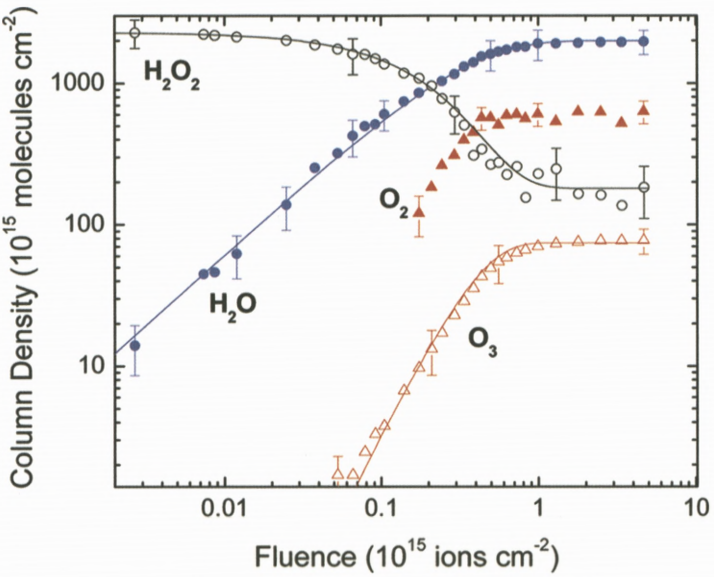

Figure 7. The production of water, O_2, and ozone in a film of 2.6×10^{18} H_2O_2 cm^{-2} irradiated with 50 keV H^+. From Loeffler et al. (2006a).

Another scenario for the thermal evolution of radiation processed ice is the diurnal cycle of the surface of icy satellites immersed in the magnetosphere of giant planets. This is one aspect of more general phenomena. The state of the surface of these bodies is determined by a competition of radiation damage and erosion due to energetic particles, photons, meteorite impact, and sublimation, by thermal diffusion, by interactions with the atmosphere, and radiation enhanced chemical processes, such as synthesis of radicals and new molecules, creation of optically active centers, phase transitions, release of trapped gases, and surface roughening. While one can study each aspect individually, it is important to consider the different ways in which synergism can occur and plan experiments to test them.

Several laboratory studies have shown the presence of trapped radicals in radiolyzed or photolyzed condensed gases. Here I summarize the results for water ice, by far the most abundant of those substances. Dissociation of water in the solid state often leads to immediate reformation of the molecule, since the dissociation fragments suffer collisions with surrounding molecules and cannot escape. The consequence of this phenomenon, called the *cage effect*, is a substantially smaller yield of radiation products in solids as compared to the gas phase. For radiation of slow linear energy transfer (LET, deposited dE/dx) isolated H, O and OH radicals

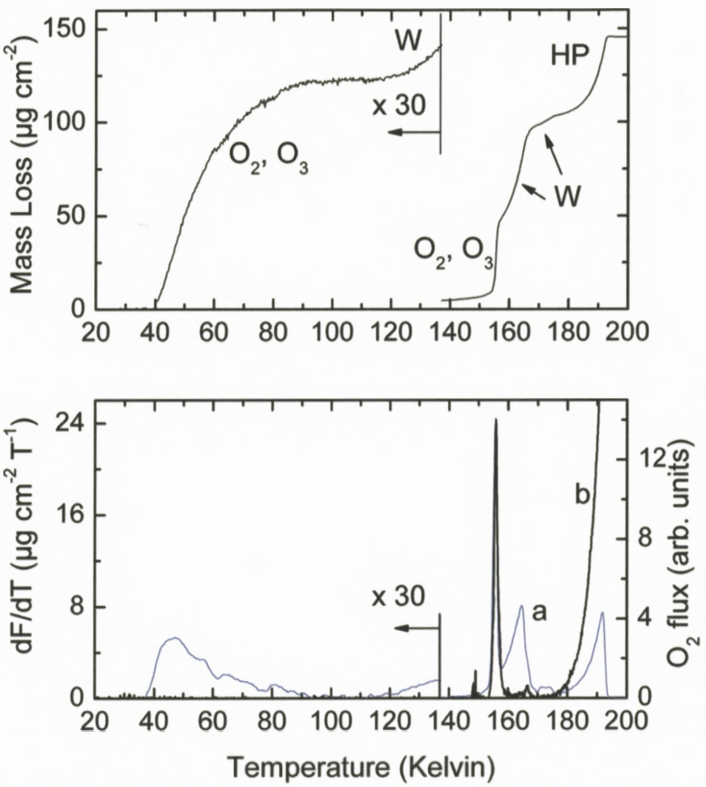

Figure 8. Thermal desorption for an initially solid hydrogen peroxide film irradiated with 50 keV protons at 17 K to a final composition of 69.2% H_2O, 22% O_2, <6.2% H_2O_2 and 2.6% O_3. The amounts of water and hydrogen peroxide include a few percent of the radical OH. Top: Mass loss due to sublimation, measured with a quartz-crystal microbalance. W: water, HP: hydrogen peroxide. Bottom: Mass loss rate *versus* temperature while heating at a constant rate and mass spectrometer reading at mass 32. The large rise in (b) beginning at 180 K is O_2 from H_2O_2 decomposition off the vacuum chamber walls. From Loeffler et al. (2006b).

produced at low temperatures become mobile at ~100–120 K, and react to form stable molecular products such as H_2O_2, O_2, and HO_2. Energetic ions, on the other hand, can produce a high density of radicals in their track, which can recombine immediately. This causes a higher yield of new molecular products as compared with the case of gamma rays or fast electrons. It is very important to stress this differences since one often finds in the literature the erroneous claim that, since fast ions produce many low energy secondary electrons in the solid, fast ion solid interactions can be reproduced using incident 5–100 eV electrons.

3.4.1. *O_2 Synthesis from Water Ice*

Of the molecular products of water ice, oxygen is particularly important because it was detected in its solid form on Ganymede, a satellite of Jupiter. This detection is very perplexing because, at the reported high diurnal temperatures in Ganymede, the vapor pressure of O_2 exceeds the atmospheric pressure by several orders of magnitude. Although it was clear that the oxygen must come from radiolysis of water it is not clear if the pathway occurs in the atmosphere or within the surface ice. The first prediction was that enough O_2 could be generated by ice radiolysis and trapped in the surface ice.

Although O_2 ejection from ice had been demonstrated in sputtering experiments (reviewed by Baragiola et al., 2003), O_2 trapping was found to be orders of magnitude too small to explain the Ganymede observations (Vidal et al., 1997; Bahr et al., 2001). Recent, more elaborate experiments by Teolis et al. (2005) using 100 keV argon ions confirmed the low concentrations of trapped oxygen and shed light on the production mechanism. The authors found a complex dependence of O_2 sputtering on irradiation fluence that is correlated with that of the total sputtering yield. The results suggest that O_2, formed in the projectile track by recombination of radicals, diffuses to the surface where it is trapped and then ejected via sputtering or thermal desorption. Depth profiling by sputtering shows that a high concentration of O_2 can trap in a sub-surface layer during bombardment at 130 K due to the formation of hydrogen and its escape from that region. Although the details of the microscopic processes have not yet been worked out, it is apparent that radiation induced diffusion is important and that hydrogen peroxide, often cited as a precursor for molecular oxygen, is of minor significance (Teolis et al., 2005).

3.4.2. *Ozone Synthesis*

Whenever O_2 is present in a radiation experiment, the synthesis of ozone is expected, but at a very low level. In the case of pure water ice, no ozone was found in decades of experimentation. This presents a problem for the interpretation of the presence of ozone on Saturn's satellites Rhea and Dione (Noll et al., 1997). One could argue for the presence of condensed oxygen from which ions readily synthesize ozone (Baragiola et al., 1999; Famá et al., 2002). However, this would not explain why there is no ozone at Tethys, a satellite of similar size which is in an environment with more oxygen.

A recent development may help to solve the puzzle, the discovery that the amount of radiolytic O_2 trapped can be increased dramatically by co-deposition of water during ion irradiation. The co-deposition simulates the return of sputtered water molecules to the surface of an icy satellite due to gravity or by the effect

of regolith porosity/topography and causes the burial of a high concentration of radiolytic O_2. Teolis et al. (2006) showed that ozone, which cannot be formed from ice under vacuum, can readily be synthesized from the high concentration of buried O_2. The amount of O_3 (and O_2) trapped depends sensitively on the ratio of re-deposition to sputtering fluxes, that should vary with the type of terrain and the flux of magnetospheric ions.

3.4.3. *Synthesis of Hydrogen Peroxide*

The hydrogen peroxide molecule is important because it was identified in the Galilean satellite Europa through the absorption of solar infrared and ultraviolet light. This observation attracted significant attention and led to laboratory studies of H_2O_2 synthesis in ice by energetic protons and heavy ions, using infrared spectroscopy (Moore and Hudson, 2000; Gomis et al., 2004; Loeffler et al., 2006a, 2006c). In addition, Bahr et al. (2001) observed that thermal desorption of ice radiolyzed by 100 keV protons released not only water, as expected, but also HO_2 and H_2O_2 molecules. All these results not only explain the levels of H_2O_2 detected on Europa but the detailed analysis of infrared reflectance also serve to identify the state of the peroxide at the molecular level.

3.4.4. *Other Ices*

The cases described above are relatively simple and, in principle, could be modeled by using what we know of collision physics to obtain the spatial and temportal distribution of species that will then be used as input in chemical kinetics programs. More complicated pathways result from organic ices, and from ice mixtures (Delitsky and Lane, 1998). Significant recent research of ion interactions with ices containing carbon-bearing species includes the papers of Gerakines et al. (2000), Strazzulla and Palumbo (2001), Baratta et al. (2002), Moroz et al. (2004), Hudson et al. (2005), Ruiterkamp et al. (2005) and Brunetto et al. (2006).

4. Was Ion Irradiation Needed for Primordial Life?

Since Louis Pasteur falsified the Aristotelian dictum that life can arise spontaneously from non-living matter, one of the grandest unsolved scientific problems of all times has been: what is the origin of life? (Outside science there are answers to this question that are simple but lack predictive power.)

There are four main connections between ion impacts and life: (1) the possible synthesis of the first complex organic molecules (prebiotic molecules) that were used in the first microorganisms, (2) triggering life (biogenesis), (3) the well known effect of radiation in producing mutations and cell death, (4) the production of molecules that can be the energy source to sustain life.

The famous experiment of Stanly Miller and Harold Urey of half a century ago was aimed at recreating some of the organic compounds that make up life on Earth. They passed a spark discharge through a mixture of hydrogen, methane and ammonia simulated the primordial Earth's atmosphere. After a week of operation of the apparatus they found they produced amino acids: glycine, α-alanine and β-alanine. Subsequent research has shown that amino acids can be synthesized when replacing the spark discharge with well defined ion or photon beams and when using condensed gases.

However, the relevance of the Urey and Miller experiment on life synthesis on Earth is questioned today because these researchers used a strongly reducing mixture of gases for the atmosphere whereas the current understanding is that the early atmosphere was mildly reducing. In addition, the chirality of the artificially produced amino acids is wrong. Life favors left-handed amino acids (they cause polarized light to rotate left), whereas the experiments show that the molecules are racemic: in equal proportion of left-and right-handed polarities.

Alternatively, one can think that the molecules came from outer space in comets or meteorites. This is the theory of exogenesis, supported by circumstantial evidence such as the Murchison meteorite. This object, which fell in Australia in 1969, contained amino acids glycine, alanine and glutamic acid and other unusual types. The chirality was slightly non-racemic, at a few percent level (Pizzarello and Cronin, 2000), a very weak support for the idea that they may be related to extraterrestrial life. Still, how those amino acids were formed is an open question.

More radical is the panspermia conjecture that life is everywhere and comes into Earth from space and is distributed to other worlds from Earth. The support for this idea does not come from evidence but from respect to authority – it has been endorsed by many eminent personalities: Anaxagoras, Alexander von Humboldt, Sven Arrhenius, Fred Hoyle, and Francis Crick. The weakest point of this idea is the frailty of life against atomic collisions. It is extremely unlikely that a microbe can survive the cosmic ray background in the very long travel through interstellar space.

I end this section with reference to an old topic in ion beam science that bears on the question of this section: ion beam polymerization. It can come to the aid of overcoming an obstacle: the huge distance between the amino acids synthesized till today and the complexity of life (not to mention the functionality). The largest synthesized molecules that have been identified contain 12 atoms. In contrast, a small protein contains 100 atoms, and a small cell 10^{10} atoms. Open questions are therefore: What are the conditions for formation of large molecules by ion impact? What is the largest molecule that can be synthesized? The last question arises because ions can on one hand polymerize and on the other hand break up

intra- and intermolecular bonds, as demonstrated in the previous section and in the use of radiation therapy, a topic discussed elsewhere in this volume.

4.1. Energetic Ions as a Source of Biotic Energy

There has been great interest in determining if there is life elsewhere in the solar system. High hopes were placed on Mars, but the Viking spacecraft and further missions produced no evidence of life. Reports on fossilized life forms in Martian meteorites, that made headlines ten years ago, have been largely discredited. New explorations to Mars will, nevertheless, continue. Now the quest is to find evidence below the surface since energetic radiation and an oxidizing environment makes it extremely unlikely that life or remnant molecules would have survived on the surface.

The focus of astrobiologists has shifted in part to the outer solar system. Clues for the existence of an ocean on Europa, a satellite of Jupiter, tens or hundreds of kilometers below the icy crust, stimulated speculation that life might exist there. This brings up the question of the source of energy required for life, at the depths below the surface where photosynthesis is not possible. Chyba (2000) proposed that this energy may be provided by magnetospheric ions striking Europa's surface through radiolytic oxidants such as oxygen, hydrogen peroxide or ozone, would in turn release energy in reactions with hydrocarbon compounds. There has been a surge of laboratory studies in this area, which have served to quantify the radiation chemical products, as discussed above. The next question is the transport of the oxidants kilometers deep to reach the ocean, where they could fuel bacterial life, since the penetration of radiation is limited to depths of typically microns and at most a few centimeters. Such transport mechanism could be sporadic surface cracking and melting of the surface ice, created by tidal stresses, tectonic activity or meteorite impact. However, on Earth, bacteria are found in deep-sea hydrothermal vents, and in rocks kilometers below the surface, possibly fed by hydrogen and oxygen released from water by energetic ions from natural radioactivity. There is recent evidence that bacteria may subsist on an energy input of 2.8×10^{-13} Joules/year (1.8 MeV/year) (Kerr, 2006). Such a situation may exist in underground oceans of Europa, Ganymede, Enceladus, Charon and possible other satellites in the outer solar system. Further progress beyond the speculative stage requires an *in situ* exploration of the surfaces; currently there are exploration missions being planned to Europa and Enceladus.

5. Summary and Outlook

Multiple topics in ion-solid interactions are of relevance to astrophysics. The list includes: Energy deposition, knock-on sputtering (including preferential sputtering and ion emission), electronic sputtering, radiation synthesis of molecules, decomposition of molecules, formation of bubbles and blisters by ion implantation and decomposition of H-bearing compounds, ion implantation and trapping, radiation enhanced diffusion, phase changes (amorphization, crystallization), electron emission and charging. The solids of interest are mostly minerals and condensed gases and the extant knowledge of atomic collisions – mostly on elemental solids – is usually not transferable.

The most promising lines of enquiry to make an impact on astrophysics are: (1) the study of the effect of fast heavy ions, (2) the dependence of sputtering yields of ices on deposited energy, (3) the magnitude of the sputtering yield of small grains, (4) the degree to which large molecules (e.g., organic molecules) can be synthesized and/or destroyed in condensed mixed gases, (5) the conditions necessary for a particular microorganism to survive space travel, (6) synergistic effects, (7) sputtering, amorphization and compositional changes of multi-component solids for light ions; measurements and predictive theories (not just computer simulations), (8) Auger desorption of condensed gases.

Acknowledgements

In concluding, the author would specially like to thank Peter Sigmund for organizing a high-level, stimulating symposium and for his kind invitation and support to attend it. The National Science Foundation supported the preparation of this manuscript through Grant No. 0506565.

References

Bahr D.A., Famá M.A., Vidal R.A. and Baragiola R.A. (2001): Radiolysis of water ice in the outer solar system: sputtering and trapping of radiation products. J Geophys Res E **106**, 33285–33290

Baker D.N. (2002): How to cope with space weather. Science **297**, 1486–1487

Baragiola R.A. (2005): Energetic electronic processes on extraterrestrial surfaces. Nucl Instr Meth Phys Res B **232**, 98–107

Baragiola R.A., Atteberry C.L., Bahr D.A. and Jakas M.M. (1999): Solid-state ozone synthesis by energetic ions. Nucl Instr Meth Phys Res B 157, 233-238

Baragiola R.A., Vidal R.A., Svendsen W., Schou J., Shi M., Bahr D.A. and Atteberry C.L. (2003): Sputtering of water ice. Nucl Instr Meth Phys Res B **209**, 294–303

Baragiola R.A., Loeffler M.J., Raut U., Vidal R.A. and Wilson C.D. (2005): Laboratory studies of radiation effects in water ice in the outer solar system. Rad Phys Chem **72**, 187–191

Baratta G.A., Leto G. and Palumbo M.E. (2002): A comparison of ion irradiation and UV photolysis of CH_4 and CH_3OH. Astron & Astrophys **384**, 343–349

Boogert A.C.A. et al. (2004): Spitzer Space Telescope spectroscopy of ices toward low-mass embedded Protostars. Astrophys J Suppl Ser **154**, 359–362

Bringa E.M. and Johnson R.E. (2004): A new model for cosmic-ray ion erosion of volatiles from grains in the interstellar medium. Astrophys J **603**, 159–164

Brucato J.R., Strazzulla G., Baratta G. and Colangeli L. (2004): Forsterite amorphization by ion irradiation: Monitoring by infrared spectroscopy. Astron & Astrophys **413**, 395–401

Brunetto R., Barucci M.A., Dotto E. and Strazzulla G. (2006): Ion irradiation of frozen methanol, methane, and benzene: Linking to the colors of Centaurs and trans-Neptunian objects. Astrophys J **644**, 646–650

Burnett D.S., Barraclough B.L., Bennett R., Neugebauer M., Oldham L.P., Sasaki C.N., Sevilla D., Smith N., Stansbery E., Sweetnam D. and Wiens R.C. (2003): The Genesis Discovery mission: Return of solar matter to Earth. Space Sci Rev **105**, 509–534

Cassidy T.A. and Johnson R.E. (2005): Monte Carlo model of sputtering and other ejection processes within a regolith. Icarus **176**, 499–507

Chapman C.R. (2004): Space weathering of asteroid surfaces. Ann Rev Earth Planet Sci **32**, 539–567

Chyba C.F. (2000): Energy for microbial life on Europa. Nature **403**, 381–382

Cooper J. F., Johnson R.E., Mauk B.H., Garrett H.B. and Gehrels N. (2001): Energetic ion and electron irradiation of the icy Galilean satellites. Icarus **149**, 133–159

Delitsky M.L. and Lane A.L. (1998): Ice chemistry on the Galilean satellites. J Geophys Res E **103**, 31391–31403

Demyk K., d'Hendecourt L., Leroux H., Jones A.P. and Borg, J. (2004): IR spectroscopic study of olivine, enstatite and diopside irradiated with low energy H^+ and He^+ ions. Astron & Astrophys **420**, 233–243

d'Hendecourt L. and Dartois E. (2001): Interstellar matrices: The chemical composition and evolution of interstellar ices as observed by ISO. Spectrochimica Acta A **57**, 669–684

Dukes C.A., Baragiola R.A. and McFadden L. (1999): Surface modification of olivine by H^+ and He^+ bombardment. J Geophys Res **104**, 1865–1872

Famá M., Bahr D.A., Teolis B.D. and Baragiola R.A. (2002): Ion beam induced chemistry: the case of ozone synthesis and its influence on the sputtering of solid oxygen. Nucl Instr Meth Phys Res **193**, 775–780

Garrett H.B. and Whittlesey A.C. (2000): Spacecraft charging, an update. IEEE Trans Plasma Sci **28**, 2017–2028

Gerakines P.A., Moore M.H. and Hudson R.L. (2000): Carbonic acid production in H_2O: CO_2 ices – UV photolysis vs. proton bombardment. Astron & Astrophys **357**, 793–800

Gomis O., Leto G. and Strazzulla G. (2004): Hydrogen peroxide production by ion irradiation of thin water ice films. Planet Space Sci **52**, 405–410

Hansen G.B. and McCord T.B. (2004): Amorphous and crystalline ice on the Galilean satellites: A balance between thermal and radiolytic processes. J Geophys Res **109**, E01012

Hapke B. (2001): Space weathering from Mercury to the asteroid belt. J Geophys Res **106**, 10039–10073

Hapke B. and Cassidy W. (1978): Is the Moon really as smooth as a billiard ball? Remarks concerning recent models of sputter-fractionation on the lunar surface. Geophys Res Lett **5**, 297–300

Hudson R.L., Moore M.H. and Cook A.M. (2005): IR characterization and radiation chemistry of glycolaldehyde and ethylene glycol ices. Adv. Space Res **36**, 184–189

Johnson R.E. and Baragiola R.A. (1991): Lunar surface: Sputtering and secondary ion mass spectrometry. Geophys Res Lett **18**, 2169–1272

Johnson R.E. and Schou J. (1993): Sputtering of inorganic insulators. Mat Fys Medd Dan Vid Selsk **43**, 403–494

Kerr R.A. (2006): Life slow enough to live on radioactivity (report on Astrobiology Science Conference 2006). Science **312**, 179

Killen R.M., Sarantos M., Potter A.E. and Reiff P. (2004): Source rates and ion recycling rates for Na and K in Mercury's atmosphere. Icarus **171**, 1–19

Jurac S., Johnson R.E., Baragiola R.A. and Sittler E.C. (1995): Charging of ice grains by low-energy plasmas: Application to Saturn's E ring. J Geophys Res **100**, 14821–14832

Loeffler M.J., Teolis B.D. and Baragiola R.A. (2006a): Decomposition of solid amorphous hydrogen peroxide by ion rrradiation. J Chem Phys **124**, 104702

Loeffler M.J., Teolis B.D. and Baragiola R.A. (2006b): A model study of thermal evolution of astrophysical ices. Astrophys J Lett **639**, L103–L106

Loeffler M.J., Raut U., Vidal R.A., Baragiola R.A. and Carlson R.W. (2006c): Synthesis of hydrogen peroxide in water ice by ion irradiation. Icarus **180**, 265–273

Meftah A., Brisard F., Costantini J.M., Dooryhee E., Hage-Ali M., Hervieu M., Stoquert J.P., Studer F. and Toulemonde M. (1994): Track formation in SiO_2 quartz and the thermal-spike mechanism. Phys Rev B **49**, 12457–12463

Messenger G.C. and Ash M. (1997): Single Event Phenomena. Springer, Berlin

Mewaldt R.A., Cohen C.M.S., Labrador A.W., Leske R.A., Mason G.M., Desai M.I., Looper M.D., Mazur J.E., Selesnick R.S. and Haggerty D.K. (2005): Proton, helium, and electron spectra during the large solar particle events of October–November 2003. J. Geophys Res **110**, A09S18

Mitchell C.J., Horányi M., Havnes O. and Porco C.C. (2006): Saturn's spokes: Lost and found. Science **311**, 1587–1589

Moore M.H. and Hudson R.L. (2000): IR detection of H_2O_2 at 80 K in ion-irradiated laboratory ices relevant to Europa. Icarus **145**, 282–288

Moore M.H., Hudson R.L. and Gerakines P.A. (2001): Mid- and far-infrared spectroscopic studies of the influence of temperature, ultraviolet photolysis and ion irradiation on cosmic-type ices. Spectrochimica Acta A **57**, 843–858

Moroz L., Baratta G., Strazzulla G., Starukhina L., Dotto E., Barucci M.A., Arnold G. and Distefano E. (2004): Optical alteration of complex organics induced by ion irradiation: 1. Laboratory experiments suggest unusual space weathering trend. Icarus **170**, 214–228

Noll K.S., Roush T.L., Cruikshank D.P., Johnson R.E. and Pendleton Y.J. (1997): Detection of ozone on Saturn's satellites Rhea and Dione. Nature **388**, 45–47

Pizzarello S. and Cronin J.R. (2000): Non-racemic amino acids in the Murray and Murchison meteorites. Geochimica et Cosmochimica Acta **64**, 329–338

Ruiterkamp R., Peeters Z., Moore M.H., Hudson R.L. and Ehrenfreund P. (2005): A quantitative study of proton irradiation and UV photolysis of benzene in interstellar environments. Astron & Astrophys **440**, 391–402

Schutte W.A. (1996): Formation and evolution of interstellar icy grain mantles. In: Greenberg J.M. (Ed.), The Cosmic Dust Connection, 1. Kluwer, Dordrecht, pp 1–84

Shi M., Baragiola R.A., Grosjean D.E., Johnson, R.E., Jurac S. and Schou J. (1995): Sputtering of water ice surfaces and the production of extended neutral atmospheres. J Geophys Res **100**, 26387–26395

Simpson J.A. (1983): Elemental and isotopic composition of the galactic cosmic rays. Ann Rev Nucl Part Sci **33**, 323–382

Strazzulla G. and Palumbo M.E. (2001): Organics produced by ion irradiation of ices: Some recent results. Adv Space Res **27**, 237–243

Strazzulla G., Baratta G.A. and Palumbo M.E. (2001): Vibrational spectroscopy of ion-irradiated ices. Spectrochimica Acta A **57**, 825–842

Teolis B.D., Vidal R.A., Shi J. and Baragiola R.A. (2005): Mechanisms of O_2 sputtering from water ice by keV ions. Phys Rev B **72**, 245422+8

Teolis B.D., Loeffler M.J., Raut U., Famá M. and Baragiola R.A. (2006): Ozone synthesis on the icy satellites. Astrophys J Lett **644**, L141–L144

Trachenko K. (2004): Understanding resistance to amorphization by radiation damage. J Phys Cond Matter **16**, R1491–R1515

Vidal R.A., Bahr D.A., Baragiola R.A. and Peters M. (1997): Oxygen on Ganymede: Laboratory studies. Science **276**, 1839–1842

Wehner G.K. (1964): Sputtering effects on the lunar surface. In: Salisbury J.W. and Glaser P.E. (Eds), The Lunar Surface Layer. Academic Press, New York, pp 311–322

Weingartner J.C. and Draine B.T. (2001): Electron-ion recombination on grains and polycyclic aromatic hydrocarbons. Astrophys J **563**, 842–852

Hadron Therapy: Radiotherapy Using Fast Ion Beams

Oliver Jäkel*

German Cancer Research Center
Department for Medical Physics in Radiation Oncology
Im Neuenheimer Feld 280, 69120 Heidelberg, Germany

Abstract

Charged particle beams offer an improved dose conformation to the target volume as compared to photon radiotherapy, with better sparing of normal tissue structures close to the target. In addition, beams of ions heavier than helium exhibit a strong increase of the LET in the Bragg peak as compared to the entrance region. These physical and biological properties make ion beams more favorable for radiation therapy of cancer than photon beams. As a consequence particle therapy with protons and heavy ions has gained increasing interest worldwide.

This contribution summarizes the physical and biological principles of charged particle therapy with ion beams and highlights some of the developments in the field of beam delivery and beam monitoring for a scanned ion beam, as well as the principles of treatment planning and the determination of absorbed dose in ion beams. The clinical experience gathered so far with carbon ion therapy is briefly reviewed.

Contents

1 Introduction: Status of Ion Therapy in 2006 **38**

2 Physical Properties of Ion Beams **39**

3 Radiobiological Properties of Ion Beams **41**

* E-mail: o.jaekel@dkfz.de

4 Clinical Results Obtained with Ion Beams **42**

5 Beam Application and Beam Diagnostics **44**

6 Therapy Planning **48**
6.1 Absorbed Dose Calculation 48
6.2 Biologic Modeling 49
6.3 Secondary Neutrons 50
6.4 Empirical Range Calculation 51

7 Dosimetry **52**
7.1 Stopping Power Ratios and Ionization Potential 52
7.2 w-Values for Ions 54
7.3 Perturbation Factors 54

8 Dose Verification **55**

9 Conclusion **55**

References **56**

1. Introduction: Status of Ion Therapy in 2006

In 2004, radiation therapy with hadron beams celebrated its 50th anniversary. The proposal to use heavy charged particles in radiation medicine dates back to 1946, when Dr. Robert R. Wilson, a physicist who had worked on developing particle accelerators, was the first to propose the use of protons for cancer therapy (Wilson, 1946). Less than 10 years later, in 1954 protons were used to treat cancer patients for the first time in Berkeley and in 1957 also helium ions were used at the same facility (Sisterson, 2005). In the 70s, heavier ions, like neon, silicon and argon were introduced for cancer therapy also at the Lawrence Berkeley Laboratory and many encouraging results (esp. in skull base tumors and paraspinal tumors) were achieved (Castro et al., 1994; Castro, 1997).

Today, particle therapy with protons and carbon ions has gained increasing interest. Worldwide, there are about 25 therapy units for treating patients with protons. The majority of the particle therapy centers are located in physics research laboratories, and only a few centers are available in a hospital environment. This situation is currently changing: There are more then 20 centers under construction or in the planning phase which will start to treat patients within the next 5 years (Sisterson, 2005), and nearly all those future installations will be hospital based. Obviously, the time has come that particle therapy is merging into clinics.

The availability of heavy ion RT is currently limited, as worldwide only 3 facilities offer carbon ion RT: two hospital based facilities in Japan (HIMAC/Chiba and HIBMC/Hyogo) and a physics research facility at GSI, Darmstadt in Germany. There is, however, an increasing interest in ion radiotherapy especially in Europe, where new facilities are being built in Germany (Heeg et al., 2004) and Italy (Amaldi, 2004) or are in an advanced planning phase like in Austria, France and Sweden (Sisterson, 2005).

This contribution gives an overview on the physical and biological background and of some of the physics problems connected to the use of heavy charged particles in cancer therapy.

2. Physical Properties of Ion Beams

As the physical and biological properties of proton beams differ significantly from beams of heavier particles, there is a distinction between the two categories "proton-therapy", characterized by low linear energy transfer (LET) and "heavy-ion therapy", with high LET properties.

Charged particles passing through tissue slow down losing energy in atomic interactions. This reduces the energy of the particles, which in turn causes increased energy loss, reaching a maximum at the end of range and causing the maximum dose deposition within the target area. In addition, due to nuclear interactions the number of primary particles is reduced and light fragments are produced. The primary rationale for radiotherapy with heavy charged particles is this sharp increase of dose in a well defined depth (Bragg peak) and the rapid dose fall-off beyond that maximum (Figure 1).

Mono-energetic Bragg peaks are usually not wide enough to cover most treatment volumes. By superimposing a set of beams with decreasing energies and weights, a "Spread out Break Peak" (SOBP) is generated, which delivers the desired dose to the whole treatment volume (Figure 1).

The ratio of Bragg peak dose *versus* dose in the entrance region is larger for heavy ions than for protons. Due to their larger mass, angular and energy straggling becomes negligible for heavy ions as compared to protons. Heavy ions therefore offer an improved dose conformation as compared to photon and proton RT, with better sparing of normal tissue structures close to the target.

The possibility to concentrate the radiation dose to the tumor while sparing the surrounding normal tissue is called dose conformation. The rational for the development of conformal radiation therapy techniques is found in radiobiology. The probability to control the growth of a tumor is increasing with the delivered dose. The same is true, however, for the probability of radiation related side effects

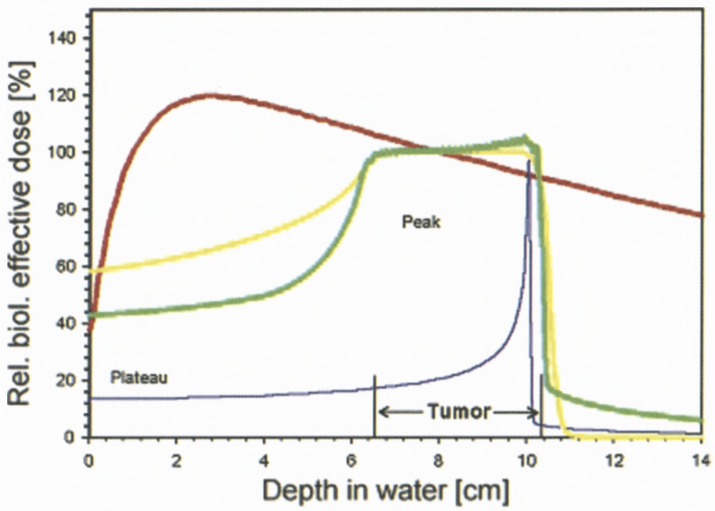

Figure 1. Biologically effective dose, as a function of the penetration depth in water, for high energy photon beams (red line), a mono-energetic carbon ion Bragg peak (blue line) and spread-out Bragg peaks of protons (yellow line) and carbon ions (green line). The given numbers are relative units, normalized to dose at 8 cm depth. For photons the biologically effective dose is equivalent to the absorbed dose, while for protons a constant RBE of 1.1 is assumed. The RBE for carbon was calculated using the track structure model by Scholz (see text).

in normal tissue. In many clinical cases, the dose that can be delivered to a tumor (and hence the tumor control) is limited by the radiation tolerance of the surrounding normal tissue. It has been observed, however, that the radiation tolerance of many organs is increasing if the irradiated volume of that organ is decreased (the so-called dose-volume effect). Consequently, if the irradiated volume of normal tissue can be minimized by conformal radiation therapy, a higher dose can be delivered to the tumor and thus a better outcome can be achieved without increasing the risk of side effects. This effect is the basis of most developments in the field of radiation therapy in the last decades. The highest degree of dose conformation can currently be achieved with proton and ion beams.

Ion beams undergo nuclear fragmentation processes during their passage through tissue. Most energetic fragments are produced in the projectile fragmentation (resulting in a spectrum of proton, helium, lithium, beryllium, boron and carbon ions for a primary carbon beam), while the fragmentation of target nuclei plays only a minor role. Monte Carlo transport simulations show, that when a beam of 290 MeV/u carbon ions penetrates into a depth in water of 15 cm, only about 40% of the primary ions reach the Bragg peak and only about 43% of

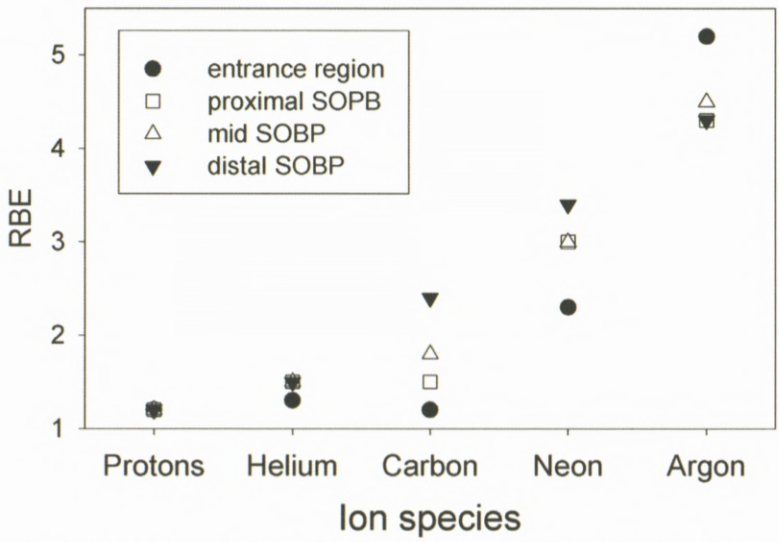

Figure 2. Relative biological effectiveness for crypt cells of mice after irradiation with ions in different positions of the spread-out Bragg peak (SOBP). The modulation depth of the SOBP was 8–10 cm, the initial beam energy was 160, 225, 400, 557 and 570 MeV/u for p, He, C, Ne and Ar ions, respectively. Figure reprinted from Jäkel (2006).

the total beam energy is deposited by carbon ions (Geithner et al., 2006). About 50% of the initial energy is transferred to lighter fragments and neutrons and the remainder is spent into gammas and nuclear binding energies.

The resulting complex radiation spectrum is of importance for the understanding of the biological effects of ion beams, but also to model the response of radiation detectors, like ionization chambers, thermo-luminescence detectors or even radiochromic film response. Modeling of these nuclear fragmentation effects is therefore an important problem in the application of ion beams in cancer therapy.

3. Radiobiological Properties of Ion Beams

In addition to the dose conformation, heavy ions exhibit a strong increase of the linear energy transfer (LET) in the Bragg peak as compared to the entrance region. The radiobiological advantage of high LET radiation in tumor therapy is well known from neutron therapy. Unlike in radiotherapy with neutron beams, in heavy ion radiotherapy the high LET region can be conformed to the tumor. The increasing biological effectiveness of ions with larger charge is shown in Figure 2.

While helium ions are very similar to protons in their biological properties, carbon or neon ions exhibit an increased relative biological effectiveness (RBE) in the Bragg peak as compared to the entrance region (see Figure 2). The RBE ratio (Bragg peak *versus* entrance region) is highest for carbon ions. For ions heavier than neon, the RBE in the entrance region is even higher than in the Bragg peak (like for argon).

Another disadvantage of heavy ions for radiotherapy is the increase of nuclear fragmentation processes, which leads to a fragment tail in the depth dose distribution that extends beyond the Bragg peak (see Figure 1).

The higher biological effectiveness of high LET radiation as compared to low LET radiation can be modeled by so-called track-structure models (Scholz and Kraft, 1994, 1997). According to these models the basic difference of high and low LET radiation, is the high local dose that is deposited close to the primary particle track of a high LET particle. If one assumes that the nonlinear relation between cell survival and dose can be applied also for subvolumes of a cell nucleus (where "lethal events" in the cell nucleus are considered) it becomes clear, that the integral effect for the cell nucleus is dependent on the pattern of the local dose distribution: irradiation of small subvolumes with a high dose is more effective than a homogeneous dose over the whole nucleus (keeping the average dose constant). If assumptions on the local radial dose distributions are made, this can be used to extract the relative biological effectiveness for ions beams from known survival data for cells after low LET irradiation.

It should be noted that besides the larger effect in cell killing, there are some more radiobiological effects, which make heavier ions beneficial for tumor therapy. It is known e.g., that for low LET radiation the survival of cells depends critically on the oxygen saturation of tissue. This is due to the production of oxygen radicals in the cell due to radiation. Many solid tumors, which exhibit hypoxic areas are therefore very resistant to low LET radiation. For high LET radiation, it is known, that the oxygen saturation of tissue plays only a minor role. High LET particles should therefore be especially useful in the treatment of radio-resistant tumors. There is also a smaller variation in the sensitivity of cells in different parts of the cell cycle when using high LET radiation instead of low LET radiation.

4. Clinical Results Obtained with Ion Beams

Since the availability of ion beams is still limited, there is only very little clinical experience with ion beams, especially, when ions heavier than Helium are considered. In 2006 roughly 2500 patients have been treated worldwide with carbon

ions. About 2000 patients were treated at the Japanese heavy ion facility HIMAC, which has been in operation since 1994.

At HIMAC a number of studies are ongoing using ion RT for the treatment of tumors of the head and neck, prostate, lung, liver as well as sarcomas of soft tissue and bone and uterine carcinomas. A report on the clinical results is found in Tsujii et al. (2004).

The fractionation scheme used is generally 16 fractions in 4 weeks for head and neck tumors as well as for sarcomas of bone and soft tissue. It was significantly shortened for lung cancer (9 fractions in 3 weeks) and liver tumors (12 fractions in 3 weeks) and is being further shortened to 4 fractions in 1 week for both indications. The latest results are from dose escalation studies in lung tumors and soft tissue sarcoma.

In two phase I/II trials non-small cell lung cancer (NSCLC), using different fractionation schemes (18 fractions in 6 weeks and 9 fractions in 3 weeks), a dose escalation was performed from 59.4 to 94.5 Gye[1] and from 68.4 to 79.2 Gye, respectively (Miyamoto et al., 2003; Koto, 2004). The resulting overall control rates for the 6- and 3-week fractionation were 64% and 84%, respectively. The total recurrence rate was 23.2%.

For unresectable bone and soft tissue sarcomas, a further phase I/II trial was performed with doses between 52.8 to 73.6 Gye (Kamada et al., 2002), applied in 16 fractions over 4 weeks. The observed overall control rates were 88% and 73% at 1 year and 3 years, respectively.

At GSI, about 300 patients have been treated with carbon ions since 1997. An overview over the results is found in Schulz-Ertner et al. (2004). The majority of patients was treated for skull base tumors. The median dose was 60 Gye (20 fractions each 3 Gye). The 3-year overall local control rate was 91%. The observed side effects were only very moderate (Schulz-Ertner et al., 2002).

Figure 3 shows an example of a treatment plan for patient with a chondrosarcoma close to the brain stem treated with carbon ions at GSI. The excellent dose conformation of the 90% isodose to the target is clearly demonstrated, although only two horizontal treatment fields were used here. The dose sparing of the relevant organs at risk can also be seen in the dose distribution.

Another group of patients was treated at GSI for a malignant salivary gland tumor (adenoid cystic carcinoma) using a combination of photon therapy and a carbon ion boost. The carbon therapy is given only to the macroscopic tumor residual (dose 18 Gye), while the photon dose is given to a much larger volume.

An analysis showed an actuarial local control rate of 62% at 3 years can be achieved, while in patients treated with photons alone, only 25% control rate could

[1] Gye stands for "Gray equivalent" and is commonly used to specify biologically effective dose.

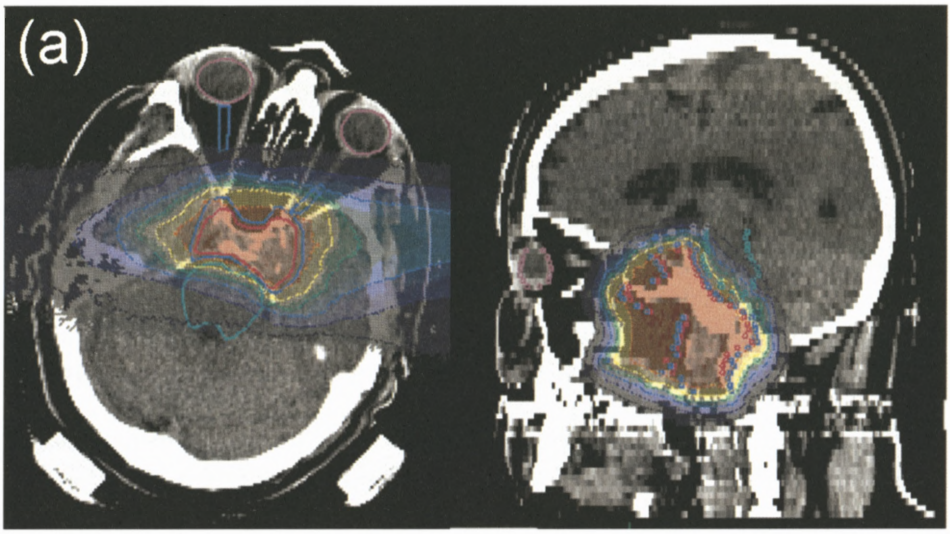

Figure 3. Example of a treatment plan for fully fractionated radiotherapy using 2 nearly opposing fields of carbon ions. The dose distribution at isodoses of 10%, 30%, 50%, 70% and 90% of the total dose (60 Gye) is shown, respectively. The colored lines indicate the primary and secondary target volume (red, blue), the brain stem (green line), optical nerves (blue) and eyes (pink), respectively.

be achieved (Schulz-Ertner et al., 2003). Again, severe side effects were observed only in few patients.

5. Beam Application and Beam Diagnostics

There exist two principal methods to shape the beam and thus to tailor the dose to the target volume, which will be described in the next section.

Passive beam delivery techniques (Figure 4a) use double-scattering systems or wobbling-magnets in combination with scatterers to produce large particle fields (Kanai, 1999). The particle field is then confined to the tumor cross-section by individually manufactured collimators or multi-leaf-collimators. To generate the SOBP, a rotating modulator wheel is inserted into the beam. This device introduces periodically material of varying thickness into the beam which results in a periodical modulation of the range. Alternatively, a static filter of varying thickness may be applied. This so-called ridge-filter uses lateral scattering to produce a homogeneous range modulation over the lateral extension of the treatment field. Each modulator-wheel or ridge filter is connected to a specific SOBP and is selected according to the extension of the tumor in depth. To adjust the SOBP to the distal edge of the tumor, range shifters are used. Finally, compensators

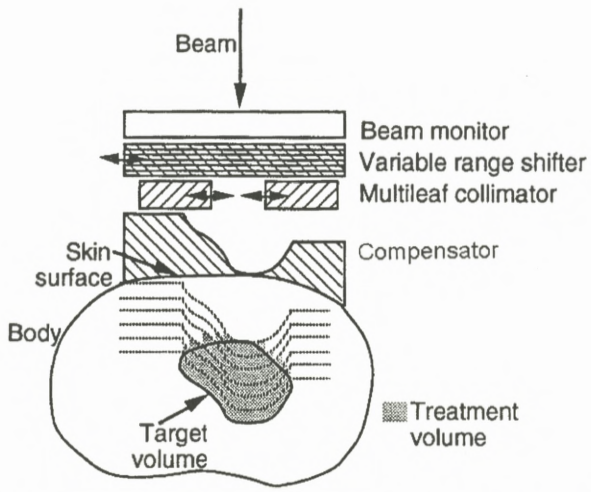

Figure 4a. Principle of the passive dose delivery. Shown is the incoming broadened beam that is modulated in depth. The range shifter shifts the SOBP to the desired depth, while collimator and compensator are patient specific devices. The lines in the body represent the distal dose fall-off that can be shifted in depth with the range shifter. Figure reproduced from Jäkel (2006).

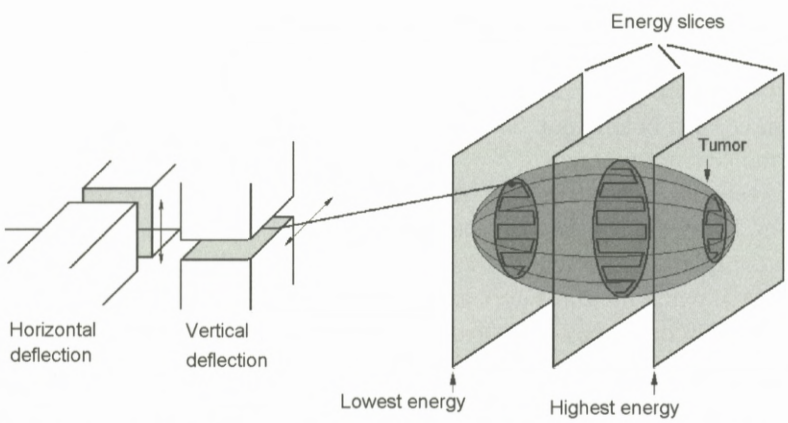

Figure 4b. Principle of an active beam delivery: a mono-energetic pencil beam is scanned over the tumour cross section. After one slice is irradiated the energy of the beam extracted from the synchrotron can be switched to the next energy.

manufactured for the individual field of each patient can be used to adjust the dose distribution to the distal edge of the tumor. As the extension of the SOBP remains constant over the tumor cross-section, the dose conformation at the distal edge is connected to high doses in the normal tissue at the proximal edge of the tumor (Figure 4a).

Another way of beam delivery is called active beam shaping (Haberer et al., 1993). This system takes advantage of the electric charge of the particles, in order to produce a tightly focused pencil beam that is then deflected laterally by two magnetic dipoles to allow a scanning of the beam over the treatment field. When the beam is produced with a synchrotron, the energy can be switched from pulse to pulse in order to adapt the range of the particles in tissue. This way, a target volume can be scanned in three dimensions and the dose distribution can be tailored to any irregular shape without any passive absorbers or patient specific devices, like compensators or collimators. Therefore, the high dose region can also be conformed to the proximal end of the target volume and the integral dose as well as the non-target volume receiving high LET radiation is minimized. Figure 4b shows the principle of the active beam delivery system.

There is only one facility (GSI) where beam scanning for carbon ions is already applied clinically. The GSI beam delivery system allows for a 3D scanning of arbitrarily shaped volumes with a spatial resolution of 1mm in all three directions. Typically, a beam width of 3–10 mm full-width half-maximum is scanned over a regular grid of points with typically 2–3 mm spacing. The accelerator energy can be switched from pulse to pulse and the energy can be selected from a library of 252 accelerator energies.

An essential prerequisite for such a beam scanning system is a suitable beam diagnostic system that is capable of monitoring the exact position and intensity of the beam at each beam spot. The monitoring system is connected via a feedback loop to the scanner magnets.

The system designed at GSI, relies on three large area ionization chambers (18 cm by 18 cm size of the active area) for the intensity measurement. Two chambers are completely identical in their design and readout, (using a chamber gas of Argon:CO_2), while the third uses a different electronic system (and air filling), in order to have redundancy and diversity built into the system. The resolution of the chambers in terms of particle number is around 1000 particles per sampling interval (which reflects an accuracy of about 1% in dose). The sampling interval is around 12 μs, in order to allow for a number of measurements at each beam position.

The intensity monitors are calibrated in terms of particle number and are used to switch the beam via the feedback loop to the next scan point if a predefined par-

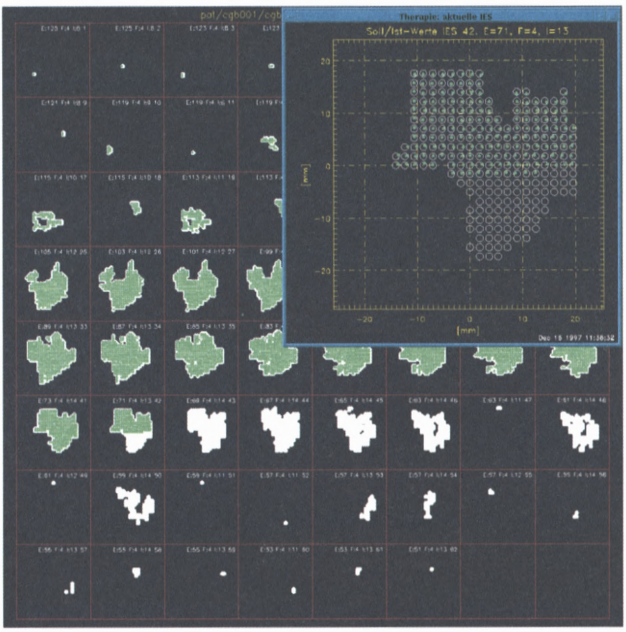

Figure 5. Screenshot of the therapy online monitor (TOM) developed at GSI. It displays the measured data on the actual position of the beam and indicates if the correct particle number was delivered by varying colors. The data from the monitoring system are displayed nearly in real-time.

ticle number for a given scan point has been reached. The chambers are operated at a high voltage which yields a charge collection efficiency of 99.5%.

For detection of the beam position, two additional large area multi wire proportional chambers are installed. They are made up of two wire planes with 112 wires with a spacing of 2 mm. This allows a determination of the beam position with a spatial resolution of better than 0.5 mm at a sampling interval of 150 μs. The position data are again fed back to the scanning magnets, so that any deviation of the measured from the desired beam position is immediately corrected for at the next scan point.

The time resolution of the monitoring system is designed such that it is still capable of monitoring even the large variations of intensity during the extraction cycle of the synchrotron and delivering a well defined particle number to each scan spot. It also allows for a rapid beam shut off within less than 200 ms in case of any interlock from the control system. Moreover, the total water equivalent thickness of all five chambers in the monitoring system is only about 0.7 mm.

The data of the monitoring system are also displayed in real-time on a screen, to allow a visualization of the ongoing treatment. A screenshot of this therapy online monitor is shown in Figure 5.

6. Therapy Planning

For the active beam shaping system at GSI, a research therapy planning system (TPS) was developed (Krämer et al., 2000; Jäkel et al., 2001), which fulfills the needs of the beam scanning system at GSI. While a modulator for passive beam shaping is designed to achieve a prescribed homogeneous biologically effective dose for a single field. A 3D scanning system can produce nearly arbitrary shapes of the spread out Bragg peak (SOBP). The shape of the SOBP therefore has to be optimized separately for every scan point in the irradiation field. The introduction of a 3D scanning system thus has some important consequences for the TPS:

- The beam intensity of every scan point at each energy has to be optimized separately to obtain a homogeneous biological effect.
- As the system is able to apply any complicated inhomogeneous dose distribution, the capability for intensity modulated radiotherapy with ions should be taken into account.
- All fields of a treatment plan are applied at the same day to avoid uncertainties in the resulting dose due to setup errors.
- The dose per fraction should be variable for every patient.
- The scanner control data (energy, beam position, particle number at every beam spot) have to be optimized for each field of every patient.
- An RBE model has to be implemented, that allows the calculation of a local RBE at every point in the patient depending on the spectrum of particles at this point.

6.1. Absorbed Dose Calculation

The dose calculation for active beam shaping systems relies on measured data for the depth dose curves. Instead of the measured depth dose data for the SOBPs resulting from the modulators, data for the single energies are needed. If the applied dose is variable, it is necessary to base the calculation of absorbed dose on absolute particle numbers rather than on relative values. For the calculation of absorbed dose, the integral data including all fragments are sufficient.

Before the actual dose calculation starts, the target volume is divided into slices of equal radiological depth. (Here the same empirical methods of range

calculation as for passive systems are used.) Each slice then corresponds to the range of ions at a certain energy of the accelerator. The scan positions of the raster scanner are then defined as a quadratic grid for each energy. In the last step, the particle number at each scan point is optimized iteratively until a predefined dose at each point is reached.

6.2. Biologic Modeling

To fulfill the demands of an active beam delivery on the TPS concerning the biological effectiveness, a more sophisticated biological model is needed. Such a model was developed e.g. at GSI (Scholz and Kraft, 1994, 1996; Scholz et al., 1997). Its main idea is to transfer known cell survival data for photons to ions, assuming that the difference in biological efficiency arises only from a different pattern of local dose deposition along the primary beam. It is therefore also called the local effect model (LEM).

The model takes into account the different energy deposition patterns of different ions and is thus able to model the biological effect resulting from these ions. An important prerequisite for this is, however, the detailed knowledge of the number of fragments produced as well as their energy spectrum. The calculated RBE shows a dependence on the dose level and cell type, if the underlying photon survival data for this respective cell type are known.

Another important prerequisite for the LEM model is the knowledge on the particle track structure, i.e. the radial dose distribution around the ion track, as a function of the particle charge and energy.

The LEM allows the optimization of a prescribed biologically effective dose within the target volume (Krämer et al., 2000) using the same iterative optimization algorithm as for the absorbed dose. At each iteration step, however, the RBE has to be calculated anew, as it is dependent on the particle number (or dose level). Since this includes the knowledge of the complete spectrum of fragments, the optimization is rather time consuming. Again, it has to be pointed out, that the dose dependence of the RBE demands the use of absolute dose values during optimization.

In Figure 6, the absorbed and biologically effective dose as a function of depth along the central axis in a typical treatment field for a base of skull tumor is shown. In order to achieve a homogeneous biological effect in the tumor, an optimization of the physical dose distribution (as shown in the right image) is necessary.

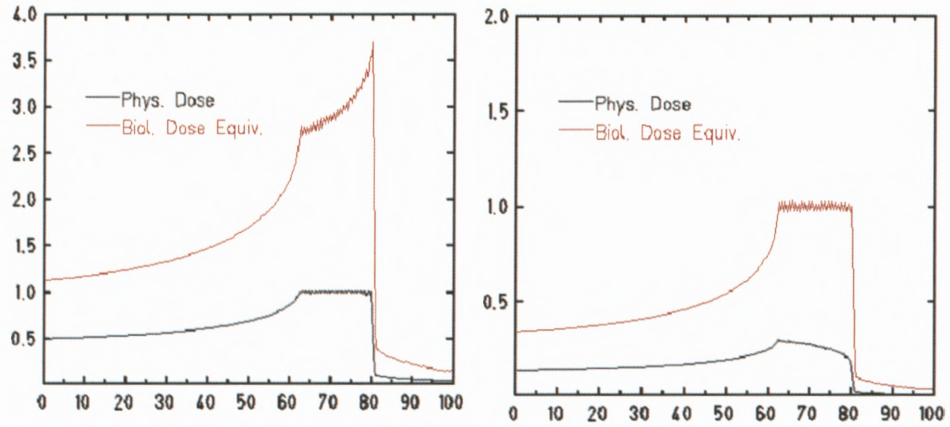

Figure 6. Absorbed and biologically effective dose resulting from a homogeneous absorbed dose (left) and from a direct optimization of a homogeneous biologically effective dose (right). Doses are given in Gy (or Gye) and depths in mm, respectively.

6.3. Secondary Neutrons

An open question arising from the nuclear fragmentation of ions is the detrimental effect of secondary neutrons. Although a number of calculations (Pshenichnov et al., 2005) and measurements (Gunzert-Marx et al., 2004) of the number of secondary neutrons produced during irradiation with carbon ions exist, it is difficult to accurately determine the effective equivalent dose due to these neutrons. This is due to a lack of knowledge on the kerma factors for the high energy secondary neutrons (neutrons up to twice the primary energy of the carbon ions are observed, i.e. up to 500 MeV neutrons for a beam of 250 MeV/μ carbon ions). It has been estimated that the dose due to secondary neutrons is less than 1% of the absorbed dose of the primary ions. The resulting risk of late effects resulting from this neutron dose is very difficult to determine. Two things should, however, clearly be noted. First, the neutrons produced are predominantly produced in forward direction, and are thus leading to irradiation of a relatively small part of the body. The biological effects will depend strongly on the direction of the beam and the type of tissues involved in that location. Second, it has been shown, that the use of an active beam delivery system leads to a production rate of neutrons, which is much lower than for a passive system (Schneider et al., 2002).

6.4. Empirical Range Calculation

In treatment planning, the selection of beam energies and the determination of ion ranges are crucial for the calculation of the delivered dose. The synchrotrons used to produce the ion beams, usually provide a very well defined and reproducible beam energy. Precision measurements of the ionization in water are used to determine the exact position and form of the Bragg curve. The accuracy of measured ion ranges in water, which can be achieved with such measurements, is better than 0.1 mm (Jäkel et al., 2001). Range calculations in tissue are then based on X-ray CT images and make use of the dependence of both, X-ray attenuation and stopping powers from the electron density. There is, however, no clear functional relation between the ion ranges and (polychromatic) X-ray attenuation since there are second order effects depending on other tissue specific quantities (the logarithmic dependence of the stopping power in the ionization potential and the strong Z-dependence of the photo-effect).

Therefore, in charged particle therapy purely empirical relations between the relative photon attenuation coefficients (called the Hounsfield units, or HU[2]) and ion ranges are used. These relations are established for phantom materials or samples of real tissues. The accuracy of the range calculation in tissue is influenced strongly by the accuracy of HU numbers. Therefore an imaging protocol for each CT scanner and treatment site has to be defined that specifies all parameters that may influence the value of the HU.

Furthermore, there are a number of effects that may disturb the quality of Hounsfield units (e.g. a contrast agent which is often used may influence the range calculation in the patient). Another unavoidable problem arises from metal artifacts. These artifacts play a role especially for tumors in the head and pelvic region, stemming from gold fillings in teeth or hip prostheses, respectively.

The described range calculation for heavy charged particles based on CT images is one of major uncertainties in ion beam therapy. Using a well defined imaging protocol for each scanner and treated anatomical site the uncertainty in the range calculation for carbon ions can be reduced to about 2–3 mm for the head and neck region. In the presence of artifacts uncertainties up to 10 mm can be observed.

---

[2] Given the linear absorption coefficients of a material μ and μ_W for water, the HU value is defined as $HU = 1000 \cdot (\mu - \mu_W)/\mu_W$.

7. Dosimetry

The determination of absorbed dose to water in all operating ion facilities is currently based on ionization chamber dosimetry (Kanai et al., 1999; Hartmann et al., 1999). For this purpose, commercial ionization chambers (mainly thimble type chambers) are used which are calibrated by the manufacturer in a field of Co-60 in terms of absorbed dose to water. Initially at HIMAC chambers calibrated in terms of air kerma were used, but the transition to water absorbed dose was performed recently.

This procedure is recommended also in the latest Code of Practice of the International Atomic Energy Agency, the technical report series TRS-398, which is currently the only international guideline for clinical dosimetry of ion beams (IAEA, 2000).

According to TRS-398, the absorbed dose to water at an effective point of measurement, P_{eff}, of the chamber in an ion beam is determined by:

$$D_{\text{w}}(P_{\text{eff}}) = M_{\text{corr}}\, N_{D,\text{w,Co60}}\, k_Q. \tag{1}$$

where M_{corr} is the dosimeter reading M, corrected for changes in air density, incomplete saturation, and polarity effects of the chamber. The calibration factor, N_D, w, Co60, is given by the manufacturer and k_Q is a chamber specific factor that corrects for the different beam quality of ^{12}C ions and the calibration beam quality (^{60}Co).

In TRS 398 it is suggested, that the k_Q factor is calculated theoretically as:

$$k_Q = \frac{(w_{\text{air}}/e)^{\text{C12}}}{(w_{\text{air}}/e)^{\text{Co60}}}\, \frac{\bar{s}^{\text{C12}}_{\text{w,air}}}{(\bar{L}/\rho)^{\text{Co60}}_{\text{w,air}}}\, \frac{p^{\text{C12}}}{p^{\text{Co60}}}, \tag{2}$$

which is a product of the ratios of the w values,[3] the stopping power ratios of water to air and the chamber specific perturbation factors for ^{12}C and ^{60}Co, respectively. The overall uncertainty of this determination of absorbed dose is stated to be about 3%. These three terms will be discussed briefly in the following.

7.1. Stopping Power Ratios and Ionization Potential

The calculation of the stopping power ratio has to take into account not only the fluence of primary carbon ions but also the fragments that arise from nuclear interactions and also their energy distribution. The value $s_{\text{w,air}}$ for for light ion beams in TRS-398 can be obtained as a fluence-weighted average ratio of stopping

[3] w is the mean energy required to create an electron-ion pair by a charged particle in a gas.

powers (henceforth referred to as "stopping-power ratio", not to be confused with a direct ratio of stopping powers) over the complete spectrum of primary particles and secondary particles at the reference depth:

$$s_{\mathrm{w,air}} = \frac{\sum_i \int_0^\infty \Phi_{E,i} \cdot (S_i(E)/\rho)_{\mathrm{w}} \, \mathrm{d}E}{\sum_i \int_0^\infty \Phi_{E,i} \cdot (S_i(E)/\rho)_{\mathrm{air}} \, \mathrm{d}E} \,. \tag{3}$$

Here, $(S_i(E)/\rho)$ is the mass stopping power for a particle i with energy E in water or air and $\Phi_{E,i}$ is the particle fluence differential in energy, in water for particles of type i. This method is, however, only practical if the particle fluence is well known.

In an analysis done by Hartmann et al. (1999) it was found that for energies above 10 MeV/μ the ratio of stopping powers for various light ions varies only little, and that an average constant value can be used with an uncertainty of about 2%. As a practical approach in clinical dosimetry, TRS-398 proposed to use a fixed value of 1.130.

In a recent investigation (Geithner et al., 2006), a Monte Carlo simulation of the nuclear fragmentation processes was used to analyze the dependence of the fluence averaged stopping power ratio (similar to Equation 3) on the beam energy and penetration depth. Two findings have been observed: first, the relative variation of $s_{\mathrm{w,air}}$ for various energies and depths is below 1%, except for a small region around the Bragg peak, where a maximum deviation of 4% was found. Secondly, it was found that the absolute values at high energies obtained with stopping power data from the new ICRU-73 were about 1% higher than the value recommended by TRS-398.

The reason for this discrepancy is probably a difference in the ionization potential used for various stopping power calculations. In the evaluation of the TRS-398, the ICRU-49 for proton and alpha particles and calculations by Salamon (1980) played an important role. Both data sets used I-values for water between 75 eV (ICRU 49) and 79 eV (Salamon). In the new ICRU 73, an I-value for water of 67 eV is used, which gives rise to the higher stopping power ratios. It should be noted, that a change in the I-value of 2 eV leads to a shift of the ion ranges in the order of 1 mm (Gudowska et al., 2004; Krämer et al., 2000). Therefore, a consistent analysis of stopping power data and precision range measurements would be highly desirable in order to improve the uncertainty of the dosimetry for ion beams.

7.2. W-Values for Ions

The mean energy required to produce an ion pair in air (w_{air}) is another crucial quantity in the determination of the quality correction factor. Precise measurements of the w-value are, however, difficult to perform and consequently on little experimental data for protons and ions exist (Jones, 2006; IAEA, 2000). Since the w-value again depends on the ion type and energy, in principle the same fluence averaging can be used as for the stopping power ratio (see Equation 3). Since no detailed data on the w-value for ion beams at various energies are available, TRS-398 again proposed to use a single fixed value of 34.5 eV. The uncertainty of this value was determined again from a weighting of the various sources and amounts to 1.5%. It is the second largest source of uncertainty in the dose determination for ion beams.

It is common sense that a more accurate w-value can be obtained by dosimetric measurements using an independent method, namely the water calorimetry. This method is commonly established as the primary standard for absorbed dose to water in many countries and needs only few, small corrections even for ion beams. A comparison of calorimetry with ionometry therefore might result in an indirect determination of the w-value for ion beams.

7.3. Perturbation Factors

The perturbation factor, P, for the different beam qualities includes all departures from ideal Bragg–Gray detectors, which are essentially connected to the equilibrium of secondary electrons. These are the correction for cavity effects, the displacement factor, and the effects from the chamber wall and central electrode. There are currently no data on these correction factors, which are chamber specific, in ion beams. The corresponding correction factors in photon beams are already very small. Since the secondary electrons produced in a carbon ion beam have an average energy which is lower than in the case of photon beam, the corrections are expected to be even smaller than for photons (for proton beams some estimates for the corrections exist, but the general situation is similar).

Consequently, the perturbation factors for a standard chamber in a ^{12}C ion beam, was set to unity, since no data exist that indicate a significant deviation from unity. The uncertainty of the perturbation factors in the determination of absorbed dose is stated to be 1%.

8. Dose Verification

The verification of the dose delivered to a patient by a certain treatment plan is one of the crucial points of any quality assurance system in radiotherapy. For a dynamic dose delivery, like the 3D raster scanning system, this procedure is even more important, since the dose delivery may be correct at one point in the treatment field, but deviations may appear at another point. Therefore, the dose has to be verified simultaneously at many points in the field. Such a method was introduced at the GSI, using a set of 24 small volume ionization chambers connected to a motor-driven phantom (Karger et al., 1999). It allows an efficient check of the absorbed dose in the treatment field at many points and furthermore the direct comparison with the treatment planning dose at these points. There are currently a number of ongoing developments in order to develop integrated systems with much more channels of independent ionization chambers. The aim is to get a three-dimensional sample of measured dose data in a single measurement for a certain treatment field.

At the Japanese facility HIMAC, a system was introduced (Mizota et al., 2002), that uses a 64 channel multi-layer ionization chamber with a 3×3 m^2 sensing area to measure depth dose distributions. Using the corresponding radiological depths, the dose values are transformed to the respective point in treatment planning CT. The dose distribution is then measured by sweeping the chamber through the field and reconstructing the dose on the CT-image. This procedure is certainly extremely useful for a static treatment field. For a dynamic beam application, it is not possible to move the chamber during beam application and comparable solutions have yet to be developed.

9. Conclusion

In the last decade, in 30 centers worldwide valuable clinical experience has been gained in charged particle therapy. Together with the development of new technologies especially for beam application and treatment planning there will certainly be a broader implementation of ions in clinical settings that allow for an optimal exploitation of the physical and biological potential of protons and heavy ions.

In order to allow for a successful clinical application of ion beams, a number of open questions in the field of medical physics have to be addressed. Among these are the improvements of the existing dosimetry protocols, which still lack the degree of accuracy which is current standard in conventional therapy with photon beams. Important aspects here are especially connected to the description

of the nuclear fragmentation of the heavy ions, the stopping power ratios for water to air as well as the w-values for air. Also the recommendations for I-values may have to be reconsidered in view of their importance for the stopping power and range calculations.

Another important area of physics research for particle therapy is the development of radiation detectors, which either serve as beam monitors or are used for dosimetric purposes.

References

Amaldi U. (2004): CNAO – The Italian Centre for Light-Ion Therapy. Radiother Oncol **73 Suppl 2**, S191–S201

Castro J.R., Linstadt D.E., Bahary J.-P. et al. (1994): Experience in charged particle irradiation of tumors of the skull base 1977–1992. Int J Radiat Oncol Biol Phys **29**, 647–655

Castro J.R. (1997): Clinical programs: A review of past and existing hadron protocols. In: Amaldi U., Larrson B. and Lemoigne Y. (Eds), Advances in Hadron Therapy. Elsevier Science, Amsterdam, Netherlands, pp 79–94

Geithner O., Andreo P., Sobolevsky N., Hartmann G. and Jäkel O. (2006): Calculation of stopping power ratios for carbon ion dosimetry. Phys Med Biol **51**, 2279–2292

Gudowska I., Sobolevsky N., Andreo P., Belki D. and Brahme A. (2004): Ion beam transport in tissue-like media using the Monte Carlo code SHIELD-HIT. Phys Med Biol **49**, 1933–1958

Gunzert-Marx K., Schardt D. and Simon R.S. (2004): Fast Neutrons produced by nuclear fragmentation in treatment irradiations with C12 beam. Rad Prot Dos **110, nos 1–4**, 595–600

Haberer T., Becher W., Schardt D. and Kraft G. (1993): Magnetic scanning system for heavy ion therapy. Nucl Instrum Meth A **330**, 296–305

Hartmann G.H., Jäkel O., Heeg P., Karger C.P. and Krießbach A. (1999): Determination of water absorbed dose in a carbon ion beam using thimble ionization chambers. Phys Med Biol **44**, 1193–1206

Heeg P., Eickhoff H. and Haberer T. (2004): Conception of heavy ion beam therapy at Heidelberg University (HICAT). Z Med Phys **14**, 17–24

International Atomic Energy Agency (IAEA) (Ed.) (2000): Absorbed Dose Determination in External Beam Radiotherapy. Technical Report Series No. 398, Vienna

Jäkel O. (2006): Heavy ion radiotherapy. In: Schlegel W., Bortfeld T. and Grosu A.L. (Eds), New Technologies in Radiation Oncology. Springer, Heidelberg, pp 365–378

Jäkel O., Jacob C., Schardt D., Karger C.P. and Hartmann G.H. (2001a): Relation between carbon ions ranges and X-ray CT numbers. Med Phys **28, no. 4**, 701–703

Jäkel O., Krämer M., Karger C.P. and Debus J. (2001b): Treatment planning for heavy ion radiotherapy: Clinical implementation and application. Phys Med Biol **46**, 1101–1116

Jones D. (2006): The w-value in air for proton therapy beams. Radiat Phys Chem **75**, 541–550

Kamada T., Tsujii H., Tsuji H., et al. (2002): Efficacy and safety of carbon ion radiotherapy in bone and soft tissue sarcomas. J Clin Oncol **20**, 4466–4471

Kanai T., Endo M., Minohara S., et al. (1999): Biophysical characteristics of HIMAC clinical irradiation system for heavy-ion radiation therapy. Int J Radiat Oncol Biol Phys **44**, 201–210

Karger C.P., Jäkel O., Hartmann G.H. and Heeg P. (1999): A system for three-dimensional dosimetric verification of treatment plans in intensity-modulated radiotherapy with heavy ions. Med Phys **26**: 2125–2132

Koto M., Miyamoto T., Yamamoto N., et al. (2004): Local control and recurrence of stage I non-small cell lung cancer after carbon ion radiotherapy. Radiother Oncol **71**, 147–156

Krämer M., Jäkel O., Haberer T., Kraft G., Schardt D. and Weber U. (2000): Treatment planning for heavy ion radiotherapy: Physical beam model and dose optimization. Phys Med Biol **45**, 3299–3317

Miyamoto T., Yamamoto N., Nishimura H., et al. (2003): Carbon ion radiotherapy for stage I non-small cell lung cancer. Radiother Oncol **66**, 127–140

Mizota M., Kanai T., Yusa K., et al (2002): Recontruction of biologically equivalent dose distribution on CT-image from measured physical dose distribution of therapeutic beam in water. Phys Med Biol **47**, 935–945

Pshenichnov I., Mishustin I. and Greiner W. (2005): Neutrons from fragmentation of light nuclei in tissue-like media: A study with the GEANT4 toolkit. Phys Med Biol **50**, 5493–5507

Salamon M.H. (1980): A range-energy program for relativistic heavy ions in the region $1 < E < 3000$ MeV/amu. LBL Report 10446, LBL, Berkeley

Schneider U., Agosteo S., Pedroni E. and Besserer J. (2002): Secondary neutron dose during proton therapy using spot scanning. J Rad Oncol Biol Phys **53**, 244–251

Scholz M. and Kraft G. (1994): Calculation of heavy ion inactivation probabilities based on track struckture, X-ray sensitivity and target size. *Radiat Prot Dosim* **52**, 29–33

Scholz M. and Kraft G. (1996): Track structure and the calculation of biological effects of heavy charged particles. Adv Space Res **18**, 5–14

Scholz M., Kellerer A.M., Kraft-Weyrather W. and Kraft G. (1997): Computation of cell survival in heavy ion beams for therapy – The model and its approximation. Rad Environ Biophys **36**, 59–66

Schulz-Ertner D., Haberer T., Scholz M., et al. (2002): Acute radiation-induced toxicity of heavy ion radiotherapy delivered with intensity modulated pencil beam scanning in patients with base of skull tumors. Radiother Oncol **64**, 189–195

Schulz-Ertner D., Didinger B., Nikoghosyan A., et al. (2003): Optimization of radiation therapy for locally advanced adenoid cystic carcinomas with infiltration of the skull base using photon intensity modulated radiation therapy (IMRT) and a carbon ion boost. Strahlenther Onkol **179**, 345–351

Schulz-Ertner D., Nikoghosyan A., Thilmann C., et al. (2004): Results of carbon ion radiotherapy in 152 patients. Int J Radiat Oncol Biol Phys **58**, 631–640

Sisterson J. (Ed.) (2005): Particle Newsletter 36, Harvard

Tsujii H., Mizoe J.E., Kamada T. et al. (2004): Overview of clinical experiences on carbon ion radiotherapy at NIRS. Radiother Oncol **73 Suppl 2**, S41–S49

Wilson R.R. (1946): Radiological use of fast protons. Radiology **47**, 487–491

Spatial Distribution of DNA Double-Strand Breaks from Ion Tracks

A. Hauptner[1], W. Friedland[2], S. Dietzel[3], G.A. Drexler[4], C. Greubel[5], V. Hable[5], H. Strickfaden[3], T. Cremer[3], A.A. Friedl[4], R. Krücken[1], H.G. Paretzke[2] and G. Dollinger[5,*]

[1]Physik Department E12, TU-München
D-85748 Garching, Germany
[2]Institut für Strahlenschutz, GSF
D-85764 Neuherberg, Germany
[3]Department Biologie II, LMU-München
D-82152 Martinsried, Germany
[4]Strahlenbiologisches Institut, LMU-München
D-80336 München, Germany
[5]Angewandte Physik und Messtechnik, LRT2, UniBw-München
D-85577 Neubiberg, Germany

Abstract

Theoretical and experimental approaches are developed to investigate the spatial distribution of DNA damage induced by energetic ions in cell nuclei, with a special emphasis on DNA double-strand breaks (DSB). Using a phenomenological description for the relationship between energy dose and DSB induction, the total number of DSBs and their average number per unit pathlength can be calculated analytically for single ion tracks in cell nuclei. A simple approach to microscopic DNA damage description is offered by analytical representations which give the average energy dose in dependence of the radial distance from the ion track. However, the extreme fluctuations in the DNA damage per volume, which is due to the inhomogeneous ionisation events of the individual secondary electron paths and the structure of chromatin in the nucleus, make a true follow-up of the ionisation and excitation events desirable, e.g. by using Monte Carlo methods. The visualisation of DSBs

* E-mail: guenther.dollinger@unibw.de

by staining proteins which accumulate in large amounts at DSB repair sites, thus forming so-called foci, allows to analyse the spatial distribution of DSB sites under the fluorescence microscope. With this method, generally a much lower number of DSB sites along an ion track is observed than expected on basis of calculations. This observation hints at insufficient consideration of gross structures in the organisation of nuclear DNA or at a fast clustering of DSBs, possibly to form repair factories.

Contents

1 Introduction **60**

2 Experimental Techniques **62**
2.1 Microirradiation of Cells by a High Energy Ion Microprobe 62
2.2 Optical Detection of DSB Sites in Cell Nuclei Using Immunofluorescence Technique 65

3 Microscopic DSB Distribution **65**
3.1 General Considerations 65
3.2 Radial Distributions of Energy Dose and DSBs 71
3.3 Influence of Chromatin Structure on DSB Distribution 74
3.4 Longitudinal DSB Distributions 77

4 Future Prospects **80**

Acknowledgements **83**

References **83**

1. Introduction

Double-strand breaks (DSBs) in the DNA are a major threat for each living cell since they affect the genome integrity. Ionising radiation is known to be one of the main elicitors of DSBs. Natural sources of ionising radiation are cosmic rays and radiation from radioactive isotopes in the environment (e.g. in minerals or in the atmosphere) or directly incorporated into living organisms, like ^{14}C or ^{40}K. Medical x-ray diagnostics, single photon emission computed tomography (SPECT) or positron emission tomography (PET), as well as tumour treatment by ionising radiation (x-rays, electrons, protons, heavy ions), are further sources of unintended or intended DSB induction. The number and the 3D arrangement of DSBs induced by a given dose are important quantities for the understanding of cellular reactions like DSB repair, programmed cell death (i.e. apoptosis) or

the induction of mutations. There are several models available which predict the spatial distribution of energy dose or of generated DSBs by analytical (Butz and Katz, 1967; Chatterjee and Schaeffer, 1976; Xapsos, 1992; Chen et al., 1994) or numerical (i.e. Monte Carlo calculation) (Krämer and Kraft, 1994; Nikjoo et al., 1999; Friedland et al., 2005) approaches. The latter models are mainly based on the simulation of primary ionisation and excitation processes, as well as the follow-up reactions from the interaction cascades of the secondary electrons. All relevant differential cross sections for ionisation and excitation as well as the angular and energy spectra of secondary electrons from the various interactions have to be known accurately for the detailed Monte Carlo studies. There has been substantial progress in the last years to include relevant cross section data (Dingfelder et al., 1998; Dingfelder, 2002) into Monte Carlo codes to calculate local dose and especially DSB distributions. However, there is still a lack of accuracy in the cross section data for heavy ion primary particles at energies where the stopping force (LET, linear energy transfer) is close to its maximum, and at lower energies. On the other hand, the most severe problem remains to model the chemical effects on DSB induction which result from radicals produced by the ionising radiation not directly on DNA sites. Since the DNA content in a cell nucleus is only a very small fraction of the total mass, molecules other than DNA, mainly water molecules, are much more likely to be hit by the radiation. In addition, a realistic model for the organisation and structure of the DNA within the cell nucleus is needed in order to calculate accurate DSB distributions from such a bottom-up approach.

From the experimental side, the recently developed high energy ion microprobes offer new possibilities to investigate ion track structures in cell nuclei with respect to DSB production, the ensuing dynamics of DSB sites, and the complex spatio-temporal behaviour of proteins and chromatin modifications involved in DSB repair.

In this work we want to present some theoretical aspects and experimental findings on how DSBs are distributed around and along an ion track. We will first present how individual cells can be targeted by focussed ions at a high energy ion microprobe and how double-strand breaks can be visualised in cells. In a second part, we will describe the analytical and numerical approaches to calculate local dose and DSB distributions. The aim is a comparison of the measured spatial distributions of DSB sites with the calculated distributions, in order to further understand the processes of DNA damage induction in biological systems after ion irradiation.

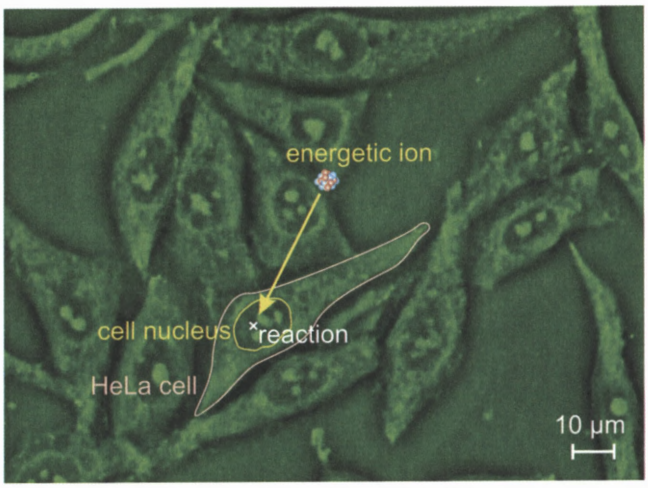

Figure 1. Micrograph of living HeLa cells in optical phase contrast. The nucleus of one cell is schematically subjected to a single ion hit.

2. Experimental Techniques

2.1. Microirradiation of Cells by a High Energy Ion Microprobe

The purpose of a microirradiation experiment on living cells is to target a certain position within a cell by a definable amount of ionising radiation damage. Especially the cell nucleus, which contains the genetic material DNA, represents the object of radiobiological interest (Figure 1). Ion microprobes allow to target sub-cellular structures by a single or a counted number of ions. To do so, high energy ions are focussed to beam spots well below 1 μm in diameter, for example by a set of magnetic quadrupole lenses (Fischer, 1985; Datzmann et al., 2001; Greif et al., 2004). A less expensive arrangement with a resolution of only about 2 μm employs microcollimators (Folkard et al., 1997a; Randers-Pehrson et al., 2001). As an example for a focussing ion microprobe the Munich microprobe setup SNAKE (Superconducting Nanoprobe for Applied nuclear (Kern-) physics Experiments) and the corresponding cell irradiation technique are described here. The schematic ion beam transport system of SNAKE (and in principle of comparable microprobes) is shown in Figure 2. An ion beam well-defined with respect to beam energy, charge state and mass is prepared using a 90° magnet located behind a high energy ion accelerator. With a system of precision slits the ion beam is trimmed, thus forming the object for an ion optical transformation and defining the aperture of the beam. The result of this beam trimming is a flow of

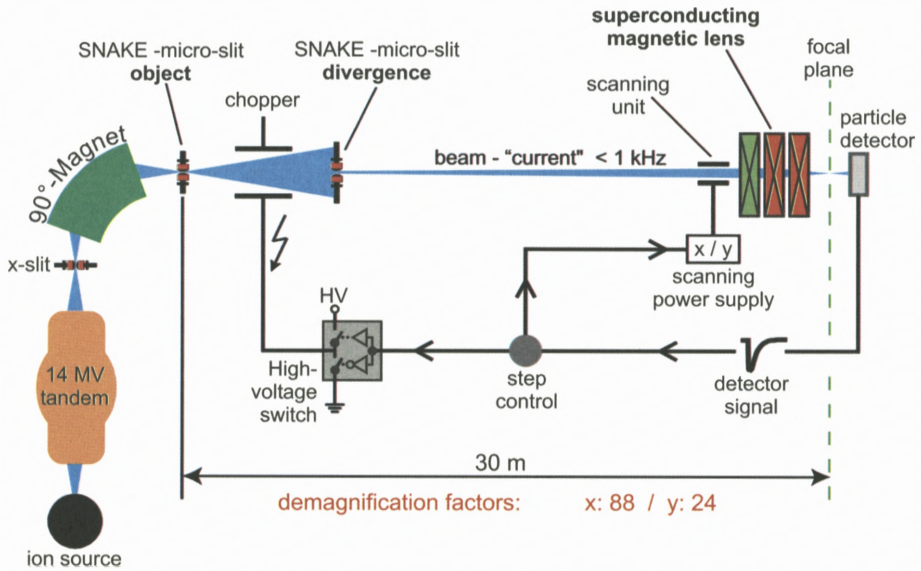

Figure 2. Beamline system of the ion microprobe SNAKE at the Munich tandem accelerator.

ions with a particle rate of not more than 10^3 per second, which then is focussed by a superconducting magnetic lens into the focal plane of the microprobe. An electrostatic scanning unit in front of the magnetic lens allows to scan the beam focus over the target without moving the sample mechanically. In order to irradiate samples with defined numbers of ions the described beam transport system is completed with an electrostatic beam shutter (chopper) enabling on-off-switching times in the order of 1 μs.

As living cell samples can only be handled under normal atmospheric pressure, the ion beam has to leave the vacuum of the beam transport line for cell irradiation. To separate vacuum from atmosphere, thin foils (e.g. made of Kapton or silicon nitride) are used which are traversed by the ion beam. The ion energy has to be sufficiently high to limit the lateral straggling caused by small angle scattering and to ensure a sufficient penetration depth in matter.

Suitable cell chambers have to be designed to make the cells accessible for the ion beam while ensuring favourable culture conditions (see an example in Figure 3). In general, these chambers contain a thin polymeric foil (e.g. Mylar foil) on which the cells are grown. For the detection of energetic ions during irradiation of cells different concepts exist. The three most common concepts base upon the detection of secondary electrons from the inner wall of vacuum windows (Fischer et al., 2003), the scintillation light of thin plastic foils placed in front of the cell

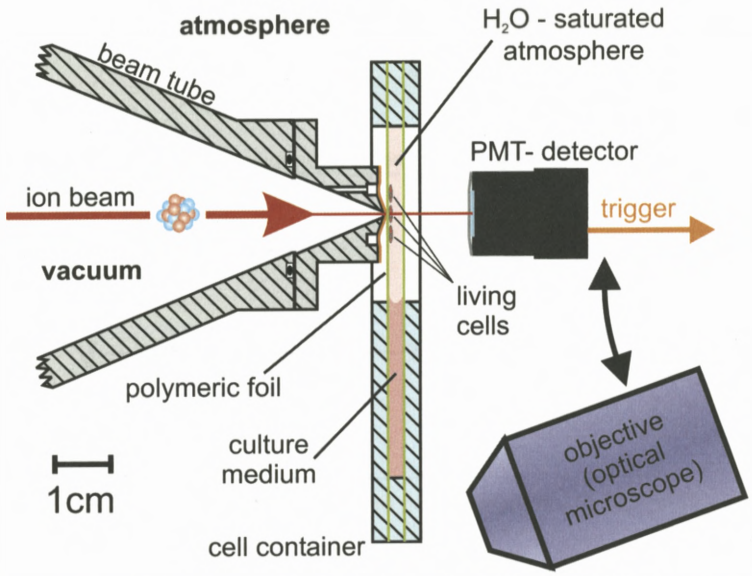

Figure 3. Arrangement for microirradiation of living cells with energetic ions. The ion beam exits the vacuum system through a bore in the beam tube covered by a thin foil. This vacuum window touches the back side of the cell carrier, polymeric foil to reduce beam spot broadening caused by angular scattering of the beam.

sample (Folkard et al., 1997b), or the ion-stop detection in a silicon or scintillation detector behind the sample (Hauptner et al., 2004). In the SNAKE setup the latter concept is realised. Detecting each ion on its arrival, the beam to the target can be switched off after a certain number of counted ions, e.g. after the first ion, and using the beam scanning unit (Figure 2) the ion beam can be directed to a new position, to which the next ion will be delivered. To perform targeted irradiations of cellular structures, an optical microscope has to be integrated into the irradiation setup. At present, the Munich irradiation configuration uses a standard inverted optical microscope devised for cell biology applications. With the help of this instrument the optical focussing of the ion beam on a fluorescent screen is performed, as well as the positioning of target locations relative to the beam position.

In order to study the DNA damage structure along the ion tracks (see Section 3.4), it is advantageous to perform irradiation experiments with a small angle between ion beam direction and the carrier foil of the cells (Jakob et al., 2003; Aten et al., 2004). Due to the optical properties of the analysing fluorescence microscope with the optical axis perpendicular to the cell substrate, a much better resolution along the track direction is obtained with this kind of irradiation

geometry than with the placement of the specimen perpendicular to the ion beam described above. At the Munich setup cells can be irradiated with an angle of 10° between beam direction and carrier foil. However, with this setup the ability to perform targeted irradiation is lost due to angular scattering and the large distance between vacuum exit window and target.

2.2. Optical Detection of DSB Sites in Cell Nuclei Using Immunofluorescence Technique

The induction of a DSB in the DNA of a living cell is a process taking place on the molecular level. A direct observation of a DSB using optical microscopy or electron microscopy is not possible due to lack of resolution and unsuitable sample structure. Visualisation of regions containing DSBs has, however, recently become possible with the help of cell biology and fluorescence microscopy methods. The first step in this procedure is done by the living cells themselves, which accumulate repair factors (proteins) at the sites of DSBs in order to initiate and execute repair of damaged DNA molecules. The experimenter can then fix the cells, i.e. kill them while preserving the biological structure, and treat them with antibodies which enter the cell nucleus. These primary antibodies are chosen to specifically recognize and bind to selected repair factors. Then secondary antibodies carrying a fluorescent dye molecule are added which bind to the primary antibodies (see schematic sketch in Figure 4a). Using an optical fluorescence microscope the distribution of the secondary antibodies and therefore of DSB sites in the form of so-called fluorescence foci can be observed with a resolution of about 200 nm (see Figure 4b).

In the near future, repair factors stained by green fluorescent proteins (GFP) will be used to follow DNA repair dynamics also in living cells on site at the ion microirradiation setup of SNAKE.

3. Microscopic DSB Distribution

3.1. General Considerations

It has been known for several decades that the biological effects of ionising radiation, such as cell killing or mutation, depend mainly on the energy dose $D = E/m$ (measured in Gy = J/kg), that is the ratio of the energy E deposited into a certain volume to its mass m. Scaling this quantity down to the cellular or subcellular level leads to so-called microdosimetry (Figure 5). As an extrapolation of the macroscopic dose, a local dose D_{loc} is defined as $D_{\mathrm{loc}} = \mathrm{d}E/\mathrm{d}m$ when the amount of energy $\mathrm{d}E$ is delivered into an infinitesimal small volume of mass $\mathrm{d}m$.

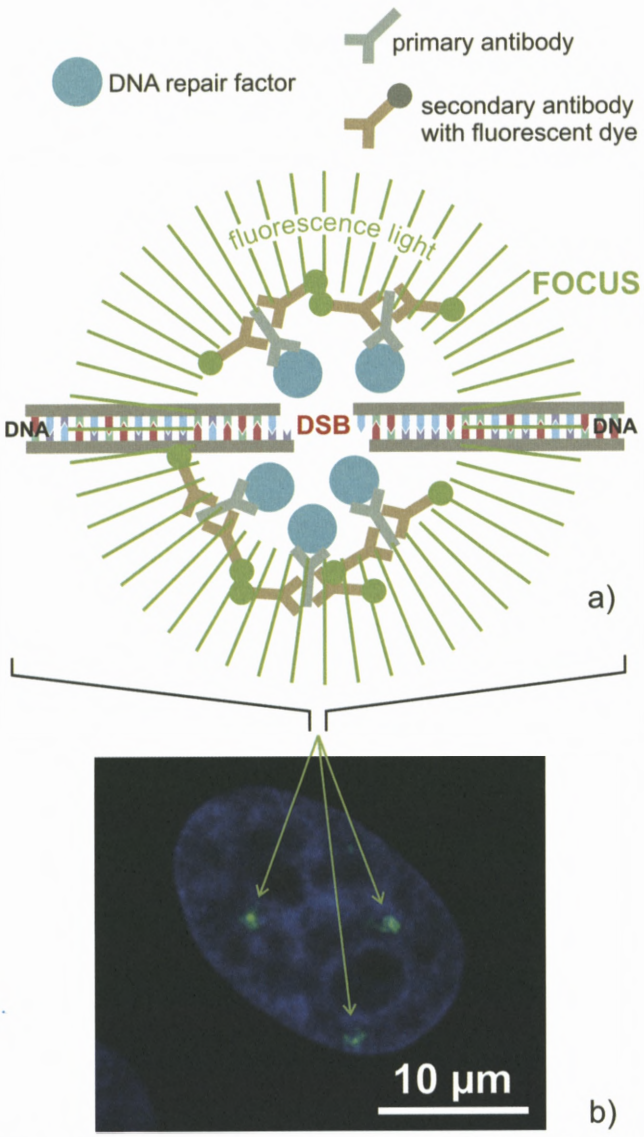

Figure 4. (a) DNA repair factors accumulating at DSB sites are marked with fluorescent antibodies (schematic drawing, not to scale). (b) Optical micrograph of a HeLa cell nucleus irradiated by single 55 MeV ^{12}C ions. The direction of the ion tracks is perpendicular to the image plane shown. Accumulated 53BP1 repair proteins are made visible as bright foci (green colour, see arrows) using immunofluorescence technique. The chromatin in the cell nucleus is marked by DAPI-counterstaining (blue colour) of DNA. The image is taken from an image stack (i.e. several optical slices perpendicular to the line of sight). Deconvolution software was used to reconstruct unmixed image information of single optical slices.

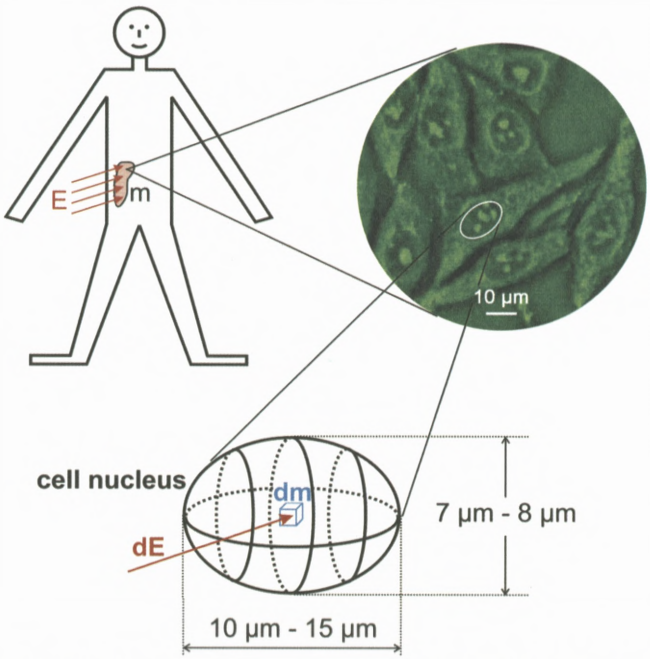

Figure 5. From macro- to micro-dosimetry: The mass element, in which one regards the deposition of radiation energy is scaled to a subcellular size.

X-ray and γ-ray irradiation damages living cells through the tracks of energetic electrons released mainly due to Compton scattering and photo effect. This so-called sparsely ionising radiation yields about $Y_{\mathrm{SSB}} = 1000$ single-strand breaks (SSBs) per Gy and about $Y_{\mathrm{DSB}} = 35$ DSBs per Gy within a diploid mammalian cell nucleus (Hall, 2000), over a wide range of absorbed doses. Using this linear relationship between energy dose and DSBs, a given local dose distribution $D_{\mathrm{loc}}(\mathbf{r})$ would result in a number $N_{\mathrm{DSB},\gamma}$ of induced DSBs within a certain voxel volume V_{Vox}:

$$N_{\mathrm{DSB},\gamma} = \frac{Y_{\mathrm{DSB}}}{V_{\mathrm{nucl}}} \int_{V_{\mathrm{Vox}}} D_{\mathrm{loc}}(\mathbf{r})\,\mathrm{d}V. \tag{1}$$

Using this equation one should obtain reasonable results as long as V_{vox} is sufficiently large so that it contains the average DNA concentration as found in the whole cell nucleus. V_{nucl} is the volume of the cell nucleus. For HeLa cells,[1] we have determined $V_{\mathrm{nucl}} = 710\ \mu\mathrm{m}^3$ (i.e. 0.71 ng of mass) on average, by measuring

[1] HeLa cells are immortalised human cells often used for biological experiments.

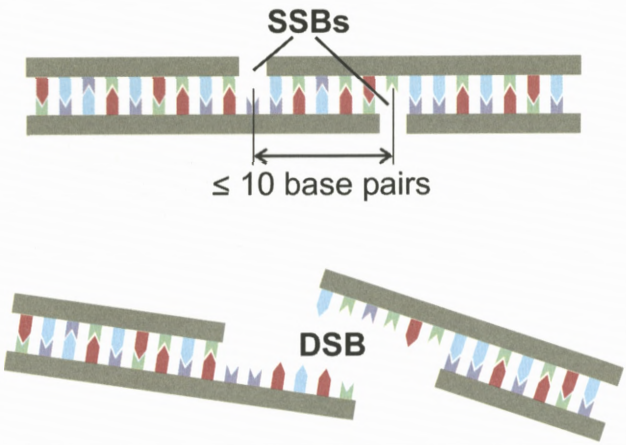

Figure 6. Generation of a double-strand break (DSB) from adjacent single-strand breaks (SSBs) on opposite strands of the DNA molecule.

a set of hundred HeLa cell nuclei using optical microscopy. Thus, an average dose of 1 Gy deposits an energy of 0.71 pJ into a HeLa cell nucleus. After irradiation with ions, the number of DSBs induced per unit dose may differ from that observed after X- or γ-irradiation. Thus, the ions' relative biological effectiveness for DSB induction, $\mathrm{RBE}_{\mathrm{DSB}}$, has to be considered in the determination of $N_{\mathrm{DSB,ion}}$, yielding

$$N_{\mathrm{DSB,ion}} = \frac{Y_{\mathrm{DSB}}\mathrm{RBE}_{\mathrm{DSB}}}{V_{\mathrm{nucl}}} \int_{V_{\mathrm{Vox}}} D_{\mathrm{loc}}(\mathbf{r})\,\mathrm{d}V = \mathrm{RBE}_{\mathrm{DSB}} N_{\mathrm{DSB},\gamma}. \tag{2}$$

DSBs occur if there are two SSBs on opposite strands on a DNA molecule within a distance smaller than 10 base pairs (i.e. 3 nm distance, see Figure 6). The probability for generation of two SSBs in close vicinity will be increased at sites of high local dose. Therefore, $\mathrm{RBE}_{\mathrm{DSB}}$ values are expected to exceed unity when the stopping force of the ions is close to or larger than the stopping force of electrons at their stopping force maximum (26 keV/μm). The effects from nuclear energy transfers, which are important for fast neutrons or slow ions, have to be treated differently, but little is known about dose-DSB relationships from atomic knock-on collisions.

A swift ion loses the energy $\Delta E = \int_{\ell}(\mathrm{d}E/\mathrm{d}x)\,\mathrm{d}x$ when it passes through a cell nucleus along a path of length ℓ. If the ion is fast enough (specific energies larger than 1 MeV/nucleon), the stopping force $\mathrm{d}E/\mathrm{d}x$ within one cell is nearly

constant and is dominated by electronic interaction. Thus, the energy deposited in the nucleus can be approximated by

$$\Delta E = \frac{\mathrm{d}E}{\mathrm{d}x}\,\ell, \tag{3}$$

where ℓ is the length of the track in the cell nucleus. On the other hand, if ion velocities are not too high (i.e. less than 20 MeV/nucleon), the secondary electrons ejected along the ion track in a cell nucleus are mostly stopped within that cell nucleus, and the energy ΔE is fully deposited there. Although the ions' nuclear energy loss may show enhanced biological effectiveness compared to electronic energy loss, these effects should be negligible at high ion energies since only about 0.1% of the energy loss is of nuclear origin.

The average height of a HeLa cell nucleus grown on foil was determined as 7.6 μm. If this nucleus is traversed perpendicularly to the substrate by a swift ion, an average dose D_{av} is deposited in the cell nucleus (mass density approximated by $\rho_{\mathrm{H_2O}}$) of mass m_{nucl}:

$$D_{\mathrm{av}} = \frac{\Delta E}{\rho_{\mathrm{H_2O}} V_{\mathrm{nucl}}} = \frac{\Delta E}{m_{\mathrm{nucl}}}\,. \tag{4}$$

Thus, the number $N_{\mathrm{DSB,ion}}$ of DSBs obtained from a single ion passage through a cell nucleus is given by:

$$N_{\mathrm{DSB,ion}} = D_{\mathrm{av}} Y_{\mathrm{DSB}} \mathrm{RBE}_{\mathrm{DSB}}. \tag{5}$$

The energy deposition in a HeLa cell nucleus, the average energy dose D_{av} and the numbers of DNA strand breaks when applying uniformly the dose effect relationship for sparsely ionising radiation created by the passage of a single particle through a cell nucleus are plotted in Figure 7 for various kinds of ions and in addition for electrons in dependence of their velocity. Dividing N_{DSB} by the average height of the nucleus, one obtains the number of DSBs per unit path length of the particle (see rightmost scale in Figure 7). This number varies over orders of magnitude from less than 0.01 DSBs averaged per micrometer for protons with more than 100 MeV energy to about 100 DSBs per micrometer (and even more considering $\mathrm{RBE}_{\mathrm{DSB}}$ values) for the heaviest ions around their stopping force maximum.

Fast protons have stopping forces close to those of energetic electrons at the same speed, while the stopping forces of heavier ions exceed it by several orders of magnitude. The most severe difference between sparsely ionising radiation and heavy projectiles penetrating tissue lies in the local energy deposition around the ion track. This results in high local doses in the vicinity of the ion track in the

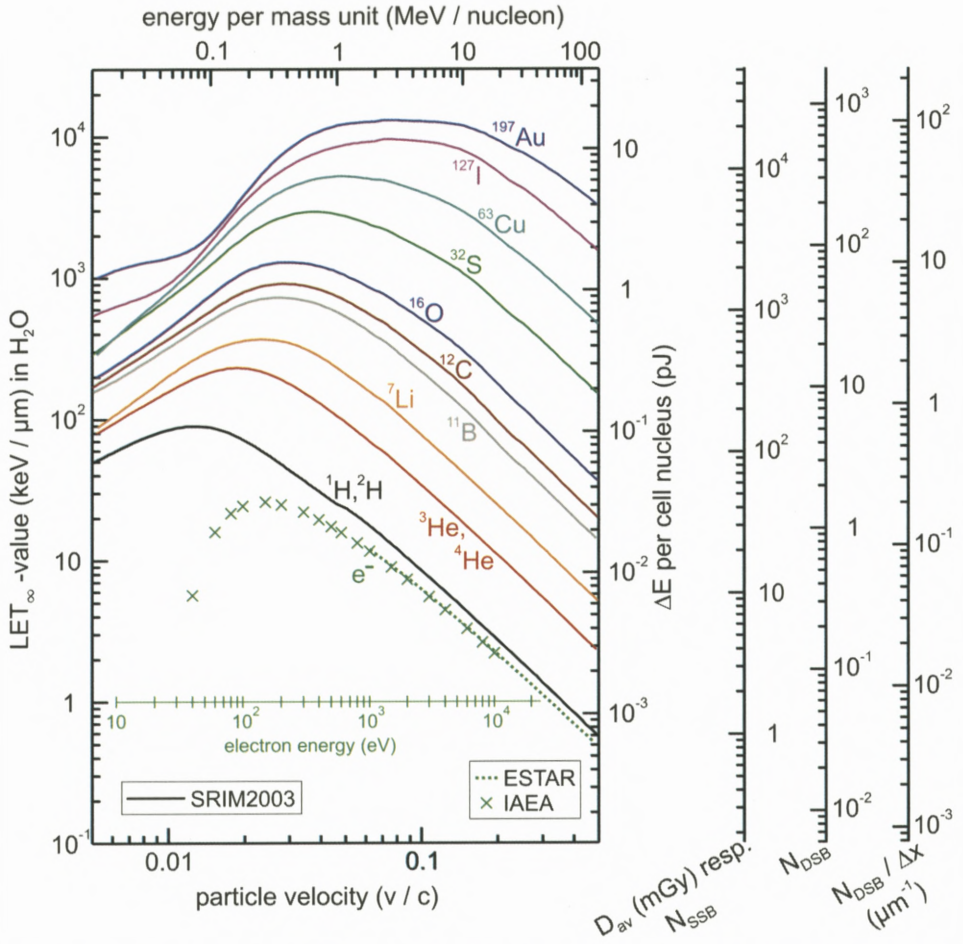

Figure 7. Damage induction in cell nuclei for single hits of different ions and electrons: The amount of energy ΔE deposited in the nucleus assumes a particle track length of 7.6 μm within the nucleus. The additional precondition for the average energy dose D_{av} is a cell nucleus mass of 0.71 ng. The numbers of SSBs N_{SSB} and DSBs N_{DSB} are obtained by a strict scaling as known from sparsely ionising radiation. Especially for DSB induction at heavy ion tracks the values shown do not consider enhanced effectiveness (i.e. $RBE_{DSB} = 1$ for all values shown). Note also that for the lower particle energies shown the stopping force value (LET_∞) cannot be assumed to be constant along the track through the whole cell nucleus. In that case, the absolute values shown for energy deposition, average dose and numbers of strand breaks are not applicable. Stopping force data were taken from SRIM (Ziegler and Biersack, 2003) for ions and from IAEA (1995) as well as from ESTAR (Berger et al., 2005) for electrons.

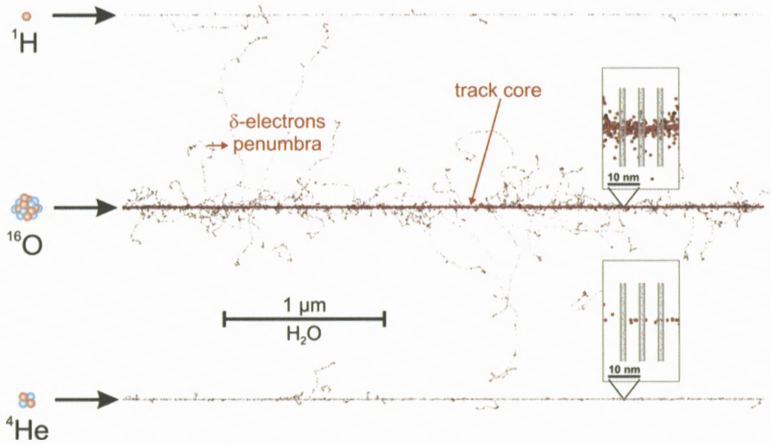

Figure 8. Projections of PARTRAC calculations (ionisation and excitation events in water) for three different ion tracks with the same specific energy 6.25 MeV/nucleon. The magnified cut-outs with overlaid DNA (schematic) demonstrate the difference between densely and sparsely ionising radiation.

case of heavy ions, while sparsely ionising radiation creates fluctuations of dose only through the statistical nature of electron trajectories and their ionisation and excitation processes.

3.2. Radial Distributions of Energy Dose and DSBs

The local dose distribution has been subject to various theoretical approaches. The most detailed calculations stem from Monte Carlo simulations where the primary reactions of the ion along its trajectory are calculated in a statistical way and the probability for a reaction to happen is calculated from the relevant differential cross sections (Dingfelder et al., 1998; Dingfelder, 2002). A snap shot of the ionisation and excitation events along charged particle tracks in water as target material is plotted in Figure 8. It has been projected from a 3D Monte Carlo calculation with the code PARTRAC (Friedland et al., 1998, 1999, 2003), applied to a proton, an oxygen and a helium ion, respectively, at a specific energy of 6.25 MeV/nucleon, corresponding to a velocity of $0.115c$, where c is the speed of light. While especially for the proton track the single events along the center of the track (= core) can be resolved on the given scale, a continuous ionisation path is generated by the oxygen track where an ionisation is created within every atomic distance. Ionisation paths are also visible where secondary electrons carry some energy leading to ionisations at larger distances from the core. This more sparsely ionised region around the track core is sometimes called "penumbra".

Although the average dose is smaller by orders of magnitudes in the penumbra than in the core, there are areas of relatively high dose close to the ends of the secondary electrons paths, where the highest stopping force of electrons occurs (see Figure 7). At these end points the ionisation density is high enough that there also exists a significant probability for DSB induction. A number of radicals is also formed from various molecules besides the DNA molecules, which can potentially create additional DSBs.

Monte Carlo simulations are laborious, and for certain applications it may be helpful to estimate the average energy dose at a given radial distance to the ion track center using an analytical expression. Analytical models have already been used for longer times for the calculation of microscopic dose distributions. Microdosimetry experiments were performed, where ionisation doses were measured in diluted gases and scaled to fluid water densities. Therewith dose distributions have been seen to scale with $1/r^2$ with r being the radial distance from the ion track core. Several analytical representations of such dose distributions were given by Butz and Katz (1967), Chatterjee and Schaeffer (1976), Xapsos (1992) and Chen et al. (1994). For some of them it is argued, that the energy deposited should be divided equally between core and penumbra region, which leads to some incongruities in the radial dose distribution at the core/penumbra interface (Chatterjee and Schaeffer, 1976). For other representations less crude assumptions on the track core are made (Butz and Katz, 1967). In general, comparisons of the analytical representations with the Monte Carlo calculations show quite good agreement in the penumbra region, where all calculations are also in good agreement with measured data. The agreement is, however, less favourable in the core region and also at the very far distances, where the $1/r^2$ scaling ends. There, the analytical representations assume a sharp drop while the Monte Carlo calculations show only a faster decrease in dose. This decrease may be approximated by a $1/r^4$ scaling.

Using this approximation, an improved analytical representation was fitted to Monte Carlo simulation data of average radial dose distributions in water (Krämer and Kraft, 1994) for high ion energies ($E/A > 1$ MeV/nucleon):

$$D = \begin{cases} \frac{B}{r} & r \le r_i \\ \frac{Br_i}{r^2} & r_i < r \le r_k \\ \frac{Br_i r_k^2}{r^4} & r_k < r \le r_{\max} \\ 0 & r > r_{\max} \end{cases} \quad \text{with the radii} \quad \begin{aligned} r_i &= 1 \text{ nm} \\ r_k &= 45 \text{ nm}(E/A)^{1.75} \\ r_{\max} &= 5r_k \end{aligned} \tag{6}$$

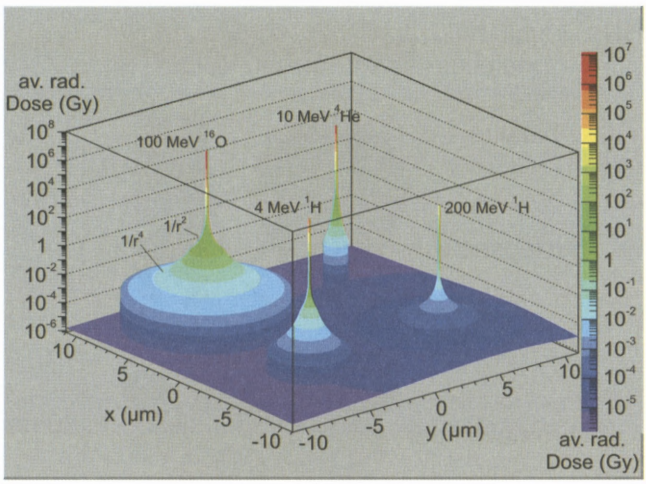

Figure 9. Average radial dose distributions given by Equation (6) for four different ions with track directions perpendicular to the x–y plane. Looking at the dose distribution of 100 MeV ^{16}O one can distinguish between the two different radial dependences ($1/r^2$ and $1/r^4$, respectively) used in the analytical expression. The dose background over the whole area shown originates from the track of the fast 200 MeV proton. To avoid an infinite high dose in the center of the tracks the dose has been restricted to B/(0.1 nm) in the track centers. Because of graphical reasons the drawn surfaces near the track centers were radially expanded and are not to scale. Moreover, one should always keep in mind that the average radial dose distributions shown in this figure veil the stochastic nature of energy deposition due to the tracks of secondary electrons (compare Figure 8).

with

$$B = \frac{1}{\rho_{H_2O}} \frac{dE}{dx} \frac{1}{2\pi r_i (5.28 + 1.75 \ln(E/A))} ,$$

$\rho_{H_2O} = 1.0$ g/cm^3 and $E/A =$ kinetic energy divided by the mass of the particle measured in MeV/nucleon.

One has to be aware that, outside the core and up to r_k, the integrated radial dose scales with $\ln(r)$ due to the $1/r^2$ dependence of the radial dose distribution. Thus a significant fraction of the energy is deposited in that region. Since the end point r_k of the $1/r^2$ scaling increases disproportionate to the ion velocity ($r_k \sim (E/A)^{1.75} \sim v^{3.5}$), the interaction volume, where DSBs are most likely generated, depends heavily on the ion velocity. The absolute dose values depend on the stopping force dE/dx of the ion which again is a function of ion velocity and scales close to Z^2 at high ion velocities (with $Z =$ atomic number). The unreal infinity of the given dose distribution at $r = 0$ is meaningless if doses in real voxel volumina are determined.

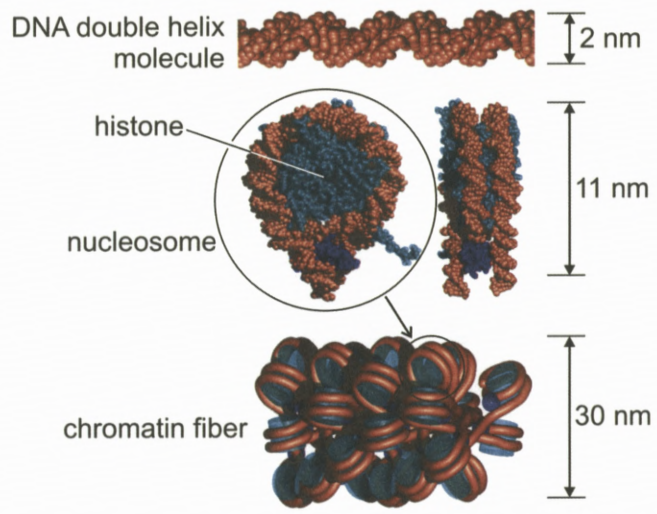

Figure 10. Organisation of the DNA molecule in nucleosomes where DNA is wrapped around histone proteins (side and front view, atomic resolution), and condensation of nucleosomes into the 30 nm chromatin fiber. This photorealistic visualisation was copied from the work of Bernhardt (2002).

In order to illustrate the situation for different ions, the average radial dose distributions according to Equation (6) are plotted in Figure 9. Assuming a strict linear dose – DSB relationship and knowing the corresponding RBE_{DSB} values (e.g. from experiments) one could scale these distributions also to average radial DSB distributions. Note that the diameter $2r_k$ exceeds the diameter of a normal cell nucleus of about 10 μm at energies exceeding 20 MeV/nucleon. At those high energies the total number N_{DSB} of DSBs created in a cell nucleus traversed by a single ion is lower than calculated based on Equations (3–5) since a fraction of the energy is deposited outside the cell nucleus.

3.3. Influence of Chromatin Structure on DSB Distribution

Since the damaging events are inhomogeneously distributed on a microscopic scale, Monte Carlo calculations offer the possibility for a detailed modelling of DSB distributions along the ion track and also of their radial distributions. To do so, a detailed model of the DNA and chromatin structure and its organisation within a cell nucleus is needed. In addition, all mechanisms, direct ionisation and excitation processes on DNA as well as the effects of radicals created by the radiation in the vicinity to a DNA molecule have to be taken into account. The

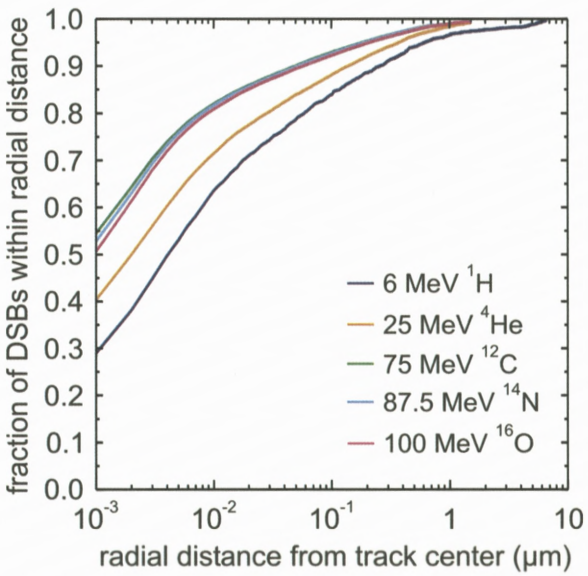

Figure 11. Average fraction of DSBs found within a given radial distance from the ion track center as calculated by the PARTRAC code for different ions with the same velocity.

microscopic double-helical structure of the DNA, its organisation around nucleosomes and its compaction into the 30 nm chromatin fibers are well investigated (Figure 10). To what degree higher order chromatin organisations are present in the cell nucleus, and how these structures look like, is still under discussion. From the total length of 30 nm chromatin fibers (5.5 cm) in a human cell (corresponding to 6×10^9 base pairs of DNA) the volume occupied by chromatin within one cell nucleus can be calculated to 39 μm^3. Regarding the average volume of the nucleus (710 μm^3) one can estimate that only about 5% of the cell nucleus is made of chromatin. The remaining space is filled mainly by water and an additional fraction of other organic molecules.

The current PARTRAC code assumes a homogeneous distribution of chromatin fibers in the cell nucleus. Basic elements are 150 nm long chromatin fiber rods arranged in rosette-like structures with stochastic variations (Friedland et al., 2003). Based on this model for a cell nucleus the PARTRAC code is able to calculate the spatial distribution of radiation induced DSBs. The average fraction of DSBs found within a given radial distance from the ion track center is plotted in Figure 11 for various ions which all have the same specific energy ($E/A = 6.25$ MeV/nucleon). Each curve is the average of 10000 individual ion trajectories for protons and alpha particles and 5000 trajectories for the heavier

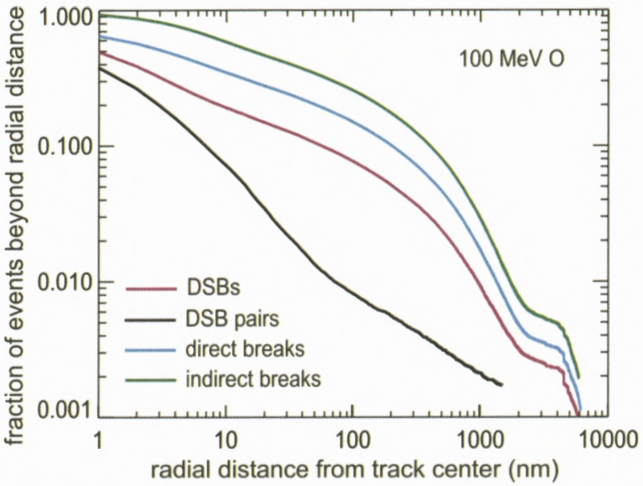

Figure 12. Average fraction of different DNA damage events generated beyond a given radial distance from a 100 MeV ^{16}O ion track center as calculated by the PARTRAC code. Each curve is normalised to a value of 1 for the track center (i.e. $r = 0$).

ions. The plots were normalised to an integrated value of 1 and have to be multiplied with the total number of DSBs created along a given ion track segment in order to obtain the average number of DSBs generated within the radius r. The calculations show that a significant proportion of the DSBs are found in the core region (i.e. 1 nm) but that there is still a considerable fraction of DSBs which is created at a distance from the core exceeding 100 nm. It is also remarkable that there is a difference in the DSB distribution for the heavier ions as compared to protons. The heavier ions have a higher relative yield for DSBs in or close to the core. This effect may be explained by the high density of damaging events induced by different primary or secondary reactions and which interact to enhance DSB induction in the core region. Speaking strictly in terms of RBE_{DSB} values a definition of radial dependent values $RBE_{DSB}(r)$ would be necessary with higher values for small radial distances. This means that a global scaling of radial dose distributions using an uniform RBE_{DSB} value as mentioned at the end of Section 3.2 is not expected to give accurate radial DSB distributions, especially not for heavy ion tracks. Besides radial distributions the PARTRAC calculation can also give an overview in which way DNA strand breaks are created (see an example for 100 MeV ^{16}O ions in Figure 12), whether by direct breaks from ionisation and excitation of the DNA molecules themselves or by indirect interaction from radicals produced mainly in water surrounding the DNA. The latter is about two times more efficient in damage creation than the direct processes (Michael and

O'Neill, 2000). Figure 12 shows in addition the fraction of DSBs and of DSB pairs generated beyond a given radial distance from the ion track center. A DSB pair consists of two lesions on the same modeled DNA fiber rod and constitutes an even more serious damage to the DNA than an isolated DSB. Since the DNA is organised in higher order structures the probability of creating a second lesion on the DNA molecule in close vicinity to another lesion is enhanced. This enhancement is especially prominent in the core of the ion track where the ionisation density is the highest. Thus, the radial distribution of DSB pairs decreases faster with increasing distance from the ion track center than the DSB distribution. Up to now, there is no experimental information available to prove and maybe to refine the predicted radial DSB and DSB pair distributions.

3.4. Longitudinal DSB Distributions

There would be a random distribution of DSBs in longitudinal direction along the ion track if the DNA molecules were distributed homogeneously inside the cell nucleus. However, the fiber structure of the chromatin exerts a strong influence on the longitudinal distribution of DSBs. In a first approximation the situation is illustrated in Figure 13. Here schematic chromatin fibers without internal structure are projected from a cuboid (1 μm $\times$ 1 μm lateral, 300 nm projected onto image plane) assuming a statistical distribution of the fibers within the volume. The ionisation track structure of a 100 MeV oxygen ion is overlaid onto this chromatin distribution. The probability that the ion passes directly through a chromatin fiber is low, but if it hits a fiber it produces a DSB cluster, which means several DSBs in close vicinity which are separated by a larger distance from the next DSB cluster. Some additional DSBs are created at larger radial distances from the ion path when secondary electron cascades end in or close to a DNA fiber. It is important to note that in reality the 30 nm fiber is arranged in a higher-order conformation, which as yet is not characterised. Already in Figure 4b it is evident that the chromatin is not distributed homogeneously inside the cell nucleus.

Experimental analysis of repair factor foci by conventional optical microscopy cannot resolve reliably the individual DSBs within one DSB cluster, due to the ultimate resolution of optical microscopy (200 nm) and the repair factor dependent extension of the fluorescent foci ($\approx$1 μm). Thus, the number of visible foci corresponding to DSB clusters or sufficiently separated DSB sites (i.e. $\approx$1 DSB), respectively, is expected to be lower than the calculated number of DSBs. The number of DSB clusters can also be estimated from the PARTRAC code. In our analysis we put all DSBs into one cluster which are generated on one 150 nm long fiber section (corresponding to 1.8×10^4 base pairs). Figure 14 shows, for a variety of ions and ion energies, the numbers of DSBs per path length expected when

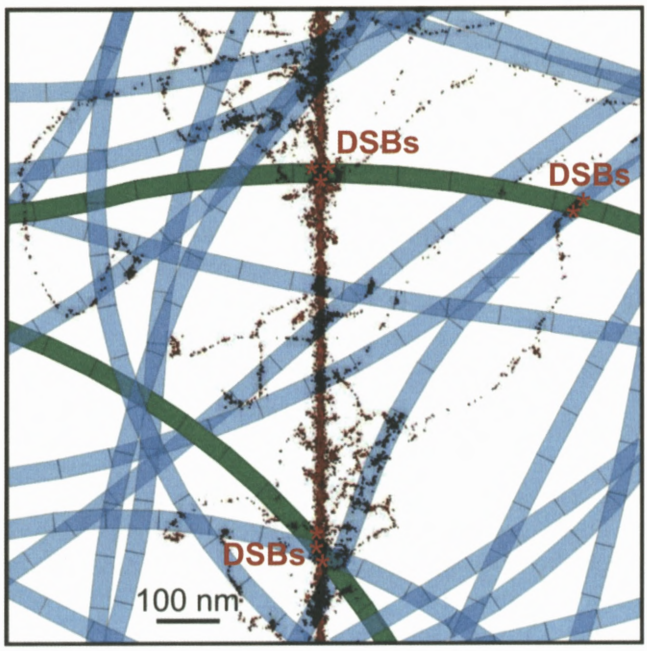

Figure 13. Illustrative visualisation of DSB and DSB-cluster induction along the track of an energetic ion. The projection of a 100 MeV ^{16}O ion track structure (PARTRAC) is overlaid on a simple model for a cell nucleus containing homogeneously distributed chromatin fibers. The fibers occupy a volume fraction of about 5%. A 300 nm thick layer of this model is projected perpendicularly to the image plane. Green marked fiber sections are thought to be directly hit by the ion track center.

assuming the linear extrapolation from sparsely ionising radiation (left column). The middle column shows the numbers of DSBs per path length as calculated from the PARTRAC code, which demonstrates an increased formation of DSBs due to the high ionisation density in the core region of the heavier ions. The relative biological effectiveness for DSB induction, RBE_{DSB}, was found to lie between $RBE_{DSB} = 1.3$ for 6.25 MeV protons and $RBE_{DSB} = 2.6$ for 75 MeV carbon and comparable ions. For comparison, experimentally determined RBE_{DSB} data ranging from 1.2 (for 21 MeV protons) to 2.8 (for 65.6 MeV oxygen ions) are also shown. These data were deduced from a comparison of experimentally obtained DNA fragment-size distributions with the outcome of simulations based on an analytical model for the radial dose distribution and Monte Carlo models for the distribution of chromatin in the nucleus (Friedl et al., 2003). The numbers of DSB clusters per path length, as determined by the PARTRAC code, are shown in the right column in Figure 14. For the densely ionising tracks of heavy ions where a strong clustering of DSBs can be expected these numbers are even lower than the

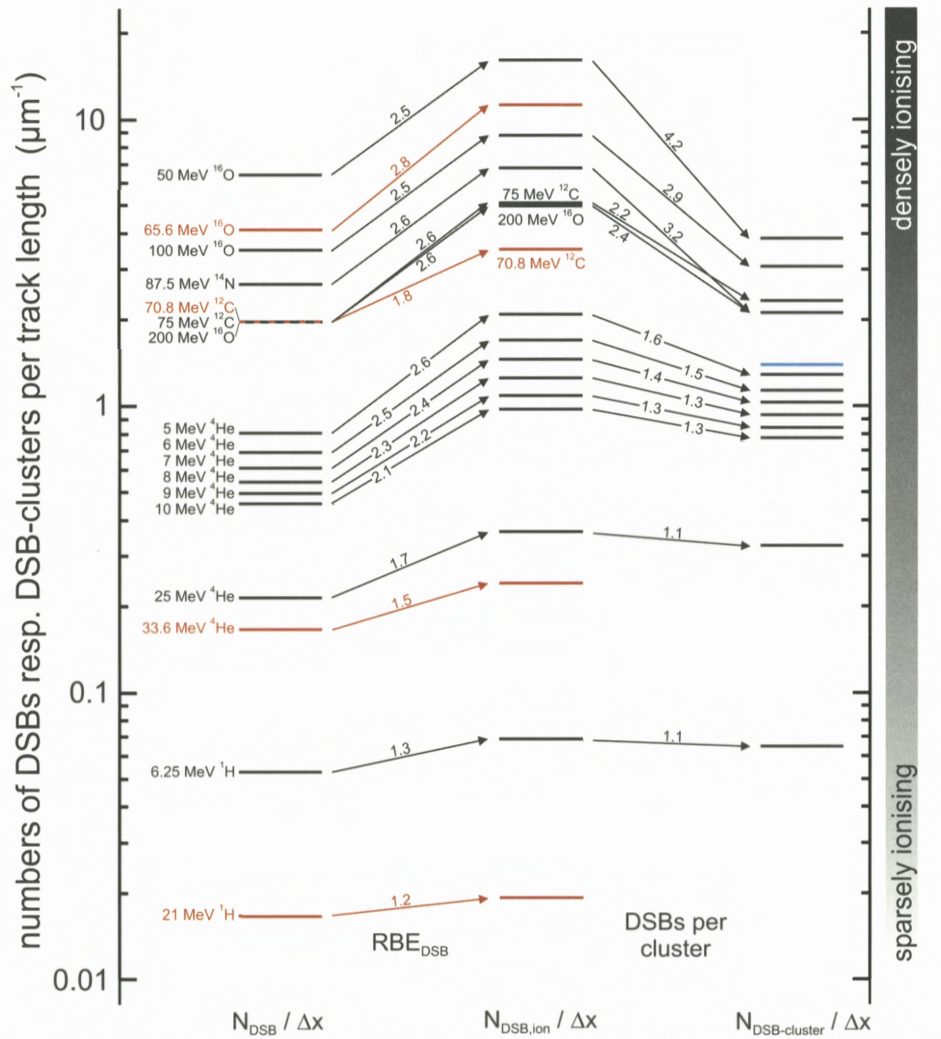

Figure 14. Left column: numbers of DSBs per ion track length ($N_{\mathrm{DSB}}/\Delta x$) for different ions obtained by extrapolating from sparsely ionising radiation (i.e. $\mathrm{RBE}_{\mathrm{DSB}} = 1$). Middle column: numbers of DSBs per ion track length ($N_{\mathrm{DSB,ion}}/\Delta x$) weighted by the corresponding $\mathrm{RBE}_{\mathrm{DSB}}$ value. $\mathrm{RBE}_{\mathrm{DSB}}$ data stem from PARTRAC monte carlo simulations (black) and experiments (red), respectively. Right column: numbers of DSB clusters per ion track length ($N_{\mathrm{DSB\ cluster}}/\Delta x$) as obtained from PARTRAC calculations. These values are reduced relative to the values of the middle column by the average number of DSBs found within one cluster. A simple geometric estimation concerning directly hit chromatin fibers (further explanation in the text) is also shown in the right column (blue).

numbers of DSBs per path length obtained from linear approximation (compare right and left column).

One can also estimate the minimum number of expected DSB clusters per track length considering the volume fraction of 5% occupied by chromatin fibers. For dense ion tracks, where each hit of a fiber by the track center should lead to the generation of a DSB site, counting simply the number of these hits leads to an average of about 1.4 predicted DSB sites per μm (see also right column in Figure 14).

To investigate the relationship between expected DSB sites and repair protein foci HeLa cells were irradiated by 29 MeV ^{7}Li and by 24 MeV ^{12}C ions at an angle of about 10° to the image plane of the epifluorescence microscope. Using an interpolation between the PARTRAC data the number of DSB clusters is predicted as 1 to 1.5 clusters per μm for 29 MeV ^{7}Li and as 3–4 clusters per μm for 24 MeV ^{12}C ions. Considering the optical resolution during fluorescence analysis and the extension of foci one would expect a more or less continuous line in the fluorescence micrograph along the tracks for the last-mentioned ion type. Our experiments show a much lower linear focus density than expected (Figure 15), namely on average about 0.8 foci per μm for both kinds of ions, albeit with a large statistical variation. Note that the counting of foci is difficult because of the presence of sub-structures visible at the larger foci where several small foci might be resolvable in higher resolution micrographs. These sub-structures might be due to clustering of foci by diffusion within the nucleus of the living cell to form larger foci several minutes after irradiation (Aten et al., 2004). Another reason for the larger than expected distance between the foci may lie in an additional higher order organisation of the chromatin. A recent model (Cremer et al., 2006) based on high resolution fluorescence images and electron microscopy proposes that the chromatin occupies small domains of high chromatin density while an interchromatin compartment consisting of channel- and lacuna-like structures separates the chromatin domains (for an illustration, see Figure 16). Such a gross structure would enhance the number of DSBs per cluster, resulting in larger clusters, but in a lower number of separated clusters.

4. Future Prospects

The most important advantage of Monte Carlo calculations over analytical models is the capability to include the microscopic dose fluctuations caused by secondary electron cascades and their end points where the electron energy loss is largest. In order to obtain reliable data for DSB induction and distribution, accurate differential cross sections for the electronic interaction of energetic ions in matter

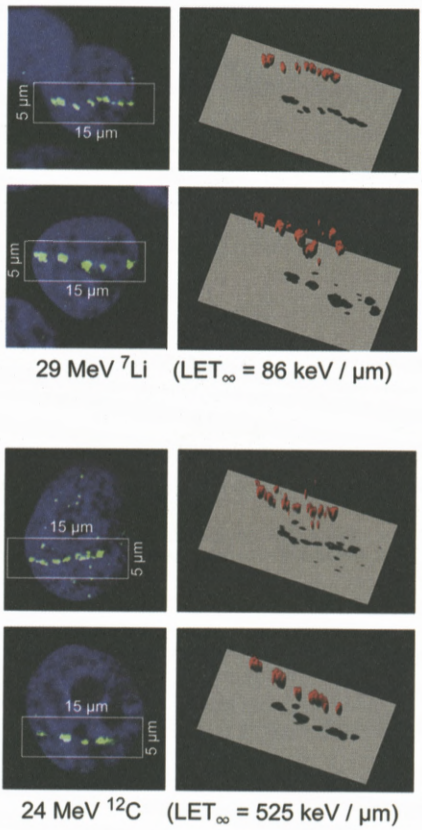

Figure 15. Left side: fluorescence micrographs (optical slices) of HeLa cell nuclei irradiated with single 29 MeV ^{7}Li or 24 MeV ^{12}C ions, respectively. The direction of the ion tracks encloses an angle of 10° with the image plane. 15 min after irradiation the cells were fixed and 53BP1 DNA repair factor accumulations were visualised by indirect immunofluorescence (green signal). Image stacks were taken using a motorized epifluorescence microscope and processed by deconvolution software. Right side: Corresponding three-dimensional reconstructions of image stacks were performed for the immunofluorescence signal using rendering software. The foci structures (red colour) of the DNA repair factor accumulations along the ion tracks reveal the distribution of DSB sites at the time of cell fixation.

and a realistic model for the DNA organisation within cell nuclei are needed. In particular, the present disagreement observed between calculations and observations of longitudinal DSB distributions along ion tracks may reflect a higher-order chromatin organisation that has not yet been adequately considered in the Monte Carlo approaches.

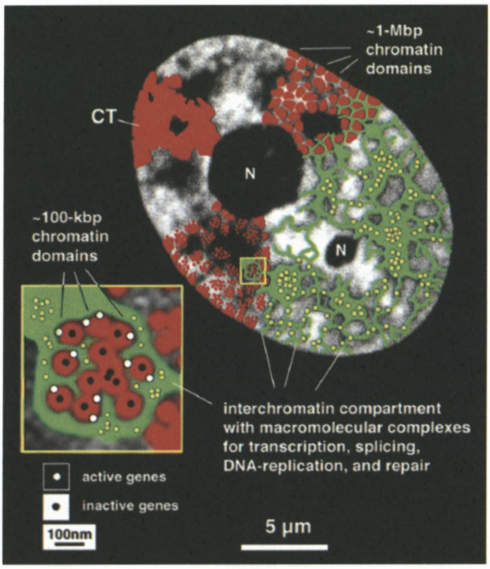

Figure 16. Chromosome territory-interchromatin compartment (CT-IC) model (Cremer et al., 2006). This model emphasizes that chromosomes occupy distinct territories in the cell nucleus. Chromosome territories (CTs) are built up from focal chromatin domains representing higher order chromatin structures with a DNA content in the range of about 10^6 base pairs. Each of these chromatin domains is thought to consist of a series of chromatin loop domains of about 10^5 base pairs. The model also emphasizes the presence of an interchromatin compartment (IC) with the most peripheral branches connected to the nuclear pores and protruding to the nuclear interior both between neighbouring CTs and into the interior of individual CTs. Actively transcribed genes locate at the chromatin surfaces exposed to the IC which contains nuclear bodies involved in various functions like transcription, splicing, replication and repair.

From the physical viewpoint, DSB induction is a certain endpoint resulting from interaction processes of ionising radiation with tissue. The energy transfers through ionisation, excitation and radical formation are the starting points which may end in the creation of DSBs. After completion of this physical and chemical stage within a timescale of nanoseconds biological processes occupied with the answer to the DNA damage take place in the living cell. Although a lot of DNA repair factors have been identified over the last decade, little is known on the spatiotemporal organisation of DSB repair, especially with respect to the structural organisation of DSBs within the cell nuclei. Even simple questions are not yet answered: Are there certain repair factories in the cell nucleus where damaged DNA is treated by the repair factors? Are the repair factories created at the damaged chromatin or has the damaged chromatin to move to the repair centers? What is the dynamical behaviour of the foci which are known to be formed by a number

of repair factors around DSBs? Do the foci move around and at what speed? What is the sequence of recruitment of repair factors, which one is earliest, which repair factors depend on each other?

These questions may be answered by radiation biology experiments preferentially performed at high energy ion microprobes. There the damaging action of ionising radiation can be induced by targeted irradiation which makes the cellular follow-up reactions accessible in space and time.

Acknowledgements

The experimental part of this work was supported by DFG grants Do438/9 and Cr59/23-1 as well as by the Maier Leibnitz Laboratorium of the TU-München and the Ludwig-Maximilians-Universität München.

References

Aten J.A., Stap J., Krawczyk P.M., Van Oven C.H., Hoebe R.A., Essers J. and Kanaar R. (2004): Dynamics of DNA double-strand breaks revealed by clustering of damaged chromosome domains. Science **303** (5654), 92–95

Berger M.J., Coursey J.S., Zucker M.A. and Chang J. (2005): Stopping-power and range tables for electrons (ESTAR) [online]. National Institute of Standards and Technology (NIST), Physics Laboratory, Gaithersburg, Maryland, USA. Available from: http://physics.nist.gov/PhysRefData/Star/Text/ESTAR.html (accessed 28 September 2006)

Bernhardt P. (2002): Strukturierte Targets in der Modellierung von strahlungsinduzierten DNS Schäden. Thesis (PhD), Technical University of Munich

Butz J.J. and Katz, R. (1967): Theory of RBE for heavy ion bombardment of dry enzymes and viruses. Rad Res **30**, 855–871

Chatterjee A. and Schaeffer H.J. (1976): Microdosimetric structure of heavy ion tracks in tissue. Rad Env Biophys **13**, 215–227

Chen J., Kellerer A.M. and Rossi H.H. (1994): Radially restricted linear energy transfer for high-energy protons: a new analytical approach. Rad Env Biophys **33**, 181–187

Cremer T., Cremer M., Dietzel S., Müller S., Solovei I. and Fakan S. (2006): Chromosome territories – A functional nuclear landscape. Curr Opin Cell Biol **18, no. 3**, 307–316

Datzmann G., Dollinger G., Goeden C., Hauptner A., Körner H.J., Reichart P. and Schmelmer O. (2001): The Munich microprobe SNAKE: First results using 20 MeV protons and 90 MeV sulfur ions. Nucl Instr Meth Phys Res B **181, nos 1–4**, 20–26

Dingfelder M. (2002): Cross section calculations in condensed media: Charged particles in liquid water. Radiation Protection Dosimetry **99, no. 1**, 23–27

Dingfelder M., Hantke D., Inokuti M. and Paretzke H.G. (1998): Electron inelastic-scattering cross sections in liquid water. Rad Phys Chem **53, no. 1**, 1–18

Fischer B.E. (1985): The scanning heavy ion microprobe at GSI. Nucl Instr Meth Phys Res B **10/11, no. 2**, 693–696

Fischer B.E., Heiss M. and Cholewa M. (2003): About the art to shoot with single ions. Nucl Instr Meth Phys Res B **210**, 285–291

Folkard M., Vojnovic B., Prise K.M., Bowey A.G., Locke R.J., Schettino G. and Michael B.D. (1997): A charged-particle microbeam: I. Development of an experimental system for targeting cells individually with counted particles. Int J Rad Biol **72, no. 4**, 375–385

Folkard M., Vojnovic B., Hollis K.J., Bowey A.G., Watts S.J., Schettino G., Prise K.M. and Michael B.D. (1997): A charged-particle microbeam: II. A single-particle micro-collimation and detection system. Int J Rad Biol **72, no. 4**, 387–395

Friedl A.A., Quicken P. and Kellerer A.M. (2003): Analyse räumlich korrelierter DNA-Schäden zur Bestimmung der relativen biologischen Wirksamkeit dicht-ionisierender Strahlung (BMU – 2003-616) [online]. Bundesministerium für Umwelt, Naturschutz und Reaktorsicherheit, Germany. Available from: http://www.bmu.de/strahlenschutz/doc/text/2476.php (accessed 28 September 2006)

Friedland W., Jacob P., Paretzke H.G. and Stork T. (1998): Monte Carlo simulation of the production of short DNA fragments by low-linear energy transfer radiation using higher-order DNA models. Rad Res **150**, 170–182

Friedland W., Jacob P., Paretzke H.G., Merzagora, M. and Ottolenghi, A. (1999): Simulation of DNA fragment distributions after irradiation with photons. Rad Env Biophys **38, no. 1**, 39–47

Friedland W., Jacob P., Bernhardt P., Paretzke H.G. and Dingfelder M. (2003): Simulation of DNA damage after proton irradiation. Rad Res **159, no. 3**, 401–410

Friedland W., Dingfelder M., Jacob P. and Paretzke H.G. (2005): Calculated DNA double-strand break and fragmentation yields after irradiation with He ions. Rad Phys Chem **72, nos 2–3**, 279–286

Greif K.D., Brede H.J., Frankenberg D. and Giesen U. (2004): The PTB single ion microbeam for irradiation of living cells. Nucl Instr Meth Phys Res B **217, no. 3**, 505–512

Hall E.J. (2000): Radiobiology for the Radiologist, 5th edn. Philadelphia: Lippincourt Williams & Wilkins.

Hauptner A., Dietzel S., Drexler G.A., Reichart P., Krücken R., Cremer T., Friedl A.A. and Dollinger G. (2004): Microirradiation of cells with energetic heavy ions. Rad Env Biophys **42, no. 4**, 237–245

IAEA (1995): Atomic and molecular data for radiotherapy and radiation research (IAEA-TECDOC-799), page 440 [online]. IAEA (International Atomic Energy Agency), Vienna, Austria. Available from: http://www-pub.iaea.org/MTCD/publications/PDF/te_799_prn.pdf (accessed 28 September 2006)

Jakob B., Scholz M. and Taucher-Scholz G. (2003): Biological imaging of heavy charged-particle tracks. Rad Res **159, no. 5**, 676–684

Krämer M. and Kraft G. (1994): Calculations of heavy-ion track structure. Rad Env Biophys **33, no. 2**, 91–109

Michael B.D. and O'Neill P. (2000): A sting in the tail of electron tracks. Science **287** (5458), 1603–1604

Nikjoo H., O'Neill P., Terrissol M. and Goodhead D.T. (1999): Quantitative modelling of DNA damage using Monte Carlo track structure method. Rad Env Biophys **38, no. 1**, 31–38

Randers-Pehrson G., Geard C.R., Johnson G., Elliston C.D. and Brenner D.J. (2001): The Columbia University single-ion microbeam. Rad Res **156, no. 2**, 210–214

Xapsos M.A. (1992): A spatially restricted linear energy transfer equation. Rad Res **132**, 282–287

Ziegler J.F. and Biersack J.P. (2003): The stopping and range of ions in matter (SRIM2003) [online]. Available from: http://www.srim.org (accsessed 28 September 2006)

Magnetic Confinement Fusion: Ions in ITER – Beams and Surfaces

A.W. Kleyn[1,2,⋆]

[1]FOM-Institute for Plasma Physics Rijnhuizen
Association Euratom-FOM, Trilateral Euregio Cluster
Nieuwegein, The Netherlands
[2]Also at: Leiden Institute of Chemistry, Leiden University
Leiden, The Netherlands

Abstract

Ions play a dominant role in the experimental fusion reactor ITER. In this article some aspects of ion interactions will be discussed briefly: fast ion beams to produce fast neutral beams used for current drive and heating, and plasma surface interaction. The fusion plasma with a typical temperature of several tens of keV has to be brought into contact with a physical wall in order to remove the helium produced and drain the excess energy in the fusion plasma. Without cooling, the plasma would degrade the wall and the debris from the wall would extinguish the plasma. Therefore, schemes are developed to cool the plasma edge. The resulting plasma-surface interaction concerned in ITER is facing several challenges including surface erosion, material redeposition and tritium retention.

Contents

1 Introduction **88**

2 ITER and Fusion Energy **89**

3 Neutral Beam Heating **92**

⋆ E-mail: kleyn@rijnh.nl

4 Plasma-Surface Interaction in Fusion Devices **94**
4.1 Divertor Physics 96
4.2 Wall Materials and Lifetime 98
4.3 Tritium Retention 100
4.4 Research on ITER Relevant Plasma Surface Interaction 100

5 Experiments to Study ITER Relevant Plasma-Surface Interaction **101**

6 Conclusions **104**

Acknowledgements **105**

References **105**

1. Introduction

Ion beams provide unique opportunities to probe and modify matter as witnessed at the ION06 conference and the present volume. Ions created in a dedicated source have properties that can be tailored very precisely in an ion beam. Consequently, such beams have important applications in determining surface and interface structure, and in addition in modification of materials near a surface. Another way to produce quasi unbound ions is in plasma. In the plasma the total charge state is zero, it is quasi neutral, but the properties of the plasma can widely vary because the ion and electron translational temperatures in the plasma can vary from close to zero to phenomenal, multi keV temperatures in laboratory plasma and stars (McCracken and Stott, 2005). In fact, the plasma state is the predominant state of matter in the universe.

Fusion of light elements is the energy source of the stars and when carried out in a controlled fashion would make an almost unlimited amount of energy available on earth. There is two ways to achieve this in principle: inertial confinement fusion where the density and temperature of a small volume are raised to extreme levels during very short pulses, as discussed elsewhere at this conference, and magnetic confinement fusion, in which the nuclei to be fused are magnetically confined in a hot (tens of keV) plasma for so long, that a stable plasma heated internally by nuclear fusion reactions can deliver excess energy to the outside world. Very recently, a major step towards the realisation of fusion energy has been taken. On June 28th 2005, the ITER partners China, the European Union, Japan, the Russian Federation, South Korea and the USA agreed to construct ITER in Cadarache, France. ITER is the large international fusion reactor and a major step on the way (ITER is Latin for "the way") to commercial exploitation of nuclear fusion for the production of electricity. Later India joined the project, and

it is expected that before the end of 2006 all treaties bringing ITER into existence will have been signed and ratified by all parties concerned.

ITER is a fusion reactor of the "tokamak"-type, in which a hydrogen plasma is confined in a torus by means of strong magnetic fields (Braams and Stott, 2002; McCracken and Stott, 2005). ITER must demonstrate tenfold power multiplication in a controlled fusion process, at a power level in excess of 500 MW and during pulses of 10 minutes or longer. Experiments with ITER should lead to the solution of the remaining physics problems on the way to fusion (ITER Physics Basis Editors et al., 1999). It will be used to address a number of technological issues that will be important in the construction of commercial reactors (ITER; Ongena and vanOost, 2002; Samm, 2003; Lister and Weisen, 2005).

In ITER's very large vacuum vessel, filled with plasma with a degree of ionization of unity, a very high temperature can be realized. Therefore, ITER is a place where many complex interactions involving ions take place. In this article I will only mention two, the use of ion beams to heat the plasma, and the interaction of the plasma and the physical wall of the device.

2. ITER and Fusion Energy

Nuclear fusion reactions proceed only at temperatures which are roughly six orders of magnitude higher than those required for regular chemical reactions, because of the Coulomb repulsion of the nuclei concerned. The reaction with the lower activation energy is the one between deuterium and tritium. This is the reaction of choice in ITER:

$$^2\mathrm{D}^+ + {}^3\mathrm{T}^+ \rightarrow n + {}^4\mathrm{He}^{++} + 17.6\ \mathrm{MeV}.$$

For comparison we list the energetics of carbon monoxide combustion:

$$2\mathrm{CO} + \mathrm{O}_2 \rightarrow 2\mathrm{CO}_2 + 10\ \mathrm{eV}.$$

The six orders of difference in magnitude of the barrier is reflected in the exothermicity of the two reactions. Per unit of mass of the "fuel" the energy release of the fusion reaction is even seven orders of magnitude larger than that of the chemical reaction.

Most (80%) of the energy of the DT-fusion is carried away by the neutron. It is captured in a blanket containing Li, in a reaction in which also tritium is regenerated:

$$^6\mathrm{Li} + n \rightarrow {}^3\mathrm{T} + {}^4\mathrm{He} + 4.78\ \mathrm{MeV}.$$

This yields the overall reaction equation for a fusion reactor:

$$^2\mathrm{D} + {}^6\mathrm{Li} \rightarrow 2\,{}^4\mathrm{He} + 22.4\ \mathrm{MeV}.$$

This reaction shows that ^{2}D and ^{6}Li constitute the fuel for fusion. ^{2}D and ^{6}Li are abundantly available. The exhaust of a 1 GigaWatt fusion plant is only 250 kg of benign He per year. The latter is to be compared to 7.2×10^9 kg of CO_2, which is released by a 1 GigaWatt coal fired power plant.

The DT fusion reaction is not a chain reaction, a fusion reactor cannot have an energetic runaway. A fusion reactor is thus inherently safe and will not cause a nuclear explosion. Some components inside the fusion reactor become activated during the operational lifetime, but the total radio toxicity decays rapidly, dropping by four orders of magnitude within the first 100 years, to a level that allows recycling of the material. In addition, operation of a fusion plant does not require transport of radioactive fuel or waste. The fuel is abundant, practically unlimited, very cheap, and available to everyone, which could greatly reduce political tension. Fusion is one of the few options for large scale power generation. In summary, a fusion plant would be a very desirable addition to the world's capabilities to generate energy in a sustainable fashion.

The rate coefficient $\langle \sigma v \rangle$ for the DT- reaction peaks at a value of 10^{-21} m^{-3}s^{-1}. The peak occurs at a Maxwellian temperature of 70 keV. For the fusion power output also the ion density plays an important role. For a given product of density and temperature (pressure) we find that the maximum output of fusion power is given around an operation temperature of a fusion reactor of 10–30 keV. At those temperatures all light atoms are fully stripped of their electrons. Obviously, the contact of the hot plasma with a material wall has to be avoided, because the wall will be evaporated, the evaporated matter will be ejected into the hot plasma, and the plasma will be extinguished by the resulting fast cooling. In ITER, and other so-called Tokamak reactors this is done by confining the plasma in a doughnut-shaped magnetic field. In the picture of ITER in Figure 1, the doughnut-shaped plasma chamber, surrounded by magnets, can clearly be seen. The magnetic field is so strong that the ions and electrons can only move along the field lines, reducing the plasma transport perpendicular to the magnetic field lines by 14 orders of magnitude. This brings the thermal conduction of the hot plasma to the wall down so much, that a temperature difference of 100 Million K over a distance of about a meter can be sustained. The magnetic field is produced by superconducting coils, which implies that the vacuum vessel of ITER containing the hottest (macroscopic) volume on earth is placed inside the worlds largest liquid-He cryostat.

Perhaps the most crucial element of magnetic confinement fusion is the stability of its confinement. Most efforts of the fusion community in the past have been

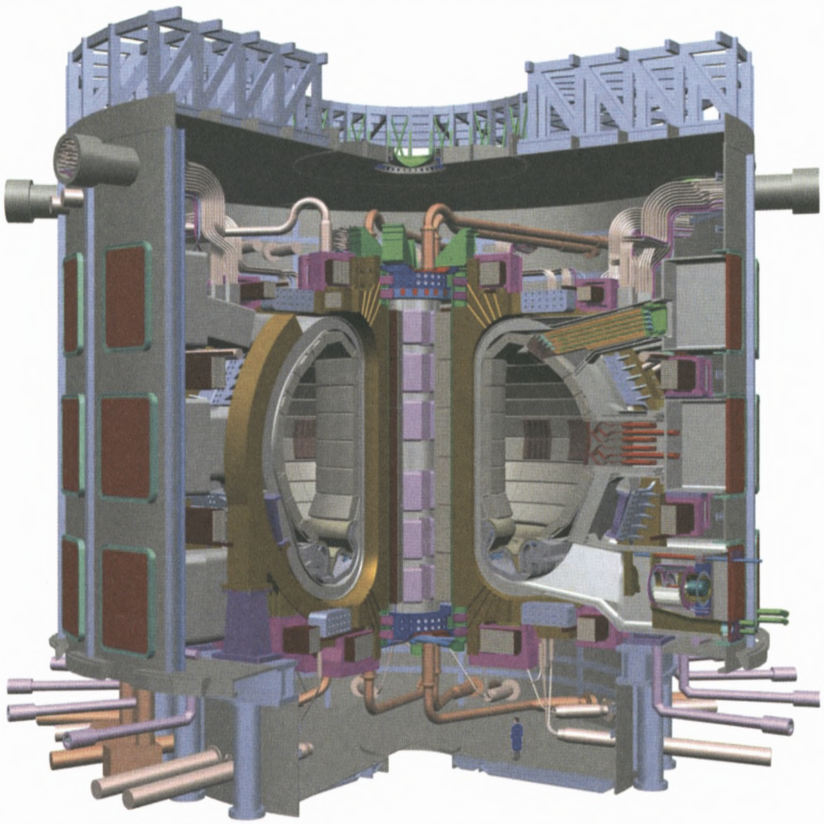

Figure 1. Artists view of ITER. The toroidal plasma chamber is clearly visible. Some parameters are: major radius 6.2 m; minor radius, 2 m; vertical elongation, 1.86; plasma current, 15 MA; magnetic field, 5.3 T; plasma volume, 850 m3; fusion power, 500 MW; power multiplication Q, 10. From (ITER).

devoted to proper confinement of the plasma and major breakthroughs have been realised. This is nicely illustrated in Figure 2, where the experimental confinement time of plasma in many different tokamaks is plotted against the confinement time as derived from various models. From the figure it is clear that ITER is a direct extrapolation from existing machines and scaling such as the one shown here demonstrate that ITER will be built on very solid grounds. Nevertheless, ITER is a scientific experiment and the last step between fusion science and fusion reactor engineering. It is obvious, that this article is not the place to discuss the scientific issues for ITER in any detail. The reader is referred to other sources, notably

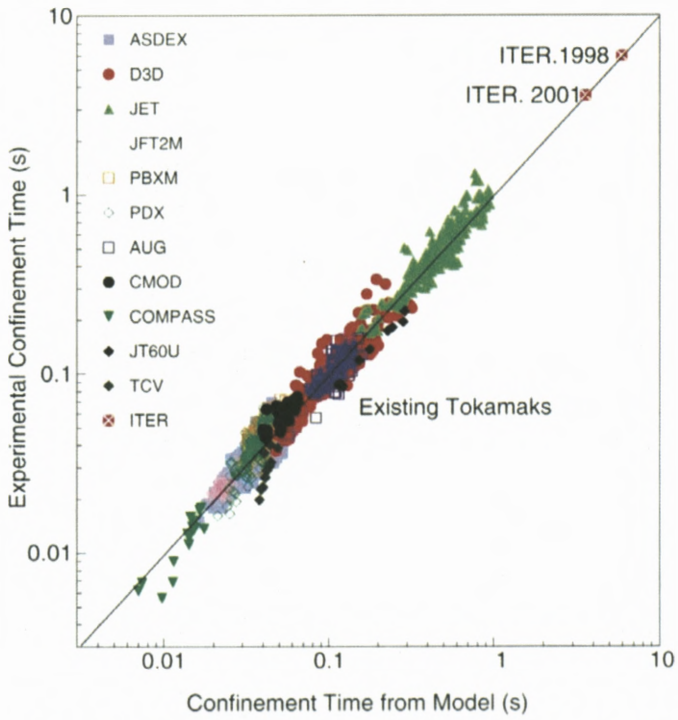

Figure 2. Experimental data from all the major tokamaks in the international fusion program, showing how the measured confinement time fits model calculations of the confinement time. Extrapolating this scaling, the confinement time is predicted to be almost an order of magnitude higher for the present and previous ITER design. The confinement time is a measure how much external energy needs to be provided to run the tokamak in steady state. From McCracken and Stott (2005).

also on the web (ITER; Samm, 2003). In this report we limit ourselves to briefly introducing neutral beam heating and plasma-surface interaction.

3. Neutral Beam Heating

The very high temperatures of many keV in a fusion reactor can only be created by extensive heating systems. In Tokamaks several heating schemes are used (Braams and Stott, 2002; McCracken and Stott, 2005). Each of these schemes should be able to deposit tens of MW's into the plasma. Using a coil around the inner structure of the tokamak, inside the doughnut, as the primary winding of a transformer, currents can be induced in the plasma, which lead to Ohmic heating. Besides, electromagnetic radiation of several frequencies can be employed to resonantly

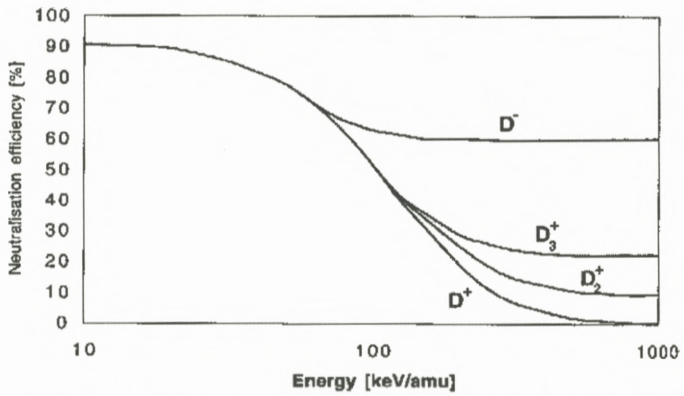

Figure 3. Neutralization rate for hydrogenic ions in a gas neutraliser as a function of the ion energy. The figure demonstrates that for high neutral beam energies, negative ion beams have to be used. From Koch (2006).

heat modes of motion of either the electrons or the ions. Finally, the plasma can be heated and directional current can be driven by injecting energetic hydrogenic ions into the plasma (Pamela, 1995). Due to the very strong magnetic field of tokamaks these particle beams can not be charged when entering the tokamak through the magnetic field. The ions would be deflected away from the plasma. Therefore, ion beams need to neutralized before passing through the magnetic field into the plasma. In the plasma the neutral beam will be gradually ionized. The easiest way to neutralise ion beams is by using a gas neutraliser. The efficiency of neutralization in this case is plotted in Figure 3 (taken from Koch, 2006). It is clearly seen that for positive ions the neutralization efficiency drops markedly above 100 keV. The reason for this is that at the corresponding velocities the nuclear velocity is much higher than the classical orbit velocity of an electron in a hydrogen atom, and those electrons would have to "jump" on to the moving deuteron. Conversely, a negative ion can easily detach its most weakly bound electron at any velocity. Since each neutral beam heating system has to deposit several MW into the core of plasma, neutral beam energies of 1 MV or more are foreseen to obtain the proper penetration, and those cannot be realized starting by using positive ion sources. Negative ion beam based neutral beam heating is applied on several machines and a representative example is shown in Figure 4, where the neutral beam heating system of the large helical device (LHD) in Japan is shown (Kaneko et al., 2003). The LHD is not a tokamak but a stellerator, another type of magnetic confinement. From the overview drawing it can be seen that the neutral beam injection system consists of a negative ion source, followed by a

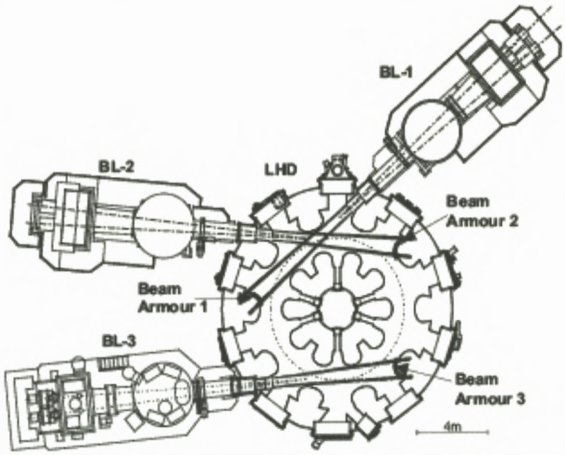

Figure 4. Arrangement of beam lines and the location of beam armour plates in the vacuum vessel of the Large Helical Device in Japan. Three tangential beam lines are installed, and each beamline has two negative ion sources side by side, followed by a single neutraliser. Note the scale in the lower right. From Kaneko et al. (2003).

gas neutraliser. In 2002 the total power of the three beams was about 10 MW, at acceleration voltages of 160–180 keV, and pulse lengths of 2 s. The interaction between the beam and the plasma is a complex issue not to be addressed here. In fact, the stopping power of the fusion plasma is a property analogous to the well know stopping power for ions in solids. If under circumstances not all the power available in the beams is transferred to the plasma, the walls might be damaged. Therefore, special armour is installed to protect the vacuum vessel to the very high power load imposed by the beams. For ITER the building of megavolt accelerators of multi-ampere D^- beams will be a major challenge.

4. Plasma-Surface Interaction in Fusion Devices

Another major area where ion interactions play a crucial role is where energetic ions hit physical surfaces. This is part of the well studied field of plasma-surface interaction (PSI). This is an area of very exciting research, where PSI in ITER will be radically different from PSI in its predecessors, and in other areas such as plasma etching (Winters and Coburn, 1992). A typical plasma pulse in a contemporary, non-superconducting tokamak lasts at most tens of seconds. An ITER pulse will last at least 500 seconds and continuous operation is foreseen. While the electron, ion and power fluxes to the wall in ITER will be only a factor of 2–3 higher, the accumulated particle and energy loads of the surfaces concerned

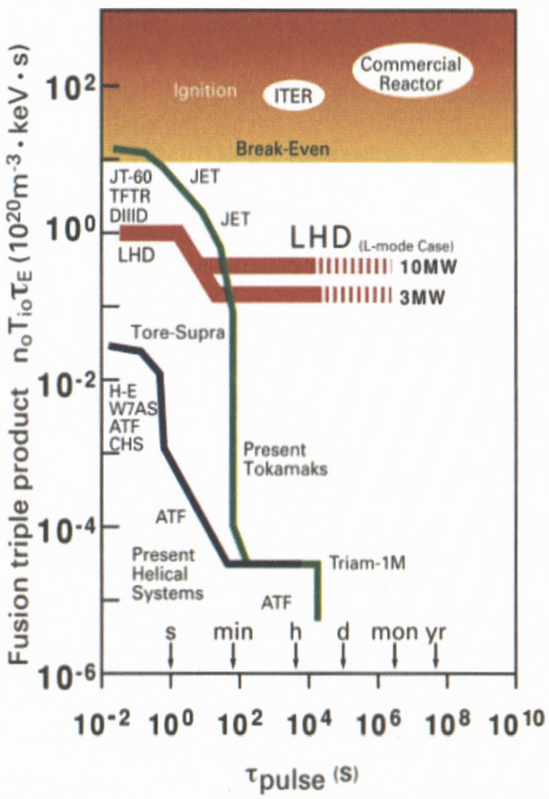

Figure 5. Parameter space for fusion devices plotted against fusion triple product, a measure for confinement, and pulse duration. It is clear that most devices operate at short pulses and that up to now the path towards a working reactor was chosen to follow an increase in triple product first, only later to be followed by long pulse experiments. From the website of the large helical device: http://www.lhd.nifs.ac.jp/en/home/lhd.html.

in ITER will be up to 4 orders of magnitude higher than for the earlier machines. In terms of wall-load, a single ITER pulse is comparable to at least a year of operation of JET, presently the largest fusion device in the world. It is a very large challenge to construct walls that can sustain the loads to be expected in ITER. It is a very interdisciplinary problem (Kleyn et al., 2006b).

The development of fusion devices and PSI therein can be summarized very nicely with Figure 5. Here is plotted the performance of various machines as a function of the fusion triple product, the key figure of merit for reaching ignition in a magnetic confinement device, and the pulse duration (Braams and Stott, 2002; Motojima et al., 2002, 2004; McCracken and Stott, 2005). It is seen that most

effort has been devoted to reach very high plasma densities, high temperatures and sometimes even break even for a short time. It is also seen that there are devices such as Triam in Japan, Tore Supra in France, and LHD in Japan, where plasma operation for extended periods was achieved, but at lower plasma performance (see e.g. Mutoh et al., 2006). In ITER the ambitious goal is sustained burn with a power amplification of 10, which is a formidable job as far as PSI is concerned.

The first PSI question to be addressed here is: where does the plasma hit the surface and why (Federici et al., 2001, 2003; Philipps, 2002, 2005; Philipps et al., 2003 Samm, 2002, 2003, 2005)? The primary wall is supposed to be completely protected against impact of the plasma by the confining magnetic field. Diffusion across this field is strongly suppressed. But some diffusion across the field always occurs. Delicate equipment inside the toroidal plasma chamber is protected from plasma impact by so-called limiters. Impact on those devices is also unlikely under normal conditions, but they are designed to take a large power load in exceptional cases. In the so-called divertor the plasma is deliberately brought in contact with the wall. The reason for this is simple: in a burning DT-plasma He is produced. If the He remains in the core of the plasma, it will gradually dilute the burning DT mixture, and eventually extinguish the nuclear fire. In addition, the heating power released into the plasma volume by the He^{++} formed and the initial external heating has to be exhausted via the wall.

4.1. Divertor Physics

In Figure 6 a cross section perpendicular to the toroidal field shows the divertor. The magnetic field surrounding the plasma core is designed to block any transport across it to the wall. The field lines form nested flux surfaces as shown on which the particles run around the torus according to their thermal speed. The outmost of such magnetic flux surfaces is called "last closed flux surface" or LCFS. Below the LCFS the so-called X-point is shown. The magnetic field lines outside the LCFS are designed to intersect the wall in the divertor region. Plasma that by diffusion has moved outside the LCFS in the divertor region will eventually hit the divertor surface. The angle between magnetic field lines and divertor surface is very small, a few degrees only, to reduce the specific heat load.

At the divertor plate the ions from the plasma are neutralised on the surface. The neutralization step will result in electron or photon emission and surface heating. In addition, neutral particles will be formed on the surface, that leave the divertor plates as atoms, molecules, clusters or even dust particles and are reionized when entering the plasma. Once ionised the magnetic field guides the ions and the plasma flow forces them to return to the surface, where again neutralisation occurs. Resonant charge transfer reactions with neutral gas produces

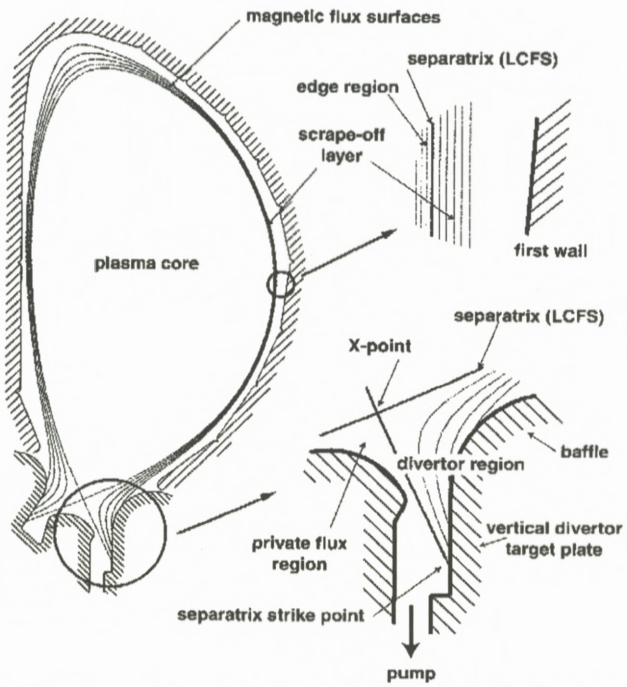

Figure 6. Poloidal cross section of a tokamak, defining the various regions of the plasma and the boundary walls. Important regions are: the plasma core, the edge region just inside the separatrix, the scrape off layer outside the separatrix and the divertor region, which is an extension of the scrape off layer plasma along field lines into the divertor chamber. The divertor structure is designed to prevent neutrals from leaving the divertor. In the magnetic flux region below the X-point, the magnetic field lines are spiralling downward to intersect the wall at the vertical divertor target plates, and are isolated from the rest of the plasma. In the divertor region intense plasma surface interaction will take place. From Federici et al. (2001).

hot, electronically excited neutral atoms, which exhaust a significant fraction of plasma energy by radiation onto large sections of the walls when leaving the plasma. In addition, neutrals and impurity ions are excited by electron impact which leads to more electromagnetic radiation. Electrons and ions originating from the core plasma are thus effectively cooled by radiation and charge exchange processes from the keV range to preferably below 1 eV (Samm et al., 1993; Samm, 2002). The plasma ions can undergo many neutralization-reionization cycles before they leave the plasma regions as neutrals towards the vacuum pumps under the divertor. At plasma temperatures around a few eV inside the divertor the plasma is in a so-called detached state (Stageby, 2000). The surface is thus protected by a dense plasma with a low degree of ionization. This dissipative layer

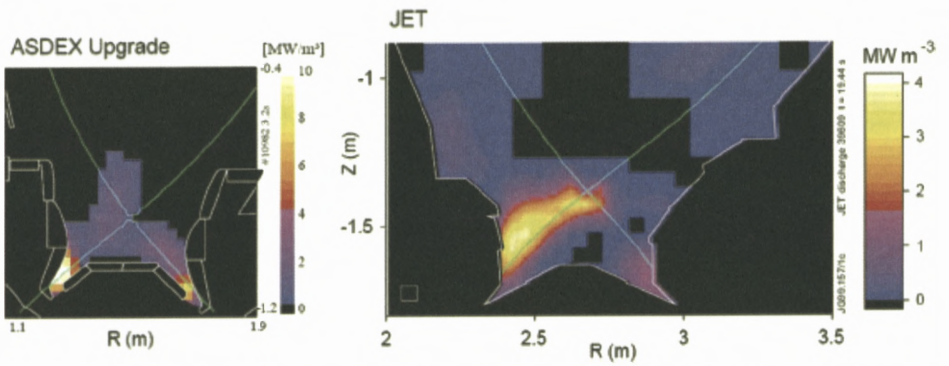

Figure 7. A vertical cross section through the ASDEX and JET tokamaks, with a measurement of the emission from the plasma. It is clear that below the X-point the plasma is efficiently cooled by radiation, and that the maximum of the radiation is detached from the divertor surfaces. From Kallenbach et al. (1999).

that radiates large amounts of the power carried by the incident plasma has been studied extensively, and a nice view on it is reproduced in Figure 7 (Kallenbach et al., 1999). It is seen that most of the power radiated does not come from the surface region but slightly above it. The plasma is detached from the wall and the wall is protected by it. Nevertheless, the power load on the surface of the divertor in steady state is still formidable in ITER, up to 10 MWm^{-2}.

4.2. Wall Materials and Lifetime

The materials of the various walls are of critical importance, because they might be emitted in some form into the divertor plasma, contributing to the plasma chemistry and to the radiation level in the plasma. The role of the divertor surface and its material composition require much more study. Requirements for divertor materials are:

- Good thermal and electrical conductivity,
- Low probability of ending up in the core plasma, and
- If ending up in the core plasma: low Z.

The low Z requirement follows from the fact, that ions which are not fully stripped act as a heat sink in the plasma, due to continuous excitation/de-excitation cycles of inner shell electrons by plasma electrons. If the plasma can be tailored such, that divertor material will never end up in the core, the low Z requirement can

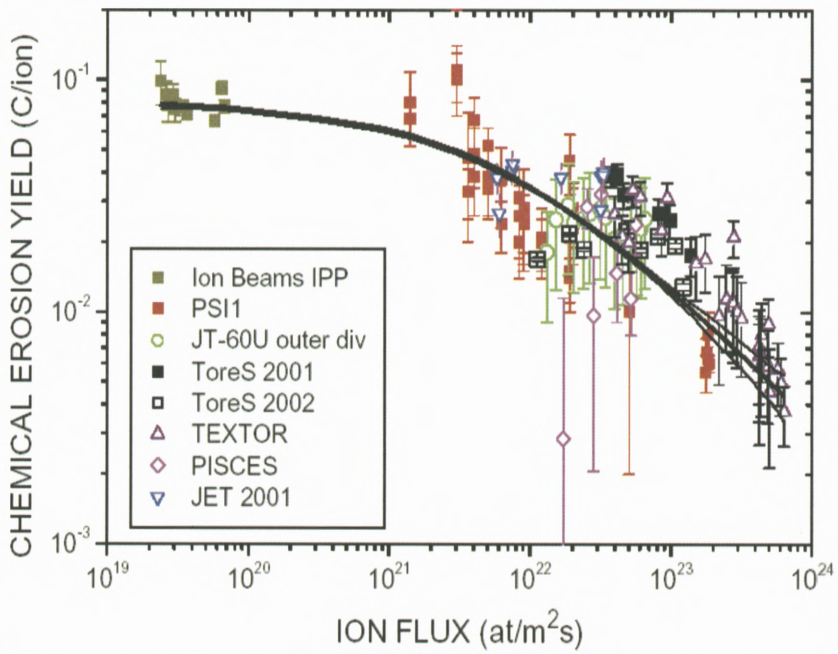

Figure 8. Erosion rates for Carbon surfaces by low temperature plasma. From Roth et al. (2005).

be relaxed. Because this is not yet completely certain, the provisional choice of materials for ITER is:

- W for limiters,
- Be for the primary wall, and
- Carbon for the divertor target plates.

The argument in general for this choice is beyond the present paper, and the reader is referred to other papers (Federici et al., 2001, 2003; Samm, 2003). Some arguments will be touched on later in this article.

The erosion rate for carbon surfaces as a function of the incident plasma flux is shown in Figure 8 (from Roth et al., 2005). What is seen is that the erosion rate drops remarkably with the incident flux. This might be at first sight very surprising, because several erosion mechanisms such as physical sputtering or chemical etching can be expected to be linear in the flux of the etching particle. This is because the PSI enters into the so-called strongly coupled regime (Kleyn et al., 2006a). This means that the mean free path of the plasma particles and the etch products is much smaller than the system size. The particles can simply

be atoms, but also hydrocarbon molecules and even carbon containing dust. Dust particles in the critical size range of 1–10 nanometres are thought to play an essential role (Hollenstein et al., 1996; Hollenstein, 2000; Winter, 2000). The particles produced at the surface are interacting in the plasma, getting reionized and are redeposited at the surface, because these ions are confined by the strong magnetic field available. The eroded particles are thus effectively recycled near the surface. The higher the plasma flux, the higher the recycling probability and thus the lower the effective erosion yield. In fact, in certain regions deposition will be the result of the recycling in the strongly coupled region and wall material can effectively be transported inside the machine. This has important consequences when tritium is present in the machine.

4.3. Tritium Retention

Because tritium is radioactive, most of the tritium should be in the plasma volume or in the gas processing plant, but not retained or trapped elsewhere. Hydrogen and its heavier isotopes deuterium and tritium can be adsorbed with long residence time in deep pores in the walls. In addition, they readily form compounds with carbon. In these compounds the deuterium and tritium present in a fusion reactor are not available for the fusion reactions in the plasma, but are retained somewhere in the vacuum vessel or walls. For hydrogen and deuterium this is only an operational problem, because there is hardly an upper limit to the amount of hydrogen in a tokamak. For tritium the retention in the walls is a serious problem, because the amount of tritium allowed in the reactor is small.

From present tokamak experience it is definitely concluded that the overwhelming majority of the long term tritium retention is due to co-deposition of tritium along with eroded carbon forming tritium saturated carbon co-deposits. Like H and D, T is very reactive with carbon and can form a variety of molecules. To evaluate the scientific basis of this process and to improve our predictions for future devices comprehensive action is needed. The reactivity of D and T will be considered to be similar, so that the majority of studies can be carried out with D.

4.4. Research on ITER Relevant Plasma Surface Interaction

Of course ITER itself will serve as an important test bed for the divertor design. However, supporting experiments in smaller devices are indispensable in approaching a deeper understanding of the processes. The issue of PSI and wall materials in reactor conditions is far from settled. Tokamaks are needed to study the complex interplay of main chamber plasma and divertor plasma in toroidal geometry. The most important large scale experiment in this context is planned

to be conducted on JET by modifying the JET wall with an ITER-like mix of materials (www.JET.org). On a smaller scale, but addressing the processes in more detail with specialised diagnostics, experiments on plasma-wall interaction are performed on other tokamaks, like e.g. on TEXTOR in Jülich. TEXTOR is operated by the Trilateral Euregio Cluster collaboration (TEC: FOM Institute for Plasma Physics Rijnhuizen The Netherlands, Institute for Plasma Physics Forschungszentrum Jülich Germany, Royal Military School Brussels Belgium). However, most present tokamaks are short-pulsed compared to ITER. Their rather small duty cycle and lack of easy access for PSI diagnosis give rise to uncertainties with respect to long term erosion and deposition processes. From this problem the need for steady-state experiments with the relevant PSI parameters will be obvious. Such experiments should allow addressing the issues discussed above in an open and well-accessible, steady state flexible laboratory environment. The accessibility allows the use of *in-situ* real time plasma and surface diagnostics, so that processes can be studied while they happen, with the plasma on. Samples should be transferable, if necessary under vacuum, to surface analysis facilities. Modifications, changes to materials etc should be introduced relatively quickly. Thus, smaller scale laboratory experiments, with steady-state capability and heavily equipped with diagnostic tools, will complement the studies of plasma-wall interaction in tokamaks.

5. Experiments to Study ITER Relevant Plasma-Surface Interaction

The ideal experiment is sketched in Figure 9. Essentially, a small slice out of the circular ITER divertor is taken. Please note that the ITER magnetic field is almost perpendicular to the plane of the paper. In fact, in ITER the magnetic field intersects the divertor plates at an angle of a few degrees. Above it, a plasma generator needs to be build delivering a plasma of ITER-like characteristics with a temperature and density that is high enough that the plasma will diffuse perpendicular to the field lines and intersect the surfaces to be studied with the ITER-like powers and fluxes. Basically, this is not possible, because such a plasma generator does not exist, other than a real Tokamak that the smaller scale experiment tries to mimic but not to copy. The only way to realise such an experiment is to use the geometry given in Figure 10.

A plasma source delivers the plasma the required energy and particle density. This plasma is magnetically confined and impinges on a target at grazing incidence. The device has opportunities for heating the plasma by radio-frequency radiation, and by biasing the target. It should be noted that the similarity to the ITER case and Figure 10 is limited. The aim in the linear experiment of Figure 10

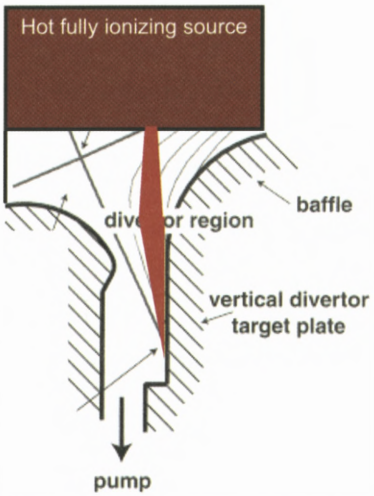

Figure 9. Schematic diagram showing how to construct an experiment to mimic interactions at the ITER divertor. The divertor region is taken from Figure 6.

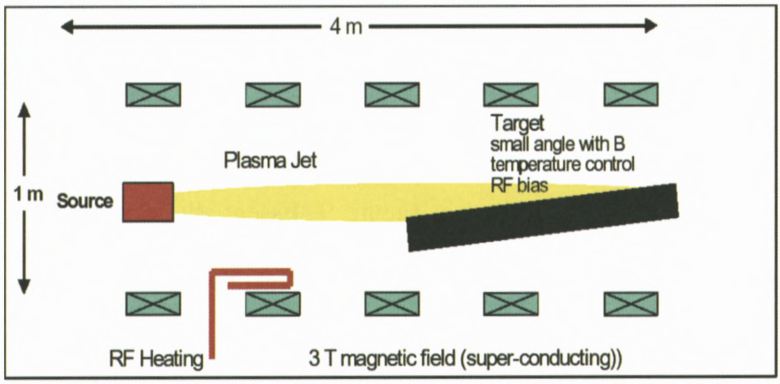

Figure 10. Schematic drawing of a linear experiment to study plasma surface interaction.

is to have conditions similar to those in ITER in the last 1–2 centimetres before the target plate.

As part of the TEC collaboration and within the framework of Euratom the FOM Institute is building a new machine, Magnum-psi, providing an important new experimental facility in the range of experiments that are available to PSI research for ITER and reactors beyond ITER (Groot et al., 2005; van Eck et al., 2005). The uniqueness of Magnum-PSI lies first in its ability to access simultane-

ously the multitude of aspects of PSI in the combination of which ITER differs essentially from present day experiments:

1. Large ion fluence and continuous operation, which leads to "macroscopic" modification of plasma-facing surfaces.
2. High power density (5–10 MWm^{-2}) with low plasma temperature (<5 eV) such that materials are close to, or at the energy threshold for sputtering, but have high surface temperature and are therefore near their materials limits for stress/strain, etc.
3. Strong plasma-surface coupling: the high plasma density leads to short mean free paths for dissociation/ionisation of eroded atoms or molecules in comparison with the linear dimensions of the plasma.
4. Access to plasma diagnostics and *in-situ* surface analysis.

With a steady-state high flux of up to 10^{24} ions $m^{-2}s^{-1}$ at a plasma temperature in the eV range, a magnetic field of 3 T, and large beam diameter, Magnum-psi will be a unique experiment, bringing the relevant parameters typically an order of magnitude beyond what is presently available in linear plasma devices, and into the realm of the ITER divertor.

A device providing the parameters as described above is currently not available to the magnetic fusion community although a number of smaller devices do exist, following the basic design of Figure 10. These include the PISCES experiment at the University of California in San Diego (Hollmann et al., 2002), the PSI-2 experiment at the Humboldt University in Berlin (Grote et al., 1997), the NAGDIS-II at the Nagoya University (Hollmann et al., 2001), and the Pilot-PSI experiment at FOM Rijnhuizen (de Groot et al., 2003, 2005). The latter device, Pilot-PSI, is shown in Figure 11. The plasma generator, a high pressure cascaded arc source, can be seen clearly at the left (VanDeSanden et al., 1992). The cylindrical vacuum vessel is surrounded by magnetic field coils (blue and yellow). The target is at the right of the vessel, and not visible in the figure. The vacuum (roots) pump is at the far right. This experiment has a number of characteristics of the Magnum-PSI experiment. The ITER-like flux needed in those experiments has been demonstrated recently at our laboratory and dramatically high etching rates have been shown. These rates are way off the curve of Figure 8. It demonstrates that in the small linear device Pilot-PSI the erosion products are not recycled, and real ITER relevant experiments can only be carried out if recycling takes place in the experiment. In Magnum-PSI the dimensions and density of the plasma will be sufficiently large to ensure recycling. Another difference between Pilot-PSI and the ITER divertor region is, that the pressure in the Pilot vessel can considerably exceed

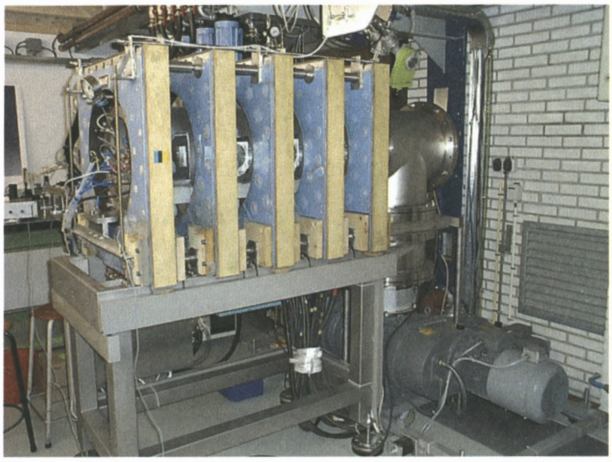

Figure 11. Picture of the Pilot-PSI experiment.

the one near the ITER divertor, a few Pa, because the degree of ionization of the plasma as it exits the source is only 10% or so, and in contrast to ITER, where it is 100%. Therefore, a linear simulator based upon high pressure cascaded arc plasma generators needs differential pumping to make sure, that the neutral gas around the target plates is only created by neutralization of the plasma, not by a steady flux from the source. In the design of Magnum-PSI this differential pumping has been incorporated, as can be seen in a schematic drawing in Figure 12. In this drawing one sees the vacuum vessel, moved into a large bore superconducting magnet. To the right of the magnet the target chamber with tubing to its pumps and an analysis chamber for the retractable target can be seen. In the main vacuum vessel one sees from left to right the source, a skimmer leading to the heating chamber followed by the target irradiation chamber. Magnum-PSI is described in more detail in other papers (vacuum) (de Groot et al., 2005; van Eck et al., 2005).

6. Conclusions

Plasma-surface interaction will be one of the areas determining the availability of ITER and the ultimate viability of generating fusion power under steady state conditions. Erosion and redeposition, handling the steady state power, and preventing tritium retention by the walls, are issues to be solved for and by ITER. Although a lot of knowledge is available an extension of our knowledge base at all levels is necessary for the ultimate success of ITER.

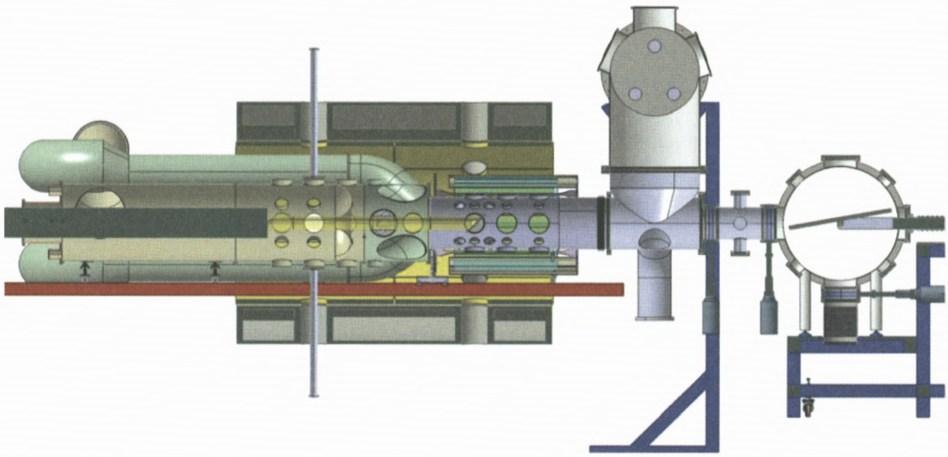

Figure 12. Total overview of the Magnum-PSI experiment with target station and target manipulator. Shown are (from left to right) the source-, heating- and target chamber with pump ducts. Next to these, the pumping station for the third stage is shown. On the right hand side, the target station with target and target manipulator are visible. In the target analysis station, the targets can be analyzed in detail with surface analysis equipment.

Acknowledgements

The author thanks all members of the Pilot-PSI and Magnum-PSI teams for their contributions to this article. He thanks Dr. Tony Donne and Dr. K. Tsumori for their comments on the manuscript. This work, supported by the European Communities under the contract of Association between EURATOM and FOM, was carried out within the framework of the European Fusion Programme with financial support from NWO. The views and opinions expressed herein do not necessarily reflect those of the European Commission

References

Braams C.M. and Stott P.E. (2002): Nuclear Fusion, Half a Century of Magnetic Confinement Fusion Research. IOPP, Bristol

de Groot B. et al. (2003): Magnum-psi, a new linear plasma generator for plasma-surface interaction studies in ITER relevant conditions. Fusion Engineering and Design **66, no. 8**, 413–417

de Groot B. et al. (2005): Magnum-psi, a plasma generator for plasma-surface interaction research in ITER-like conditions. Fusion Engineering and Design **74, nos 1–4**, 155–159

ITER Physics Basis Editors, ITER Physics Expert Group Chairs and ITER Joint Central Team and Physics Integration Unit (1999): ITER Physics basis: Overview and summary. Nuclear Fusion **39, no. 12**, 2137–2174

Federici G. et al. (2001): Plasma-material interactions in current tokamaks and their implications for next step fusion reactors. Nuclear Fusion **41, no. 12**, 1967–2137

Federici G. et al. (2003): Key ITER plasma edge and plasma-material interaction issues. Journal of Nuclear Materials **313–316**, 11–22

Grote H. et al. (1997): Comparison of chemical sputtering yields for different graphites at high ion flux densities. Journal of Nuclear Materials **241–243**, 1152–1155

Hollenstein C. (2000): The physics and chemistry of dusty plasmas. Plasma Physics and Controlled Fusion **42**, R93–R104

Hollenstein C. et al. (1996): Anionic clusters in dusty hydrocarbon and silane plasmas. Journal of Vacuum Science & Technology A – Vacuum Surfaces and Films **14, no. 2**, 535–539

Hollmann E.M. et al. (2001): Evidence for the importance of radial transport in plasma detachment in the Nagoya University Divertor Simulator (NAGDIS-II). Physics of Plasmas **8, no. 7**, 3314–3320

Hollmann E.M. et al. (2002): Particle balance measurements during detachment in a gas-target diverter simulator. Physics of Plasmas **9, no. 4**, 1226–1232

ITER, www.iter.org.

Kallenbach A. et al. (1999): Closed divertor operation in ASDEX Upgrade and JET. Plasma Physics and Controlled Fusion **41, no. 12B**, B177–B189

Kaneko O. et al. (2003): Engineering prospects of negative-ion-based neutral beam injection system from high power operation for the large helical device. Nuclear Fusion **43, no. 3**, 692–699

Kleyn A.W., Koppers W. and Cardozo N.L. (2006a): Plasma-surface interaction in ITER. Vacuum **80, no. 10**, 1098–1106

Kleyn A.W., Lopes Cardozo N.J. and Samm U. (2006b): Plasma-surface interaction in the context of ITER. Physical Chemistry Chemical Physics **8, no. 15**, 1761–1774

Koch R. (2006): Plasma heating by neutral beam injection. Transactions of Fusion Science and Technology **49, no. 2**, 167–176

Lister J. and Weisen H. (2005): What will we learn from ITER. Europhysics News **36, no. 2**, 48–51

McCracken G. and Stott P. (2005): Fusion, the Energy of the Universe. Elsevier Academic Press, London

Motojima O. et al. (2002): Review developments of LHD experiment. Journal Plasma Fusion Research SERIES **5, no. 1**, 22–27

Motojima O. et al. (2004): Review on the progress of the LHD experiment. Fusion Science and Technology **46, no. 1**, 1–12

Mutoh T. et al. (2006): Thirty-minute plasma sustainment by real-time magnetic-axis swing for effective divertor-load-dispersion in the Large Helical Device. Physics of Plasmas **13, no. 5**, 056118

Ongena J. and vanOost G. (2002): Energy for future centuries; Will fusion be an inexhaustible, safe and clean energy source? Transactions of Fusion Science and Technology **41, no. 1**, 3–14

Pamela J. (1995): The physics of production, acceleration and neutralization of large negative ion beams. Plasma Physics and Controlled Fusion **37**, A325–A336

Philipps V. (2002): Plasma wall interaction and its control by wall conditioning. Fusion Science and Technology **41, no. 2t**, 319–329

Philipps V. (2005): Wall conditioning on TEXTOR. Fusion Science and Technology **47, no. 2**, 119–125

Philipps V., Roth J. and Loarte A. (2003): Key issues in plasma-wall interactions for ITER: A European approach. Plasma Physics and Controlled Fusion **45**, A17–A30

Roth J. et al. (2005): Flux dependence of carbon erosion and implication for ITER. Journal of Nuclear Materials **337-39, nos 1–3**, 970–974

Samm U. (2002): Radiation cooling experiments and reactor application. Fusion Science and Technology **41, no. 2T**, 352–358

Samm U. (2003): Controlled thermonuclear fusion at the beginning of a new era. Contemporary Physics **44, no. 3**, 203–217

Samm U. (2005): Textor: A pioneering device for new concepts in plasma-wall interaction, exhaust, and confinement. Fusion Science and Technology **47, no. 2**, 73–75

Samm U. et al. (1993): Radiative edges under control by impurity fluxes. Plasma Physics and Controlled Fusion **35**, B167

Stageby P.C. (2000): The Plasma Boundary of Magnetic Fusion Devices. IOPP, Bristol

van Eck H.J.N. et al. (2005): A 3 T magnet system for MAGNUM-PSI. IEEE Transactions on Applied Superconductivity **15, no. 2**, 1303–1306

VanDeSanden M.C.M. et al. (1992): A combined Thomson–Rayleigh scattering diagnostic using an intensified photodiode array. Review of Scientific Instruments **63, no. 6**, 3369–3377

Winter, J. (2000): Dust: A new challenge in nuclear fusion research? Physics of Plasmas **7, no. 10**, 3862–3866

Winters H.F. and Coburn J.W. (1992): Surface science aspects of etching reactions. Surface Science Reports **14, nos 4–6**, 162–269

High Energy Density Matter Generated by Heavy-Ion Beams, and Application to Fusion Energy

A. Blazevic[1], B. Rethfeld[1] and D.H.H. Hoffmann[1,2,⋆]

[1]Gesellschaft für Schwerionenforschung mbH
GSI-Darmstadt, Plasmaphysik
Planckstr. 1, 64291 Darmstadt, Germany
[2]Institut für Kernphysik, Technische Universität Darmstadt
Schlossgartenstr. 9, 64289 Darmstadt, Germany

Abstract

A detailed understanding of interaction phenomena of intense ion- and laser radiation with matter is important for a large number of applications in different fields of science, from basic research of plasma properties to application in energy science. Energy loss processes of heavy ions in plasma and cold matter are important for the generation of high energy density states in general and especially in the hot dense plasma of an inertial fusion target. Of special interest are phase transitions and the associated time scales when matter passes the warm dense matter regime of the phase diagram at high density but relatively low temperature. We present an overview on recent results and developments of beam plasma, and beam matter interaction processes studied with heavy ion beams from the GSI accelerator facilities.

Contents

1 Introduction **110**

2 Accelerator and Laser Facilities at GSI-Darmstadt **111**

3 Heavy Ion Plasma Interaction **112**

⋆ E-mail: d.hoffmann@gsi.de

4 Charge State Distribution of Heavy Ions Penetrating Thin Target Foils 115
4.1 Experimental Setup 115
4.2 Charge State Distributions 116
4.3 Charge State Dependent Energy Loss 119

5 Timescales of Phase Transitions from Solid to Warm Dense Matter 121
5.1 Absorption of Energy within the Solid 121
5.2 Electronically Induced Ultrafast Phase Transitions 123
5.3 Thermal Phase Transitions of the Heated Lattice 124
5.4 Further Phase Transitions 125

6 Summary and Open Problems 125

Acknowledgement 127

References 127

1. Introduction

The early theoretical work by Bethe (1930, 1932), Bloch (1933) and later Bohr (1948) paved the ground for a theoretical understanding of ion-matter interaction and the stopping power of matter. Since the discovery of fission fragments in the beginning of the 20th century the interaction of heavy ions with solid or gaseous matter has been investigated intensively in experiments, resulting in a vast number of semi- or empirical formulas, tables or codes for the mean charge of the projectile, its charge state distribution or the stopping power (Lindhard and Scharff, 1961; Northcliffe and Schilling, 1970; Ziegler et al., 1985; Hubert et al., 1990; ICRU, 2005). Despite the vast amount of theoretical and experimental work, a proper general microscopic description of the physical processes is still lacking or at least needs improvement.

Even less is known about the details of the interaction of ions with plasmas, a field with increasing interest especially for astrophysics, where plasma is the usual state of matter. Fusion physics is another field that shows great interest for beam plasma interaction since accelerators are a candidate for a primary driver in inertial confinement fusion, ICF-scenario, where a small pellet, filled with a deuterium-tritium mixture, is heated by X-rays in a hohlraum. The X-rays can be generated by powerful lasers, Z-pinches or by ion-beam interaction with matter. In the latter case the ion beam is stopped in a converter target and its energy is converted into X-rays. During the stopping process of an intense bunch of ions the converter target will be heated to approximately 300 eV in about 10 ns. Therefore the major part of the ion beam energy is deposited into hot and dense matter,

which is then a partially ionized plasma. For the optimization of the converter parameters a detailed knowledge of the ion-plasma interaction is needed (Badger et al., 1990).

2. Accelerator and Laser Facilities at GSI-Darmstadt

The perspectives of intense ion beams to drive an inertial fusion targets motivated a number of major accelerator laboratories like LBNL-Berkeley, ITEP-Moscow, TIT-Tokyo, University of Paris, Orsay and GSI-Darmstadt to start plasma physics research programs to study the interaction of heavy ion beams with ionized matter (Logan et al., 2006; Roy et al., 2005; Sharkov et al., 2005; Someya, 2006; Oguri et al., 2005; Gardes et al., 1989; Deutsch et al., 1989; Hoffmann et al., 2005). Today, the GSI-heavy ion accelerator laboratory in Germany operates the most powerful and versatile heavy ion accelerator worldwide and in addition to this there is an approved project to build a new accelerator facility at GSI called FAIR (Facility for Antiproton and Ion research). This new accelerator (Figure 1) will consist of two powerful heavy ion synchrotrons and a number of storage rings and experimental facilities for various research projects. The centerpiece of the accelerator assembly will be a 100 Tm heavy ion synchrotron. This will extend the available beam deposition power from the current level of 50 GW/g by at least two orders of magnitude up to 12000 GW/g. Many aspects of high power beam physics associated with inertial confinement fusion driven by intense heavy ion beams can be addressed there, even though this facility will not provide enough beam power to ignite a fusion pellet.

GSI-Darmstadt is also the first accelerator laboratory where in addition to a powerful and intense heavy ion beam a high-energy laser beam is available for experiments using laser and particle beams simultaneously. The already existing laser facility nhelix (nanosecond high energy laser for ion experiments) is currently complemented by a new laser PHELIX (Petawatt High Energy Laser for Ion Experiments). This is a laser system in the kJoule regime with the option to produce ultra-short, high-intensity light pulses with a total power above 1 PW (10^{15} Watt). It will be able to produce a light pulse pressure exceeding the pressure in the interior of the sun. The full potential of the PHELIX laser will be exploited in high energy density physics experiments with the high intensity heavy ion beams of the future accelerator at GSI. The unique combination of ion and laser beams facilitates novel and pioneering beam-plasma interaction experiments to investigate the structure and the properties of matter under extreme conditions of high energy density.

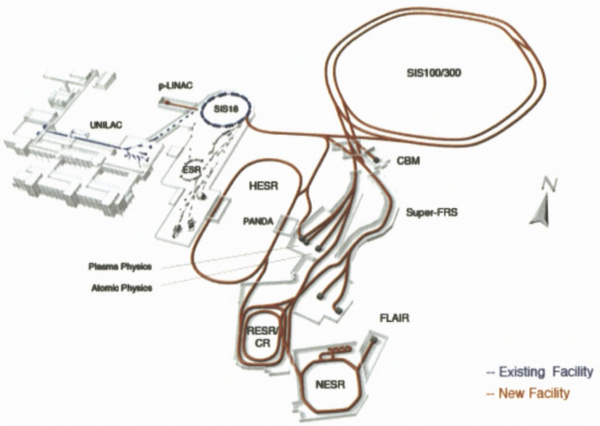

Figure 1. GSI accelerators and the experimental areas of plasma physics. The FAIR project at GSI will greatly improve the experimental option for beam-plasma experiments. The arrows point to the future experimental areas of plasma physics and atomic physics at FAIR.

3. Heavy Ion Plasma Interaction

Early stopping power experiments for protons and heavy ions in ionized matter have used discharge plasma and Z-pinch plasma as well as laser produced plasma (Ogawa et al., 2001; Belyaev et al., 1996; Couillaud, 1994; Gardes et al., 1988; Hoffmann et al., 1988). The most effective method to determine the ion energy loss was based on time-of-flight measurements where the rf-frequency of the accelerator was used for timing purposes. The experiments using gas discharge plasmas as stopping medium, reached densities up to 10^{17} free electrons/cm^3 and plasma temperatures of a few eV for hydrogen plasma (Hoffmann et al., 1990; Weyrich et al., 1989; Jacoby et al., 1995). The results show a clearly enhanced stopping power of the projectiles in the plasma compared to cold matter. In contrast to cold matter the projectiles do not interact with neutral atoms but with target ions and additionally with a free electron gas. Stopping power models applicable for this experimental situation can be based on theories given by Bethe, Bohr and Bloch, taking into account the Barkas corrections for the gas case. Since the Barkas correction nearly cancels out the Bloch ones we find that the situation for partially ionized plasmas can be well described in the frame of the standard stopping model, based on the Bethe formalism as suggested by Peter (1988):

$$-\frac{\mathrm{d}E}{\mathrm{d}x} = \frac{16\pi a_0^2 I_\mathrm{H}^2 Z_\mathrm{eff}^2}{m_\mathrm{e} v^2}\left[\sum_{Z=0}^{Z_\mathrm{t}}(Z_\mathrm{t}-Z)n_z \ln\left(\frac{2m_e v^2}{\bar{I}_Z}\right) + n_\mathrm{e}\ln\left(\frac{2m_\mathrm{e}v^2}{\hbar\omega_\mathrm{P}}\right)\right], \quad (1)$$

with a_0: the Bohr radius, I_H: the mean ionization potential of hydrogen, Z_{eff}^2: effective projectile charge, $m_e v^2$: electron mass times projectile velocity, Z_t: target atomic number, n_Z, n_e: density of plasma ions of charge Z and free electrons, respectively, $\bar{I}_Z$: the mean plasmon energy energy transfer in a collision with a plasma ion of charge Z, and $\hbar\omega_P$: the plasma frequency. The Coulomb logarithm is split up into two contributions. The first term describes the energy transfer to the remaining bound electrons in the plasma. As in a plasma a charge state distribution is created it is necessary to sum over all charge states Z and take into account the varying mean ionization potential of the different charge states. In the second term the contribution of free electrons is described. In this case the projectile can transfer its energy in collisions to free electrons and by plasmon excitation.

In the case of fully ionized plasma the first term of the equation given above is zero. This case prevails in our experiments with fully ionized hydrogen plasma from discharges and z-pinches, and we find that in this case the experimental data are well represented by the model given by Peter (1988). Figure 2 shows experimental data of energy loss measurements for Kr ions in cold hydrogen gas and fully ionized hydrogen plasma from discharge plasma. The red hatched area is the energy loss expected for Kr ions with different effective charge states. The blue graph represents Northcliffe and Schilling stopping values.

Mainly two effects contribute to the stopping power enhancement of ions in fully ionized hydrogen plasma:

(a) An efficient energy transfer to the free electron gas.
For free electron densities below $10^{21}/cm^3$ the plasmon energy $\hbar\omega_P$ is less than 1 eV, thus much smaller than the average of the excitation or ionization energy of bound electrons in hydrogen. This leads to an increase of the stopping power by a factor of up to 2.5.

(b) An increase of the projectile charge state.
Since for a free electron it is nearly impossible to fulfill energy conservation and momentum conservation at the same time in a capture process, the dynamic equilibrium of capture and ionization processes is shifted towards a higher mean projectile charge state, which in turn leads to an increase of the effective charge Z_{eff}.

The stopping power of ionized matter depends strongly on Z_{eff}. There is no simple relation between Zeff and the charge state of the projectile. The experimental results and the arguments given above suggest however, that the charge state of an ion traversing fully ionized hydrogen plasma is higher than the charge state of the projectile under the same conditions of density in cold hydrogen gas.

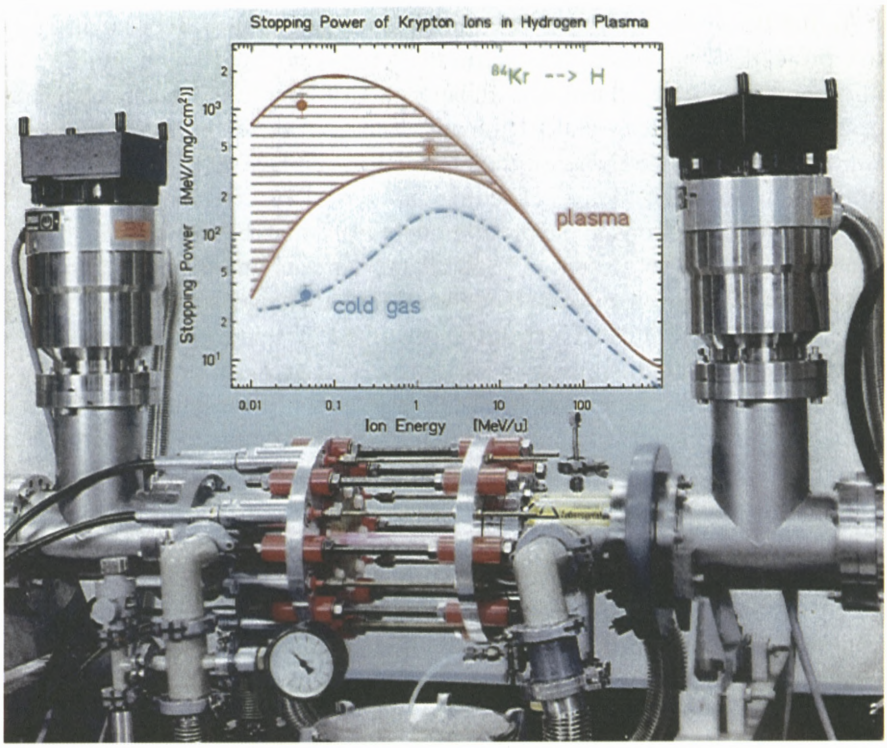

Figure 2. Hydrogen discharge plasma to provide fully ionized hydrogen plasma for plasma stopping power measurements. Red data points are stopping power data of plasma for Kr ions at 1.4 MeV/u and 45 keV/u respectively. The blue data points represent data in cold hydrogen gas. (From Jacoby et al., 1995.)

In different laboratories experiments were carried out to measure and calculate the charge state of ions passing through ionized matter (Nardi et al., 2006; Kojima et al., 2002; Golubev et al., 2001; Dietrich et al., 1992). The GSI plasma physics group has dedicated their efforts to extend the experimental data base for the stopping power of ions in plasmas to higher densities and higher temperatures. At the experimental area Z6, a branch of the UNILAC (Universal linear accelerator), an experimental setup has been built up for the investigation of the interaction of ions with laser produced plasmas. Therefore a thin foil, mainly a carbon foil with a thickness of a few hundred μg/cm^2, is irradiated by the nhelix laser (amplified NdYAG laser with $\lambda = 1064$ nm, energy up to 100 J in 5–15 ns (FWHM)) transforming the foil into a dense and hot plasma with densities close to solid density and temperatures of over 200 eV in the very hot spot. As the plasma is expanding there will be density and temperature gradients, which have to be mea-

sured experimentally. At the same time an ion pulse with a length of a few hundred μs, built up of micro bunches with a length of 3 ns FWHM and a frequency of 108 MHz, is probing the plasma parallel to the laser direction. This means the expanding plasma is being investigated each 9.2 ns. The delay between the laser and the ion bunch can be shifted with an accuracy of 1 ns. The ions first penetrate a still cold part of the foil, and then enter dense and hot plasma, which is expanding and cooling. Finally all matter along the interaction path has vanished and the ions fly through vacuum with their initial energy. The energy loss as a function of time is determined by a time of flight measurement. Additionally a dipole magnet behind the target chamber can be used to measure the charge state distribution of each single bunch penetrating the plasma. As a result we obtain a set of energy loss data and charge state distributions of ions probing expanding plasma. As the target conditions with respect to density and temperature during the interaction time are important, a set of plasma diagnostic tools is used e.g. laser interferometry for a space resolved measurement of the free electron density n_e, time resolved X-ray spectroscopy for the temperature determination, a visible streak camera measuring the expansion velocity, pinhole cameras, etc. Nevertheless, the very dense and hot part of the plasma is not accessible with all these diagnostics. Therefore results of the plasma diagnostic serve to benchmark hydrodynamic simulation of the laser-matter interaction and plasma expansion. From these simulations the necessary density and temperature profiles along the ion path can be extracted for the theoretical calculation of the energy loss and charge state distributions.

4. Charge State Distribution of Heavy Ions Penetrating Thin Target Foils

The theoretical description of the charge state distributions faces the problem that until now no reliable theory or code to calculate all the relevant charge exchange cross sections exists. Therefore we used the high resolution spectrometer of the Hahn–Meitner Institut in Berlin to measure them along with energy loss data as a function of the projectiles charge state, to extract charge state dependent stopping powers $S(q)$. Measurements of this type have been pioneered at Harwell and Chalk River many years ago and were greatly improved by Ogawa et al. (1992, 1997) and references therein. Calculations have been carried out by Winterbon (1977), Sigmund (1992) and Sigmund and Schinner (2001) and references therein.

4.1. Experimental Setup

The investigated system was Argon interacting with thin Carbon target foils. The projectile energy was chosen to be 4 MeV/u, a suitable energy for the ion-plasma

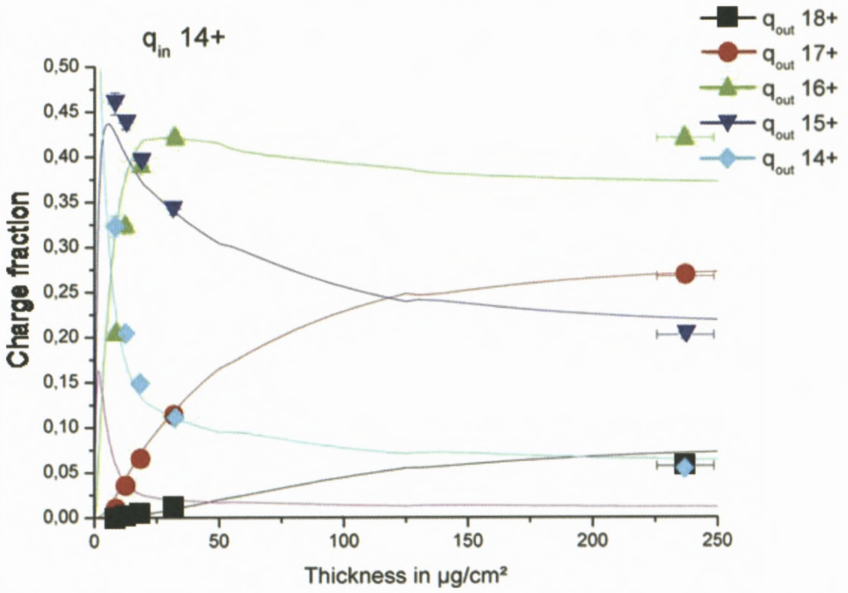

Figure 3. Evolution of the charge state distribution for Ar ions with the incoming charge $q_{\text{in}} = 14+$.

interaction experiments. The initial charge state was varied between 14+ and 18+, covering over 99% of the equilibrium charge state distribution of Ar at 4 MeV/u.

The thicknesses of the target foils were 8.1, 12, 18, 32.2 and 231.6 μg/cm^2, measured by the energy loss of α particles with energies of 5.80 and 5.76 MeV emerging from an open ^{244}Cm source. Such thin foils were used on the one hand to cover the pre-equilibrium region, so that the evolution of the charge state distributions can be measured to fix the charge exchange cross sections, on the other hand to measure a difference in the energy losses as function of the charge states, $\Delta E(q)$. We measured the evolution of the incoming charge states 14+, 16+ and 18+ using increasing foil thicknesses until charge state equilibrium is reached.

4.2. Charge State Distributions

In contrast to equilibrium charge state measurements, the pre-equilibrium region allows to determine the cross sections absolutely. Figures 3 to 5 show the evolution of the charge state distributions in this region for the three incoming charge states (symbols). To the statistical error, marked by the error bars, a systematic error of 3% must be added.

The interpretation of these results can be done by model calculations in two ways (Blazevic et al., 2000): (a) by solving the coupled-channel rate equations

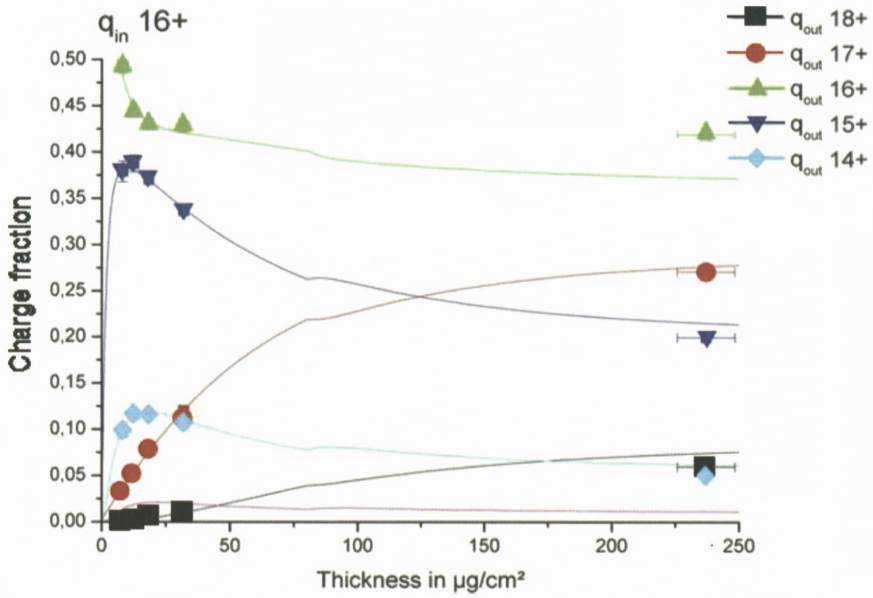

Figure 4. Evolution of the charge state distribution for Ar ions with the incoming charge $q_{\mathrm{in}} = 16+$.

for the individual charge state probabilities, or (b) by a Monte Carlo simulation following the history of each ion on its way through the foil. Both methods need a complete set of cross sections for all possible interactions between the projectile and the target atoms. In our studies both methods were applied. First the rate equation model will be described, which results are shown as lines in Figures 3 to 5.

The solving of the rate equations was performed with the ETACHA code of Rozet et al. (1996), taking into account the following processes for the first three projectile and target shells including the sub-shells:

- radiative and mechanical electron capture;
- ionization;
- excitation;
- radiative and Auger decay, auto ionization.

The cross sections enter into the rate equations, which can be written as

$$\frac{\mathrm{d}Y_i(x)}{\rho \cdot \mathrm{d}x} = \sum_j Y_j(x)\sigma_{ji} - Y_i(x)\sum_j \sigma_{ij}, \tag{2}$$

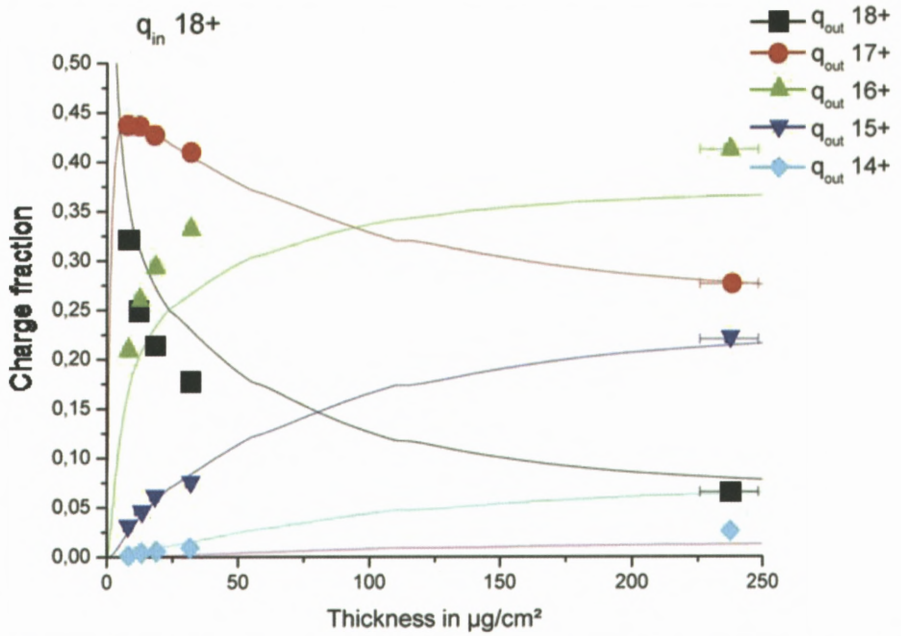

Figure 5. Evolution of the charge state distribution for Ar ions with the incoming charge $q_{\mathrm{in}} = 18+$.

where $Y_i(x)$ denotes the fraction of ions in charge state i including excited states; x is the traversed target thickness and σ_{ij} denotes the collision cross section from state i to state j. The code calculates the cross sections for bare projectile ions in the case of capture processes or a hydrogen like configuration for the ionization, excitation and decay processes, taking into account the screening effects of the residual electrons. As the code was initially written for energies above 10 MeV/u, it had to be adapted to the experimental situation. In contrast to the equilibrium charge distributions, the data for the pre-equilibrium region allows to determine absolute values for the cross sections. Figures 3–5 show that charge state equilibrium of Ar ions is obtained with carbon foils of more than 200 μg/cm^2.

The analysis results in a set of cross sections, which were used in our Monte Carlo Simulation to describe the charge exchange processes inside the foil. From these calculations we deduce, that even for the thinnest foil and an initial charge state of $q_{\mathrm{in}} = 16+$ far less than half of all ions keep their charge state during the passage through the foil. Therefore no measured charge state dependent parameter can be regarded as "frozen charge state" result.

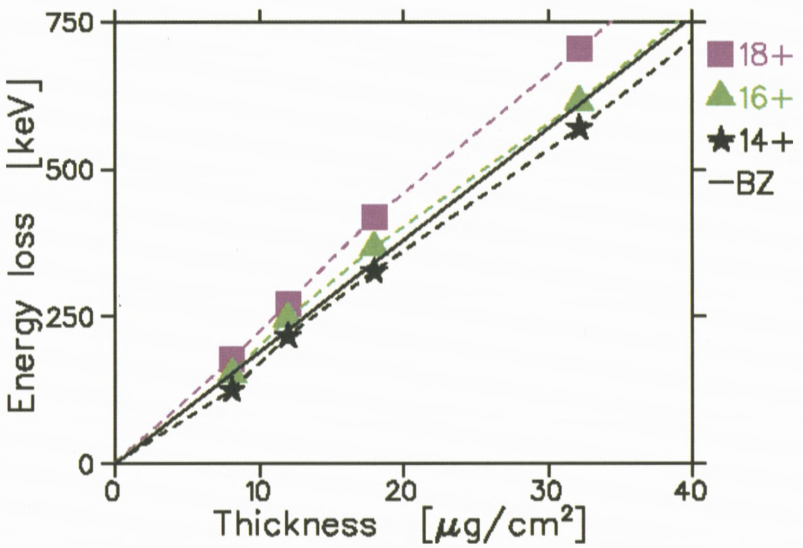

Figure 6. Measured energy loss for varying incoming charge states, $\Delta E(q_{\text{in}} = q_{\text{out}})$, of Argon projectiles at 4 MeV/u penetrating Carbon foils. BZ corresponds to energy loss calculations with the Biersack–Ziegler code SRIM.

4.3. Charge State Dependent Energy Loss

The magnetic field of the spectrometer selects a specific charge state for energy loss measurements. Figure 6 shows the $\Delta E(q_{\text{in}} = q_{\text{out}})$ results for thin foils and charge states from 14+ to 18+. As discussed above, these values are not generated by the "frozen charge state", since the majority of ions have undergone several charge state fluctuations before leaving the foil with q_{out}. As described in detail in Blazevic et al. (2002), we have developed an iterative Monte Carlo simulation method to eliminate the influence of the charge exchange and to extract "frozen charge state" stopping powers $S(q)$. In other words, we used the charge exchange cross sections from the charge state distribution measurements, combined them with charge dependent stopping powers and succeeded to reproduce the measured energy losses including all the charge exchange effects. The result is plotted in Figure 7.

These data can now be used to test some theoretical calculations of the $S(q)$ values. Four of them shall be discussed below:

- Kaneko derived an analytical formula for $S(q)$ for swift lithium- and beryllium-like ions based on first-order perturbation theory. The bound

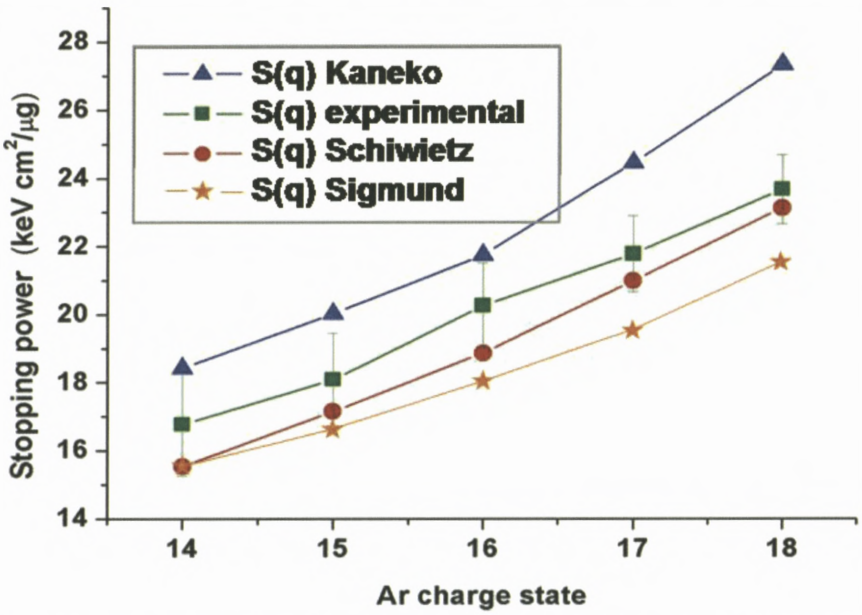

Figure 7. Experimental and theoretic charge state dependent stopping power $S(q)$ for Argon ions interacting with Carbon.

electrons attached to the ion in the ground state were described by the Hartree–Fock–Slater determinant (Kaneko, 1994).

- Schiwietz and Grande developed the CASP code to calculate the impact parameter dependence of the electronic energy loss of bare ions. This perturbative convolution approximation is based on first order perturbation theory, which is only valid for fast projectiles with low charges. But using Bloch's stopping power results and a scaling, they could overcome these restrictions and derived a unitary convolution approximation (Schiwietz and Grande, 1999).
- Maynard expressed the stopping power of swift heavy ions within the convergent kinetic Lindhard theory, based on a modified Bloch correction term, devoted to correctly describe the close collisions contribution to the energy loss process (Maynard et al., 2001).
- Sigmund and Schinner treated charged particle stopping via a binary scattering theory, assuming free binary collisions governed by a suitable effective potential (Sigmund and Schinner, 2000).

Kaneko's first order perturbation theory is known to overestimate the $S(q)$ values for heavier projectiles, so it can be seen as an upper limit. On the other hand

the theory of Schiwietz and Grande lacks some correction terms, which should increase the calculated stopping powers; hence it is a lower limit for the $S(q)$ values. Our experimental data are between these limits.

5. Timescales of Phase Transitions from Solid to Warm Dense Matter

In order to be able to study the stopping power of ions in laser-generated plasmas, knowledge of the transient material state of the laser-irradiated target foil, which is initially in solid state, is essential. Numerical codes, simulating the interaction of the target with the laser and the subsequent hydrodynamic expansion, usually assume a cold plasma as initial condition. However, the transition from solid to warm dense matter may proceed through different pathways and may be completed on different timescales, depending on target material and energy of excitation. Here, we can benefit from experimental and theoretical studies on the dynamics of a solid during and after irradiation with an ultrashort laser pulse. Examples of such studies will be reviewed below.

The time-resolved description of the excitation of the solid and the induced phase transitions is a challenging task: On ultrashort time scales the highly excited material passes through non-equilibrium states of different kinds. Therefore, the theoretical description of the investigated processes may differ strongly from the classical descriptions valid for equilibrium or steady-state conditions. A temporal separation of the basic processes as excitation, melting and material removal can be achieved, applying an ultrashort laser pulse of about a hundred femtosecond duration. This allows a separate investigation of each of these key-processes.

Figure 8 shows a schematic view of the typical time scales and intensity ranges of some phenomena, discussed in the following. The pathway of the material after irradiation depends strongly on the type of material and on laser properties as intensity and wavelength. Note that in real laser experiments due to laser intensity variations in space, as well as for excitation with ion beams, a large variety of these phenomena (and probably further transient states and pathways which are not shown) may play a role leading to a rather complex behaviour.

5.1. Absorption of Energy within the Solid

Heavy ions of sufficient high energy lose energy within solid material through electronic stopping, thus the energy input proceeds by heating of the electron gas of the solid. Also laser energy absorption is usually dominated by free carrier absorption. In metals, free electrons are inherent in the conduction band of the metal. At moderate intensities, these electrons absorb photons and thus gain higher energy. Following absorption, this energy is transferred from electrons to phonons by

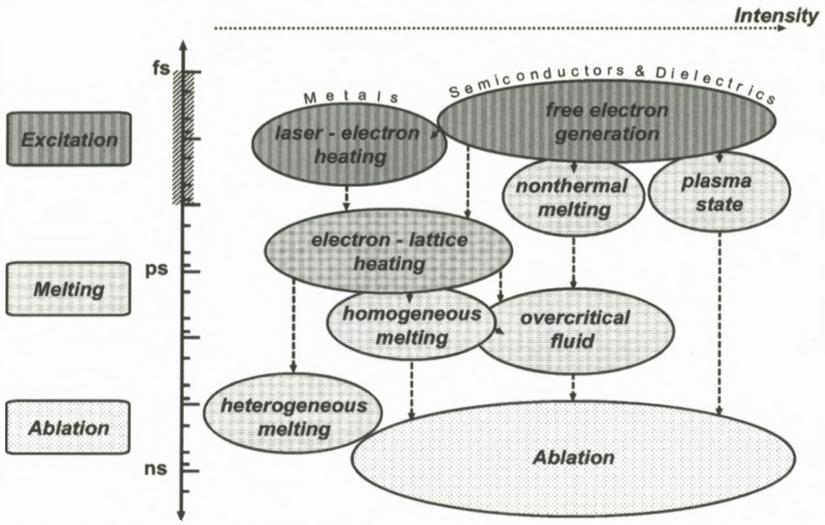

Figure 8. Schematic view of typical time scales and intensity ranges of some phenomena occurring during and after irradiation of a solid with an ultrashort laser pulse of about 100 fs duration. Excitation occurs during irradiation, while the time scale of melting may vary for different processes depending on excitation strength. Material removal, i.e. ablation, lasts up to the nanosecond regime (Rethfeld et al., 2004). The intensities, this overview applies to, ranges from about 10^{10} to 10^{14} W/cm^2.

electron-phonon interaction, that is, lattice heating occurs. For timescales longer than the electron-electron collision time, the two-temperature model (Kaganov et al., 1957; Anisimov et al., 1974) provides an applicable description for the heat transfer and heat conduction for the case of laser irradiation as well as for the case of ion impact.

If the timescale of interest is shorter or in the range of the electron-electron thermalization time, the two-temperature model is not applicable at first. We have extensively studied the dynamics of laser-excited electrons in this regime, including the influence of a nonequilibrium electron distribution on the electron-phonon energy transfer (Rethfeld et al., 2002b).

In dielectrics there is only a negligible amount of free electrons inherent in the conduction band. However, in the case of irradiation of a dielectric with laser or particle beams of sufficiently high intensity or energy, respectively, ionization processes may transfer electrons from the valence band to the conduction band. The transient characteristics of electron excitation with visible lasers in the intensity regime below $I_L \approx 10^{14}$ W/cm^2 have been studied in Kaiser et al. (2000) and Rethfeld (2004, 2006).

For the case of ion impact on insulating materials, mainly two models of track formation are discussed. The first model expects that along the projectile path the target atoms are fully ionized, leading to repulsive forces between them. The resulting movement of atom is termed "Coulomb explosion" and leads directly to material damage (Fleischer et al., 1967, 1975). In contrast, the "thermal spike model" provides a description of electron heating followed by electron-phonon energy transfer (Toulemonde et al., 2000). This description is based on the two-temperature model (Kaganov et al., 1957; Anisimov et al., 1974). The role of these two processes is not finally clarified; however, both processes may occur successively for certain energy ranges of the impinging ion (Bringa and Johnson, 2002).

In the following we review different mechanisms for phase transitions occurring on different timescales after electronic excitation. The mentioned experiments are performed after laser excitation taking advantage of the large lateral spatial scale of the laser spot. We believe that the microscopic mechanisms in the material are in certain parameter ranges the same as occurring during phase transitions of a solid target after ion bombardment. Thus, studies of laser excitation and the induced processes may provide general insight also to the physical processes induced by heavy ion bombardment.

5.2. Electronically Induced Ultrafast Phase Transitions

As mentioned above, the process of Coulomb explosion is discussed to be responsible for damage of dielectric material irradiated by swift heavy ions (Fleischer et al., 1967; Bringa and Johnson, 2002). This process is initiated by locally high charges occurring after electron excitation leading to ionization of target atoms. Repulsive Coulomb forces may lead to material damage and ablation. For the case of laser irradiation it was found that Coulomb explosion can lead to removal of the top surface layers of excited dielectrics (Stoian et al., 2002; Bulgakova et al., 2004).

For the macroscopic removal of material by this process, a net charge of the surface must be present. If electronic transport rapidly neutralizes the surface region, as may be expected for metals and semiconductors (Bulgakova et al., 2004; Stoian et al., 2004), the material does not disrupt. However, in this case one may speak about a rapid transition to the plasma state at solid density.

Another rapid, directly electronically induced phase transition to the *liquid* state is known for covalently bonded semiconductors. This rapid transition occurs at lower intensities than possible direct transitions to the *plasma* state at solid density, as discussed above. Here, the photo excited high density electron-hole plasma may lead to a lattice instability (Stampfli and Bennemann, 1994), resulting

in a disordering of the lattice and thus a transition to the liquid state on a time scale of approximately 100 fs. This process is often called *non-thermal* melting, since the disordering occurs faster than lattice heating. Experimentally the process of ultrafast non-thermal melting was detected directly by time-resolved X-ray diffraction (Siders et al., 1999; Sokolowski-Tinten et al., 2001).

Also for metals, processes of ultrafast non-thermal melting have been under discussion (Falkovsky and Mishchenko, 1997, 1999), but they are not yet unambiguously demonstrated. Most of the studies claiming the experimental observation of ultrafast melting of metals could be explained with the mechanism of homogeneous melting discussed in the following subsection.

5.3. Thermal Phase Transitions of the Heated Lattice

The typical time scale for thermal lattice heating due to electron-phonon collisions is in the range of a few to tens of picoseconds. However, depending on excitation strength, already a few picoseconds after irradiation the crystal may be strongly superheated, i.e. the lattice temperature greatly exceeds the equilibrium melting temperature (Rethfeld, 2004a). Usually subsequent *thermal* melting is supposed to start at the surface, where the energy barrier for heterogeneous nucleation of a liquid layer at the solid-vapour interface is zero. In this case, a melting front proceeds from the surface into the material with a velocity limited by the speed of sound. A natural limit for the melting time is therefore the thickness of the heated layer divided by the melting front velocity. Typical times for melting by this mechanism of *heterogeneous* nucleation are in the range of about 100 nm/10^3 m/s = 100 ps.

In Rethfeld et al. (2002a) the possibility of laser-induced melting of crystals due to *homogeneous* nucleation was considered. It was shown that a sufficiently superheated bulk crystal would melt completely in less than one picosecond. Thus, the time for homogeneous melting is limited only by the time for lattice heating, and is therefore expected to be longer than the time for non-thermal melting mentioned above, but significantly faster than the time needed for a melting front to sweep from the surface through the heated layer (i.e. heterogeneous melting). Homogeneous melting can thus explain experimental observations of rapid melting of solids without invoking nonthermal mechanisms (Ashitkov et al., 2002; Siwick et al., 2003).

Also molecular dynamic simulations have confirmed the microscopic view of melting by homogeneous nucleation (Jin, 2001). For the case of laser excitation, extended molecular dynamic simulations have shown the dynamics of short-pulse laser-induced melting, studying in detail the interplay of homogeneous and het-

erogeneous melting mechanisms (Ivanov and Zhigilei, 2003a, 2003b; Lorazo et al., 2006).

5.4. Further Phase Transitions

Once the material has lost the crystalline order, further phase transitions are usually connected with a remarkable density decrease. In this case, the timescale of phase transition strongly depends on the spatial dimensions of the heated volume and the position of a possible free surface where expansion may be initiated.

The timescale of expansion can be estimated by dividing the spatial target dimensions with the sound velocity. Typical timescales for the density decrease of laser-heated material are in range of 100 ps. Note that the liquid-gas phase transition is connected with a strong drop of sound velocity, resulting in a complex density profile during expansion (Sokolowski-Tinten et al., 1998; Anisimov et al., 1999; Zhakhovskij et al., 2000).

In the case of ion bombardment of larger volumes, the material in the center of the target can be kept in the state of warm dense matter at solid state density for long times up to the range of 100 ns (Tahir et al., 2005).

6. Summary and Open Problems

The perspectives to use intense ion beams as drivers has initiated many experimental and theoretical programs to investigate ion beam plasma interaction phenomena. It was clearly demonstrated that fully ionized plasma consisting of bare ions is a very effective stopping medium. The stopping power enhancement is almost a factor of 40 for Kr ions at an energy of 45 keV/u passing through a fully ionized hydrogen discharge plasma. This is well explained by the effective energy transfer in collisions with free electrons and the higher charge state of projectile ions in a fully ionized plasma. Enhanced charge states of heavy ions in plasma were observed in experiments and we have a sufficient theoretical modelling for this phenomenon (Nardi and Zinamon, 1982; Boine-Frankenheim and Stockl, 1996). This led to the proposal to use plasma strippers for accelerators, where foil strippers or gas strippers are routinely used to generate ions in high charge states for effective acceleration (Alton et al., 1992; Neuner et al., 1999; Oguri et al., 2000).

It is very difficult to generate a plasma situation of fully ionized ions and free electrons for materials other than hydrogen. In the case of carbon this requires plasma temperatures well above 200 eV, a situation which is expected to prevail in the converter material of a in inertial fusion target. The PHELIX laser system at GSI (Neumayer, 2005) is designed for this experiment. Here the problem is not

the temperature but the fact that the plasma conditions have to be provided in a way to be suitable for ion beam-plasma interaction experiments. To this extend a large focal spot of the order of 1mm with low temperature and density gradients is necessary and this is an experimental challenge, which has not yet been met.

In the situation where the plasma ions still have bound electrons the experimental data base is very small. In the case of z-pinch plasma an enhanced stopping power has been observed, but there are no reliable charge state measurements available. Therefore efforts are underway to revisit the problem of projectile charge states inside matter with new high resolution spectroscopy (Rosmej et al., 2005) and to scale the results to plasma target conditions with less bound electrons, free electrons, changes in binding energies and screening.

For the theoretical description of the charge state distributions, the cross sections must be scaled to plasma target conditions. This allows to simulate the passage through the laser generated plasma, giving information about the charge state history of the projectiles. Combined with the charge dependent stopping powers $S(q)$ for bound electrons together with the energy transfer to the free electron gas a microscopic description of the energy deposition of swift ions in plasmas will be given.

We have reviewed studies on the dynamics of a solid during and after irradiation with an ultrashort laser pulse of moderate intensity. For a pulse duration in the subpicosecond regime, the basic processes as excitation and subsequent phase transitions are temporally separated. We have discussed electronically induced ultrafast "non-thermal" phase transitions as well as mechanisms of thermal phase transitions, following lattice heating. Qualitatively, the results can be directly applied to the studies of ion tracks in solids, where similar mechanisms are discussed. For a quantitative adaptation, the specific geometry and parameter range of ion-solid interaction has to be taken into account.

In future, we will study phase transitions induced by a high-intensity laser and ion beam pulse, transforming the initial solid directly to the plasma state. A detailed understanding of the materials pathway on a nanosecond timescale is essential for the interpretation of time-resolved experiments on the interaction of ions with laser produced plasmas. The initial conditions for corresponding hydrodynamic simulations of laser-matter interaction and plasma expansion must be improved; ideally, also phase transitions should be taken into account. To this end, the transient description of the dynamics of a solid during and after laser irradiation should be provided for a large range of intensities and timescales. Specific features of solid carbon and hydrogen will be studied.

Acknowledgement

We thank C. Trautmann for helpful discussions.

References

Alton G.D., Sparrow R.A. and Olsen, R.E. (1992): Plasma as a high-charge-state projectile stripping medium. Phys Rev A **45, no. 8**, 5957–5963

Anisimov S.I., Kapeliovich B.L. and Perel'man T.L. (1974): Electron emission from metal surfaces exposed to ultrashort laser Pulses. Sov Phys JETP **39**, 375–377

Anisimov S.I., Inogamov N.A., Oparin A.M., Rethfeld B., Yabe T., Ogawa M. and Fortov V.E. (1999): Pulsed laser evaporation: Equation-of-state effects. Appl Phys A **69**, 617–620.

Ashitkov S.I., Agranat M.B., Kondratenko P.S., Anisimov S.I., Fortov V.E., Temnov V.V., Sokolowski-Tinten K., Zhou P. and von der Linde D. (2002): Ultrafast structural transformations in graphite. JETP Lett **75**, 87.

Badger B. et al. (1990): HIBALL – A conceptual heavy ion beam driven fusion reactor study. Kernforschungszentrum Karlsruhe Report KfK-3202

Bethe, H. (1930): Zur Theorie des Durchgangs schneller Korpuskularstrahlen durch Materie. Ann Phys **5**, 324–400

Bethe H.A. (1932): Bremsformel für Elektronen relativistischer Geschwindigkeit. Z Phys **76**, 293

Belyaev G., Basko M., Cherkasov A., Golubev A., Fertman A., Roudskoy I., Savin S., Sharkov B., Turtikov V., Arzumanov A., Borisenko A., Gorlachev I., Lysukhin S., Hoffmann D.H.H. and Tauschwitz A. (1996): Measurement of the Coulomb energy loss by fast protons in a plasma target. Phys Rev E **53, no. 3**, 2701–2707

Blazevic A., Bohlen H.G. and von Oertzen W. (2000): Charge-state changing processes for Ne ions passing through thin carbon foils. Phys Rev A **61**, 032901

Blazevic A., Bohlen H.G. and von Oertzen W. (2002): Stopping power of swift neon ions in dependence on the charge state in the non-equilibrium regime. Nucl Instr Meth Phys Res B **190**, 64.

Bloch F. (1933): The slow down of rapidly moving particles in their passing through solid matter. Ann Phys (Leipzig) **16**, 285–320

Bohlen H.G. (1983): The magnetic spectrometer at VICKSI. In: Symposiom of Detectors in Heavy Ion Reactions, Lecture Notes in Physics, Vol. 178, Springer Verlag, Berlin, pp 105

Bohr N. (1948): The penetration of atomic particles through matter. Mat Phys Medd K Dan Vidensk Selsk **18, no. 8**, 1–144

Boine-Frankenheim O. and Stockl C. (1996): Charge state and nonlinear stopping power of heavy ions in a fully ionized plasma. Laser and Particle Beams **14, no. 4**, 781–788

Bringa E.M. and Johnson R.E. (2002): Coulomb explosion and thermal spikes. Phys Rev Lett **88**, 165501

Bulgakova N.M., Stoian R.,Rosenfeld A., Hertel I.V. and Campbell E.E.B. (2004): Electronic transport and consequences for material removal in ultrafast pulsed laser ablation of materials. Phys Rev B **69**, 054102

Couillard C., Deicas R., Nardin Ph., Beuve M.A., Guihaume J.M., Renaud M., Cukier M., Deutsch C. and Maynard G. (1994): Ionization and stopping of heavy ions in dense laser-ablated plasmas. Phys Rev E **49, no. 2**, 49

Dietrich K.G., Hoffmann D.H.H., Boggasch E., Jacoby J., Wahl H., Elfers M., Haas C.R., Dubenkov V.P. and Golubev A.A. (1992): Charge state of fast heavy-ions in a hydrogen plasma. Phys Rev Lett **69, no. 25**, 3623–3626

Deutsch C., Maynard G., Bimbot R., Gardes D., Dellanegra S., Dumail M., Kubica B., Richard A., Rivet M.F., Servajean A., Fleurier C., Sanba A., Hoffmann D.H.H., Weyrich K. and Wahl H. (1989). Ion beam-plasma interaction – A standard model approach. Nucl Instr Meth Phys Res A **278, no. 1**, 38–43

Falkovsky L.A. and Mishchenko E.G. (1997): Lattice deformation from interaction with electrons heated by ultrashort laser pulse. JETP Lett **66**, 208

Falkovsky L.A. and Mishchenko E.G. (1999): Electron lattice kinetics of metals heated by ultrashort laser pulses. J Exp Theor Phys **88**, 84

Fleischer R.L., Price P.B., Walker R.M. and Hubbard E.L. (1967): Criterion for registration in dielectric track detectors. Phys Rev **156**, 353

Fleischer R.L., Price P.B. and Walker R.M. (1975): Nuclear Tracks in Solids. Principles and Applications, University of California Press, Berkeley, CA

Gardes D., Bimbot R., Dellanegra S., Dumail M., Kubica B., Richard A., Rivet M.F., Servajean A., Fleurier C., Sanba A., Deutsch C., Maynard G., Hoffmann D.H.H., Weyrich K. and Wahl H. (1988): Interaction of heavy-ion beams with a hydrogen plasma – Plasma lens effect and stopping power enhancement. Europhys Lett **7, no. 8**, 701–705

Gardes D., Bimbot R., Dumail M., Kubica B., Richard A., Rivet M.F., Servajean A., Fleurier C., Sanba A., Hong D., Deutsch C., Maynard G., Hoffmann D.H.H., Weyrich K. and Dietrich K.G. (1989): Experimental investigation of beam-plasma interactions enhanced stopping power – Plasma lens effect. Rad Eff Defects Solids **110, nos 1–2**, 49–53

Golubev A., Turtikov V., Fertman A., Roudskoy I., Sharkov B., Geissel M., Neuner U., Roth M., Tauschwitz A., Wahl H., Hoffmann D.H.H., Funk U., Suss W. and Jacoby J. (2001): Experimental investigation of the effective charge state of ions in beam-plasma interaction. Nucl Instr Meth Phys Res A **464, nos 1–3**, 247–252

Hoffmann D.H.H., Weyrich K., Wahl H., Peter T., Meyertervehn J., Jacoby J., Bimbot R., Gardes D., Rivet M.F., Dumail M., Fleurier C., Sanba A., Deutsch C., Maynard G., Noll R., Haas R., Arnold R. and Maurmann S. (1988): Experimental-observation of enhanced stopping of heavy-ions in a hydrogen plasma. Z Phys A **330, no. 3**, 339–340

Hoffmann D.H.H., Weyrich K., Wahl H., Gardés D., Bimbot R and Fleurier C. (1990): Energy loss of heavy ions in a plasma target. Phys Rev A **42**, 2313–2321

Hoffmann D.H.H., Blazevic A., Ni P., Rosmej O., Roth M., Tahir N.A., Tauschwitz A., Udrea S., Varentsov D., Weyrich K. and Maron Y. (2005): Present and future perspectives for high energy density physics with intense heavy ion and laser beams. Laser and Particle Beams **23, no. 1**, 47–53

Hubert F., Bimbot R. and Gauvin H. (1990): Range and stopping power table for 2.5-500 Me V/nuclean heavy ions in solids. At Data Nucl Data Tables **46**, 1–213

ICRU (2005): Stopping of ions heavier than helium, Vol. 73 of ICRU Report. J ICRU **5**, 1–253

Ivanov D.S. and Zhigilei L.V. (2003a): Effect of pressure relaxation on the mechanisms of short-pulse laser melting. Phys Rev Lett **91**, 105701

Ivanov D.S. and Zhigilei L.V. (2003b): Combined atomistic-continuum modeling of short-pulse laser melting and disintegration of metal films. Phys Rev B **68**, 064114

Jacoby J. et al. (1995): Stopping of heavy ions in a hydrogen plasma. Phys Rev Lett **74**, 50

Jin Z.H., Gumbsch P., Lu K. and Ma E. (2001): Melting mechanisms at the limit of superheating. Phys Rev Lett **87**, 055703

Kaganov M.I., Lifshitz I.M. and Tanatarov L.V. (1957): Relaxation between electrons and the crystalline lattice. Sov Phys JETP **4**, 173

Kaiser A., Rethfeld B., Vicanek M. and Simon G. (2000): Microscopical processes in dielectrics absorbing a subpicosecond laser pulse. Phys Rev B **61**, 11437

Kaneko T. (1994): Energy loss of swift projectiles with n ($n \leq 4$) bound electrons. Phys Rev A **49, no. 4**, 2681

Kojima, M., Mitomo, M., Sasaki, T., Hasegawa, J., Ogawa, M. (2002): Charge-state distribution and energy loss of 3.2-MeV oxygen ions in laser plasma produced from solid hydrogen. Laser and Particle Beams **20, no. 3**, 475–478

Lindhard J. and Scharff M. (1961): Energy dissipation by ions in the keV region. Phys Rev **124**, 128–130

Logan B.G., Bangerter R.O., Callahan D.A., Tabak M., Roth M., Perkins L.J. and Caporaso G. (2006). Assessment of potential for ion-driven fast ignition. Fusion Sci Technol **49, no. 3**, 399–411

Lorazo P., Lewis L.J. and Meunier M. (2006): Thermodynamic pathways to melting, ablation, and solidification in absorbing solids under pulsed laser irradiation. Phys Rev B **73**, 134108

Maynard G. et al. (2001): Modeling of swift heavy ions interacting with dense matter. Nucl Instr Meth Phys Res A **64**, 86

Nardi E. and Zinamon Z. (1982): Charge state and slowing of fast ions in a plasma. Phys Rev Lett **49, no. 17**, 1251–1254

Nardi E., Fisher D.V., Roth M., Blazevic A. and Hoffmann D.H.H. (2006): Charge state of Zn projectile ions in partially ionized plasma: Simulations. Laser and Particle Beams **24, no. 1**, 131–141

Neumayer P., Bock R., Borneis S., Brambrink E., Brand H., Caird J., Campbell E.M., Gaul E., Goette S., Haefner C., Hahn T., Heuck H.M., Hoffmann D.H.H., Javorkova D., Kluge H.J., Kuehl T., Kunzer S., Merz T., Onkels E., Perry M.D., Reemts D., Roth M., Samek S., Schaumann G., Schrader F., Seelig W., Tauschwitz A., Thiel R., Ursescu D., Wiewior P., Wittrock U. and Zielbauer B. (2005): Status of PHELIX laser and first experiments. Laser and Particle Beams **23, no. 3**, 385–389

Neuner U., Horioka K., Nakajima M., Ogawa M., Oguri Y., Takizawa M. and Yamauchi S. (1999): Performance of a carbon plasma stripper for intense beams. Fusion Engrg Design **44**, 285–286

Northcliff L.C. and Schilling R.F. (1970): Range and stopping-power tables for heavy ions. Nucl Data Tab A **7**, 233–463

Ogawa H., Katayama I., Sugai I., Haruyama Y., Aoki A ., Tosaki M ., Fukuxawa F., Yoshida K. and Ikegami H. (1992): Charge state dependent energy loss of light ions. Nucl Instr Meth Phys Res B **69**, 108–112

Ogawa H., Sakamoto N., Katayama I., Haruyama Y., Saito M., Yoshida K., Tosaki M., Susuki Y. and Kimura K. (1997): Energy loss of 10 MeV/amu atomic helium in carbon, Nucl Instr Meth Phys Res B **132**, 36–40

Ogawa M., Oguri Y., Neuner U., Nishigori K., Sakumi A., Shibata K., Kobayashi J., Kojima M., Yoshida M. and Hasegawa J. (2001): Laser heated dE/dX experiments in Japan. Nucl Instr Meth Phys Res A **464, nos 1–3**, 72–79

Oguri Y., Tsubuku K., Sakumi A., Shibata K., Sato R., Nishigori K., Hasegawa J. and Ogawa M. (2000): Heavy ion stripping by a highly-ionized laser plasma. Nucl Instr Meth Phys Res A **161**, 155–158

Oguri Y., Hasegawa J., Kaneko J., Ogawa M. and Horioka K. (2005): Stopping of low-energy highly charged ions in dense plasmas. Nucl Instr Meth Phys Res A **544, nos 1–2**: 76–83

Peter T. (1988): Energieverlust von Schwerionenstrahlen in dichten Plasmen. MPQ Report 137

Rethfeld B. (2004): Unified model for the free-electron avalanche in laser-irradiated dielectrics. Phys Rev Lett **92**, 187401

Rethfeld B. (2006): Free-electron generation in laser-irradiated dielectrics. Phys Rev B **73**, 035101

Rethfeld B., Sokolowski-Tinten K., Anisimov S.I. and von der Linde D. (2002a): Ultrafast thermal melting of laser-excited solids by homogeneous nucleation. Phys Rev B **65**, 092103

Rethfeld B., Kaiser A., Vicanek M. and Simon G. (2002b): Ultrafast dynamics of nonequilibrium electrons in metals under femtosecond laser irradiation. Phys Rev B **65**, 214303

Rethfeld B., Sokolowski-Tinten K., Anisimov S.I. and von der Linde D. (2004): Timescales in the response of materials to femtosecond laser excitation. Appl Phys A **79**, 767

Rosmej O.N., Blazevic A., Korostiy S., Bock R., Hoffmann D.H.H., Pikuz S.A., Efremov V.P., Fortov V.E., Fertman A., Mutin T., Pikuz T.A. and Faenov A.Y. (2005): Charge state and stopping dynamics of fast heavy ions in dense matter. Phys Rev A **72, no. 5**, 052901

Roy P.K., Yu S.S., Henestroza E., Anders A., Bieniosek F.M., Coleman J., Eylon S., Greenway W.G., Leitner M., Logan B.G., Waldron W.L., Welch D.R., Thoma C., Sefkow A.B., Gilson E.P., Efthimion P.C. and Davidson R.C. (2005): Drift compression of an intense neutralized ion beam. Phys Rev Lett **95, no. 23**, 234801

Rozet J.P., Stephan C. and Vernhet D. (1996): ETACHA: A programm for calculating charge states at GANIL energies. Nucl Instr Meth Phys Res B **107**, 67

Schiwietz G. and Grande P.L. (1999): A unitary convolution approximation for the impact-parameter dependent electronic energy loss. Nucl Instr Meth Phys Res B **153**, 1–9

Siders C., Cavalleri A., Sokolowski-Tinten K., Toth C., Guo T., Kammler M., Horn von Hoegen M., Wilson K., von der Linde D. and Barty C. (1999): Detection of nonthermal melting by ultrafast x-ray diffraction. Science **286**, 1340

Sigmund P. (1992): Statistical theory of charged-particle stopping and straggling in the presence of charge exchange. Nucl Instr Meth Phys Res B **69**, 113–122

Sigmund P. and Schinner A. (2000): Binary stopping theory for swift heavy ions. J Eur Phys D **12**, 425

Sigmund P. and Schinner A. (2001): Nonperturbative theory of charge-dependent heavy-ion stopping. Physica Scripta T **92**, 222–224

Siwick B.J., Dwyer J.R., Jordan R.E. and Miller R.J.D. (2003): An atomic-level view of melting using femtosecond electron diffraction. Science **302**, 1382

Sharkov B.Y., Alexeev N.N., Basko M.M., Churazov M.D., Koshkarev D.G., Medin S.A., Orlov Y.N. and Suslin V.M. (2005): Power plant design and accelerator technology for heavy ion inertial fusion energy. Nucl Fusion **45, no. 10**, S291–S297

Sokolowski-Tinten K., Bialkowski J., Cavalleri A., von der Linde D., Oparin A., Meyer ter Vehn J. and Anisimov S.I. (1998): Transient states of matter during short pulse laser ablation. Phys Rev Lett **81**, 224

Sokolowski-Tinten K., Blome C., Dietrich C., Tarasevitch A., Horn von Hoegen M., von der Linde D., Cavalleri A., Squier J. and Kammler M. (2001): Femtosecond x-ray measurement of ultrafast melting and large acoustic transients. Phys Rev Lett **87**, 225701

Someya T., Miyazawa K., Kikuchi T. and Kawata S. (200): Direct-indirect mixture implosion in heavy ion fusion. Laser and Particle Beams **24, no. 3**, 359–369

Stampfli P. and Bennemann K.H. (1994): Time dependence of the laser-induced femtosecond lattice instability of Si and GaAs: Role of longitudinal optical distortions. Phys Rev B **49**, 7299

Stoian R., Boyle M., Thoss A., Rosenfeld A., Korn G., Hertel I.V. and Campbell E.E.B. (2002): Laser ablation of dilectrics with temporally shaped femtosecond pulses. Appl Phys Lett **80**, 353

Stoian R., Rosenfeld A., Hertel I.V., Bulgakova N.M. and Campbell E.E.B. (2004): Comment on "Coulomb explosion in femtosecond laser ablation of si(111)" [Appl Phys Lett 82, 4190 (2003)]. Appl Phys Lett **85**, 694

Tahir N.A., Deutsch C., Fortov V.E., Gryaznov V., Hoffmann D.H.H., Kulish M., Lomonosov I.V., Mintsev V., Ni P., Nikolaev D., Piriz A.R., Shilkin N., Spiller P., Shutov A., Temporal M., Ternovoi V., Udrea S. and Varentsov D. (2005): Proposal for the study of thermophysical properties of high-energy-density matter using current and future heavy-ion accelerator facilities at GSI Darmstadt. Phys Rev Lett **95, no. 3**, 035001

Toulemonde M., Dufour Ch., Meftah A. and Paumier E. (2000): Transient thermal processes in heavy ion irradiation of crystalline inorganic insulators. Nucl Instr Meth Phys Res B **166–167**, 903

Weyrich K., Hoffmann D.H.H., Jacoby J., Wahl H., Noll R., Haas R., Kunze H., Bimbot R., Gardes D., Rivet M.F. and Deutsch C. (1989): Energy-loss of heavy-ions in a hydrogen discharge plasma. Nucl Instr Meth Phys Res A **278, no. 1**, 52–55

Winterbon K.B. (1977): Electronic energy loss and charge-state fluctuations of swift ions. Nucl Instr Meth **144**, 311–315

Zhakhovskij V.V., Nishihara K., Anisimov S.I. and Inogamov N.A. (2000): Molecular-dynamics simulation of rarefaction waves in media that can undergo phase transitions. JETP Lett **71**, 167

Ziegler J.F., Biersack J.P. and Littmark U. (1985): The Stopping and Ranges of Ions in Solids. Pergamon Press, New York.

Ion Beam Analysis of Lower Dimensional Structures

L.C. Feldman*

Department of Physics and Astronomy
Vanderbilt University
Nashville, TN 37215, USA

Abstract

The use of ion beam analysis for the characterization of lower dimensional structures is reviewed. Fundamental limitations as well as practical sources of uncertainty are described. A number of recent examples illustrate the useful information extracted by such analysis, and the critical role that ion beam analysis plays in modern materials science.

Contents

1 Introduction **134**

2 Ion Scattering **135**
2.1 Depth Resolution 136
2.2 Thin Film Stoichiometry 137
2.3 Ultimate Sensitivity 137
2.4 Lateral Resolution 138

3 Semiconductor-Dielectric Interfaces **138**
3.1 The Si/SiO_2 Interface 138
3.2 "Alternate" Dielectrics-Necessity of High K Materials 142
3.3 SiC/SiO_2 143
3.4 CdSe Quantum Dots 146

4 Conclusions and Questions **147**

* E-mail: leonard.c.feldman@vanderbilt.edu

Acknowledgements **149**

References **149**

1. Introduction

A major theme within condensed matter physics and materials science is the creation and characterization of nanostructures, solids with characteristic dimensions less than 100 nm.

Ion beam technology is having a major influence on nanoscience, primarily through ion implantation of nanostructured solids, ion beam lithography at the nanoscale, finely focused ion beam technology, single ion implantation schemes and ion beam analysis. This paper considers some of the ways in which ion beams are impacting nanoscience characterization and analysis, with a special emphasis on the characterization of lower dimensional nanostructures. This paper describes the current limits of ion beam analysis and outstanding problems in the field. The emphasis in this paper will be on the use of ion scattering in the control of semiconductor surfaces, both for two dimensional problems (planar technologies) and zero dimensional problems (quantum dots). Ion beam analysis of thin films is a major field unto itself and has been applied to a large variety of thin film structures. In this paper we focus on the semiconductor dielectric interface, which is of extensive interest and illustrates many of the features and limitations of ion beam analysis.

I first review the basic concepts on ion beam analysis with an emphasis on the simple aspects of Rutherford backscattering (RBS). RBS in all its forms provides a vehicle for understanding the limitations and issues associated with the ion beam analysis. I then provide a detailed discussion of the limits of ion scattering in its various applications. Finally the applicability of these concepts to a number of nanoscience investigations is illustrated. The discussion will focus on the region of incident energies from 100 KeV to ~2 MeV, the most used region for precision material analysis.

This paper is not meant to be a comprehensive or complete overview of ion scattering analysis. Rather it cites few examples, many from the author's work, that allow us to illustrate and discuss the advantages and limitations of ion scattering analysis at the nanoscale.

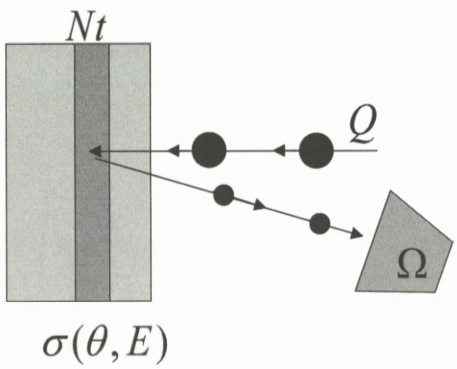

Figure 1. Schematic of a standard RBS set-up indicating the sample-detector configuration and using a solid state detector subtending a solid angle Ω. The measured yield from a thin layer of material of thickness t, volume concentration N may be approximated as $Nt\sigma(\theta, E)\Omega \cdot \Omega$, where $\sigma(\theta, E)$ is the cross-section for scattering to an angle θ and Q represents the number of incident ions.

2. Ion Scattering

The basic physics that governs the interaction of energetic ion beams with solids has its roots in the atomic and nuclear physics of the last century. The central formalisms of Rutherford, Bohr, Lindhard, and others, describing the "ion-solid interaction", provide a valuable quantitative guide to statistically meaningful quantities such as energy loss, ranges, range straggling, channeling effects, sputtering coefficients and damage intensity and profiles. This approach has been an important pillar of the field, leading to a wealth of science and applications. Modern materials science requires atomic scale control and the ability to characterize grown structures on the atomic scale. At this level a reexamination of the ion beam probe is appropriate to either seek enhancements to the technique or to understand the limitations for application at this nanometer level.

Rutherford backscattering has emerged as the most general and used application of ion beam analysis. Indeed both the high level of understanding of the process and its simplicity has combined to underpin this broad application. The process and its description are well-known to the broader community and described in detail in the books by Chu et al. (1978), Feldman and Mayer (1986) and others. The basic scheme is shown in Figure 1. Often RBS is combined with channeling to enhance the surface component of the scattering (Feldman et al., 1982). The apparatus that is employed in RBS also lends itself to a number of other techniques useful in the quantitative analysis of solids. These include particle induced x-ray emission (PIXE), elastic recoil detection analysis (ERDA),

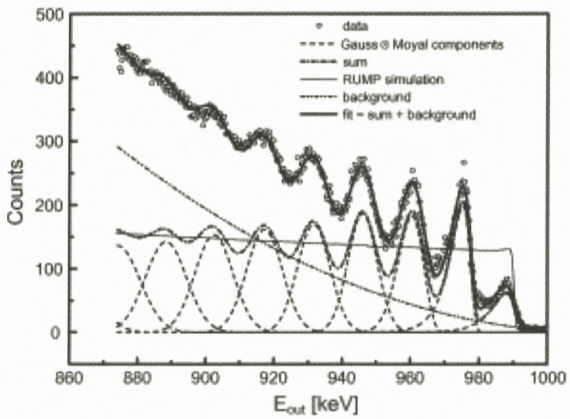

Figure 2. High energy resolution RBS spectrum from a HOPG sample. The first seven carbon layers of the sample are well resolved. (Incident beam: 1 MeV N^+ ions, analyzed ions: N^{2+}, scattering angle: 7°, angles of incidence and exit: 3.5° each.) from Srivastava et al. (2004).

forward recoil scattering (FRS), and nuclear reaction analysis (NRA). Each has their own specific applications. However the straightforward discussion of RBS provides simplicity, while the discussion of limitations may also apply to these other techniques. We first review, with literature examples, the current state of the art of RBS.

2.1. Depth Resolution

Depth resolution has been optimized over recent times through the use of new geometries, grazing angle techniques and the use of high resolution spectrometers. The latest probes can achieve monolayer resolution at the surface of a single crystal (Vrijmoeth et al., 1991; Kimura and Mannami, 1996; Srivastava et al., 2004). A famous example, shown in Figure 2, reveals the monolayer-by-monolayer depth resolution that is achievable (Srivastava et al., 2004).

Such depth resolution is satisfactory for the investigation of clean surfaces, a relevant two-dimensional nanostructure. Ion scattering has been an important tool in understanding surface structures, surface adsorption/desorption kinetics, and ultra-thin (of order a few monolayers) film structures.

Nanostructured materials often comprise buried interfaces. The region in the immediate vicinity of the interface, usually less than 100 nm below the surface, is the critical element of these structures. In such cases the exquisite depth resolution afforded by ion scattering probes is dominated by energy straggling. Indeed finite and insufficient depth resolution is a characteristic of almost all material

probes, including electron spectroscopys such as Auger analysis in combination with sputtering where the depth resolution may be defined by sputter induced ion beam mixing; photoelectron spectroscopy, where the depth resolution is defined by the extinction length; and secondary ion mass spectroscopy (SIMS) where the depth resolution may be determined by ion beam mixing. In the ion scattering case the resolution broadening mechanism, straggling, is relatively well understood in terms of the statistical aspects of the energy loss process. Nevertheless for either experimental and/or theoretical reasons the unfolding of the straggling contribution to depth resolution has not yet been established.

2.2. Thin Film Stoichiometry

As mentioned above the formation of nanostructures often begins with the growth or deposition of a thin film on a substrate. For semiconductor structures the dielectric plays the role of a surface passivator, with the goal of eliminating surface states. In such applications the overlayer dielectric must be of high quality, stoichiometrically ideal and able to withstand high voltages to avoid breakdown.

Ion scattering is an ideal tool for the determination of stoichiometry. Some of the most precise work in this type of problem is reported in the InGaAs system, where the authors report a stoichiometry determination to better than 1% (Jeynes et al., 1997). The limitation of improved stoichiometry determination is primarily the statistical accuracy of an experiment and the knowledge of the scattering cross-section to considerably better than 1%.

2.3. Ultimate Sensitivity

In many applications it is critical to explore impurity levels at very low concentrations. For semiconductor/dielectric problems this often means at the impurity level that can affect the electronic properties of the material, as small as $10^{10}/cm^2$.

The ultimate sensitivity of the ion beam probe is discussed by Feldman and Mayer (1986). Basically the technique is limited by the ion beam sputtering process. Obviously one requires that the probing beam not remove (sputter) the impurity before the completion of the analysis. Such a formulation can be quantitatively established using accepted formulae for ion scattering and sputtering yields. Questions of the appropriate sputtering coefficient to apply to the ultimate surface problem persist. How do you describe the sputtering coefficient for a small fraction of Au on a silicon substrate?

Ultimate sensitivity in ion scattering has been established by the Sandia group (Banks et al., 1998) using low energy – heavy ion beams, time-of flight detection techniques and optimal geometries. This work shows detection sensitivities of

$\sim 1 \times 10^{10}/\text{cm}^2$, an amazing result and certainly in the range where correlation with electrical measurements would be meaningful.

2.4. Lateral Resolution

Lateral resolution, comparable to electron beam spectroscopy, has long been a goal of the ion beam community. Recent years have seen an explosion of developments in the ability to develop such beams using a variety of focusing tools and elements. Current limits are at the 100 nm level and it seems difficult to achieve smaller spot size. (One caveat – the conventional focused ion beam tool typically produces a ~10 nm 30 KeV Ga beam. This paper concentrates on the higher energy regime but one can expect substantial progress in this area, with higher energy and multiple ion beams). Issues associated with the effects of ion source brightness on nuclear microprobe performance is described in the work of Szymanski and Jamieson (1997). Practical examples of ~500 nm ion beam analysis are given in Dollinger et al. (2006).

A new development in focused ion beams is the use of tapered glass capillary optics (Nebiki et al., 2003). In this procedure glass capillaries are formed with opening apertures of ~1 mm and outlet diameters of sub-microns. A surface channeling effect is involved which results in approximately 1% of the beam forming a suitable analysis beam. Although the beam loss is large, and there is some loss of energy resolution due to side-wall scattering, this may be a most convenient and useful mode of placing ion beam analysis in the sub-micron regime. Clearly such simplified and useful methods of forming focused ion beams will receive considerable attention in the future.

3. Semiconductor-Dielectric Interfaces

In the following we illustrate RBS analysis of a number of semiconductor dielectric interfaces. It should be remembered that each of these studies is a multi-technique investigation involving a substantial number of electronic and structural probes. The following discussion focuses only on the ion scattering part to reveal the strengths and limitations of this aspect of particle-solid interactions.

3.1. The Si/SiO_2 Interface

To a large extent the silicon revolution is based on the wonderful properties of the silicon/silicon dioxide interface (Queisser, 1998). The importance of this structure has been documented and cited in many articles and books on the history of technology. Clearly it is the most important materials interface in current process

technologies. Briefly, oxidation of pure silicon results in a large band-gap, uniform, dielectric layer of amorphous SiO_2, with the proper band-offsets to allow both p and n channel devices to be fabricated. Most importantly, modern growth and annealing techniques result in interface defect levels that are sufficiently small so that carrier transport is close to theoretical limits. These excellent qualities have served the community well and been preserved as the basic metal-oxide-semiconductor field effect transistor (MOSFET) device has scaled down over the last five decades.

The success of the MOSFET hinged on a most important and fundamental element of solids, namely the limitations imposed by surface states. Even ideal surfaces can possess electronic states that represent sufficient charge to make the MOSFET inoperable. Hans Quiesser, in his exciting book, *Conquest of the Microchip*, notes: "what finally saved the day was that an incredibly stable oxide of silicon can be wrapped around the crystal to protect it" (Queisser, 1998). Another historical account, *The History of Engineering & Science in the Bell System* (Millman, 1983), states "surface state problems were resolved by an unexpected discovery .... Kahng and Atalla found that silicon and clean, thermally grown SiO_2 interfaces contain sufficiently small surface states to realize a true field effect transistor in silicon". Frosch and Derick (1957) first reported the beneficial properties of the SiO_2/Si materials system.

Research in the last twenty years has exploited almost every conceivable surface/thin film probe to establish the underlying physical nature of this critical solid-state interface (Feldman et al., 1998). Of particular interest has been the nature of the starting silicon surface, the kinetics of the oxidation process, the structure and solid-state chemistry of the silicon-silicon dioxide interface and the relationship of the structure to the electronic properties.

Nevertheless outstanding scientific issues remain at the very forefront, limiting the further evolution of silicon science and technology. Indeed these issues have become even more prominent. For as the device has scaled down, with the corresponding reduction of silicon dioxide thickness from microns to nanometers, the silicon/silicon dioxide interface becomes more prominent and more limiting. We are close to fundamental limits where the need for understanding and atomic control becomes ever more critical.

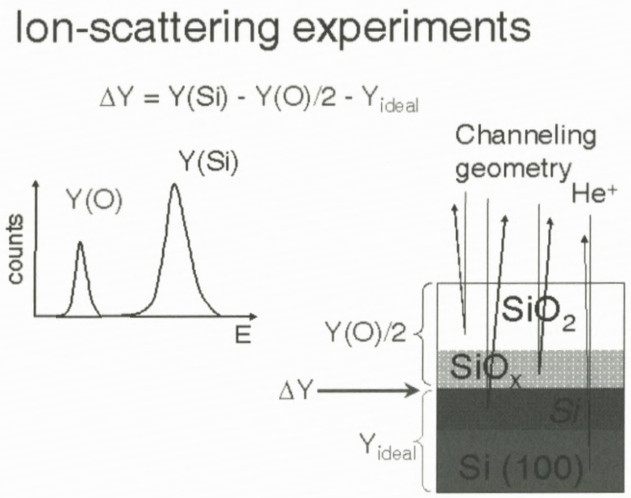

Figure 3. Schematic of the ion scattering/channeling configuration with the beam oriented parallel to the major ⟨100⟩ channeling direction for a Si/SiO_2 structure. The spectrum schematically indicates the scattering from the oxygen in the oxide and the silicon contributions from the SiO_2, the SiO_x and the Si surface peak. The "excess yield", ΔY, is indicated as the silicon yield over and above that expected from an ideal, stoichiometric oxide and Y_{ideal}, the contribution from the ideal surface peak.

It is generally agreed that there is a transition region (of altered structure and/or stoichiometry) between crystalline silicon and SiO_2. Ion scattering experiments on this interface have contributed to the sophisticated characterization required for the determination of the structure (Bongiorno et al., 2003). Measurements are usually done in a channeling geometry as shown schematically in Figure 3. Because of the channeling condition the ion scattering spectrum is dominated by silicon and oxygen in the amorphous oxide and the Si surface peak, as shown in Figures 3 and 4.

In a channeling direction the ion beam encounters at least the first monolayer of a clean surface with a full scattering intensity. Scattering from deeper layers is suppressed due to the channeling (shadowing) effect. In practice the "surface peak" encompasses scattering yields from the first few monolayers of the solid due to thermal vibrations, which cause the first few sub-surface layer atoms to extend beyond the shadow established by the first atom in the string. The total yield of surface scattering for an ideal crystal can be estimated through a variety of numerical simulations (Feldman et al., 1982). Figure 5b shows the good agreement between the measured and calculated surface scattering intensity for the Si(100)-H-(1×1) surface, a surface structure that is established to have a near "bulk-like"

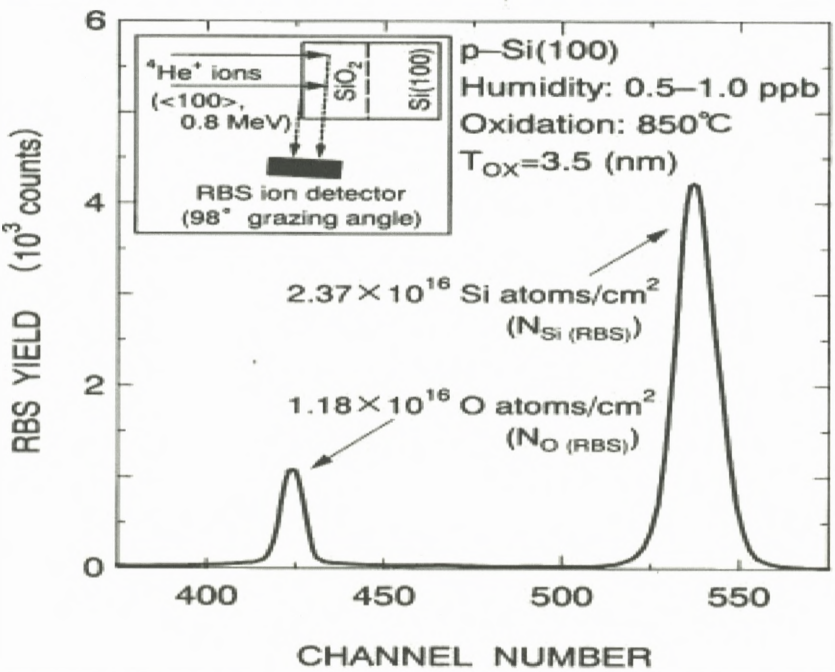

Figure 4. Rutherford backscattering spectrometry (RBS) spectrum for the 3.5 nm-thick silicon oxide film grown on a *p*-type Si(100) substrate at 850°C with 0.5–1.0 ppb humidity. This was obtained in the channeling grazing-exit-angle geometry using 0.8 MeV $^4He^+$ incident ions along a Si ⟨100⟩ -axial-aligned channeling direction and an ion detector arranged at a grazing-exit angle of 95° relative to the incident ion beam (Yamada, 2001).

surface termination. The good agreement between experiment and calculation for the "bulk-like" surface establishes the validity of the technique and the value of the intrinsic surface contribution to the total silicon scattering intensity (Stensgaard et al., 1981).

The essential results of the measurements indicates an excess of Si scattering over that expected from an ideal structure for the Si/SiO_2 material (Jackman et al., 1980). This excess is attributed to the distortion of the first few monolayers of silicon at the amorphous oxide/crystal interface. This "excess" has been compared to theory (Bongiorno et al., 2003) to provide a total description of the interface structure and distortions (Figure 5). The significance of these few monolayers of distortion may be understood when it is realized that the electronic wave function of the conduction electrons is confined to ~10 monolayers near the interface and the crystal distortion can seriously affect the electron probability density and the (inversion layer) electron mobility. This latter quantity ultimately determines

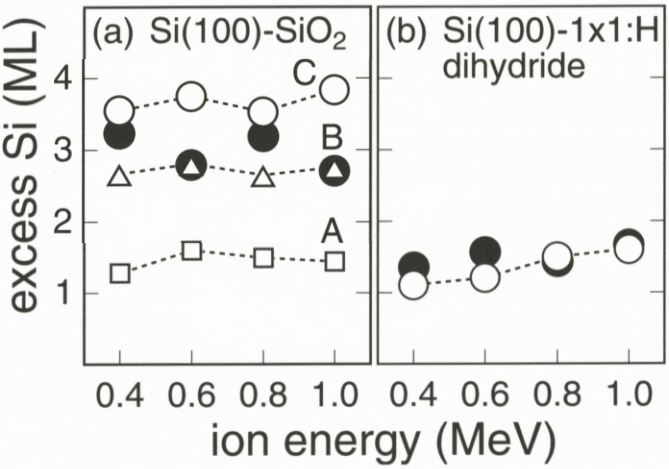

Figure 5. Measured (full circles) and calculated excess Si yields *versus* ion energy for (a) the Si(100)-SiO_2 interface and (b) the Si(100) 1× 1:H surface. The agreement for the hydrogen terminated surface demonstrates the high level of understanding of the intrinsic surface peak. In (a) the calculated values are obtained for different models of the interface structures; the contribution from partially oxidized silicon is shown by a shaded band. The models are most completely explained in Bongiorno et al. (2003), but may be briefly described as (A) near ideal termination with no distruption; (B) in-plane dimers and (C) a mixture of dimers and nonstoichiometric oxide.

the speed of the device. Other authors have also measured this Si distortion and considered its extent as a function of oxidation parameters (Stedile et al., 1996; Yamada, 2001, 2002).

3.2. "Alternate" Dielectrics-Necessity of High K Materials

One of the fundamental limits of ultrathin oxide/oxynitride films is direct tunneling (current) which grows exponentially with decreasing film thickness (Feldman et al., 1998). For sub 2 nm films, the tunneling current becomes large, which requires a significant (and unacceptable) power dissipation in logic devices, especially for portable applications. To overcome the direct tunneling problem, the "physical" thickness of the dielectric should be kept large, much thicker than the direct tunneling limit ~2.0 nm. On the other hand, ULSI scaling is driving a reduction in thickness (increasing capacitance) for next generation of fast switching devices. One way to ameliorate these conflicting needs is to replace conventional SiO_2 by a material with a higher dielectric constant, preferably a much higher one. This would allow a dielectric with a thicker "physical" thickness, but the "equivalent" capacitance (with respect to pure SiO_2) and the direct tunneling current would be much reduced.

Several high K materials are now being explored as a gate dielectric. Recent examples include ZrO_2, HfO_2, hafnium silicates, scandium oxide and others. The material of choice must have a set of important properties including: (i) a high dielectric constant (preferably > 25), (ii) high thermal stability (especially with respect to Si); (iii) perfect stoichiometry (which presumably minimizes intrinsic defects and traps in the film), (iv) a low concentration of interface states and stability of the interface during thermal treatments and external radiation; (v) resistance to dopant diffusion, (vi) low leakage currents; (vii) large band gap (>4 eV) and an appropriate barrier offset with respect to silicon; (viii) a low thermal budget, defect free processing; and (ix) manufacturability and integration with silicon technology. Ideally, this material should have properties as good as SiO_2 on Si, but with a much higher dielectric constant. This is a "tall order" and there is no clear favorite at the moment. The search for the alternate dielectric is an intense on-going activity in the semiconductor community.

Furthermore, a very thin buffer layer of silicon oxide, oxynitride or nitride may still be required between the silicon substrate and the high K dielectric in order to minimize interface states and to act as a diffusion barrier between the layers. In this case, the equivalent thickness of the stacked dielectric will have contributions from both the thickness of the buffer layer and the equivalent thickness of the high K layer. To keep the overall equivalent thickness less than $\sim$1.0 nm, the buffer layer should consist of not more than 1–2 atomic layers. Needless to say, this mono/double layer should be nearly perfect and the new interface between the buffer layer and the high K material should be as high quality as the SiO_2/Si interface. This fact motivates and justifies the continuing, atomic-scale studies of ultrathin silicon oxides, oxynitrides and nitrides, in conjunction with the exploration of the optimum alternate dielectric.

Ion scattering analysis plays a significant role in the search for the "alternate dielectric" (Gustafsson et al., 2001). Figure 6 shows an important contribution of ion scattering for the case of a ZrO_2 layer. With the clever use of isotopes and making use of the mass selectivity and depth resolution of ion scattering the authors show that oxidation (in ^{18}O) of a SiO_2/ZrO_2 stack results in oxygen exchange within the ZrO_2 and additional oxidation of the underlying silicon increasing the underlying SiO_2 layer. Such results are critical to questions of reliability and processing of these new structures.

3.3. SiC/SiO_2

Si-based metal-oxide-semiconductor field-effect transistors are at the heart of microelectronics. However, for many applications, such as systems operating at high power, high temperature, and high frequency, it is very desirable to have

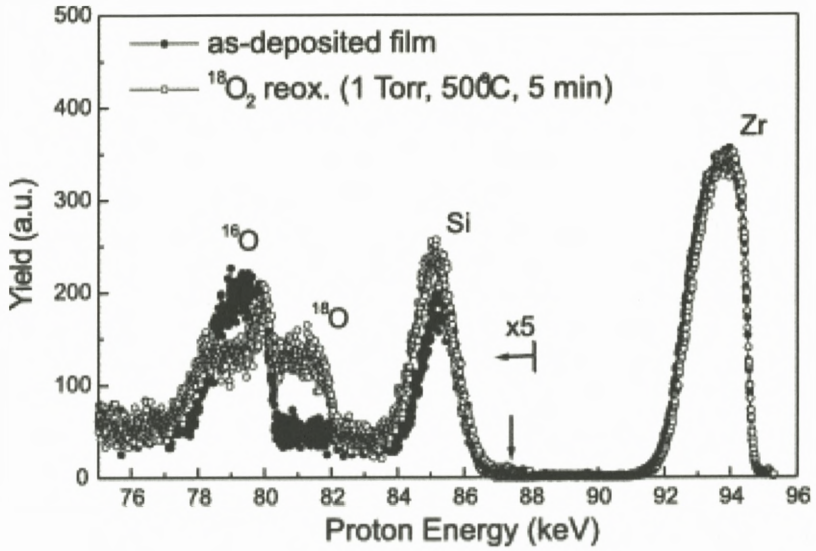

Figure 6. Medium Energy Ion Scattering (MEIS) proton spectrum from the as-deposited ZrO_2 film on Si(100), and a film subsequently re-oxidized in $^{18}O_2$ (1 Torr, 500°C, 5 min). Signals from ^{16}O, ^{18}O, Si and Zr are clearly resolved. The arrow at 87.3 keV indicates the energy where surface Si would be detected. The data clearly show the growth of SiO_2 at the interface between the ZrO_2 film and Si substrate (as seen by shifts of the O and Si signals to lower energy), and a dramatic oxygen exchange within the film (Gustafsson et al., 2001).

MOSFETs based on a wide-band-gap semiconductor. High temperature at high power operation has become increasingly important as society considers energy efficient systems.

Several wide-band-gap semiconductors have been investigated extensively, but all are limited by the lack of a suitable dielectric. The problem is generic as Si-SiO_2 is the only semiconductor-dielectric combination that yields functional MOSFETs. No other semiconductor has a native oxide that meets the crucial requirements of low densities of interface traps that control channel mobility. Deposited non-native oxides have not proven adequate either. From this perspective, SiC is a unique semiconductor because it is the only other material, besides Si, whose native oxide is the well understood SiO_2. 4H-SiC also has high thermal conductivity, high breakdown field strength, reasonable mobility and mobility anisotropy and high saturated electron drift velocity, all of which make it a prime candidate for high-power, high-temperature, and high-frequency devices. Obviously the critical role of the dielectric requires that the material, its stoichiometry and its electrical properties be well characterized and understood. The stoichiom-

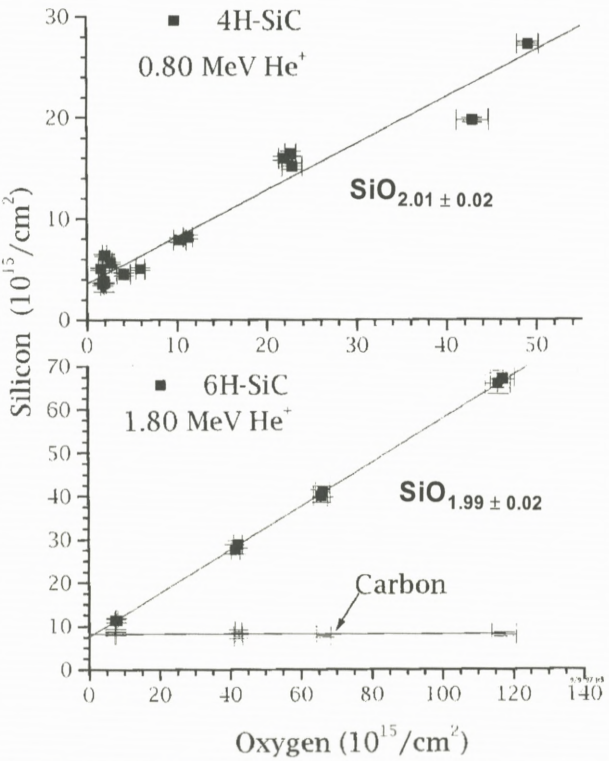

Figure 7. Determination of the Si to oxygen ratio as a function of thickness for SiO_2 grown layers on SiC. The values of the slope of the line indicate that the oxide is stoichiomentric SiO_2. The *y*-axis intercept is a measure of the intrinsic Si surface intensity. Note that the carbon content, which arises from the crystalline carbon surface peak, is constant with growth indicating no carbon incorporation (at the level of $10^{15}/cm^2$) in the oxide.

etry determination is an ideal problem for ion beam analysis. Figure 7, shows the results of ion scattering studies, in a channeling direction, to determine the composition of the grown oxide on 4H-SiC. Clearly the material is stoichimeteric SiO_2, within the error of the determination. Furthermore, there is essentially no carbon within the film. The baseline of the carbon content arises from the carbon surface peak and is constant with increasing oxide thickness. Such measurements, as a function of processing conditions and in concert with other experimental studies, demonstrate that the oxide is essentially pure SiO_2, similar in all ways to the high quality oxide on Si. The successful growth of this oxide followed by specialized processing has opened up the possibility for a new high power, energy efficient SiC technology (Song et al., 2004).

3.4. CdSe Quantum Dots

Nanostructures, particularly "quantum dots", with their very large surface to volume ratio and their non-planar geometry, present an important challenge to surface scientists. New issues arise as to surface characterization, quantification, and interface formation and surface passivation.

A nanocrystal is essentially a three-dimensional quantum square well. By precisely controlling a nanocrystal's size and surface, its properties can be engineered. CdSe nanocrystals vary in size from ~2–11 nm and contain a few hundred to ten thousand atoms. Through quantum confinement of the photo-created electron hole pair the optical properties of the nanocrystal can be tuned by size. For example, a 2.2 nm nanocrystal will have 88% of its atoms on the surface and absorb light at 420 nm while a 8.5 nm nanocrystals consists of 20% surface atoms and absorbs light at 650 nm. Nanocrystals are usually chemically synthesized in an organic surfactant that passivates the surface. The choice of surfactant can control the growth of the nanocrystal and its size and shape. The surfactant/nanocrystal organic/inorganic interface also controls the ultra-fast carrier dynamics in the nanocrystal and the fluorescence quantum yield. Alternatively the surface of the CdSe nanocrystal can be passivated with a second inorganic material, such as CdS, ZnS, or ZnSe to create a core-shell nanocrystal. When wrapped in a wider band gap material the electron-hole pair is further confined and surface states dangling bonds are minimized. If the interface between the two inorganics is perfect nearly unity quantum yield materials result. Here again characterization of the interface is crucial in order to engineer a quantum dot with desired properties (McBride et al., 2006).

Given their large surface to volume ratio and their non-planar geometry, nanocrystals present an important challenge to surface scientists. Recent investigations use Rutherford backscattering spectroscopy (RBS) and atomic number-contrast scanning transmission electron microscopy (Z-STEM) to determine composition and size (McBride et al., 2006). When combined these techniques give information on nanocrystal composition, surface composition, surface ligand coverage, and nanocrystal structure, including the interior, interfaces, and surfaces of the quantum dot.

Figure 8 shows an example of the insights to be gained by the accuracy afforded in a stoichiometry measurement via RBS. Here the quantity of interest is the stoichiometry as accurately determined via the Cd/Se ratio. Systematic studies as a function of size and crystal growth procedures revealed that nanocrystals grown in TOPO (trioctyphosphine oxide) showed excess Cd. The systematic

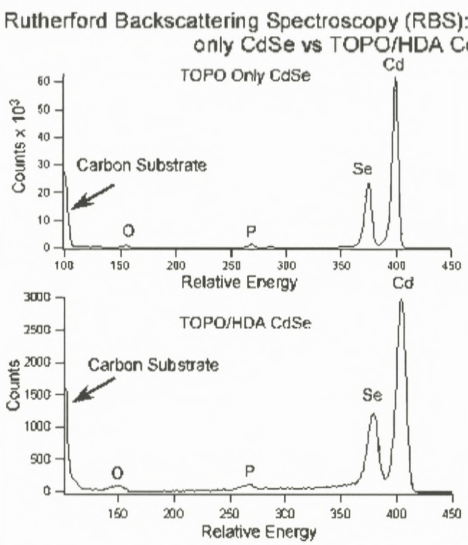

Figure 8. RBS spectrum comparison of CdSe nanocrystals grown in TOPO and HAD. The ideal stoichiometry, 1:1, is achieved in the HAD grown material leading to more uniform size distributions and more efficient optical properties (McBride et al., 2006).

series of measurements indicate that the excess was a surface component, easily envisioned when it is recognized that the surface contains ~50% of all the atoms in the structure. Growth in hexadecylamine (HAD) results in a stoichiometric nanocrystal with superior surface properties, compared to growth in TOPO. These core structures may then be encapsulated in a wide-band gap semiconductor to provide surface passivation and reduce surface recombination.

The RBS analysis reveals intriguing insight in the structure of these TOPO only nanocrystals. The excess Cd is due to the stabilization of Cd dangling bonds by the passivating TOPO. An outcome of this analysis was the successful capping of the stoichiometric nanocrystals with a wide band gap semiconductor, ZnCdS. The wide band gap material plays the same role in these nanocrystals as SiO_2 on Si-namely it passivates surface states. The final structure had exceedingly high quantum yields of >80%, indicative of a well passivated surface.

4. Conclusions and Questions

These examples illuminate the strengths, weaknesses and physical limitations of ion scattering spectroscopy. It is important to distinguish between limitations that

arise because of well-understood physics and limitations that might be overcome with new experimental and computational approaches.

A complete discussion of the limitations to depth resolution in ion scattering experiments has recently been presented by Schulte et al., focusing on the shape of the surface peak in "clean surface" experiments (Schulte et al., 2001). Good agreement between experiment and theory depends on the understanding of the impact parameter dependent stopping power, understanding the thermal vibrations of surface atoms, and the possibility of specific inelastic losses. All of these quantities require further testing and more precise comparisons between experiment and theory. A fascinating aspect of this question is the possible effects of modified energy loss and energy loss straggling in these lower dimensional structures consisting of a two-dimensional electron gas (Borisov et al., 2006).

Buried interfaces provide an additional set of issues for the ion scattering community. Undoubtedly new methods to deconvolute straggling contributions could be a substantial benefit in analysis. This is a formidable task both experimentally and theoretically. Nevertheless success in this venture will represent a substantial benefit and applicability to the technique. It is clear that all of the buried structures described above would benefit from a sophisticated deconvolution of the straggling contribution to the resolution broadening.

On the experimental side there needs to be considerable efforts at higher resolution and more efficient detectors. Efficiency here might mean the ability for three dimensional analysis in the channeling-blocking configuration, to minimize ion beam damage. The convenience of the solid state detector also needs to be recognized. The great advances that have occurred in semiconductor heterostructures suggest that new solid state detectors might be conceived with better energy resolution.

Many contributions to nanoscience will depend on the successful utilization of focused ion beams. It is important to explore new and convenient ways of forming such beams, with optimal geometries to reduce probing beam damage effects. The glass capillary approach mentioned above is such an example (Nebiki et al., 2003).

Finally, as noted above, thin film stoichiometry is a great strength of the RBS technique. In the limit of high statistical accuracy the stoichiometric determination will be limited by absolute knowledge of the scattering cross-sections, indicating the need for more precise measurements of these fundamental quantities, particularly for low Z elements.

All of the examples cited above could yield more detailed and specific information with the potential advances cited above.

Acknowledgements

It is a pleasure to acknowledge colleagues with whom I have collaborated concerning the issues discussed in this manuscript: S.J. Rosenthal, J. McBride, S. Dhar, Y. Song, S. Dixit, J. Williams, A. Bongiorno and A. Pasquarello.

References

Banks J.C., Doyle B.L., Knapp J.A., Werho D., Gregory R.B., Anthony M., Hurd T.Q. and Diebold A.C. (1998): Using Heavy Ion Backscattering Spectrometry (HIBS) to solve integrated circuit manufacturing problems. Nucl Instrum Meth Phys Res B **137**, 1223–1228

Bongiorno A., Pasquarello A., Hybertson M.S. and Feldman L.C. (2003): Transition structure at the Si(100)-SiO_2 interface. Phys Rev Lett **90**, 186101

Borisov A.G., Juaristi J.I., Muino R.D., Sanchez-Portal D. and Echenique P.M. (2006): Quantum size effects in the energy loss of charged particles interacting with confined two-dimsional electron gas. Phys Rev A **73, no. 1**, 012901

Chu W.K., Mayer J.W. and Nicolet M.A. (1978): Backscattering Spectrometry. Academic Press, New York

Dollinger G., Bergmaier A., Hauptner A., Dietzel S., Drexler G.A., Greubel C., Hable V., Relchart P., Krucken R., Cremer T. and Friedl A.A. (2006): Hydrogen microscopy and analysis of DNA repair using focused high energy ion beans. Nucl Instr Meth Phys **249**, 270–277

Feldman L.C. and Mayer J.W. (1986): Fundamentals of Surface and Thin Film Analysis. North Holland-Elsevier, New York [Translated into Japanese, Kaibundo Publishing (1988); translated into Russian, MIR Publishing (1989)]

Feldman L.C., Mayer J.W. and Picraux T.A. (1982): Materials Analysis by Ion Channeling: Submicron Crystallography. Academic Press, New York

Feldman L.C., Gusev E.P. and Garfunkel E. (1998): Ultrathin dielectrics in Si microelectronics – An overview. In: Garfunkel E., Gusev E.P. and Yavul A. (Eds), Fundamental Aspects of Ultrathin Dielectrics on Si-Based Devices. Kluwer Academic Publishers, Dordrecht

Frosch C.J. and Derick L. (1957): Surface protection and selective masking during diffusion in silicon. Proc Electrochem Soc **547**

Gustafsson T., Lu H.C., Busch B.W., Schulte W.H. and Garfunkel E. (2001): High-resolution depth profiling of ultrathin gate oxides using medium-energy ion scattering. Nucl Instrum Meth Phys Res B **183**, 146–153

Jackman T.E., MacDonald J.R., Feldman L.C., Silverman P.J. and Stensgaard I. (1980): (100) and (110) Si-SiO_2 interface studies by MeV ion backscattering. Surf Sci **100**, 35–41

Jeynes C., Jafri Z.H., Webb R.P., Kimber A.C. and Ashwin M.J. (1997): Accurate RBS measurements of the indium content of InGaAs thin films. Surf Sci Interface Anal **25**, 254

Kimura K., and Mannami M. (1996): RBS single monolayer resolution. Nucl Instrum Meth Phys Res B **113**, 270

McBride J., Treadway J., Feldman L.C., Pennycook S.J. and Rosenthal S.J. (2006): Structeral basis for near unity quantum yield core/shell nanostructures. NanoLetters **6**, 1496

Millman, S. (Ed.) (1983): A History of Engineering and Science in the Bell System. AT&T Bell Laboratories, New York

Nebiki T., Yamamoto T., Narusawa T., Breese M.B.H., Teo E.J. and Watt F. (2003): Focusing of MeV ion beams by means of tapered glass capillary optics. J Vac Sci Technol A **21**, 1671–1674

Queisser H. (1998): The Conquest of the Microchip. Harvard University Press, Cambridge, MA

Schulte W.H., Busch B.W., Garfukel E., Gustafsson T., Schwietz G. and Grande P.L. (2001): Limitations to depth resolution in ion scattering experiments. Nucl Instr Meth B **183**, 16

Song Y., Dhar S., Feldman L.C., Chung G. and Williams J.R. (2004): Modified deal grove model for the thermal oxidation of silicon carbide. J Appl Phys **95**, 4953–4957

Srivastava S.K., Plachke D., Szokefalvi-Nagy A., Major J. and Carstanjen H.D. (2004): Counting individual atom layers in graphite – High-resolution RBS experiments on highly oriented pyrolytic graphite. Nucl Instrum Meth Phys Res B **219/220**, 364

Stedile F.C., Baumvol I.J.R., Oppenheim I.F., Trimaille I., Ganem J.J. and Rigo S. (1996): Thickness of the SiO_2/Si interface and composition of silicon oxide thin films: Effect of wafer cleaning procedures. Nucl Instrum Meth Phys Res B **118**, 493–498

Stensgaard I., Feldman L.C. and Silverman P.J. (1981): Evidence of multilayer distortions in the reconstructed Si(001) surface. Surf Sci **102**, 1–6

Szymanski R. and Jamieson D.N. (1997): Ion source brightness and nuclear microprobe applications. Nucl Instrum Meth Phys Res B **130**, 80–85

Taylor J., Kippeny T., Bennett J.A., Huang M., Feldman L.C. and Rosenthal S.J. (1999): Proceedings of the Materials Research Society, Microcrystalline and Nanocrystalline Semiconductors, Vol 536, p 413.

Vrijmoeth J., Zagwijn P.M., Frenken J.W.M. and Vanderveen J.F. (1991): Monolayer resolution in medium-energy ion-scattering experiments on the $NiSi_2(111)$ surface. Phys Rev Lett **67**, 1134–137

Yamada H. (2001): Microscopic composition difference related to oxidizing humidity near the ultrathin silicon oxide-Si(100) interface. J Vac Sci A **19**, 627

Yamada H. (2002): Changes in the density of ultrathin silicon oxide films related to excess Si atoms near the oxide-Si(100) interface. J Appl Phys **91**, 1108

Solved and Unsolved Problems in Ion-Beam Analysis: The Influence of Single Collisions

P.L. Grande[1,*], A. Hentz[1], R.P. Pezzi[1,2], I.J.R. Baumvol[1,3] and G. Schiwietz[4]

[1]Instituto de Física da Universidade Federal do Rio Grande do Sul
Avenida Bento Gonçalves 9500
91501-970, Porto Alegre, RS, Brazil
[2]IBM Research Division, T.J. Watson Research Center
P.O. Box 218, Yorktown Heights, NY 10598, USA
[3]Centro de Ciências Exatas e Tecnologia, UCS
Caxias do Sul, R.S., Brazil 95070-560
[4]Hahn-Meitner-Institut, Abteilung SF4
Glienicker Str. 100, 14109 Berlin, Germany

Abstract

In this work we explore some unsolved problems in ion-beam techniques involving backscattered projectiles or nuclear reactions. In particular, we focus on the influence of a single violent collision on the depth resolution. In high-resolution experiments, where the surface or near surface interfaces are investigated, the energy straggling becomes very asymmetric. The corresponding energy-loss distributions are skewed for larger energy losses due to the ionization and excitation of the inner-shell electrons. We determine the electronic energy-loss distribution using the coupled-channel calculations. Then these *ab-initio* calculations are used as benchmark for simple models of energy-loss lineshapes that can be used in ion-beam analysis to replace the standard Gaussian distribution.

* E-mail: grande@if.ufrgs.br

Contents

1 Introduction **152**

2 Open Problems in IBA **154**

3 Asymmetric Energy Loss Straggling **155**

4 Energy Loss in a Single Collision **156**
4.1 Coupled-Channel Method 156
4.2 Independent-Particle Model 158
4.3 Higher-Order Effects 160
4.4 Reference Results 164
4.5 Simple Model for Energy-Loss Distributions 167
4.5.1 Model for the Mean Energy-Loss 167
4.5.2 Energy-Loss Moments 169
4.5.3 Analytical Formula 171

5 Examples **172**
5.1 Depth Profiling in Ultra Thin Films 172
5.2 Description of the Al Surface Peak 173
5.2.1 Transport: Stochastic and Monte-Carlo Approaches 175

6 Conclusions **180**

Acknowledgements **182**

References **182**

1. Introduction

The ideal ion-beam technique is the one that is non-destructive, has high sensitivity, atomic selectivity and high lateral and well as depth resolution.

However, this is not the case for the real ion-beam techniques. In fact, most of the open problems in ion-beam analysis (IBA) are concerned with how to increase sensitivity and resolution without damaging the target.

Many improvements have been achieved during the last years in order to increase sensitivity and resolution in IBA. From the experimental point of view, the increasing use of magnetic, electrostatic and time-of-flight spectrometers has strongly enhanced the resolution compared to standard surface barrier detectors. The detection efficiency has been improved by using a larger number of detectors

as well as by increasing the solid angle with the corresponding geometrical corrections (Dollinger et al., 2004). Furthermore, ultra high vacuum conditions have allowed for surface and near-surface investigations (Woodruff and Delchar, 1994). On the side of the data analysis, nowadays there are many fitting procedures and simulation programs, which have been recently reviewed by Rauhala et al. (2006). From the theoretical point of view, the equilibrium and non-equilibrium stopping forces as function of the projectile charge-state can be obtained using different approaches and programs, as for example the Unitary Convolution Approximation UCA (Schiwietz and Grande, 1999; Grande and Schiwietz, 2002), the Friedel Sum extended to finite velocities (Arista and Lifschitz, 1998; Arista, 2002) and the Binary model (Sigmund and Schinner, 2000, 2002; Sigmund, 2004). In these approaches the projectile charge-state enters as an input parameter. Recently, Grüner and Bell (2006) has extended the CTMC (Classical Trajectory Monte-Carlo) method (Olson, 1989) to calculate not only the stopping force but also the charge-states for heavy ions at high energies. Concerning the statistical treatment, the use of the stochastic theory to analyze, for instance, the nuclear reaction analysis (NRA) using nuclear resonant reactions, has established this ion-beam technique as a powerful method for depth profiling light isotopes (Maurel et al., 1982).

The improved experimental conditions have allowed for energy resolved monolayer resolution, using medium energy ion scattering (MEIS) (Vrijmoeth et al., 1991), Rutherford backscattering (RBS) (Kimura et al., 1994) and also recoil detection analysis (ERDA) (Dollinger et al., 1998b). The fundamentals for monolayer resolution analytics using the energy loss of ionic projectiles is, besides the high resolution, grazing incidence or detection conditions (only few degrees with respect to the surface), because the ratio of the energy loss straggling to the mean energy loss decreases for increasing projectile pathlength. Recently, Carstanjen and coworkers (Srivastava et al., 2004) have performed a remarkable experiment, where individual atom layers in graphite have been observed by RBS using 1 MeV N projectiles. In this experiment we may find two open problems in IBA, namely a non-Gaussian energy loss distribution for atomic layers near the surface and a reduced yield for the first monolayer due to charge exchange processes.

The present paper is organized as follows. Some unsolved problems in IBA are addressed in Section 2. Then, we will focus on the problem of asymmetric energy loss distributions in Section 3 and subsequent sections. The energy loss straggling in a single collision (in Section 4) will be described using *ab-initio* calculations (in Sections 4.1 to 4.4) and a simplified model (in Section 4.5). The importance and correct modeling of the energy loss in a single collision is discussed in Section 5 for depth profiling of Hf in sub-nanometric high-k oxide films (in Section 5.1)

and for the description of the surface peak in Al (in Section 5.2). Finally the conclusions are presented in the last section. If not indicated otherwise, atomic units ($e = m = \hbar = 1$) will be used throughout the paper.

2. Open Problems in IBA

In most used ion-beam techniques including analysis (RBS, MEIS, ERDA, NRA, etc.) (Tesmer and Nastasi, 1995) and ion therapy (Debus et al., 2004), the energy scale can be converted to depth and the measured yield to concentration. In this way, the accurate knowledge of the projectile energy-loss distribution and charge-states are of fundamental importance. Not only the knowledge of stopping forces are required but also the energy straggling (Gaussian or non-Gaussian) as a function of the projectile charge-state must be accurately known, even within a 1% level, for some applications.

For ion-beam techniques dealing with heavy ions, there are additional problems in the data analysis related to non-equilibrium projectile charge-states. It has been observed (Dollinger et al., 1998a; Carstanjen, 1998) that the yield of detected heavy ions depends on the projectile charge-state and the charge-state populations depend on the depth. In fact, the correct data analysis in such experiments is a quite complex problem, since many charge-changing cross-sections have to be known accurately as a function of the projectile charge and energy. An experimental way out of this problem is the measurement of the yield for all projectile-charge states, which is extremely time consuming especially for electrostatic and magnetic spectrometers.

There are numerous other problems, which limit the use of ion-beam analysis. For instance, it would be very interesting to use ion-beam techniques for elemental depth profiling in materials that are not planar such as nanostructures embedded in a homogenous host target. However, all data analysis procedures assume translation invariance in the direction perpendicular to the sample normal.

Another problem is the determination of the instrumental resolution function without any influence of the target, particularly in magnetic and electrostatic spectrometers (Munoz-Marquez et al., 2005b). In fact, what can be measured is the convolution of the instrumental spectrometer function with the energy-loss straggling. The accurate knowledge of the instrumental function as well as of the Doppler effect coming from target thermal vibrations are of ultimate importance to understand the asymmetric energy-loss distributions in future ultra-high resolution experiments.

Among many open problems for ion-beam analysis, here we will focus our present study to address asymmetric energy-loss distribution laws. As will be

shown below, the understanding and corresponding modeling of such asymmetries is crucial to use the ion-beam analysis in subnanometric regions near the surface.

3. Asymmetric Energy Loss Straggling

The use of Gaussian distributions for the electronic energy loss in IBA techniques has been widely used in the literature not only because its simplicity but also because for thick enough targets the energy-loss distribution does tend to a normal distribution according to the central limit theorem (for $\Omega^2 \gg T_{\max}^2$ – see Sigmund, 2006). In other words, a Gaussian energy-distribution results from the convolution of many small energy losses due to individual events.

There are two significant improvements of the existing formalism: impact-parameter-dependent straggling (Kabachnik et al., 1993) (adopted here) and non-Gaussian straggling based on realistic and non-realistic energy-transfer cross-sections (for a very nice and self containing review, see Sigmund, 2006).

Differently from other ion-beam techniques, the modeling of nuclear reaction profiling (NRP) (Maurel et al., 1982) does not assume Gaussian energy-loss distributions. Instead many self-convolutions are determined numerically for an approximate single collision spectrum. The nuclear reaction yield is then obtained by considering Poisson statistics of collisions, the cross-section for the resonant reaction, the beam spread and Doppler broadening effect. Thus, experimental excitation curves are fitted using trial concentration profiles. In this way, highly accurate depth profiling of light isotopes has been obtained with remarkable depth resolution (Driemeier et al., 2006), though the electronic excitations for the ion-nucleus nuclear reaction are also important for an improved depth resolution in ultra-thin films (Schulte et al., 2001).

In summary, the asymmetry in the energy-loss distribution arises from the statistics of collisions, which are uncorrelated in amorphous materials and correlated in crystals. On the other hand, collisions with very small impact parameters to the nucleus as the backscattering collision in scattering techniques may be responsible for very large asymmetries since the inner-shells can be ionized. This will be of ultimate importance for the cases where there are collisions with high inner-shell ionization probability and large binding energy.

Moreover, the inner-shell binding energy has to exceed the projectile-energy straggling before the violent collision, and of course, the experimental resolution must have a variance smaller than (or comparable to) the inner-shell binding energy. This scenario occurs, for instance, in surface and near-surface investigations using typically few hundred keV of protons or helium in MEIS experiments (Hoshino et al., 2005).

4. Energy Loss in a Single Collision

During the last years we have investigated the electronic energy loss of bare and screened ions for light targets using the coupled-channel method. This first principle calculation (Schiwietz, 1990; Grande and Schiwietz, 2004), based on an expansion of the time-dependent electronic wave function in terms of atomic orbitals, has been successfully applied to evaluate the impact-parameter and angular dependence of the electronic energy loss and the total stopping cross-section of ions (antiprotons, H and He) colliding with H and He atoms at energies ranging between 1 to 500 keV/amu. It has also been applied to calculate the entrance-angle dependence of the stopping force for He ions channeling along the Si main crystal directions (dos Santos et al., 1997) as well the shape of the surface peak for protons backscattered from Al under channeling and blocking conditions (Grande et al., 2004).

These benchmark calculations have also been used to check simplified models that account for the basic energy loss processes without the need of large scale calculations (Grande and Schiwietz, 1998; Schiwietz and Grande, 1999) and to calculate the probability of multiphoton ionization in the case of intense fs-laser pulses (Schiwietz et al., 2001; Grande and Schiwietz, 2004).

4.1. Coupled-Channel Method

Here we will focus the attention on atomic treatments of the energy-transfer process. Thus, we will not consider solid-state effects such as intra-band transitions, collective excitations (bulk and surface plasmons) and the corresponding dynamic projectile screening. The coupled-channel was already reviewed in Grande and Schiwietz (2004). In what follows we review the most important points for completeness. Any additional information can be found in Grande and Schiwietz (2004) and references therein.

The theoretical formulation of atomic excitation and ionization processes is conveniently discussed by introducing the quantum-mechanical Hamilton operator. For a three-body system the Hamiltonian reads

$$\mathcal{H} = T_{\mathrm{p}}(\vec{r}_{\mathrm{p}}) + T_{\mathrm{t}}(\vec{r}_{\mathrm{t}}) + T_{\mathrm{e}}(\vec{r}_{\mathrm{e}}) + V_{\mathrm{pt}}(\vec{R}) + V_{\mathrm{te}}(\vec{r}) + V_{\mathrm{pe}}(\vec{R} - \vec{r}) \tag{1}$$

with the kinetic and potential energies denoted T and V, respectively. The subscripts p, t, and e refer to the projectile ion, target core, and electron as indicated in Figure 1.

In the following we will use the impact-parameter method, i.e., it is assumed that $\vec{r}_{\mathrm{p}}$ and $\vec{r}_{\mathrm{t}}$ are given by classical paths $\vec{r}_{\mathrm{p}} = \vec{r}_{\mathrm{p}}(t, b)$, $\vec{r}_{\mathrm{t}} = \vec{r}_{\mathrm{t}}(t, b)$ (determined

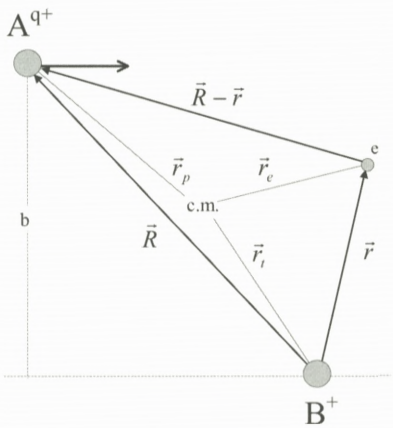

Figure 1. Vector diagram for the projectile ion A^{q+}, the ionic target core B^+, and one active electron. The impact parameter b is indicated. $\vec{r}_p$, $\vec{r}_t$ and $\vec{r}_e$ are position vectors of projectile, target, and electron in the center-of-mass system.

by the impact parameter b). This concept was first introduced by Mott (1931) and Bang and Hansteen (1959).

If, additionally, an independent motion of the electron (McGuire and Weaver, 1977) is assumed, one may solve the time-dependent Schrödinger equation for one active electron:

$$\left(i\frac{\partial}{\partial t} - \mathcal{H}_e\right)\Phi_e(t) = 0 \tag{2}$$

with

$$\mathcal{H}_e(t) = \mathcal{H}_{te} + V_{pe}(\vec{R}(t) - \vec{r}) \tag{3}$$

and

$$\mathcal{H}_{te}(t) = T_e(\vec{r}_e) + V_{te}(\vec{r}_e - \vec{r}_t(t)). \tag{4}$$

In the subsequent treatment the electron coordinate will be measured from the accelerated target nucleus and is the only dynamical variable. Thus the target system is the frame of reference. In such a non-inertial system non-Newtonian forces arise. The corresponding Hamiltonian $\mathcal{H}_{te}$ is

$$\mathcal{H}_{te} = -V_{te}(\vec{r}) + T_e(\vec{r}) + V_{recoil}(\vec{r}, \vec{r}_t(t)). \tag{5}$$

It is reasonable to neglect the last term V_{recoil}. By doing this, transitions are excluded which are due to the interaction of the active electron with the recoiling

target nucleus. This so-called recoil effect leads to insignificant contributions to total cross-sections, but may be important for very close collisions ($b < 10^{-3}$ a.u.) (Rösel et al., 1982). Before the solution of Equation (2) is explained in more detail, the classical path $\vec{R}(t)$ should be defined. Given the time-dependent electronic wave function Φ_e, a classical Hamiltonian for the heavy particles may be defined:

$$\mathcal{H}_h = T_p(\vec{r}_p) + T_t(\vec{r}_t) + V_{pt}(\vec{R}) + \langle \Phi_e | V_{pe}(\vec{R} - \vec{r}) | \Phi_e \rangle + \langle \Phi_e | V_{te}(\vec{r}) | \Phi_e \rangle. \quad (6)$$

With this Hamiltonian the classical equations of motion are solved. The last term in Equation (6) was neglected because of its small influence on the motion of the target core in case of a strongly target-centered wave function Φ_e. It is emphasized that the concept defined by Equation (6) introduces for the first time a dynamically curved projectile trajectory in the impact-parameter method. Thus the projectile motion is coupled to the motion of the active electron. We note that this procedure goes far beyond the Born–Oppenheimer approximation.

It is noted that some calculations have been performed with hyperbolic projectile paths. In this case only the first three terms in Equation (6) are considered. However, most of the previous calculations have been performed for straight line paths, as given by the first two terms in Equation (6). Such calculations are equivalent to quantum-mechanical solutions of the three-body Schrödinger equation with plane projectile waves.

4.2. Independent-Particle Model

The electronic many-body Hamiltonian in Equation (1) is treated in the framework of the independent-electron frozen-core model. This means that there is only one active electron, whereas the other electrons are passive (no dynamic correlation is accounted for) and no relaxation occurs. In this model the electron-electron interaction is replaced by an initial-state Hartree–Fock–Slater potential (Herman and Skillmann, 1963).

The independent-electron approximation allows for a distinction of target electrons and projectile-centered electrons which screen the projectile nuclear charge. One of the most important dynamic correlation effects (deviations from the independent-electron approximation) is the collision of a target electron with a projectile-centered electron (McGuire and Simony, 1981). This will directly enhance the energy loss and reduce the projectile screening.

The time-dependent Schrödinger equation may be solved by expanding $\Phi_e(\{\vec{r}\}, t)$ in terms of unperturbed eigenfunctions φ_i of the target with coefficients

$a_i(t) = \langle \varphi_i \mid \Phi_e(t) \rangle$. Thus, Equation (2) is replaced by a set of coupled first-order differential equations, the so-called coupled-channel equations:

$$i \frac{\mathrm{d}}{\mathrm{d}t} a_i(t) = \sum_j a_j(t)\, \mathrm{e}^{i(E_i - E_j)t} V_{j \to i}(\vec{R}(t)) \tag{7}$$

with the internuclear distance $\vec{R}$ and

$$V_{j \to i}(\vec{R}(t)) = \langle \varphi_i | V_{\mathrm{pe}}(\vec{R}(t), \vec{r}) | \varphi_j \rangle. \tag{8}$$

E_i is the orbital energy associated with the target wave function φ_i. Here V_{pe} is an effective potential seen by the active electron, which contains the screening effect produced by other electrons from the medium. For bare incident ions, the active-electron projectile interaction V_{pe} is just the Coulomb potential. However, in the case where the projectile carries electrons, we use a screened potential made up of the Coulomb part due to the projectile-nuclear charge and the static potential produced by the target electrons that screen the projectile-nuclear charge,

$$V_{\mathrm{pe}}(\vec{R} - \vec{r}) = -\frac{Z_{\mathrm{p}}}{|\vec{R} - \vec{r}|} + \sum_n^{\mathcal{N}} \int \mathrm{d}^3 r' \frac{|\chi_n(\vec{r'})|^2}{|\vec{R} - \vec{r} - \vec{r'}|}, \tag{9}$$

where Z_{p} is the projectile nuclear charge, χ_n is the projectile-electron wave function and $\mathcal{N}$ is the number of projectile electrons. The wave functions χ_n for each electron n of the projectile are obtained according to the Hartree–Fock–Slater procedure (Herman and Skillmann, 1963). Thus, we neglect dynamic screening (a time dependence of χ_n due to target induced polarization respectively excitation/ionization), Pauli correlation (antisymmetrization of the projectile- and target-centered wave functions) as well as dynamic correlation effects due to the residual electron-electron interaction. It is pointed out, that the dynamic electron-electron interaction is not included in the present model since there is only one active electron.

For high projectile speeds and low projectile charge-states the transition matrix-elements $V_{j \to i}$ are small. This is the domain of first-order perturbation theory (semi-classical approximation SCA, first-order Born approximation); see for example Kabachnik et al. (1993). In this case, most transitions are governed by the direct step from the initial state j to the final i. Thus, we may drop the summation over j and use $a_j(t) = 1$ (the state j corresponds to the ground-state). Hence, the time-consuming solution of the coupled-channel equations is reduced to a set of simple integrals over time within perturbation theory.

The coupled-channel equations are solved numerically in order to obtain the coefficients a_i after the collision ($t \to \infty$). In contrast to other coupled-channel

calculations we do not use pseudo states to represent the electron continuum wave functions. Instead we use a large number of continuum wave-packets that are composed out of a superposition of exact continuum eigenstates (up to 500 gerade states with partial waves up to $l = 10$), since the computation of the stopping power demands high accuracy of the emitted electron energy spectrum.

Each excited or continuum state corresponds to a well-defined energy transfer ΔE_i $(= E_i - E_0)$. Then the cross-section for a such an energy-transfer process will read

$$\sigma_i = 2\pi \int_0^\infty b \, \mathrm{d}b |a_i|^2(b) \tag{10}$$

and average electronic energy loss $Q(b)$ is given by

$$Q(b) = \sum_i |a_i|^2(b) \Delta E_i. \tag{11}$$

The electronic stopping cross-section S_e and energy straggling W per atom can be computed directly from:

$$S_\mathrm{e} = \sum_i \sigma_i \Delta E_i = 2\pi \int_0^\infty b \, \mathrm{d}b \; Q(b) \tag{12}$$

and

$$W = \sum_i \sigma_i \Delta E_i^2. \tag{13}$$

For the electronic energy-loss distribution $\mathrm{d}P_i/\mathrm{d}T$ we use

$$\frac{\mathrm{d}P_i}{\mathrm{d}T}(b) = \sum_f |a_{i\to f}(b)|^2 \delta(T - (\epsilon_f - \epsilon_i)), \tag{14}$$

It is pointed out that for elastic collisions $(f = i)$ as well as for "bound-state" excitation the energy-loss distribution defined above contains spikes due to the atomic level structure. Broadening effects originating from state lifetime, band width and the Doppler effect are not considered explicitly since they are much smaller than the experimental resolution. It is noted that the above sums have to be replaced by integrals in the case of continuum states.

4.3. Higher-Order Effects

The coupled-channel calculations allow for accurate calculations of higher-order effects. At high energies the electronic energy loss may be expanded in terms of the projectile charge Z_p according to

$$Q(b) = q_1 Z_p^2 + q_2 Z_p^3 + q_3 Z_p^4 + \cdots . \tag{15}$$

The quadratic term is the leading one at high energies. It is well described by first-order Born theory and involves only direct ionization and excitation of the target atom. With decreasing ion energy higher-order effects become important. They either depend on the sign of the projectile charge Z_p (polarization and binding effects) or only on the absolute value of Z_p. All higher-order effects (deviations from the Z_p^2 proportionality) can be related to multiple successive interactions of the active electron with the projectile and the (screened) target within a single collision. The number of these interactions increases for high projectile charges, small impact parameters and low projectile velocities. We can distinguish different higher-order contributions as a function of the strength of the perturbation.

For small perturbations of outer-shell electrons the polarization of the electronic density appears first. Positively charged particles attract and negatively charged projectiles repel the electron cloud during an early stage of the collision, which leads to a change of the density around the projectile path and correspondingly to a change in the stopping power. This is a second-order effect (proportional to Z_p^3).

By decreasing the ion energy the influence of the projectile is no longer a small perturbation and effects such as saturation and binding-energy modifications will appear. In standard first-order treatments, the sum over all probabilities exceeds one since no reduction of the of the initial-state population is accounted for. This leads to an artificial creation of electrons (overestimated stopping power proportional to Z_p^4). The corresponding experimentally observed saturation (stopping power reduction compared to Z_p^2 for heavy ions) may roughly be described within the unitary first-order Magnus approximation (Ryufuku and Watanabe, 1978, 1979). A different treatment by Bloch (1933) also takes into account this effect and the term proportional to Z_p^4 agrees quite well with the one from coupled-channel calculations.

For inner-shell electrons the so-called binding effect gains importance. The resulting change of the stopping power is proportional to Z_p^3 but its sign is opposite to the change induced by the polarization effect. The binding effect can be viewed as an increased binding energy of the bound electron in the vicinity of positively charged projectiles, which reduces the stopping power for small impact parameters (or large scattering angles).

Finally, at low energies the projectile represents a strong perturbation and effects such as electron capture for positive projectiles and adiabatic ionization (Fermi–Teller effect; Schiwietz et al., 1996) for negative charged projectiles turn out to be very important. The electron capture may be viewed as a very strong

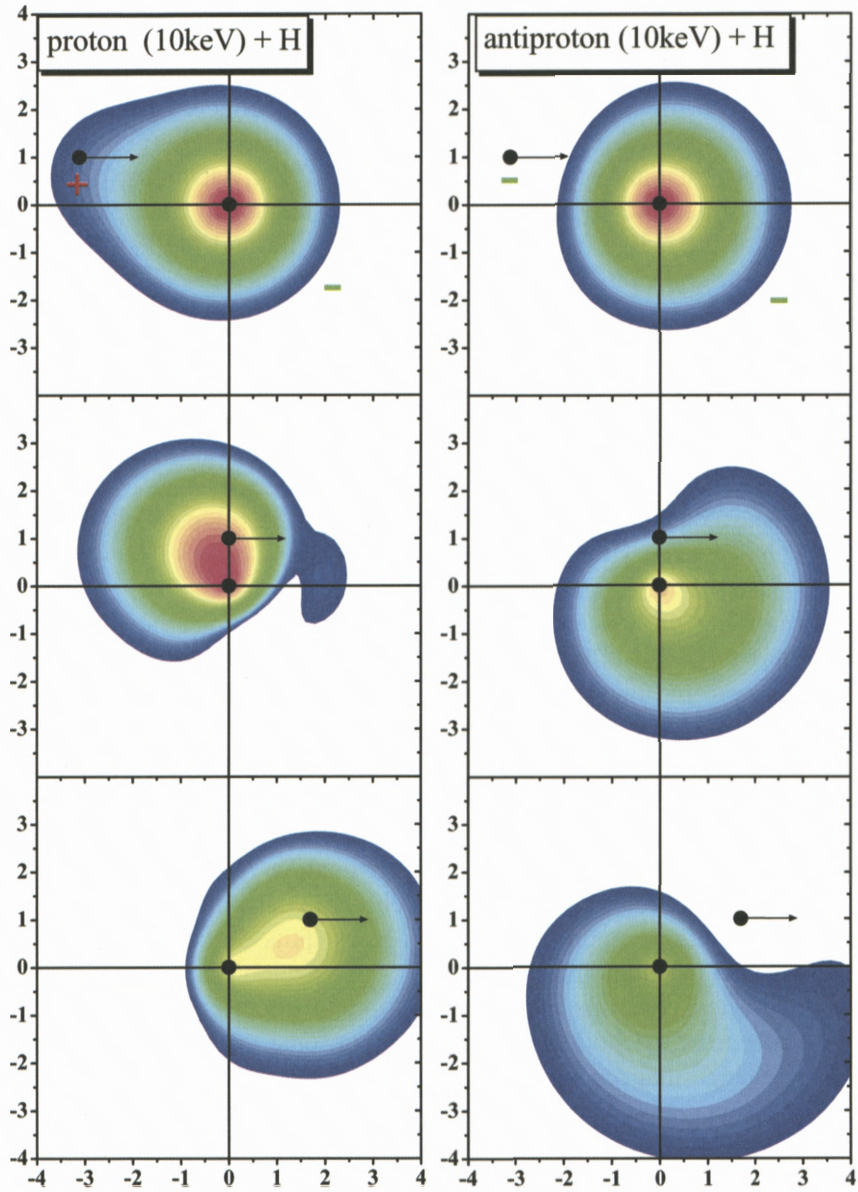

Figure 2. Contour plot of the time-dependent electronic density of a hydrogen atom disturbed by a 10keV proton (on the left) and antiproton (on the right) at $b = 1$. The plot corresponds to a cut of the density across the collision plane.

polarization effect (target electrons are attracted by and finally travel with the projectile). If the electronic motion is described in a target-centered basis all orders of the perturbation are necessary to yield the time-dependent electron-density. In other words, the interaction between electron and projectile never stops. In the Fermi–Teller effect, collisions with negative heavy projectiles are involved. For the case antiprotons on H, the electrons move in the field of a transient "quasidipole" formed by the heavy particles. The electronic states of the quasidipole experience a rapid loss of binding energy when the distance between the heavy particles decreases, and become even unbound at a certain non-zero "critical" distance.

Besides these effects we also observe for increasing perturbations (high Z_p at low energies) a diffusion-like effect in the energy spectrum of emitted electrons (Grande and Schiwietz, 1995). The first excitation step gives rise to an excitation spectrum with a maximum at low energy transfers. Successive interactions (continuum-continuum couplings) yield a broadening of the excitation spectrum. Hence, low electron energies are suppressed due to this diffusion-like process and the mean stopping power as well as the straggling are enhanced. This energy-diffusion effect may be viewed as the onset of the Fermi shuttle effect, where multiple head-on collisions between projectile and electron in the field of target lead to extremely high electron energies.

Figure 2 shows a contour plot of the time-dependent electron density for a hydrogen atom disturbed by a positively (displayed on left) and negatively (displayed on right) charged Coulombic point particle at 10 keV per atomic mass unit (amu) at an impact parameter of 1 a.u. These electronic densities correspond to a cut in the collision plane and were obtained directly from the calculated transition amplitudes $a_i(t)$ according to

$$\rho(\vec{r},t) = \sum_{i,j} a_i a_j^* \, \mathrm{e}^{-i(E_i-E_j)t} \varphi_i(\vec{r}) \varphi_j^*(\vec{r}), \tag{16}$$

using about 200 gerade states. An inspection of this figure shows several interesting features. First, the positively charged particle (proton) attracts the electron on the incoming path; the so-called polarization process. One may see that the electron density moves towards the projectile. The opposite effect takes place for the negatively charged particle (antiproton).

Second, for protons at the distance of closest approach, the maximum of the electron-density points to the backward direction at an angle of about 120 degrees with respect to the beam axis. It is clearly visible that the electron density lies behind the projectile, although the proton is attracting the electron. The reason for this behavior is a delayed response of the electron cloud (the inertia due to

the electron mass). Third, the proton enables electron-capture in the outgoing path of the collision and large fraction of the electron density is finally bound to and moving with the projectile. Since an antiproton repels the target-electron, the electron density near the projectile on the outgoing path of the collision is almost zero.

For collisions of antiprotons with atomic hydrogen, a quasi dipole is formed during the collisions. The dipolar antiproton-proton system does not support bound states for inter-particle distances below 0.64 a.u. (Schiwietz et al., 1996). For finite velocities and larger impact parameters b (in the figure, $b = 1$) there is still a significant ionization contribution. As can be observed in the figure at the distance of closest approach there is a high transition probability (blowing up of the density).

4.4. Reference Results

In the framework of the independent-electron model, the probability for a certain total electronic energy-loss ΔE transferred during an individual ion-atom collision can be written as

$$\frac{\mathrm{d}P_{\mathrm{atom}}^{\mathrm{elec}}}{\mathrm{d}\Delta E}(b) = \left(\prod_i \int \mathrm{d}T_i \, \frac{\mathrm{d}P_i}{\mathrm{d}T_i}(b)\right) \times \delta\left(\Delta E - \sum_i T_i\right), \tag{17}$$

where the index i runs over all electrons for each subshell, for example, the 1s, 2s, 2p, 3s and 3p of the Al atom. Equation (17) corresponds to a series of convolutions of individual single-electron energy-loss distributions from Equation (14). In this way, multiple ionizations/excitations are taken into account.

Figure 3 shows the results of the coupled-channel calculations for the energy-loss probability of 100 keV H^+ projectiles colliding with atomic Al at $b = 0$. The elastic peak (the peak at $\Delta E = 0$) is represented here by a Gaussian distribution with a very small standard deviation (about 10 eV) in order to keep the normalization and to avoid the use of a Dirac function. In the present case, backscattering is almost always accompanied by excitation or ionization events, involving mainly electrons from the 2p shell (due to the large number of electrons) and from the 3s and 3p bands. This is the reason for high backscattering yields at non-zero energies in the figure.

The main feature of the energy-loss distribution in Figure 3 is the significant contribution of the L-shell at large energy transfers. The contribution of the valence electrons for the surface peak is of minor importance since the corresponding M-shell energy loss is much smaller than the experimental resolution. K-shell ionization of Al atoms is kinematically suppressed for protons at incident energies below about 1 MeV.

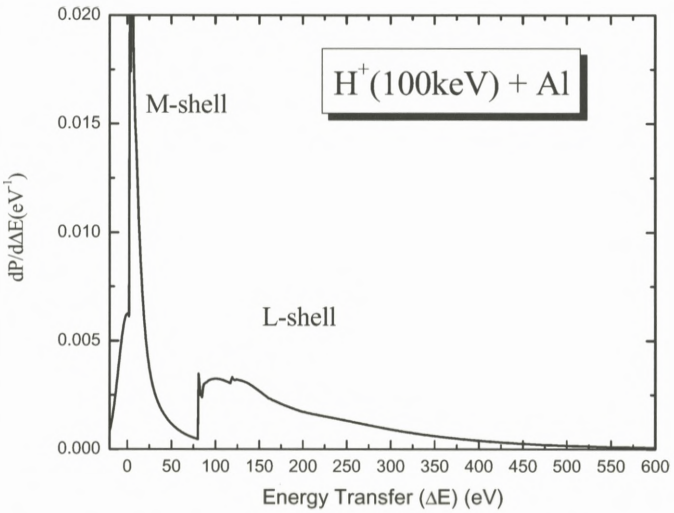

Figure 3. Energy transfer in a single collision for 100 keV H^+ on atomic Al for a near central collision ($b \rightarrow 0$).

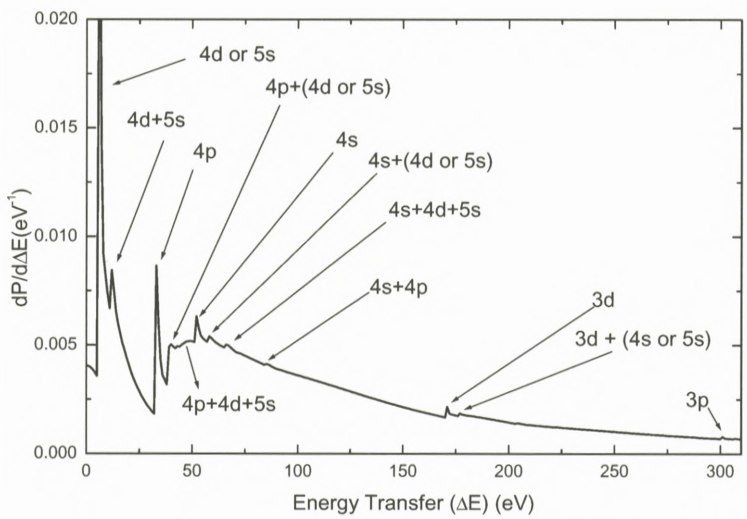

Figure 4. Energy transfer in a single collision for 100 keV H^+ on atomic Y for a near central collision ($b \rightarrow 0$).

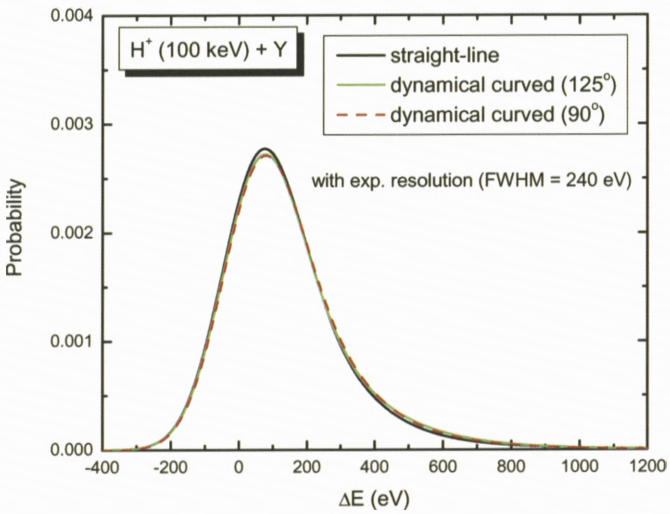

Figure 5. Energy transfer in a single collision for 100 keV H^+ on atomic Y using different projectile trajectories in a near central collision ($b \to 0$).

The same can be seen in Figure 4 but for an Y atom, which has much more subshells than Al. In this case we can observe many peaks indicated by arrows. Some of arising from double inner-shell ionization and even triple ionization are visible. However, all theses peaks are washed out after considering the experimental resolution or Doppler effect due to the thermal motion of the target atoms in a solid. But the energy-loss distribution remains very asymmetric (see Figure 5) because of large energy transfer to ionization of the inner-shells.

The influence of different ion trajectories on the electronic excitations can be seen in Figure 5 for 100 keV protons on Y atom. Here the coupled-channel results from Equation (17) were convoluted with a typical experimental resolution (of about 240 eV) found in MEIS experiments. The curve denoted as straight-line, corresponds to coupled-channel calculations using a straight-line trajectory for the projectile (passing through the Y atom) while the other curves stand for dynamic curved trajectories calculated from the hamiltonian described by Equation (6). For dynamic curved trajectories, the final scattering angle is indicated in Figure 5. As can be observed from this figure, the electronic energy-loss distribution is nearly insensitive to projectile trajectories as far as very small impact parameters are concerned. In fact there is a narrow range of impact parameters corresponding to a large variation of the scattering angle, where the energy-loss distribution is about the same (even for scattering angle of few degrees almost no change has

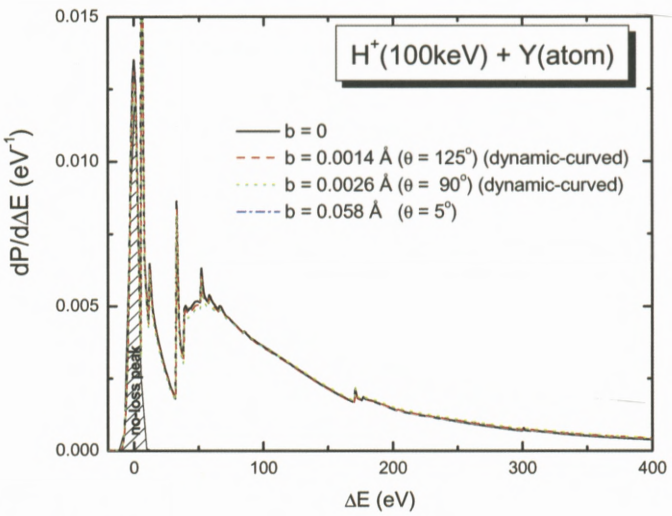

Figure 6. The same as in Figure 5 but unfolded results and including an additional scattering angle of 5 degrees.

been observed, see Figure 6). The *near central collision* regime is determined by this range of impact parameters. We have also checked the recoil effect described in Section 4.1 but it is negligible for protons with some hundred keV colliding with heavy targets such as Al or Y.

4.5. Simple Model for Energy-Loss Distributions

The coupled-channel calculations demand a computational effort that precludes its direct use in any analysis of ion-beam data. Therefore, we search for an approximate solution without the necessity of performing a large-scale calculation. For this purpose, the close coupling calculations shall be used as benchmark results to check simple models for the energy loss distribution at near central collisions. A detailed description of such models may be found elsewhere (Grande et al., 2006). Here we present only a short outline of the method.

4.5.1. *Model for the Mean Energy-Loss*

The first ingredient of a model for the electronic energy-loss distribution is the mean energy-loss value as a function of the impact parameter $Q(b)$. In recent works (Grande and Schiwietz, 1998; Schiwietz and Grande, 1999) we have proposed a simple formula for $Q(b)$ – called Perturbative Convolution Approximation (PCA) and Unitary Convolution Approximation (UCA) – realized by the CasP Program (Grande and Schiwietz, 2006). This formula reproduces first-order

Born results for all impact parameters for bare and also for screened projectiles (in the PCA mode) and contains some higher-order terms, reproducing the Bloch formula (Bloch, 1933) at high velocities (in the UCA mode). The UCA model can also be seen as the impact-parameter realization of the Bloch formula and resembles the Binary model of Sigmund and Schinner (2000). The following simple formula

$$Q(b) = \int \mathrm{d}^2 r_T \, \mathcal{K}(\vec{b} - \vec{r}_T) \int \mathrm{d}z \, \rho(\vec{r}_T, z) \tag{18}$$

with

$$\mathcal{K}(b) = \frac{2Z^2}{v^2 b^2} \times h\left(\frac{2vb}{\eta}\right) \times \sum_i f_i \, g\left(\frac{\omega_i b}{v}\right) \tag{19}$$

joins smoothly all regions of impact parameters b for which two-body ion-electron (small b) and dipole (large b) approximations are valid (see Figure 7).

The function $h(2vb)$ (see Grande and Schiwietz, 1998) approaches zero for $b \ll 1/v$ (relative impact parameter smaller than the electron de Broglie wavelength in the projectile frame) and it reaches 1 for large values of b. The first two product terms in Equation (19) resemble the classical energy transfer to a statistical distribution of electrons at rest and describe violent binary collisions. The last term, involving the g function (see Grande and Schiwietz, 1998) and the oscillator strengths f_i, accounts for the long ranged dipole transitions as depicted in fig(7) where the energy transfer is about $1/\Delta t$ (Δt is the collision time and is about the impact parameter b divided by the projectile velocity v). For intermediate impact-parameters the closure approximation in applicable (Grande and Schiwietz, 1998), which links smoothly the two body projectile-electron scenario with the dipole approximation.

The first integral $\int \mathrm{d}^2 r_T \ldots$, in Equation (18) describes a convolution with the initial electron density also outside the projectile path and yields non-local contributions to the energy loss. It is noted that these non-local contributions are neglected in most previous simple energy loss models. With the parameter η equal to one, this formula mimics the first-order Born approximation very well (Grande and Schiwietz, 1998) and it is denoted *PCA* (perturbative convolution approximation). For increasing projectile-charge first-order calculations (on which PCA is based) break down. They do not take in account, for instance, that each electron transition gives rise to an increased final-state population and a corresponding reduction of the initial state population. It is clear that the ionization probability cannot increase indefinitely with the strength of the perturbation (the so-called saturation effect). Since these ionization processes come mostly from

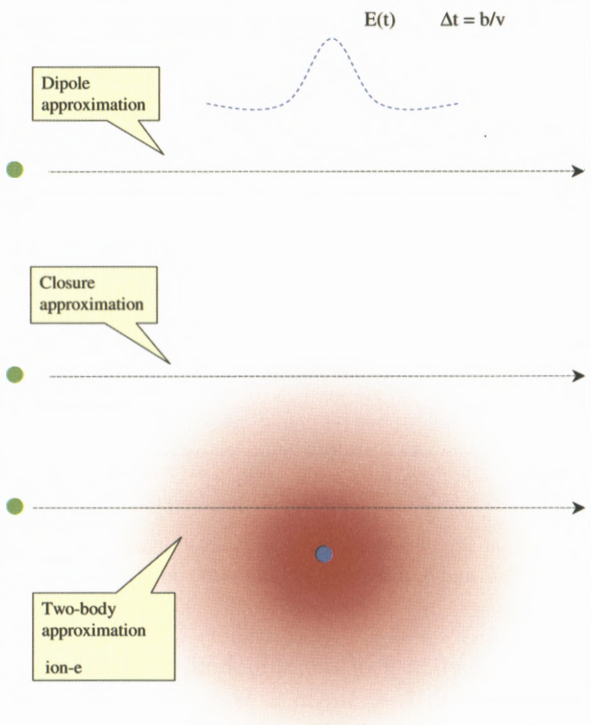

Figure 7. Impact parameter regions that are interpolated by the PCA/UCA models.

small impact parameters, we have introduced in Schiwietz and Grande (1999), a scaling parameter η in the function h that enforces unitarity in accordance with the Bloch model (Bloch, 1933).

Nevertheless, the UCA model, as other stopping power models (Sigmund and Schinner, 2002; Arista, 2002), only calculates the mean electronic energy loss. Except for the model from Grande et al. (2006) no simple calculation for the energy loss distribution as a function of the impact parameter is available so far.

4.5.2. *Energy-Loss Moments*

Using the mean energy loss $Q(b)$ calculated from the UCA model, as shown in Grande et al. (2006), we can determine the moments of the energy loss distribution by assuming the following model.

The energy-loss distribution due to a single electron in a given sub-shell has two parts. A no-loss part, represented by a delta function at zero energy transfer, and a loss part, separated from the no-loss part by an energy gap corresponding

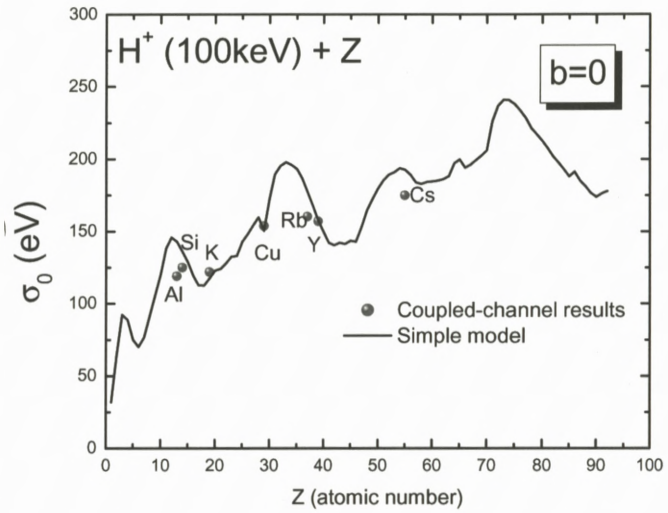

Figure 8. Standard deviation for the electronic energy-loss distribution in a single collision for impinging protons at 100 keV and $b = 0$ as a function of the atomic number of the target.

essentially to the binding energy of the sub-shell. The loss part involves a fixed averaged energy loss $\bar{E}$ (with $\bar{E} = \ln(2mv^2/I_b)$, where m is the electron mass, v the projectile velocity and I_b is the binding energy). The ratio of the loss to no-loss part (P_{reaction}), as a function of the impact parameters is determined from the mean energy loss $Q(b)$. The second and the third moments of the distribution, related to the standard deviation and skewness respectively, are determined by assuming a $1/\Delta E^2$ law starting from the binding energy value I_b up to the maximum energy transfer $2mv^2$. Then, the effect of all electrons is determined by adding the moments (relative to the first moment) according to the additivity rule found in convolutions of probability distributions. Further details can be found in Grande et al. (2006).

Figure 8 displays the results of this simple model for the standard deviation of the electronic energy-loss spectrum as a function of the atomic number of the target, for impinging 100 keV protons at an impact parameter close to zero (near central collision). The results are compared to coupled-channel results (Grande et al., 2006). In general the agreement is very good although some significant deviations can be observed. We note that the maxima and minima are not related the valence structure. Indeed they are due to the interplay between inner-shell ionization probability and binding energy.

Nonetheless, despite of the crudeness of the present model, it may be already sufficiently accurate to be used in MEIS or other ion-beam technique.

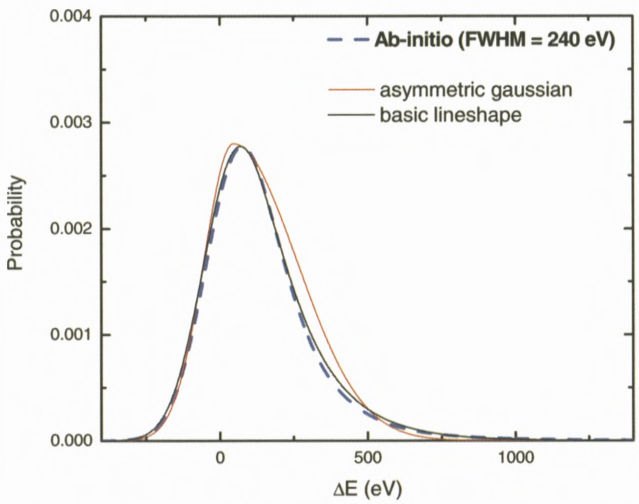

Figure 9. Coupled-channel results for 100 keV proton colliding with Y at a impact-parameter close to zero in comparison with analytical formulas. All results have been convoluted with the experimental resolution of 240 eV.

4.5.3. *Analytical Formula*

The coupled-channel calculations have also been used (see Grande et al., 2006) as a benchmark for simple analytical formulas of the electronic energy-loss distribution, which replace the Gaussian distribution when the asymmetry cannot be neglected.

In Figure 9 two analytical formulas for the energy-loss distribution are compared with coupled-channel results for 100 keV protons colliding with a Y atom at $b = 0$. The asymmetric Gaussian (two Gaussians linked at the same point – the absolute maximum – with different standard deviations below and above this common point), used to analyze some MEIS experiments (Munoz-Marquez et al., 2005a; Okazawa et al., 2005) and the basic lineshape

$$\begin{aligned} f(\Delta E) &= \alpha \exp(-\alpha \Delta E)\Theta(\Delta E) * \text{gauss}(\Delta E, \sigma) \\ &= \frac{\alpha}{2} \exp\left(-\frac{\alpha}{2}(2\Delta E - \sigma^2 \alpha)\right)\left(1 + \text{erf}\left(\frac{\Delta E - \sigma^2 \alpha}{\sqrt{2}\sigma}\right)\right) \end{aligned} \tag{20}$$

proposed in Grande et al. (2006), are also displayed in Figure 9. All curves have the same standard deviation. For the basic lineshape, σ is the experimental resolution ($\sigma = \text{FWHM}/2.355$) and $\alpha = 1/\sigma_0$ (σ_0 from Figure 8) quantifies the effect of the single collision contribution.

Further advantages of the basic lineshape (Equation 20) are the following: (i) the corresponding self-convolutions are analytical and (ii) the Bothe–Landau equation (Sigmund, 2006) for an exponential decay energy-loss cross-section has also an analytical solution. Thus, the transport in a diluted medium can be easily computed. This is important for depth profiling techniques in amorphous targets.

5. Examples

The correct modeling of the energy-loss distribution in a single collision is very important for investigations of surface and near-surface interfaces as will be seen in the following examples.

5.1. Depth Profiling in Ultra Thin Films

Microelectronic devices based on metal-oxide-semiconductor (MOS) structures have continuously and exponentially advanced for decades without any substantial revolution regarding materials employed in integrated circuit fabrication. The main driving force for this tremendous evolution has been the downsizing of devices and integration.

Research of new gate oxide materials requires characterization tools in the nanometer scale, a straightforward consequence of the nanoscopic dimensions of the devices to which research is devoted. Medium energy ion scattering (MEIS) and narrow nuclear resonant reaction profiling (NRP) are the most important ion-beam characterization tools with nanometric depth resolution.

Gate oxides with high dielectric constant are currently being investigated to replace silicon oxide in MOS transistors. Hf-based oxides, silicates and aluminates are the best candidates for replacing SiO_2 as the gate dieletric because of their superior dielectric constant, electrical compatibility in the Si technology, and thermal and chemical stability (Wilk et al., 2001). Therefore, the depth profile of Hf in ultra thin films is of high importance.

In Figure 10 we show MEIS experimental results (the symbols) and the corresponding simulations for $Hf_{1.06}Zr_{0.1}O_2$ oxide with different thicknesses (see Figure 10 caption) taken with 100 keV protons (Pezzi et al., 2006). Here, the simulations (noted as standard ones) are based on Gaussian-shape energy-loss distributions, where the mean energy value has been taken from the SRIM code (Ziegler, 2006) and the straggling value from Chu's formula (Chu, 1976). We observe a decrease in the quality of the simulation for films with thicknesses smaller than one nanometer, when a homogenous oxide layer is assumed. Nevertheless, a good agreement can be obtained by fitting each spectrum, independently, without considering that they are in fact normalized to each other. Indeed, this is a pitfall,

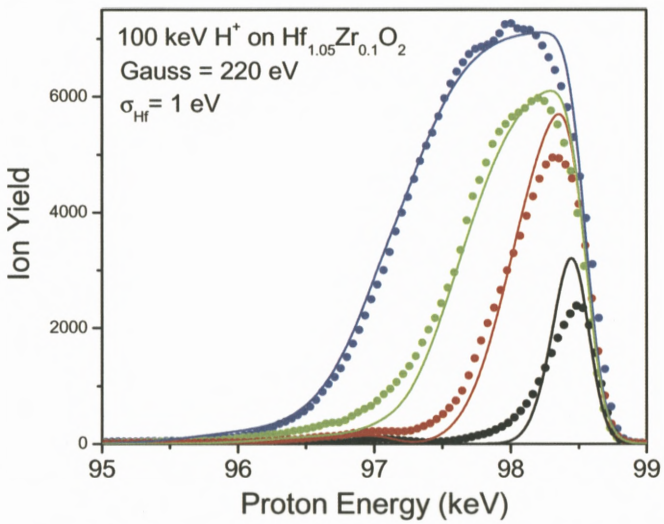

Figure 10. MEIS spectra obtained with 100 keV protons incident in thin HfO_2 (with small amount of Zr). The thicknesses of the films are 0.2 (black full circles), 0.5 (red full squares), 1 (green up triangles) and 2nm (blue down triangles).

since the corresponding thickness will not be realistic. Furthermore, as shown in Pezzi et al. (2006), the areal density of Hf as a function of the resulting film thickness as obtained by fitting the simulation results to the data in Figure 10 is a straight-line that has a large negative value of Hf when the thickness is extrapolated to zero.

On the other hand, when the energy-loss straggling during the strong head-on collision is included, agreement between experimental data and simulation is recovered, as shown in Figure 11.

Here we have used the basic lineshape from Equation 20 to describe the energy-loss distribution in a single, violent collision, responsible for the backscattering. The exponential decay α was obtained from Figure 8 for Hf, and amounts to 1/217 eV^{-1}. In this case the assumed experimental resolution of about 100 eV that is much smaller than used in Figure 10 because of the extra broadening arising from the backscattering collision. In addition, the total Hf quantity as a function of the film thickness is a linear function that crosses the origin (Pezzi et al., 2006).

5.2. Description of the Al Surface Peak

Medium-energy ion scattering (MEIS) in connection with shadowing and blocking techniques is a powerful method for the determination of structural and

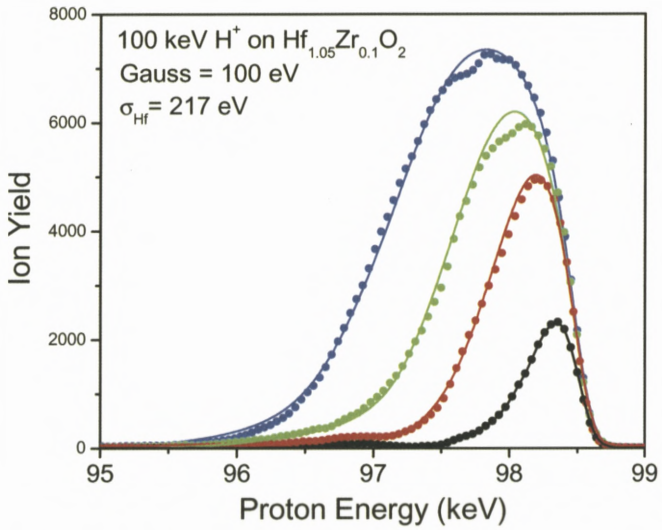

Figure 11. The same as in Figure 10 but the simulations include the effect a the energy loss spreading in a backscattering collisions.

vibrational parameters of crystalline surfaces (van der Veen, 1985). In this context, the shape of ion energy-loss spectra is usually not analyzed, because this requires a detailed knowledge on the energy-transfer mechanisms. Thus, standard energy-loss theories or semi-empirical methods based on Gaussian energy-loss distributions cannot be used successfully. Instead, an atomistic description of the electronic excitation process and its impact parameter dependence have to be taken into account in a stochastic approach which leads, in general, to an asymmetric line shape. Nevertheless, many groups use Gaussian line shapes to fit the surface peak area (using high resolution and grazing conditions) in order to get the fractions for adlayers or adatoms (Hoshino et al., 2005), which may lead to questionable interpretations by neglecting the asymmetry of all backscattered-ion distributions.

The surface peak is due to collisions at and near the surface, involving just the first few atomic layers. The deflection of incoming projectiles by surface atoms results in the formation of a volume behind this atom, practically free of ion trajectories, the so-called shadow cone. If the incident ion beam is aligned with a main axis of the crystal, shadowing greatly reduces the chance of backscattering from successive atoms along the row. In a similar way, the backscattered flux from sub-surface atoms cannot propagate in directions corresponding to vectors that point to atoms closer to the surface. This will result in pronounced minima

in the angular distribution of the backscattered flux. Such blocking dips provide a sensitive method to determine surface-atom displacements. An angular shift in the position of a blocking dip away from the bulk crystal blocking direction is a direct indication of layer relaxation. Accurate determination of structural parameters (atomic location and vibrational amplitudes) using Medium Energy Ion Scattering (MEIS) is a well-established technique. This is accomplished by comparing the angular scattering intensity to results of Monte-Carlo type computer simulations for models of the surface structure, as implemented, e.g., in the VEGAS (Frenken et al., 1986) code for trial atomic crystal structures. The atomic positions in the trial structure are changed until a convincing fit to the measured data (shape and minimum position) is obtained. This method, however, takes into account only the ballistic part of the backscattering events. The information contained in the detailed peak shape is usually not considered.

Since solid-state effects are of minor importance due to the large energy transfers involved, the valence-band contributions to the backscattering signal may therefore to a good approximation be described within an atomic model. This provides the best scenario for the use of advanced atomic-physics models, such as coupled-channel calculations.

Here we describe the energy-loss distribution of the surface peak for protons impinging with 60° (and $\phi = 35.3°$) with respect with the main axes of a clean Al(110) surface and being backscattered along a blocking direction also 60° off normal. Further details may be found in Grande et al. (2004) and Grande et al. (2005).

The configuration of the scattering experiment is schematically sketched in Figure 12(a). The top view of the Al(110) surface with a scattering plane perpendicular to the Al(110) surface is given in Figure 1(b). The incoming beam is aligned with the [−101] direction. For a bulk-terminated static lattice this geometry completely eliminates scattering events from all layers except the topmost one. Due to thermal vibrations and surface relaxation the deeper layers contribute to the surface peak as well.

5.2.1. *Transport: Stochastic and Monte-Carlo Approaches*

The energy lost by the projectile after several collisions is given by a series of convolutions of the energy-loss distribution for each single collision. Thus, each single collision is characterized by one impact parameter b_α. When a sequence of collisions is described by a set of impact parameters $\{b_\alpha\}$, for example along the incoming path before hitting the target nucleus, the energy-loss distribution of the projectile will be

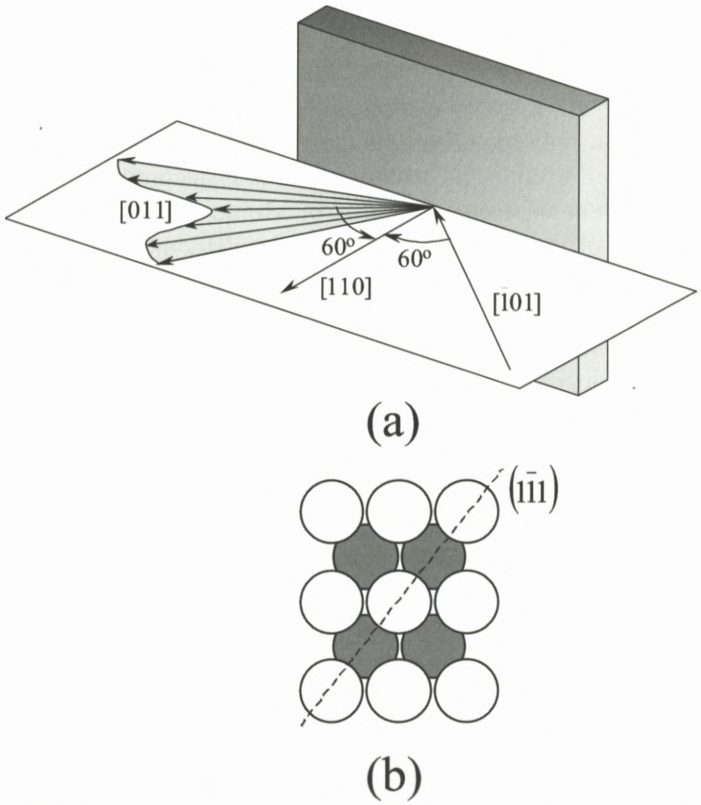

Figure 12. (a) Schematic figure of the scattering geometry used in this work; the scattering plane is shown in (b) in a top view of the Al(110) surface. Taken from Grande et al. (2004).

$$\frac{\mathrm{d}P_{\mathrm{in}}}{\mathrm{d}\Delta E}(\{b_\alpha\}) = \left(\prod_\alpha \int \mathrm{d}\Delta E_\alpha \frac{\mathrm{d}P_{\mathrm{atom}}}{\mathrm{d}\Delta E_\alpha}(b_\alpha)\right) \times \delta\left(\Delta E - \sum_\alpha \Delta E_\alpha\right). \tag{21}$$

The measurable sequences of impact parameters $\{b_\alpha\}$ are however only those that lead to a hitting event (a close backscattering encounter) and will depend on shadowing effects due to the atomic layers, which the ions pass through. In this way, the thermal vibrations as well as the relaxation of the first layers must also be

taken into account to determine the impact-parameter-averaged energy loss due to a target atom from the layer L' for the projectile that hits a target atom from layer L. The same holds true for the outgoing path after the backscattering. Then, the projectile energy distribution for a sequence of collisions that hit a target atom from layer L and reach the detector reads

$$
\begin{aligned}
Y_L(E) = & \prod_{L'=1}^{L} \int \mathrm{d}\Delta E_{L'}^{\mathrm{in}} \left(\frac{\mathrm{d}P_{\mathrm{atom}}}{\mathrm{d}\Delta E_{L'}^{\mathrm{in}}} \right)_{L',L}^{\mathrm{av}} \\
& \times \int \mathrm{d}\Delta E^{\mathrm{hit}} \left(\frac{\mathrm{d}P_{\mathrm{atom}}}{\mathrm{d}\Delta E^{\mathrm{hit}}}(b=0) \right) \\
& \times \prod_{L'=1}^{L} \int \mathrm{d}\Delta E_{L'}^{\mathrm{out}} \left(\frac{\mathrm{d}P_{\mathrm{atom}}}{\mathrm{d}\Delta E_{L'}^{\mathrm{out}}} \right)_{L',L}^{av} \\
& \times \delta \left\{ E - \left[K \left(E_0 - \sum_{L'} \Delta E_{L'}^{\mathrm{in}} - \frac{1}{2} \Delta E^{\mathrm{hit}} \right) - \sum_{L'} \Delta E_{L'}^{\mathrm{out}} - \frac{1}{2} \Delta E^{\mathrm{hit}} \right] \right\},
\end{aligned}
\tag{22}
$$

which turns out to be a series of convolutions. Here the symbol "av" stands for thermal averaging according to Grande et al. (2004), E_0 is the incident projectile energy and K is the kinematical factor describing the two-body kinematics for the backscattering collision. All impact parameters involved in the equations above are small compared to the L- and M-shell radii (they are given by the thermal vibrations of about 0.1 Å). We have assumed a straight-line motion for the incoming and outgoing ion path for the averaging of the energy-loss over the impact parameter. In fact the angular deviations affect the kinematical factor (Grande et al., 2004). All above energy distributions are by definition normalized to one. The measurable projectile energy-loss function can be determined by (neglecting the energy resolution of the detection system)

$$
Y_{\mathrm{detected}}(E) = \sum_{L} p_{\mathrm{HD}}(L) Y_L(E), \tag{23}
$$

where p_{HD} is the hitting-detecting probability for a backscattering collision at a given layer L. The hitting probability p_{H} is the chance to hit a certain target atom in a close backscattering encounter and will depend basically on shadowing effects due the layers the ions pass through. The detecting probability p_{D} is the chance for a particle emerging from that target position to leave the crystal in the detector direction and will depend strongly on blocking. For the upper layers p_{HD} is very close to the product of hitting p_{H} and detecting p_{D} probabilities as

observed also previously (Frenken et al., 1986). Thus, for the layers $L < 4$ the effect of connected in and out tracks is minor.

The surface peak was also calculated using the Monte-Carlo SILISH code (Munoz-Marquez et al., 2005c). As in the well-established VEGAS code, the lattice positions of the Y and Si atoms are stored in an array. For each impinging projectile the target atoms are displaced according to their one-dimensional root-mean-square thermal vibrations, and the ion trajectory is determined by a sequence of binary collisions. In each of them, the scattering angle is obtained by using the Moliere scattering potential, the ion energy and the impact parameter. The scattering angle is used to determine the new ion direction as well as the recoil-energy transfer to the target atom. This impact parameter is also used to select the associated inelastic energy-loss tabulated from calculations based on Equation (17) for different targets and impact parameters. The target atoms are selected by considering the atoms inside a cylinder with radius r_{max} and axis parallel to the ion incident direction. The flux of incident ions at each lattice position is then stored in a 2D matrix, where each bin, representing the transverse ion position, contains not only the number of projectiles, but also the histogram of ion directions and energy losses. The same calculation is performed for the outgoing ions in the detection direction using time reversibility. The incoming and outgoing tracks are connected by using the corresponding flux matrices, together with the position of the backscattering atom according to its thermal vibration. Only trajectories having the same scattering plane are connected. The corresponding energy loss for the whole ion trajectory therefore consists of the energy loss due to the incoming and outgoing paths, as well as to the elastic and inelastic energy loss in the hard scattering collision. In this way, the variation of the kinematical factor due to different scattering angles is also taken into account. While quite large values of the cylinder radius r_{max} (about 4 Å) are needed to fully converge the calculation, some improvement in computational speed was achieved without significant loss of precision by using a somewhat smaller value (about 2 Å) and including a correction to the final energy loss spectrum. Moreover, this method of calculation avoids "double counting" of energy losses from more distant atoms, which may fall into both the ingoing and outgoing trajectory cylinders if these cylinders are too large.

The energy-loss distribution of each visible backscattering layer is displayed in Figure 13. The contribution of the first layer corresponds to a single collision with the first atom on the Al surface (see Figure 3). The deeper layers involve differences in the impact-parameter distribution and a convolution of these layer-specific distributions. For backscattering layers $L > 3$ the resulting shape is approaching a Gaussian distribution, as expected for electronic energy-losses.

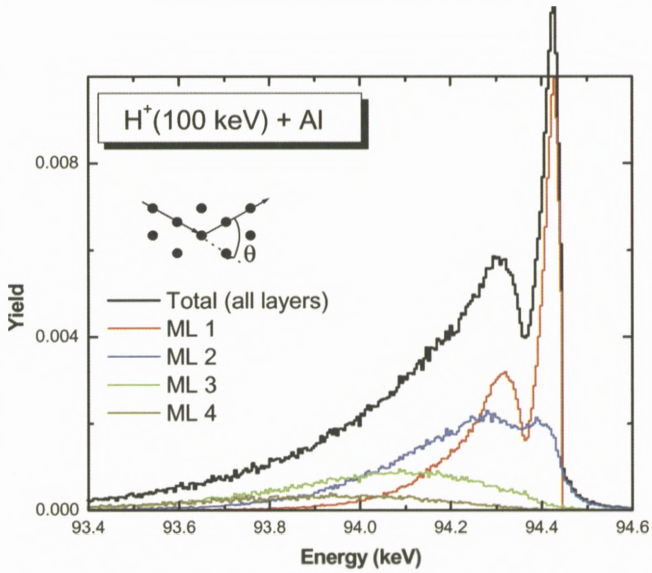

Figure 13. Contribution of each visible layer for the surface peak of 100 keV H^+ backscattered from the Al(110) surface for a 60–60 degree geometry.

According to Equation (23) the area of each curve in Figure 13 corresponds to the hitting-detecting probability p_{HD}. The backscattering yield of the first and second layers are similar because of a comparatively large surface relaxation, leading to a layer offset of about 0.1 Å. The third and fourth layers are still visible because of the thermal vibrations, which are of the order of the shadow cone radius for the ion energy used. For large energy losses even the fifth layer gains some importance. However, layers $L > 7$ have been neglected in the present work, since their contribution to the spectrum is very small.

The calculated curves in Figure 13 have been convoluted with the experimental resolution. The dashed curve AO (Atomic Orbital coupled-channel calculations) corresponds the simulations according to Equation (23) using a fixed impact parameter of $b = 0$ for the calculation of excitation/ionization probabilities in Al. The effect of the thermal vibrations along the ion history is represented by the dotted curve. Hence, the possible impact-parameters due to thermal vibrations are restricted to those outside of the shadow cone for a given hitting as well as detecting event. The solid curve includes additionally the effect of surface relaxation.

The results of the simulation show that although the surface relaxation is very important for the total yield, it affects the shape of energy-loss distribution very little. This is because backscattering collisions taking place in deep layers that

can contribute to the surface peak are due to trajectories having large impact parameters in the first layers (resulting in relatively insignificant energy losses) because of shadowing for the incoming path and blocking for the outgoing path. Thus, the surface relaxation plays a minor role for the energy-loss shape, but is very important for the total yield.

The simulation represented by the solid curve includes all-important terms that can be computed within the framework of the independent-electron model (IEM). In this simulation the effects concerning the electronic and atomic structure of Al(110) and ion-atom collisions including all higher-order effects have been very accurately included (within the IEM). Other effects such as a better description of the valence electrons, dynamically curved ion trajectories and/or the influence of a small H^0 charge-state fraction are of minor importance. This has been checked using test calculations. Furthermore, previous investigations have shown that correlated vibrations do only have a minor influence on the results (Frenken et al., 1986). Also the approximations used to calculate the impact-parameter distributions for each collision as well as the angular spreading have been cross-checked by performing full Monte-Carlo calculations SILISH. As can be observed in Figure 14, there is reasonable agreement between the present analytical simulation (solid line) and a full Monte-Carlo calculation for the same problem (dashed-dotted curve). The maximum relative deviation between both model results slightly exceeds 10% at backscattering energies below 93.8 keV.

The experimental data show a steeper decrease towards lower energies than our best analytical prediction (solid line) or the Monte-Carlo result (dashed-dotted curve). The remaining difference between both calculations and the experimental data clearly exceeds 30% at low backscattering energies, which is much larger than the present experimental and numerical uncertainties. We attribute this disagreement between the simulation and the experimental data to a breakdown of the independent-electron model (IEM). It was shown in Grande et al. (2005) that the dynamic modification of the target-electron density as well as the modification of the electron binding energy in multiple ionizations lead to a reduction of the ionization/excitation probabilities and are responsible for the observed differences. For other geometries these effects are expected to be of minor importance and a much better agreement with the experimental data have been observed (Grande et al., 2005).

6. Conclusions

Among other "unsolved" problems in IBA, the use of a more realistic (a non-Gaussian distribution) description for the electronic energy-loss distribution is

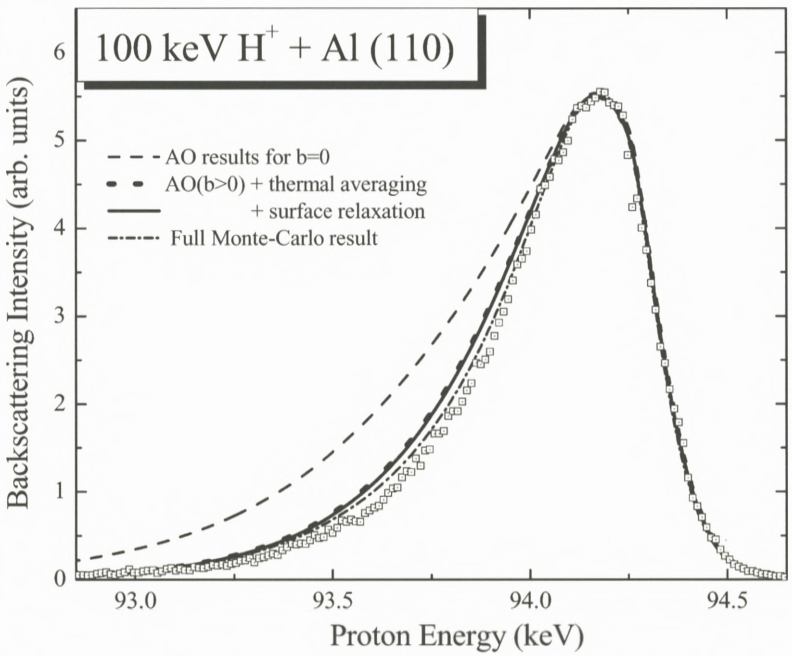

Figure 14. Experimental data (open squares) for 100 keV H^+ backscattered from Al(110) in comparison with simulations using the coupled-channel method (AO). Dashed line: energy-loss calculations for $b = 0$ only (no thermal averaging), weighted with the hitting-detecting probabilities. Dotted line: energy-loss calculations averaged over thermal vibrations and considering the weighted impact-parameter dependence of the energy-transfer distributions. Solid curve: energy-loss calculations including thermal vibrations and additionally the Al surface relaxation. Dashed-dotted curve: full Monte-Carlo calculations (SILISH) including thermal vibrations and surface relaxation.

crucial for high-resolution near-surface experiments. In this work we have shown some recent developments, which go far beyond the usual Gaussian approximation. In particular we have provided an accurate description of the energy-loss spectrum in a single collision using the coupled-channel method as well as the statistics of collisions (the ballistics) for amorphous and crystalline materials.

We have observed that large energy losses arising from inner-shell (e.g. the L-shell for Al) ionization/excitation are responsible for the energy-loss asymmetry at near central collisions (b close to zero) with a considerable fraction of double ionization. We note that the appropriate methods to handle the energy-loss in such violent collisions are those from the atomic physics field.

Using the coupled-channel calculations as a benchmark we have analyzed a simple energy-loss model for the energy-loss moments. Also, these *ab-initio*

calculations have been used to check some analytical formulas for the energy-loss distribution in order to replace the standard Gaussian distribution. Thus, the so-called basic lineshape is a step forward for near surface ion-beam analysis.

The energy loss in a single violent collision (as the backscattering collision in RBS or MEIS) firstly leads to a "degradation" of the depth resolution. Then, the real experimental resolution in high-resolution experiments is indeed often better than the one reported. For instance, concerning proton or He bombardment of few hundred keV, the difference between the nominal and real experimental resolution is large in the case of heavy targets (for RBS and MEIS) and less relevant for IBA techniques (such as NRA) involving light targets.

Nevertheless, as observed in the examples given in Section 5, the correct modeling of the energy-loss distribution is important to get reliable depth profiles in oxides and the shape of the surface peak.

Acknowledgements

This work was partially supported by CAPES -PROBRAL, by CNPq and by the Alexander-von-Humboldt foundation. Part of this work is a result of fruitful collaborations with D.P Woodruff (Warwick), T. Gustafsson (Rutgers), and M. Copel (IBM).

References

Arista N.R. (2002): Energy Loss of ions in solids: Non-linear calculations for slow and swift ions. Nucl Instr Methods **195**, 91–105

Arista N.R. and Lifschitz A. (1998): Velocity-dependent screening in metals. Phys Rev A **57**, 200–207

Bang J. and Hansteen J.M. (1959): IPM. Kgl Dan Vidensk Selsk Mat Fys Medd **31**, 13

Bloch F. (1933): The slow down of rapidly moving particles in the their passing through solid matter. Ann Physik **16**, 285

Carstanjen H.D. (1998): Ion beam analysis with monolayer resolution. Nucl Instr Methods **136–138**, 1183–1190

Chu W.K. (1976): Calculation of energy straggling for protons and He ions. Phys Rev A **13**, 2057–2060

Debus J., Schultz-Ertner D., Haberer T., Kraft G. and Jaekel O. (2004): Heavy charged particle therapy: From the technical challenge to the clinical role. Radiotherapy and Oncology **73**, 122

Dollinger G., Boulouednine M., Bergmaier A. and Faestermann T. (1998a): Nonequilibrium charge states of recoil ions in high resolution elastic recoil detection analysis. Nucl Instr Methods **136–138**, 574

Dollinger G., Frey C.M., Bergmaier A. and Faestermann T. (1998b): Elastic recoil detection with single atomic layer depth resolution. Nucl Instr Methods **136-138**, 603

Dollinger G., Bergmaier A., Goergens L., Neumaiera P., Vandervorst W. and Jakschik S. (2004): High resolution elastic recoil detection. Nucl Instr Methods **219–220**, 333

dos Santos J.H.R., Grande P.L., Behar M., Boudinov H. and Schiwietz G. (1997): Angular dependence of the electronic energy loss of 800-keV He ions along the Si[100] direction. Phys Rev B **55**, 4332–4342

Driemeier C., Miotti L., Pezzi R.P., Bastos K.P. and Baumvol I.J.R. (2006): The use of narrow nuclear resonances in the study of alternative metal-oxide semiconductor structures. Nucl Instr Methods Phys Res B **249**, 278–285

Frenken J.W.M., Tromp R.M. and van der Veen J.F. (1986): VEGAS code. Nucl Instr Methods **17**, 334

Grande P.L. and Schiwietz G. (1995): On classical calculations of the electronic stopping power at intermediate energies. J Phys B: At Mol Opt Phys **28**, 425–433

Grande P.L. and Schiwietz G. (1998): Impact-parameter dependence of the electronic energy loss of fast ions. Phys Rev A **58**, 3796–3801

Grande P.L. and Schiwietz G. (2002): The unitary convolution approximation for heavy ions. Nucl Instr Methods **195**, 55–63

Grande P.L. and Schiwietz G. (2004): Ionization and energy loss beyond perturbation theory – Advances in Quantum Chemistry, first edn., Elsevier Academic Press, Amsterdam

Grande P.L. and Schiwietz G. (2006): Convolution approximation for swift particles. Free download from `http://www.hmi.de/people/schiwietz/casp.html`

Grande P.L., Hentz A., Schiwietz G., Schulte W.H., Busch B.W., Starodub D. and Gustafsson T. (2004): Nonperturbative treatment of medium-energy proton scattering under shadowing-blocking conditions in Al(110). Phys Rev B **69**, 104112

Grande P.L., Hentz A., Schiwietz G., Starodub D., Garfunkel E. and Gustafsson T. (2005): Observation of collective inner-shell effects for protons backscattered from the Al(110) surface. Phys Rev A **72**, 012902

Grande P.L., Hentz A., Pezzi R.P. and Schiwietz G. (2006): Improved energy-loss formulas for high resolution ion-beam analysis. Nucl Instr Methods, to be published

Grüner F. and Bell F. (2006): First-principles-simulation of both charge state and stopping power of swift heavy ions in solids. Nucl Instr Methods **245**, 15–18

Herman F. and Skillmann S. (1963): *Atomic Structure Calculations*. Prentice-Hall, Inc. Englewood Cliffs, New Jersey, first edn.

Hoshino Y., Fukuyama R., Nishimura T., Tanaka S., Kohyama M. and Kido Y. (2005): Atomic structure of Si-rich 6H-Si(0001) – 2 × 2 surface. Phys Rev B **71**, 195331

McGuire N.S. and Simony P.R. (1981): Screening and anti-screening by projectile electrons in high-velocity atomic-collisions. Phys Rev A **24**, 97–102

Kabachnik N.M., Chumanova O.V. and Chumanov V.Y. (1993): Impact parameter dependence of energy-loss straggling in ion-atom collisions. Nucl Instr Methods **83**, 591–593

Kimura K., Ohshima K. and Mannami M. (1994): Monolayer analysis in Rutherford backscattering spectroscopy. Appl Phys Lett **64**, 2232–2234

Maurel B., Amsel G. and Nadai J.P. (1982): Depth profiling with narrow resonances of nuclear reactions: theory and experimental use. Nuclear Instr and Methods **197**, 1–13

McGuire J.H. and Weaver L. (1977): Independent electron approximation for atomic scattering by heavy particles. Phys Rev A **16**, 41–47

Mott N.F. (1931): On the theory of excitation by collision with heavy particles. Proc Cambr Phil Soc **27**, 553–560

Munoz-Marquez M.A., Parkinson G.S., Quinn P., Gladis M., Tanner R., Woodruff D.P., Bailey P. and Noakes T.C.Q. (2005a): N-induced pseudo-(100) reconstruction of Cu(111): One layer or more? Surf Sci **582**, 97–109

Munoz-Marquez M.A., Parkinson G.S., Woodruff D.P., Hentz A., Grande P.L., Schiwietz G., Wood T.J., Bonet C., Tear S.P., Bailey P. et al. (2005b): Energy loss in medium-energy ion scattering: A combined theoretical and experimental study of the model system Y on Si(111). Phys Rev B **72**, 075415 (pages 10). `http://link.aps.org/abstract/PRB/v72/e075415`

Munoz-Marquez M.A., Parkinson G.S., Woodruff D.P., Hentz A., Grande P.L., Schiwietz G., Wood T.J., Bonet C., Tear S.P., Bailey P. et al. (2005c): Energy loss in medium-energy ion scattering: A combined theoretical and experimental study of the model system Y on Si(111). Phys Rev B **72**, 075415

Okazawa T., Takeuchi F. and Kido Y. (2005): Enhanced and correlated thermal vibrations of Cu(111) and Ni(111) surfaces. Phys Rev B **72**, 075408

Olson R.E. (1989): Energy deposition by energetic heavy-ions in matter. Rad Eff and Deff in Solids **110**, 1–5

Pezzi R.P., Grande P.L., Copel M., Schiwietz G. and Baumvol I.J.R. (2006): Stochastic modeling of ion energy loss at intermediate energies: profiling with subnanometric resolution. Surf Sci, to be published

Rauhala E., Barradas N.P., Fazinic S., Mayer M., Szilagyi E. and Thompson M. (2006): Status of ion beam data analysis and simulation software. Nucl Instr Methods **244**, 436–456

Rösel F., Trautmann D. and Bauer G. (1982): Recoil effects in atomic inner shell ionization. Nucl Instr Methods **192**, 43–52

Ryufuku H. and Watanabe T. (1978): Charge transfer in collisions of atomic hydrogen with O^{8+}, He^{2+}, and H^{+}. Phys Rev A **18**, 2005–2015

Ryufuku H. and Watanabe T. (1979): Charge transfer cross sections for collisions of Li^{3+}, Be^{4+}, B^{5+}, and C^{6+} ions with atomic hydrogen. Phys Rev A **19**, 1538–1549

Schiwietz G. (1990): Coupled-channel calculation of stopping powers for intermediate-energy light-ions penetrating atomic H and He targets. Phys Rev A **42**, 296–306

Schiwietz G. and Grande P.L. (1999): A unitary convolution approximation for impact-parameter dependent electronic energy loss. Nucl Instr Methods **153**, 1–9

Schiwietz G., Wille U., Muiño R.D., Fainstein P.D. and Grande P.L. (1996): Comprehensive analysis of the stopping power of antiprotons and negative muons in He and H-2 gas targets. J Phys B: At Mol Opt Phys **29**, 307–321

Schiwietz G., Grande P.L. and Roth M. (2001): Electronic stopping of protons at intermediate velocities. ISL Annual Report HMI B587 (ISSN 1610-0638), 20

Schulte W.H., Busch B.W., Garfunkel E., Gustafsson T., Schiwietz G. and Grande P.L. (2001): Limitations to depth resolution in ion scattering experiments. Nucl Instr Methods **183**, 16–24

Sigmund P. (2004): Stopping of Heavy Ions – A Theoretical Approach, first edn., Springer, Berlin

Sigmund P. (2006): Particle Penetration and Radiation Effects, first edn. Springer, Berlin

Sigmund P. and Schinner A. (2000): Binary stopping theory for swift heavy ions. Europ Phys J D **12**, 425–434

Sigmund P. and Schinner A. (2002): Binary theory of the electronic stopping. Nucl Instr Methods **195**, 64–90

Srivastava S.K., Plachke D., Szokefalvi-Nagy A., Mayor J. and Carstanjen H.D. (2004): Counting individual atom layers in graphite – High-resolution RBS experiments on highly oriented pyrolytic graphite. Nucl Instr Methods **219–220**, 364–368

Tesmer J.R. and Nastasi M.A. (1995): Handbook of Modern Ion Beam Materials Analysis: Materials Research Society, first edn., MRS, Pittsburgh

van der Veen J.F. (1985): Ion beam crystallography of surfaces and interfaces. Surf Sci Rep **5**, 199–288

Vrijmoeth J., Zagwijn P.M., Frenken W.M. and van der Veen J.F. (1991): Monolayer resolution in Medium-Energy-Ion-Scaterring on $NiSi_2(111)$ surface. Phys Rev Lett **67**, 1134

Wilk G.D., Wallace R.M. and Anthony J.M. (2001): High-κ gate dielectrics: Current status and materials properties considerations. Appl Phys Rev **89**, 5243

Woodruff D.P. and Delchar T.A. (1994): Modern Techniques of Surface Science, second edn., Cambridge University Press, Cambridge

Ziegler J.F. (2006): SRIM code. Free download from `http://www.SRIM.org`

Nanoscale Morphology Control Using Ion Beams

M.J. Aziz

Division of Engineering and Applied Sciences
Harvard University
Cambridge, MA 02138, U.S.A.

Abstract

Ion irradiation of a solid surface can be used to control surface morphology on length scales from 1 micron to 1 nanometer. Focused or unfocused ion irradiation induces a spontaneous self-organization of the surface into nanometer-sized ripples, dots, or holes; it also induces diameter increases and decreases in pre-existing nanopores. The phenomenology of the surface morphological evolution under ion beam erosion is reviewed with an emphasis on semiconducting materials, including recent experiments on the influence of boundary conditions on guiding self-organized pattern formation; the development of shock fronts that sharpen features at sufficiently steep angles; and the kinetics governing the fabrication of nanopores for single-biomolecule detectors. The theory underlying the surface morphology evolution is reviewed and areas of agreement and disagreement with experiment are identified.

Contents

1 Introduction **188**

2 Sputter Patterning **189**
2.1 Formation of Sputter Patterns 189
2.2 Guided Self-Organization by Templating 191
2.3 Theory of Sputter Pattern Formation 192
2.3.1 Linear Stability Theory 193
2.3.2 Nonlinear Perturbative Approach 196
2.3.3 Erosion of Tall, Steep Features 197

3 Single Biomolecule Detectors **200**

4 Surface Morphological Relaxation and Nanostructure Stability **202**

Acknowledgements **203**

References **204**

1. Introduction

Nanoscale surface morphologies spontaneously develop from uniform ion irradiation of an initially flat surface in a non-equilibrium self-organization process termed "sputter patterning". Spontaneous self-organization processes such as this have no fundamental throughput limitations and have been used to create patterns with lateral feature sizes as small as 15 nm, and good short-range order (Facsko et al., 1999) as shown in Figure 1. As in most self-organization processes, the major challenge is the flexibility one has over the resulting pattern. A combination of "top-down" approaches for flexibility and "bottom-up" approaches for size and throughput is likely to be a successful strategy for mass production of functional nanoscale devices. The importance of the "bottom-up" approaches will be determined to a significant degree by the answer to the question, "how much control do we have over the morphology?" A great deal of fundamental research must be done before this question can be answered.

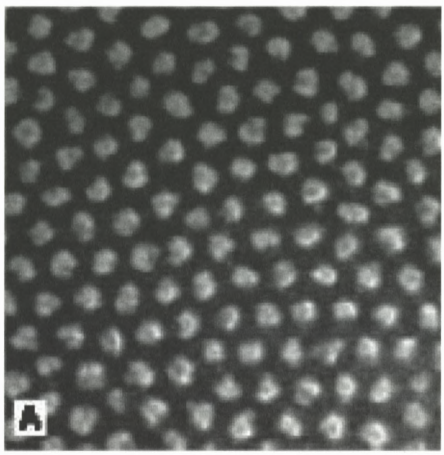

Figure 1. "Quantum dots" on GaSb, fabricated by normal-incidence sputter patterning using 420 eV Ar^+. From Facsko et al. (1999). Image 500 nm × 500 nm. Dots as small as 15 nm have been reported.

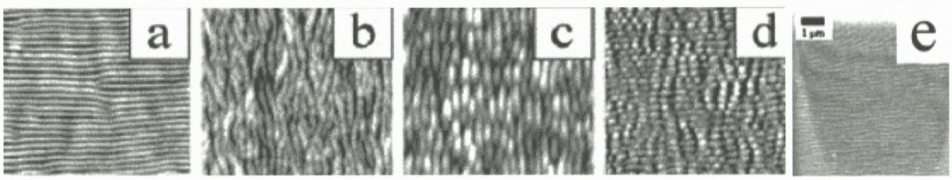

Figure 2. Sputter patterns formed on Si. (a) highly aligned "parallel mode" ripples on Si(111), from Brown et al. (2005), (b) wavy "perpendicular mode" ripples on Si(001) (Erlebacher et al., 1999), (c) wavy perpendicular mode ripples on Si(111), from Brown et al. (Brown et al., 2005), (d) two dimensional dot arrays on Si(111), from Brown et al. (Brown et al., 2005), (e) ripples in *a*-Si formed by uniform FIB rastering (Cuenat and Aziz, 2002). Projected ion beam direction is from bottom to top in all images. AFM scan size for (a)–(d) is 10 microns. Scale bar in SEM image in (e) is 1 micron.

In a related phenomenon, ion irradiation permits nanopore morphology control on the single-digit nanometer level and is consequently termed "ion beam nano sculpting". Solid state nanopores with diameters of molecular dimensions have been fabricated this manner (Li et al., 2001). The technology is being used to make single biomolecule detectors that are now capable of analyzing biomolecule lengths and molecular conformations in vitro and are envisaged as ultra-rapid DNA sequencers.

In this paper we discuss the scientific aspects of ion-solid interactions underlying these developments.

2. Sputter Patterning

2.1. Formation of Sputter Patterns

It has long been known that under some conditions of uniform ion irradiation of a solid surface, a spontaneously-arising sputter pattern topography arises that often takes the form of one-dimensional ripples or two-dimensional arrays of dots. The periodicity is understood to arise as a result of a kinetic competition between the surface roughening effect of the ion beam and morphological relaxation.

There is a significant body of experimental and theoretical work on ion-stimulated formation and relaxation of self-organized topographic features on solid surfaces (Navez et al., 1962; Bradley and Harper, 1988; Erlebacher and Aziz, 1997; Habenicht, 2001; Makeev et al., 2002; Valbusa et al., 2003; Brown and Erlebacher, 2005). Figure 2 shows representative surface morphologies on Si, including regular and irregular one-dimensional ripples formed at off-normal ion beam incidence (Erlebacher et al., 1999; Cuenat and Aziz, 2002; Brown and Erlebacher, 2005; Brown et al., 2005), and also transient two-dimensional ripple

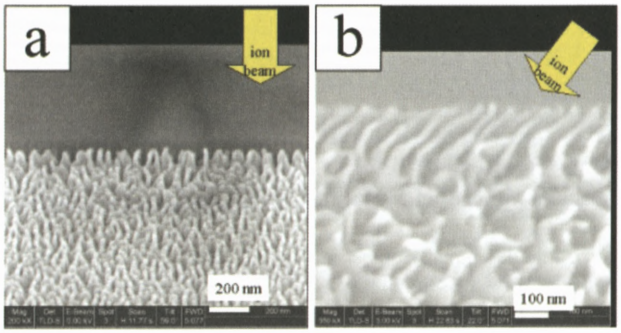

Figure 3. SEM image of Ge "nanograss" formed by uniform rastering with 30 keV Ga^+ FIB. (a) incident angle 90 degrees; (b) incident angle 60 degrees.

morphologies. For sputter patterns on Si, on which we will focus, the in-plane length scales (wavelengths) are typically of order 100 nm, and the out-of-plane length scales (amplitudes) are of order 10 nm. Spontaneously self-organized ripples and dots as small as 15 nm have been formed in other materials systems such as GaSb (Facsko et al., 2001) and SiO_2 (Mayer et al., 1994). We are studying the larger lateral length scales in Si because of the ready availability of *in-situ* probes, e.g. optical diffraction techniques (Chason et al., 1998; Erlebacher et al., 1999) and Focused Ion Beam (FIB)-Scanning Electron Microscopy (SEM) (Zhou et al., 2003) and because Si is a monatomic system highly amenable to atomistic modeling. With measurements at these length scales, we hope to rapidly develop a deep understanding of the fundamental aspects of the phenomenon. Ultimately we expect to develop sufficient understanding to design and guide experiments at sub-lithographic length scales that permits us to answer the question, "How much morphology control can one attain without having to write each individual feature?"

A significant recent discovery (Cuenat and Aziz, 2002; Habenicht et al., 2002) has been sputter patterning under uniform rastering of a focused ion beam (FIB), which is a machine typically used to micromachine surfaces in computer-controlled patterns. The rapid feedback possible with *in-situ* real-space imaging in a FIB instrument has accelerated the understanding of the phenomena believed to be common to both focused and unfocused ion irradiation. Not only has this observation of pattern evolution under FIB irradiation served as an excellent test of theory and motivated new theory, it has also lead to unanticipated developments, such as germanium "nanograss" shown in Figure 3 (Cuenat and Aziz, 2002).

2.2. Guided Self-Organization by Templating

Methods for the fabrication of large areas of nanoscale features with controlled period and intra-period organization are of interest because of the potential for high-throughput mass production of nanoscale devices. Due to their potential in this regard, much recent attention has been devoted to self-organization processes (Teichert et al., 1996; Facsko et al., 1999; Shchukin and Bimberg, 1999; Thurn-Albrecht et al., 2000). Although the short-range order can be quite high, some envisaged applications require long-range order, which is destroyed by uncontrolled topological defects arising spontaneously from the self-organization process. A potentially successful hierarchical fabrication strategy is the fabrication of controlled features at a small, but lithographically tractable, length scale by methods such as conventional mask or optical standing wave lithography, in order to guide a self-organization process at the finest length scale (Peters et al., 2000; Cheng et al., 2004). Lithographically- and Focused Ion Beam (FIB)-patterned topographies have recently been used to template quantum dot growth in linear chains (Yang et al., 2004), periodic 2D lattices (Karmous et al., 2004), and in more complex configurations promising for novel nanoelectronics architectures such as quantum cellular automata (Gray et al., 2004). The finest features have been templated by serial writing with the FIB, a prohibitively expensive process for mass production that might be circumvented by the hierarchical fabrication strategy. Self-organized sputter-ripple topographies have been used to template metal islands (Brown, 2005) and colloidal particles (Mathur et al., 2005) in linear chains.

We measured the influence of patterned boundaries on a Si(001) substrate in guiding self-organized sputter ripples (Cuenat et al., 2005). We showed that the long-range order of the features can be greatly enhanced by this lateral templating approach (Figure 4). The emerging pattern can be manipulated by changing the boundary spacing and misorientation with respect to the projected ion beam direction. We developed a scalar figure of merit, a dimensionless topological defect density, to characterize the degree of order of the pattern. At small boundary separation, the greatest order is observed when the separation is near an integer multiple of the spontaneously arising feature size. The defect density is exceedingly low up to a critical misorientation angle, beyond which topological defects develop in proportion to the incremental misorientation. No theory has been shown to predict the lateral templating effect and the documented behavior of the defect density, or to address the maximum distance between template boundaries over which it is possible to deterministically set the pattern that evolves within the intervening area. These remain open questions.

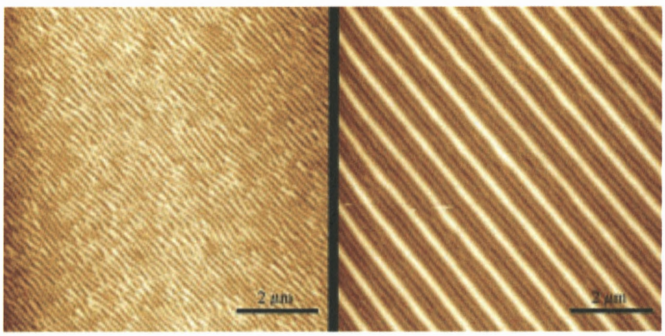

Figure 4. Lateral templating under ion beam sputtering (Cuenat et al., 2005). AFM topographs of sputter-rippled Si(001) just outside (left) and inside (right) lithographically templated region of same sample. High regions are white.

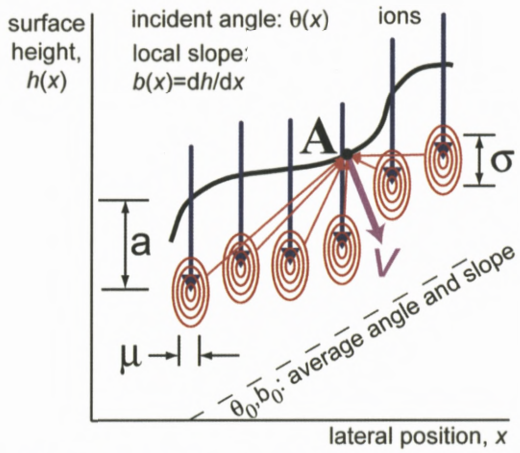

Figure 5. Sigmund's (1973) model of sputter morphology evolution. Iso-energy contours are illustrated. Average ion range is a, longitudinal and transverse straggling are σ and μ. As illustrated by red arrows, some energy from ions impinging at all points contributes to erosion at point **A**. Concave regions such as **A** are closer to the energy deposition maxima than convex regions and thereby erode faster.

2.3. Theory of Sputter Pattern Formation

All theories of sputter pattern formation originate from Sigmund's (1973) model demonstrating the instability of a planar surface to uniform ion beam erosion. Although treatments in two independent spatial dimensions are common, for the purpose of simplicity we will restrict our exposition to a single independent spatial dimension. As shown in Figure 5, let the ion beam approach the solid in the y

direction and let surface height be described by the function $y = h(x, t)$, where t is time. The rate of recession of an eroding surface (excluding surface relaxation and noise) can be written as $\partial h/\partial t = -V\sqrt{1 + b^2}$, where $b \equiv \partial h/\partial x$ is the local slope of the surface and V is the erosion speed normal to the surface. Generally, V is a function of the surface slope, curvature, and higher order derivatives of the morphology. According to Sigmund, V at point **A** at position **x** on the surface is proportional to the energy $E(x, x')$ deposited per unit depth at **x** from the collision cascades originating from ions impinging on the surface at all other points **x**′, as shown in Figure 5. The speed of erosion at **x** is then given by an integral over all points **x**′:

$$V(x) \propto \int \mathrm{d}x' E(x, x'). \tag{1}$$

As can be seen from Figure 5, concave regions of the surface, such as point **A**, are closer to the energy deposition maxima than convex regions and so erode faster. For simplicity, Sigmund modeled the distribution of deposited energy as centered a distance a below the impingement site (along the initial ion direction) and decaying outward as a Gaussian with an ellipsoidal shape. $E(x, x')$ then becomes simply

$$E(x, x') = \text{const.} \cdot \exp\left(-\frac{[h(h') - a - h(x)]^2}{2\sigma^2} - \frac{[x' - x]^2}{2\mu^2}\right). \tag{2}$$

We shall refer to the r.h.s. of Equation (1) as the *Sigmund sputter integral* and Equation (2) as the *Sigmund kernel*. Note that the only materials parameters controlling morphology evolution in this model are a, σ, and μ: parameters such as the surface binding energy merely scale the rates for all points on the surface by a multiplicative factor through the proportionality sign in Equation (1).

2.3.1. *Linear Stability Theory*

Bradley and Harper (BH) (1988) performed a linear stability analysis of a flat surface undergoing erosion according to the Sigmund kernel while simultaneously undergoing surface relaxation toward flatness by surface diffusion. They showed that the instability survives no matter how much relaxation by surface diffusion is occurring simultaneously. By expanding the height function for small curvature, slope difference, and height difference from a planar surface, they found that the leading order instability arises from the curvature coefficient of the sputter yield. The same expansion for the diffusional relaxation term is taken from the classical Mullins–Herring (Herring, 1950; Mullins, 1959) theory of morphological relaxation kinetics: The chemical potential is proportional to the surface tension

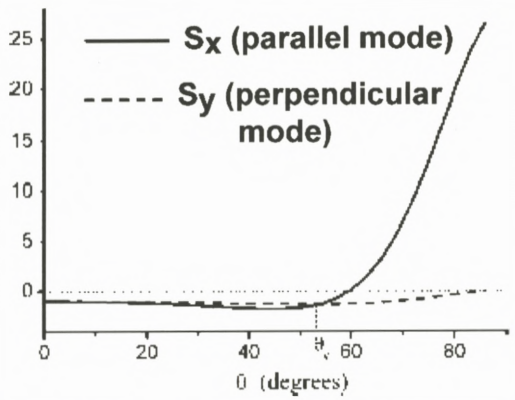

Figure 6. Variation of the curvature coefficient S of the vertical erosion rate (arbitrary units) in Equation (3) with inclination angle. Linear instability ($S < 0$) exists at all angles. When surface diffusion is isotropic, mode with most negative value of S is expected to dominate topography. Adapted from Feix et al. (2005).

times $\partial^2 h/\partial x^2$; the gradient of the chemical potential ($\sim\partial^3 h/\partial x^3$) determines the surface diffusion flux; and the divergence of the flux ($\sim\partial^4 h/\partial x^4$) gives the rate of change of height. The resulting partial differential equation (PDE) of BH for the change in height, relative to the average height, is

$$\frac{\partial h(x,t)}{\partial t} = S\frac{\partial^2 h}{\partial x^2} - B\frac{\partial^4 h}{\partial x^4}, \tag{3}$$

where the curvature coefficient S is negative, leading to instability. As a linear PDE, Equation (3) can be solved using Fourier methods. The amplitude of each Fourier component of the surface morphology $h_q(t)$ with wavenumber q should grow or decay exponentially with rate constant $R(q) = -Sq^2 - Bq^4$. BH thus predict a maximal value of $R(q)$ at a fastest growing spatial frequency $q^* = (-S/2B)^{1/2}$, so after a while the surface should be dominated by sinusoidal ripples with spatial period $\lambda^* = 2\pi/q^2$.

In two independent spatial dimensions, Bradley and Harper solved for the stability with respect to sinusoidal perturbations with wavevector either parallel or perpendicular to the direction of the projected ion beam on the surface ("parallel mode" and "perpendicular mode", respectively, Figure 2). As shown in Figure 6, all surfaces, at all angles of inclination θ, are predicted to be linearly unstable to perpendicular mode ripples, whereas all surfaces below a certain inclination angle (measured from normal) are predicted to be unstable to parallel mode ripples. Where instabilities to both modes arise, the resulting topography is expected to be

dominated by the mode with the greatest value of R. When surface diffusion is isotropic, this would be the mode with the most negative value of S.

The BH model also predicts the dependence of q^* and $R(q)$ on control parameters such as flux f and temperature T, and predicts that as long as the curvature and range of slope remain sufficiently small, the fastest growing spatial period should be time-independent. The model has been tested under a wide variety of conditions and has been found to describe some aspects of evolution but not others Chason, in these proceedings, describes tests of BH for copper surfaces under a wide range of conditions. For silicon, the flux-dependence and temperature-dependence of λ^* is consistent with BH (Erlebacher et al., 1999); λ^* is time-independent for Si(001) (Erlebacher et al., 1999, 2000b) but, contrary to BH, coarsens with time for Si(111) (Brown and Erlebacher, 2005). One commonly observes amplitude saturation at long times, which one expects would arise from nonlinear terms missing from a linear stability theory, but in silicon saturation is occurring at surprisingly small slopes ($\sim 10°$) that are difficult to understand (Erlebacher et al., 2000b; Brown and Erlebacher, 2005). Transient topographies not predicted by BH are observed on Si(111) (Brown et al., 2005).

One common example of the curious failure of BH theory is for normal-incidence unfocused ion irradiation, where an instability with a characteristic length scale is predicted but rarely observed (Cuenat and Aziz, 2002) (with a few notable exceptions, e.g. Facsko et al., 2001). Beyond this, the experimental conditions for stability are not clear. We now have evidence that under certain conditions the sputter instability is actually a sputter metastability, i.e., an initially flat, amorphous surface is metastable.

Because the BH linear stability results are a rigorous consequence of formulae (1, 2), one must examine the validity of the Sigmund theory underlying just about every treatment of morphological development. Recently Feix et al. (2005) reported molecular dynamics simulations of the sputter erosion of copper crystals by 5 keV Cu. They looked at the spatial distribution of sites from which the sputtered atoms were emitted with respect to the point of impact and found that Equation (1) describes their results pretty well (assuming V is proportional to the atom emission rate, which they tracked), except that the Sigmund kernel, Equation (2), needed to be replaced by a kernel of a somewhat different form. This permitted them to explain a reduction in sputter yield with increasing angle at very high angles, which is not explained by the Gaussian ellipsoid kernel (see Figure 10), but otherwise the results of the Sigmund model seem to be qualitatively unchanged. In particular, with a modified sputter kernel of Feix et al., the qualitative features of Figure 6 remain the same: all surfaces at all inclinations *should* exhibit a linear instability.

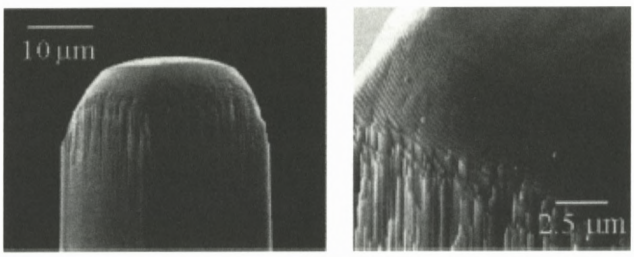

Figure 7. Example of tall, steep features that cannot be modeled with a perturbative approach. Single crystal diamond curved tip microindenter fabricated by FIB, from Adams et al. (2003). High-magnification view on the right shows three different morphologies, including rippled "phase" and flat "phase".

We have accumulated reasons to believe that other forms of the sputter kernel qualitatively change the conclusions on stability. Other kernels may result from a variety of effects. For example, under some conditions, ion impacts create craters with rims (Bringa et al., 2001). In all cases, the ion-induced change in topography $\Delta h(x - x')$ can be characterized quantitatively (Moseler et al., 2005). Because of effects such as thermal spikes or ion-stimulated mass transport at or near the surface, V is *not* necessarily proportional to the atom emission rate. We are working on understanding the consequences when the Sigmund kernel is replaced in Equation (1) by an expression for the local topography change (Kalyanasundaram et al., unpublished), resulting in

$$\frac{\partial h(x,t)}{\partial t} = \int J(x')\Delta h(x, x'; b)\, \mathrm{d}x', \tag{4}$$

where J is the ion flux and b is the local slope. Our conjecture is that this will create a term $S'\partial^2 h/\partial x^2$ that can overwhelm the first term on the r.h.s. of Equation (3), thereby becoming the predominant source of linear stability or instability.

2.3.2. *Nonlinear Perturbative Approach*

Enhancements to BH theory have been made to include noise (Mayer et al., 1994), nonlinear effects at larger amplitudes (Park et al., 1999; Makeev et al., 2002; Castro et al., 2005), and the identification (Makeev and Barabasi, 1997) of a fourth-order "effective surface diffusion" term $-D_{xx}\partial^4 h/\partial x^4$ through which we can understand how patterns may form even when surface diffusion is essentially turned off at low temperature where $B = 0$.

The inclusion of nonlinear effects is an area of very active research. Makeev and co-workers (Makeev et al., 2002) developed from the Sigmund kernel a general expression for V in terms of arbitrary topography and the parameters a, σ,

and μ describing the ion collision cascade in the solid. To obtain solutions, they then expanded V in powers of slope and derived an erosion equation of the form (for simplicity we report only the most noteworthy terms in a one-dimensional version although the actual theory is for two independent spatial dimensions)

$$\frac{\partial h}{\partial t} = S_x \left(\frac{\partial^2 h}{\partial x^2}\right) + \xi_x \left(\frac{\partial h}{\partial x}\right)\left(\frac{\partial^2 h}{\partial x^2}\right) + \Omega_1 \frac{\partial^3 h}{\partial x^3} - D_{xx}\frac{\partial^4 h}{\partial x^4} + \frac{\lambda_x}{2}\left(\frac{\partial h}{\partial x}\right)^2, \quad (5)$$

where S_x, x_x, and W_1 are roughening prefactors determining the anisotropic erosion rate, D_{xx} describes ion induced "effective surface diffusion", and λ_x controls the early stages of nonlinear evolution. Makeev et al. solved for these ion-related coefficients as functions a, σ, and μ. Solutions to the two-dimensional counterpart of Equation (5) have been obtained for shallow ripples (Makeev et al., 2002; Makeev and Barabasi, 2004b) and self-affine surfaces (Makeev and Barabasi, 2004a).

Makeev et al.'s small-slope expansion, Equation (5), is valid for slope excursions of several tens of degrees, but cannot be used to describe our observed lateral templating of sputter ripples (Figure 4) because experimentally the initial surface possesses regions of widely differing slopes. Likewise, understanding and controlling the effects of the FIB on morphology evolution in the micromachining of tall, steep features remains open (Vasile et al., 1999; Adams et al., 2003; Tseng et al., 2004). What we need in cases such as these is a non-perturbative approach that can handle arbitrarily large excursions in inclination angle

2.3.3. *Erosion of Tall, Steep Features*

We have reported a new regime of ion beam sputtering that occurs for sufficiently steep slopes (Chen et al., 2005). High slopes propagate over large distances without dissipating the steepest features. Both the propagation velocity and the dynamically selected slope are universal, independent of the details of the initial shape of the surface. The SEM image in Figure 8 shows a pit with steep side walls that has been micromachined into silicon using a Focused Ion Beam, and to the right the same pit, with sides that have not smeared out, after uniform ion irradiation of the entire wafer. The left panel of Figure 9 shows predictions of the new theory of sputter morphology evolution that is valid for arbitrarily large slopes when the curvature is small. Under uniform ion irradiation the pit wall, initially at $t = 0$, propagates laterally and, for this particular set of conditions, evolves to maintain a uniform slope that is steeper than the original slope. The theory also predicts that sufficiently shallow slopes dissipate, which is the conventionally observed behavior. The experimental sequence in Figure 9, obtained with an optical profilometer, shows striking confirmation of the predictions of the

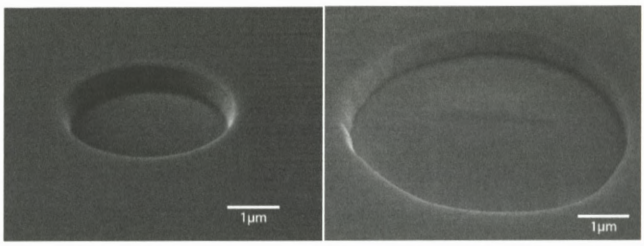

Figure 8. (a) SEM image of an initial circular pit in Si with 3 μm diameter, 0.5 μm depth, and steep side walls. (b) The wall of the enlarged pit is still sharp after uniform ion exposure. From Chen et al. (2005).

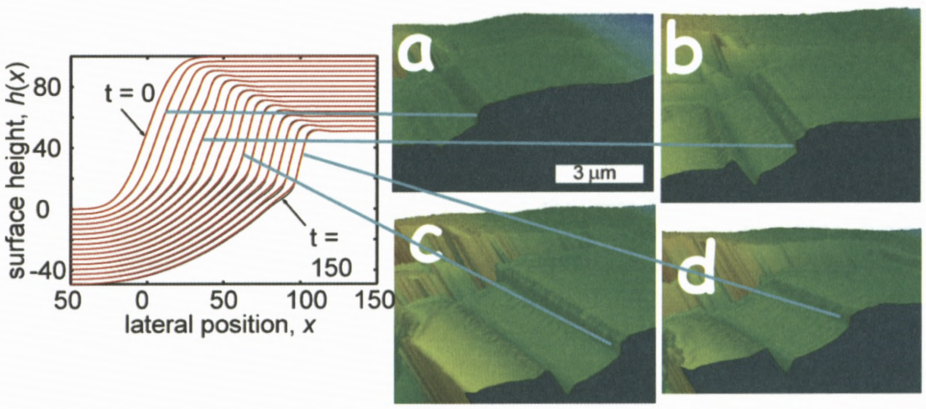

Figure 9. (Left) Theoretical profile evolution. Red curves: solution of advection-diffusion PDE; black curves: numerical integration of Sigmund kernel. (a)–(d) Experimental profiles illustrating propagation of shock front with decreasing height and increasing size of trailing rarefaction wave. The blue lines are for illustrative purposes and do not signify a quantitative one-to-one correspondence between theoretical and experimental profiles. Adapted from Chen et al. (2005).

theory. An important implication of the transition from dissipative behavior to propagative behavior at high slopes is that a structure (e.g. line or dot) can be fabricated at a large length scale and, with uniform ion irradiation, reduced to a smaller length scale while preserving, or even sharpening, the steepest features.

The non-perturbative approach for steep features develops from the Sigmund sputter kernel a small-curvature approximation that is valid for *all* slopes. Combining this with Mullins–Herring surface diffusion mediated surface smoothening results in a nonlinear PDE called the advection-diffusion equation,

$$\frac{\partial b(x,t)}{\partial t} = -C\frac{\partial b}{\partial x} - S\frac{\partial^2 b}{\partial x^2} - B\frac{\partial^4 b}{\partial x^4}, \tag{6}$$

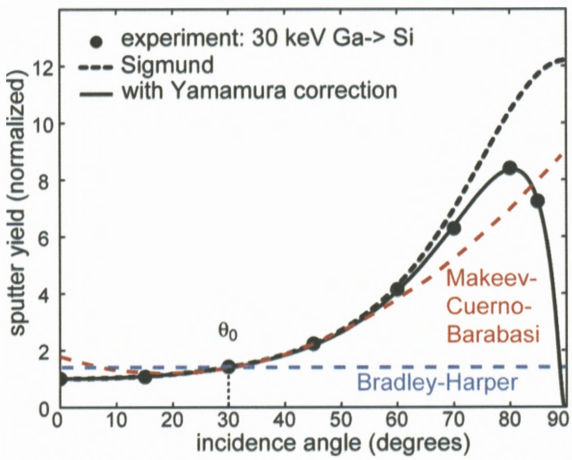

Figure 10. Sputter yield of flat surface *versus* incidence angle. Adapted from Vasile et al. (1999). Dashed curve: full Sigmund sputter integral with Sigmund kernel(Gaussian ellipsoids). Solid black: with empirical Yamamura correction (Yamamura et al., 1983; Vasile et al., 1999). Applying Bradley–Harper analysis to large amplitudes assumes all coefficients are constant at their initial value, e.g. illustrated here for an initial slope of 30°. Red curve: Makeev et al.'s quadratic expansion in powers of slope. The entire black curve goes into the non-perturbative theory of Chen et al.; shock fronts result in the region where the curvature is downward.

where $b \equiv \partial h/\partial x$ b is the slope, $C = C(b) \equiv \partial Y/\partial b$ turns out to be the propagation speed, and Y is the sputter yield (see Figure 10). The solutions of this equation predict behavior that can be understood as the propagation of a shock front that self-selects a stable slope; the mathematical structure of the solutions is the same as that previously observed in thin-film fluid flows. The shock front behavior turns out to be a generic feature of the non-monotonic behavior of the sputter yield *versus* slope. As the slope increases, the center of the energy deposition gets closer to the surface; hence the sputter yield increases with slope. But at high enough slope, the sputter yield turns down again due to effects such as reflection at grazing incidence (Yamamura et al., 1983) and incomplete development of the collision cascade (Sigmund, 1981), and possibly to deviations of the true collision cascade shape from Gaussian ellipsoids (Feix et al., 2005). This qualitative behavior of the sputter yield *versus* slope, combined with the kinetics of surface diffusion, turns out to be sufficient for propagative rather than dissipative solutions to the morphology evolution equation arising from the Sigmund sputter kernel and fourth-order diffusion.

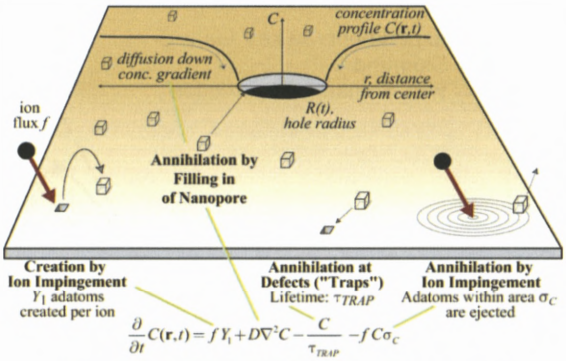

Figure 11. Processes in adatom diffusion model.

3. Single Biomolecule Detectors

The physics and materials science of sputter patterning are important in the development of nanopore single- molecule detectors (Figure 12). Focused and unfocused ion beam irradiation has been used to fabricate single nanopores in insulators, control their diameters to molecular dimensions, and use them in sensitive devices to detect and analyze single biomolecules in solution (Li et al., 2001, 2003; Stein et al., 2002, 2004; Chen et al., 2004; Mitsui et al., 2006) Such detectors are envisaged as DNA sequencers $\sim 10^6$ times faster than those in current use (Meller et al., 2000). Using a FIB of 50 keV Ga^+, single nanopores of diameter $\sim$ 50 nm are drilled through a membrane of silicon dioxide or silicon nitride supported along its perimeter by attachment to a silicon wafer substrate. Subsequent broad irradiation with an unfocused beam of 3 keV Ar^+ results in the gradual closure of the nanopore. Feedback on the transmitted ion current permits an exquisite level of control on the final pore diameter, which can be tuned to pass molecules with diameters under a desired value. An adatom-diffusion model (Figure 11), which is an extension of the model of the atomistic processes occurring in sputter patterning of Si(001) (Erlebacher et al., 1999), accounts for many aspects of the ion-sputter-induced closing of nanopores in silicon nitride membranes (Li et al., 2001) (Figure 12). This model posits that the spatiotemporal evolution of the concentration field $C(\mathbf{r}, t)$ of surface-diffusing mobile species ("adatoms") created by the ion beam is governed by the following PDE:

$$\frac{\partial}{\partial t}C(\mathbf{r}, t) = fY_1 - \frac{C}{\tau_{\text{trap}}} - fC\sigma + D\nabla^2 C, \tag{7}$$

where f is the ion flux, Y_1 is the number of adatoms created per incident ion, τ_{trap} is a time constant for annihilation by fixed traps, σ is the cross section for adatom

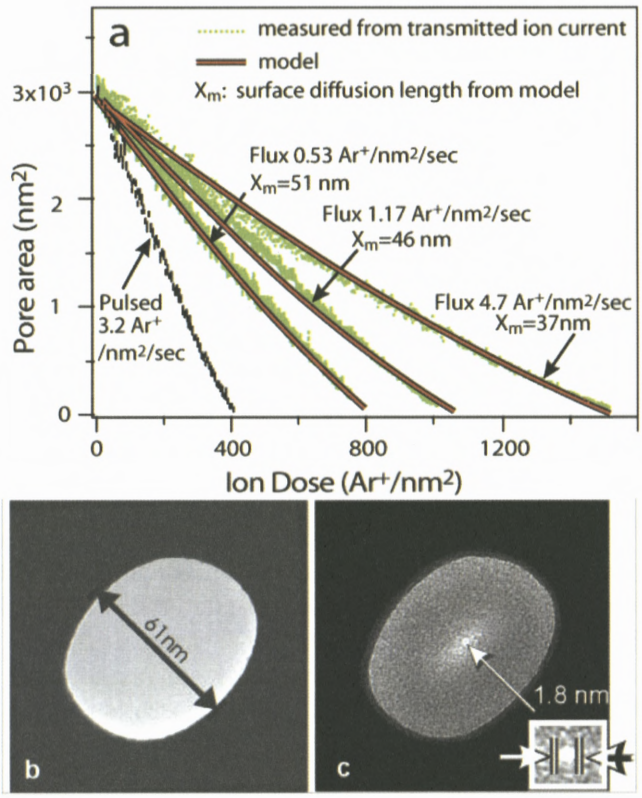

Figure 12. (a) Pore area determined by ion beam current transmitted through nanopore *versus* dose. (b) TEM image of initial ~ 60 nm pore in a 500 nm thick Si_3N_4 membrane made by focused ion beam. (c) TEM image of sample after subsequent unfocused 3 keV Ar^+ ion irradiation during which pore fills with electron transparent (~ 10 nm thick) membrane; final diameter 1.8 nm. Adapted from Li et al. (2001).

annihilation by direct ion impingement, and D is the adatom diffusivity. Adatoms that diffuse to the edge of the pore fill it in; the diffusional flux to the edge of the pore is determined by the concentration gradient at the edge of the pore in the steady-state solution to Equation (7). This flux then determines the closing rate of the pore, which is given by

$$\frac{\mathrm{d}}{\mathrm{d}t}(\pi R^2) = \frac{2\pi R\Omega f}{H}\left(Y_p - Y_a X_m \frac{K_1(R/X_m)}{K_0(R/X_m)}\right), \tag{8}$$

where R is the pore radius, Ω is the adatom volume, H is the pore thickness, Y_p is the opening contribution from ion beam sputter erosion of the edge of

the pore, Y_a is the adatom yield, X_m is the average surface diffusion length of adatoms before annihilation by fixed traps or ion impingement, and K_0 and K_1 are Bessel functions that arise from the solution to the diffusion equation in polar coordinates.

The model successfully accounts for several observations including (a) the measured time-dependence of the nanopore area during irradiation; (b) the decreased effectiveness of nanopore closing, per ion, at higher fluxes due to increased beam-induced "adatom" annihilation; (c) the increased effectiveness of nanopore closing, per ion, if the same flux is delivered in pulses separated by "offtime", to the same total fluence; (d) the strong temperature-dependence of the closing rate; (e) the existence of a maximum size pore that can be closed under ion exposure. Representative results are shown in Figure 12(a).

Although nanopores close in SiO_2 (Stein et al., 2002), the material appears to respond differently than silicon nitride, e.g. the rate is rather insensitive to temperature. We are considering the possibility that ion stimulated viscous flow (Snoeks et al., 1995; Umbach et al., 2001), possibly in conjunction with ion-stimulated compressive stress (Brongersma et al., 2000; van Dillen et al., 2005), mediates morphology evolution in this system. Electrostatic effects and ionic conduction during irradiation also appear to be important (Mitsui et al., 2006).

We anticipate that different classes of materials may be found in which different mechanisms mediate transport. For example, surface-confined viscous flow via an ion-enhanced fluidity has been identified as the transport mechanism in sputter rippling of SiO_2 with keV ion beams (Mayer et al., 1994; Umbach et al., 2001). The nanopore-closing results on amorphous silicon nitride are quantitatively consistent with the adatom diffusion model and qualitatively inconsistent with at least one key aspect of the ion-enhanced fluidity mechanism, namely the observed dependence of closure-per-ion on flux and on offtime between ion pulses: in current models for ion-enhanced fluidity, only the ion fluence matters and not its temporal dependence. Results in SiO_2 are also qualitatively inconsistent with this same key aspect of the ion-enhanced fluidity mechanism in its current form (Stein et al., 2002). It is more difficult to envisage viscous flow as an important mechanism in materials that remain crystalline under ion irradiation, in either single-crystal or large-grain polycrystal form, as metals do at typical temperatures and Si and Ge do at sufficiently high temperature.

4. Surface Morphological Relaxation and Nanostructure Stability

Much recent research has been focused on a better understanding of the sputter yield and its nonlinear dependence on elements of the surface topography.

However, all analytical treatments of morphology evolution under ion erosion generally assume surface diffusion mediated smoothening governed by the final term in Equation (3), $B\partial^4 h/\partial x^4$, where B contains the surface diffusion coefficient. This classical Mullins–Herring term is known to be valid for amorphous solids and crystalline surfaces above the thermodynamic roughening transition temperature. However, we have shown that under thermal annealing conditions after the ion beam is turned off, sputter patterned Si(001) surfaces obey non-classical relaxation kinetics inconsistent with $B\partial^4 h/\partial x^4$ (Erlebacher et al., 2000a; Pedemonte et al., 2003). As are most crystalline surfaces under typical materials processing conditions, these surfaces are well below their roughening transition temperature. Non-classical effects appear to be responsible for the change of the decay kinetics of the corrugation amplitude $A(t)$ from exponential decay to inverse linear,

$$A(t) = \frac{A(0)}{1 + kt}, \tag{9}$$

where k is a wavelength and temperature dependent rate constant. An important element of a non-classical approach leading to inverse linear decay under the observed conditions appears to be a description of the surface as a collection of atomic steps separated by flat terraces (Israeli and Kandel, 2000; Margetis et al., 2005; Margetis, 2006). It remains an open question whether a crystalline surface below its thermodynamic roughening transition temperature can be driven by ion beam irradiation into a dynamically roughened state for which the classical description remains valid.

Acknowledgements

I am indebted to my students, postdocs and collaborators, whose contributions have been critical to the understanding of many of the phenomena discussed here: Jack Blakely, Dan Branton, Michael Brenner, Ari Brown, Kee-Chul Chang, Eric Chason, Henry Chen, Alexandre Cuenat, Benny Davidovitch, Jonah Erlebacher, Jerry Floro, Jonathan Freund, H. Bola George, Jene Golovchenko, Stefan Ichim, Harley Johnson, Nagarajan Kalyanasundaram, Jiali Li, Dionisios Margetis, Ciaran McMullan, Humberto Rodriguez, Mike Sinclair, Derek Stein, Howard Stone, Omar Urquidez, and Wei Zhou. This research was supported initially by U.S. Department of Energy grant DE-FG02-01ER45947 and subsequently by U.S. National Science Foundation grant DMR-0306997.

References

Adams D.P., Vasile M.J., Mayer T.M. and Hodges V.C. (2003): Focused ion beam milling of diamond: Effects of H_2O on yield, surface morphology and microstructure. J Vac Sci Technol B **21**, 2334–2343

Bradley R.M. and Harper J.M. (1988): Theory of ripple topography induced by ion bombardment. J Vac Sci Technol A **6**, 2390

Bringa E.M., Nordlund K. and Keinonen J. (2001): Cratering-energy regimes: From linear collision cascades to heat spikes to macroscopic impacts. Phys Rev B **64**, 235426–235437

Brongersma M.L., Snoeks E., van Dillen T. and Polman A. (2000): Origin of MeV ion irradiation-induced stress changes in SiO_2. J Appl Phys **88**, 59–64

Brown A.D. (2005). Studies of ion sputtered Si(111) surfaces. Ph.D. Thesis, Johns Hopkins University, Baltimore, MD

Brown A.D. and Erlebacher J. (2005): Temperature and fluence effects on the evolution of regular surface morphologies on ion-sputtered Si(111). Phys Rev B **72**, 075350

Brown A.D., Erlebacher J., Chan W.L. and Chason E. (2005): Transient topographies of ion patterned Si(111). Phys Rev Lett **95**, 056101

Castro M., Cuerno R., Vazquez L. and Gago R. (2005): Self-organized ordering of nanostructures produced by ion-beam sputtering. Phys Rev Lett **94**, 016102

Chason E., Sinclair M.B., Floro J.A., Hunter J.A. and Hwang R.Q. (1998): Spectroscopic light scattering for real- time measurements of thin film and surface evolution. Appl Phys Lett **72**, 3276

Chen H.H., Urquidez O.A., Ichim S., Rodriguez L.H., Brenner M.P. and Aziz M.J. (2005): Shocks in ion sputtering sharpen steep surface features. Science **310**, 294–297

Chen P., Gu J.J., Brandin E., Kim Y.R., Wang Q. and Branton D. (2004): Probing single DNA molecule transport using fabricated nanopores. Nano Lett **4** 2293–2298

Cheng J.Y., Mayes A.M. and Ross C.A. (2004): Nanostructure engineering by templated self-assembly of block copolymers. Nature Materials **3**, 823–828

Cuenat A. and Aziz M.J. (2002): Spontaneous pattern formation from focused and unfocused ion beam irradiation. Mater Res Soc Symp Proc **696**, N2.8.1

Cuenat A., George H.B., Chang K.C., Blakely J. and Aziz M.J. (2005): Lateral templating for guided self-organization of sputter morphologies. Advanced Materials **17**, 2845–2849

Erlebacher J.D. and Aziz M.J. (1997): Ion-sputter induced rippling of Si(111). Mater Res Soc Symp Proc **440**, 461–466

Erlebacher J., Aziz M., Chason E., Sinclair M. and Floro J. (1999): Spontaneous pattern formation on ion bombarded Si(001). Phys Rev Lett **82**, 2330–2333

Erlebacher J., Aziz M.J., Chason E., Sinclair M.B. and Floro J.A. (2000a): Nonclassical smoothening of nanoscale surface corrugations. Phys Rev Lett **84**, 5800–5803

Erlebacher J., Aziz M.J., Chason E., Sinclair M.B. and Floro J.A. (2000b): Nonlinear amplitude evolution during spontaneous patterning of ion-bombarded Si(001). J Vacuum Sci Technol A **18**, 115–120

Facsko S., Dekorsy T., Koerdt C., Trappe C., Kurz H., Vogt A. and Hartnagel H.L. (1999): Formation of ordered nanoscale semiconductor dots by ion sputtering. Science **285**, 1551–1553

Facsko S., Bobek T., Dekorsy T. and Kurz H. (2001): Ordered quantum dot formation by ion sputtering. Phys Stat Sol B **224**, 537–540

Feix M., Hartmann A.K., Kree R., Munoz-Garcia J. and Cuerno R. (2005): Influence of collision cascade statistics on pattern formation of ion-sputtered surfaces. Phys Rev B **71**, 125407

Gray J.L., Atha S., Hull R. and Floro J.A. (2004): Hierarchical self-assembly of epitaxial semiconductor nanostructures. Nano Lett **4** 2447–2450

Habenicht S. (2001): The morphology of graphite surfaces after ion beam erosion. Phys Rev B **63**, 125419

Habenicht S., Lieb K.P., Koch J. and Wieck A.D. (2002): Ripple propagation and velocity dispersion on ion-beam-eroded silicon surfaces. Phys Rev B **65**, 115327

Herring C. (1950): Effect of change of scale on sintering phenomena. J Appl Phys **21**, 301–303

Israeli N. and Kandel D. (2000): Decay of one-dimensional surface modulations. Phys Rev B **62**, 13707–13717

Kalyanasundaram N., Davidovitch B., Johnson H.T., Freund J.B., Brenner M.P. and Aziz M.J. (unpublished).

Karmous A., Cuenat A., Ronda A., Berbezier I., Atha S. and Hull R. (2004): Ge dot organization on Si substrates patterned by focused ion beam. Appl Phys Lett **85**, 6401–6403

Li J., Stein D., McMullan C., Branton D., Aziz M.J. and Golovchenko J. (2001): Ion beam sculpting at nanometre length scales. Nature **412**, 166–169

Li J., Gershow M., Stein D., Brandin E. and Golovchenko J.A. (2003): DNA molecules and configurations in a solid state nanopore microscope. Nature Materials **2**, 611–615

Makeev M.A. and Barabasi A.-L. (1997): Ion-induced effective surface diffusion in ion sputtering. Appl Phys Lett **71** 2800–2802

Makeev M.A. and Barabasi A.-L. (2004a): Effect of surface morphology on the sputtering yields. I. Ion sputtering from self-affine surfaces. Nucl Instrum Meth B **222**, 316–334

Makeev M.A. and Barabasi A.-L. (2004b): Effect of surface morphology on the sputtering yields. II. Ion sputtering from rippled surfaces. Nucl Instrum Meth B **222**, 335–354

Makeev M.A., Cuerno R. and Barabasi A.-L. (2002): Morphology of ion-sputtered surfaces. Nucl Instrum Meth B **197**, 185–227

Margetis D. (2006): Unified continuum approach to crystal surface morphological relaxation. Submitted

Margetis D., Aziz M.J. and Stone H.A. (2005): Continuum approach to self-similarity and scaling in nanostructure decay. Phys Rev B **71**, 165432

Mathur A., Brown A.D. and Erlebacher J. (2005): Self-ordering of colloidal particles in shallow nanoscale surface corrugations. Langmuir **22**, 582–589

Mayer T.M., Chason E. and Howard A.J. (1994): Roughening instability and ion-induced viscous relaxation of SiO_2 surfaces. J Appl Phys **76** 1633–1643

Meller A., Nivon L., Brandin E., Golovchenko J. and Branton D. (2000): Rapid nanopore discrimination between single polynucleotide molecules. Proc Nat Acad Sci USA **97**, 1079–1084

Mitsui T., Stein D., Kim Y.R., Hoogerheide D. and Golovchenko J.A. (2006): Nanoscale volcanoes: Accretion of matter at ion-sculpted nanopores. Phys Rev Lett **96**, 036102

Moseler M., Gumbsch P., Casiraghi C., Ferrari A.C. and Robertson J. (2005): The ultrasmoothness of diamond-like carbon surfaces. Science **309**, 1545–1549

Mullins W.W. (1959): Flattening of a nearly plane solid surface due to capillarity. J Appl Phys **30**, 77

Navez M., Chaperot D. and Sella C. (1962): Microscopie electronique – étude de lattaque du verre par bombardement ionique. C R Hebdomadaires Seances Acad Sci **254**, 240

Park S., Kahng B., Jeong H. and Barabasi A.-L. (1999): Dynamics of ripple formation in sputter erosion: Nonlinear phenomena. Phys Rev Lett **83**, 3486–3489

Pedemonte L., Bracco G., Boragno C., Mongeot F.B. and Valbusa U. (2003): Smoothing of nanoscale surface ripples studied by He atom scattering. Phys Rev B **68**, 115431

Peters R.D., Yang X.M., Wang Q., de Pablo J.J. and Nealey P.F. (2000): Combining advanced lithographic techniques and self-assembly of thin films of diblock copolymers to produce templates for nanofabrication. J Vac Sci Technol B **18**, 3530–3534

Shchukin V.A. and Bimberg D. (1999): Spontaneous ordering of nanostructures on crystal surfaces. Rev Mod Phys **71**, 1125–1171

Sigmund P. (1973): A mechanism of surface micro-roughening by ion bombardment. J Mater Sci **8**, 1545–1553

Sigmund P. (1981): Sputtering by ion bombardment: Theoretical concepts. In: Sputtering by Particle Bombardment I, Behrisch R. (Ed.), Springer-Verlag, Berlin, pp 9–71

Snoeks E., Weber T., Cacciato A. and Polman A. (1995): MeV ion irradiation-induced creation and relaxation of mechanical stress in silica. J Appl Phys **78**, 4723–4732

Stein D., Li J. and Golovchenko J.A. (2002): Ion beam sculpting time scales. Phys Rev Lett **89**, 276106

Stein D.M., McMullan C.J., Li J.L. and Golovchenko J.A. (2004): Feedback-controlled ion beam sculpting apparatus. Rev Sci Instrum **75**, 900–905

Teichert C., Lagally M.G., Peticolas L.J., Bean J.C. and Tersoff J. (1996): Stress-induced self-organization of nanoscale structures in SiGe/Si multilayer films. Phys Rev B **53**, 16334–16337

Thurn-Albrecht T., Schotter J., Kastle C.A., Emley N., Shibauchi T., Krusin-Elbaum L., Guarini K., Black C.T., Tuominen M.T. and Russell T.P. (2000): Ultrahigh-density nanowire arrays grown in self-assembled diblock copolymer templates. Science **290**, 2126–2129

Tseng A.A., Insua I.A., Park J.S., Li B. and Vakanas G.P. (2004): Milling of submicron channels on gold layer using double charged arsenic ion beam. J Vac Technol B **22**, 82–89

Umbach C.C., Headrick R.L. and Chang K.C. (2001): Spontaneous nanoscale corrugation of ion-eroded SiO2: The role of ion-irradiation-enhanced viscous flow. Phys Rev Lett **87**, 246104

Valbusa U., Boragno C. and de Mongeot F.B. (2003): Nanostructuring by ion beam. Mater Sci Engrg C **23**, 201–209

van Dillen T., Polman A., Onck P.R. and van der Giessen E. (2005): Anisotropic plastic deformation by viscous flow in ion tracks. Phys Rev B **71**, 024103

Vasile M.J., Xie J.S. and Nassar R. (1999): Depth control of focused ion-beam milling from a numerical model of the sputter process. J Vac Sci Technol B **17**, 3085–3090

Yamamura Y., Itikawa Y. and Itoh N. (1983): Angular dependence of sputtering yields of monatomic solids. Nagoya, Japan, Institute of Plasma Physics, Nagoya University

Yang B., Liu F. and Lagally M.G. (2004): Local strain-mediated chemical potential control of quantum dot self-organization in heteroepitaxy. Phys Rev Lett **92**, 025502

Zhou W., Cuenat A. and Aziz M.J. (2003): Formation of self-organized nanostructures on Ge during focused ion beam sputtering. In: Microscopy of Semiconducting Materials 2003: Proceedings of the 13th International Conference on Microscopy of Semiconducting Materials, Cullis A.G. and Midgley P.A. (Eds), IOP

Ion-Induced Surface Evolution in the Linear Instability Regime: Continuum Theory and Kinetic Monte Carlo Simulations

Eric Chason* and Wai Lun Chan

Division of Engineering, Brown University
Providence RI 02912, USA

Abstract

Low energy ion sputtering produces spontaneous pattern formation on many surfaces. A continuum theory that balances the processes of roughening by sputter removal of atoms and smoothing by surface diffusion of defects explains many features of the early stages of pattern formation. The sputtering is based on a mechanism proposed by Sigmund (1969, 1973) which couples the rate of atom removal to the local surface morphology. Results of kinetic Monte Carlo simulations of surface evolution using the Sigmund mechanism for sputtering are found to agree quantitatively with the predictions of the continuum theory in the linear regime. This suggests that the continuum theory correctly accounts for many of the essential physical mechanisms that lead to the initial formation of the ion-induced pattern.

Contents

1 Introduction **208**

2 Continuum Theory of Sputter Ripple Formation **209**
2.1 Sigmund Mechanism for Sputtering 210
2.2 Sputter Roughening of Surface 211
2.3 Surface Diffusion 211
2.4 Ion-Induced Smoothing and Higher Order Effects 212
2.5 Ehrlich–Schwoebel Barriers to Interlayer Transport 213

* E-mail: eric_chason@brown.edu

2.6 Surface Evolution in the Linear Regime 214

3 Kinetic Monte Carlo Simulations **216**

4 Results of KMC Simulations and Comparison with Continuum Theory **218**

5 Conclusion **221**

Acknowledgements **222**

References **222**

1. Introduction

Bombardment by low energy ions (ion sputtering) is a real workhorse when it comes to modifying and characterizing thin films and surfaces. The virtue of low energy ions is that they are able to remove material from the surface without creating so much damage that they destroy the structures that are of interest. Therefore, ion sputtering is frequently used to prepare atomically clean surfaces and to create thin samples for transmission electron microscopy. Analyzing the sputtered surface or the atoms that are sputtered away is used to profile the depth distribution of atoms in thin layers. More recently, focused ion beams (FIB) have enabled nanoscale regions of the sample to be removed selectively for analysis or to create unique structures.

Although the damage by the ion beam is confined mostly to the near surface region, it has been noted by many (Bradley and Harper, 1988; Carter, 2001; Makeev et al., 2002; Valbusa et al., 2002) that prolonged sputtering can lead to the development of pronounced patterns on the surface (sputter ripples). The type of pattern depends on the ion beam, the material being sputtered, and the processing conditions so that arrays of one-dimensional ripples (Mayer et al., 1994; Chason et al., 1994; Carter and Vishnyakov, 1996; Rusponi et al., 1998; Erlebacher et al., 1999; Habenicht, 2001; Umbach et al., 2001), two-dimensional mounds and pits (Ritter et al., 1996; Ernst, 1997; Murty et al., 1998b; Costantini et al., 2001; Michely et al., 2001; Kalff et al., 2001; Malis et al., 2002) and even quantum dot-like structures (Facsko et al., 1999; Gago et al., 2001; Frost et al., 2004) have been observed under different conditions. The wavelength of these patterns ranges from the micron range down to nanometers. From the materials analysis point of view, the excess roughness created by these patterns can degrade the depth resolution (Stevie et al., 1988; Cirlin, 1992; Wittmaack, 1998) and there is interest in understanding their origin in order to control or eliminate them. On the other hand, because ion-induced patterns form spontaneously without needing

any external templates or beam modulation, they are also interesting as a way of inexpensively producing nanoscale structures by means of self-organization. Moreover, the patterning behavior can be used to study the ion-surface interaction and the resulting ion-induced defect kinetics on the surface.

Understanding how sputter ripples form has been the subject of significant analysis over the past twenty-odd years. The fact that the sputter ripples form spontaneously indicates that they originate from the interaction between different processes occurring on the surface during ion bombardment. In the early stages, the behavior can be modeled using a simple linear theory of morphology evolution. As described below, the heart of this model is a sputtering theory developed by Sigmund in which the sputter yield is dependent on the local surface curvature. The overall surface evolution is described analytically in terms of a dynamic balance between roughening by the sputtering process and smoothing by diffusion of point defects (adatoms and surface vacancies) on the surface. As pointed out by Bradley and Harper (BH) (1988), the appearance of a characteristic wavelength can be explained by the mechanism of a linear instability where the competition between different surface processes results in the selection of a preferred range of spatial frequencies that grow faster than any others on the surface.

The goal of this article is to describe the physical mechanisms that determine the evolution of the sputter ripples in the early stage. To explore the validity of this analytical approach, we compare the continuum predictions with recent results of kinetic Monte Carlo (KMC) simulations. The KMC simulations use the Sigmund mechanism to model the sputtering process coupled with diffusion of defects using a solid-on-solid (Chason and Dodson, 1991) model of atomic hopping. Unlike experiments, in the KMC simulations we are able to completely specify all the important parameters for the ion beam and the surface diffusion. The resulting surface morphology enables us to monitor how the surface evolves under the simultaneous action of the sputtering and surface diffusivity for direct comparison with the continuum theory. In addition, the KMC simulations enable us to quantify the surface defect concentrations on the surface during the simulated sputtering process which is not possible in experiments.

2. Continuum Theory of Sputter Ripple Formation

In this section, we discuss different physical mechanisms that operate during low energy ion bombardment to control the evolution of the surface morphology. We use continuum approximations of these mechanisms to derive an analytical expression for the evolution of the surface height $[h(x, y)]$ at different positions x and y on the surface. This treatment follows the approach originally used by

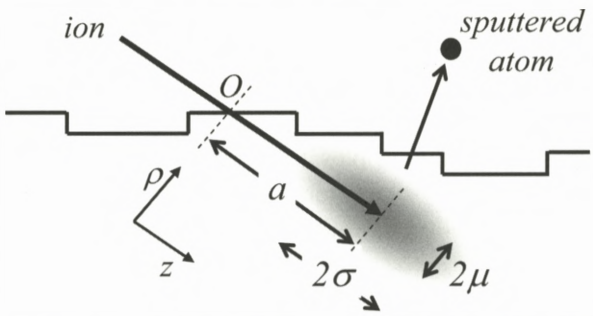

Figure 1. Schematic of Sigmund mechanism for sputtering of atom. The energy deposited by the ion per unit volume is approximated by a Gaussian form that creates elliptical contours around the stopping point. The sputter yield from each surface site is taken to be proportional to the energy deposited there.

Bradley and Harper (1988) to explain the origin of ripple formation in terms of a linear instability mechanism.

2.1. Sigmund Mechanism for Sputtering

The Sigmund theory is an approximation that makes it possible to calculate where an incoming ion will cause an atom to be sputtered from on the surface. In the actual process of sputtering, the energetic ion gives up its kinetic energy in a series of atomic collisions (called the binary collision approximation or BCA). Monte Carlo programs such as SRIM (Ziegler and Biersack, 2000) that are based on the BCA can calculate the details of a series of collisions for an incident ion trajectory. However, because each trajectory contains only a few collisions and is very sensitive to the exact impact parameter, it is not possible to use the BCA approach in an analytical formulation. This difficulty is avoided in the Sigmund theory, where the energy deposited per unit volume averaged over a large number of incident ion trajectories is approximated by a smooth form in which the contours of constant energy deposition form ellipsoids around the center of the distribution (Sigmund 1969, 1973). Therefore, even though each individual trajectory is difficult to predict, the behavior averaged over a large number of incident ions may be treated analytically.

The energy distribution derived by Sigmund is shown schematically in Figure 1. In this figure, the ion enters the surface at the point O and the center of the distribution is at a distance a along the initial ion trajectory. Using coordinates where z is the distance from O along the ion trajectory and ρ is the distance

normal to the trajectory, the energy per unit volume deposited by collisions at each point in the material is described by

$$E(\rho, z) = \varepsilon_0 \exp\left\{-\left[\frac{(z-a)^2}{2\sigma^2} + \frac{\rho^2}{2\mu^2}\right]\right\}, \tag{1}$$

where ε_0 is a normalization factor and the parameters σ and μ describe the width of the energy deposition profile in the directions parallel and perpendicular to the initial trajectory. The amount of material sputtered from each site on the surface is taken to be proportional to the energy deposited at that site, as calculated from Equation (1). The sputter yield, Y, is proportional to the total amount of energy deposited at the surface.

2.2. Sputter Roughening of Surface

Bradley and Harper (1988) used the Sigmund theory to calculate the evolution of the surface topography by integrating the erosion rate calculated from Equation (1) over the entire surface. For topographies in which the radius of curvature on the surface remains large compared to the ion's range a, the erosion rate at each point x and y on the surface can be approximated by the form:

$$\frac{\partial h}{\partial t} = -v_0(\theta) + \Gamma\frac{\partial h}{\partial x} + v_x\frac{\partial^2 h}{\partial x^2} + v_y\frac{\partial^2 h}{\partial y^2}. \tag{2}$$

In this equation, x is oriented parallel to the direction of the ion beam projected onto the surface, i.e., in the same direction as z in Figure 1 projected along the surface and y is in the orthogonal direction on the surface. v_0 is the average rate of erosion of the surface and depends on the angle of incidence, θ, relative to the surface normal Γ accounts for the variation of the sputter yield with the slope of the surface and is equal to $\partial v_0/\partial\theta$. v_x and v_y relate the sputter yield locally to the surface curvature with values that depend on the ion parameters (a, Y, σ, μ) and the angle of incidence; a detailed calculation of v_x and v_y is provided in Makeev et al. (2002). The dependence of the sputter rate on the local curvature means that for a surface with a rough topography the peaks on the surface will sputter slowly and the valleys will sputter quickly. Therefore, in the absence of all other effects, the Sigmund mechanism will make a rough surface become even rougher due to sputtering.

2.3. Surface Diffusion

Surface diffusion will act to smoothen a rough surface by transport of material from regions of high surface energy to regions of low surface energy (as shown

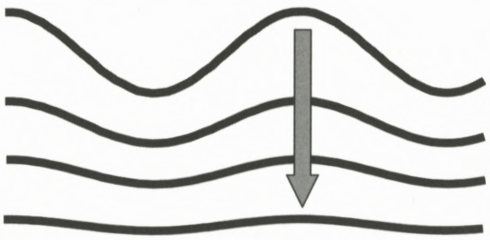

Figure 2. Surface diffusion is modeled using the classical theory of Mullins (1959) and Herring (1950). Surface defects diffuse to decrease the amplitude of modulations on the surface.

schematically in Figure 2). The analytical form for this was described by Mullins (1959) and Herring (1950) and given by:

$$\frac{\partial h}{\partial t} = -B\nabla^4 h, \tag{3a}$$

where

$$B = \frac{\gamma D_s C}{n^2 k_B T}, \tag{3b}$$

and γ is the surface energy, D_s is the diffusivity of a mobile surface defect, C is the concentration of mobile defects on the surface (number per unit area) and n is the number of atoms per unit volume. We define D_s and C in terms of mobile defects (rather than simply adatoms) because surface transport may occur by diffusion of adatoms or surface vacancies when ion bombardment is used. Note that this model for the surface diffusivity does not take into account effects of surface crystallinity and therefore is strictly only appropriate for amorphous surfaces or crystalline surface above the roughening transition. The complications that this entails have been discussed elsewhere (Jeong and Williams, 1999; Israeli and Kandel, 2000; Erlebacher et al., 2000; Pedemonte et al., 2003; Shenoy et al. 2003, 2004; Chan et al., 2004b; Margetis et al., 2004), however we will use this simple linear theory in this work.

2.4. Ion-Induced Smoothing and Higher Order Effects

Makeev and co-workers (Makeev and Barabasi, 1997; Makeev et al., 2002) carried out the calculation of the surface evolution to higher order and recognized that there are other terms that are linear in the surface height besides those included by Bradley and Harper. The effect of this is to add additional terms to Equation (2) of the form:

$$-B_{I,x}\frac{\partial^4 h}{\partial x^4} - B_{I,xy}\frac{\partial^4 h}{\partial x^2 \partial x^2} - B_{I,y}\frac{\partial^4 h}{\partial y^4}. \tag{4}$$

These terms have functional forms that are similar to the diffusional smoothing in Equation (3), i.e., they depend on the fourth derivative of the height and they tend to make the surface smoother. However, these terms derive directly from the interaction of the ion with the surface and have no relation to surface diffusion.

Higher order terms of the form $\partial^3 h/\partial x^3$ and $\partial^3 h/\partial x \partial y^2$ are also present in the linear continuum equation (Makeev et al., 2002). Similar to the effect of the Γ term, these terms affect the propagation of the ripples along the ion beam direction and account for dispersion in the ripple velocity with respect to the wavevector. These effects are observed in our simulation (Chason et al., 2006) but are not discussed further here. Other non-linear terms can be added to these equations to account for long-time behavior (Makeev et al., 2002). However, since the purpose of this work is comparing the continuum theory with KMC simulations, we limit the discussion to the early linear regime of pattern formation where the KMC model is expected to be most valid.

2.5. Ehrlich–Schwoebel Barriers to Interlayer Transport

On metal surfaces, measurements of pattern formation during ion bombardment may depend on the crystallography of the surface and not just the direction of the ion beam. It is suggested (Rusponi et al., 1998; Costantini et al., 2001; Valbusa et al., 2002) that the presence of Ehrlich–Schwoebel barriers that modify interlayer transport can modify the roughening process in a way similar to the mechanism proposed by Villain (1991) and Politi and Villain (1996). Although this effect is not linear, they proposed that in the early stages the roughening behavior could be approximated by a form in which the roughening depends on the local curvature with coefficients S_x and S_y that depend on the barriers to interlayer transport.

In contrast with the BH mechanism, the parameters S_x and S_y depend on temperature while the BH roughening terms (v_x, v_y) only depend on the ion beam parameters. Since the curvature dependence is similar to the BH mechanism, these terms can compete directly with the BH roughening terms. Under certain sputtering conditions, these effects can dominate to produce a different class of surface morphology. In this paper, however, we will only concentrate on regimes in which the BH mechanism is dominant so that roughening induced by Ehrlich–Schwoebel barrier will be neglected. Experimentally, these conditions are fulfilled when the surface is sputtered at a relatively high temperature and flux (Chan et al., 2004a), when the surface has a low Schwoebel barrier (Chason et al., 1994; Erlebacher et al., 1999; Brown and Erlebacher, 2005) or when the surface becomes amorphous (Mayer et al., 1994; Carter and Vishnyakov, 1996; Facsko et al., 1999; Umbach et al., 2001; Habenicht, 2001; Gago et al., 2001; Frost et al., 2004).

2.6. Surface Evolution in the Linear Regime

These mechanisms can be put together to predict the evolution of the surface morphology. Combining Equations (2)–(4), in the linear regime (i.e., the early stages of pattern formation), the continuum equation is written as:

$$\begin{aligned}\frac{\partial h}{\partial t} &= -v_0(\theta) + \Gamma\frac{\partial h}{\partial x} + v_x\frac{\partial^2 h}{\partial x^2} + v_y\frac{\partial^2 h}{\partial y^2} + S_x\frac{\partial^2 h}{\partial x^2} + S_y\frac{\partial^2 h}{\partial y^2} \\ &\quad - B\nabla^4 h - B_{I,x}\frac{\partial^4 h}{\partial x^4} - B_{I,xy}\frac{\partial^4 h}{\partial x^2\partial x^2} - B_{I,y}\frac{\partial^4 h}{\partial y^4}\,. \end{aligned} \tag{5}$$

This equation can be Fourier transformed so that the amplitude of individual Fourier components on the surface can be calculated. The amplitude of each Fourier component at time t is given by:

$$h_k(t) = h_k(0)\,\mathrm{e}^{r(k_x,k_y)t}\,\mathrm{e}^{ik_x(x+\Gamma t)}, \tag{6a}$$

where $h_k(0)$ is the value of the Fourier coefficient initially and

$$\begin{aligned} r(k_x, k_y) &= -v_x(f)k_x^2 - v_y(f)k_y^2 - S_x(f,T)k_x^2 - S_y(f,T)k_y^2 \\ &\quad - B(f,T)(k_x^2 + k_x^2)^2 - B_{I,x}(f)k_x^4 \\ &\quad - B_{I,xy}(f)k_x^2k_y^2 - B_{I,y}(f)k_y^4\,. \end{aligned} \tag{6b}$$

We call $r(k_x, k_y)$ the amplification factor because it determines the rate at which the amplitude grows or decays. The parameters that determine $r(k_x, k_y)$ have been explained above. The dependence of each parameter on the flux, f, and the temperature, T, has been written explicitly to indicate how f and T impact the growth rate of the ripples.

For positive values of r, the amplitude will increase while for negative values it will decrease. The evolution of the surface morphology is therefore completely determined (in this model, at least) by the value of the amplification factor, r. For a range of parameters, the dependence of r on the magnitude of k has a form that can be represented schematically as shown in Figure 3. Under these conditions, there is a range of k values for which the amplification factor is positive and other values for which it is negative. The amplification factor has a maximum value of r^* which occurs at the wavevector k^*. As a function of time, the amplitude of the Fourier coefficient with wavevector k^* will grow faster than all others and the surface will develop a characteristic periodicity at this spatial frequency.

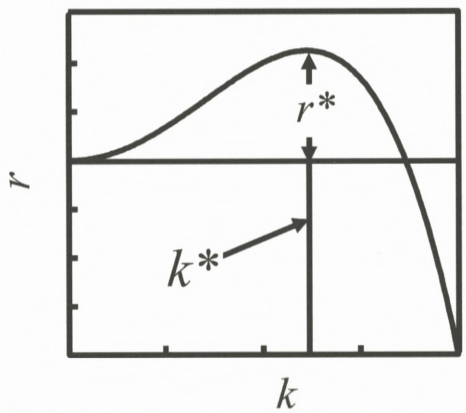

Figure 3. Schematic representation of the amplification rate r as a function of the wavevector k. The amplification factor is maximum (r^*) at the fastest growing wavevector (k^*).

From a linear stability analysis of $r(k_x, k_y)$, we can determine how the wavelength and growth rate of the pattern depend on the parameters of the model:

$$r^* = \frac{v_{\max}^2}{4(B + B_{I,\max})}, \tag{7a}$$

$$k^* = \left(\frac{v_{\max}}{2(B + B_{I,\max})}\right)^{1/2} \tag{7b}$$

The subscript "max" refers to the value $|v_x|$ or $|v_y|$ which has the greater magnitude, i.e., the one that will grow faster on the surface. The wavevector of the pattern will align along the direction corresponding to the larger of these parameters.

From these equations, we have a prediction of how the pattern will evolve based on the parameters of the continuum model. In the following section, we will compare these predictions with results of our KMC simulation to determine how well the instability model compares with an atomistic sputtering picture based on the Sigmund model. Note that in this analysis we have set the value of S_x and S_y equal to zero so that we are ignoring the effect of the Schwoebel barrier. Also note that we are only considering a linear model for the pattern formation here. Non-linear terms are certainly expected to become important as the amplitude of the ripples increases. The comparison with the KMC simulations is therefore only relevant to the early stages of the pattern formation. However, the direct comparison of the model with the simulations is useful even if it is only over a limited range of ripple amplitude.

3. Kinetic Monte Carlo Simulations

The approach to pattern formation described above is based on developing a rate equation for the evolution of the surface height using continuum models for the sputter removal and surface transport. An alternative approach, discussed here, is to develop kinetic Monte Carlo (KMC) computer simulations in which atomistic processes are modeled by transitions on a surface following rules designed to mimic kinetic processes such as diffusion and sputtering. The surface morphology that develops from this approach is the result of the interaction of many independent events that are analogous to the motion of individual atoms and vacancies on the sputtered surface. By comparing the surface morphology evolution between the simulations and the continuum theory, we can directly determine if the continuum theory is a valid approximation for the collective action of the numerous atomic-level events controlling the surface evolution. Furthermore, because we can monitor all the atomic level processes in the KMC simulation, we can also study the defect kinetics that underlie the ion-induced pattern formation.

Previously, simulations have been performed that use the Sigmund mechanism for sputtering but these did not use the same approach as this work for surface transport. In these works, either a simplified relaxation process or a process based on a Monte Carlo (MC) algorithm to determine the equilibrium state was employed (Cuerno et al., 1995; Koponen et al., 1997; Hartmann et al., 2002; Stepanova and Dew 2004; Yewande et al., 2005) so that they did not model the non-equlibrium surface dynamics. On the other hand, previous simulations that do employ diffusion processes with thermally activated hopping rates did not use the Sigmund mechanism for the sputtering process (Murty et al., 1998a; Strobel et al., 2001). Unlike these other simulations, our model considers both the Sigmund mechanism and thermally activated diffusion of surface defects satisfying detail balance.

A brief description of the concept behind the KMC simulation is discussed below; a fuller description can be found in Chason et al. (2006). The positions of all the atoms on a surface are assigned to an element in a two-dimensional lattice (known as a solid-on-solid model). A schematic representation of different surface processes considered in the KMC is shown schematically in Figure 4. Note that we also allow the motion of vacancies in the surface to occur by the hopping of atoms adjacent to it. This is important because we believe that mobile vacancy defects play a significant role in surface evolution during ion sputtering.

All the transitions that can occur on the surface are assigned a rate based on the local configuration. The rate of transition between two sites i and j is based on a thermally activated process in which the barrier to the transition ($E_{i,j}$) is

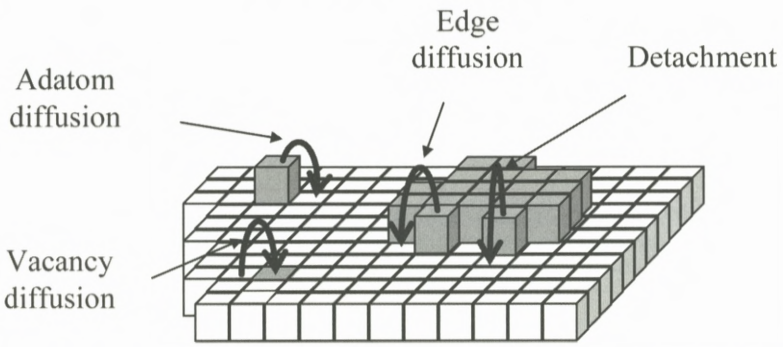

Figure 4. Schematic of surface transport processes considered in the kinetic Monte Carlo simulation of sputtering. Each surface process has an activation energy and transition rate associated with it. Note that in the simulation vacancy diffusion is allowed to occur at a rate equal to adatom diffusion.

equal to an activation energy (E_a) plus the difference in bond energy between the two configurations. The change in bond energy between two configurations is determined by counting the change in the number of nearest neighbors ($n_i - n_j$) and multiplying by a constant energy per bond (E_{bond}) if the number of bonds decreases. The rate of a transition is therefore

$$R_{i,j} = \omega \, \mathrm{e}^{-E_{i,j}/kT}, \tag{8}$$

where $E_{i,j} = E_a$ if the number of bonds does not decrease ($n_i \leq n_j$) or $E_{i,j} = E_a + (n_i - n_j)E_{\text{bond}}$ if the number of bonds decreases ($n_i > n_j$). The attempt frequency ω is a constant that is taken as 10^{12} s^{-1} in the current work. Keeping track of bond energy in this way ensures that detailed balance is preserved, i.e., the rate of a transition between two sites in the forward and backward direction is properly related to the difference in energy between the sites.

Lists of all the surface positions at which atomic transitions can occur and their associated transition rates are maintained in the computer simulation as the surface evolves. Events are chosen from these lists randomly with a probability that is proportional to the transition rate. In this way, atomic level events are performed on the surface at a rate that is on average proportional to the transition rate for that process.

The process described above is able to simulate the evolution of the surface due to diffusive processes. The removal of atoms from the surface via sputtering requires an additional mechanism. We use the same Sigmund mechanism utilized in the continuum approach to model the sputtering process in the KMC simulations. For an individual incident ion trajectory, the position at which it strikes the surface is chosen randomly and the energy deposition at all the points on the surface is

Table 1. List of parameters used in the kinetic Monte Carlo simulations.

Activation energy (E_a)	0.8 eV Note: a value of 1.0 eV was used for diffusion along the edge of a step.
Bond energy (E_{bond})	0.2 eV
Temperature (T)	187–250°C
Flux (f)	0.15–6.0 monolayers/s
Ion parameters:	
θ	45 deg
a	20
$\sigma = \mu$	10
Y	2 atoms/ion

then calculated using Equation (1). Unlike the continuum approach, the surface height is not reduced incrementally at each point based on the calculated energy deposition. Instead the energy deposition is used to determine the probability of sputtering from each site on the surface; the Monte Carlo algorithm is then used to choose which site to perform the sputtering event based on the relative probabilities.

4. Results of KMC Simulations and Comparison with Continuum Theory

We performed KMC simulations of surface evolution during sputtering under a range of processing conditions in order to study the dependence of the ripple growth rate and wavelength on the processing conditions. The parameters used in the simulation are given in Table 1. The results described here have been presented more fully in Chason et al. (2006) but are reviewed here in order to provide a comparison between the simulations and the continuum theory.

The morphology of ripples produced by the KMC program under different simulation conditions is shown in Figure 5. Figure 5a corresponds to simulated sputtering at $f = 1$ monolayer/s, $T = 187$°C and a fluence of 45 monolayers and Figure 5b corresponds to $f = 1$ monolayer/s, $T = 250$°C and a fluence of 70 monolayers. The time evolution of the simulated ripple amplitude and wavelength for the same conditions is shown in Figure 6. Aside from an initial transient, the wavelength of the ripples remains fairly constant over the entire range of the sim-

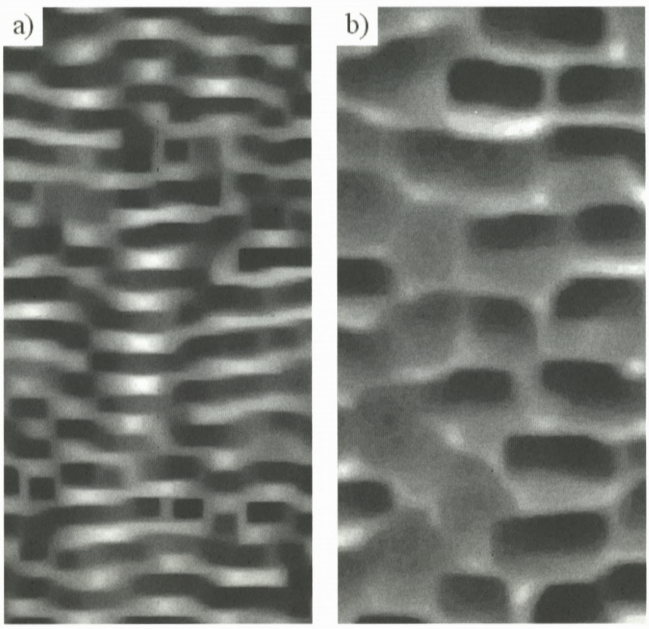

Figure 5. Surface morphology produced by KMC simulation with (a) $T = 187°C$, fluence = 45 monolayers and (b) $T = 250°C$, fluence = 70 monolayers. The flux for both cases is 1 monolayer/s.

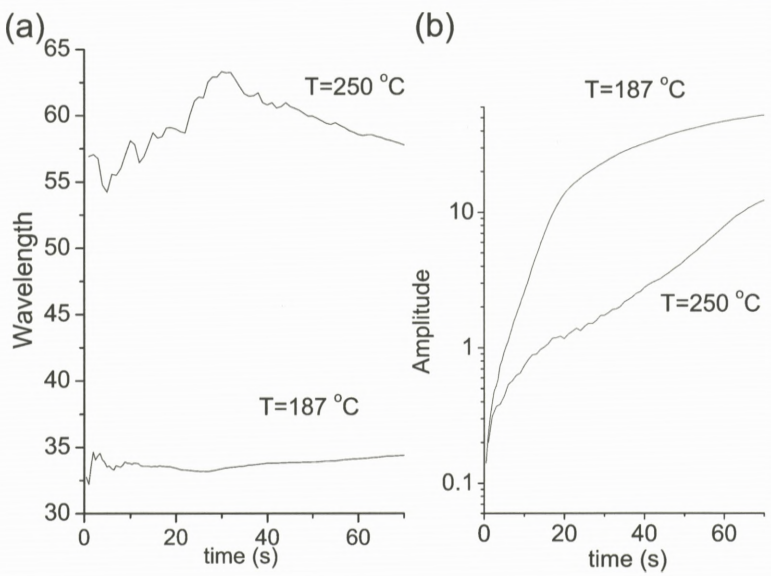

Figure 6. Evolution of (a) wavelength and (b) amplitude of the ripples produced by the KMC simulations. Temperature for the simulation is indicated on the figure.

ulation. The amplitude increases exponential in the early stages, though saturation is reached for larger amplitudes. Both of these features, a fixed wavelength and an exponential growth in the early stages are consistent with the expected behavior from the instability model. The amplitude saturation can also be addressed by including higher order non-linear terms (Cuerno and Barabasi, 1995; Park et al., 1999) in the continuum theory, but we have restricted our analysis of the KMC studies to the linear regime where amplitudes are small and the approximations of the Sigmund model are most valid.

Surface defects (adatoms and vacancies) play a major role in determining smoothing processes on the surface (Erlebacher et al., 1999; Chan and Chason, 2005). Unlike experiments, in the KMC simulation we can monitor the concentration of defects on the surface directly during the surface morphology evolution. The primary defect that we observe on the surface is the vacancy, which is consistent with the fact that we directly produce vacancies in the simulation when atoms are removed from surface sites by sputtering. The concentration of defects across the surface appears to be uniform and is not correlated with the surface morphology. The defect concentration depends on both the temperature and the ion flux with the concentration increasing with increasing ion flux and decreasing with increasing temperature. Fitting the temperature and flux dependence to a power law behavior gives good agreement over the entire range of the simulation conditions using the form $(f/D)^{0.48}$.

By performing simulations under different conditions, we have also studied the flux and temperature dependence of the ripple wavelength. The temperature dependence of the simulated ripple wavelength (shown in Figure 7) can be compared directly with the continuum theory using Equation (7b). Using the fact that $v_{\max}$ and $B_{I,\max}$ depend only on the flux and not on temperature, the continuum theory predicts that the wavelength should depend on the following parameteric form:

$$\lambda^*(T, f) = \frac{2\pi}{k^*} \propto \sqrt{\frac{D_s C}{fT} + A_I}, \tag{9}$$

where A_I is a constant independent of flux or temperature. In evaluating this expression, we can use the measured value of the defect concentration for each temperature and flux. The only unknown parameters required to compare this form with the data are A_I, an overall normalization constant and the activation energy for the diffusivity. The fit to this form is shown as the solid line in Figure 7. The value for the activation energy determined from the fit is 0.86 eV, in good agree with the value of 0.8 used as an input in the simulation.

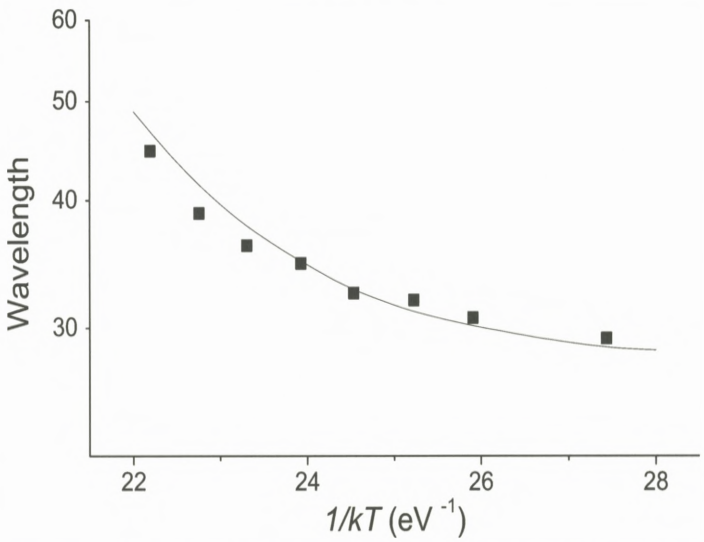

Figure 7. Dependence of simulated ripple wavelength on temperature. The solid line represents least squares fit to analytical form described in text.

5. Conclusion

The morphological evolution produced by the KMC simulation shows that the Sigmund theory captures the essential physics required to produce Bradley–Harper type ripples in the early stages of sputtering. Furthermore, comparison of the continuum theory with the KMC results indicates that the analytical theory does a good job of capturing the balance between roughening by sputter removal and smoothing by surface diffusion, e.g., the continuum equations quantitatively account for the temperature dependence of the wavelength of ripples produced by the simulation. The agreement is somewhat surprising since the diffusional smoothing used in the continuum model is not appropriate for the crystalline, stepped surface used in the simulation. In spite of this, it provides good agreement over a wide range of parameters studied. It is worth noting that non-linear effects such as amplitude saturation are observed in the simulation, even though we have restricted our analysis to the linear instability regime. These effects can incorporated into the continuum analysis by using higher-order non-linear terms but we have not considered them here.

Although the simulations agree well with the continuum theory, this does not mean that the Bradley–Harper theory is a complete description for early-stage ripple formation in experimental systems. Measurements of the rate of ripple

formation on Cu (Chan et al., 2004a), Ge (Chason et al., 1994) and Si (Brown and Erlebacher, 2005) surfaces are significantly lower than predicted by the theory. This suggests that there may be other roughening mechanisms in experimental systems beyond the Sigmund that have not been included in the simulations or the continuum model.

Furthermore, over a wider range of parameters than those discussed here, transitions to other type of roughening behavior can be observed both in the experiments and the simulations. These studies are discussed in other references (Chan and Chason, 2006; Chason and Chan, 2006).

Acknowledgements

This work has benefited greatly from collaboration and helpful discussions with many others including Vivek Shenoy, Jonah Erlebacher, Michael Aziz, Ashwin Ramasubramanian and M.S. Bharathi. The authors also gratefully acknowledge the support of the US Department of Energy under contract DE-FG02-01ER45913 and EC acknowledges the National Science Foundation under contract CMS-0210095.

References

Bradley R.M. and Harper J.M.E. (1988): Theory of ripple topography induced by ion Bombardment. J Vac Sci Technol A **6**, 2390–2395

Brown A.-D. and Erlebacher J. (2005): Temperature and fluence effects on the evolution of regular surface morphologies on ion-sputtered Si(111). Phys Rev B **72**, 075350

Carter G. (2001): The physics and applications of ion beam erosion. J Phys D: Appl Phys **34**, R1–R22

Carter G. and Vishnyakov V. (1996): Roughening and ripple instabilities on ion-bombarded Si. Phys Rev B **54**, 17647–17653

Chan W.L. and Chason E. (2005): Sputter ripples and radiation-enhanced surface kinetics on Cu(001). Phys Rev B **72**, 165418

Chan W.L. and Chason E. (2006): Morphology of ion sputtered Cu(001) surface: Transition from unidirectional roughening to bidirectional roughening. Nucl Instrum Methods B **242**, 228–231

Chan W.L., Pavenayotin N. and Chason E. (2004a): Kinetics of ion-induced ripple formation on Cu(001) surface. Phys Rev B **69**, 245413

Chan W.L., Ramasubramaniam A., Shenoy V.B. and Chason E. (2004b): Relaxation kinetics of nano-ripples on Cu(001) surface. Phys Rev B **70**, 245403

Chason E. and Chan W.L. (2006): Kinetics mechanisms in ion-induced ripple formation on Cu(001) surfaces. Nucl Instrum Methods B **242**, 232–236

Chason E. and Dodson B.W. (1991): Effect of step edge transition rates and anisotropy in simulations of epitaxial-growth. J Vac Sci Technol A **9**, 1545–1550

Chason E., Mayer T.M., Kellerman B.K., McIlroy D.T. and Howard A.J. (1994): Roughening instability and evolution of Ge(001) surface during ion sputtering. Phys Rev Lett **72**, 3040–3043

Chason E., Chan W.L. and Bharathi M.S. (2006): Kinetic Monte Carlo simulations of ion-induced ripple formation. Submitted

Cirlin E.-H. (1992): Auger electron spectroscopy and secondary ion mass spectrometry depth profiling with sample rotation. Thin Solid films **220**, 197–203

Costantini G., Rusponi S., de Mongeot F.B., Boragno C. and Valbusa U. (2001): Periodic structures induced by normal-incidence sputtering on Ag(110) and Ag(001): Flux and temperature dependence. J Phys: Condens Matter **13**, 5875–5891

Cuerno R. and Barabasi A.L. (1995): Dynamic scaling of ion-sputtered surfaces. Phys Rev Lett **74**, 4746–4749

Cuerno R., Makse H.A., Tomassone S., Harrington S.T. and Stanley H.E. (1995): Evolution from ripple morphology to rough morphology. Phys Rev Lett **75**, 4464–4467

Erlebacher J., Aziz M.J., Chason E., Sinclair M.B. and Floro J.A. (1999): Spontaneous pattern forming on ion bombarded Si(001). Phys Rev Lett **82**, 2330–2333

Erlebacher J., Aziz M.J., Chason E., Sinclair M.B. and Floro J.A. (2000): Nonclassical smoothening of nanoscale surface corrugations. Phys Rev Lett **84**, 5800–5803

Ernst H.-J. (1997): The pattern formation during ion bombardment of Cu(001) investigated with helium atom beam scattering. Surf Sci **383**, L755–L759

Facsko S., Dekorsy T., Koerdt C., Trappe C., Kurz H., Vogt A. and Hartnagel H.L. (1999): Formation of ordered nanoscale semiconductor dots by ion sputtering. Science **285**, 1551–1553

Frost F., Ziberi B., Höche T. and Rauschenbach B. (2004): The shape and ordering of self-organized nanostructures by ion sputtering. Nucl Instrum Methods B **216**, 9–19

Gago R., Vazquez L., Cuerno R., Varela M., Ballesteros C. and Albella J.M. (2001): Production of ordered silicon nanocrystals by low-energy ion sputtering. Appl Phys Lett **78**, 3316–3318

Habenicht S. (2001): Morphology of graphite surfaces after ion-beam erosion. Phys Rev B **63**, 125419

Hartmann A.K., Kree R., Geyer U. and Kölbel M. (2002): Long-term effect in a simulation model of sputter erosion. Phys Rev B **65**, 193403

Herring C. (1950): Effect of change of scale on sintering phenomena. J Appl Phys **21**, 301–303

Israeli N. and Kandel D. (2000): Decay of one-dimensional surface modulations. Phys Rev B **62**, 13707–13717

Jeong H.-C. and Williams E.D. (1999): Steps on surfaces: Experiment and theory. Surf Sci Rep **34**, 175–294

Kalff M., Comsa G. and Michely T. (2001): Temperature dependent morphological evolution of Pt(111) by ion erosion: destabilization, phase coexistence and coarsening. Surf Sci **486**, 103–135

Koponen I., Hautala M. and Sievanen O.-P. (1997): Simulations of ripple formation on ion-bombarded solid surfaces. Phys Rev Lett **78**, 2612–2615

Makeev M.A. and Barabasi A.-L. (1997): Ion-induced effective surface diffusionin ion sputtering. Appl Phys Lett **71**, 2800–2802

Makeev, M.A., Cuerno R. and Barabasi A.L. (2002): Morphology of ion-sputtered surfaces. Nucl Instrum Methods B **197**, 185–227

Malis O., Brock J.D., Headrick R.L., Yi M.-S. and Pomeroy J.M. (2002): Ion-induced pattern formation on Co surfaces: An x-ray scattering and kinetic Monte Carlo study. Phys Rev B **66**, 035408

Margetis D., Aziz M.J. and Stone H.A. (2004): Continuum description of profile scaling in nanostructure decay. Phys Rev B **69**, 041404

Mayer T.M., Chason E. and Howard A. (1994): Roughening instability and ion induced viscous relaxation of SiO_2 surfaces. J Appl Phys **76**, 1633–1643

Michely T., Kalff M., Comsa G., Strobel M. and Heinig K.H. (2001): Step edge diffusion and step atom detachment in surface evolution: Ion-erosion of Pt(111). Phys Rev Lett **86**, 2589–2592

Mullins W.W. (1959): Flattening of a nearly plane solid surface due to capillarity. J Appl Phys **30**, 77–83

Murty M.V.R., Cowles B. and Cooper B.H. (1998a): Surface smoothing during sputtering: Mobile vacancies versus adatom detachment and diffusion. Surf Sci **415**, 328–335

Murty M.V.R., Curcic T., Judy A., Cooper B.H., Woll A.B., Brock J.D., Kycia S. and Headrick R.L. (1998b): X-ray scattering study of the surface morphology of Au(111) during Ar^+ ion irradiation. Phys Rev Lett **80**, 4713–4716

Park S., Kahng B., Jeong H. and Barabasi A.-L. (1999): Dynamics of ripple formation in sputter erosion: Nonlinear phenomena. Phys Rev Lett **83**, 3486

Pedemonte L., Bracco G., Boragno C., de Mongeot F.B. and Valbusa U. (2003): Smoothing of nanoscale surface ripples studied by He atom scattering. Phys Rev B **68**, 115431

Politi P. and Villain J. (1996): Ehrlich-Schwoebel instability in molecular beam epitaxy: A minimal model. Phys Rev B **54**, 5114–5129

Ritter M., Stindtmann M., Farle M. and Baberschke K. (1996): Nanostructuring of the Cu(001) surface by ion bombardment: A STM study. Surf Sci **348**, 243–252

Rusponi S., Costantini G., Boragno C. and Valbusa U. (1998): Scaling laws of the ripple morphology on Cu(110). Phys Rev Lett **81**, 4184–4187

Shenoy V.B., Ramasubramaniam A. and Freund L.B. (2003): A variational approach to nonlinear dynamics of nanoscale surface modulations. Surf Sci **529**, 365–383

Shenoy V.B., Ramasubramaniam A., Ramanarayan H., Tambe D.T., Chan W.-L. and Chason E. (2004): Influence of step-edge barriers on the morphological relaxation of nanoscale ripples on crystal surfaces. Phys Rev Lett **92**, 256101

Sigmund P. (1969): Theory of sputtering I. Sputtering yield of amorphous and polycrystalline targets. Phys Rev **184**, 383–416

Sigmund P. (1973): A mechanism of surface microroughening by ion bombardment. J Mater Sci **8**, 1545–1553

Stepanova M. and Dew S.K. (2004): Surface relaxation in ion-etch nanopatterning. Appl Phys Lett **84**, 1374–1376

Stevie F.A., Kahora P.M., Simons D.S. and Chi P. (1988): Secondary ion yield changes in Si and GaAs due to topography changes during O_2^+ or Cs^+ ion bombardment. J Vac Sci Technol A **6**, 76–80

Strobel M., Heinig K.H. and Michely T. (2001): Mechanisms of pit coarsening in ion erosion of fcc(111) surfaces: A kinetic 3D lattice Monte-Carlo study. Surf Sci **486**, 136–156

Umbach C.C., Headrick R.L. and Chang K.-C. (2001): Spontaneous nanoscale corrugation of ion-eroded SiO_2: The role of ion-irradiation-enhanced viscous flow. Phys Rev Lett **87**, 246104

Valbusa U., Borangno C. and de Mongeot F.B. (2002): Nanostructuring surfaces by ion sputtering. J Phys: Condens Matter **14**, 8153–8175

Villain J. (1991): Continuum model of crystal – Growth from atomic-beams with and without desorption. J Phys (Paris) **1**, 19–42

Wittmaack K. (1998): Artifacts in low-energy depth profiling using oxygen primary ion beams: Dependence on impact angle and oxygen flooding conditions. J Vac Sci Technol B **16**, 2776–2785

Yewande E.O., Hartmann A.K. and Kree R. (2005): Propagation of ripples in Monte Carlo models of sputter-induced surface morphology. Phys Rev B **71**, 195405

Ziegler J.F. and Biersack J.P. (2000): SRIM-2000.40, IBM Co., Yorktown, NY

Some Ion-Beam Modification Issues: Ion-Induced Amorphisation and Crystallisation of Silicon

J.S. Williams*, G. de M. Azevedo[1] and A. Kinomura[2]

Research School of Physical Sciences and Engineering
Australian National University, Canberra, 0200 Australia
[1]Present address: Brazilian Synchrotron Light Laboratory (LNLS), 6192–CEP 13084-971, Campinas, SP, Brazil
[2]Present address: Advanced Defect-Characterization Research Group
Research Institute of Instrumentation Frontier
National Institute of Advanced Industrial Science and Technology
1-1-1 Umezono, Tsukuba, Ibaraki 305-8568, Japan

Abstract

This paper reviews the crystalline to amorphous and amorphous to crystalline phase transformations which can be induced in silicon by energetic ion irradiation. An overview of ion disordering and amorphisation is treated first. At temperatures or irradiation conditions under which the defects generated by the ion bombardment are relatively stable, disorder builds up with ion dose until complete amorphisation occurs. At elevated temperatures, the disordering and amorphisation processes can be considerably more complex. In this regime, dynamic annealing can occur during irradiation, whereby defects can annihilate and cluster to form defect bands. If the temperature is not too high, amorphisation can be nucleated with increasing dose at such defect bands but also at surfaces and interfaces, often well away from the maximum in the (nuclear) energy deposition distribution. Such nucleation-limited amorphisation is difficult to model, particularly as the critical dose for amorphisation depends in a complex way on irradiation temperature, ion mass, ion energy and ion flux. Once an amorphous layer forms

* E-mail: director.RSPSE@anu.edu.au

in this regime, it can extend with increasing dose in a layer-by-layer manner. Again, there is no accepted model for this process. At higher irradiation temperatures, crystallisation of pre-existing amorphous layers can be induced. This ion beam induced epitaxial crystallisation (IBIEC) process occurs at temperatures well below that at which normal thermal epitaxial crystallisation takes place. This paper then gives an overview of the experiments and observations that have been made to study the IBIEC phenomenon. Studies of the dependence of the growth rate on irradiation temperature, ion dose, ion mass and ion flux again point to a complex process, but it is clear that the crystallisation is induced by ion displacements at or close to the amorphous-crystalline interface. Irradiations under ion channeling conditions, coupled with simulations of displacement distributions, have been used to probe the mechanism in more detail. Although it is now possible to establish that ion-induced defect generation precisely at the amorphous-crystalline interface is responsible for IBIEC, modelling of the process is again difficult. Such difficulties result from complex temperature, ion mass and flux dependencies, whereby the density of the collision cascade and inter-cascade effects appear to play dominant roles. Although much is known about both ion-induced amorphisation and crystallisation processes, the observed dependencies over a broad temperature range cannot as yet be quantitatively modelled.

Contents

1 Introduction **229**

2 Overview of Ion-Induced Amorphisation **230**
2.1 The Effect of Temperature on Defect Accumulation 230
2.2 Preferential Amorphisation at Surfaces and Defect Bands 232
2.3 Mechanisms of Amorphisation: The Role of Defects 234
2.4 Layer-by-Layer Amorphisation 237

3 Overview of Ion Beam Induced Epitaxial Crystallisation **239**
3.1 IBIEC Temperature Dependence 239
3.2 IBIEC Observations and Dependencies 239
3.3 IBIEC and Early Channeling Studies 245
3.4 IBIEC Models 248

4 Cascade Effects on IBIEC: Observations and Interpretation **249**
4.1 Experimental Observations 249
4.2 Comparison with Simulations 252

5 Some Answered and Unanswered Questions **257**

References **258**

1. Introduction

When materials are irradiated with energetic ions, the ion-induced disorder can lead to a number of interesting structural transformations, including amorphisation and crystallisation. The behaviour is particularly interesting when irradiation is carried out at temperatures where the defects produced by the ion beam are mobile. Silicon is an ideal material to observe and understand such processes, but, despite extensive studies over the past two decades, there are still many unanswered questions relating to ion-induced defects and their influence on amorphisation and crystallisation. For ion irradiation at or below room temperature in silicon, the disorder produced is essentially stable since point defects are readily immobilised within disordered regions. Under such conditions, ion damage generated within collision cascades builds up with ion dose, leading to amorphisation of the silicon. At higher implant temperatures, where defects begin to move and interact during ion bombardment, significant defect annihilation can occur and it can be difficult to induce amorphisation. In this regime, preferential amorphisation can be observed at regions where extended defects first form, for example, at nanocavities or at surfaces. Continued irradiation can lead to layer-by-layer amorphisation.

At even higher temperatures ion irradiation may not cause amorphisation. Incomplete defect annihilation during bombardment can lead to the formation of defect clusters and even extended defects in an otherwise crystalline matrix. In this elevated temperature regime, where defects are mobile, the understanding of the observed defect-mediated processes is far from complete. Irradiation under these conditions can even lead to the recrystallisation of previously-amorphised layers. This latter process, so called ion-beam-induced-epitaxial crystallisation (IBIEC), occurs at temperatures well below that at which normal thermally-induced crystallisation of amorphous silicon occurs. IBIEC has been shown to be an activated process, dependent on the generation of mobile "defects" by ion irradiation. There has been considerable controversy as to the role of defects in IBIEC but recent experiments have assisted in partly clarifying this issue. Indeed, studies of ion-induced amorphisation and crystallisation not only indicate much about the behaviour of defects and defect-induced phase changes in silicon but also provide considerable insight into the fundamental physics of defect interactions and epitaxial crystallisation at an atomic level. This review first gives an

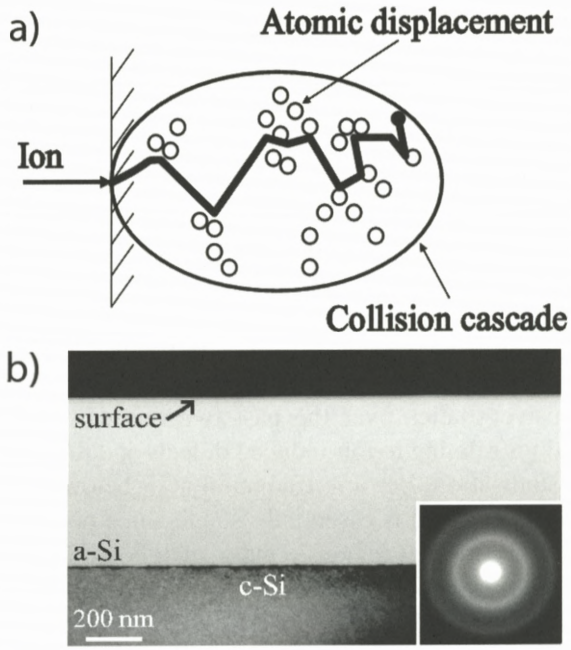

Figure 1. (a) Schematic of displacements within a collision cascade. (b) A cross-sectional transmission electron microscope (XTEM) image of a continuous amorphous layer (a-Si) generated in silicon by 245 keV Si ion irradiation at room temperature to a dose of 3×10^{15} cm^{-2}. The sample surface is indicated, as is the underlying crystalline silicon (c-Si).

overview of ion-induced amorphisation and crystallisation phenomena that have been observed in silicon and identifies some unanswered questions. More recent experiments, that provide insight into both ion-induced defect interactions and IBIEC, are then presented and interpreted with the aid of computer simulations. Finally, a summation of what is known and what is not known in these areas is presented.

2. Overview of Ion-Induced Amorphisation

2.1. The Effect of Temperature on Defect Accumulation

At sufficiently low irradiation temperatures, residual lattice disorder in semiconductors is controlled by the energy deposited by swift ions in nuclear collisions with lattice atoms. Individual heavy ions can generate dense displacement cascades (Figure 1a) that result directly in amorphous zones (Howe and Rainville,

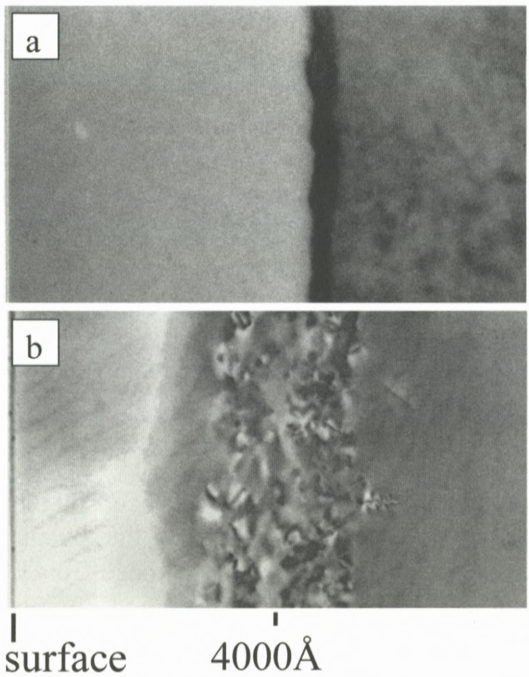

Figure 2. XTEM images corresponding to 245 keV Si ion irradiation of silicon (100) to a dose of $4 \times 10^{15}\text{cm}^{-2}$ at (a) room temperature, and (b) 350°C. After Williams (1998).

1987) and the overlap of such zones with increasing dose leads to a continuous amorphous layer (Morehead et al., 1970; Dennis and Hale, 1978), as shown in the cross-sectional transmission electron micrograph (XTEM) in Figure 1b. For light ions, cascades are less dense and the lattice can collapse to an amorphous phase when a sufficiently high defect density builds up and the local free energy of the defective lattice exceeds that of the amorphous phase (Swanson and Quennevi, 1971; Vook and Stein, 1969; Christel et al., 1981). These two extremes of damage build up at low temperatures can be successfully treated by heterogeneous (heavy ion) or homogeneous (light ion) models, such as those of Morehead et al. (1970) and Vook and Stein (1969), respectively.

Implantation temperature can determine whether the defects generated within collision cascades are stable or whether they can migrate and annihilate. An example of temperature dependent effects is shown in Figure 2 (Williams, 1998). Figure 2a is a XTEM micrograph depicting a continuous amorphous layer in silicon, produced by 245 keV Si ions at room temperature to a dose of 4×10^{15} cm^{-2}. The ion range is around 3800 Å but, under these implant conditions,

the amorphous layer is around 5000 Å thick. Note that the boundary between the amorphous layer and the underlying silicon substrate is quite sharp, indicating that defects produced in the tail of the Si implant distribution can annihilate quite effectively at this implant temperature. If the implant temperature is raised to 350°C, irradiation-produced defects are considerably more mobile and annihilate or cluster to effectively suppress amorphisation (Williams 1992), as shown in the XTEM micrograph in Figure 2b. Here, there are clearly observed interstitial clusters that evolve into well defined interstitial-based line defects such as {311} defects and dislocation loops (Takeda et al., 1994) on annealing. It will be shown later that, at such implant temperatures where defects can annihilate, irradiation-induced displacements can induce crystallisation of pre-existing amorphous layers.

Between the two extreme regimes illustrated in Figure 2, the close balance between the rate of damage production within collision cascades and the rate of dynamic annealing (defect annihilation and clustering) can give rise to interesting defect-mediated phenomena, with strong dependencies on implantation temperature, dose and dose rate. Small changes in any of these parameters can result in dramatic differences in residual implantation damage from almost damage-free structures, as a result of efficient defect annihilation, to continuous amorphous layers. In this regime, amorphisation can occur in an entirely different way, as a result of nucleation-limited or preferential amorphisation processes (Goldberg et al., 1999). For example, as the implantation dose increases and the density of defects increases, amorphous layers can spontaneously form at the depth of maximum disorder. Such layers can then grow to encompass the entire defective region (Goldberg et al., 1995). Further examples of the critical balance between defect creation and defect annihilation, including preferential amorphisation, are given below.

2.2. Preferential Amorphisation at Surfaces and Defect Bands

Amorphous layers can be observed to nucleate preferentially at depths significantly away from the maximum in the ion's energy deposition distribution, at, for example, surfaces (Williams et al., 1994b), interfaces and pre-existing defects (Goldberg et al., 1999; Williams et al., 1994a). Figure 3 illustrates the case of preferential amorphisation at a silicon surface or, more precisely, at a SiO_2-Si interface. Figure 3a (Goldberg et al., 1995) shows an RBS/channeling spectrum for an 80 keV Si implant into silicon at 160°C for a dose of 10^{16} cm^{-2} at a beam flux of 2.7×10^{13} ions cm^{-2} s^{-1}. The spectrum shows a strong disorder peak at the surface and a buried peak around the end-of-ion-range at about 1200 Å. (The end-of-ion-range refers to the region in the tail of the ion range distribution, about two standard deviations deeper than the projected ion range.) The corresponding

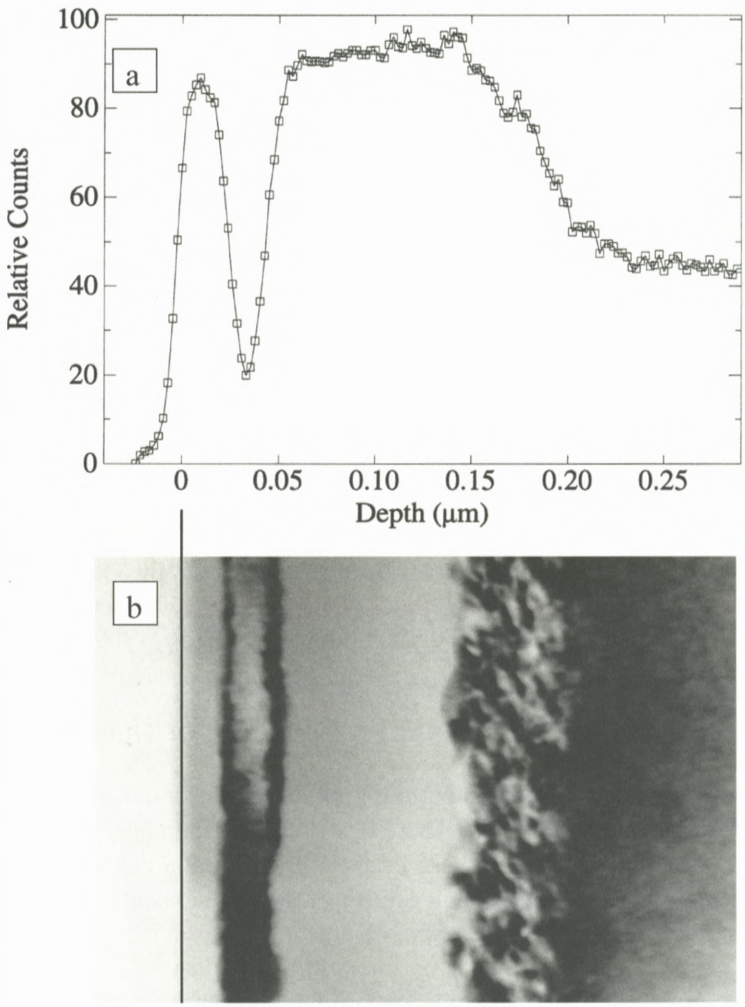

Figure 3. (a) An RBS/channeling spectrum for an 80 keV Si implant into silicon at 160°C to a dose of 10^{16} cm^{-2} at a beam flux of 2.7×10^{13} ions cm^{-2} s^{-1}. After Goldberg et al. (1995). (b) XTEM image of the sample in (a). After Goldberg (1995).

XTEM micrograph in Figure 3b (Goldberg, 1995) indicates that there are two amorphous layers present, one extending 300 Å from the surface and a buried layer from 500 to 1500 Å. Between these layers is a region of crystalline silicon containing few defects but below the buried layer there is a region of crystalline silicon, rich in (interstitial-type) defect clusters. This result shows not only the

nucleation of an amorphous region around the maximum in the nuclear energy distribution at about 800 Å but nucleation of an amorphous layer well away from the maximum disorder depth, at the surface. When the evolution of this defect structure was examined as a function of ion dose (Goldberg, 1995), it was found that the deep disorder first accumulated as defect clusters of interstitial character at lower doses. This defective region then appeared to collapse into an amorphous layer as the dose increased. In addition, the surface amorphous layer was found to thicken with increasing dose. This behaviour suggests that, in a regime where substantial dynamic annealing occurs during ion irradiation, mobile defects not only annihilate and locally form defect clusters, but can also migrate and accumulate at SiO_2-Si interfaces. Collapse of such disorder to an amorphous phase can occur at a sufficiently high implantation dose. It has also been shown that a pre-existing dislocation band can act as a nucleation site for amorphisation, even when it is situated well away from the disorder peak (Goldberg et al., 1999). Furthermore, such dislocation bands were found to "getter" interstitial-based defects from deeper in the material during irradiation (Goldberg et al., 1999). Thus, it would appear that both dislocation bands, surfaces (actually SiO_2-Si interfaces) and amorphous layers themselves are good trapping sites or sinks for mobile defects that may otherwise form stable clusters close to where they come to rest, in the absence of such sinks.

2.3. Mechanisms of Amorphisation: The Role of Defects

The mechanism for the above defect trapping and preferential amorphisation behaviour deserves some comment. There has been considerable speculation in the literature (Williams, 1992; Goldberg et al., 1999; Elliman et al., 1988; Jackson, 1988) as to the specific defects that are trapped at pre-existing defects, surfaces and amorphous layers. Clearly, open volume defects such as vacancies or divacancies, as well as interstitials or interstitial complexes, are candidates. As we discuss more fully below, some experiments on the kinetics of amorphous layer formation, in the regime where the irradiation-induced amorphous phase is nucleation-limited, have suggested that divacancies (Elliman et al., 1988) may be the main defects preferentially trapped at amorphous layers. However, other experiments, where amorphous layers are nucleated at pre-existing dislocation bands, suggest (Goldberg et al., 1999) that interstitial trapping also may have a major role to play. Nevertheless, regardless of the specific defects that accumulate prior to amorphisation, it would appear to be the local free energy that ultimately determines the collapse of a defective crystalline lattice to the amorphous phase. This mechanism (Williams, 1994) is illustrated schematically in Figure 4. The free energy of an amorphous phase exceeds that of a crystalline phase. In the

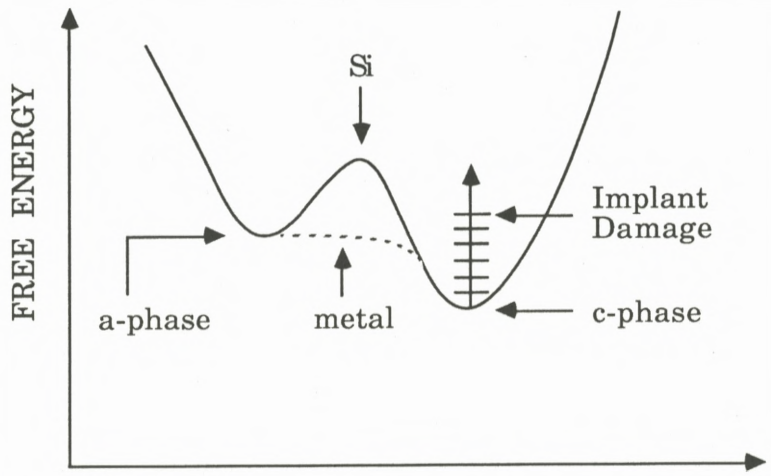

Figure 4. Schematic illustrating free energy differences and pathways between amorphous and crystalline materials. After Williams (1994).

case of silicon, the amorphous phase is metastable since there is a kinetic barrier that must be overcome before crystallisation can occur. In contrast, for pure metals, an amorphous phase is unstable even at extremely low temperatures, since there is essentially no barrier to crystallisation. Thus, under appropriate implantation conditions, implantation-induced disorder in silicon can build up until the local free energy exceeds that of the amorphous phase. It can then be energetically favourable for the defective crystalline lattice to collapse to the amorphous phase that provides a local minimum in free energy. Such behaviour suggests that, in cases where there is some defect mobility, defect annihilation and agglomeration occurs and the amorphous phase can preferentially form at sites which minimise the local free energy. Under such situations amorphisation can be nucleation-limited.

In cases where there are no pre-existing nucleation sites for amorphisation, the onset of amorphisation (at elevated temperatures) usually occurs at the ion-end-of-range. Here, nucleation of the amorphous phase normally occurs where there is an interstitial excess and this corresponds roughly to the end-of-ion-range. In this regime, amorphisation can exhibit interesting dependencies, including situations where the ion flux controls the critical amorphisation temperature (Elliman et al., 1988), as illustrated in Figure 5. For a fixed dose of 5×10^{15} cm^{-2} for 1.5 MeV Xe ions irradiating silicon, amorphisation at the end-of-ion-range can be observed only below 200°C if the average beam flux is kept below 10^{12} ions

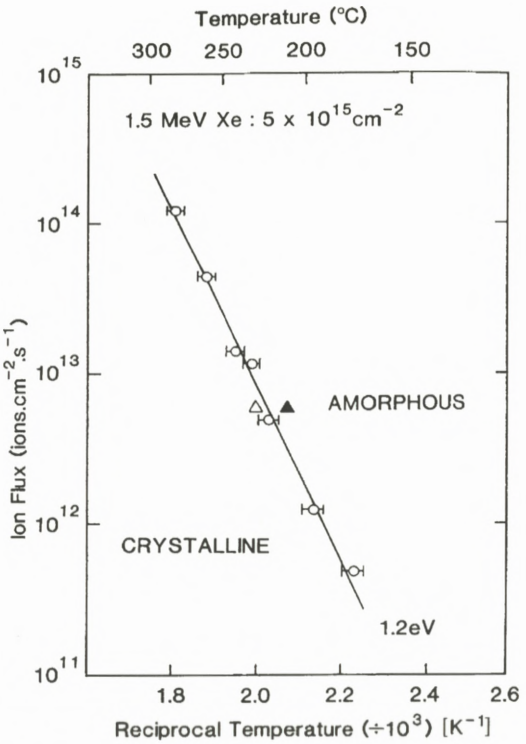

Figure 5. Ion flux as a function of $1/T$ for ion irradiation conditions (1.5 MeV Xe ions at a dose of 5×10^{15} cm^{-2}) under which a buried amorphous layer is just formed in silicon. The solid and open triangles represent the cases in Figures 7b and 8b, respectively. After Elliman et al. (1988).

cm^{-2} s^{-1}, but up to 300°C if the ion flux is raised above 10^{14} ions cm^{-2} s^{-1}. This demonstrates the critical dependence of amorphisation on the balance between the rate of disorder production (controlled by ion flux in the case of Figure 5) and the extent of dynamic annealing, which is controlled by irradiation temperature. For implantation conditions on the left hand side of the solid line in Figure 5, no amorphous silicon was formed (only defect clusters in crystalline silicon), whereas buried amorphous layers are generated under conditions on the right. Note that the onset of amorphisation in Figure 5 fits well to an activation energy of 1.2 eV. Elliman et al. (1988) noted that this value corresponds to the dissociation energy of silicon divacancies and, consequently, suggested that the stability of divacancies may control amorphisation in silicon. However, more recent studies, that use other ion beams to examine the dependence of the onset of amorphisation on ion flux and temperature, have shown a range of activation energies between

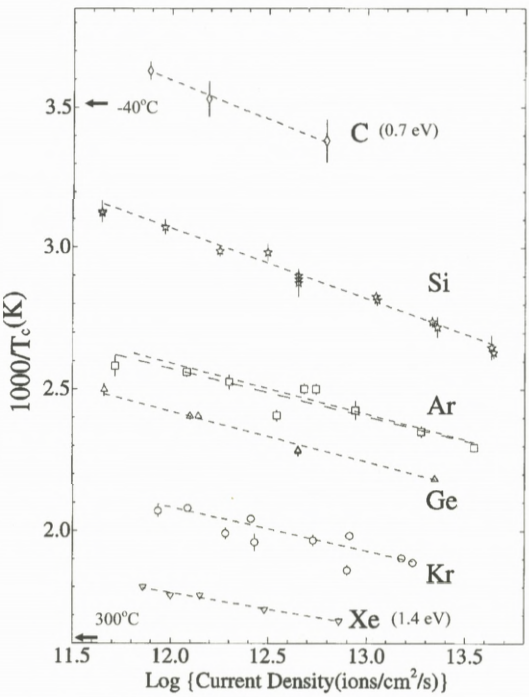

Figure 6. Ion flux as a function of $1/T$ for ion irradiation conditions under which a buried amorphous layer is just formed in silicon for a number of ions at a dose of 10^{15} cm^{-2} except C where the dose was 2×10^{15} cm^{-2}. After Goldberg et al. (1993).

0.5 and 1.7 eV as shown in Figure 6, taken from the work of Goldberg et al. (1993). The conclusion is that more complex defects and defect interaction processes may control amorphisation, depending on the implant conditions used, particularly the implantation temperature.

2.4. Layer-by-Layer Amorphisation

Another intriguing case of preferential amorphisation is layer-by-layer amorphisation, which has been observed in some cases when silicon containing pre-existing amorphous layers is re-irradiated at elevated temperatures (Linnros et al., 1988b). An example of such behaviour is illustrated by the XTEM micrographs in Figure 7 (Elliman et al., 1987). Clearly, the near-surface amorphous layer in Figure 7a has increased in thickness when irradiated with 1.5 MeV Xe ions at 208°C (Figure 7b). It is also interesting to note that a buried amorphous layer has also formed at the Xe end-of-ion-range under these conditions. The region between

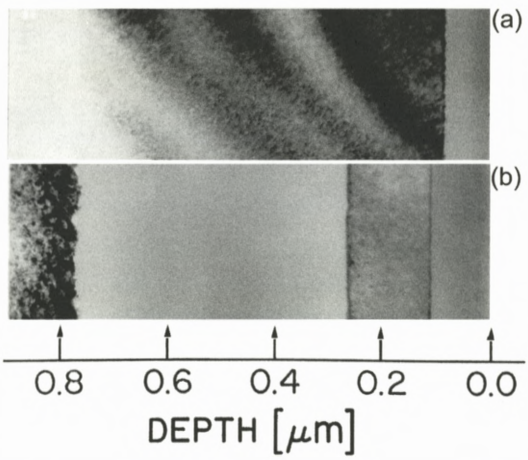

Figure 7. XTEM images illustrating layer-by-layer amorphisation of silicon by 1.5 MeV Xe ion irradiation to a dose of 5×10^{15} cm^{-2}. (a) A pre-existing surface amorphous layer on silicon prior to Xe irradiation, and (b) following Xe irradiation at 208oC. After Elliman et al. (1987).

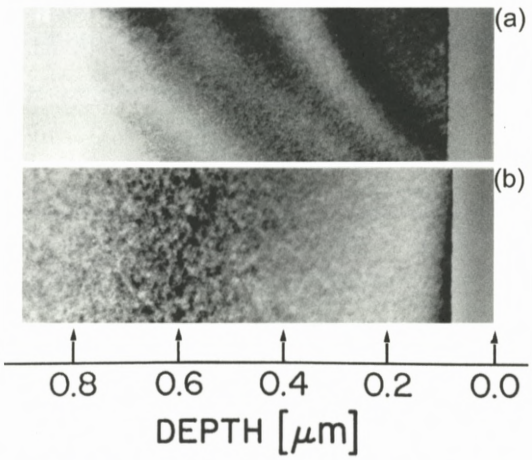

Figure 8. XTEM images illustrating IBIEC of a pre-existing amorphous layer in silicon (a) using 1.5 MeV Xe ions to a dose of 5×10^{15} cm^{-2} at a temperature of 227°C. After Elliman et al. (1987).

the two amorphous layers is essentially free of defects, as a result of near perfect defect annihilation in this region. Both amorphous layers are observed to extend layer-by-layer with increasing ion dose, presumably by the preferential trapping of mobile defects at the respective amorphous-crystalline interfaces.

3. Overview of Ion Beam Induced Epitaxial Crystallisation

3.1. IBIEC Temperature Dependence

The previous section illustrated implantation conditions where amorphisation by ion irradiation is nucleation-limited and can give rise to preferential amorphisation and layer-by-layer amorphisation phenomena. If the implantation conditions are changed to further favour the rate of dynamic annealing over defect production, by raising the temperature for example, pre-existing amorphous layers can be observed to crystallise epitaxially by the IBIEC process. IBIEC is illustrated for the case of 1.5 MeV Xe irradiation in Figure 8 (Elliman et al., 1987). At an irradiation temperature of 227°C, the pre-existing surface amorphous layer is observed to shrink. Increasing the dose causes further epitaxial growth of the amorphous layer. It is interesting to note that a slight reduction in irradiation temperature to 208°C, keeping the other irradiation conditions the same, induces layer-by-layer amorphisation, as previously shown in Figure 7. If the temperature is increased further, above that corresponding to the data in Figure 7b, the IBIEC rate speeds up. The temperature dependence of IBIEC is illustrated in Figure 9 for the case of 600 keV Ne irradiation of silicon (Williams et al., 1985b). Note that a well-defined activation energy can be extracted from the data (0.24 eV), the magnitude of which is suggestive that defect-mediated processes control IBIEC, possibly vacancies (Elliman et al., 1987; Williams et al., 1985b). In Figure 9, the kinetics of thermally-induced epitaxial growth is also shown, with the normal activation energy of 2.8 eV (Olson and Roth, 1988). It was accepted in early IBIEC studies (Williams et al., 1985b; Olson and Roth, 1988) that the low IBIEC activation energy arose as a result of athermally generated displacements. These displacements provide the defects for stimulating bonding rearrangements at the interface and hence crystallisation. In the thermal case, the high activation energy was attributed (Williams et al., 1985b) to two activation terms, nucleation of the defects influencing epitaxial crystallisation and a second term involving migration and bond rearrangement. In IBIEC, the first term is eliminated by athermal defect generation and only the second activation term applies. More detailed treatment of IBIEC mechanisms will be given in Section 3.4.

3.2. IBIEC Observations and Dependencies

Early studies (Linnros et al., 1985, 1988b; Elliman et al., 1987; Williams et al., 1985b; Priolo et al., 1989b) indicated that the IBIEC rate was proportional to ion dose and was controlled by nuclear energy deposition. This demonstrates that atomic displacements are crucial for IBIEC. Indeed, experiments with electron

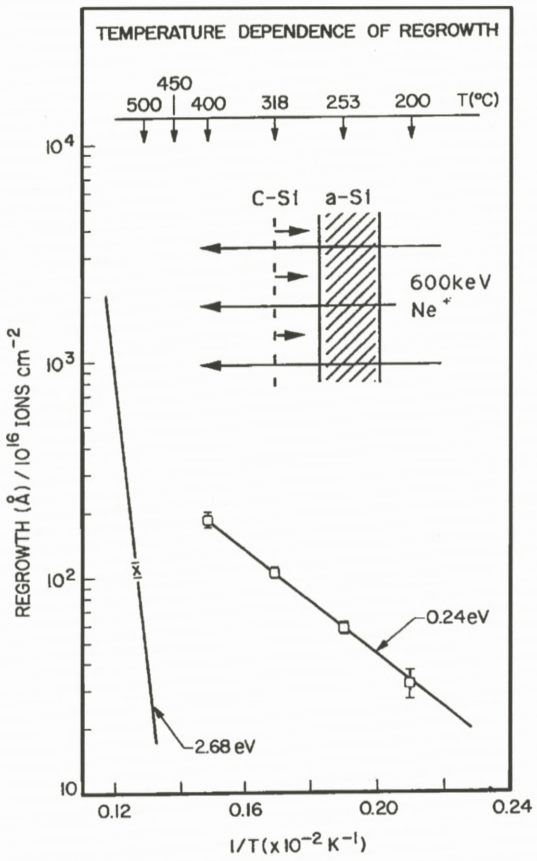

Figure 9. IBIEC regrowth for a dose of 10^{16} Ne ions cm^{-2} (600 keV) as a function of $1/T$ (open squares) in silicon. The activation energy for thermally-induced epitaxy (2.8 eV) is also shown. After Williams et al. (1985b).

beams (Lulli et al., 1987) have clearly shown that recrystallisation only occurs if the energy of the electron beam is sufficient to produce atomic displacements in silicon in the region of the amorphous-crystalline interface. Several studies (Linnros et al., 1985, 1988b; Elliman et al., 1987; Williams et al., 1985b; Priolo et al., 1989b; Lulli et al., 1987; Priolo and Rimini, 1990) have suggested that atomic displacements generated by nuclear collisions very close to the amorphous-crystalline interface are responsible for IBIEC. For example, Figure 10 from Williams et al. (1985a) shows the dependence of IBIEC on nuclear energy deposition at the interface. In Figure 10a, the RBS/channeling spectra show that for 1.5 MeV Ne ions at 318oC the extent of regrowth is linear with dose for this

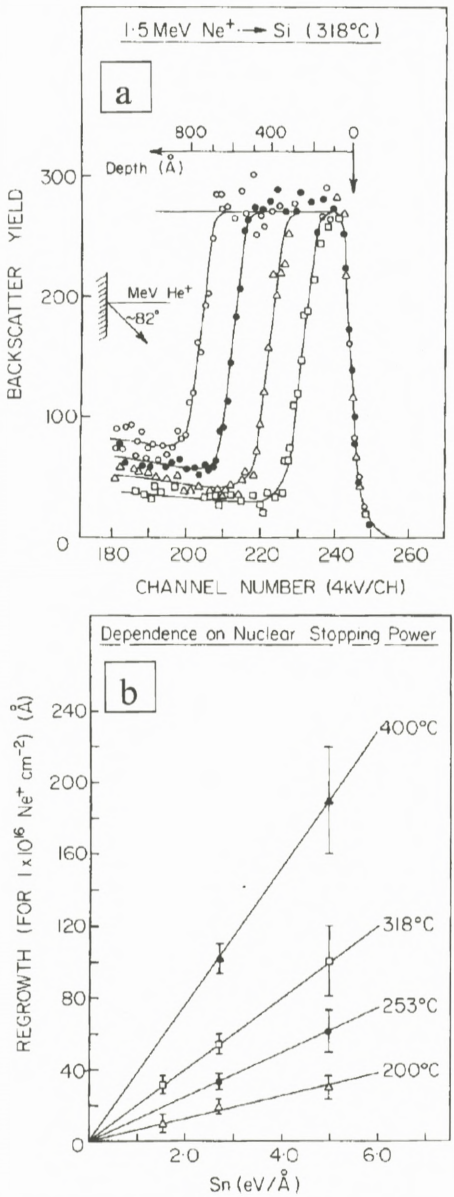

Figure 10. (a) RBS/channeling spectra from a silicon sample (with a pre-amorphised layer) held at 318°C and irradiated sequentially with 1.5 MeV Ne ions at dose increments of 3×10^{16} cm^{-2}. The open circles data show the spectrum corresponding to the pre-existing amorphous layer. (b) IBIEC growth normalised to a Ne dose of 10^{16} cm^{-2} as a function of nuclear stopping power (S_n) for different substrate temperatures. After Williams et al. (1985a).

irradiation situation, where the nuclear energy deposition is relatively constant at the interface as regrowth proceeds. In Figure 10b, IBIEC growth is plotted as a function of nuclear energy deposition at the interface (Sn) for Ne ion irradiation at 4 temperatures. Here, three Ne ion energies were used (0.6, 1.5 and 3 MeV) and the atomic displacements generated by the ion beam at the amorphous-crystalline interface (Sn) were obtained from simulations using the TRIM code (Ziegler et al., 1985). The IBIEC rate is observed to scale with the nuclear energy deposition at the interface. This result strongly suggests that long range diffusion of defects from the amorphous or crystalline sides of the interface do not contribute significantly to IBIEC but does not rule out short range diffusion, an issue we return to later.

The IBIEC growth rate is also found to be significantly different for different substrate orientations (Priolo et al., 1989b; Cannavo et al., 1986; Maher et al., 1987), where a 2–4 times slower rate is observed for ⟨111⟩ compared with ⟨100⟩ orientations. No difference between ⟨100⟩ and ⟨110⟩ orientations is observed for IBIEC. These trends are somewhat similar to those found in normal thermally-induced epitaxial growth but the scale of the difference is greater for thermal epitaxy, where a 25 times difference in rates between ⟨111⟩ and ⟨100⟩ substrates is obtained and there is also a 2.5 times difference between ⟨110⟩ and ⟨100⟩ substrates (Olson and Roth, 1988). Furthermore, the slower rates of thermally-induced epitaxial growth observed in ⟨111⟩ oriented layers are consistent with models which suggest that solid phase epitaxy is mediated by bond breaking and remaking processes at kinks and ledges on the amorphous-crystalline interface (Spaepen and Turnbull, 1982; Williams and Elliman, 1983). Indeed, the interface is expected to be resolved into surfaces of minimum free-energy by the formation of terraces with a {111} orientation and epitaxial growth proceeds by thermally activated atomic rearrangements at energetically favourable kink sites on ledges connecting two consecutive (111) terraces, as proposed in the phenomenological models of Spaepen and Turnbull (1982) and Williams and Elliman (1983). Rate differences arise from the different concentrations of kink sites, depending on the interface geometry or orientation. Priolo et al. (1990) have suggested that similar processes may account for the IBIEC orientation dependence.

The effects of impurity species on IBIEC are also qualitatively similar to those observed for thermal epitaxy (Olson and Roth, 1988; Kennedy et al., 1977; Poate et al., 1987). For example, slow diffusing electrically active dopants, such as B and P, are observed to enhance the IBIEC growth rate (Priolo et al., 1990), whereas species such as oxygen, that form strong bonds with silicon, are observed to retard the rate (Priolo et al., 1989a). However, the magnitudes of the rate changes are considerably smaller than those observed for thermal epitaxy, again suggesting

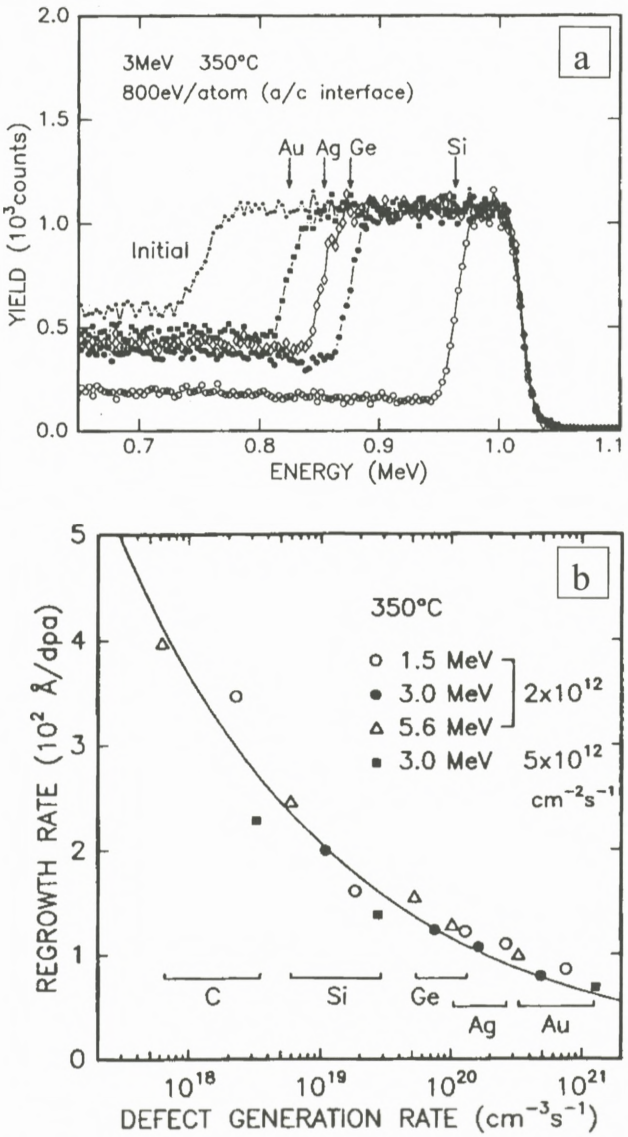

Figure 11. (a) Channeling spectra showing the difference in regrowth thicknesses among four different ion species (Au, Ag, Ge, and Si) at 3.0 MeV. Irradiation doses were adjusted to provide the same total nuclear energy deposition (800 eV per atom) to the initial amorphous/crystalline interfaces. (b) Normalised regrowth rates as a function of defect generation rate for five ion species (C, Si, Ge, Ag, and Au) at three energies (1.5, 3.0, and 5.6 MeV) with two dose rates (2×10^{12} and 5×10^{12} cm^{-2} s^{-1}). After Kinomura et al. (1999).

that the lower temperatures of IBIEC growth may not achieve thermal equilibrium behaviour (Priolo and Rimini, 1990). Priolo and Rimini (1990) have also reviewed the IBIEC behaviour of fast diffusing species, such as Au and Ag, and again noted the similar tendency for such impurities to strongly prefer to remain in the amorphous phase as growth proceeds. This leads to segregation at the moving amorphous-crystalline interface. IBIEC allows such segregation phenomena to be studied at low temperatures, where the interface velocity can exceed the impurity diffusivity in the amorphous phase (Poate et al., 1988). These intriguing impurity segregation effects are not further treated in this paper, which concentrates more on the mechanisms of IBIEC.

Although studies of the energy and depth dependence of IBIEC growth, such as that in Figure 10, indicate that the IBIEC rate scales with nuclear energy deposition, such scaling across widely different ion masses does not occur. Indeed, ion mass effects were appreciated early (Linnros et al., 1988a), but only relatively recently have they been quantified in terms of an influence of cascade density on IBIEC rate (Kinomura et al., 1999). Furthermore, a small ion flux dependence of IBIEC (Linnros et al., 1988a, 1988b) was also found in early studies and the scale of this effect has only recently been examined over a wide flux range (Kinomura et al., 1999; Heera et al., 1993). Such mass effects, which illustrate the role of cascade density on IBIEC, and flux effects, which indicate the interaction times of defects contributing to IBIEC, are illustrated in Figure 11, taken from the work of Kinomura et al. (1999). Figure 11a shows RBS/channeling spectra that illustrate the mass dependence of IBIEC. Here 3 MeV Au, Ag, Ge and Si ions were used to irradiate an amorphous silicon layer of about 2000 Å in thickness on a silicon ⟨100⟩ substrate. Different doses were chosen to provide the same total nuclear energy deposition at the amorphous-crystalline interface and MeV ions were chosen to provide a near constant energy deposition at the interface during IBIEC growth. It is clear from Figure 11a that the regrown thickness increases with decreasing ion mass, even though the total nuclear energy deposition is similar for each ion within the range of the measured depth. This clearly shows that, at the same average ion flux, the *rate* of nuclear energy deposition, or the cascade density, clearly influences IBIEC. Another effect observed by Kinomura et al. (1999) was a flux dependence, whereby higher fluxes of the same ions under otherwise identical conditions resulted in less regrowth. This is again consistent with the observation that the rate of nuclear energy deposition influences IBIEC. Figure 11b plots the IBIEC regrowth rate (normalised to constant nuclear energy deposition at the interface) as a function of defect (ie vacancy) generation rate at the interface for five ion masses, four ion energies and two fluxes at 350°C. The defect generation was calculated using TRIM (Ziegler et al., 1985). Note that

the defect generation rate varies over more than 4 orders of magnitude from C to Au and the normalised growth rate for C is about 4 times that of Au under these conditions. A similar dose rate dependence for 300 keV ions has also been demonstrated by Linnros and Hólmen (1986) and Heera et al. (1993). Furthermore, Heera et al. (1995) proposed a diffusion limited model to explain IBIEC, where the regrowth thickness, normalised to dose, was proportional to ion beam current to the $-1/4$ power. Kinomura et al. (1999) have extended this treatment and the solid curve in Figure 11b is a fit to the equation

$$r_d = cg^{-1/4}, \tag{1}$$

where r_d is the regrowth thickness normalised to the number of displacements, c is a constant and g is the defect generation rate. The curve is a good fit to the data points for the conditions employed in Figure 11b but, as we show below, it does not fit particularly well to more extended dose rate data.

As indicated in Figure 11b, there are two parameters that conveniently change the defect generation rate, namely ion mass and ion flux. Figure 11b would appear to indicate that these different ways of changing defect generation rate, by altering cascade density (instantaneous displacement density within a single collision cascade) and ion flux (which changes the average time between the spatial overlap of subsequent cascades), have similar effects on IBIEC. However, Kinimora et al. (1999) subsequently varied the ion flux for similar mass ions over a wide range and found that cascade density and ion flux changes do not give identical changes to IBIEC rates. These results are shown in Figure 12a for Au and Ag ions, where the IBIEC rate seems to vary linearly with defect generation rate rather than the proposed Heera et al. (1995) fit. These data suggest that cascade size and ion flux give rise to separate influences on IBIEC rate, in addition to their common influence on defect generation rate, as we discuss more fully below. In Figure 12b we illustrate another case where more extensive recent data provide further insight into IBIEC processes. These data show that the apparent activation energy of IBIEC extracted from temperature dependent studies can vary from 0.18 to 0.4 eV, depending on ion mass. We also discuss the significance of these observations in the discussion of IBIEC mechanisms in Section 3.4.

3.3. IBIEC and Early Channeling Studies

A further series of observations relate to the influence of channeling of the incident ion beam on IBIEC rate. Experiments under channeling conditions can, in principle, help to clarify where the defects that influence IBIEC are generated, since channeling allows selective reduction in the number of defects produced in the crystalline region. However, in the early measurements using channeling

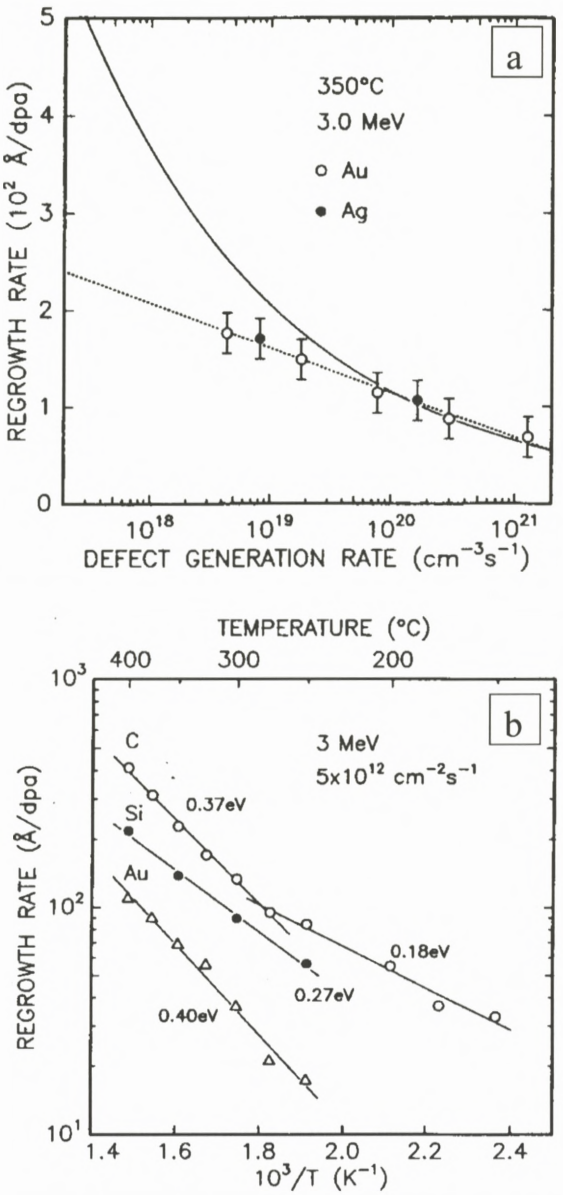

Figure 12. (a) Dose rate dependence of IBIEC for 3.0 MeV Au and Ag compared with the fitting curve of Figure 11b (solid curve). (b) Temperature dependence of IBIEC regrowth rates normalised to the number of displacements for 3.0 MeV Si, Ge and Au with a dose rate of 2×10^{12} cm^{-2} s^{-1}. After Kinomura et al. (1999).

(Williams et al., 1985b; Linnros and Hólmen, 1986; Elliman et al., 1986), the interpretation of the results has not been conclusive, mainly because it was difficult to estimate the exact number of point defects generated in the crystalline region, particularly after an ion beam had traversed an amorphous layer before entering the crystal. In cases of a surface amorphous layer and the incident beam aligned with a channeling direction in the underlying crystal, the IBIEC rate appeared to be reduced in some cases (Linnros and Hólmen, 1986) and not in others (Williams et al., 1985b). The multiple scattering of the beam in the amorphous layers was suggested as a reason for such differences and hence defects migrating short distances to the interface from the crystalline side of the interface may still play a role in the IBIEC process (Linnros and Hólmen, 1986). However, other studies, where no channeling effect was observed for surface amorphous layers (Williams et al., 1985b; Elliman et al., 1986), suggested that defects created away from the interface on the crystalline side played no role. Experiments with buried amorphous layers and measuring IBIEC rates under channeling conditions were more conclusive (Williams et al., 1985b; Elliman et al., 1986). A large reduction in IBIEC growth rate was observed for the near-surface interface of the buried layer (40–100%), compared with a random case. However, again such results were interpreted differently (Williams et al., 1985b; Priolo and Rimini, 1990; Elliman et al., 1986) to argue for either a role of mobile defects from the crystalline side or, alternatively, displacements produced exactly at the interface, as the main contribution to IBIEC. A more recent example of the channeling effect on IBIEC for a buried amorphous layer is shown in Figure 13 (Williams et al., 2000). Here, the regrowth differences are compared for channeled and random irradiations of an initially 1000 Å amorphous layer with 2 MeV C ions at 320°C to a dose of 1.2×10^{16} cm^{-2} in each case. Clearly, the front interface under channeling grows only 60% of that under random alignment, whereas the rear interface appears to show no differences between the two irradiations. The authors of this study (Williams et al., 2000) argued that, if mobile defects from the crystalline side were dominating IBIEC, then a much larger effect should have been expected. This conclusion is based on the difference in the magnitude of the nuclear energy deposition in the crystal between channeling and random alignments (whereby the channeled value is only about 5–10% of the random case). However, it was also argued that more detailed simulations would be necessary before a more precise determination of the origin of defects responsible for IBIEC could be made, as we illustrate in Section 4.

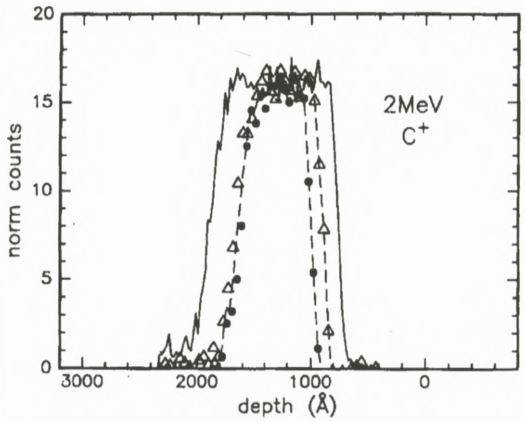

Figure 13. Random and channeled IBIEC regrowth extracted from RBS/channeling spectra (1.8 MeV He ions) for a 1000 Å amorphous silicon layer buried about 1000 Å below the surface. The data has been corrected for channeled He energy loss effects. The 2 MeV C ion dose was 1.2×10^{16} cm^{-2} in both random (filled circles) and channeled (open circles) cases. After Williams et al. (2000).

3.4. IBIEC Models

Priolo and Rimini (1990) have given an overview of various models to explain IBIEC observations up to about 1990. An early proposal suggested that annealing processes, which occur in the quenching of thermal spikes that overlap the amorphous-crystalline interface, were responsible for IBIEC (Kachurin, 1980). In addition, minimum free energy arguments and differences in free energy of amorphous and crystalline silicon have also been used to explain the temperature dependence of ion-induced amorphisation and crystallisation (Atwater et al., 1988). However, such proposals do not address many of the observations and fail to suggest the "defects" that may stimulate IBIEC. Furthermore, vacancies were suggested by several authors (Linnros et al., 1988a; Lulli et al., 1988; Nakata et al., 1981) as the prime defect involved. Firstly, the similarity of the initial activation energy of IBIEC (around 0.3 eV) to that of vacancy migration led Linnros et al. (1988a) to propose that migrating vacancies, produced athermally by the ion beam, mediated IBIEC, whereas, if the temperature was lowered, then the increased stability of divacancies, with a dissociation energy of 1.2 eV, may cause amorphisation at the interface. This two-defect model qualitatively explains both the layer-by-layer amorphisation and IBIEC processes but presupposes the migration of such defects in crystalline silicon to the interface. Other defects proposed to mediate IBIEC are (charged) kinks (Williams et al., 1985b; Priolo and Rimini,

1990) and dangling bonds (Mosley and Paesler, 1984) that are formed athermally by the ion beam directly at the interface. A difficulty with a single defect model is the fact that the apparent activation energy of IBIEC has been shown to vary from about 0.18 to 0.4 eV (see Figure 12b), which led Kinomura et al. (1999) to suggest that the rate limiting effect in IBIEC may involve several different defect-mediated processes, depending on the cascade density at the interface and the temperature. This proposal does not necessarily preclude kinks or other specific interface defects as the final step in the IBIEC process, but rather suggests that more complex defect processes may be involved in the annealing of dense cascades before discrete kinks are formed. A particular concern of vacancy models is that there is now considerable weight to arguments suggesting that defects produced right at the interface dominate IBIEC, as we illustrate more clearly in Section 4.

Another explanation for both layer-by-layer amorphisation and IBIEC is due to Jackson (1988), who developed an intracascade model in which each ion penetrating through the interface creates a disordered zone. Subsequent local interaction between defects in this zone can either lead to amorphisation or crystallisation. The onset of either amorphisation or crystallisation is controlled by a rate equation in which the net rate of interface movement, R, is given by the difference between a crystallisation term, Rx, and an amorphisation term, Rà, according to:

$$R = \frac{\mathrm{d}x}{\mathrm{d}\varphi} = R_x - R_\alpha, \tag{2}$$

where x is the distance of interface motion and φ is the ion beam dose. The amorphisation term can be written as $R_\alpha = V_\alpha \varphi$, where V_α is the volume of the amorphous zone created by a single ion. Crystallisation arises when defects produced by the ion beam annihilate in pairs at the interface. The simplicity of the Jackson model is attractive but it does not adequately account for ion mass and flux effects. Indeed, no single model appears to adequately explain all observations. We now move on to more recent channeling measurements and simulations that address more directly the origin of defects that influence IBIEC.

4. Cascade Effects on IBIEC: Observations and Interpretation

4.1. Experimental Observations

In this section, we present more detailed results of IBIEC rates obtained with random and channeled incident beams (Azevedo et al., 2002). In this study the recrystallisation rates of both surface and buried amorphous layers were studied with high resolution by *in situ* time resolved reflectivity (TRR) and *ex situ* RBS analysis.

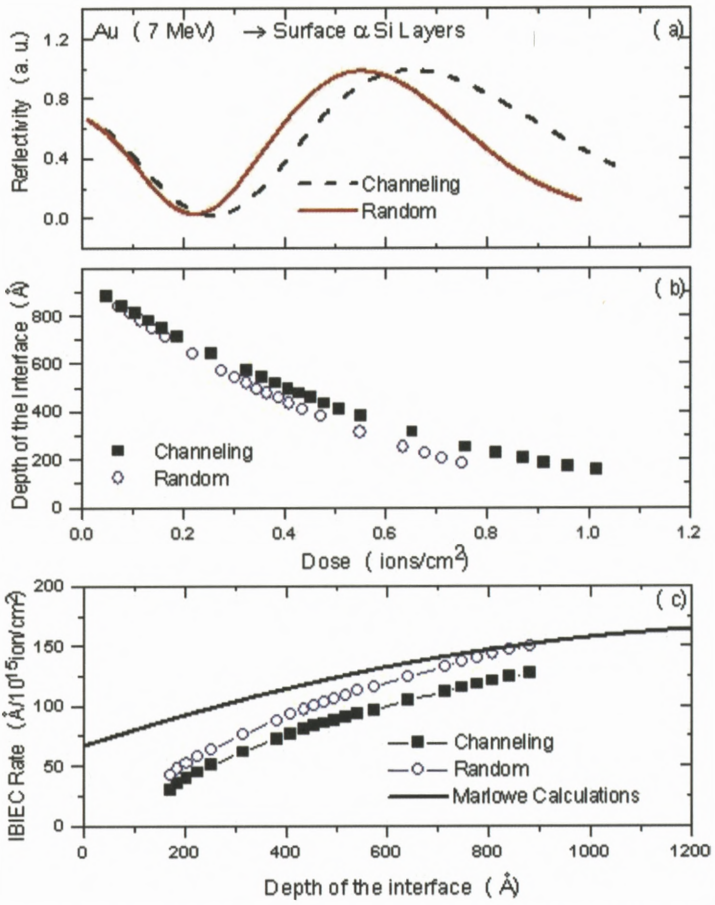

Figure 14. (a) Experimental reflectivity traces, as a function of dose, for 7 MeV Au ions irradiating a surface amorphous layer in silicon. The solid and dashed lines correspond to the random and channeling irradiations, respectively. (b) Depth of the interface as a function of the ion dose. (c) IBIEC rates for channeling (solid symbols) and random (open symbols) cases as a function of the interface depth. The solid line corresponds to MARLOWE calculations for the number of vacancies produced per ion per Å at the interface. After Azevedo et al. (2002).

In Figure 14, we present the results for surface amorphous layers in silicon irradiated under both random and channeling conditions (Azevedo et al., 2002). The experimental TRR traces for random (dashed line) and channeling (solid line) cases are plotted in panel (a). Note that for TRR from silicon using a 6328 Å laser, every 330 Å traversed by the interface corresponds to an oscillation between a maximum and a minimum of the reflectivity. Our results clearly indicate a reduc-

tion of the recrystallisation rate under channeling bombardment. This difference can be better appreciated by an examination of panels (b) and (c), where we plot, respectively, the interface depth as a function of the irradiation dose and the IBIEC rate as a function of the interface depth. These curves indicate that the magnitude of the channeling effect on interface motion is quite small in this case. For example, the maximum difference in the interface depths is of the order of 80 Å, whereas the IBIEC rate for channeling implants is only 20% smaller than the rate observed for random implants.

Unlike the results presented above, in previous measurements of IBIEC induced by 1.5 MeV Ne^+ (Williams et al., 1985a, 1985b) and 2.0 MeV C^+ (Williams et al., 2000) (see Figure 13) in samples consisting of an amorphous silicon surface layer, no channeling effect was observed. The lack of channeling effect was interpreted by Williams et al. (1985a) as evidence that displacements produced exactly at the interface were responsible for IBIEC. However, in these experiments the interface movement was monitored by RBS/channeling with alpha particles with energies between 1.5 and 1.8 MeV. Hence, limited depth resolution (even in the glancing angle backscattering geometry) of RBS (see Figure 13), means that RBS will not detect 20% reduced IBIEC growth under channeling conditions when this difference is of the order of the depth resolution.

In Figure 15, we present results of IBIEC for buried amorphous layers in silicon (Azevedo et al., 2002). In this case, the simultaneous movement of two amorphous-crystalline interfaces produces complicated patterns on the TRR traces, making their interpretation less evident than in the case of surface amorphous layers. For the sake of clarity, we only present IBIEC results extracted from RBS analysis of samples irradiated with increasingly higher doses. Panel (a) displays the RBS spectra for the buried layer before irradiation (solid line) and after 3×10^{15} Au/cm^2 random and channeling bombardments (squares and circles, respectively). Again, a clear channeling effect is observed. This difference is better quantified by an inspection of panel (b), where we plot the position of the amorphous-crystal interfaces as a function of the ion dose. It is apparent in this figure that the deeper interface (circles) advances at the same rate (281 ± 10 Å and 274 ± 14 Å per 10^{15} ions cm^{-2}) for channeling and random implants, respectively. However, the shallower interface (squares) advances much faster in random irradiations than in channeling cases (262 ± 10 Å and 124 ± 5 Å per 10^{15} ions cm^{-2}, respectively). A similar channeling effect was reported by Linnros and Hólmen (1986) for IBIEC in buried layers induced by 300 keV N and Ne beams and by Williams et al. (2000) in experiments with a 2 MeV C beam.

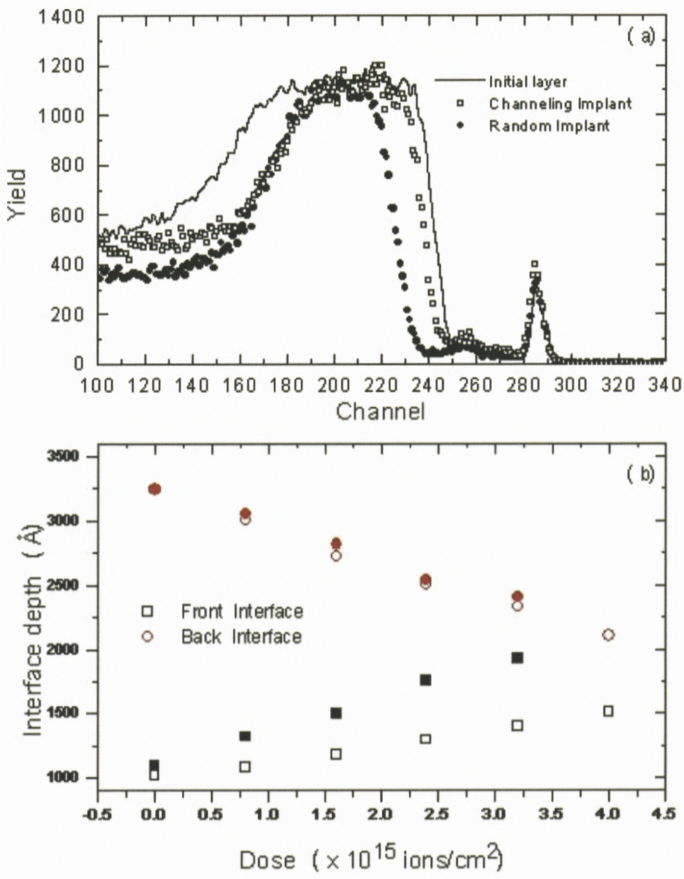

Figure 15. (a) RBS spectra for a buried amorphous layer irradiated with 1.6×10^{15} Au cm^{-2}. The solid line is the spectrum for the buried layer before the irradiation. Symbols (squares and circles) correspond to the random and channeling irradiations, respectively. (b) Position of the interfaces as a function of dose. Open and solid symbols correspond to channeling and random irradiations, respectively. After Azevedo et al. (2002).

4.2. Comparison with Simulations

The IBIEC growth data presented above are now compared with the results of computer simulations of collision cascades (atomic displacements). For the simulations, all displacements (point defects), both in random and channeled alignments, were calculated with the aid of the MARLOWE code (Robinson and Torrens, 1974; Robinson, 1990). MARLOWE has been specifically developed for the simulation of atomic displacements in both amorphous and crystalline

solids. The code is based on the binary collision approximation (BCA) (Azevedo et al., 1999) to construct particle trajectories. The atomic scattering is governed by screened potentials, such as ZBL (Ziegler et al., 1985) and Molière (1947). Thermal vibrations are simulated by a random gaussian distribution of the lattice atoms around their equilibrium positions, with amplitude given by the Debye–Waller (Eckstein, 1991) model. In the simulations performed here, we have used version 13c of the MARLOWE (Robinson, 1990) code with a ZBL potential to describe the Au-Si and Si-Si interactions and 490 K for the value of the silicon Debye temperature, in accordance with the results of references (Azevedo et al., 1999; Dygo et al., 1992; Hobler et al., 1996).

Figure 16a displays the result of MARLOWE calculations for a 300 Å surface layer (Azevedo et al., 2002). A reduction in the number of vacancies produced per ion per Å (η) in the crystalline region is apparent, even for random bombardments. This feature can be explained as follows. Even though the nuclear energy dissipation occurs mainly in cascades initiated by high energy primary knock ons, the average energy transferred to a silicon target atom by 7 MeV Au ions is of the order of 0.5 keV only. Such low energy primary knock-ons have a large critical angle for channelling (of the order of several degrees) and hence the number of displacement collisions that they initiate in crystalline silicon is less than in amorphous silicon. This explains the reduction of η in the crystalline region, even for a random orientation of the beam. Additional simulations show that the value of η in the crystalline region (Figure 16a) corresponds to the value predicted by MARLOWE for a random irradiation in a crystalline target without a surface amorphous layer. Furthermore, when the Au beam is aligned with the $\langle 100 \rangle$ channeling direction in the underlying crystalline silicon, the number of vacancies generated at the interface and within the crystalline region is lower than for the random case. Its also interesting to note that, under channeling conditions, η is slightly reduced in the amorphous region, in comparison with random implants. Simulations show that this difference is reduced as the thickness of the amorphous layer is increased. This latter observation implies that cascades initiated in the crystalline region can produce displacements in the amorphous region, even though it is closer to the surface. A comparison of the experimentally observed $\sim$20% lower IBIEC rate for channeling beam alignment with the simulation data in Figure 16a, indicates that the scale of difference between channeled and random IBIEC rates is most consistent with vacancies produced precisely at the interface than with vacancies produced in the amorphous or crystalline regions.

Figure 16b displays the results of simulations for a buried layer in silicon with the same configuration as those we have used in our experiments. It is apparent that, for channeling implants, η is strongly reduced in the crystalline region near to

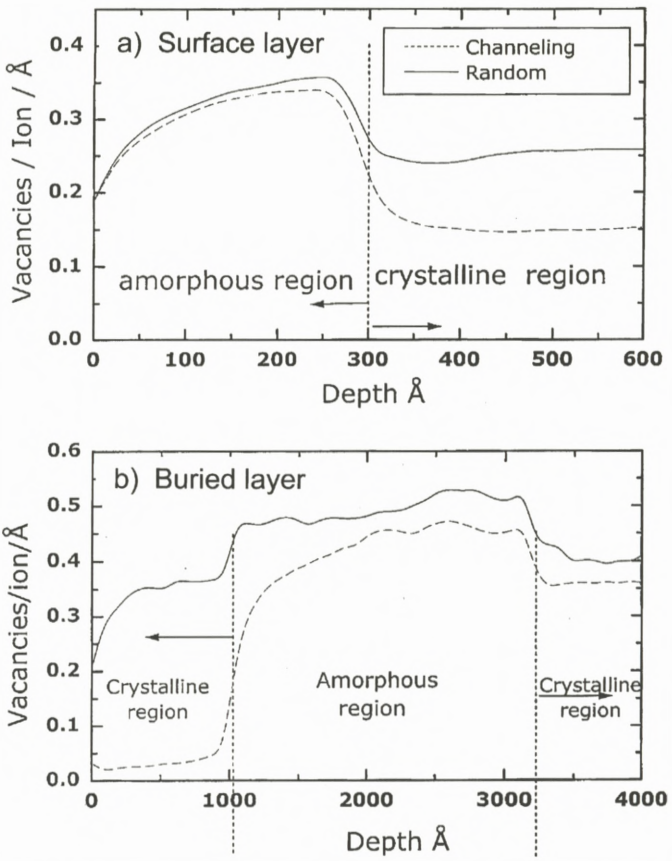

Figure 16. Point defect profiles calculated with MARLOWE for channeling (dashed lines) and random irradiations (solid lines) in surface and buried amorphous layers shown in upper and lower panels, respectively. After Azevedo et al. (2002).

the surface, as one might expect. However, only a small reduction of η is observed after the deeper interface. These features can be explained by the same arguments utilised above to explain the results for surface layers. Therefore, the most important feature displayed in Figure 16b is that, assuming IBIEC is controlled by point defects generated at the amorphous-crystalline interface, MARLOWE predicts a large channeling effect at the front interface and a very small effect at the back interface, consistent with our experimental data for a buried amorphous layer. Furthermore, the scale of the experimental IBIEC reduction under channeling conditions (~50%) appears to best correlate with the relative num-

ber of vacancies produced at the front interface (Figure 16b), rather than in the amorphous-crystalline regions, as we discuss below.

The solid line in Figure 14c corresponds to the predictions of MARLOWE for η at the amorphous-crystalline interface. As can be readily observed, η drops quickly as the interface approaches the surface. This feature is a result of the reduction in the cascade density for shallow depths and the experimental IBIEC rates (γ) display a similar trend. However, γ is clearly steeper than η when the thickness of the amorphous layer is smaller than about 500 Å. The same dependence of γ with the thickness of the amorphous layer has been observed in previous experiments with 5 MeV Au (Kinomura et al., 2001) and 7 MeV I (Heera et al., 1995) ions, and this effect was attributed to diffusion of point defects in the amorphous layer. However, this proposal is not consistent with our channeling data, particularly the large front interface effect. We suggest that other effects could be responsible for this behaviour and for the discrepancies with MARLOWE predictions. For example, it has been demonstrated previously that the IBIEC rate is affected by defect interactions within individual cascades (i.e. the cascade density) as well as by defect interactions between cascades (Kinomura et al., 1999). This suggests that the observed thickness dependence of γ could be related to a distortion of the point defect profiles at the interface when the interface is close to the surface, due to cascade density differences and cascade interactions, rather than being related to point defect diffusion. Furthermore, Kinomura et al. (2001) have demonstrated that oxygen impurity atoms recoiling from the surface native oxide contribute partially to a decrease in the IBIEC rates close to the surface. Therefore, the comparison of MARLOWE predictions with the experimental results for shallow surface amorphous layers is not straightforward.

In order to more precisely determine the origin of the defects that control IBIEC, we will compare the ratio between the channeling and random IBIEC rates ($\Gamma = \gamma_c/\gamma_r$) to the ratio between the corresponding simulated defect profiles. Proceeding in this way, in particular for shallow surface layers, the chemical contamination and cascade interaction effects are cancelled out. As indicated earlier, an examination of our simulation results indicate that the observed channeling effect can be better quantitatively explained by assuming that defects produced at the interface control the IBIEC process. From our results for amorphous layers, we can exclude defects coming from the amorphous region since the simulations show that η is reduced by only $\sim$5% (surface layer) or 10% (buried layer) in that region while the observed channeling effect is of the order of 20% and 50% for surface and buried layers, respectively. On the other hand, the simulations for a buried layer indicate that defects produced in the crystalline region are not likely to be participating in IBIEC, since the simulations predict a 90% reduction of

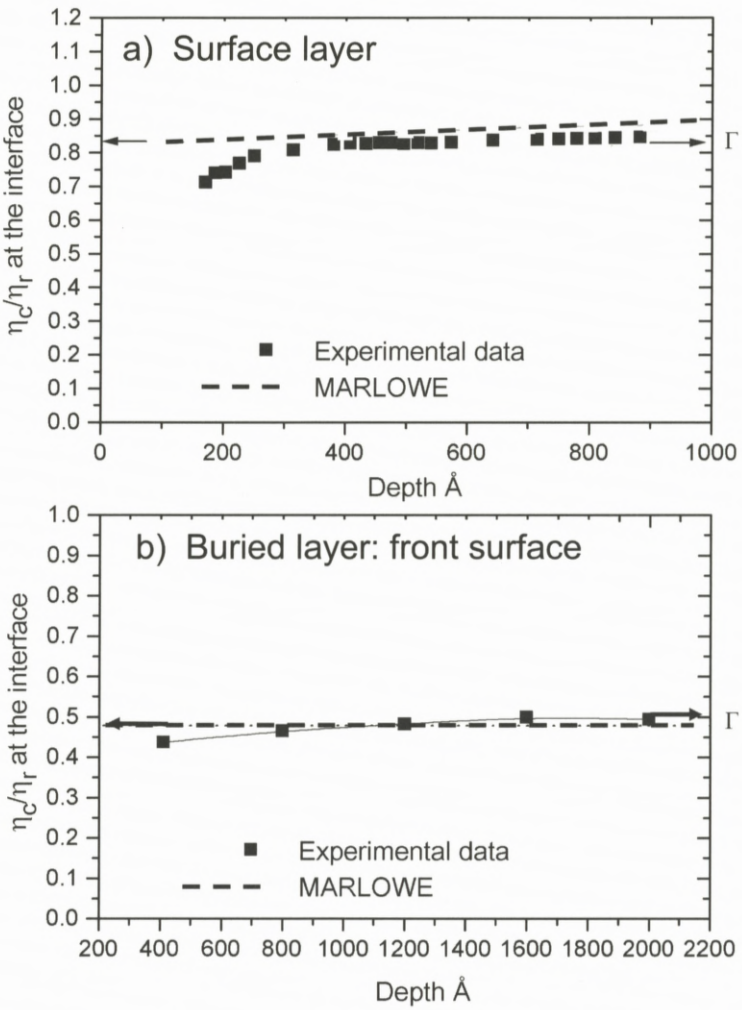

Figure 17. Ratio of η_c/η_r between the experimental growth rates and the calculated displacements at the interfaces. Upper and lower panels depict results for surface and buried layers, respectively. Adapted from Azevedo et al. (2002).

η in the crystalline region close to the surface, while the observed channeling effect is of the order of 50%. In Figure 17, adapted from the data of Azevedo et al. (2002), we present the ratio Γ between the experimentally determined IBIEC rates under channeling and random conditions, compared to the ratio between the corresponding calculated defect levels (η_c/η_r) at the amorphous-crystalline

interface. As can be observed, the magnitude of the experimentally determined Γ is in good agreement with MARLOWE calculations for the ratio η_c/η_r. Therefore, combining all experimental and simulation comparisons, we conclude that defects produced at or very near the amorphous-crystalline interfaces are most likely to control IBIEC. Although the precise interface defect controlling IBIEC is not revealed by these results, the data is consistent with any crystallisation-enabling defect, such as a kink, produced at the interface by the ion beam.

5. Some Answered and Unanswered Questions

In terms of disorder, defect generation and amorphisation in silicon, a reasonable qualitative description of observed phenomena exists. For example, for a given ion at fixed fluence and flux (or temperature and flux), it is possible to model the observed build up of disorder with temperature (fluence). It is also possible to model the accumulation of interstitial-based defects, located mostly near the ion's end-of-range, that evolve into line defects and loops on annealing. In contrast, a vacancy excess exists towards surface, evolving into voids on annealing. It is also known that mobile defects are gettered to and trapped at pre-existing defects and at the surface both during irradiation at elevated temperature (leading to the local nucleation of amorphous layers) and during subsequent annealing (leading to defect accumulation away from the depth of the maximum in nuclear stopping power).

The key deficiency in our understanding of ion-induced disorder and amorphisation relates to the lack of availability of quantitative models (with predictability) to treat defect accumulation and evolution. Available quantitative models (e.g. kinetic Monte Carlo and MD simulations) are only partially successful at best at describing observations when dynamic annealing is important during irradiation. Similarly, models of defect evolution on annealing are also not quantitative in most cases, since they rely on a precise knowledge of little-known defect parameters such as concentration and activation energies for defect formation, migration and annihilation. Defect gettering to and trapping at other defects can often control disorder accumulation and amorphisation behaviour but few data and models exist to describe such processes. Finally, a major unknown involves how cascade energy density determines defect generation and residual disorder. For example, amorphisation is not scalable with ion mass and flux and appears to depend in a complex manner on cascade density as well as instantaneous and average defect generation rates.

In terms of ion beam induced epitaxial crystallisation, there are several features of the phenomenon that are known and work well. For example, there is

now strong evidence that the process is driven by atomic displacements at the amorphous-crystalline interface. The Marlowe simulation code that calculates atomic displacements for random and channeled ion irradiations can successfully predict the effect of channeling on IBIEC growth (ie linear scaling of growth rate with atomic displacements at the interface) for individual ion species. The excellent agreement of simulations with experiment, suggests that individual values used in the simulations are accurate, such as nuclear energy deposition, atomic displacement distributions for random and aligned irradiations, as well as multiple scattering through amorphous layers and associated angular spreads.

The issue that is not understood at all well is the effect of cascade density on IBIEC. For example, the dependence of IBIEC on ion mass has no understandable scaling and the trends are the exact opposite to those for the ion mass dependence observed for amorphisation. Finally, if the driving force for IBIEC is atomic displacements at the amorphous-crystalline interface then the interface "defects" that mediate IBIEC are not known.

References

Atwater H.A., Thompson C.V. and Smith H.I. (1988): Interface-limited grain-boundary motion during ion-bombardment. Phys Rev Lett **60**, 112–115

Azevedo G. de M., Martini J.C., Behar M. and Grande P.L. (1999): Depth profiles and amorphization behavior under channeling condutions for low energy Bi ions implanted into Si crystals. Nucl Instrum Meth B **149**, 301–311

Azevedo G. de M., Williams J.S., Young I.M., Conway M.J. and Kinomura A. (2002): In-situ measurements of the channeling dependence of ion-beam-induced recrystallization in silicon. Nucl Instrum Meth B **190**, 772–776

Cannavo S., La Ferla A., Rimini E., Ferla G. and Gandolfi L. (1986): Ion-beam annealing during high-current density implants of phosphorous into silicon. J Appl Phys **59**, 4038–4042

Christel L.A., Gibbons J.F. and Sigmon T.W. (1981): Displacement criterion for amorphization of silicon during ion-implantation. J Appl Phys **52**, 7143–7146

Dennis J.R. and Hale E.B. (1978): Crystalline to amorphous transformation in ion-implanted silicon – Composite model. J Appl Phys **49**, 1119–1127

Dygo A., Smoulders P.J.M. and Boerma D.O. (1992): Simulation analysis of ion channeling spectra – Thermal vibrational amplitude in Si. Nucl Instrum Meth B **64**, 701–705

Eckstein W. (1991) Computer Simulation of Ion-Solid Interaction. Springer, Berlin

Elliman R.G., Williams J.S., Maher D.M. and Brown W.L. (1986): Kinetics, microstructure and mechanisms of ion beam induced epitaxial crystallisation of semiconductors. Mat Res Soc Symp Proc **51**, 319

Elliman R.G., Williams J.S., Brown W.L., Leiberich A., Maher D.A. and Knoell R.V. (1987): Ion-beam-induced crystallization and amorphization of silicon. Nucl Instrum Meth Phys Res B **19–20**, 435–442

Elliman R.G., Linnros J. and Brown W.L. (1988): Amorphization of silicon by ion irradiation: The role of the divacancy. Mat Res Soc Symp Proc **100**, 363

Goldberg R.D. (1995): Ion-induced disordering processes in Silicon. PhD Thesis, University of Melbourne

Goldberg R.D., Elliman R.G. and Williams J.S. (1993): The kinetics of self ion amorphization of silicon. Nucl Instrum Meth Phys Res B **80–81**, 596–599

Goldberg R.D., Williams J.S. and Elliman R.G. (1995): Amorphization of silicon by elevated temperature ion irradiation. Nucl Instrum Meth Phys Res B **106**, 242–247

Goldberg R.D., Williams J.S. and Elliman R.G. (1999): Preferential amorphization at extended defects of self-ion-irradiated silicon. Phys Rev Lett **82**, 771–774

Heera V., Henkel T., Kögler R. and Skorupa W. (1995): Evidence for diffusion-limited kinetics of ion-beam-induced epitaxial crystallization in silicon. Phys Rev B **52**, 15776–15784

Heera V., Kögler R., Skorupa W. and Grötzschel R. (1993): Dose-rate dependence of the ion-beam-induced epitaxial crystallization in silicon. Nucl Instrum Meth Phys Res B **80–81**, 538–542

Hobler G., Simionescu A., Palmetshofer L., Jahnel F., Von Criegern R., Tian C. and Stingeder G. (1996): Verification of models for the simulation of boron implantation into crystalline silicon. J Vac Sci Technol B **14**, 272–277

Howe L.M. and Rainville M.H. (1987): Heavy-ion damage in silicon and germanium. Nucl Instrum Meth Phys Res B **19–20**, 61–66

Jackson K.A. (1988): A defect model for ion-induced crystallization and amorphization. J Mater Res **3**, 1218–1226

Kachurin G.A. (1980): Mechanism of ion-stimulated crystallization of amorphous layers. Sov Phys Semicond **14**, 461–462

Kennedy E.F., Csepregi L., Mayer J.W. and Sigmon T.W. (1977): Influence of 0-16, C-12, N-14 and Noble-gases on crystallization of amorphous Si layers. J Appl Phys **48**, 4241–4246

Kinomura A., Williams J.S. and Fuji K. (1999): Mass effects on regrowth rates and activation energies of solid phase epitaxy induced by ion beams in Silicon. Phys Rev B **59**, 15214–15224

Kinomura A., Chayahara A., Tsubouchi N., Heck C., Horino Y. and Miyagawa Y. (2001): Movement of defects and atoms during ion beam induced crystallization. Nucl Instrum Meth B **175–177**, 319–323

Linnros J and Hólmen G. (1986): Channeling dependence of ion-beam-induced epitaxial recrystallization in silicon. J Appl Phys **59**, 1513–1517

Linnros J., Hólmen G. and Svensson B. (1985): Proportionality between ion-beam-induced epitaxial regrowth in silicon and nuclear-energy deposition. Phys Rev B **32**, 2770–2777

Linnros J., Brown W.L. and Elliman R.G. (1988a): Pulsed ion beam induced crystallization and amorphization of silicon. Mat Res Soc Symp Proc **100**, 369

Linnros J., Elliman R.G. and Brown W.L. (1988b): Divacancy control of the balance between ion-beam-induced epitaxial crystallization and amorphization in silicon. J Mater Res **3**, 1208–1211

Lulli G., Merli P.G. and Vittori Antisari M. (1987): Solid-phase epitaxy of amorphous-silicon induced by electron irradiation at room-temperature. Phys Rev B **36**, 8038–8042

Lulli G., Merli P.G. and Vittori Antisari M. (1988): Solid phase epitaxy of implanted silicon by electron irradiation at room temperature. Mat Res Soc Symp Proc **100**, 375

Maher D.M., Elliman R.G., Linnros J., Williams J.S., Knoell R.V. and Brown W.L. (1987): Epitaxial crystallization of amorphous silicon layers under ion irradiation: Orientation dependence. Mat Res Soc Symp Proc **93**, 87

Molière G. (1947): Theorie der Streuung schneller geladener Teilchen, 1. Z Naturforsch Sect A-A J Phys Sci **2**, 133–145

Morehead F.F. Jr., Crowder B.L. and Title R.S. (1970): Formation of amorphous Si by ion bombardment as a function of ion, temperature and dose. Bull Amer Phys Soc **15**, 396

Mosley L.E. and Paesler M.A. (1984): Electronic effect on crystallization growth velocities produced by charged dangling bonds in A-Si. Appl Phys Lett **45**, 86–88

Nakata J., Takahashi M. and Kajiyama K. (1981): Insitu self ion-beam annealing of damage in Si during high-energy (0.53 MEV–2.56 MEV As^+ ion-implantation. Jpn J Appl Phys **20**, 2211–2221

Olson G.L. and Roth R.A. (1988): Kinetics of solid phase crystallization in amorphous silicon. Mat Sci Rep **3**, 1

Poate J.M., Jacobson D.C., Williams J.S., Elliman R.G. and Boerma D.O. (1987): Diffusion of implanted impurities in amorphous Si. Nucl Instrum Meth B **19–20**, 480–483

Poate J.M., Linnros J., Priolo F., Jacobson D.C., Batstone J.L. and Thompson M.O. (1988): Nonequilibrium segregation and trapping phenomena during ion-induced crystallization of amorphous Si. Phys Rev Lett **60**, 1322–1325

Priolo F. and Rimini E. (1990): Ion-beam-induced epitaxial crystallization and amorphization in silicon. Mat Sci Rep **5**, 319

Priolo F., Spinella C., La Ferla A., Battaglia A., Rimini E., La Ferla G., Carnera A. and Gasparotto A. (1989a): Ion-assisted regrowth of deposited Si layers: Mechanism and morphology. Mat Res Soc Symp Proc **128**, 563

Priolo F., Spinella C., La Ferla A., Rimini E. and La Ferla G. (1989b): Ion-assisted recrystallization of amorphous silicon. Appl Surf Sci **43**, 178–186

Priolo F., Spinella C. and Rimini E. (1990): Phenomenological description of ion-beam-induced epitaxial crystallization of amorphous-silicon. Phys Rev B **41**, 5235–5242

Robinson M.T. (1990): The temporal development of collision cascades in the binary-collision approximation. Nucl Instrum Meth B **48**, 408–413

Robinson M.T. and Torrens I.M. (1974): Computer-simulation of atomic-displacement cascades in solids in binary-collision approximation. Phys Rev B **9**, 5008–5024

Spaepen F. and Turnbull D. (1982): Crystallization processes. In: Poate J.M. and Mayer J.W. (Eds), Laser Annealing of Semiconductors. Academic Press, New York, p 15

Swanson M.L. and Quennevi A.F. (1971): Effect of compressional plastic deformation on superconducting transition temperature of indium and tin. Scripta Metall **5**, 1081

Takeda S., Kohyama M. and Ibe (1994): Interstitial defects on (113) in Si and Ge – Line defect configuration incorporated with a self interstitial atom chain. K Phil Mag A **70**, 287–312

Vook F.L. and Stein H.J. (1969): Relation of neutron to ion damage annealing in Si and Ge. Rad Eff **2**, 23

Williams J.S. (1992): Subsurface processing of electronic materials assisted by atomic displacements. MRS Bull **17**, 47–51

Williams J.S. (1994): Ion induced damage and dynamic annealing processes. Trans Mat Res Soc Jpn **17**, 417

Williams J.S. (1998): Unpublished article

Williams J.S. and Elliman R.G. (1983): The role of electronic processes in epitaxial recrystallisation of amorphous semiconductors. Phys Rev Lett **51**, 1069–1072

Williams J.S., Elliman R.G., Brown W.L. and Seidel T.E. (1985a): Beam induced crystallisation of silicon. Mat Res Soc Symp Proc **37**, 127

Williams J.S., Elliman R.G., Brown W.L. and Seidel T.E. (1985b): The dominant influence of beam induced interface rearrangements on solid phase epitaxial crystallisation of amorphous silicon. Phys Rev Lett **55**, 1482–1485

Williams J.S., Goldberg R.D., Petravic M. and Rao Z. (1994a): Phase transformations and compound formation during ion irradiation of material. Nucl Instrum Meth Phys Res B **84**, 199–203

Williams J.S., Tan H.H., Goldberg R.D., Brown R.A. and Jagadish C. (1994b): Dynamic annealing & amorphous phase formation in Si, GaAs, AlGaAs under ion irradiation. Mat Res Soc Symp Proc **316**, 15

Williams J.S., Young I.M. and Conway M.J. (2000): Ion-beam-induced epitaxy experiments in silicon under channeling and random alignments. Nucl Instrum Meth Phys Res B **161–163**, 505–509

Ziegler J.F., Biersack J.P. and Littmark U. (1985): The Stopping and Range of Ions in Solids. Pergamon, New York

Experimental Phenomena and Thermal Spike Model Description of Ion Tracks in Amorphisable Inorganic Insulators

M. Toulemonde[1,*], W. Assmann[2], C. Dufour[3], A. Meftah[4], F. Studer[5] and C. Trautmann[6]

[1]CIRIL, Laboratoire commun CEA, CNRS, ENSICAEN, UCBN
Bd H. Becquerel, BP 5133, 14070 Caen Cedex 5, France
[2]Departement of Physics, University of Munich
85748 Garching, Germany
[3]SIFCOM, Laboratoire commun CNRS, ENSICAEN, UCBN
6 Bd Maréchal Juin, 14050 Caen Cedex, France
[4]LRCPSI, Université de Skikda
BP 26, Route d'El-Hadaiek, 21000 Skikda, Algeria
[5]CRISMAT, Laboratoire commun CNRS, ENSICAEN, UCBN
6 Bd Maréchal Juin, 14050 Caen Cedex, France
[6]Materialforschung/GSI, Planckstr. 1, 64291 Darmstadt, Germany

Abstract

Experimental investigations of ion tracks produced with energetic heavy projectiles in the electronic energy loss regime are reviewed. Focusing on amorphisable insulators as target material, we present an overview of track phenomena such as the dependence of the track size on energy loss and beam velocity, the critical energy loss for track formation, and damage morphology along the ion tracks. Different characterization techniques for track dimensions are compared including direct, e.g. microscopic observations, as well as quantification of beam-induced damage. In the second part, we present a theoretical description of track formation based on an inelastic thermal spike model. This thermodynamic approach combines the initial size of the energy deposition with the subsequent diffusion process

* E-mail: toulemonde@ganil.fr

in the electronic subsystem of the target. The track size, resulting from the quench of a molten phase, is determined by the energy density deposited on the atoms around the ion path. Finally, we discuss the general validity of this model and its suitability to describe tracks in non-amorphisable insulators.

Contents

1 Introduction **264**

2 Electronic Energy Loss of Swift Ions and Energy Density **265**

3 Quantification of Damage Cross Section and Track Radius **268**
3.1 Determination of Damage Cross Sections 268
3.2 Direct Determination of Track Radii 270

4 Tracks in Amorphisable Insulators **272**
4.1 Damage Cross Sections 272
4.2 Comparison of Track Radii from Direct Measurements 273
4.3 Damage Morphology 273
4.4 Comparison of Damage Cross Sections and Track Radii 274
4.5 Velocity Effect 276
4.6 Summary of Track Observations in Amorphisable Insulators 278

5 Model Calculations with the Inelastic Thermal Spike **279**
5.1 Introduction 279
5.2 The Inelastic Thermal Spike Model 279
5.3 Determination of the Electron Mean Free Path 281
5.4 Effect of Beam Velocity 282
5.5 Thermal Spike Description of Electronic Sputtering of Surface Atoms . . 283

6 Conclusions **285**
6.1 Amorphisable Materials 285
6.2 Unsolved Problems 286

References **287**

1. Introduction

When swift heavy ions penetrate matter they create electronic excitations. In many solids, this process results in the formation of cylindrical damage zones, so-called *ion tracks*. Since their discovery in the late 50s of the last century (Young, 1958; Silk and Barnes, 1959), the understanding of track formation has

largely improved mainly due to dedicated irradiation experiments at large accelerator facilities for heavy ions developed in the 80s. Ion-induced material modifications and track studies were performed for crystalline (Iwase et al., 1987; Dufour et al., 1993b; Dunlop et al., 1994) as well as amorphous metals (Klaumünzer et al., 1986; Hou et al., 1990; Audouard et al., 1991), semiconductors (Levalois et al., 1992; Wesch et al., 2004; Szenes et al., 2002), ionic insulators (Schwartz et al., 1998; Trautmann et al., 2000a), and numerous oxide materials (Fuchs et al., 1987; Studer and Toulemonde, 1992; Meftah et al., 2005). Although a large amount of experimental data is now available, several important issues are still not clarified such as damage and track formation in semiconductors (Wesch et al., 2004), the different response of amorphisable (Toulemonde et al., 1987; Toulemonde and Studer, 1988) and non-amorphisable insulators such as ionic crystals (Khalfaoui et al., 2005; Trautmann et al., 2000a), or the role of internal and external pressure (Trautmann et al., 2000b; Glasmacher et al., 2006; Rizza et al., 2006). Finally, there is the open question, which model (Chadderton and Montagu-Pollock, 1963; Seiberling et al., 1980; Fleischer et al., 1975; Bringa and Johnson, 2002) is suitable to describe existing track phenomena.

The aim of this paper is not to present a complete overview of the present track knowledge for all different material classes, but we rather restrict the discussion to inorganic amorphisable insulators and consider the following two aspects: (1) Observation of track radii and damage cross sections and (2) the description by the inelastic thermal spike model. In the first section we discuss the energy deposition of energetic projectiles in a solid, in particular the density of the energy initially transferred to the target electrons. Section 3 describes experimental methods typically used to determine track radii and the electronic energy loss threshold for damage creation. The important role of the velocity of the incident ion on those two parameters is indicated. Section 4 gives a summary of the specific signatures and the present knowledge of tracks in amorphisable insulators. Section 5 shows how different aspects of track formation such as track size, formation threshold, and the projectile velocity effect are described by the inelastic thermal spike model. The conclusions finally resume the main features observed in amorphisable materials and point out questions concerning the specific response of non-amorphisable materials.

2. Electronic Energy Loss of Swift Ions and Energy Density

When a swift heavy ion of MeV to GeV energy penetrates a solid, the slowing down process is dominated by interactions with the target electrons (electronic energy loss) whereas slower projectiles of keV energy mainly undergo direct

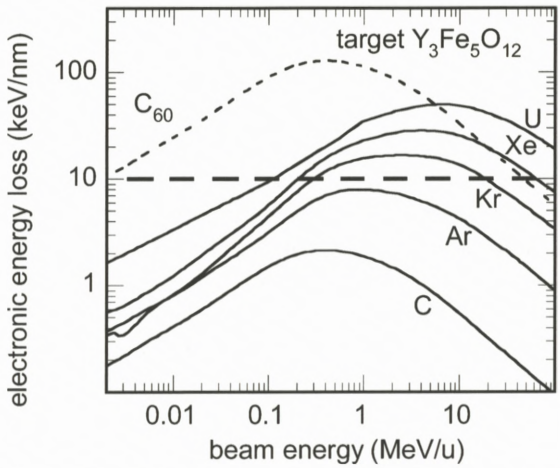

Figure 1. Electronic energy loss (S_e) *versus* specific energy for different monoatomic ions and for C_{60} cluster projectiles in $Y_3Fe_5O_{12}$ target as calculated with the SRIM2003 code (for energies below 0.1 MeV/u, these S_e values probably contain large uncertainties).

elastic collisions with the target atoms (nuclear energy loss). In the following we concentrate on specific aspects related to electronic stopping processes.

The electronic energy loss (S_e) depends on the charge state and the velocity of the projectile (see contribution by Sigmund, this volume) (Biersack and Haggmark, 1980; Huber et al., 1990; Sigmund and Schinner, 2002) typically given as specific energy, E_p, in MeV per nucleon (MeV/u). When an accelerated particle moves through a solid, it strips off those orbital electrons that are slower than the projectile velocity and acquires an equilibrium charge state Z_p^*. Most accelerator facilities deliver ions of charge states lower than Z_p^*, and the energy loss at the sample surface thus differs from tabulated S_e values given e.g. by the SRIM code (Ziegler, 1999). Experimentally, the equilibrium charge state can easily be obtained by inserting a thin stripper foil (e.g. carbon) in front of the target (Betz, 1972).

Figure 1 shows the electronic energy loss as a function of specific energy for different projectiles and yttrium iron garnet as target. For a given ion, the maximum energy loss is obtained at the so-called Bragg peak (at ~0.5 MeV/u for carbon and ~5 MeV/u for uranium). Using cluster beams of C_{60} projectiles, S_e values even higher than for uranium ions can be obtained, because the energy loss of a C_{60} cluster is in good approximation equal to the sum of the electronic energy loss of the 60 carbon constituents (Baudin et al., 1994).

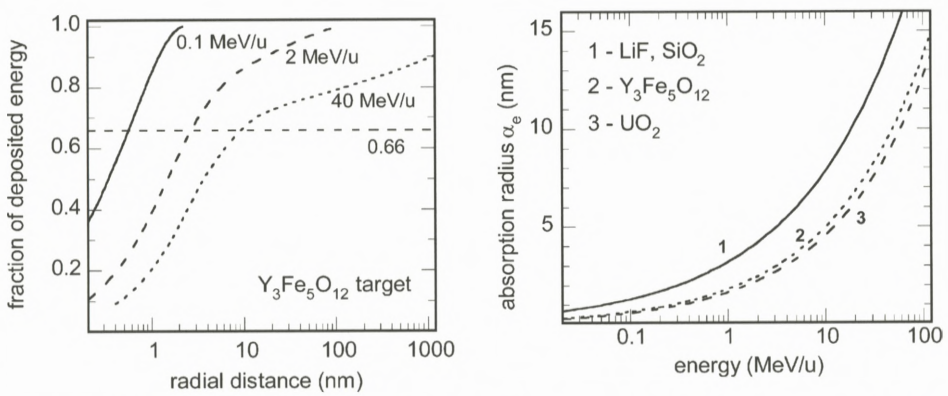

Figure 2. Left: Fraction of energy deposited on the electrons of a $Y_3Fe_5O_{12}$ target as a function of the radial distance from the ion trajectory. The calculations assume cylindrical geometry and are based on Monte Carlo simulations. Right: Absorption radius α_e defined as a cylinder radius in which 0.66 of the electronic energy loss is deposited as a function of beam velocity for different insulators.

Figure 1 also shows that a certain S_e value can be reached for a given ion either below or above the Bragg peak (see dashed line, e.g., Xe at 0.2 MeV/u and 60 MeV/u) or for different ion species (e.g., Kr at 17 MeV/u and Xe at 60 MeV/u). Although the nominal S_e is the same, there is a significant difference given by the deposited energy density ("velocity effect"). The target volume in which S_e is deposited depends on the maximum energy transfer to electrons which increases with beam velocity. The relative radial distribution of the energy, deposited on the electrons, is estimated by means of Monte Carlo simulations (Waligorski et al., 1986) that follow the evolution of the energy in the electron cascades (assuming free electron scattering) as a function of space ($\sim$1 μm) and time ($\sim 10^{-15}$ to 10^{-14} s) (Gervais and Bouffard, 1994). Figure 2 (left) shows the energy density for different beam energies *versus* the radial distance from the ion trajectory as calculated with an analytical formula derived from MC calculations. As criterion we defined an absorption radius α_e of a cylinder in which 0.66 of the electronic energy loss is stored on the target electrons. Larger ion velocities result in larger α_e values (Figure 2, left). High-velocity ions therefore spread their energy into a larger volume leading to a lower energy density. Figure 2 (right) presents α_e values *versus* beam energy for different materials. It should be noted that the extrapolation of the analytical formula of Waligorski et al. (1986) to low energies ($\alpha_e < 1$ nm) is questionable. In this regime new MC calculations are needed.

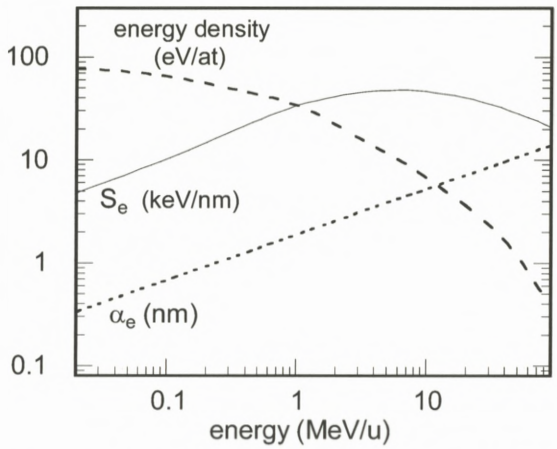

Figure 3. Electronic energy loss S_e (solid line), absorption radius α_e (dotted), and energy density (given in eV per atomic volume) (dashed) in the electronic system as a function of specific beam energy for a $Y_3Fe_5O_{12}$ target irradiated with U ions.

Combining the absorption radius α_e and the energy loss S_e allows us to determine the deposited energy density. Figure 3 illustrates the dependence of α_e, S_e, and the mean energy density of the electrons (S_e divided by $N_y \pi \alpha_e^2$, where N_y is the atomic density of the target) for the case of $Y_3Fe_5O_{12}$ target irradiated with U ions. In contrast to S_e, the energy density steadily increases with decreasing beam energy. If we presume that the energy density in the electronic subsystem is transferred to the lattice, low beam energies should allow significant atomic motion.

3. Quantification of Damage Cross Section and Track Radius

3.1. Determination of Damage Cross Sections

Material modifications induced by swift heavy ions can be investigated by many different techniques. Structural changes, e.g., can be examined by x-ray diffraction (Chailley et al., 1996; Hémon et al., 1997) and by Channelling Rutherford Backscattering (Figure 4 left) (Meftah et al., 1993). The creation of defects are studied by electrical resistivity measurements (Costantini et al., 1993), UV (ionic crystals; Schwartz et al., 1998) or IR (vitreous SiO_2; Busch et al., 1992) spectroscopy. In magnetic materials, the appearance of a paramagnetic phase (Figure 4 right) (Toulemonde et al., 1987) can be detected by Mössbauer spectrometry. Ion-induced volume changes (swelling) are quantified by surface profilometry

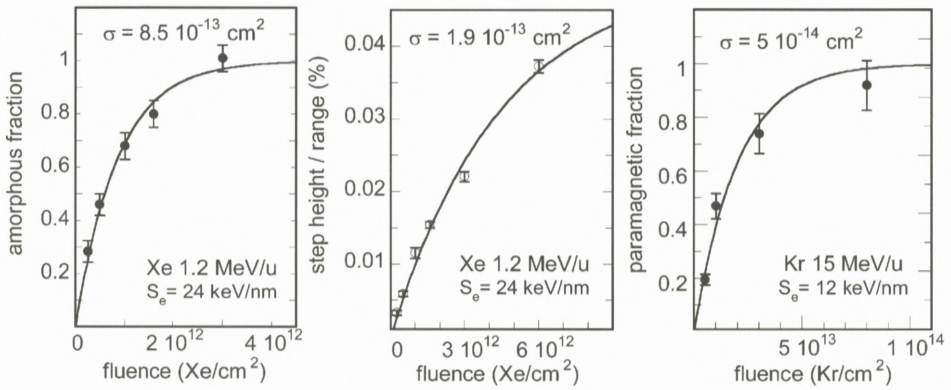

Figure 4. Evolution of special physical properties as a function of fluence for $Y_3Fe_5O_{12}$ targets exposed to Xe and Kr ions of different energy and electronic energy loss. Left: The amorphous fractions of ion-irradiated crystals are quantified by Channeling Rutherford Backscattering. Center: Step height of out-of-plane swelling normalized by the ion range as recorded by profilometry. Right: Fraction of ion-induced paramagnetic structure deduced from Mössbauer spectrometry.

(Figure 4 center) (Trautmann et al., 2002) and anisotropic growth by optical or electron microscopy (Benyagoub et al., 1992; Klaumünzer et al., 1986). Except for Channelling Rutherford Backscattering which probes the damage close to the surface and, thus, allows an assignment of the damage to a better defined S_e value (provided that the ion projectiles used are in equilibrium charge state (Toulemonde, 2006)), most of the techniques test bulk samples and thus associate property changes with an energy loss averaged along the entire track length.

Ion-induced material changes are typically studied as a function of the ion fluence. In the regime of well separated individual tracks, the observed parameter usually follows a linear function and evolves towards saturation at high fluences due to track overlapping. Figure 4 shows the evolution of disorder obtained by Channeling Rutherford Backscattering (left), out-of-plane swelling from profilometry (center), and the fraction of a paramagnetic phase from Mössbauer spectrometry (right) for a $Y_3Fe_5O_{12}$ target. Analyzing such a fluence evolution by a Poisson law that takes into account overlapping track regions, one can extract the damage cross section σ and also the radius of the tracks provided that the damage is continuous and of cylindrical geometry. With increasing S_e the damage cross section typically becomes larger (cf. Figure 4 right and left). The absolute value of σ may depend on the characterization technique (cf. Figure 4 left and center) and the kind of modification tested.

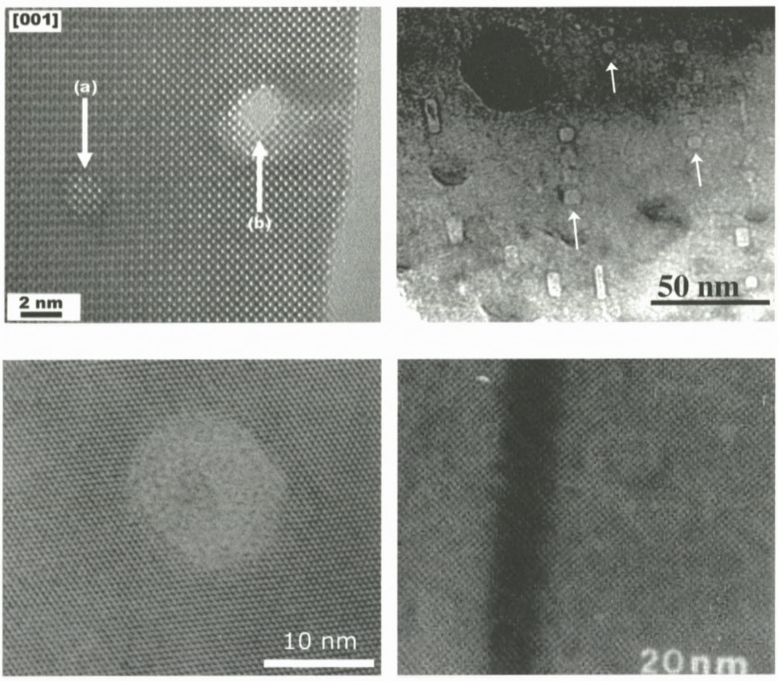

Figure 5. High-resolution transmission electron microscopy images of ion tracks in non-amorphisable (top) and amorphisable (bottom) insulators. Top left: Cross section of two tracks (a and b) in non-amorphisable SnO_2 irradiated with Cd ions (9 MeV/u) (Berthelot et al., 2000). Close to the border where the sample is extremely thin, the ion projectile created a hole (b). Top right: CaF_2 irradiated with Bi ions of 10 MeV/u. The arrows indicate the trajectories of non-continous facetted defect clusters (Khalfaoui et al., 2005). Bottom left: Cross section of a single track of a Pb ion in mica. The amorphous track zone is surrounded by the intact crystal matrix (Vetter et al., 1998). Bottom right: Continuous amorphous track region created along the trajectory of a Xe ion (~24 MeV/u) in $Y_3Fe_5O_{12}$ (Toulemonde and Studer, 1988).

3.2. Direct Determination of Track Radii

In the past, direct measurements of track radii were performed by visualizing tracks with Transmission Electron Microscopy (TEM) (Groult et al., 1988; Bursill and Braunshausen, 1990; Träholt et al., 1996) and scanning force microscopy (Ackermann et al., 1996; Müller et al., 2003; Khalfaoui et al., 2005; Thibaudau et al., 1991) or by applying small angle x-ray (or neutron) scattering (Albrecht et al., 1985; Schwartz et al., 1998; Saleh and Eyal, 2005).

The observation of individual tracks by TEM is limited to samples of small thickness (<~100 nm) which can be prepared either after or before the ir-

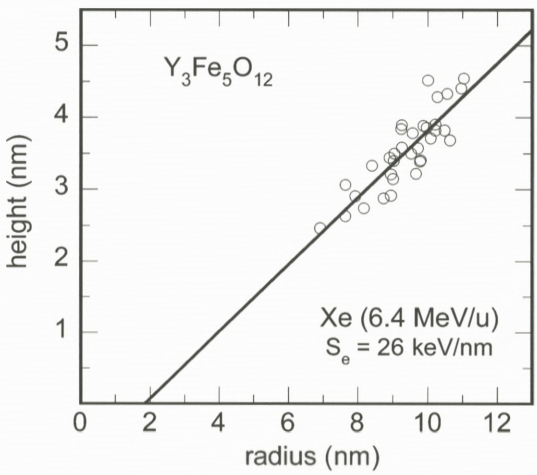

Figure 6. Height *versus* radius (half-width at half maximum) of hillocks on a $Y_3Fe_5O_{12}$ surface irradiated with Xe ions. By extrapolation to height zero, the curvature radius of the scanning tip can be extracted. This allows a deconvolution of the hillock diameter and the tip size (Khalfaoui et al., 2005).

radiation. The latter case has the advantage that the S_e value is well defined but special attention should be paid to possible thickness and surface effects (Berthelot et al., 2000). If a thick sample is thinned down after beam exposure, damage by the thinning process has to be avoided. TEM reveals ion-induced changes of the material structure such as amorphous (Groult et al., 1988) or otherwise modified (Jensen et al., 1998) tracks embedded in a cristalline matrix. Figure 5 shows TEM images of tracks in non-amorphisable SnO_2 and CaF_2 crystals and in amorphisable materials such as mica and $Y_3Fe_5O_{12}$ garnet.

On the sample surface, high-resolution imaging of individual tracks is possible by means of scanning force microscopy. Under suitable conditions, each ion impact produces a nanometric hillock (Thibaudau et al., 1991; Ackermann et al., 1996). The determination of the height is straightforward if the surface roughness is sufficiently small, whereas for the extraction of the hillock width (e.g. half width at half maximum) it is necessary to take into account the size of the scanning tip (typically of same order of magnitude as the hillock) (Müller et al., 2003). Figure 6 presents the height and the diameter of hillocks recorded with the same scanning tip. There is obviously a correlation, i.e. hillocks with a bigger diameter have a larger height (Khalfaoui et al., 2005).

In contrast to transmission electron and scanning force microscopy, small-angle scattering experiments give information for bulk samples averaging over

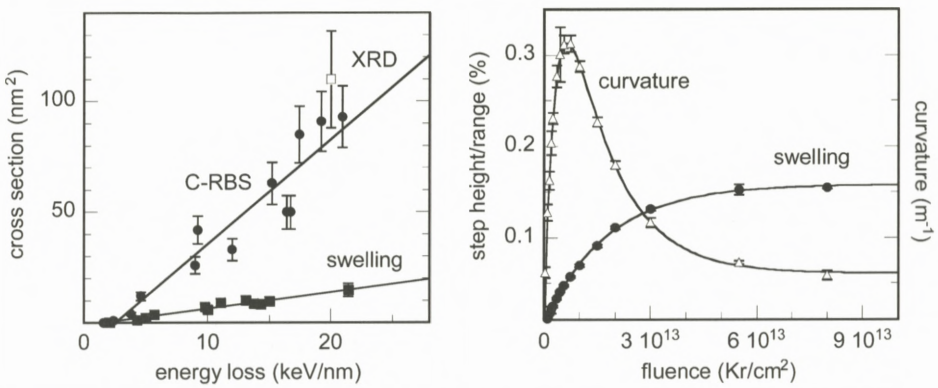

Figure 7. Left: Damage cross sections of tracks in SiO_2 quartz as a function of electronic energy loss (Ziegler, 1999). The data are extracted from x-ray diffraction (XRD), Channelling Rutherford Backscattering (C-RBS), and swelling measurements. The irradiations were performed using beam energies between 1 and 4 MeV/u (Meftah et al., 1994). The lines are linear fits to the experimental cross sections. Right: Step height from out-of-plane swelling normalized by the ion range and sample curvature as a function of ion fluence of a mm thick quartz sample irradiated with 3-MeV/u Kr ions (range ~24 μm, $S_e = 11.5$ keV/nm) (the lines are guides to the eye).

many tracks along their full length (Schwartz et al., 1998). To deduce track parameters such as size and material density, the analysis requires a more or less complex geometrical model of tracks as scattering objects (Albrecht et al., 1985; Saleh and Eyal, 2005).

4. Tracks in Amorphisable Insulators

4.1. Damage Cross Sections

For a small number of solids (e.g. SiO_2, $Y_3Fe_5O_{12}$) there exists a rather broad set of track data obtained from irradiation experiments with many different ion beams and analyzed by various complementary techniques. The track size or the damage cross section is typically plotted as a function of the electronic energy loss as deduced from the TRIM or SRIM code (Ziegler, 1999) (Figure 7, left). The track data for SiO_2 quartz were deduced from x-ray diffraction, Channelling Rutherford Backscattering, profilometry, and electron spin resonance measurements (Meftah et al., 1994; Trautmann et al., 1998; Douillard et al., 1992), and the linear extrapolation yields the same S_e threshold of ~2 keV/nm. Also the cross sections of the different techniques are in good agreement, except for swelling. The smaller swelling cross section is probably linked to stress phenomena. As a

consequence of the amorphisation of the quartz, the irradiated volume expands and stress builds up at the interface to the underlying non-irradiated substrate. Depending on the crystal thickness and ion range, the entire sample bends. Figure 7 right shows the curvature of a thick quartz sample as a function of the fluence. In the initial stage of the irradiation, the curvature increases with a high rate. Maximum bending occurs around 6×10^{12} ions/cm^2, where swelling is still far from saturation but a large part of the irradiated volume is amorphised. At that stage, stress release becomes easier and with continuing irradiation the bending of the sample relaxes (Trautmann et al., 2002). This example demonstrates that a complete analysis of the swelling data is rather complex.

Another material for which damage cross sections and S_e threshold were deduced with different physical characterization techniques is $Y_3Fe_5O_{12}$. Channelling Rutherford Backscattering, Mössbauer spectrometry, and magnetization measurements (Toulemonde and Studer, 1988) give consistent track size and threshold data, except that the swelling cross section is also smaller (cf. Figure 4 left and center). It remains to be clarified if this is a general property of amorphisable solids.

4.2. Comparison of Track Radii from Direct Measurements

Concerning track observations by direct techniques such as transmission-electron and scanning force microscopy and small angle x-ray scattering, mica is probably the most intensively studied insulator. The track zone in mica is amorphous, and the track radii obtained with these three methods show good overall agreement in a wide energy loss regime (Figure 8). However due to missing systematic data, it is not clear if this finding is universal and applies for all amorphisable crystals.

4.3. Damage Morphology

By combining the information from different techniques (TEM, Mössbauer spectrometry and chemical etching), the damage morphology of tracks is best investigated for $Y_3Fe_5O_{12}$ garnet (Figure 9) (Houpert et al., 1989). Energetic projectiles of small energy loss produce individual spherical defects (of radius $R \sim 1.6$ nm) aligned along the ion path. For projectiles with larger energy loss, neighboring spherical defects overlap forming a discontinuous damage zone with the same radial size. Once the defects strongly percolate, further increasing of the energy loss leads to larger track radii, and the damage becomes more and more continuous and homogeneous. The evolution of this damage morphology seems to be a general characteristic and independent of the solids (Lang et al., 2004; Villa et al., 1999; Liu et al., 2001; Gaiduk et al., 2002). The peculiarity of the track morphology has

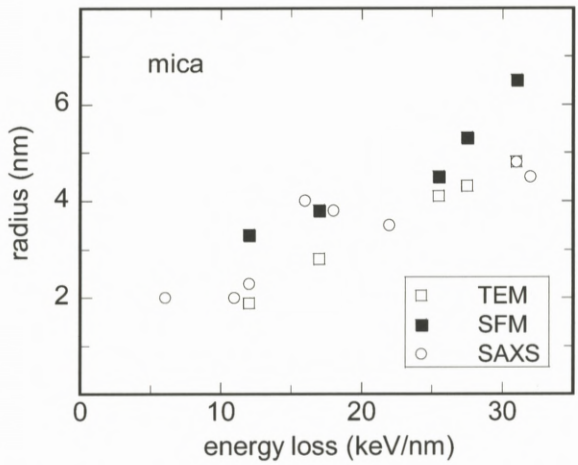

Figure 8. Track radii in mica as a function of electronic energy loss obtained by means of transmission electron microscopy (TEM), scanning force microscopy (SFM), and small angle x-ray scattering (SAXS). All irradiations were performed with beam energies around 11 MeV/u.

to be kept in mind when trying to deduce the track-formation threshold from direct track measurements. Due to the discontinuous damage at small energy losses, the track diameter remains constant and an extrapolation to $R = 0$ does not make sense.

At present, the discontinuous character of the track damage is not well understood, but it may result from the non-homogeneous energy deposition along the ion path since the energy transfer from the incident ion to the target atoms is a statistical process (Dartyge and Sigmund, 1985). Spherical defects may also be related to criteria responsible for the Rayleigh instability.

4.4. Comparison of Damage Cross Sections and Track Radii

Besides the direct visualisation of tracks, we can also deduce a track radius from measurements of the damage cross section σ by $R_e = \sqrt{\sigma/\pi}$. Here, R_e corresponds to an effective track radius because at small energy losses, as discussed above, the track damage deviates from cylindrical geometry and thus R_e yields values smaller than the diameter of the spherical defects. This is clearly visible in Figure 10 (left) where radii (R) from direct measurements by high-resolution TEM are compared to effective radii (R_e) deduced from Mössbauer damage cross sections. Tracks larger than 2 nm show good agreement between R and R_e (Toulemonde and Studer, 1988), whereas R_e is smaller than R below $S_e \sim 10$ keV/nm because of the discontinuity of the damage. Figure 10 (right) shows a

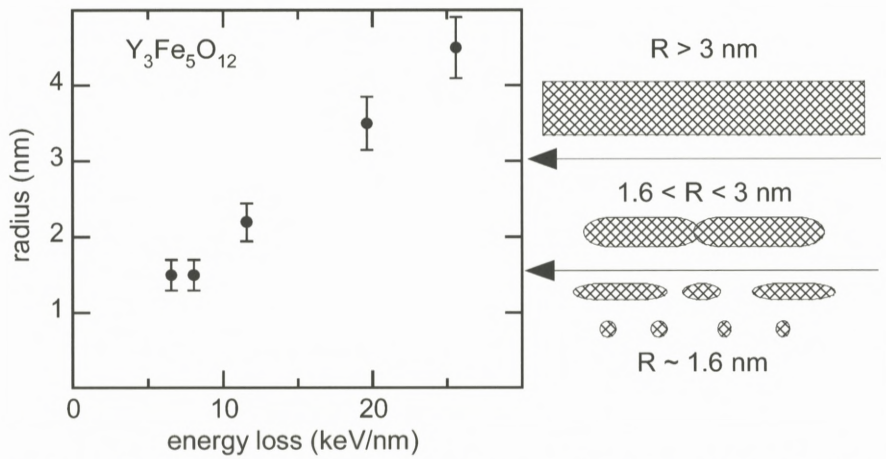

Figure 9. Damage morphology and track radii as a function of the electronic energy loss deduced from high-resolution electron microscopy (Studer and Toulemonde, 1992; Houpert et al., 1989). The irradiations of $Y_3Fe_5O_{12}$ were performed with ions of about 15 MeV/u.

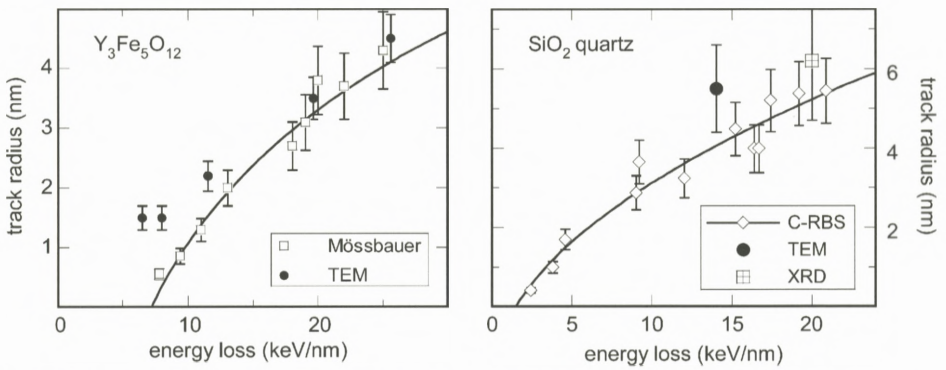

Figure 10. Track radii from transmission electron microscopy (full symbols) and effective radii (R_e) deduced from damage cross sections (open symbols) as a function of electronic energy loss. Left: Tracks in $Y_3Fe_5O_{12}$ for beam energy around 15 MeV/u. R is measured by high-resolution TEM (Houpert et al., 1989) and R_e is deduced from Mössbauer spectrometry (Toulemonde et al., 1987). Right: Tracks in SiO_2 quartz for beam energy between 1 and 4 MeV/u. R is measured by high-resolution TEM (circle) (Meftah et al., 1994) and R_e is deduced from Channelling Rutherford Backscattering (C-RBS, diamonds) (Meftah et al., 1994) and x-ray diffraction (XRD, square). The line in both plots is a square-root fit to R_e.

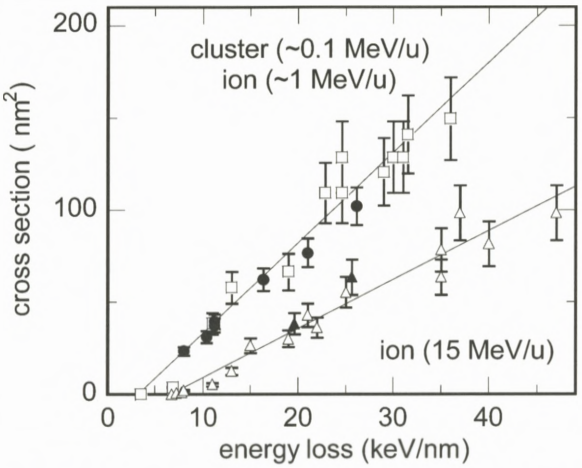

Figure 11. Damage cross sections of tracks in $Y_3Fe_5O_{12}$ as a function of electronic energy loss. The irradiations were performed with C_{2-10} clusters (~0.1 MeV/u, full circles) and with ions in two different energy regimes (~1 MeV/u and ~15 MeV/u). The damage cross section was deduced from Mössbauer spectrometry (open triangles (Toulemonde and Studer, 1988)), high-resolution TEM (full triangles (Toulemonde and Studer, 1988) and circles (Jensen et al., 1998)) assuming $\sigma = \pi R^2$ (restricted to $R > 2$ nm), and Channelling Rutherford Backscattering (open squares (Meftah et al., 1993)). The lines are linear fits to the low-energy and high-energy data group.

similar comparison of direct and indirect determined track radii in SiO_2 quartz. Radii obtained by means of x-ray diffraction and TEM agree well with results from Channelling Rutherford Backscattering experiments. Above the electronic energy loss threshold, the effective radius of both materials is well fitted by the square root of S_e (solid line in Figure 10) corresponding to a linear increase of the damage cross section (Figures 11 and 7 left).

4.5. Velocity Effect

Evidence for the velocity effect mentioned in Section 2 is given in Figure 11 showing damage cross sections as a function of energy loss for different specific beam energies. Independent of the characterization technique, the data for high-energy ions (~15 MeV/u) group around one line whereas low-energy ions (~1 MeV/u) and carbon cluster projectiles (C_n with $n = 2$–10, ~0.1 MeV/u) group around a second line. The track cross sections for high-energy ions are about a factor of 2–3 smaller compared to the low-energy group. This effect is ascribed to the difference in the initial electron energy density. The relation to the beam velocity seems not to be linear because the energy density is as small as ~1 eV/at for high-energy

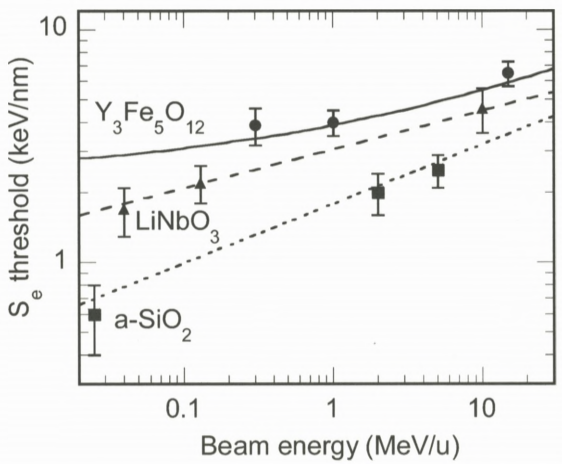

Figure 12. Electronic energy loss threshold for track formation as a function of specific beam energy for 3 different oxides $Y_3Fe_5O_{12}$ (Meftah et al., 1993), $LiNbO_3$ (Canut et al., 1997; Canut et al., 1996; Bentini et al., 2004), and vitreous SiO_2 (Benyagoub et al., 1992; Rotaru, 2004; Van Dillen et al., 2003). The lines are the electronic stopping power threshold values *versus* beam energy according to calculations performed with the thermal spike model (see Section 5.4).

ions and about 10 and 100 eV/at for 1-MeV/u monoatomic ions and 0.1-MeV/u clusters, respectively.

Also the critical electronic energy loss for track formation is sensitive to the beam velocity or energy density as illustrated in Figure 12: The threshold of several materials becomes smaller with decreasing beam energy (e.g. for $LiNbO_3$ the threshold shifts from 4.4 keV/nm at 10 MeV/u to 1.7 keV/nm at 0.04 MeV/u). This could be a chance for nanotechnology at smaller accelerator facilities providing typically ions of lower energy loss.

Another example for damage creation by electronic energy loss in the low-energy regime is illustrated in Figure 13 showing Channelling Rutherford Backscattering data of SiO_2 quartz irradiated with Au ions of ~0.02 MeV/u. With increasing beam velocity, the damage rate first decreases (following the evolution of the nuclear energy loss) and then steeply increases above 0.02 MeV/u at ~1.5 keV/nm (following the electronic stopping). This shows that at rather low beam velocities, synergetic effects of nuclear and electronic energy losses may play some role for damage creation.

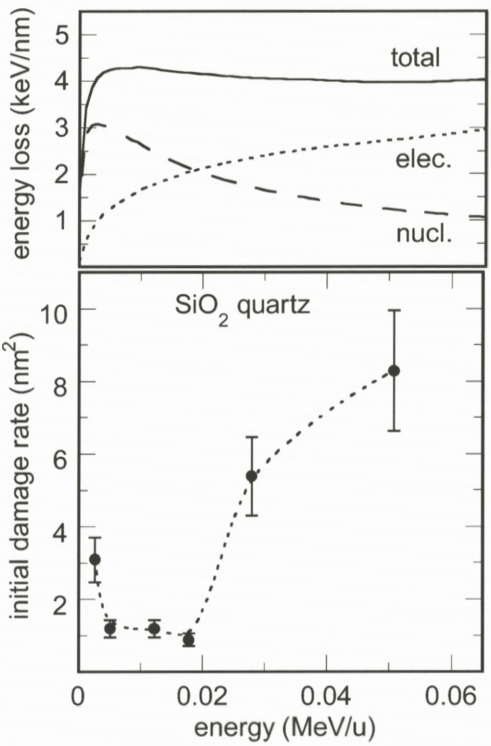

Figure 13. Nuclear, electronic, and total energy loss (top) and damage rate (bottom) as a function of specific beam energy for SiO_2 quartz irradiated with Au ions and analyzed by Channelling Rutherford Backscattering (Toulemonde et al., 2001).

4.6. Summary of Track Observations in Amorphisable Insulators

Assuming that the results described above represent characteristic track properties for amorphisable insulators in general, the following conclusions can be made: (1) The specific energy and thus the velocity of the projectiles have a direct influence on the energy density deposited to the electrons of a given target. The higher the ion velocitiy, the more is the energy smeared out into a larger volume around the ion path. Hence for a given ion species and energy loss, the resulting damage cross sections and track radii become smaller with increasing beam velocity. To avoid misinterpretation, any data comparison should therefore only be performed within the same velocity range. (2) Damage cross sections obtained with a variety of characterization techniques show good agreement, except swelling measurements which yield smaller values. A direct relation between the

track radius and the damage cross section is restricted to tracks with continuous damage morphology. The critical track radius is of the order of 2 nm. Above this value, radii deduced from damage cross sections and from direct e.g. microscopic observations are in good agreement. (3) The energy loss threshold for a given material appears to be independent of the characterization method (including swelling measurements), but it should be extracted only from cross section data. Direct radius measurements suffer from the problem that close to the threshold, the track fragments into a discontinuous damage trail of constant radius.

5. Model Calculations with the Inelastic Thermal Spike

5.1. Introduction

Since the discovery of ion tracks several decades ago, various efforts have been made (e.g. Fleischer et al., 1975; Ithoh and Stoneham, 1998; Chadderton and Montagu-Pollock, 1963; Lesueur and Dunlop, 1993; Seiberling et al., 1980; Szenes, 1995; Trinkaus and Ryazanov, 1995) in order to give a realistic scenario of the complex track formation process and describe quantitatively experimental track data in different materials and under different irradiation conditions.

In this section we concentrate on the inelastic thermal spike model that tries to establish a link between the initial energy deposition on the electrons as described in Section 3 and the resulting damage creation in the lattice (Meftah et al., 1994). For many metallic targets, the thermal spike concept has been successfully applied predicting track recording metals and quantifying threshold values for track formation and the dependence of track radii on the electronic energy loss (Dufour et al., 1993b; Wang et al., 1994/1995). In a slightly modified version, the same concept is also used for a wide variety of insulators (Toulemonde et al., 2000; Meftah et al., 2005).

5.2. The Inelastic Thermal Spike Model

In this model, the electron and the lattice subsystem are included as two coupled systems. The kinetic energy of the projectiles is deposited into the electron system of the target, where thermalization occurs within about 10^{-15} s. The hot electrons then transfer their energy by electron-phonon coupling to the cold lattice in which thermal equilibrium is reached after about 10^{-13} s (typical time for lattice vibrations). The heat diffusion in the electron and lattice subsystem is described by the classical heat equations with the electronic energy loss being the heat source term. The energy exchange term is given by the product $g \times (T_e - T_a)$ with g being the coupling constant and $(T_e - T_a)$ the temperature difference between the

two subsystems. Due to the straight trajectory of energetic projectiles, the two differential heat equations are expressed in cylindrical geometry as follows:

$$C_e(T_e)\frac{\partial T_e}{\partial t} = \frac{1}{r}\frac{\partial}{\partial r}\left[rK_e(T_e)\frac{\partial T_e}{\partial r}\right] - g(T_e - T_a) + A(r,t), \tag{1a}$$

$$C_a(T_a)\frac{\partial T_a}{\partial t} = \frac{1}{r}\frac{\partial}{\partial r}\left[rK_a(T_a)\frac{\partial T_a}{\partial r}\right] + g(T_e - T_a), \tag{1b}$$

where T, C, and K are respectively the temperatures, the specific heat coefficients, and the thermal conductivities of the electronic (index e) and lattice subsystem (index a).

$A(r,t)$ denotes the spatiotemporal energy deposition of the projectile to the electron subsystem described by a Gaussian time distribution and a radial distribution $F(r)$ of the delta-electrons according to the Katz model (Waligorski et al., 1986)

$$A(r,t) = bS_e\, e^{-(t-t_0)^2/2s^2} F(r). \tag{2}$$

The initial width of the electron cascade is described by α_e (cf., Figure 2 left), and the half width s of the Gaussian distribution corresponds to the time the electrons need to reach thermal equilibrium (Gervais and Bouffard, 1994). The majority of the electrons deposit their energy close to the ion path within $t_0 = 10^{-15}$ s. The normalization factor b ensures that the integration of $A(r,t)$ in space and time is equal to the total electronic energy loss S_e (Dufour et al., 1993b).

In insulators the values of the thermal parameters of the electronic subsystem C_e and $K_e = C_e \times D_e$ (D_e is the electron diffusivity), are problematic since there exist no free electrons. However, according to Baranov et al. (1988), we can suppose that hot electrons in the conduction band of an insulator behave like hot free electrons in a metal and consequently $C_e \sim 1.5 k_B n_e$, ($\sim$1 J cm^{-3} K^{-1}) where k_B is the Boltzmann constant and n_e the number of excited electrons per atoms ($\sim$1). D_e is equal to the product of the electron Fermi velocity and the inter-atomic distance ($\sim$2 cm^2 s^{-1}) (Toulemonde et al., 2000). The electron-phonon coupling constant g of insulators is linked to the electron-phonon mean free path λ by the relation $\lambda^2 = C_e D_e / g$. When the electronic temperature has cooled down to T_a, electrons are supposed to be trapped in the lattice and consequently the lattice cooling by cold free electrons is inhibited. The thermodynamical lattice parameters of insulators such as specific heat, thermal conductivity, solid and liquid mass density, melting and vaporisation temperatures (and corresponding latent heat values and sublimation energy) are extracted from experimental data available in the literature.

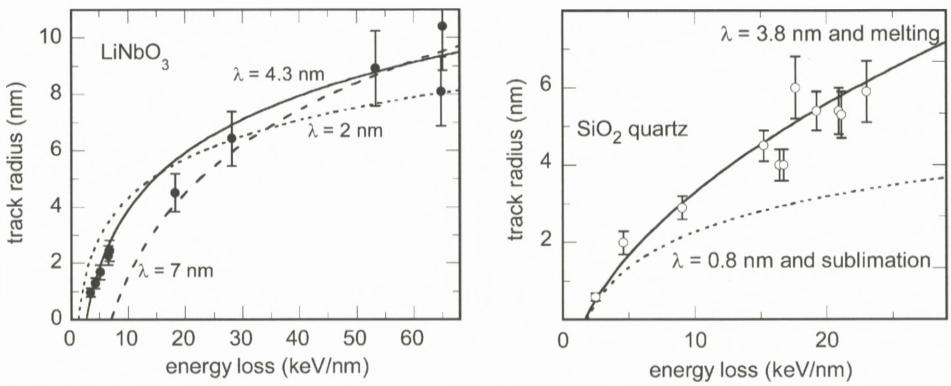

Figure 14. Left: Experimental track data for $LiNbO_3$ irradiated with carbon clusters (C_n, $n = 6, 8, 60$) (Canut et al., 1996, 1997) and thermal spike calculations (lines) testing different λ values. Best agreement for the radius dependence on the electronic energy loss is obtained for $\lambda = 4.3 \pm 0.3$ nm (Meftah et al., 2005). Right: Experimental radii *versus* electronic energy loss for ion tracks in SiO_2 quartz. A fit value of $\lambda = 3.8 \pm 0.3$ nm in combination with the melting criterion (solid line) gives best agreement with experimental data in the entire energy loss regime (Toulemonde et al., 2002). The fit fails if the sublimation energy is used as criterion for track formation (dashed line).

5.3. Determination of the Electron Mean Free Path

The two differential heat equations are solved numerically (Dufour et al., 1993a; Toulemonde et al., 2000) and give the lattice temperature $T_a(t, r)$ around the projectile trajectory as a function of time (t) and space (r). In the thermal spike model, the track size is defined by the radial zone which contains sufficient energy for melting (defined by the energy to reach the melting temperature plus the latent heat of fusion) (Wang et al., 1994/1995; Meftah et al., 2005). Tracks are formed when during subsequent rapid cooling the molten material is quenched. In the heat equations (Equations 1a and 1b), λ is the only free parameter to be fitted to the experimental track radii. A suitable λ value has to describe track data in a wide range of electronic energy losses and beam velocities. Figure 14 (left) shows as example a set of experimental track data in $LiNbO_3$ together with thermal spike calculations for different λ values. It should be emphasized that experimental data close to the energy loss threshold (e.g. radii deduced from cross section measurements) are important for reliable extraction of the λ value.

The dependence of the track radius on the energy loss is rather strongly influenced by the track formation criterion as demonstrated in Figure 14 (right) demonstrating that for SiO_2 quartz, the melting criterion and $\lambda = 3.8$ gives good agreement, whereas no suitable lambda value can be found in combination with the sublimation criterion. Such a test was also performed for other amorphisable

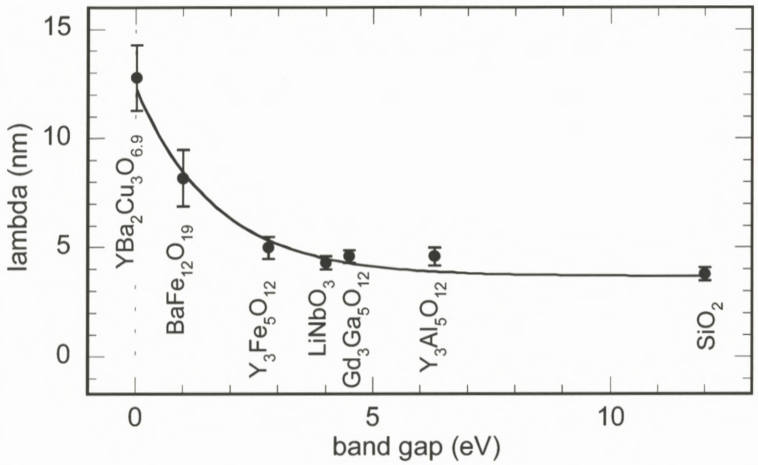

Figure 15. Electron mean free path λ from thermal spike fitting as a function of the band gap energy for several crystalline oxide materials (Meftah et al., 2005).

insulators revealing that in all cases the melting criterion seems to yield best fit results.

Figure 15 presents λ values of thermal spike calculations based on the melting criterion obtained by fitting track data for various oxides. The extracted values appear to be directly related to the inverse of the band gap energy (Toulemonde et al., 2000; Meftah et al., 2005). This evolution is reasonable if we consider that the cooling of hot electrons occurs via excitation of peripheral cold electrons from the valence to the conduction band which is directly linked to the band gap energy (Haglund and Kelly, 1992). More systematic investigations are required to show if this relation to the band gap is universal, so that the electron mean free path can be deduced for any insulator. In this case, λ could be inserted in the heat equations as a predetermined parameter.

5.4. Effect of Beam Velocity

In the thermal spike code, the velocity of the ion beam enters via the initial energy distribution. The calculations should therefore describe the track radii of ions of different velocities using the same λ value. An example is shown in Figure 16, where the experimental track data (same as shown in Figure 11) for monoatomic and cluster projectiles of low and high velocity are well described by thermal spike calculations (solid lines) for $\lambda = 5$ nm. In the calculation, the energy distribution of these different beams, characterized by α_e, goes into the heat equations via $F(r)$ in Equation (2). During the coupling time between the electronic and lattice

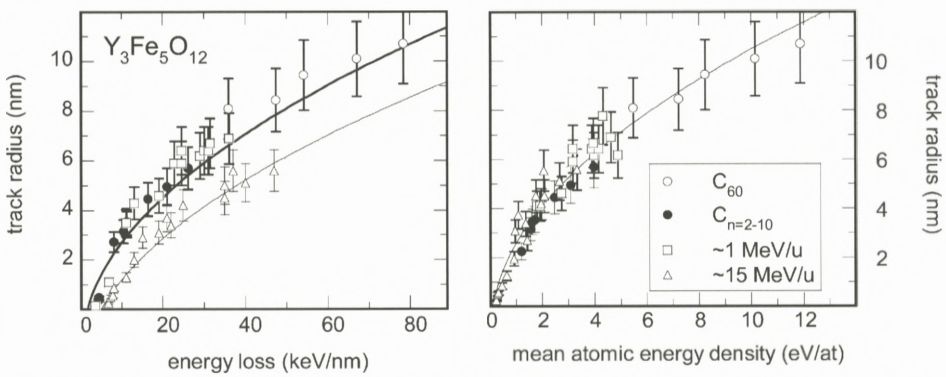

Figure 16. Track radii in $Y_3Fe_5O_{12}$ irradiated with projectiles of different velocities (see caption of Figure 11) and thermal-spike calculations using a fixed electron–phonon mean free path of $\lambda = 5$ nm but different initial energy distributions. Left: Track radius as a function of electronic energy loss. Right: Track radius as a function of mean atomic energy density.

system, α_e and the electron-phonon mean free path λ contribute to the increase of the energy distribution in the lattice system to a radius of $\alpha_a = \sqrt{\lambda^2 + \alpha_e^2}$. For low-energy projectiles (including clusters), the initial energy distribution α_e is much smaller than λ and has therefore only a small influence on the resulting track radius. In contrast, for high-energy ions where $\alpha_e \sim \lambda$, the energy spread in the lattice increases leading to smaller energy densities and smaller track radii. At extremely high beam velocities, the contribution of λ becomes negligible and the energy distribution is governed by α_e. When plotting the track radius *versus* the atomic energy density (obtained by dividing the electronic energy loss S_e by $N_y \pi \alpha_a^2$ with N_y being the atomic density of the target), all data follow one universal curve as illustrated in Figure 16 (right). Thermal spike calculations of this type also confirm the experimental findings that the damage creation threshold S_e decreases for smaller beam energies (cf. Figure 12) (Meftah et al., 2005).

5.5. Thermal Spike Description of Electronic Sputtering of Surface Atoms

To test if the thermal spike approach can also describe surface processes such as sputtering of atoms, the thermal spike code was extended by the possibility to calculate the number of particles evaporated when an energetic ion impinges the sample surface (Mieskes et al., 2003; Toulemonde et al., 2002). As in the case of elastic-collision spikes, the evaporation is determined by the local temperature (Sigmund and Claussen, 1981). Since the temperature around the ion path decreases as a function of the radial distance, the total sputter yield Y_{tot} has

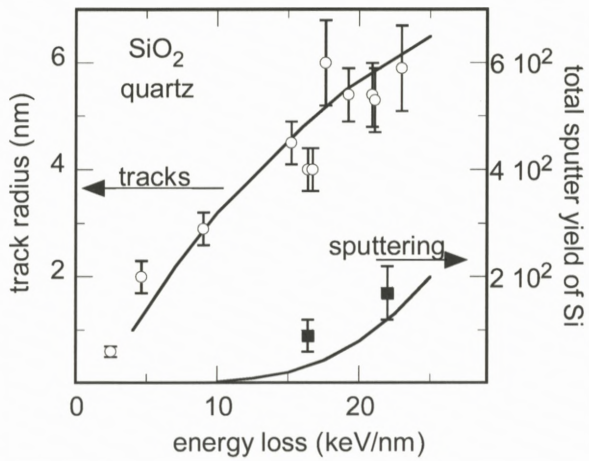

Figure 17. Track radii and total sputtering yields as a function of energy loss for SiO_2 quartz. The thermal spike model calculations (solid lines) for track formation (melting) and sputtering (evaporation) are performed with the same electron mean free path $\lambda = 3.8$ nm, and the known sublimation energy.

to be determined from the time and space integral of the local evaporation rate $\Phi(T_a(t, r))$. The temperature is calculated with the heat equations (Equations 1a and 1b) using a λ value determined by fitting track radii as described above. The temperature dependence of the evaporation rate is given by statistical thermodynamics and the Maxwell–Boltzmann equation:

$$Y_{\text{tot}} = \int_0^\infty \mathrm{d}t \int_0^\infty \Phi(T_a(r, t)) 2\pi r \, \mathrm{d}r, \tag{3a}$$

$$\Phi(T_a(r, t)) = N_y \sqrt{\frac{kT_a(t, r)}{2\pi M}} \exp\left(\frac{-U}{kT_a(t, r)}\right), \tag{3b}$$

where N_y denotes the atomic density and M the molecular mass of the target, k is the Boltzmann constant, and U is the surface binding energy assumed to be equal to the sublimation energy per atom or molecule (for compound materials). For temperatures above vaporization, the thermal diffusivity of the lattice is assumed to increase with the square root of the temperature as derived by Sigmund (1974/1975).

At present we can apply this approach only for SiO_2 quartz because track and simultaneously sputtering data exist only for this material.[1] Figure 17 shows how

[1] Sufficient data exist for $Y_3Fe_5O_{12}$ but the sublimation energy necessary for the thermal spike calculation is not available.

well thermal spike calculations with a fixed λ value of 3.8 nm can describe track radii and sputtering yields.

The good agreement indicates that tracks can be attributed to the appearance of a "molten" phase while sputtering is linked to "vapor" phase, i.e. to surface sublimation. To confirm this relation, additional experiments are needed to provide data of track radii (or damage cross sections) and simultaneously total sputtering yields for other materials.

6. Conclusions

6.1. Amorphisable Materials

Based on many investigations, track radii can be quantitatively determined either from direct observations or deduced from cross section measurements. The track formation threshold can be reliably extrapolated from the dependence of the cross section on electronic energy loss. Track radii deduced from different analysis techniques show overall agreement for radii larger than 2 nm. Deviations below 2 nm have to be ascribed to the discontinuous damage morphology i.e. the track shape deviates from cylindrical geometry. The overall agreement between the different characterization techniques may be linked to the fact that all these methods probe structural modifications such as ion-induced disorder or amorphization. Track radii from profilometer measurements seem to be different probably because the out-of-plane swelling includes additional effects. In any case swelling yields the same track formation threshold as other techniques.

For track formation it is important to consider the deposited energy density and not only the linear energy transfer. The energy density is given by the initial radial distribution of the recoil electrons, and the subsequent diffusion of the energy in the electronic subsystem prior its transfer to the lattice atoms. The inelastic thermal spike model considers (1) the initial energy deposition on the electrons in a cylinder of radius α_e, which scales with the ion velocity, and (2) the electron-phonon mean free path λ to characterize the diffusion length of the electrons in a specific material. λ is not known *a-priori* and is thus the unique fit parameter in the model. Finally a clear correlation can be seen between the calculated atomic energy density and the measured track radius.

Thermal spike calculations allow a consistent description of a series of experimental track phenomena, despite the fact that the application of thermodynamics to short time events occurring in a nanometric volume and the strong simplification of the description of the energy dissipation (see chapter by Klaumünzer, this volume) may be questionable. Tracks in amorphisable insulators are ascribed

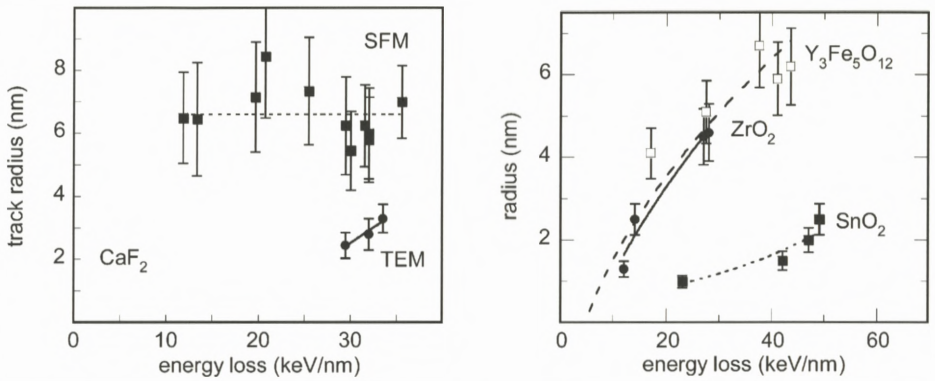

Figure 18. Track radii as a function of electronic energy loss for different materials. Left: Tracks in CaF_2 observed by scanning force microscopy (SFM) and transmission electron microscopy (TEM) (Khalfaoui et al., 2005). Right: Tracks in amorphisable $Y_3Fe_5O_{12}$ garnets (Meftah et al., 1993) and in non-amorphisable ZrO_2 (Benyagoub, 2005) and SnO_2 (Berthelot et al., 2000) crystals.

to a quench of a molten phase, and electronic sputtering of surface atoms is associated with thermal spike induced sublimation. For different materials, the electron-phonon mean free path values, derived from a fit to track radii and S_e thresholds, follow a monotonic decrease with the band gap energy. The model considers the effect of the ion velocity, by combining the size of the initial electron energy distribution (α_e) with the electron-phonon mean free path (λ). Simulations show that the mean energy density deposited in the lattice is mainly governed by α_e for high-velocity projectiles and by λ for low-velocity beams.

6.2. Unsolved Problems

Various thermal spike calculations show that the melting concept suitable for amorphisable materials does not directly apply for tracks in non-amorphisable materials. One of the problems is given by the difficulty to define a suitable track diameter (Trautmann et al., 2000a). The response of non-amorphisable material to energetic ion beams is not just an amorphous cylindrical track but exhibits manifold effects (cf., Figure 5). For instance, in ionic crystals such as alkali and earth alkali halides, point defects and defect clusters are created. The size of hillocks formed on the surface of CaF_2 is not related to tracks directly observed by transmission electron microscopy (in contrary to mica) (Figure 18, left). Also in SnO_2 (Berthelot et al., 2000) and UO_2 (Wiss et al., 1997), TEM reveals track sizes much smaller than typically recorded for amorphisable material (Figure 18, right). Other solids, e.g. ZrO_2, change their structure from the monoclinic to the tetrag-

onal phase but with rather large cross sections (Benyagoub, 2005) (Figure 18, right). At present, it is not clear, if trends found for tracks in amorphisable crystals are of general validity.

Tracks in CaF_2 and SnO_2 cannot be described by thermal spike calculations using the melting criterion and a λ value deduced from the λ *versus* band gap plot (Figure 15). Triggered by the observations that energetic ions may produce empty holes in SnO_2 (Figure 5 top, left), the criterion of track formation was modified to sublimation instead of melting (Berthelot et al., 2000). Under this condition, track sizes in SnO_2 as well as in CaF_2 could be described quantitatively (Toulemonde et al., 2000). It remains to be shown if in non-amorphisable solids tracks can be produced from a quench of a molten phase. A possible case could be ZrO_2, where the track radii deduced from the cross sections of the monoclinic to tetragonal phase change is well described by the thermal spike model using the energy necessary to melt ($\sim$1 eV/at) and a λ value of 4 nm. As proposed for Y_2O_3 (Hémon et al., 1997), the tracks, resulting from melt quenching, probably consist of small nanograins instable regarding the monoclinic phase (Djurado et al., 2000). Although coherent with the description made for amorphisable materials, this interpretation is in contradiction with a phase change resulting only from a rise of temperature to 1100 K, according to the phase diagram (Benyagoub, 2005) of ZrO_2 (this corresponds to an energy of $\sim$0.2 eV/at and can be fitted by the thermal spike with $\lambda \sim 10$ nm).

Last but not least, it should be mentioned that experiments studying track formation and electronic sputtering of surface atoms can help to shed more light onto the basic ion-matter interaction processes. Huge sputtering yields for ionic crystal and new phenomena such as jet-like sputtering normal to the surface do not have a straightforward link to the same beam and material parameters as track formation (Assmann et al., 2006; Toulemonde et al., 2002).

References

Ackermann J., Angert N., Neumann R., Trautmann C., Dischner M., Hagen T. and Sedlacek M. (1996): Ion track diameters in mica studied with scanning force microscopy. Nucl Instr Meth B **107**, 181–184

Albrecht D., Armbruster P., Spohr R., Roth M., Schaupert K. and Stuhrmann H. (1985): Investigation of heavy ion produced defect structures in insulators by small angle scattering. Appl Phys A **37**, 37–46

Assmann W., Toulemonde M. and Trautmann C. (2006): Electronic sputtering with swift heavy ions. In: Behrisch R. and Eckstein W. (Eds), Sputtering by Particle Bombardment, Sputtering with Ion Energies from Threshold to MeV – Experiments and Computer Simulation. Springer, pp 313–361 (in press)

Audouard A., Balanzat E., Jousset J.C., Chamberod A., Fuchs G., Lesueur D. and Thom L. (1991): Effects of electronic energy loss in crystalline and amorphous Ni_3B irradiated by high-energy heavy ions. Phil Mag B **63**, 727–738

Baranov I.A., Martynenko Yu.V., Tsepelevich S.O. and Yavlinskii Yu.N. (1988): Inelastic sputtering of solids by ions. Sov Phys Usp **31**, 1015–1034

Baudin K., Brunelle A., Chabot M., Della-Negra S., Depauw J., Gardes D., Hakanson P., Le Beyec Y., Billebaud A., Fallavier M., Remilleux J., Poizat J.C. and Thomas J.P. (1994): Energy loss by MeV carbon clusters and fullerene ions in solids. Nucl Instr Meth B **94**, 341–344

Bentini G.G., Bianconi M., Correra L., Chiarini M., Mazzoldi P., Sada C., Argiolas N., Bazzan M. and Guzzi R. (2004): Damage effects produced in the near-surface region of x-cut $LiNbO_3$ by low dose, high energy implantation of nitrogen, oxygen and fluorine ions. J Appl Phys **96**, 242–247

Benyagoub A. (2005): Mechanism of the monoclinic-to-tetragonal phase transition induced in zirconia and hafnia by swift heavy ions. Phys Rev B **72**, 094114 (1–7)

Benyagoub A., Löffler S., Rammensee M., Klaumünzer S. and Saemann-Ischenko G. (1992): Plastic deformation in SiO_2 induced by heavy-ion irradiation. Nucl Instr Meth B **65**, 228–231

Berthelot A., Hémon S., Gourbilleau F., Dufour C., Domengès B. and Paumier E. (2000): Behaviour of a nanometric SnO_2 powder under swift heavy-ion irradiation: from sputtering to splitting. Phil Mag A **80**, 2257–2281

Betz H.D. (1972): Charge states and charge-changing cross sections of fast heavy ions penetrating through gaseous and solid media. Rev Mod Phys **44**, 465–539

Biersack J.P. and Haggmark L.G. (1980): A Monte Carlo computer program for the transport of energetic ions in amorphous targets. Nucl Instr Meth **174**, 257–269

Bringa E.M. and R.E Johnson R.E. (2002): Coulomb explosion and thermal spikes. Phys Rev Lett **88**, 165501 (1–4)

Bursill L.A. and G. Braunshausen G. (1990): Heavy-ion irradiation tracks in zircon. Phil Mag **62**, 395–420

Busch M.C., Slaoui A., Siffert P., Dooryhee E. and Toulemonde M. (1992): Structural and electrical damage induced by high-energy heavy ions in SiO_2/Si structures J Appl Phys **71**, 2596–2601

Canut B., Ramos S.M.M., Brenier R., Thevenard P., Loubet J.L. and Toulemonde M. (1996): Surface modifications of $LiNbO_3$ single crystals induced by swift heavy ions. Nucl Instr Meth B **107**, 194–198

Canut B., Ramos S.M.M., Bonardi N., Chaumont J., Bernas H. and Cottereau E. (1997): Defect creation by MeV clusters in $LiNbO_3$. Nucl Instr Meth B **122**, 335–338

Chadderton L.T. and Montagu-Pollock H.M. (1963): Fission fragment damage in crystal lattices: Heat-sensitive crystals. Proc R Soc London A **274**, 239–252

Chailley V., Dooryhee E. and Levalois M. (1996): Amorphization of mica through the formation of GeV heavy ion tracks. Nucl Instr Meth B **107**, 199–203

Costantini J.M., Brisard F., Meftah A., Studer F. and Toulemonde M. (1993): Conductivity modifications of calcium-doped yttrium iron garnet by swift heavy ion irradiations. Rad Eff Def Sol **126**, 233–236

Dartyge E. and Sigmund P. (1985): Tracks of heavy ions in muscovite mica: Analysis of the rate of production of radiation defects. Phys Rev B **32**, 5429–5431

Djurado E., Bouvier P. and Lucazeau G. (2000): Crystallite size effect on the tetragonal-monoclinic transition of undoped nanocrystalline zirconia studied by XRD and Raman spectrometry. J Sol St Chem **140**, 399–407

Douillard L., Jollet J., Duraud J.P., Devine R.A.B. and Dooryhee E. (1992): Radiation damage produced in quartz by energetic ions. Radiat Eff Def in Sol **124**, 351–370

Dufour C., Lesellier de Chezelles B., Delignon V., Toulemonde M. and Paumier E. (1993): A transient thermodynamic model for track formation in amorphous semi-conductors: A possible mechanism. In: Mazzoldi P. (Ed.), Modifications Induced by Irradiation in Glasses, Europ. Mat. Res. Soc. (E-MRS) Symp. Proc. Vol. 29. North Holland, Amsterdam, pp 61–66

Dufour C., Audouard A., Beuneu F., Dural J., Girard J.P., Hairie A., Levalois M., Paumier E. and Toulemonde M. (1993): A high resistivity phase induced by swift heavy ion irradiation of Bi: A probe for thermal spike damage. J Phys: Condens Matter **5**, 4573–4584

Dunlop A., Lesueur D., Legrand P., Dammak H. and Dural J. (1994): Effects induced by high electronic excitations in pure metals: A detailed study in iron. Nucl Instr Meth Phys B **90**, 330–338

Fleischer R.L., Price P.B. and Walker R.M. (1975): Nuclear Tracks in Solids, Principles and Applications, University of California Press, Berkeley

Fuchs G., Studer F., Balanzat E., Groult D., Toulemonde M. and Jousset J.C. (1987): Influence of the electronic stopping power on the damage rate on yttrium-iron garnets irradiated by high-energy heavy ions. Europhys Lett **3**, 321–325

Gaiduk P.I., Nylandsted Larsen A., Trautmann C. and Toulemonde M. (2002): Discontinuous tracks in arsenic-doped crystalline $Si_{0.5}Ge_{0.5}$ alloy layers. Phys Rev B **66**, 045316 (1–5)

Gervais B. and Bouffard S. (1994): Simulation of the primary stage of the interaction of swift heavy ions with condensed matter. Nucl Instr Meth **B** 88, 355–364

Glasmacher U.A., Lang M., Keppler H., Langenhorst F., Neumann R., Schardt D., Trautmann C. and Wagner G.A. (2006): Phase transitions in solids stimulated by simultaneous exposure to high pressure and relativistic heavy ions. Phys Rev Lett **96**, 195701 (1–4)

Groult D., Hervieu M., Nguyen N. and Raveau B. (1988): 3.1 GeV-Xenon latent tracks in $Bi_2Fe_4O_9$: Mössbauer and electron microscopy studies. J Sol Stat Chem **76**, 248–259

Haglund R.F. and Kelly R. (1992): Electronic processes in sputtering by laser beams, Mat. Fys. Medd. Dan. Vid. Selsk 43 (1992) 527-592

Hémon S., Challey V., Dooryhée E., Dufour C., Gourbilleau F., Levesque F. and Paumier E. (1997): Phase transformation of polycrystalline Y_2O_3 under irradiation with swift heavy ions. Nucl Instr Meth B **122**, 563–565

Hou M.-D., Klaumünzer S. and Schumacher G. (1990): Dimensional changes of metallic glasses during bombardment with fast heavy ions. Phys Rev B **41**, 1144–1157

Houpert C., Studer F., Groult D. and Toulemonde M. (1989): Transition from localized defects to continuous latent tracks in magnetic insulators irradiated by high energy heavy ions: A HREM investigation. Nucl Instr Meth B **39**, 720–723

Huber F., Bimbot R. and Gauvin H. (1990): Range and stopping power tables for 2.5 to 500 MeV/u, heavy ions in solids. At Nucl Data Tables **46**, 1–215

Itoh N. and Stoneham A.M. (1998): Excitonic model of track registration of energetic heavy ions in insulators. Nucl Instr Meth B **146**, 362–366

Iwase A., Sasaki S., Iwata T. and Nihira T. (1987): Anomalous reduction of stage-I recovery in nickel irradiated with heavy ions in the energy range 100–120 MeV. Phys Rev Lett **58**, 2450–2453

Jensen J., Dunlop A., Della Negra S. and Toulemonde M. (1998): A comparison between tracks created by high energy mono-atomic and cluster ions in $Y_3Fe_5O_{12}$. Nucl Instr Meth B **146**, 412–419

Kamarou A., Wendler E. and Wesch W. (2005): Charge state effect on near-surface damage formation in swift heavy ion irradiated InP. J Appl Phys **97**, 123532 (1–6)

Khalfaoui N., Rotaru C.C., Bouffard S., Toulemonde M., Stoquert J.P., Haas F., Trautmann C., Jensen J. and Dunlop A. (2005): Characterization of swift heavy ion tracks in CaF_2 by scanning force and transmission electron microscopy. Nucl Instr Meth B **240**, 819–829

Klaumünzer S., Hou M.-D. and Schumacher G. (1986): Coulomb explosions in a metallic glass due to the passage of fast heavy ions. Phys Rev Lett **57**, 850–853

Lang M., Glasmacher U.A., Moine B., Neumann R. and Wagner G.A. (2004): Etch-pit morphology of tracks caused by swift heavy ions in natural dark mica. Nucl Instr Meth B **218**, 466–471

Levalois M., Bogdanski P. and Toulemonde M. (1992): Induced damage by high energy heavy ion irradiation at the GANIL accelerator in semiconductor materials. Nucl Instr Meth B **63**, 14–20

Lesueur D. and Dunlop A. (1993): Damage creation via electronic excitations in metallic target – Part II: A theoretical model. Radiat Eff and Def Sol **126**, 163–172

Liu J., Neumann R., Trautmann C. and Müller C. (2001): Tracks of swift heavy ions in graphite studied by scanning tunneling microscopy. Phys Rev B **64**, 184115 (1–7)

Meftah A., Brisard F., Costantini J.M., Hage-Ali M., Stoquert J.P. and Toulemonde M. (1993): Swift heavy ions in magnetic insulators: A damage cross section velocity effect, Phys Rev B **48**, 920–925

Meftah A., Brisard F., Costantini J.M., Dooryhee E., Hage-Ali M., Hervieu M., Stoquert J.P., Studer F. and Toulemonde M. (1994): Track formation in SiO_2 quartz and the thermal spike mechanism. Phys Rev B **49**, 12457–12463

Meftah A., Costantini J.M., Khalfaoui N., Boudjadar S., Stoquert J.P., Studer F. and Toulemonde M. (2005): Experimental determination of track cross-section in $Gd_3Ga_5O_{12}$ and comparison to the inelastic thermal spike model applied to several materials. Nucl Instr Meth B **237**, 563–574

Mieskes H.D., Assmann W., Grüner F., Kucal H., Wang Z.G. and Toulemonde M. (2003): Electronic and nuclear thermal spike effects in sputtering of metals with energetic heavy ions. Phys Rev B **67**, 155404 (1–9)

Müller C., Voss K.-O., Lang M. and Neumann R. (2003): Correction of systematic errors in scanning force microscopy images with application to ion track micrographs. Nucl Instr Meth B **212**, 318–325

Rizza G., Dunlop A. and Kopcewicz M. (2006): Deformation bands in metallic glasses induced by swift heavy ions. Nucl Instr Meth B **245**, 130–132

Rotaru C. (2004): SiO_2 sur Silicium: Comportement sous irradiation avec des ions lourds. PhD Thesis, University of Caen, web site http://tel.archives-ouvertes.fr/tel-00005399

Saleh S.A. and Eyal Y. (2005): Porous track cores along wakes of swift Pb ions in LiF. Nucl Instr Meth B **230**, 246–250

Schwartz K., Trautmann C., Steckenreiter T., Geiss O. and Krämer M. (1998): Damage and track morphology in LiF crystals irradiated with GeV ions. Phys Rev B **58**, 11232–11240

Seiberling L.E., Griffith J.E. and Tombrello T.A. (1980): A thermalized ion explosion model for high energy sputtering and track registration, Rad. Eff. 52 (1980) 201–210

Silk E. and Barnes R. (1959): Examination of fission fragment tracks with electron microscopy. Phil Mag **4**, 970–971

Sigmund P. (1974/1975): Energy density and time constant of heavy-ion-induced elastic-collision spikes in solids. Appl Phys Lett **25**, 169–171 and Appl Phys Lett **27**, 52

Sigmund P. and Claussen C. (1981): Sputtering from elastic-collision spikes in heavy-ion-bombarded metals. J Appl Phys **52**, 990–993

Sigmund P. and Schinner A. (2002): Binary theory of electronic stopping. Nucl Instr Meth B **195**, 64–90

Studer F. and Toulemonde M. (1992): Irradiation damage in magnetic insulators. Nucl Instr Meth B **65**, 560–567

Szenes G., Horvath Z.E., Pecz B., Paszti F. and Toth L. (2002): Tracks induced by swift heavy ions in semiconductors. Phys Rev B **65**, 045206 (1–11)

Szenes G. (1995): Ion-velocity-dependent track formation in yttrium iron garnet: A thermal-spike analysis. Phys Rev B **52**, 6154–6157

Thibaudau F., Cousty J., Balanzat E. and Bouffard S. (1991): Atomic-force-microscopy observations of tracks induced by swift Kr ions in mica. Phys Rev Lett **67**, 1582–1585

Toulemonde M., Fuchs G., Nguyen N., Studer F. and Groult D. (1987): Damage processes and magnetic field orientation in ferromagnetic oxides $Y_3Fe_5O_{12}$ and $BaFe_{12}O_{19}$ irradiated by high-energy heavy ions: A Mössbauer study. Phys Rev B **35**, 6560–6569

Toulemonde M. and Studer F. (1988): Comparison of the radii of latent tracks induced by high-energy heavy ions in $Y_3Fe_5O_{12}$ by HREM, channelling Rutherford backscattering and Mössbauer spectrometry. Phil Mag A **58**, 799–807

Toulemonde M., Dufour Ch., Meftah A. and Paumier E. (2000): Transient thermal processes in heavy ion irradiation of crystalline inorganic insulators. Nucl Instr Meth B **166–167**, 903–912

Toulemonde M., Ramos S.M.M., Bernas H., Clerc C., Canut B., Chaumont J. and Trautmann C. (2001): MeV gold irradiation induced damage in α-quartz: competition between nuclear and electronic stopping. Nucl Instr Meth B **178**, 331–336

Toulemonde M., Assmann W., Grüner F. and Trautmann C. (2002): Jetlike component in sputtering of LiF induced by swift heavy ions. Phys Rev Lett **88**, 057602 (1–4)

Toulemonde M. (2006): Irradiation by swift heavy ions: Influence of the non-equilibrium projectile charge state for near surface experiments. Nucl Instr Meth **250**, 263

Trinkaus H. and Ryazanov A.I. (1995): Viscoelastic model for the plastic flow of amorphous solids under energetic ion bombardment. Phys Rev Lett **74**, 5072–5075

Träholt C., Wiesner J., Zandbergen H.-W., Fuess H., Wirth G. and Wen J.-G. (1996): High resolution electron microscopy of heavy-ion induced defects in superconducting Bi-2212 thin films in relation to their effect on J_c. Physica C **268**, 161–172

Trautmann C., Costantini J.M., Meftah A., Schwartz K., Stoquert J.P. and Toulemonde M. (1998): Swelling of SiO_2 quartz induced by energetic heavy ions. Mat Res Symp Proc **504**, 123–128

Trautmann C., Toulemonde M., Schwartz K., Costantini J.M. and Müller A. (2000a): Damage structure in the ionic crystal LiF irradiated with swift heavy ions. Nucl Instr Meth B **164–165**, 365–376

Trautmann C., Klaumünzer S. and Trinkaus H. (2000b): Effect of stress on track formation in amorphous iron boron alloy: Ion tracks as elastic inclusions. Phys Rev Lett **85**, 3648–3651

Trautmann C., Boccanfuso M., Benyagoub A., Klaumünzer S., Schwartz K. and Toulemonde M. (2002): Swelling of insulators induced by swift heavy ions. Nucl Instr Meth B **191**, 144–148

Van Dillen T., Polman A., van Kats C.M. and Van Blaaderen A. (2003): Ion beam-induced anisotropic plastic deformation at 300 keV. Appl Phys Lett **83**, 4315–4317

Vetter J., Scholz R., Dobrev D. and Nistor L. (1998): HREM investigation of latent tracks in GeS and mica induced by high energy ions. Nucl Instr Meth B **141**, 747–752

Villa F., Grivet M., Rebetez M., Dubois C., Chambaudet A., Chevarier A., Martin P., Brossard F., Blondiaux G., Sauvage T. and Toulemonde M. (1999): Damage morphology of Kr ion tracks in apatite: Dependence on dE/dx. Radiat Meas **31**, 65–70

Waligorski M.P.R., Hawn R.N. and Katz R. (1986): The radial distribution of dose around the path of a heavy ion in liquid water. Nucl Track Radiat Meas **11**, 309–319

Wang Z.G., Dufour Ch., Paumier E. and Toulemonde M. (1994/1995): The S_e sensitivity of metals under swift-heavy-ion irradiation: A transient thermal process. J Phys Condens Matt **6**, 6733–6750 and **7**, 2525–2526

Wesch W., Kamarou A. and Wendler E. (2004): Effect of high electronic energy deposition in semiconductors. Nucl Instr Meth B **225**, 111–128

Wiss T., Matzke Hj., Trautmann C., Toulemonde M. and Klaumünzer S. (1997): Radiation damage in UO_2 by swift heavy ions. Nucl Instr Meth B **122**, 583–588

Young D.A. (1958): Etching of radiation damage in lithium fluoride. Nature **183**, 375–377

Ziegler J.F. (1999): Stopping of energetic light ions in elemental matter. J Appl Phys **85**, 1249–1272

Thermal-Spike Models for Ion Track Physics: A Critical Examination

S. Klaumünzer*

Ionenstrahllabor, Hahn-Meitner-Institut
Glienicker Str. 100, 14091 Berlin, Germany

Abstract

Thermal-spike models are often invoked for data interpretation in ion track physics. This work is devoted to a critical examination of these models with respect to links to other fields of physics and with respect to its foundations in non-equilibrium thermodynamics. Presently used thermal-spike models treat electronic excitations in a rather undifferentiated way. Based on the experience of hot-electron energy-transport in semiconductors a more complete approach will be outlined which explicitly distinguishes electrons in conduction bands and holes in valence bands. This model provides a natural basis for the incorporation of recombination processes and is intimately linked to the physics of semiconductors and insulators. Combining a thermal spike with the appropriate constitutive equations, the motion of the fluid track matter can be followed as will be demonstrated for vitreous silica. The calculations reproduce the experiments within a factor of four. Starting from the basis of non-equilibrium thermodynamics, it will be shown that the temperature gradients appearing in the presently used thermal-spike models are too large to meet the pre-requisites of non-equilibrium thermodynamics. Therefore, thermal-spike models can only be used for qualitative to semi-quantitative data interpretation. Deviations between model and experiment by a factor of 2 to 4 must be accepted and are the tribute to the enormous simplifications made.

* E-mail: klaumuenzer@hmi.de

Contents

1 Introduction **294**

2 The Starting Point for Thermal-Spike Models **296**
2.1 Insulators and Semiconductors 296
2.2 Metals 298

3 Hydrodynamic and Energy-Transport Models **299**
3.1 An Energy-Transport Model for Non-Metals (Grasser et al., 2003a) 299
3.2 Silicon 302
3.3 Quartz and Silica 303
3.4 Metals 304

4 The Thermal-Spike Model of Toulemonde et al. **305**

5 The Thermal-Spike Model of Szenes **308**

6 Ion Track Mechanics **310**
6.1 Ion Hammering of Amorphous Materials 310
6.2 The Effective-Flow-Temperature Approach (EFTA) of Trinkaus 311
6.3 Trinkaus' Constitutive Equations for Ion Hammering 313

7 Elements of Non-Equilibrium Thermodynamics **318**

8 Conclusions **322**

Acknowledgements **323**

References **323**

1. Introduction

The physics of ion tracks started in 1958, when Young reported on the etching of radiation damage in LiF (Young, 1958). A year later, Silk and Barnes (1959) published the first transmission electron microscopy images of long trails of damage created by fission fragments in mica. The combination of both discoveries generated a boom in research work stimulated by various applications in nuclear physics, geochronology, archaeology, interplanetary science, and radiation dosimetry. Soon after the discovery of ion tracks it became clear that they originated from the excitation and ionization of the target atoms and not from atomic displacements by elastic collisions, a damaging mechanism dominating at ion energies much smaller than 1 MeV/u. It became also clear that the excitation and/or

ionization density had to surpass a material-dependent threshold value in order to generate continuously etchable ion tracks. For example, 1-MeV He ions were shown to generate tracks in certain polymers, while 100-MeV Fe ions are needed for track formation in the mineral olivine. At that time, tracks could be detected in many insulators but not in metals, alloys and semiconductors like silicon or germanium. The separation line between track forming and non-track-forming materials was located at an electrical resistivity between 2×10^3 and 2×10^4 Ωcm. In 1965, Fleischer, Price and Walker proposed the Coulomb-explosion spike which accounted reasonably well for all experimental data available at that time (Fleischer et al., 1965). A concurring thermal-spike mechanism, originally devised for metals by Lifshitz et al. (1960) and proposed to apply also to insulators by Chadderton (1969), was not sufficiently developed to provide useful predictions. The work of the first fifteen years after the discovery of ion tracks is exhaustively described in the monograph of Fleischer, Price and Walker (1975). The development of the subsequent fifteen years has been summarized by Spohr (1990).

Around 1980, with the advent of large heavy-ion accelerators, much higher excitation and ionization densities became easier accessible. About fifteen years later even larger excitation densities could be realized by fullerene beams. At present, it is well-established that ion tracks can be also generated in metals (Henry et al., 1992; Dammak et al., 1995), alloys (Barbu et al., 1991; Audouard et al., 1990; Trautmann et al., 1993) and semiconductors (Scholz et al., 1993; Canut et al., 1998; Dunlop et al., 1998; Wesch et al., 2004), but the thresholds for track generation are usually larger than those for insulators. Therefore, the experimental data base on ion tracks in insulators is still wider than that for metals and semiconductors.

There have been various attempts (Klaumünzer et al. 1986; Lesueur and Dunlop, 1993) to modify the Coulomb-explosion spike to include the new experimental findings. But a prerequisite for this mechanism, the occurrence of a repulsive Coulomb force of sufficient strength and lifetime, turned out to be not fulfilled since in metals electrical space charges are virtually neutralized within femtoseconds as confirmed by spectroscopy of Auger and convoy electrons (Schiwietz et al., 1992, 2004,; Xiao et al., 1996, 1997). Therefore, it is not surprising that the thermal spike mechanism underwent a renaissance, in particular by the work of Toulemonde et al. (1993a, 1993b), Dufour et al. (1993) and Szenes (1995). An overview on the current experimental situation concerning ion tracks in insulators and on thermal-spike models is given by Toulemonde et al. (2006).

Thermal-spike models are not only used in ion-track physics, but also to describe the behavior of excited carriers generated by femtosecond lasers or by strong electrical fields in submicron semiconductor devices. Though these various

models deal with similar physical problems, they do not take much notice of each other. The consequence is that knowledge, which has been gained in one field, is not transferred to the others. A severe deficiency of the currently used thermal-spike models in ion track physics is the missing distinction between the two kinds of excitations in semiconductors and insulators, namely electrons in the conduction band and holes in the valence band. However, this distinction is essential to exploit the wealth of information available in the physics of semiconductors and insulators.

In Section 2, I briefly summarize what is known about electron-hole formation by fast ions in semiconductors and insulators. The key quantity is the so-called W-value which is the average energy needed to generate an electron-hole pair. With this quantity a surprising result will be obtained: the sum of the average kinetic energies of holes and electrons is independent of the radial distance from the ion trajectory. This result can be taken as the starting point for a thermal-spike model, which explicitly distinguishes holes and electrons. Such a model is outlined in Section 3 and compared to the thermal-spike models of ion track physics in Sections 4 and 5.

A common basis of all thermal-spike models is the validity of classical heat transport as it is described by Fourier's law. However, guided by their molecular dynamics simulations based on a Lennard–Jones potential, Bringa and Johnson (1998) argued that energy transport after ion impact does not follow classical heat conduction. Additionally, they pointed out that the atomic motion in the track, together with energy fluctuations and inertia effects should not be ignored. While atomic motion and inertia effects can easily be incorporated into thermal-spike models (see Section 6), the inadequacy of classical heat transport remains a central and unsolved issue. In Section 7 it will be shown that the inadequacy of classical heat transport is not a peculiarity of the Lennard–Jones potential but follows from an inadequate use of non-equilibrium thermodynamics.

2. The Starting Point for Thermal-Spike Models

2.1. Insulators and Semiconductors

Most of the ion-track research has been done at kinetic ion energies between 1 and 10 MeV/u, where the electronic stopping power S_e is maximal. A 5-MeV/u projectile (projectile velocity $v_{ion} = 3.1 \times 10^7$ m/s) traverses 100 atomic layers in 1 fs and interacts primarily with the electrons of the target atoms. Thus, if the projectile charge is sufficiently large, a cylindrical trail of excited and/or ionized target atoms is created on a femtosecond time-scale. In a solid with sufficiently large gap en-

ergy E_{gap} between valence band and conduction band, screening of the projectile can be ignored. The radius $b_{\max}$ of the primary interaction can be obtained from Bohr's adiabatic principle (Mozumder, 1974) and is for non-relativistic ions

$$b_{\max} = \frac{\hbar\, v_{\mathrm{ion}}}{2E_{\mathrm{gap}}}. \tag{1}$$

For the ion energy range of interest, $b_{\max}$ is of the order of 1 nm. Assuming Coulomb interaction between projectile and target electrons the differential cross-section $\mathrm{d}\sigma/\mathrm{d}w$ for an energy transfer between w and $w + \mathrm{d}w$ is proportional to $1/w^2$ (Leibfried, 1965). For a free electron gas the mean transferred energy to an electron is

$$\langle w \rangle = \frac{\int_{w_{\min}}^{w_{\max}} w(\mathrm{d}\sigma/\mathrm{d}w)\,\mathrm{d}w}{\int_{w_{\min}}^{w_{\max}} (\mathrm{d}\sigma/\mathrm{d}w)\,\mathrm{d}w} = w_{\min} \log \frac{w_{\max}}{w_{\min}}, \tag{2}$$

with the maximum transferable energy

$$w_{\max} = 4\frac{M_{\mathrm{ion}}\, m_{\mathrm{e}}}{(M_{\mathrm{ion}} + m_{\mathrm{e}})^2} E_{\mathrm{ion}}, \tag{3}$$

where M_{ion} and m_{e} denote the ion and the electron mass, respectively, and E_{ion} the projectile energy. For a 5-MeV/u projectile $w_{\max}$ is about 11 keV. In insulators and semiconductors the minimum transferable energy $w_{\min}$ is E_{gap}. With these values, Equation (2) yields $\langle w \rangle = 10.5$ eV for silicon ($E_{\mathrm{gap}} = 1.15$ eV) and $\langle w \rangle = 82$ eV for quartz ($E_{\mathrm{gap}} = 12$ eV). Obviously, the primary effect of the ion-electron interaction is the production of electron-hole pairs with average kinetic energies of $\langle w \rangle - E_{\mathrm{gap}}$. For both solids the relation $\langle w \rangle - E_{\mathrm{gap}} \gg E_{\mathrm{gap}}$ holds, so that further electron-hole pairs can be generated until the kinetic energy of the colliding participants falls below E_{gap}. The time-scale of this electron-hole production process depends on the electron-impact ionization rate, which is for electrons (holes) in silicon and quartz 5 eV above (below) the gap about 10^{14} s^{-1} and 10^{15} s^{-1}, respectively (Cartier et al., 1993; Oguzman et al., 1995; Arnold et al., 1994; Kunikiyo et al., 2003). Thus, on a time-scale of 10 fs a heavy fast ion generates an electron-hole plasma, which can be described by electron and hole distribution functions $f_n(\mathbf{r}, \mathbf{k}, t)$ and $f_p(\mathbf{r}, \mathbf{k}, t)$ in the phase space $(\mathbf{r}, \mathbf{k})$ and time t. In principle, the further evolution of $f_n(\mathbf{r}, \mathbf{k}, t)$ and $f_p(\mathbf{r}, \mathbf{k}, t)$ has to be described by Boltzmann transport equations and requires an adequate specification of the relevant scattering processes. A full solution of these equations involves enormous computational work and has not yet been performed. An early treatment based on a hydrodynamical fluid approach of the electron-hole plasma generated by the passage of a fast ion has been given by Ritchie and Claussen (1982).

In another approach, electron-energy-transport calculations have been performed, but were limited to short times and based on Monte-Carlo methods with simplified material parameters (Hamm et al., 1979; Gervais and Bouffard, 1994; Bouffard, 1996). It is well established that momentum transfers between the projectile ion and target electrons lead to an initial electrical space charge. However, quasi-neutralization occurs within a few femtoseconds (see Section 3) and in most calculations of radial dose distributions $D(r, t)$ space charge effects are not included. Because of the importance of radiation protection, much effort has been put in calculating the radial dose distribution in water and comparing these results with measurements on tissue-equivalent gases after rescaling to the density of water. With appropriate modifications arising from different mass densities and ignoring differences in electronic band structure, these results have also been applied to solids (Katz et al., 1990). With the radial dose distribution $D(r, t_0)$ with $t_0 > 10$ fs after the ion's passage the number density of electrons $n(r, t_0)$ in the conduction band and the number density of holes $p(r, t_0)$ in the valence band can be obtained from

$$n(r, t_0) = p(r, t_0) = \frac{D(r, t_0)}{W}. \tag{4}$$

For the average energy W required to generate an electron-hole pair, theory predicts $W \approx 3E_{\mathrm{gap}}$, a relation which is well confirmed by experiments – in silicon even up to high excitation densities (Alig and Bloom, 1975; Ogihara et al., 1986; Seidl et al., 2001). If we denote with $w_n(r, t_0)$ and $w_p(r, t_0)$ the average kinetic energies of electrons and holes, energy conservation demands

$$n(r, t_0)(w_n(r, t_0) + w_p(r, t_0)) = D(r, t_0) - n(r, t_0)E_{\mathrm{gap}}$$

or, by dividing by $n(r, t_0)$

$$w_n(r, t_0) + w_p(r, t_0) \approx 2E_{\mathrm{gap}}. \tag{5}$$

The surprising message of relation (5) is that the average kinetic energy per electron-hole pair is independent of the distance r from the ion trajectory. If we assume Boltzmann statistics for the electron-hole plasma and $w_n = w_p$ we obtain from Equation (5) an initial ($t_0 \sim 10$ fs) electron temperature $T_n = 2E_{\mathrm{gap}}/(3k_{\mathrm{B}}) \approx 9 \times 10^3$ K for silicon and 9×10^4 K for quartz. *A priori*, there is no reason that w_n and w_p are equal. For quartz, $w_p \approx 0.5w_n$ might be more appropriate (Mizuno et al., 1993) resulting in an electron temperature $T_n = 8E_{\mathrm{gap}}/(9k_{\mathrm{B}}) \approx 1.2 \times 10^5$ K and a hole temperature $T_p \approx 4E_{\mathrm{gap}}/(9k_{\mathrm{B}}) \approx 0.6 \times 10^5$ K. The estimate for silicon compares reasonably well with the experimental electron temperatures obtained from Auger electron spectroscopy. Depending on the interaction strength the Si-L^1VV transition (half-life 15 fs) yields electron temperatures between 7×10^3 and

1.6×10^4 K (Schiwietz et al., 2004). The same authors (Staufenbiel et al., 2005) report for the same irradiation conditions electron temperatures of $> 4.9 \times 10^4$ K. In fact, the extracted electron temperatures depend sensitively on the silicon band structure used in the data evaluation process. In the work of Staufenbiel et al. (2005), a simplified data evaluation has been performed and the obtained electron temperatures are too high (Schiwietz, 2006). Unfortunately, no experimental values are available for quartz.

2.2. METALS

In metals and semi-metals $b_{\max}$ is limited by conduction electron screening. Applying again Bohr's adiabatic principle one obtains (Mozumder, 1974)

$$b_{\max} = 1.12 \, \frac{v_{\text{ion}}}{\Omega_{\text{plasma}}} \,, \tag{6}$$

where Ω_{plasma} is the plasma frequency of the electron gas. Assuming again a free electron gas, $w_{\min}$ for metals and semi-metals can be estimated by (Leibfried, 1965).

$$w_{\min} = \frac{Z_{\text{ion,eff}}^2 q^4}{4\pi^2 \varepsilon_0^2 b_{\max}^2 w_{\max}^2 + Z_{\text{ion,eff}}^2 q^4} \, w_{\max}, \tag{7}$$

where $Z_{\text{ion,eff}}$ denotes the effective projectile charge, ε_0 the dielectric permittivity and q the (positive) elementary charge. With $b_{\max}$ from Equation (6) we find for a typical metal $w_{\min} \sim 4$ eV and thus $\langle w \rangle \sim 30$ eV. In contrast to semiconductors and insulators, the excited electrons and holes in metals belong to the same band. Thermalization within the electronic system occurred within ~10 fs and holes need not to be considered any longer. The excitation energy is shared among many conduction band electrons around the ion trajectory and, different from insulators or semiconductors, the concentration of conduction electrons is virtually independent of the distance from the ion trajectory in a spatially homogeneous material.

3. Hydrodynamic and Energy-Transport Models

In semiconductor devices of sub-micrometer dimensions hot electrons can be generated by strong electrical fields. For simulation of such devices, however, the Boltzmann transport equation is computationally very expensive. A common simplification is to investigate only the first three or four moments of the electron and hole distribution functions, which lead directly back to macroscopic transport

models, called in literature hydrodynamic or energy-transport models. A recent review of hydrodynamic and energy-transport models has been given by Grasser et al. (2003a). The various models differ in the number of moments considered and/or in the approximations made in the collision term of the Boltzmann equation. The advantage of these models is that their input and output can be directly taken from or compared with experiment. However, it has turned out that the first three moments are not sufficient to describe high-electron-mobility devices of dimensions of the order of ~100 nm. At present, there are models incorporating even the sixth moment of the Boltzmann transport equation (Grasser et al., 2003b). Because track formation occurs on a length scale much smaller than the currently envisaged electronic devices, it is possible that a reduction of the Boltzmann transport equation to macroscopic transport models may lead to serious errors. This problem will be readdressed in Section 7. In the following a three-moment model will be outlined in order to demonstrate a thermal-spike model for ion track formation, which explicitly distinguishes electrons and holes.

3.1. An Energy-Transport Model for Non-Metals (Grasser et al., 2003a)

Assume that within ~10 fs electron-hole production has finished and electron-hole collisions brought the carriers locally into thermal equilibrium. Because electrons and holes belong to different bands the corresponding energy distributions are characterized by different temperatures. The atomic motion is characterized by the lattice temperature T_L. The basic equations for mobile charge carriers in semiconductors and insulators are the Poisson equation and the continuity equations:

$$\operatorname{div}(\varepsilon_{\text{rel}}\,\varepsilon_0\,\operatorname{grad}\varphi) = q(n - p - c_{\text{dop}}), \tag{8}$$

$$\operatorname{div}\mathbf{j}_n - q\frac{\partial n}{\partial t} = q(R_{\text{dir}} + R_{\text{SHR}} + R_{\text{Auger}} + R_{\text{self trap}} + \cdots), \tag{9}$$

$$\operatorname{div}\mathbf{j}_p + q\frac{\partial p}{\partial t} = -q(R_{\text{dir}} + R_{\text{SHR}} + R_{\text{Auger}} + R_{\text{self trap}} + \cdots), \tag{10}$$

where φ denotes the electrostatic potential, ε_{rel} the relative dielectric constant, and c_{dop} the concentration of ionized dopants. In the following we assume $c_{\text{dop}} = 0$. On the right hand side of formulae (9) and (10), the R's denote various recombination processes in semiconductors and insulators (Figure 1). R_{dir} denotes the recombination rate of charge carriers by photon emission, which transports energy out of the track region because the probability of immediate reabsorption is

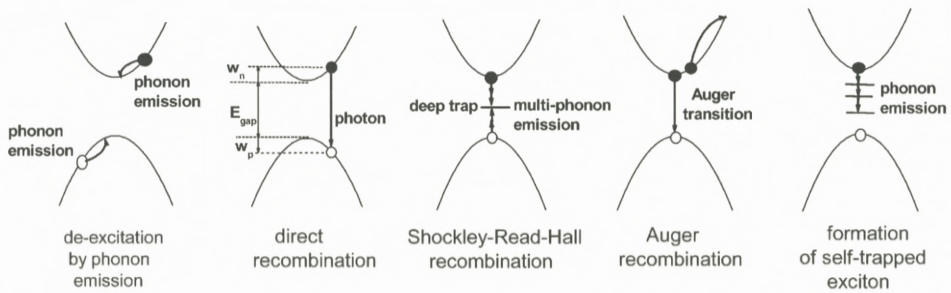

Figure 1. A schematic representation of the various de-excitation and recombination mechanisms important in semiconductors and insulators.

low. Direct recombination is particularly important in direct semiconductors like InP and GaAs. Instead of photon emission, carrier recombination can also take place by the simultaneous emission of many phonons. This process, however, is extremely improbable. But the probability of carrier recombination increases by orders of magnitude when defects or impurities exist, which have electronic states in the mid-gap region (Hall, 1952; Shockley and Read, 1952). These deep traps act as catalysts for recombination, characterized by the Shockley–Hall–Read recombination rate R_{SHR}. The recombination energy is roughly E_{gap} and is transferred to the lattice. The third recombination process is the internal Auger effect. It is particularly important at high carrier densities and is characterized by a recombination rate R_{Auger}. In this process the recombination energy contributes to electron heating. While these three recombination mechanisms are the most important ones in semiconductors, there exists another route of recombination in wide-gap insulators of low atomic density, like quartz, $LiNbO_3$ and polymers. Due to their opposite electrical charges, electrons and holes attract each other forming exciton states in the band gap. It is possible that the nearby lattice atoms undergo successive atomic rearrangements with simultaneous phonon generation so that the electron-hole pair is strongly bound and immobilized – a self-trapped exciton. The formation rate is denoted by R_{self}.

In the energy-transport model the current densities for electrons and holes read

$$\mathbf{j}_n = -q\mu_n n \operatorname{grad} \varphi + k_{\mathrm{B}}\mu_n \operatorname{grad} (nT_n), \tag{11}$$

$$\mathbf{j}_p = -q\mu_p p \operatorname{grad} \varphi - k_{\mathrm{B}}\mu_p \operatorname{grad} (pT_p), \tag{12}$$

where μ_n and μ_p denote the mobilities of electrons and holes, respectively. In Equations (11) and (12) it is assumed that the band structure of the material in spatially homogeneous. In bilayer or multilayer materials, additional terms have

to be added, which take into account spatial band structure variations. Energy conservation demands

$$\begin{aligned} \operatorname{div} \mathbf{S}_n &= -\mathbf{j}_n \operatorname{grad} \varphi - \frac{3}{2} k_\mathrm{B} \left(\frac{\partial (n T_n)}{\partial t} + \frac{T_n - T_\mathrm{L}}{\tau_n} n + T_n R_\mathrm{dir} \right) \\ &\quad + R_\mathrm{Auger} E_\mathrm{gap}, \end{aligned} \tag{13}$$

$$\operatorname{div} \mathbf{S}_p = -\mathbf{j}_p \operatorname{grad} \varphi - \frac{3}{2} k_\mathrm{B} \left(\frac{\partial (p T_p)}{\partial t} + \frac{T_p - T_\mathrm{L}}{\tau_p} p + T_p R_\mathrm{dir} \right), \tag{14}$$

$$\begin{aligned} \operatorname{div} \mathbf{S}_\mathrm{L} &= -\rho_\mathrm{L} c_\mathrm{L} \frac{\partial T_\mathrm{L}}{\partial t} + \frac{3}{2} k_\mathrm{B} \left(n \frac{T_n - T_\mathrm{L}}{\tau_n} + p \frac{T_p - T_\mathrm{L}}{\tau_p} \right) \\ &\quad + R_\mathrm{SRH}\, E_\mathrm{gap} + R_\mathrm{self\ trap} \left(E_\mathrm{gap} - E_\mathrm{exc} \right) \end{aligned} \tag{15}$$

with the energy fluxes

$$\mathbf{S}_n = -\kappa_n \operatorname{grad} T_n - \frac{5}{2} k_\mathrm{B} T_n \frac{\mathbf{j}_n}{q}, \tag{16}$$

$$\mathbf{S}_p = -\kappa_p \operatorname{grad} T_p + \frac{5}{2} k_\mathrm{B} T_p \frac{\mathbf{j}_p}{q}, \tag{17}$$

$$\mathbf{S}_\mathrm{L} = -\kappa_\mathrm{L} \operatorname{grad} T_\mathrm{L}, \tag{18}$$

where it has been assumed that the carriers obey Boltzmann statistics. τ_n and τ_p are average energy relaxation times for electrons and holes, respectively, due to interaction with the lattice. The various energy terms arising from the recombination processes can be inferred from Figure 1.

Using a generalized Wiedemann–Franz law, the thermal conductivity of the electrons is given by (Stratton, 1962; Grasser et al., 2003a)

$$\kappa_n = \left(\frac{5}{2} + c_n \right) \frac{k_\mathrm{B}^2}{q} T_n \mu_n n \tag{19}$$

and that of holes

$$\kappa_p = \left(\frac{5}{2} + c_p \right) \frac{k_\mathrm{B}^2}{q} T_p \mu_p p, \tag{20}$$

where c_n and c_p denote correction factors, the numerical values of which depend on the details of the collision term in the Boltzmann transport equation. κ_L is the phonon thermal conductivity.

For insulators and semiconductors, Equations (8) to (20) represent a closed set of differential equations which, in principle, can be solved if μ_n, τ_n, c_n, μ_p, τ_p, c_p and the recombination rates are specified. At least for technologically relevant semiconductors data are available in the literature. In this paper, Equations (8) to (20) will not be solved but two limiting cases will be considered. The first case is silicon in which carrier trapping and recombination do not play a role on a time-scale relevant for track formation (< 100 ps). Another limiting case is represented by quartz and vitreous silica in which the formation of self-trapped excitons is the dominating recombination process.

3.2. Silicon

Experiments have shown that in silicon the average energy for electron-hole production W varies by less than 5% going from low-density charge carrier production by x-ray radiation to high-density charge carrier production by 3-MeV/u Au ion bombardment (Alig and Bloom, 1975; Ogihara et al., 1986). The concomitant small deficit in charge collection in surface-barrier silicon-detectors implies that trapping and recombination of carriers are unimportant, i.e. all R_i-terms vanish in Equations (9, 10), and (13–15). Furthermore, in silicon the energy relaxation times for electrons and holes, τ_n and τ_p, are equal and are between 0.15 and 0.3 ps (Sekido et al., 1991; Bordelon et al., 1991; Roldan et al., 1996). These relaxation times are much longer than the equilibration times set by electron-electron and electron-hole collisions (Yoffa, 1980). Therefore, on a time-scale of 10 fs, the interacting electron-hole system is in a quasi-adiabatic state, which implies $T_n = T_p$.

Due to momentum transfers during the collisions between projectile ions and target electrons, there is an electrical charge proportional to $(n - p)$. The emerging electrical field in combination with the high mobility of the carriers in silicon must lead to a rapid quasi-neutralization. The neutralization time t_{neutr} can be estimated from the Debye screening length and the mobility of the fastest carrier (Lifshitz and Pitajewski, 1983)

$$t_{\text{neutr}} = \frac{\varepsilon_0 \varepsilon_{\text{rel}}}{q \mu_n(T_\text{L}, T_n) n}, \tag{21}$$

where μ_n is given by (Grasser et al., 2003a)

$$\mu_0(T_\text{L}, T_n) = \frac{\mu_n(T_\text{L})}{1 + [3k_\text{B}\mu_0(T_\text{L})/2q\tau_n v_{\text{sat}}^2](T_n - T_\text{L})}. \tag{22}$$

Assuming a cold lattice with $T_\text{L} = 300$ K and a hot electron-hole plasma with $T_n = 10^4$ K and an electron-hole density of $n = 10^{21}$ cm^{-3} we obtain $\mu_n \approx$

12×10^{-2} cm^2/Vs and $t_{\text{neutr}} \approx 0.5$ fs, where we have used the literature data for crystalline silicon $\mu_0(300\text{K}) = 1430$ cm^2/Vs, $\varepsilon_{\text{rel}} = 11.9$, $\tau_n = 0.15$ ps, and $v_{\text{sat}} = 10^7$ cm/s (Bordelon et al., 1991). Quasi-neutralization and thermalization within the electron-hole system occur approximately on the same time-scale.

Perfect neutralization would be given by $n = p$ and any electrical field would vanish (grad $\varphi = 0$ in Equation (8)). Adding Equations (9) and (10), one obtains $\text{div}(\mathbf{j}_n + \mathbf{j}_p) = \partial(n-p)/\partial t = 0$ implying $j_n = -j_p$. However, this relation is only compatible with formulae (11) and (12) if $\mu_n = \mu_p$ holds. This is usually not the case and charge neutralization cannot be perfect. Therefore, in crystalline silicon a small ion track potential is expected as it has been measured by Auger electron spectroscopy (Schiwietz et al., 2003). For $t > t_{\text{neutr}}$ electron and hole diffusion is coupled by an electric field; this effect is long known in semiconductor physics and called ambipolar diffusion.

3.3. Quartz and Silica

In silica the electrons move much faster than the holes. Using $\mu_0(300\text{K}) = 20$ cm^2/Vs (Hughes, 1973), $v_{\text{sat}} \approx 2 \times 10^7$cm/s (Hughes, 1975), $\varepsilon_{\text{rel}} = 2.4$ and $T_n = 1 \times 10^5$ K one obtains from Equations (21) and (22) $\mu_n = 1$ cm^2/Vs and $\tau_{\text{neutr}} = 2$fs. Like in silicon only a small track potential is expected. Electrons and holes with kinetic energies < 2 eV couple strongly to longitudinal optical phonons. For conduction electron energies > 2 eV acoustic phonon emission becomes also important. In this energy range, the energy relaxation time τ_n is about 0.1 ps (Arnold et al., 1994). After quasi-neutralization and cooling of the carriers by electron-phonon coupling the potential energy, which is still stored in electron-hole pairs, is partially released by the formation of self-trapped excitons. Laser experiments have shown that the mean trapping time is about 0.15 ps (Audebert et al., 1994; Guizard et al., 1996a, 1996b), only slightly longer than the energy relaxation time. On a timescale of 0.15 ps, mobile carriers disappear ($n = p = 0$ in Equations (8) to (20)) implying that energy transport in the electron-hole system has finished and energy is dissipated only by phonons. According to Ismail-Beigi and Louie (2005) the potential energy stored in the self-trapped exciton is $E_{\text{exc}} \sim 7$ eV. Thus, the fraction $1 - f$ of the energy not yet converted to heat in the atomic system is 7 eV/3$E_{\text{gap}} \approx 0.2$ (cf. Sections 5 and 6).

For $T_{\text{L}} > 300$ K self-trapped excitons often relax non-radiatively and form lattice defects (E'-centers, etc.). Thus, a track may form when the density of self-trapped excitons is sufficiently large. This mechanism has been proposed by Itoh (1996). In fact, the measured track radii can be quantitatively well explained when the exciton density matches the atomic density of quartz. However, Itoh's mechanism ignores (i) the large amount of heat in the atomic system prior to

exciton formation and (ii) the interaction between the excitons which must occur at such high exciton densities. Perhaps, the correct solution is lattice instability (Stampfli, 1996).

Of course, not all wide-gap insulators exhibit self trapping of excitons. For example, laser experiments showed that in Al_2O_3 and MgO excited electrons are not trapped within 50 ps (Guizard et al., 1996a, 1996b). Nevertheless, in both materials ion track effects can be clearly detected (Canut et al., 1995; Thevenard et al., 1996). These wide-gap materials have to be treated more or less along the route as outlined for silicon.

3.4. METALS

In metals, the lifetime of holes in the conduction band is smaller than 20 fs, if their kinetic energy is more than 3 eV below the Fermi-energy (Campillo et al., 2000). Therefore, we have $p = 0$ in Equations (8) to (20) for $t > 20$ fs and all recombination processes vanish. In Equation (8), now qc_{dop} denotes the charge density of the positive jellium background. In the presence of a time-dependent temperature gradient, a closer inspection of Equations (8) to (11) shows that even in metals an ion track potential must exist and $\mathbf{j}_n$ cannot vanish completely. From an experimental point of view we only know that the nuclear track potential for metals is below the experimental resolution limit of ± 0.4 eV (Staufenbiel et al., 2005). Nevertheless, it is often assumed that terms containing $\mathbf{j}_n$ can be neglected. With this assumption the energy-transport model yields for metals

$$C_n \frac{\partial T_n}{\partial t} = \mathrm{div}\ (\kappa_n\ \mathrm{grad}\ T_n) - C_n \frac{T_n - T_{\mathrm{L}}}{\tau_n}\,, \tag{23}$$

$$C_{\mathrm{L}} = \frac{\partial T_{\mathrm{L}}}{\partial t} = \mathrm{div}\ (\kappa_{\mathrm{L}}\ \mathrm{grad}\ T_{\mathrm{L}}) + C_n \frac{T_n - T_{\mathrm{L}}}{\tau_n}, \tag{24}$$

where we have written $C_n = 3/2nk_{\mathrm{B}}$ as specific heat of the electron system.

The same two-temperature model is used to successfully describe the evolution of an electron gas in metals after laser excitation (Rethfeld et al., 2002). One of the basic assumptions of the energy-relaxation model is that the energy relaxation time τ_n is independent of the average kinetic energy of the electrons. Therefore, the energy relaxation times obtained from laser excitation experiments should be same as those used to describe ion track formation.

4. The Thermal-Spike Model of Toulemonde et al.

In the thermal-spike model of Toulemonde et al. (1993a, 1993b, 1996) and Meftah et al. (2005) the target solid is divided into the electronic system and the atomic system (phonons). Electrons and holes are not distinguished. Both systems are coupled by electron-phonon interaction. It is also assumed that the energy deposited in the electronic system by the projectile ion is thermalized with a time constant $\tau_e \approx 10^{-15}$ s by electron-electron scattering. The evolution of the two systems is described by two coupled differential equations, one for the electronic system

$$C_n \frac{\partial T_n}{\partial t} = \text{div } (\kappa_n \text{ grad } T_n) - g(T_n - T_L) + B(r, t) \tag{25}$$

and one for the atomic system

$$C_L(T_L) \frac{\partial T_L}{\partial t} = \text{div } (\kappa_L \text{ grad } T_L) + g(T_n - T_L), \tag{26}$$

where g denotes the electron-phonon coupling parameter. $B(r, t)$ is the energy density per unit time deposited by an incident ion at radius r and at time t. It is assumed that $B(r, t)$ has the form

$$B(r, t) = cD(r) \frac{e^{-t/\tau_e}}{\tau_e}. \tag{27}$$

The choice of τ_e is not critical; variation of τ_e by a factor of 5 does not alter the final results. The radial dose distribution $D(r)$ is usually taken from microdosimetry and the normalization constant c ensures energy conservation

$$2\pi \int_{t=0}^{\infty} \int_{r=0}^{\infty} B(r, t) r \, dr \, dt = S_e. \tag{28}$$

Apart from $B(r, t)$, which can be simulated by appropriate initial conditions, formulae (25) and (26) are identical with Equations (23) and (24) if $g = C_n/\tau_n$ is taken. Therefore, the application of Equations (25) and (26) to metals and metallic alloys (Wang et al., 1994) is, apart from the terms $\sim \mathbf{j}_n$, compatible with the energy transport model. C_n can be calculated from formulas of solid-state physics textbooks if the electron density or the density of states at the Fermi energy are known. The electron thermal conductivity κ_e can be calculated from the electrical conductivity σ_e by applying the Wiedemann–Franz law. The specific heat C_L can be taken either from measured values (after subtraction of C_n) or from the rule of Dulong–Petit in the case of elemental metals or Knoop's rule in the case of

alloys. Because κ_L is usually only a minor contribution to the total conductivity, the phonon thermal conductivity is difficult to determine from experimental data. Alternatively, κ_L may be determined using the relation

$$\kappa_L = \frac{1}{3} C_L \, v_{ph} \, \ell_{ph}, \tag{29}$$

where v_{ph} denotes an appropriately averaged phonon group velocity. For T_L much larger than the Debye temperature the mean free path of the phonons ℓ_{ph} can be estimated from (Ziman, 1975)

$$\ell_{ph} = \frac{20}{\langle \gamma^2 \rangle} \frac{T_M}{T_L} a, \tag{30}$$

where $\langle \gamma^2 \rangle$ is the squared Grüneisen parameter averaged over all phonon modes, T_m the melting temperature and a the lattice constant. For most materials $\langle \gamma^2 \rangle$ is typically between 2 and 6. Thus, at $T_L = T_m$, the phonon mean free path is between 1 and 3 nm. The electron-phonon coupling parameter can be obtained from the work of Lifshitz et al. (1960), in which a free-electron gas model has been used, or from the work of Allen (1987), where the modern solid-state physics language is used.

In applying their model to insulators, Toulemonde et al. (1993a, 1993b) ignore that the carriers of heat in the valence and conduction band are just the holes and electrons generated by the projectile. Hole and electron densities vary as a function of distance from the ion's path as outlined in Section 2, and, as shown in Section 3, the (assumed) diffusive motion of the carriers changes both the spatial energy density and the carrier density. The assumption $C_n = 1$ J/(cm^{3}K) and $K_n = 2$ W/cmK for all insulators and being independent of space and time (Toulemonde et al., 1996; Meftah et al., 2005) cannot be maintained. The assumption of constant carrier densities in space and time also implies that the energy input by the passage of the fast ion appears fully as kinetic energy of the carriers as described by formulae (27) and (28). Therefore, when electron-hole production is explicitly considered, these two equations also cannot be maintained. Without following electron-hole production in detail, the concept of the W-value provides a great simplification in answering the question in which way the energy input is partitioned in carrier production and in their kinetic energy (see Section 2).

In the thermal-spike model of Toulemonde et al., the electron-phonon parameter g is treated as a free parameter and adjusted to give optimum agreement with the measured radii of amorphous tracks in crystalline solids. An amorphous track is postulated to form whenever the lattice temperature exceeds the equilibrium melting temperature T_m of the solid. With this criterion, Toulemonde et al.

(1996) and Meftah et al. (2005) succeeded in modeling track radii as a function of stopping power for a variety of insulators. Additionally, the stopping power threshold S_{e0} for track formation and the velocity effect (Toulemonde et al., 2006) could be described. Interestingly, a correlation has been found between a so-called mean diffusion length λ and E_{gap}, where λ is defined by $\lambda^2 = \kappa_n \tau_n / C_n$. The larger the gap the smaller λ is (Toulemonde et al., 2006). For example, for quartz $\lambda = 4$ nm was obtained implying $\tau_n = 0.08$ ps. This value is not too far from the energy-relaxation time of 0.1 ps as determined from laser experiments (Arnold et al., 1994). It will be interesting to see whether the discovered correlation finds a natural explanation in the energy-transport model.

The use of equilibrium melting temperatures as a criterion for the determination of track radii cannot be maintained from the viewpoint of thermodynamics, because nucleation of the new phase requires some time, leading to superheating. Classical nucleation theory predicts spontaneous decay of crystalline order when the maximum superheating temperature is exceeded. This maximum superheating temperature scales roughly with the melting temperature and is about 500 K for a material with a melting point of 2000 K and at a heating rate of 10^{14} K/s (Luo et al., 2003). A similar problem appears upon cooling of the molten track below T_{m} when recrystallization starts at the melt-crystal interface and proceeds inwards, diminishing the measurable track radius. Both, the kinetics of the decay of the crystalline order and its partial reestablishment have to be followed in greater detail before a comparison with experimental track radii is justified. The importance of this statement can be nicely illustrated in the case of track formation in glasses, which have no well defined melting point but exhibit gradual softening and a continuous transition to the melt. An example will be given in Section 6.

5. The Thermal-Spike Model of Szenes

Instead of following the complicated history of electron-hole formation, recombination, diffusion, thermalization and trapping, Szenes (1995) rigorously simplified the problem by treating the lattice system only. Time zero is chosen when the lattice temperature on the track axis attains its maximum value. The physics at earlier times is not considered. Assuming an "initial" Gaussian lattice temperature distribution of width $a(0)$, the solution of the transport equation for heat (Equation (24) without the term arising from electron-phonon coupling yields for the temperature profile

$$T_{\mathrm{L}}(r,t) = \frac{Q}{\pi a^2(t)} e^{-r^2/a^2(t)} + T_0, \tag{31}$$

where $Q = (fS_e - L\rho\pi R^2)/(\rho C_L)$ is determined by (partial) energy conservation and $a^2(t) = a^2(0) + 4\kappa_L t/(\rho C_L)$ denotes the width of the temperature profile at later times. The quantity L is the latent heat of melting. The parameter f determines the fraction of electronic excitation energy which is converted to heat at time zero. For a calculation of track diameters, Szenes uses the same melting criterion as Toulemonde et al. (1996). For insulators with amorphous tracks Szenes obtains $a(0) = 4.5$ nm independent of the material. The velocity effect is incorporated in f resulting in $f \approx 0.4$ for $E_{ion} < 2.2$ MeV/u and $f \approx 0.17$ for $E_{ion} > 8$ MeV/u (Szenes, 2005). Interestingly, Szenes found a correlation between the threshold energy loss for track formation, S_{e0}, and the thermal energy required to reach the melting temperature. This correlation was taken as evidence for a thermal spike. With the same model and the same parameters, Szenes (2002) was also able to explain ion beam mixing with fast heavy ions. But the originally claimed "rather uniform behavior" of insulators (Szenes, 2002) cannot be maintained because not all insulators exhibit amorphous tracks (Szenes, 2005).

Keeping in mind its simplicity, the model of Szenes is astonishingly successful, at least for insulators with amorphous tracks. If in these materials self-trapping of excitons is the prevailing and rapid mechanism, the idea of Szenes dealing only with the lattice heat transport could come close to reality. For quartz, e.g., Szenes's time zero would have to be identified with the mean trapping time of about 0.15 ps (Audebert et al., 1994; Guizard et al., 1996a, 1996b). However, prior to self-trapping the electrons (holes) should have cooled down to the bottom (top) of the conduction (valence) band and most (~80% in quartz) of the electronic excitation energy should be transformed to lattice heat (see Section 3.3). A factor $f \approx 0.2$ to 0.4, however, indicates the opposite trend. In Szenes's model the fate of the overwhelming part of the electronic excitation energy remains unclear.

Because the models of Toulemonde et al. and Szenes use the same track data, the same track formation criterion with same (claimed) success, the temperature profiles in the time regime of track formation should also be the same. A comparison is made in Figure 2. It turns out that the differences at the late stage ($t > 10^{-12}$ s) of track formation are not big. The reason is clear. Independent of the initial shape of the excitation profile, the solution of the heat transport equation converges towards a Gaussian profile at later times. In ion track physics this is obviously the case on a picosecond time-scale. In fact, $a^2(t)$ can be easily rewritten to $a^2(t) = 4\kappa_L/(\rho C_L) \times (t_x + t)$ with $t_x = \rho a^2(0)/(4\kappa_L)$. For silica t_x is about 3.6 ps. The solution for T_L of the model of Toulemonde et al., which require considerable numerical efforts, can be well approximated by a Gaussian for times in the picosecond range.

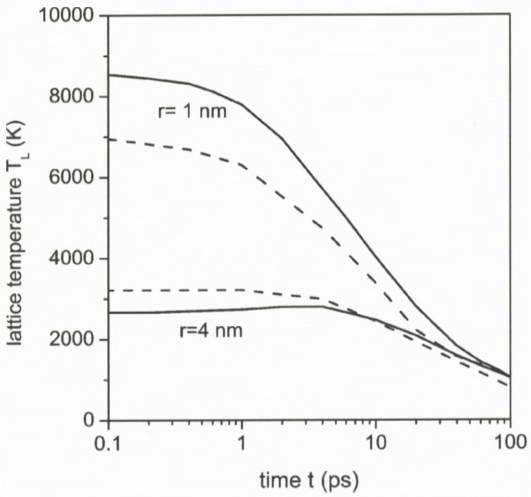

Figure 2. Lattice temperature T_L as a function of time t for vitreous silica according to the thermal-spike model of Toulemonde et al. (lines) and Szenes (dashed lines) for two distances from track centre ($r = 1$ and 4 nm) after the passage of an 340-MeV Xe ion ($S_e = 15$ keV/nm). For the model of Szenes $f = 0.6$ has been used.

All objections against the model of Toulemonde et al. can be repeated against the model of Szenes. In particular, the correlation between the stopping power threshold and the melting temperature can be put in question if superheating is taken into account. Either, superheating does not play an important role or the actual superheating temperatures scale with the equilibrium temperature, as it is suggested by classical nucleation theory (Luo et al., 2003). Then, a simple rescaling of the parameter f towards larger values would be sufficient.

6. Ion Track Mechanics

6.1. Ion Hammering of Amorphous Materials

Additional insight into the atomic motion during track formation has been gained from the so-called ion-hammering effect. It denotes the phenomenon that during bombardment with fast heavy ions, thin amorphous targets deform in a manner as if each ion would act like a little hammer. The target dimensions $\ell_\perp$ perpendicular to the beam grow while the dimension parallel to the beam shrinks so that the mass density and microscopic structure remain virtually unaltered (Klaumünzer and Schumacher, 1983; Klaumünzer et al., 1989). In this context, "thin" means that the target thickness is much smaller than the projected ion range, so that

the stopping power can be taken as constant over the specimen thickness. In this case, ion hammering is characterized by the deformation yield $A = \ell_{\perp}^{-1} \partial \ell_{\perp} / \partial \Phi t$, where Φt is the ion fluence. The deformation yield depends on irradiation temperature, on S_e and the stress state in the target. The deformation yield is maximal at low temperatures and decreases as soon as thermally activated atomic rearrangements are possible. Below the track generation threshold, A is small and decreases roughly exponentially with decreasing S_e. Above the track generation threshold, A increases linearly with S_e. Moreover, the deformation yield increases linearly with an externally applied, tensile stress. Shear stresses of the order of a few 0.1 GPa modify the deformation yield measurably (Audouard et al., 1993). Ion hammering does not occur in materials which remain crystalline during irradiation.

The link between the deformation yield and the irreversible, local radial strain ε_{loc} of the ion track is given by

$$A = \pi R_T^2 \varepsilon_{loc}, \tag{32}$$

where R_T is the track radius. Typical low-temperature values for A are between 10^{-14} and 10^{-15} cm^2 (Klaumünzer et al., 1989). Taking $R_T = 3$ nm one finds that ε_{loc} is between 3×10^{-2} and 3×10^{-3}. Assuming a characteristic deformation time of 1 ps, one obtains local rates of irreversible shear between 3×10^9 and 3×10^{10} s^{-1}. These high shear rates and their significant modification by shear stresses of the order of 0.1 GPa are strong arguments against deformations induced by shock, in which stresses of the order of 10 GPa have to be exceeded to induce plastic deformation.

The recently claimed shock-induced crystallization of an amorphous alloy by Dunlop et al. (2003) and Rizza et al. (2004a, 2004b) is not a compelling counter-argument. In those papers the difficult proof is missing that the observed crystallization proceeds within a few picoseconds after the ion passage. It is possible that the local deformation induced by the ion's passage can enhance locally the free energy of the amorphous phase so that thermally activated crystallization occurs during the warming-up period after ion bombardment.

6.2. The Effective-Flow-Temperature Approach (EFTA) of Trinkaus

The first attempt to combine a thermal spike concept with mechanical equations to follow the motion of fluid matter in a cylindrical track has been made by Ryazanov et al. (1995). However, their constitutive mechanical equations cannot explain the unsaturability of ion hammering (Trinkaus, 1998). This deficiency was removed in the papers by Trinkaus and Ryazanov (1995) and Trinkaus (1995,

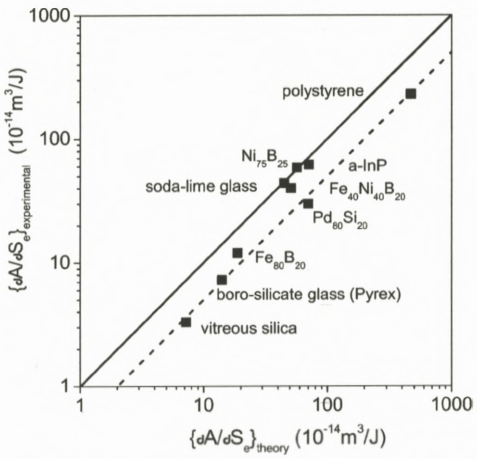

Figure 3. Comparison between the experimentally determined slopes of the deformation yield $\partial A/\partial S_e$ and the theoretical ones calculated from Equation (33) using $S'_e = f(S_e - S_{e0})$. It is obvious that all data lie between $f = 1$ (solid line) and $f = 0.5$ (dashed line).

1996). The basic ideas of the effective-flow-temperature approach are the following. Due to thermal expansion, which is constrained by the surrounding solid matrix, a cylindrical stress field emerges. Because an infinitely long track cannot expand axially the axial thermal stress is larger than the radial stress. If the track core is fluid (shear viscosity η_s) such a situation is mechanically unstable. On a time-scale, which is determined by η_S/G_∞, the fluid must relax to a state with hydrostatic pressure only, implying an additional radial strain. Here, G_∞ is the high-frequency shear modulus of the liquid, the numerical value of which is often close to the numerical value of the corresponding amorphous solid. Upon rapid cooling η_s rises dramatically and the additional radial strain may be frozen in at the effective flow temperature T^*. Neglecting inertia terms and using Eshelby's concept of elastic inclusions, Trinkaus and Ryazanov (1995) were able to obtain an analytical expression for the deformation yield. In the limit of large electronic stopping powers ($S_e \gg S_{e0}$) to ensure cylindrical geometry and with a Gaussian temperature distribution, they obtained

$$A = 0.427 \frac{1+\nu}{5-4\nu} \frac{\alpha S'_e}{\rho C_L}, \tag{33}$$

where ν is the Poisson number, α the coefficient of linear thermal expansion and ρ the target density. S'_e denotes the fraction of the stopping power S_e which is converted to heat. For comparison with experiment, S'_e is often approximated by $S'_e = f(S_e - S_{e0})$. Figure 3 shows for a wide variety of amorphous materials the

experimentally determined values for $\partial A/\partial S_e$ plotted *versus* the calculated ones assuming $f = 1$. The correlation is obvious and all data lie between $f = 1$ and $f = 0.5$.

If during ion bombardment at normal beam incidence an in-plane stress $\sigma_\perp$ exists, shear relaxation at T^* is zero when the sum of the applied stress and the thermo-elastic stress in the track yields a purely hydrostatic pressure. The EFTA yields for $\sigma_\perp$ (Trinkaus, 1995)

$$\sigma_\perp = -1.16\frac{1+\nu}{1-\nu}G_\infty\alpha(T^* - T_0). \tag{34}$$

Obviously, for $S_e \gg S_{e0}$, $\sigma_\perp$ is independent of S_e.

This in-plane stress can be determined from an experiment in which an amorphous material, the thickness of which is much larger than the projected ion range, is bombarded with track generating ions. The ion-hammering effect creates in the bombarded layer a compressive stress which bends the sample. When $\sigma_\perp$ has been reached in the bombarded layer, ion hammering ceases and bending attains its saturation value. The corresponding bending radius is directly proportional to $1/\sigma_\perp$. After applying a correction for finite irradiation temperatures using a scaling law of Trinkaus (1998), T^* can be calculated from Equation (34). The results are listed in Table 1 and can be compared with T^* determined from the relation $\eta_S(T^*)/G = 5 \times 10^{-12}$ s, where experimental data for η_S and G have been used. Details of this experiment will be published elsewhere. The agreement is astonishingly good, which demonstrates that the EFTA is self-consistent.

In the spike models of Sections 4 and 5 and in the EFTA, a common aspect is the neglect of the kinetics of the atomic motion. In the thermal-spike models instantaneous melting occurs for $T > T_m$ and instantaneous freezing to the amorphous phase for $T < T_m$. In the EFTA instantaneous shear stress relaxation occurs for $T > T^*$ and instantaneous freezing for $T < T^*$. With these assumptions the evaluation of complicated time integrals can be avoided concerning the motion of the liquid-solid interface in the spike models and the strain rates in EFTA.

6.3. Trinkaus' Constitutive Equations for Ion Hammering

In order to remove the unphysical assumption of a viscosity jump at T^* in EFTA, Trinkaus (1998) formulated the constitutive equations of fluid track matter in an amorphous matrix (shear modulus $G = G_\infty$, bulk modulus B)

$$\varepsilon_{ij} = \varepsilon_{ij}^{el} + \varepsilon_{ij}^{vis} + \alpha(T - T_0)\delta_{ij} \quad \text{(additivity of strains)}, \tag{35}$$

$$\sigma_{ij} = B\sum_{k=1}^{3}\varepsilon_{kk}^{el}\delta_{ij} + 2G\tilde{\varepsilon}_{ij}^{el} \qquad \text{(Hooke's law)}, \tag{36}$$

Table 1. In-plane stresses $\sigma_\perp$ as derived from bending radii after irradiation of various glasses by 340-MeV Xe ions with $\Phi t = 6 \times 10^{13}$ Xe/cm^2 and 120-MeV Kr ions with 3.5×10^{14} Kr/cm^2, respectively. T^* is calculated from Equation (34) after correction for finite irradiation temperatures T_i. The results should be compared with T^* in the last column, calculated from the relation $\eta(T^*)/G = 5 \times 10^{-12}$ s using experimental values for η and G. Note that for $Fe_{20}B_{80}$ T^* is independent of the stopping powers as it is predicted by Equation (34).

360 MeV Xe, $\Phi t = 6 \times 10^{13}$ Xe/cm^2

	T_i (K)	$\sigma_\perp$ (GPa) exp.	T^* from $\sigma_\perp$ (K)	T^* from η/G (K)
$Pd_{80}Si_{20}$	140	–0.42	920	960
$Fe_{80}B_{20}$	145	–1.2	1130	1130
$Fe_{81}B_{13.5}Si_{3.5}C_2$	85	–1.6	1150	1200
silica	300	–0.33	3500	3800

120 MeV Kr, $\Phi t = 3.5 \times 10^{14}$ Kr/cm^2

	T_i (K)	$\sigma_\perp$ (GPa) exp.	T^* from $\sigma_\perp$ (K)	T^* from η/G (K)
$Fe_{80}B_{20}$	140	–1.3	1150	1130
$Be_{40}Ti_{50}Zr_{10}$	160	–0.60	1100	1020

$$\tilde{\sigma}_{ij} = 2\eta_s \dot{\tilde{\varepsilon}}_{ij}^{\text{vis}} \qquad \text{(Newtonian flow)}, \tag{37}$$

where ε_{ij}, $\varepsilon_{ij}^{\text{el}}$ and $\varepsilon_{ij}^{\text{vis}}$ are the components of the total, elastic, and viscous strain tensors, respectively. The tilde restricts tensors to their deviatoric parts, for instance $\tilde{\sigma}_{ij} = \sigma_{ij} - \hat{\sigma}\delta_{ij}$ with $\hat{\sigma} = (1/3)\sum_{k=1}^{3} \sigma_{kk}$. Equations (35) to (38) have to be supplemented by the equation of motion. Trinkaus argued that in the bulk of the material, inertia terms may only be of importance at the beginning of the spike when an elastic wave packet is emitted. Thus, the equation of motion reduces to

$$\text{Div}\,\boldsymbol{\sigma} = 0. \tag{38}$$

Equations (35) to (38) can be integrated if the appropriate boundary conditions and the lattice temperature field are specified.

Because numerous experimental results are available for quartz and vitreous silica and because carrier trapping proceeds very rapidly in these materials

(see Section 3.3) the lattice temperature may be reasonably well simulated by a Gaussian temperature distribution (see Section 5)

$$T_{\mathrm{L}}(r,t) = \left(1 - \mathrm{e}^{-t/\tau_n}\right) \frac{f S_{\mathrm{e}}}{\pi \rho C_{\mathrm{L}} a^2(t)} \, \mathrm{e}^{-r^2/a^2(t)} + T_0, \tag{39}$$

with $a^2(t) = a^2(0) + 4\kappa_{\mathrm{L}} t/(\rho c_{\mathrm{L}})$ as in Section 5 and taking into account that amorphous materials have no latent heat. The following material parameters for silica have been used: $a(0) = 4.5$ nm (from Section 5), $\kappa_{\mathrm{L}} = 2.2$ W/mK, $B = 45$ GPa, $G = 34$ GPa, $C_{\mathrm{L}} = 1430$ J/kgK, $\log(\eta_{\mathrm{S}}/\mathrm{Pas}) = -6.7 + 2.67 \times 10^4/\mathrm{T}$ and $\alpha = 1.7 \times 10^{-6}\ \mathrm{K}^{-1}$. The integration of Equations (35) to (38) has been performed by the finite-element method using a commercially available code (PDEase by PDE Solutions Inc.). The temperature field of Equation (39) has been embedded in a large slab of "silica" of 200 nm radius so that cut-off effects of the Gaussian can be ignored. The thickness of the slab was chosen to be 200 nm and $T_0 = 100$ K to match the experimental conditions of Rotaru (2002). Since in Rotaru's work the silica layer was on top of a thick silicon wafer, $\boldsymbol{\varepsilon} = 0$ was chosen at the bottom and a free surface at the top of the "silica" with a specific surface energy of 5 J/m^2. The electronic energy relaxation time τ_n was varied between 0.02 and 0.2 ps without detecting large differences in the final results. Experimentally, the track radius R_{T} or the damage cross-section πR_{T}^2 is determined from a physical quantity which is sensitive to atomic rearrangements. In Trinkaus' continuum model, irreversible atomic rearrangements are incorporated in $\boldsymbol{\varepsilon}^{\mathrm{vis}}$. Accordingly, R_{T} is defined as the radial distance from the track center where $\boldsymbol{\varepsilon}^{\mathrm{vis}}$ falls to zero at any time. The deformation yield has been determined by using relation (32) with a radially averaged value of $\varepsilon_{\mathrm{r}}^{\mathrm{vis}}$. The free surface allows for outflow of matter and subsequent hillock formation due to pressure relaxation. Depending on the electronic energy loss, freezing ($\boldsymbol{\varepsilon}^{\mathrm{vis}} \to 0$) occurs between 5 and 15 ps. The calculations were extended by additional 10 ps to make sure that viscous flow has ceased completely ($\boldsymbol{\varepsilon}^{\mathrm{vis}} = 0$). Then the temperature was set to T_0 in order to calculate the quantities, which are accessible to experiment.

The results for the damage cross-sections are displayed as a function of S_{e} in Figure 4 in comparison with the experimental values taken from Meftah et al. (1994) for quartz and from Rotaru (2002) for silica. As can be seen from Figure 4, the measured damage cross-sections and the stopping power threshold are relatively well reproduced with $f = 0.6$. Even better agreement can be obtained by using $f = 0.7$. With regard to the deformation yield displayed in Figure 5, the experimentally measured slope $\partial A/\partial S_{\mathrm{e}}$ is well-reproduced with $f = 0.6$ but the calculated threshold is a factor of 3 to 4 too large.

At the free surface irreversible outflow of matter turns out to be undetectably small for ions with electronic energy losses below $S_{\mathrm{e}} = 12$ keV/nm. The height

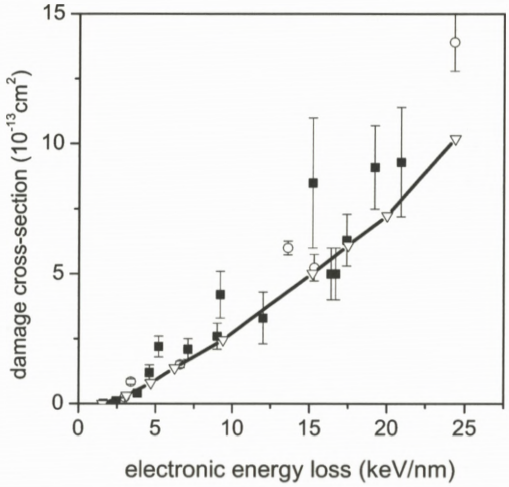

Figure 4. Damage cross-sections as a function of S_e for quartz and vitreous silica. The experimental data have been taken from Meftah et al. (1994) (full squares) and Rotaru (2002) (open circles). The open triangles represent the model calculations according to Equations (35) to (38). For the used parameters, see Section 6.3.

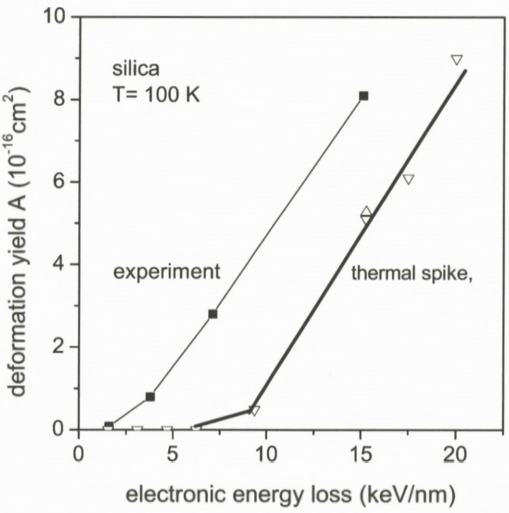

Figure 5. Comparison between experiment (Klaumünzer, 2004, full squares, thin line) and model calculations (open triangle, thick line) of the deformation yield A for vitreous silica at $T_0 = 100$ K. For the calculations the same parameters as in Figure 4 have been used.

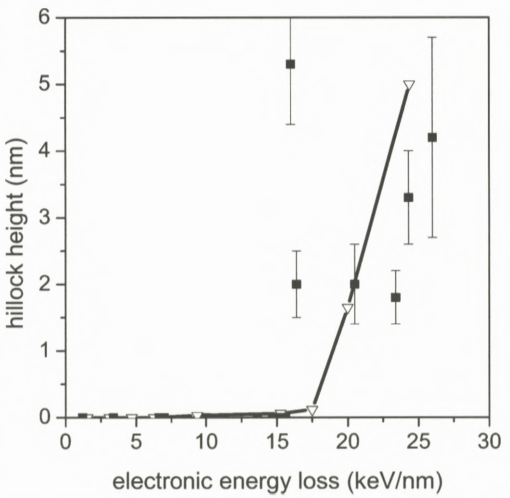

Figure 6. Hillock heights as measured by atomic force microscopy for vitreous silica *versus* S_e (Rotaru, 2002, full squares) in comparison with the model calculations of Section 6.3 using the same parameters as in Figures 4 and 5 (full line).

of hillocks due to ion impacts grows rapidly above 17 keV/nm (Figure 6). Both the height h of the hillocks and the energy loss range, where they should become visible in an atomic force microscope, agree with the experiment of Rotaru (2002). However, in the experiment, not every ion impact leads to a detectable hillock. Rather, the ratio of detected hillocks to ion impacts varies unsystematically between 0.22 and 0.68. Moreover, the experimentally measured hillock heights show no clear dependence on stopping power (see Figure 6). The origin of these "experimental fluctuations" is not yet clarified. One possibility is the desorption of matter by electronic excitations. In fact, the desorption or sputtering yield at normal beam incidence with ions of $S_e = 20$ keV/nm is about 400 SiO_2 molecules (Matsunami et al., 2003). According to Figures 4 and 6, at this stopping power, the calculated total hillock volume is about $1/3\pi R_T^2 h \approx 4 \times 10^{-20}$ cm^3 containing about 900 SiO_2 molecules. Therefore, sputtering and fluctuations in sputtering cannot be ignored and must have a significant effect on the measured height of the hillocks.

By using Equation (38) in the calculations, mechanical quasi-equilibrium has been assumed. However, the time dependence of ε shows that, for ions with $S_e = 20$ keV/nm, the matter at the track center close to the surface is accelerated to about 1000 m/s within 1 ps. Therefore, inertia terms in the equation of motion must be included and, with regard of the calculated hillock heights at large stopping powers ($S_e > 15$ keV/nm) the calculations have to be repeated.

The importance of inertia effects in surface vicinity has already been pointed out by Trinkaus (1998), Bringa and Johnson (1998), and Jakas and Bringa (2000).

In the bulk, for most of the time, the motion is always sufficiently slow so that inertia terms can be neglected. However, in the early phase of the thermal spike ($t < 1$ ps), the neglect of inertia suppresses the formation of an outgoing elastic wave. Martynenko and Umansky (1994) estimated for a spherical spike that, depending on the initial temperature and the bulk modulus of the solid, between 5 and 50% of the initially deposited energy can be carried off by an elastic wave. Jakas and Bringa (2000) found for a cylindrical spike that, depending on the stopping power, this fraction varies between 5 and 30% in the time range where viscous flow occurs. Therefore, the value $f = 0.6 \ldots 0.7$ used in the finite-element-calculations is quite plausible. However, those authors emphasize that f depends on the magnitude of the initial excitation. This effect has not been taken into account in the present calculation and has also been ignored in the model of Szenes. Obviously, inertia terms must be included in the calculations in order to eliminate this parameter and to come closer to energy conservation.

7. Elements of Non-Equilibrium Thermodynamics

The models outlined in Sections 3 to 6 are continuum models and contain "temperature" as a key quantity. Therefore, these models must be compatible with non-equilibrium thermodynamics. The basis of non-equilibrium thermodynamics is the idea that a thermodynamic system, which is not in equilibrium as a whole, can be divided into sufficiently small volume elements in which equilibrium thermodynamics applies. This idea, though not justifiable within the framework of thermodynamics, turns out to be an extremely successful physical concept. However, this concept cannot be valid down to arbitrarily small length scales and, because ion tracks are objects on the nanometer scale, special care has to be taken on the limitations of the applicability of non-equilibrium thermodynamics.

In this section the discussion is restricted to the simplest case, a homogeneous isotropic material consisting of radiation-resistant chemical building blocks and exhibiting no phase transition. Non-radiolytic amorphous materials are nature's best realization of this idealization. Sputtering, amorphization or ion-beam mixing are not considered. Furthermore, it is assumed that there exist only three degrees of freedom: temperature, a total strain tensor $\boldsymbol{\varepsilon}$, and an additional tensor $\boldsymbol{\varepsilon}^{\text{in}}$. Of course, other degrees of freedom may exist but they are not of interest in the context of this paper. Then, for a small volume element, the basic equations of thermodynamics are (Kluitenberg, 1962)

$$\frac{\mathrm{d}\rho}{\mathrm{d}t} = -\rho \,\mathrm{div}\,\mathbf{v} \qquad \text{(mass conservation)}, \tag{40}$$

$$\rho\frac{\mathrm{d}\mathbf{v}}{\mathrm{d}t} = \mathrm{Div}\,\boldsymbol{\sigma} \qquad \text{(equation of motion)}, \tag{41}$$

$$\rho\frac{\mathrm{d}u}{\mathrm{d}t} = -\mathrm{div}\,\mathbf{J}^q + \sum_{i,j=1}^{3}\sigma_{ij}\dot{\varepsilon}_{ij} \qquad \text{(first law of thermodynamics)}, \tag{42}$$

$$\rho T\frac{\mathrm{d}s}{\mathrm{d}t} = \frac{\mathrm{d}u}{\mathrm{d}t} - \sum_{i,j=1}^{3}\sigma_{ij}\dot{\varepsilon}_{ij} - \sum_{i,j=1}^{3}\tau_{ij}^{\mathrm{in}}\dot{\varepsilon}_{ij}^{\mathrm{in}} \quad \text{(Gibbs relation)}. \tag{43}$$

In these equations $\mathbf{v} = (v_i)$ denotes the velocity of the volume element, $\boldsymbol{\sigma} = (\sigma_{ij})$ the stress tensor, u the specific internal energy, $\mathbf{J}^q$ the heat flow, and s the specific entropy. The material time derivative is defined by

$$\frac{\mathrm{d}}{\mathrm{d}t} = \frac{\partial}{\partial t} + \sum_i v_i\frac{\partial}{\partial x_i} \tag{44}$$

and the tensor of total strain rate by

$$\dot{\varepsilon}_{ij} = \frac{1}{2}\left(\frac{\partial v_i}{\partial x_j} + \frac{\partial v_j}{\partial x_i}\right). \tag{45}$$

Choosing as reference state the stress-free and undeformed material at uniform temperature T_0, $\boldsymbol{\varepsilon}^{\mathrm{in}}$ is identified as the tensor of inelastic strain; i.e., in the context of this work, $\boldsymbol{\varepsilon}^{\mathrm{in}} = \boldsymbol{\varepsilon}^{\mathrm{vis}}$ from Section 6.3. Thus, in lowest order of $\boldsymbol{\varepsilon}^{\mathrm{el}}$ and T, Equations (35) and (36) can be recovered. Of course, the restriction to the lowest order of $\boldsymbol{\varepsilon}^{\mathrm{el}}$ implies the exclusion of shock phenomena.

Using the Onsager relations and exploiting the second law of thermodynamics, $\mathrm{d}s \geq 0$, Kluitenberg (1962) finds for a liquid without memory the following relations

$$\mathbf{J}^q = -\lambda\,\mathrm{grad}\,T, \tag{46}$$

$$\dot{\tilde{\boldsymbol{\varepsilon}}}^{\mathrm{vis}} = \frac{1}{2\eta_{\mathrm{S}}}\tilde{\boldsymbol{\sigma}}, \tag{47}$$

$$\dot{\hat{\varepsilon}}^{\mathrm{vis}} = \frac{1}{2\eta_{\mathrm{B}}}\hat{\sigma}, \tag{48}$$

with λ, η_S and $\eta_B > 0$ and $\boldsymbol{\tau}$ equals $\boldsymbol{\sigma}$. A liquid without memory is a liquid in which the entropy does not depend on the state of deformation or, in other words, the configurational part of the entropy is independent of the state of irreversible deformation. Equation (47) is identical with Equation (37).

Equation (48) describes an irreversible change in volume with the bulk viscosity η_B. Because irradiation experiments are typically performed between $80 \leq T_0 \leq 300$ K, the track temperature is usually much higher than T_0. Because the high-temperature thermal expansion coefficient is usually positive an overpressure exists in the track core resulting in a density increase if η_B/B matches with the lifetime of the thermal spike. With ongoing irradiation this increase must stop at some time, implying $\eta_B \to \infty$. A change in η_B, however, implies a structural change and possibly also a change in configurational entropy. Thus, in order to be self-consistent with the assumption that the track fluid has no memory, η_B must be sufficiently large for the virgin material so that ion-track-induced volume changes are zero or at least negligibly small. Therefore, in Trinkaus' constitutive equations, $\eta_B = \infty$ is assumed. They describe the simplest case of the mechanical behavior of fluid ion track matter compatible with non-equilibrium thermodynamics. Densely packed metallic glasses seem to approach this ideal case rather well (Hou et al., 1990). In Pyrex, a borosilicate glass, tracks have the same mass density as the virgin material (Klaumünzer et al., 1987). In vitreous silica, however, the track core is approximately 3% more compact than the unirradiated glass, and η_B approaches infinity after the whole sample volume is covered with tracks (Klaumünzer, 2004).

Equations (42) and (43) couple the thermodynamic quantities u and s with the mechanical quantities $\boldsymbol{\sigma}$ and $\boldsymbol{\varepsilon}$. From ion hammering of silica one can estimate that the relation

$$\kappa_L |\mathrm{div}(\mathrm{grad}\, T)| \gg \left| \sum_{i,j=1}^{3} \sigma_{ij} \dot{\varepsilon}_{ij} \right|$$

holds. In this case, the mechanical and thermodynamical equations can be solved independently. In metallic glasses, however, due to their large thermal expansion coefficient, the strain rates and stresses can be one to two orders of magnitude larger than in silica. In this case it is possible that for a correct calculation of the temperature distribution, the motion of the track matter has to be taken into account.

Writing $u = \rho C_L T$ and combining Equation (42) with Equation (46), Fourier's law of heat conduction is recovered as it is used in all models of Sections 3 to 6. It is well known that Fourier's law has the deficiency to allow for infinitely large velocities of heat dissipation, in contradiction to the fact that phonons cannot

exceed the velocity of sound. There is an attempt in thermal spike calculations (Schwartz et al., 2006) to modify Fourier's law to limit heat dissipation velocities. But one should keep in mind that this specific modification is in contradiction with the second law of thermodynamics.

Application of non-equilibrium thermodynamics must be handled with care when the characteristic length of the objects of interest approaches the mean free path of the heat carriers. Limitations of Fourier's law can be derived from solutions of the Boltzmann transport equation applying large temperature gradients (Simons, 1971). Fourier's law is valid if

$$\frac{\partial T_\mathrm{L}}{\partial r}\ell_\mathrm{ph} \ll T_\mathrm{L} \tag{49}$$

holds. For vitreous silica and high temperatures, the mean free path between phonon-phonon collisions ℓ_ph is about 1 nm (Zeller and Pohl, 1971). Taking a Gaussian temperature distribution with the parameters of Section 6.3, we find that, for all times of interest, Equation (49) is only fulfilled in the vicinity of the track center ($r < 0.5$ nm). The same situation is encountered in the spike of Toulemonde et al. As one can infer from Equation (30), $\ell_\mathrm{ph} \sim 1$ nm holds for all materials at the melting point. Therefore, in general, the lattice temperature concept of the thermal-spike models of Sections 4 and 5 has no rigorous foundation in non-equilibrium thermodynamics. In particular, the warning of Bringa and Johnson (1998) that the use of classical heat transport in ion track physics represents only a very rough approximation, is independent of the specific potential they have used.

In the case of mass transport in fluids, the limitations of Newtonian viscous flow can be inferred from modern theories on viscous flow in dense matter (Alley and Adler, 1983; Montanero and Santos, 1996; Santos et al., 1998). Equation (47) is valid if for all $i, j = 1, \ldots, 3$

$$\dot{\varepsilon}_{ij}^\mathrm{vis}\ell_\mathrm{a} \ll v_\mathrm{T} \tag{50}$$

holds, with $v_\mathrm{T} = \sqrt{2k_\mathrm{B}T/m}$ the characteristic thermal velocity of the fluid atoms of mass m and their mean free path ℓ_a between two collisions. Even for strain rates as high as 10^{11} s^{-1} the inequality (50) holds, because ℓ_a is smaller than a tenth of an atomic diameter (Turnbull and Cohen, 1970). Therefore, in spite of the smallness of ion tracks, continuum mechanics still provides a reliable basis for ion track mechanics.

In the energy-transport model, additional limitations have to be considered to make sure that thermodynamics holds. In analogy to Equation (49) application of thermodynamics to an electron gas presumes the relation

$$\frac{\partial T_n}{\partial r}\ell_n \ll T_n, \tag{51}$$

where ℓ_n denotes the mean free path of the electrons in the conduction band. For the number density n of electrons the condition

$$\frac{\partial n}{\partial r}\ell_n \ll n \tag{52}$$

must be fulfilled. Similar relations exist also for the holes of the valence band. Because the energy-transport model has not been applied yet to ion track physics, calculations have to show whether this model offers a better founded approach than the presently used thermal-spike models.

8. Conclusions

In the preceding section serious objections could be made against the thermal-spike models presently used. On the other hand, as has been demonstrated in Section 6.3, they provide a basis for data interpretation which reproduces the correct order of magnitude of experimental results. Of course, critical tests of models containing free parameters require not only comparison with track radii but other experimental quantities should be reproduced as well. It seems that, in all thermal-spike models presently in use, Fourier's law is the weakest link. Boltzmann transport equations have to be solved in order to get more insight into the errors made by the application of Fourier's law. Model solutions of the Boltzmann equation are available if only one scattering process is dominant (Stratton, 1962). But if more than one scattering process is important, the computations become expensive. Triggered by the wealth of available experimental data, thermal-spike models have been predominantly applied to insulators. However, the comparison of the thermal-spike models with the energy-transport model has shown that track physics in metals and alloys is probably much simpler. Perhaps, both, from the experimental and theoretical side, one should concentrate more on this class of materials.

Parallel to the investigations of solutions of the Boltzmann equation Trinkaus' constitutive equations should be tested for a wider variety of materials and experimental boundary conditions. Terms describing inertia and material loss at free surfaces must be included to promote at least a semi-quantitative understanding

of surface phenomena like the giant jet-like sputtering of LiF (Toulemonde et al., 2002), droplet formation on NiO (Schattat et al., 2005), and surface dewetting of NiO on silicon (Bolse et al., 2006).

Molecular dynamics simulations can help to unveil limitations of continuum mechanics, in particular, when fluctuations dominate the processes. However, the present-state-of-art molecular dynamics cannot help to bridge the gap in our knowledge, starting from the electronic excitations and ending at the atomic motion, unless the codes allow dealing simultaneously with a great number of atoms, a great number of electronic excitations, and the concomitant variations in the interatomic potentials.

Acknowledgements

I thank Bärbel Rethfeld, Christina Trautmann, Gregor Schiwietz and Helmut Trinkaus for numerous discussions, critical comments and suggestions which considerably improved this manuscript.

References

Alig R.C. and Bloom S. (1975): Electron-hole pair creation energies in semiconductors. Phys Rev Lett **35**, 1522–1525

Allen P.B. (1987): Theory of thermal relaxation of electrons in metals. Phys Rev Lett **59**, 1460–1463

Alley W.E. and Adler B. (1983): Generalized transport coefficients for hard spheres. Phys Rev A **27**, 3158–3173

Arnold D., Cartier E. and DiMaria D.J. (1994): Theory of high-field electron transport and impact ionization in silicon dioxide. Phys Rev B **49**, 10278–10297

Audouard A., Balanzat E., Bouffard S., Jousset J.C., Chamberod A., Dunlop A., Lesueur D., Fuchs G., Spohr R., Vetter J. and Thome L. (1990): Evidence for amorphization of a metallic alloy by ion electronic energy loss. Phys Rev Lett **65**, 875–878

Audouard A., Balanzat E., Jousset J.C., Lesueur D. and Thome L. (1993): Atomic displacements and atomic motion induced by electronic excitation in heavy-ion-irradiated amorphous metallic alloys. J Phys Condens Matter **5**, 995–1018

Audebert P., Daguzan Ph., Dos Santos A., Gauthier J.C., Geindre J.P., Guizard S., Hamoniaux G., Krastev K., Martin P., Petite G. and Antonetti A. (1994): Space-time observation of an electron gas in SiO_2. Phys Rev Lett **73**, 1990–1993

Barbu A., Dunlop A., Lesueur D. and Averback R.S. (1991): Latent tracks do exist in metallic materials. Europhys Lett **15**, 37–42

Bolse T., Elsanousi A., Paulus H. and Bolse W. (2006): Dewetting of nickel-oxide films on silicon under swift heavy ion irradiation. Nucl Instr Meth B **244**, 115–119

Bordelon T.J., Wang X.L., Maziar C.M. and Tasch A.F. (1991): An evaluation of energy transport models for silicon device simulation. Solid-State Electronics **34**, 617–628

Bouffard S. (1996): Relation between the basic phenomena and the observed damage. Nucl Instr Meth B **107**, 91–96

Bringa E.M. and Johnson R.E. (1998): Molecular dynamics of non-equilibrium enrgy transport from a cylidrical track. I. Test of thermal-spike models. Nucl Instr Meth B **143**, 513–535

Campillo I., Rubio A., Pitarke J.M., Goldmann A. and Echenique P.M. (2000): Hole dynamics in noble metals. Phys Rev Lett **85**, 3241–3244

Canut B., Benyagoub A., Marest G., Meftah A., Moncoffre N., Ramos S.M.M., Studer F., Thevenard P. and Toulemonde M. (1995): Swift-uranium damage in sapphire. Phys Rev B **51**, 12194–12201

Canut B., Bonardi N., Ramos S.M.M. and Della-Negra S. (1998): Latent tracks formation in silicon single crys-tals irradiated with fullerenes in the electronic regime. Nucl Instr Meth B **146**, 296–301

Cartier E., Fischetti M.V., Eklund E.A. and McFeely F.R. (1993): Impact ionization in silicon. Appl Phys Lett **62**, 3339–3341

Chadderton L. T. and Torrens I. McC. (1969): Fission Damage in Crystals. Methuen, London, pp 113 and 190

Dammak H., Dunlop A., Lesueuer D., Brunelle A., Delle-Negra S. and Le Beyec Y. (1995): Tracks in metals by MeV fullerenes. Phys Rev Lett **74**, 1135–1138

Dufour C., Paumier E. and Toulemonde M (1993): A transient thermodynamic model for track formation in amorphous metallic alloys. Rad Eff Def Sol **126**, 119–122

Dunlop A., Jaskierowicz G. and Della-Negra S. (1998): Latent track formation in silicon irradiated by 30 MeV fullerenes. Nucl Instr Meth B **146**, 302–308

Dunlop A., Jaskierowicz G., Rizza G. and Kopcewicz M. (2003): Partial crystallization of an amorphous alloy by electronic energy deposition. Phys Rev Lett **90**, 015503/1–4

Fleischer R.L., Price P.B. and Walker R.M. (1965): The ion explosion spike mechanism for formation of charged particle tracks in solids. J Appl Phys **36**, 3645–3652

Fleischer R.L., Price P.B. and Walker R.M. (1975): Nuclear Tracks in Solids. University of California Press, Berkeley

Gervais B. and Bouffard S. (1994): Simulation of the primary stage of the interaction of swift heavy ions with condensed matter. Nucl Instr Meth B **88**, 355–364

Grasser T., Tang T.W., Kosina H., Selberherr S. (2003a): A review of hydrodynamic and energy transport models for semiconductor device simulation. Proc IEEE **91**, 251–274

Grasser T., Kosina H., Gritsch M. and Selberherr S. (2003b): Using six moments of Boltzmann transport equation for device simulation. J Appl Phys **90**, 2389–2396

Guizard S., Martin P., Petite G., D'Oliveira P. and Meynadier P. (1996a): Time-resolved study of laser-induced colour centres in SiO_2. J Phys Condens Matter **8**, 1281–1290

Guizard S., D'Oliveira P., Daguzan P., Martin P., Meynadier P. and Petite G. (1996b): Time-resolved studies of carrier dynamics in wide-gap materials. Nucl Instr Meth B **116**, 43–48

Hall R.N. (1952): Electron-hole recombination in germanium. Phys Rev **87**, 387

Hamm R.N., Turner J.E., Wright H.A. and Ritchie R. H. (1979): Heavy ion track structure in silicon. IEEE Trans Nucl Sci **NS-26**, 4892–4895

Henry J., Barbu A., Leridon B., Lesueuer D. and Dunlop A. (1992): Electron microscopy observations of titanium irradiated with GeV heavy ions. Nucl Instr Meth B **67**, 390–395

Hou M.D., Klaumünzer S. and Schumacher G. (1990): Dimensional changes of metallic glasses during bombardment with fast heavy ions. Phys Rev B **41**, 1144–1157

Hughes R.C. (1973): Charge carrier transport phenomena in amorphous SiO_2: Direct measurement of the drift mobility and lifetime. Phys Rev Lett **30**, 1333–1336

Hughes R.C. (1975): Hot electrons in SiO_2. Phys Rev Lett **35**, 449–452

Ismail-Beigi S. and Louie S.G. (2005): Self-trapped excitons in silicon dioxide: Mechanism and properties. Phys Rev Lett **95**, 156401/1–4

Itoh N. (1996): Self-trapped exciton model of heavy ion track registration. Nucl Instr Meth B **116**, 33–36

Jakas M.M. and Bringa E.M. (2000): Thermal-spike theory of sputtering: The influence of elastic waves in a one-dimensional cylindrical spike. Phys Rev B **62**, 824–830

Katz R., Kim S.L., Luo D.L. and Huang G.R. (1990): An analytic representation of the radial distribution of dose from energetic heavy ions in water, Si, LiF, NaI and SiO_2. Rad Eff Def Sol **114**, 15–20

Klaumünzer S. (2004): Ion tracks in quartz and vitreous silica. Nucl Instr Meth B **225**, 136–153

Klaumünzer S. and Schumacher G. (1983): Dramatic growth of glassy $Pd_{80}Si_{20}$ during heavy ion irradiation. Phys Rev Lett **51**, 1987–1990

Klaumünzer S., Hou M.D. and Schumacher G. (1986): Coulomb explosions in a metallic glass due to the passage of fast heavy ions? Phys Rev Lett **57**, 850–853

Klaumünzer S., Li C.L. and G. Schumacher (1987): Plastic flow of borosilicate glass under bombardment with heavy ions. Appl Phys Lett **51**, 97–99

Klaumünzer S., Li C.L., Löffler S., Rammensee, M., Schumacher G. and Neitzert H.Ch. (1989): Ion-beam induced plastic deformation: A universal behavior of amorphous solids. Rad Eff Def Sol **108**, 131–135

Kluitenberg G.A. (1962): Thermodynamic theory of elasticity and plasticity. Physica **28**, 217–232

Kunikiyo T., Ishikawa K., Inoue Y., Kamakura Y., Taniguchi K. and Kotani N. (2003): Model of hole-initiated impact ionization rate in α-quartz for a full band Monte Carlo simulation. J Appl Phys **94**, 1096–1104

Leibfried G.(1965): Bestrahlungseffekte in Festkörpern. Teubner Verlagsgesellschaft, Stuttgart

Lesueur D. and Dunlop A. (1993): Damage creation via electronic excitations in metallic targets. Part II: Theoretical model. Rad Eff Def Sol **126**, 163–172

Lifshitz E.M. and Pitajewski L.P. (1983): In: Landau L.D. and Lifshitz E.M. (Eds), Lehrbuch der theoretischen Physik, Band X (Physikalische Kinetik). Akademie Verlag, Berlin, pp 112–114

Lifshitz I.M., Kaganov M.I. and Tanatarov L.V. (1960): On the theory of radiation-induced changes in metals. J Nucl Energy A **12**, 69–78 **A12**, 69

Luo S.N., Ahrens T.J., Cagin T., Strachan A., Goddard III W.A. and Swift D.C. (2003): Maximum superheating and undercooling: systematics, molecular dynamics simulations, and dynamic experiments. Phys Rev B **68**, 134206/1–11

Martynenko Yu.V. and Umansky M.V. (1994): Relaxation of thermal spikes. Rad Eff Def Sol **132**, 31–39

Matsunami N., Sataka M., Iwase I. and Okayasu S. (2003): Electronic excitation induced sputtering of insulating and semiconducting oxides by high energy heavy ions. Nucl Instr Meth B **209**, 288–293

Meftah A., Brisard F., Costantini J.M., Dooryhee E., Hage-Ali M., Hervieu M., Stoquert J.P., Studer F. and Toulemonde M. (1994): Track formation in SiO_2 quartz and the thermal spike mechanism. Phys Rev B **49**, 12457–12463

Meftah A., Costantini J.M., Khalfaoui N., Boudjadar S., Stoquert J.P., Studer F. and Toulemonde M. (2005): Experimental determination of track cross-section in $Gd_3Ga_5O_{12}$ and comparison to the inelastic thermal-spike model applied to several materials. Nucl Instr Meth B **237**, 563–574

Mizuno H., Morifuji M., Taniguchi K. and Hamaguchi C. (1993): Theoretical calculation of impact ionization rate in SiO_2. J Appl Phys **74**, 1100–1105

Montanero J.M. and Santos A. (1996): Monte Carlo simulation method for the Enskog equation. Phys Rev E **54**, 438–444

Mozumder A. (1974): Track-core radius of charged particles at relativistic speed in condensed media. J Chem Phys **60**, 1145–1148

Ogihara M., Nagashima Y., Galster W. and Mikumo T. (1986): Systematic measurements of pulse height defects for heavy ions in surface barrier detectors. Nucl Instr Meth A **251**, 313–320

Oguzman I.H., Wang Y., Kolnik J. and Brennan K. (1995): Theoretical study of hole initiated impactionization in bulk silicon and GaAs using a wave-vector-dependent numerical transition rate formulation within an ensemble Monte Carlo calculation. J Appl Phys **77**, 225–232

Rethfeld B., Kaiser A., Vicanek M. and Simon G. (2002): Ultrafast dynamics of non-equilibrium electrons in metals under femtosecond laser irradiation. Phys Rev B **65**, 214303/1–11

Ritchie E.H. and Claussen C. (1982): A core plasma model of charged particle track formation in insulators. Nucl Instr Meth **198**, 133–138

Rizza G., Dunlop A., Jaskierowicz G. and Kopcewicz M. (2004a): High electronic excitation-induced crystallization in $Fe_{37.5}Cu_1Nb_3Si_{13.5}B_9$ amorphous alloy: I. Irradiation with swift heavy monoatomic projectiles. J Phys Condens Matter **16**, 1547–1561

Rizza G., Dunlop A., Jaskierowicz G., Kopcewicz M. and Della-Negra S. (2004b): High electronic excitation-induced crystallization in $Fe_{37.5}Cu_1Nb_3Si_{13.5}B_9$ amorphous alloy: II. Carbon cluster irradiation. J Phys Condens Matter **16**, 1563–1575

Roldan J.B., Gamiz F., Lopez-Villanueva J.A. and Carceller J.E.: A Monte Carlo study on the electron-transport propertied of high-performnce strained Si and relaxed strained $Si_{1-x}Ge_x$ channel MOSFETs. J Appl Phys **80**, 5121–5128

Rotaru C. (2002): SiO_2 sur silicium: comportment sous irradiation avec des ions lourds. Thesis, University of Caen, http://tel.ccsd.cnrs.fr/documents/archives0/00/00/53/99/index_fr.html

Ryazanov A.I., Volkov A.E. and Klaumünzer S. (1995): Model of track formation. Phys Rev B **51**, 12107–12114

Santos A., Montanero J.M., Dufty J.W. and Brey J.J. (1998): Kinetic model for the hard-sphere fluid and solid. Phys Rev E **57**, 1644–1660

Schattat B., Bolse W., Klaumünzer S., Zizak I. and Scholz R. (2005): Cylindrical nanopores in NiO induced by swift heavy ions. Appl Phys Lett **87**, 173110/1–3

Schiwietz G. (2006): Private communication

Schiwietz G., Grande P., Skogvall B., Biersack J.P., Köhrbrück R., Sommer, K. and Schmoldt A. (1992): Influence of nuclear track potentials in insulators on the emission of target Auger electrons. Phys Rev Lett **69**, 628–631

Schiwietz G., Roth M., Czerski K., Staufenbiel F., Rösler M. and Grande P.L. (2003): Spectroscopy of Si-Auger electrons from the center of heavy-ion tracks. Nucl Instr Meth B **209**, 26–31

Schiwietz G., Czerski K., Roth M., Staufenbiel F. and Grande P.L. (2004): Femtosecond dynamics – Snapshots of the early ion track evolution. Nucl Instr Meth B **226**, 683–704

Shockley, W. and Read, W.T. (1952): Statistics of the recombination of holes and electrons. Phys Rev **87**, 835–842

Scholz R., Vetter J. and Hoppe S. (1993): Observation of heavy-ion latent tracks in GeS by transmission electron microscopy. Rad Eff Def Sol **126**, 275–278

Schwartz K., Volkov A.E., Voss K.-O., Sorokin M.V., Trautmann C. and Neumann R. (2006): Thermal spike effect on defect evolution in NaCl irradiated with light and heavy ions at 8 K and 300 K. Nucl Instr Meth B **245**, 204–209

Seidl M., Voit H., Bouneau S., Brunelle A., Della-Negra S., Depauw J., Jacquet D., Le Beyec Y. and Pautrat M. (2001): MeV carbon cluster-induced pulse height defect in a surface barrier detector. Nucl Instr Meth B **183**, 502–508

Sekido M., Taniguchi K. and Hamaguchi C. (1991): Direct observation of Gaussian-type energy distribution for hot electrons in silicon. Jap J Appl Phys **30**, 1149–1153

Simons S. (1971): On the use of models for phonon collision operators. J Phys C: Sol State Phys **4**, 2785–2791

Silk E.C.H. and Barnes R.S. (1959): Examination of fission fragment tracks with an electron microscope. Phil Mag **4**, 970–971

Spohr R. (1990): Ion Tracks and Microtechnology, Principles and Applications. Vieweg Verlag, Braunschweig

Stampfli P. (1996): Electronic excitation and structural stablity of solids. Nucl Instr Meth B **107**, 138–145

Staufenbiel F., Schiwietz G., Czerski K., Roth M. and Grande P.L. (2005): Electronic energy-density effects in ion tracks of metals. Nucl Instr Meth B **230**, 426–430

Stratton R. (1962): Diffusion of hot and cold electrons in semiconductor barriers. Phys Rev **126**, 2002–2014

Szenes G. (1995): General features of latent track formation in magnetic insulators irradiated with swift heavy ions. Phys Rev B **51**, 8026–8029

Szenes G. (2002): Thermal spike analysis of interface mixing induced by swift heavy ions. Appl Phys Lett **81**, 4622–4624

Szenes G. (2005): Ion-induced amorphization in ceramic materials. J Nucl Mater **336**, 81–89

Thevenard P.A., Beranger M., Canut B. and Ramos S.M.M. (1996): Damage in refractory oxides and ion beam mixing at metal-oxide interfaces induced by GeV ions and 20 MeV cluster beam. Mater Res Soc Symp Proc **396**, 127–135

Toulemonde M., Dufour Ch. and Paumier E. (1993a): Transient thermal spike process after a high-energy heavy ion irradiation of amorphous metals and semiconductors. Phys Rev B **46**, 14362–14369

Toulemonde M., Paumier E. and Dufour Ch. (1993b): Thermal-spike model in the electronic stopping power regime. Rad Eff Def Sol **126**, 201–206

Toulemonde M., Costantini J.M., Dufour Ch., Meftah A., Paumier E. and Studer F. (1996): Track creation in SiO_2 and $BaFe_{12}O_{19}$ by swift heavy ions: A thermal spike description. Nucl Instr Meth B **116**, 37–42

Toulemonde M., Assmann w., Trautmann C. and Gruner F. (2002): Jetlike component in sputtering of LiF induced by swift heavy ions. Phys Rev Lett **88**, 057602/1–4

Toulemonde M., Assmann W., Dufour C., Meftah A., Studer F. and Trautmann C. (2006): Experimental phenomena and thermal spike model description of ion tracks in amorphisable inorganic insulators. Mat Fys Medd Dan Vid Selsk **52**, 263–292

Trautmann, C., Andler S., Brüchle W. and Spohr R. (1993): Observation of etched tracks in an amorphous metal. Rad Eff Def Sol **126**, 207–210

Trinkaus H. (1995): Local stress relaxation in thermal spikes as a possible cause for creep and macroscopic stress relaxation of amorphous solids under irradiation. J Nucl Mater **223**, 196–201

Trinkaus H. (1996): Anisotropic creep and growth of amorphous solids under swift heavy ion bombardment: An asymptotic thermal spike approach. Nucl Instr Meth B **107**, 155–159

Trinkaus, H. (1998): Dynamics of viscoelastic flow in ion tracks: Origin of plastic deformation of amorphous materials. Nucl Instr Meth B **146**, 204–216

Trinkaus H. and Ryazanov A.I. (1995): Viscoelastic model for the plastic flow of amorphous solids under energetic ion bombardment. Phys Rev Lett **74**, 5072

Turnbull D. and Cohen M.H. (1970): On the free volume model of the liquid-glass transition. J Chem Phys **52**, 3038–3041

Wang Z.G., Dufour Ch., Paumier E. and Toulemonde M. (1994): The S_e sensitivity of metals under swift-heavy-ion irradiation: A transient thermal process. J Phys Condens Matter **6**, 6733–6750

Wesch W., Kamarou A. and Wendler E. (2004): Effect of high electronic energy deposition in semiconductors. Nucl Instr Meth B **225**, 111–128

Xiao G., Schiwietz G., Grande P.L., Schmoldt A., Grether M., Köhrbrück R., Stolterfoht N., Spieler A. and Stettner U. (1996): Evidence for convoy electron shifts due to induced potentials. Nucl Instr Meth B **115**, 215–219

Xiao G., Schiwietz G., Grande P.L., Stolterfoht N., Schmoldt A., Grether M., Köhrbrück R., Spieler A. and Stettner U. (1997): Indications of nuclear track guided electrons induced by fast heavy ions in insulators. Phys Rev Lett **79**, 1821–1824.

Yoffa E.J. (1980): Dynamics of dense laser-induced plasmas. Phys Rev B **21**, 2415–2425

Young D.A. (1958): Etching of radiation damage in lithium flouride. Nature **182**, 375–377

Zeller R.C. and Pohl R.O. (1971): Thermal conductivity and specific heat of noncrystalline solids. Phys Rev B **4**, 2029

Ziman J.M. (1975): Prinzipien der Festkörpertheorie. Verlag Harry Deutsch, Frankfurt/Main, pp 228

Some Solved and Unsolved Problems in Transmission Electron Microscopy Studies of Radiation Damage in Solids*

S.E. Donnelly**

Institute for Materials Research, University of Salford
Greater Manchester M5 4WT, UK

Abstract

Solved and unsolved questions from fifteen years of research using transmission electron microscopy in the study of radiation damage in materials are discussed. Examples are presented on topics that include single-ion impacts on metal surfaces, helium bubbles in semiconductors, solid xenon precipitates in metals and single-ion induced amorphous zones in silicon.

Contents

1 Introduction **330**

2 Thermal Spike-Induced Plastic Flow **331**
2.1 Background 331
2.2 Crater Formation 332
2.3 Hole Formation 336

3 Inert Gas Bubbles in Solids **337**
3.1 Background 337
3.2 Growth Mechanism for Helium Bubbles in Silicon 337
3.3 Solid Xe Bubbles in Al – Background 340
3.4 High-Resolution Observations 343

* This paper makes extensive reference to video recordings of *in-situ* TEM experiments for which video-clips are available at: http://www.imr.salford.ac.uk/fm/sed/media.php

** E-mail: s.e.donnelly@salford.ac.uk

3.4.1 Precipitate Shape Change 343
3.4.2 Precipitate Motion 345
3.4.3 Coalescence 345
3.4.4 Reversible Melting 347

4 Amorphous Zones in Silicon **348**
4.1 Background 348
4.2 *In-Situ* Observations 349

5 Conclusions **352**

Acknowledgements **353**

References **353**

1. Introduction

Transmission electron microscopy (TEM) has been used in the study of radiation damage in solids almost since the beginning of such studies; however, in recent decades, the ever-improving resolution of microscopes has enabled researchers to resolve defect structures resulting from single ion impacts, rendering this a very powerful experimental tool. In addition, in a small number of laboratories around the world, facilities exist in which it is possible to ion-irradiate thin foils *in-situ* in a TEM. These facilities add an important dimension by allowing observation of ion-induced defect morphologies as they develop during continuous ion irradiation.

The author has spent 15 years using an *in-situ* TEM/ion irradiation facility at Argonne National Laboratory, USA and has also collaborated on experiments using a high voltage electron microscope at the National Institute for Materials Science in Tsukuba, Japan. In this latter machine, displacement damage is created by the electrons used for imaging. In both these facilities, experiments have been conducted that have yielded unique insights into radiation damage processes.

This paper is an attempt to elucidate the problems in ion beam physics that have been solved by this approach and also to discuss those problems that remain to be solved. Work will be presented on single-ion impacts on metal surfaces, inert gas bubbles in semiconductors and metals and single-ion induced amorphous zones in silicon.

2. Thermal Spike-Induced Plastic Flow

2.1. Background

Above a certain energy density, the interaction of an energetic ion with a solid can no longer be successfully described as an orderly series of binary collisions involving the impinging ion and recoiling substrate atoms. As first suggested by Brinkman (1954), when the mean free path between displacing collisions approaches the interatomic spacing of the substrate, this description breaks down and instead one must think in terms of the formation of a small highly disturbed region, in which the mean kinetic energy of the atoms may be up to several eV, known as an energy or displacement spike. At some time after the initial energy deposition (of order tens of picoseconds), the kinetic energy in the spike may be shared in a continuous distribution by all the atoms within the spike region. Under some conditions this may give rise to an effective temperature within the spike zone significantly above that required for melting – this phase is generally referred to as a thermal spike.

Spikes resulting from single ion impacts were first discussed in the scientific literature more than 50 years ago; experimentally, however, until much more recently it has been difficult to study the effects of individual spikes as they are both small – typically of the order of a few nanometres in diameter – and of short duration – of order tens of picoseconds. Obtaining information on spikes resulting from individual ions thus necessitates techniques with a high spatial resolution. Unfortunately, no technique with adequate spatial resolution has a temporal resolution within orders of magnitude of spike lifetimes so that, as far as temporal resolution is concerned, observations are always of morphologies that include the effects of the displacement spike, the thermal spike and any ensuing defect annealing processes that may take place on timescales of milliseconds or more.

Over the last 30 years or so, as mentioned in the Introduction, the resolution of electron microscopes has improved and advances in the speed and capacity of computers have enabled the accurate modeling of larger and larger assemblies of atoms using molecular dynamics (MD) simulations. With this convergence, it is now possible both to image individual spike effects in the transmission electron microscope and to perform MD simulations of spike effects on "crystallites" of reasonable size. Currently, primary recoil energies are limited by the crystallite size to 100–200 keV which is more than adequate to give significant insights into spike processes with simulations running up to times of tens of picoseconds after the simulated impact.

In 1981 in a review of high-density cascade effects, Thompson (1981) posed two interesting questions on the nature of spike processes and these remained substantially unresolved until the last decade. The questions were: (i) "is it legitimate to use the concept of a vibrational temperature when the number of atoms in the spike (typically of the order of 10^4) may not be sufficient to be described by Maxwell–Boltzmann statistics?" and (ii) "is the duration of the spike (typically of the order of 10^{-11} seconds) sufficient for any major mass transport to occur?"

Recent TEM and MD work has conclusively answered question (ii) with at least empirical implications for question (i). In this sense the question of plastic flow resulting from spike effects is a solved problem in ion beam science as the next few paragraphs will illustrate.

2.2. Crater Formation

Using a facility at Argonne National Laboratory in which an ion beam is incident on thin foil specimens *in-situ* in a TEM (Allen et al., 1989), Donnelly and Birtcher (1999) studied the effect of single-ion impacts on the surfaces of a number of metals. Typically, in these experiments the specimen was tilted 15° towards the ion beam so that both ions and electrons were incident on the specimen at 15° to the foil normal and specimens were irradiated with Xe^+ ions at energies in the range 50–400 keV at fluxes of order 10^{11} ions/cm^2/s. The Au films were of thickness approximately 60 nm, made by thermal evaporation onto heated NaCl.

By defocusing the objective lens of the microscope (in a similar way to that generally done when imaging bubbles and voids), surface features arising from single ion impacts were imaged. Images were obtained under bright-field conditions, on regions of the (somewhat bent films) in which no Bragg reflection was strongly excited. Under such conditions, approximately 1000 nm of defocus of the objective lens yields images in which depressions (e.g. craters) on either surface of the foil are seen as areas of lighter contrast than the background and may be delineated by a dark Fresnel fringe. Similarly a small mound or particle on the surface appears darker than the background and may have a light fringe around it. A similar degree of overfocus gives rise to images in which this contrast is reversed. i.e. small craters appear darker than the background and small particles appear lighter than the background. In these experiments, at the magnification generally used (100 000), the area under observation measured approximately 110×85 nm and images of this area were recorded on videotape with a time resolution of a single video frame (1/30th second) and, at the flux used in the experiments (2.5×10^{11} ions/cm^2/s), approximately 20 ions impact on this area every second. With creation rates of between 0.02 and 0.05 craters per ion on Au, this results on average in a new crater appearing in the 110×85 nm area every 1–2

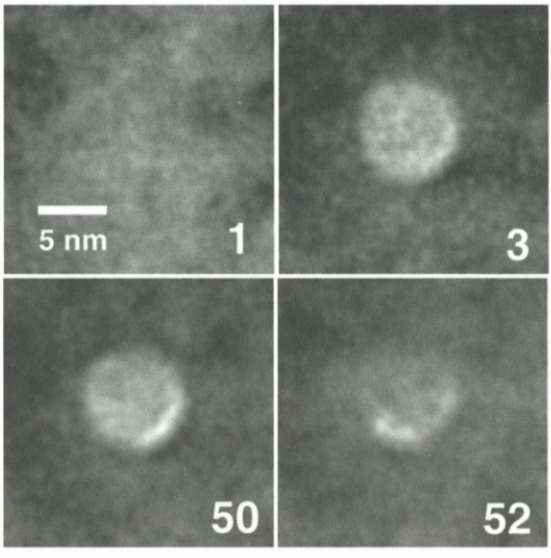

Figure 1. The creation and subsequent annihilation of a crater as a result of impacts of individual 400 keV Xe ions. Experiments carried out a room temperature. The numbers are video frame numbers (i.e. time steps in units of 1/30 s). Experiments carried out a room temperature. From Donnelly et al. (2005).

seconds. However, as will be discussed later, craters are unstable under irradiation and are rapidly filled in by material transported from other impact sites. This can be clearly seen in the "Craters" video-clip which can be streamed or downloaded via the internet (Donnelly, 2006).

The video-recording thus gives the impression of a surface exhibiting almost fluid-like properties on which a crater (sometimes along with expelled material) suddenly appears and then disappears over several seconds, during which time new craters appear. A frame-by-frame analysis, however, reveals that both crater creation and the flow that causes crater annihilation are discrete processes resulting from single ion impact effects. By using stereoscopic techniques it was also possible to show that for 400 keV irradiations, craters appeared on both the entrance and exit surfaces of the film – consistent with the results of simulations of energy/damage distributions in gold, using the Monte-Carlo code SRIM (Ziegler et al., 1985) which indicate that, in a 60 nm foil, energetic collisions take place near both surfaces at this energy.

Figure 1 shows a sequence of four images, digitized from videotape, of the same area of the gold foil. A crater is formed by a single ion impact, survives unchanged for just under two seconds and then is partially annihilated by a subse-

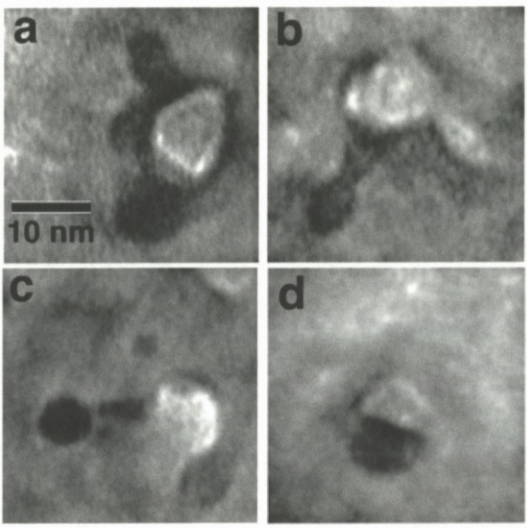

Figure 2. Examples of large features (consisting of craters and expelled material) on Au resulting from single ion impacts of Xe ions at energies of (a) 200 keV and (b) and (c) 400 keV. The images have been digitized from video recordings. Note that the imaging conditions ($\approx$1000 nm of objective lens underfocus) that give rise to craters appearing with a lighter contrast than the background, give rise to the observed darker contrast for expelled material on the surface of the foil. See text for details. Experiments carried out a room temperature. From Donnelly et al. (2005).

quent ion impact. The numbers on each part of the figure indicate the video-frame from which the image was taken and thus indicate the passage of time in units of 1/30th second. An important aspect of the study illustrated here is the general observation that craters are annihilated by subsequent individual ion impacts. As a result of this, experiments in which specimens were ion irradiated and then subsequently examined "post-mortem" for craters by TEM, such as the work by Merkle and Jäger (1981), significantly underestimated crater creation efficiencies. This is an example where *in-situ* TEM observations are essential if the dynamics of the process are to be understood.

Although the creation and annihilation of the regular crater shown in Figure 1 give little clue to the mechanisms responsible, these can be more easily gleaned from the images shown in Figure 2 where four craters resulting from impacts of Xe ions on Au at energies of (a) 50 keV, (b) 200 keV and (c) and (d) 400 keV Xe are shown. In each case, the crater appeared between successive video frames and thus resulted from a single ion impact. In particular, Figures 2b and 2c are strongly indicative of an expelled liquid droplet – fully separated from the crater in Figure 2c. This conclusion is confirmed by MD simulations of Xe ion irradiation

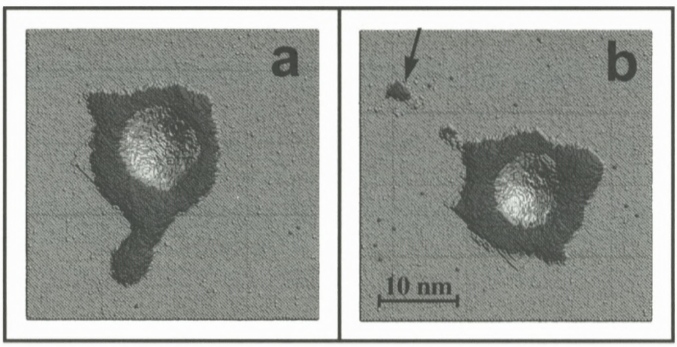

Figure 3. Structures observed in molecular dynamics simulations of impacts of 100 keV Xe ions on Au surfaces. In these images, the lighter shaded atoms are below the original surface and the darker shaded ones above. The arrow in panel "b" indicates a particle ejected from the crater by means of a "slingshot" process. From Donnelly et al. (2005).

of a {100} Au surface by Nordlund et al. recently reviewed by Donnelly et al. (2005) which exhibit a range of crater morphologies matching those observed experimentally. Examples of these are shown in Figure 3 in which MD simulations of single heavy-ion impacts have resulted in the formation of craters surrounded by expelled material and a small expelled droplet as indicated by the arrow in Figure 3b.

The comparison of the experimental results with those of the MD work makes it clear that, for many craters, there has been significant mass transport of material from the impact site, answering Thompson's question (ii) in the introduction in the affirmative. Also experimentally, the form of the expelled material (i.e. not having the same shape as its crater) provides qualitative evidence that it may have been expelled as a liquid droplet and this is exactly borne out by the MD work. Regardless of whether or not the spatial and temporal dimensions of the spike are sufficient to permit the use of Maxwell–Boltzmann statistics, the images and simulations indicate that macroscopic concepts such as melting and flow in response to surface tension forces, and quenching, provide a satisfactory description of the spike-induced crater creation process.

Although, in the majority of craters where expelled material could be seen, the above description seems appropriate, in a number of instances, small craters occasionally appeared to be accompanied by a solid plug of material having the approximate form of the crater. Such a crater is illustrated in Figure 2d). This is similar to the "lid" images recorded by Merkle and Jäger (1981). For such craters, we follow the interpretation of Merkle and Jäger that these result from spikes a sufficient distance below the surface such that a solid disc of material is

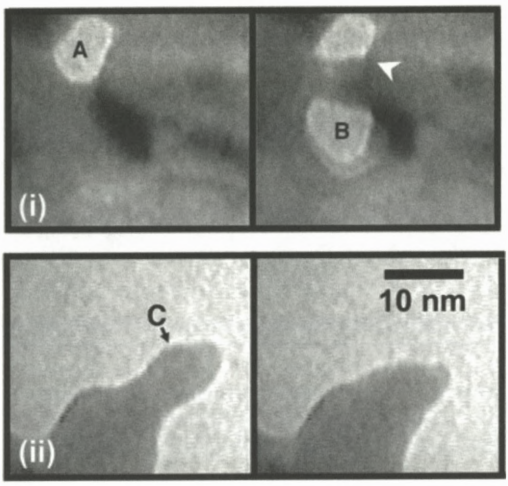

Figure 4. Microstructural evolution in Au during 200 keV Xe irradiation at room temperature: (i) the creation of a hole (B) by the impact of a single 200 keV Xe^+ ion, (ii) the change in shape of a protruding part of the gold foil following a single impact in the region indicated by "C". In each case the pair of images has been digitised from successive frames of a video-recording of the *in-situ* experiment. Experiments carried out a room temperature.

punched out by the large pressure increase that accompanies the thermal spike. MD simulations of 10 keV self ion impacts on gold (Averback and Ghaly, 1994) indeed indicate that large pressures as well as large temperatures may occur in a spike, albeit for very short periods.

2.3. Hole Formation

Finally, in an experiment in which a wedge-shaped, electro-chemically thinned gold foil was irradiated with 200 keV Xe ions, individual ion impacts were observed to produce holes through the thinnest areas of the foil (estimated to be 20–30 nm in thickness). Such an event can be seen in Figure 4(i) in which the two panels are separated by a single video frame. The light areas are holes punched entirely through the foil. Hole "B" forms due to a single ion impact next to pre-existing hole "A" which is partially filled in, in the area indicated by the arrow, by material expelled from hole "B". In addition, impacts at the edges of the foil could be seen to cause localised melting followed by a thickening of the material under the influence of surface tension forces as shown in Figure 4(ii) in which the two panels are again separated by a single video frame. This "pulsed, localized flow" resulted in a relatively rapid loss (by thickening rather than sputtering) of the thin areas of the foils. A much clearer picture of these process than it is possible

to convey from static images is to be seen in the video-clip "Holes" (Donnelly, 2006).

3. Inert Gas Bubbles in Solids

3.1. Background

Technological interest in inert gases in solids stems primarily from materials problems associated with the operation of both fission and fusion reactors. Inert gases, that are either directly injected or result from transmutation reactions in the reactor materials, tend to agglomerate at regions of low electron density and may form high concentrations of nanometre-sized bubbles. This can result in lifetime-limiting problems for reactor components such as grain-boundary embrittlement, swelling, blistering and exfoliation. More recently, however, cavities deliberately formed by ion implantation of helium into silicon have been investigated as possible proximity gettering sites for transition metal impurities. In all cases, a fundamental understanding of the nucleation and growth processes are of importance in dealing with the technological issues.

3.2. Growth Mechanism for Helium Bubbles in Silicon

Small helium bubbles are observed to form in silicon following ion implantation at room temperature. Subsequent annealing, at temperatures of 800°C or higher, results in the growth of the bubbles and the out-diffusion of the gas to yield the larger facetted voids which are of interest for potential use in the gettering of metallic impurities (Petersen et al. 1997). Until recently, an unsolved problem in ion-beam physics was the mechanism of bubble growth in helium-implanted silicon. Although a theoretical analysis by Evans (2002) had indicated that the operative mechanism should be motion and coalescence, rather than Ostwald ripening, experimental evidence on this issue was ambiguous.

This is a problem that is clearly, in principle, resolvable by TEM observations using a hot stage in which the growth of the cavities could be directly observed. Unfortunately, however, even at the moderate magnifications (≈50 000–100 000) necessary to image nanometer-sized cavities, thermal drift when using the hot-stage renders direct observation of cavity growth difficult. The area of interest drifts significantly as the temperature is raised and is periodically brought back into the centre of the field of view of the video camera resulting in a very "jerky" video sequence – particularly when the sequence is speeded up in an attempt to deduce the cavity growth mechanisms. By the time the drift has reduced to a degree that enables individual cavities to be observed, most of the motion and

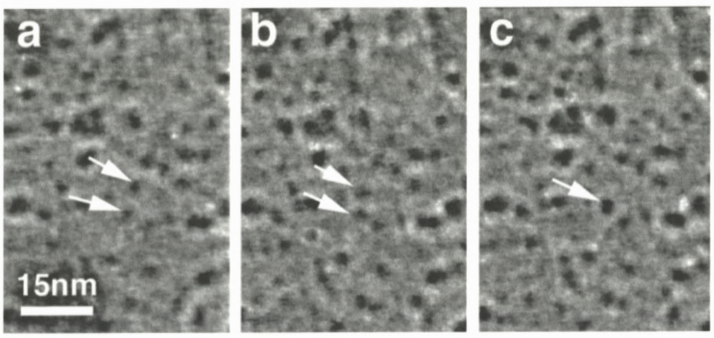

Figure 5. Bright-field underfocused images digitised from a video-recording of an annealing experiment on helium bubbles in silicon. (Note that the contrast has been reversed for clarity of reproduction.) The time interval between successive images is 3.3 seconds. The two cavities indicated by arrows in (a) have moved closer together in (b) and have coalesced into the single bubble indicated by the arrow in (c).

coalescence has occurred. Cavities are observed to have grown or disappeared due to coalescence but the motion that has led to this is not directly observed leading to the false conclusions that growth has occurred by Ostwald ripening (Donnelly et al., 2001). This is illustrated in two video clips (Donnelly, 2006). "HeBub01" is a real-time sequence which illustrates the degree of drift during an annealing experiment. "HeBub02" is a sequence that has been speeded up by a factor of 25 in which considerable bubble growth takes place; however, it is extremely difficult either by viewing the video-clip or by examining consecutive single frames to determine the mechanism of bubble growth.

The effects of this thermal drift can, however, be largely removed by centering and cropping the individual frames that make up the video-clip and reassembling the treated frames into a new video sequence. "HeBub03" (Donnelly, 2006) is a short clip, speeded up by a factor of 100, that has been treated in this way. It is perfectly clear from this clip that considerable bubble movement is taking place and that, in this temperature interval (780–840°C), cavity growth unequivocally takes place by motion and coalescence. Figure 5 shows three frames taken from this clip and illustrates the difficulty of making deductions from the static images. Having viewed the video-clip, it is fairly clear that, for instance, the bubbles indicated by the arrows undergo relative motion and coalescence. However, it would be difficult by analysis of the static images alone, to come to unambiguous conclusions regarding growth mechanisms.

During random (Brownian) motion in a solid, when a cavity migrates in any particular direction, there must be transport of substrate atoms in the opposite

direction or (equivalently) motion of vacancies in the same direction. This can occur either as a result of the diffusion of vacancies and/or interstitials through the bulk solid or by the motion of adatoms and/or surface vacancies at the surface of the cavity. Bulk diffusion in silicon occurs at an energy of 4.75 eV (Bracht et al., 1998) and thus will not be relevant at the temperatures of interest here ($\leq$1000°C). Surface diffusion occurs with a lower activation energy and is likely to be the relevant mechanism of cavity motion in the temperature range of interest.

Diffusivity is proportional to the square of the step length and the jump frequency, ν. Allen et al. (1999) have shown that, for a cavity, the step length is given by λ/N, where λ is the atomic jump distance and N is the number of vacancies in the cavity and that the cavity diffusivity, D_c, can thus be written as:

$$D_c = \frac{1}{4}\left(\frac{2\lambda}{N}\right)^2 \nu, \tag{1}$$

where the factor of 1/4 arises for observed projected displacements. Using the proportionality between r.m.s. displacement and $\sqrt{D_c t}$, where t is time, Birtcher et al. (1999) have derived the following equation for the r.m.s. distance, r_{rms}, moved by a cavity in time interval Δt:

$$r_{rms} = 2\frac{\lambda}{N}\sqrt{\nu_0 \, e^{E_s/kT} \Delta t}, \tag{2}$$

where E_s is the activation energy for surface diffusion, ν_0 is the jump attempt rate, T is temperature and k is Boltzmann's constant. This leads to the following expression for the cavity velocity, v_c, along the projected path, observed from successive video frames recorded with a frame rate of $1/\Delta t$:

$$v_c = 2\frac{\lambda}{N}\sqrt{\frac{\nu_0 \, e^{E_s/kT}}{\Delta t}}, \tag{3}$$

where Δt is 1/30 second.

Surface diffusion on silicon surfaces has been measured using scanning probe microscopy techniques to have activation energies varying from 1.3 eV to 2.1 eV for different surfaces ({100} and {111}) under different experimental conditions (Kitamura et al., 1993; Ichimiya et al., 1997). Using Equation (3) and taking an intermediate value of E_s of 1.7 eV, which has been identified as the diffusion energy of dimer vacancies on a {100} Si surface (Kitamura et al., 1993), v_c has been plotted as a function of bubble radius for a number of different temperatures in Figure 6. From this figure it can be seen that at 800°C, a cavity of radius between 20 and 40 Å would migrate at a speed from 10 to 1 Å/s – approximately consistent with the motion observed in the processed video-clip "HeBub03".

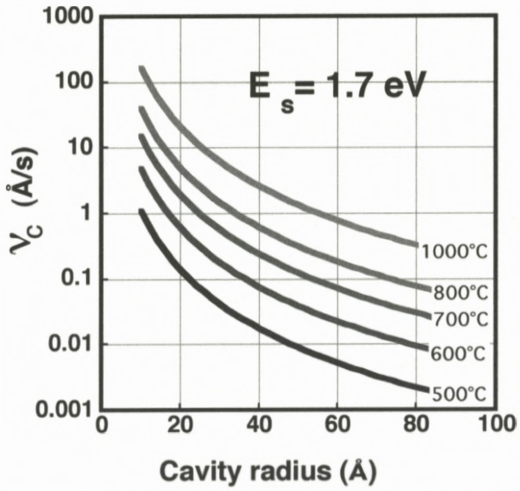

Figure 6. Calculated rate of movement of cavities at different temperatures due to surface diffusion with an activation energy of 1.7 eV as a function of radius. See text for details. From Donnelly et al. (2001).

Cavity growth in silicon thus has been unequivocally shown to occur by surface-diffusion induced motion and coalescence, in agreement with the theoretical findings of Evans (2002) and is thus now a solved problem in ion-beam physics.

3.3. Solid Xe Bubbles in Al – Background

Inert gas atoms generally have negligible solubility in metals and, as in the case of silicon, condense into nanometer-sized gas-filled cavities. Although research on inert gases in solids in general and in metals in particular has been undertaken for many decades and has established many aspects of their behaviour, until recently there have been a number of unanswered questions regarding their behaviour. For the heavier gases, in some circumstances, the inert gas in the cavities may be in solid form at room temperature so that "precipitate" probably provides a more useful description than "cavity" or "bubble". The high (Gigapascal) pressures necessary for the gases to be solid at room temperature result from simple surface energy or surface tension considerations: gas within a small three-dimensional vacancy cluster will prevent its collapse to a vacancy-type dislocation loop. For

a spherical cavity of radius R, an equilibrium pressure of P_{EQ} will prevent this collapse and result in a cavity with no stress in the surrounding material where:

$$P_{EQ} = \frac{2\gamma}{R}, \tag{4}$$

where γ is the interface free energy, which in the case of an inert gas precipitate will be close to the value for the free surface. In principle, the pressure given by Equation (4) may be a lower bound to the pressure within such precipitates with the upper limit being determined by the pressure necessary to punch a dislocation loop, P_{LP}, which has been shown by Trinkaus (1983), following Greenwood et al. (1959), to be approximately given by:

$$P_{LP} = \frac{2\gamma}{R} + \frac{\mu b}{R}, \tag{5}$$

where μ is the shear modulus of the substrate and b is the magnitude of the burgers vector of the dislocation loop (assumed to have the same radius as the precipitate). For a cavity of radius 1 nm in aluminium, Equations (4) and (5) yield pressures of approximately 2 and 9 GPa respectively.

In the 1980s, researchers first identified solid precipitates of argon, krypton and xenon in a variety of fcc metals in electron diffraction experiments and found that the precipitates were epitaxial (but non-commensurate) with the substrate (Templier et al., 1986). In hcp metals the precipitates were observed themselves to have an hcp structure again epitaxial with the substrate (Evans and Mazey, 1986), and in bcc metals they were observed to have an fcc structure with the densely packed (111) planes in the inert gas in contact with the densely packed (110) planes in the metal (Templier, 1991). The pressures determined from lattice parameter measurements obtained from diffraction patterns, coupled with bulk equations of state indicated that the precipitates were, in general, close to the equilibrium pressure given by Equation (4). The inevitable creation of vacancies (and interstitials) during the injection of inert gases by ion implantation presumably ensures that sufficient vacancies are always available for pressure equilibration to take place.

The detailed structure of inert gas precipitates was subsequently elucidated by high-resolution phase contrast electron microscopy (Donnelly and Rossouw, 1985; Birtcher et al., 1999) and a typical high resolution image of a Xe precipitate in Al is shown in Figure 7 (details of how this image was obtained will be presented below). The precipitates are generally observed to be of a tetradecahedral shape – that is an octahedral cavity bounded by {111} planes, truncated by 6 {100} facets. This shape and its projection along two low index directions is also illustrated in Figure 7.

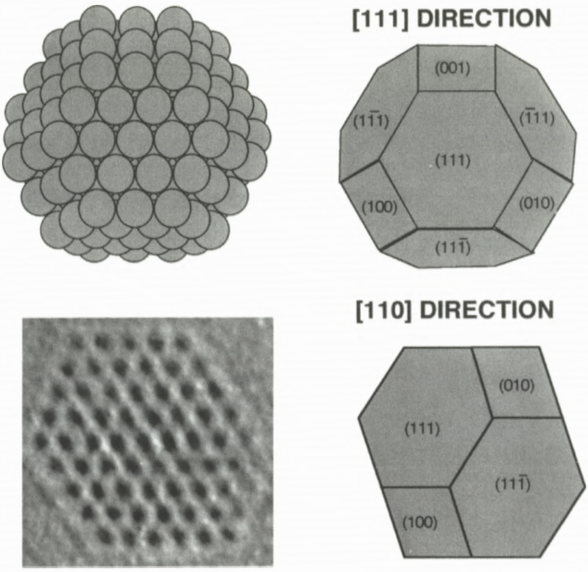

Figure 7. Schematic illustration of the tetradecahedral form of Xe precipitates in Al. Right-hand images are two different projections of the precipitate. The lower, left hand image is a high-resolution electron micrograph of a Xe precipitate in Al where the black contrast is from the Xe atom columns viewed along [110]. See text for details.

As in the case of He bubbles in Si, Xe precipitates in Al also grow on annealing and if this is as a result of motion and coalescence it is unclear as to how that process might occur – particularly given the fact that the inert gas within the cavity is in solid form. Questions that required answering in this regard include:

(i) Do solid inert gas precipitates grow by motion and coalescence?
(ii) If so, by what mechanism does a solid precipitate migrate?

and, as precipitates are generally observed to be close in shape to that shown in Figure 7:

(iii) What processes occur to bring a larger precipitate, formed by coalescence of two smaller ones, back to a compact, truncated octahedral shape?

3.4. High-Resolution Observations

These particular issues have been resolved by high-resolution TEM (HRTEM) work carried out using the JEM ARM-1000 high-voltage TEM at the National Institute for Materials Science in Tsukuba, Japan (formerly, the National Research Institute for Metals) and it is this that will be discussed below. The microscope was operated at a voltage of 1 MV and in general the HRTEM images were recorded with the incident electron beam tilted approximately 3° from an Al ⟨110⟩ direction in order to provide clear Xe images. A (non-Scherzer) defocus of approximately −76 nm was used essentially to filter out information from the aluminium substrate and provide clear Xe images (Furuya et al., 1998). Using a video camera and an on-line image processing system (giving a 5-frame average) images were obtained with sufficient contrast and intensity to be recorded directly onto standard S-VHS videotape at a frame rate of 30 s^{-1}. With the frame averaging, the temporal resolution of the system was thus 1/6 second. The specimens were 3mm Al discs (99.999%-pure) thinned by electropolishing. Ion implantations were carried out at room temperature with 30 keV Xe ions to a fluence of 2×10^{16} ions cm^{-2}. Some specimens were then vacuum-annealed at 300°C for 30 minutes to reduce radiation damage within the substrate and to consolidate the Xe within the precipitates.

3.4.1. *Precipitate Shape Change*

High voltage microscopy is *not* a non-perturbatory experimental technique. A 1 MeV electron may transfer up to 161 eV to an aluminium and also 33 eV to a Xe atom. This will result in displacements in the Al and probably in the Xe also (the displacement energy is not known in solid Xe). In addition a 161 eV Al recoil can transfer a maximum of 91 eV to a Xe atom. Under the viewing conditions used for the experiments a displacement rate of approximately 1 dpa per minute for the aluminium has been estimated. This high displacement rate means that the precipitates are continually interacting with a significant flux of vacancies and interstitials the effects of which can be seen in the video-clip "XeAl01" (Donnelly, 2006) and in still frames captured from the clip and shown in Figure 8.

The figure shows four images of a single Xe precipitate taken at different times (indicated in seconds in each image) from an arbitrary starting time. The images were recorded with the electron beam incident close to a ⟨110⟩ zone axis, under conditions such that contrast from the Al is faint but the Xe atom columns are clearly visible as black spots. The precipitate at $t = 0$ is clearly faceted and the image is consistent with a [110] projection of a truncated octahedron as shown in Figure 7 although it has departed somewhat from the equilibrium Wulff net shape (Wulff, 1901).

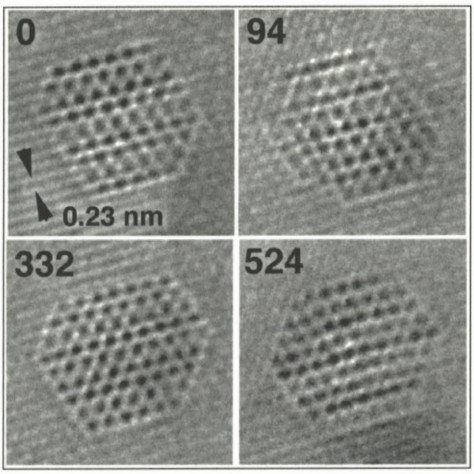

Figure 8. HRTEM images digitised from videotape of a Xe precipitate in Al undergoing shape changes induced by 1 MeV electron irradiation. Each image is an average of 5 frames. Numbers indicate time in seconds. From Donnelly et al. (1997).

With the exception of the image taken at 94 seconds, the images in Figure 8 all appear to correspond to a projection of this 14-sided shape but with facets of varying size. At 94 seconds, the precipitate departs somewhat from this shape as a consequence of having "missing" atoms at one vertex of the structure.

In many images (e.g. $t = 0$ image in Figure 8), {111} Al fringes are visible enabling a comparison to be made between the Xe and Al interplanar spacings. The ratio of the lattice constants of the two materials exhibits values ranging from about 1.4–1.5 yielding a lattice constant for the Xe in the range 0.57–0.61 nm. Assuming that a macroscopic equation of state (EOS) is valid for such small particles and using an EOS due to Ronchi (1980) the atomic density that this range of lattice spacing represents, corresponds to pressures between approximately 10 and 30 kbar.

The projected "radius" of the precipitate in Figure 8 is in the range 1.2 to 1.5 nm for which Equation (2) yields values in the range 15–18 kbar; implying that the precipitate is probably close to equilibrium pressure.

The impact of 1 MeV electrons with aluminium atoms in an Al plane immediately in front of the Xe precipitate (w.r.t. the electron beam) will tend to inject Al atoms into the Xe. Such atoms may be expected to diffuse through the Xe to one of the 14 planes making up the Al cavity. This clearly will have a randomising effect on the cavity shape; however the Al adatoms arriving on the cavity facets might be expected to surface diffuse until becoming trapped at a

ledge or vertex. In time, this process may result in the growth of an extra plane of atoms on a facet. Essentially, this is a process whereby Al atoms are transferred from one facet to another. In addition, electron impacts with the Al atoms in the rear facets of the cavity (w.r.t. electron beam) will leave additional Al vacancies at the surface of the cavity thus randomising the atomic arrangement on the facet and augmenting the cavity volume. However, the precipitate will also interact with the large numbers of mobile vacancies and self-interstitial atoms (SIAs) caused by displacement events in the aluminium. In this way, the system will act to keep the precipitate at equilibrium pressure (thus preventing any net growth) with a shape tending towards the minimum energy form defined by the Wulff construction (Wulff, 1901).

The predominant impression that is gained from viewing the speeded-up video-clip "XeAl01" is that the cavity containing the Xe is continually and randomly changing its shape by the growth or removal of planes of atoms on facets and that the Xe, always retaining its crystalline structure, is "repacking" itself into the altered cavity shape. Room temperature Xe at high pressure is a solid with a very low shear modulus so that, in the video clip, the Xe is seen to adapt to the changing shape of the cavity by shear processes. The overall effect is to cause a random variation of the position of the centre of mass of the precipitate causing it to undergo a degree of stochastic (Brownian) motion, similar to that caused by surface diffusion processes in the helium-induced cavities in Si.

3.4.2. *Precipitate Motion*

The effect of this process on a small cluster can be seen in video clip "XeAl03" (Donnelly, 2006) where such a cluster can be clearly see to migrate. Two frames from this video sequence are shown in Figures 9a and 9b. The frames are separated by 23 seconds and the cluster has moved approximately 1 nm in this time. Figure 9c shows an image of this small cluster in which it has a symmetric form from which (on the assumption of square {100} facets) one can deduce that the cluster contains 38 Xe atoms as shown in Figure 9d.

3.4.3. *Coalescence*

As in the case of thermally-induced motion, this displacement-induced motion will result in the coalescence of the Xe precipitates and, indeed the precipitate distribution is seen to coarsen under continued electron irradiation. The coalescence of two solid precipitates can be seen in the video-clip "XeAl05" (Donnelly, 2006) and four frames from this clip are shown in Figure 10. The stochastic motion discussed above is observed to result in the two precipitates coming within approximately 0.5 nm of one another, at which time the two atomic planes of Al separating them ruptures leading to coalescence into an initially elongated precip-

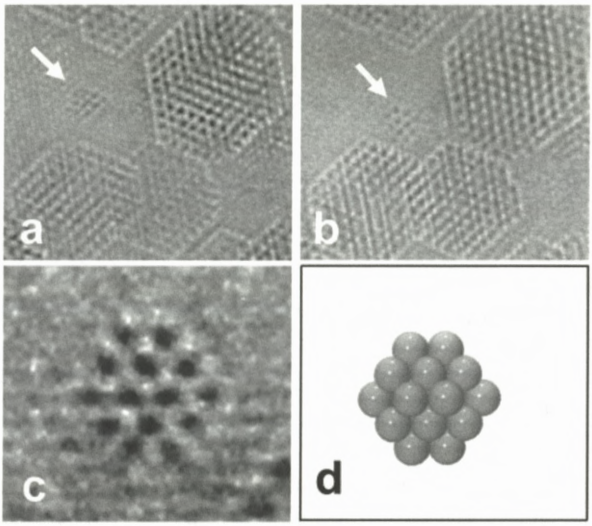

Figure 9. Motion of Xe cluster during continuous 1 MeV electron irradiation. (a) Small Xe cluster indicated by arrow. (b) Small Xe cluster 23 seconds later. Cluster has moved approximately 1 nm between images. (c) Higher magnification image of cluster in symmetrical configuration. (d) Model of small cluster containing 38 atoms.

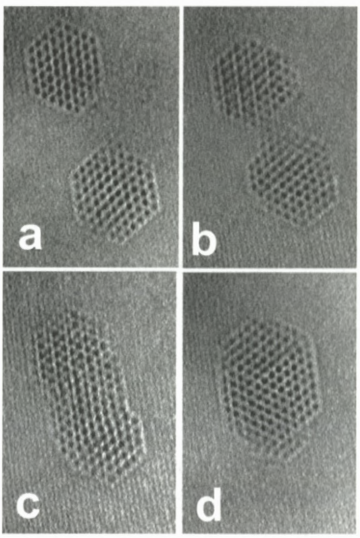

Figure 10. Coalescence of two Xe precipitates in Al during continuous 1 MeV electron irradiation. Time intervals between images are: (a)–(b) 132 seconds; (b)–(c) 34 seconds; (c)–(d) 143 seconds. From Birtcher et al. (1999).

itate. Under the continuous defect flux, however, the precipitate rapidly evolves towards the minimum-energy Wulff net shape and during these changes the Xe remains solid but repacks itself into the cavity by a multiple shearing process as described previously. Note that the large precipitate formed by the coalescence of the two smaller ones is still small enough to have an equilibrium pressure sufficiently high to keep the xenon in the solid state.

This work has clearly provided answers to the questions posed at the start of this section regarding the mobility of solid embedded nanoprecipitates. Specifically, (i) solid inert gas precipitates grow by motion and coalescence under a flux of vacancies and interstitials resulting from displacing electron irradiation. It is highly likely that the same growth process will also obtain during thermal annealing. (ii) The migration mechanism, under displacing irradiation is an interaction with the defect flux that yields changes in the shape of the cavity (without any net volume change) giving rise to a stochastic movement of the centre of mass of the precipitate. In the case of thermal annealing it is likely that similar motion will result from surface diffusion processes as with He in Si. Finally, (iii) the interaction of the cavity with defect fluxes as analysed by Allen et al. (1999) results in a precipitate, formed by coalescence of two smaller ones, evolving rapidly towards the low energy Wulff net shape. For a rigid material within the cavity this could not occur; however, having very low shear modulus, the room-temperature solid inert gas simply repacks itself into the modified shape by shear processes.

All of these are thus solved problems; however, the video clip "XeAl04" (Donnelly, 2006) illustrates one aspect of the behaviour of solid Xe precipitates in Al which remains unexplained.

3.4.4. *Reversible Melting*

The clip illustrates one cycle of a melting/solidification process that occurs up to 4 or 5 times for some precipitates. Frames from this clip are shown in Figure 11. It should be noted that the observed change in contrast does not unequivocally imply that the precipitate has melted – it could simply have rotated within the cavity. However, a detailed investigation at a range of tilts, as well as the observed volume change of the precipitate (see below) indicates strongly that the precipitate does indeed melt. This reversible melting and solidification is difficult to understand, given that the defect flux remains constant during this process. Note that the process appears to be firstly melting followed by a much slower volume change by up to 30%. The volume change then reverses and the precipitate returns slowly to its original volume whereupon it is observed to recrystallise.

A possible explanation could perhaps lie in the creation of sufficient radiation damage within the precipitate such that the Xe is ballistically amorphised, giving

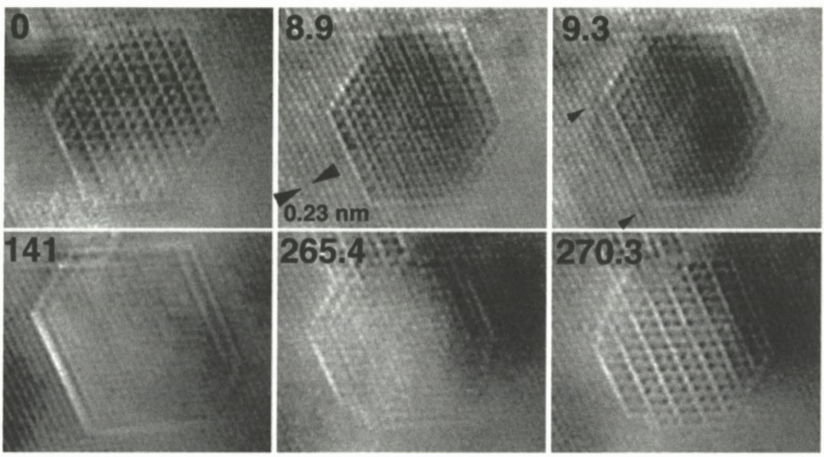

Figure 11. Melting and resolidification of Xe precipitate during continuous 1 MeV electron irradiation. Time, in seconds, is indicated on each panel.

rise to a sudden pressure increase that would (via strain fields around the precipitate) result in a greater uptake of vacancies to equilibrate the surface tension and pressure via Equation (4) thus increasing the volume. Reordering processes within the Xe may subsequently enable the precipitate to recrystallise and, by packing more efficiently, reduce its pressure so that, again by interaction with the defect fluxes, the volume would reduce. This hypothesis is currently being modelled by molecular dynamics to test its feasibility.

The reversible melting and solidification of Xe precipitates in Al under displacing electron irradiation thus remains an unsolved problem.

4. Amorphous Zones in Silicon

4.1. Background

Amorphous layers of silicon on crystalline silicon have been studied fairly extensively for over 20 years, and it has been well established that they can be re-grown to crystallinity by motion of the planar interface into the amorphous layer by thermal annealing at temperatures of 550°C or above (Jackson, 1986). Many mechanisms have been invoked to explain this re-crystallization process. These generally involve the movement and/or generation of defects at the amorphous-crystalline interface with possible defects including dangling bonds (Jackson, 1986), charged kinks on terraces (Williams and Elliman, 1983) and the so-called "bond defect" or I-V pair (Weber et al., 2000; Pelaz et al., 2004). The recrystalliza-

tion process, for the planar interface is characterized by a well-defined activation energy of 2.7 eV (Jackson, 1986).

For partially amorphized Si, where pockets of amorphous material are surrounded by crystal, the situation is more complex. Recrystallization may take place thermally and as a result of electron irradiation. For thermally induced recrystallization, amorphous zones have been observed by TEM and by Rutherford Backscattering Spectroscopy to recrystallize at lower temperatures than the continuous amorphous layer and over a wider range of temperatures.

4.2. In-Situ Observations

By ion irradiating *in-situ* in the TEM – with the specimen in a heating stage permitting subsequent annealing experiments – it is possible to follow the entire life-cycle of individual amorphous zones rather than simply obtaining averaged statistical data. Such experiments were carried out using the *in-situ* TEM/ion accelerator facility referred to in an earlier section (Allen et al., 1989) in which the ion beam is oriented 30° from the microscope axis. For this work, however, the electron energy was kept to 100 keV in order to minimize electron-beam annealing of the amorphous zones (Jencic and Robertson, 1996). Amorphous zones were imaged using structure-factor contrast (Ashby and Brown, 1963) under down-zone, bright-field conditions with the electron beam normal to the {110} surface. The recrystallization behavior of a large number of individual zones was followed on a series of negatives following different isochronal annealing steps. Recrystallization of a smaller number of zones was followed in real time during a slow temperature increase by recording on videotape.

Amorphous zones (a-zones) ranging in size from approximately 1 to 10 nm in size are observed to recrystallize over a range of temperatures from about 70°C to 400°C (Donnelly et al., 2001). In addition, however, the *in-situ* measurements yield the observation that zones with closely similar initial sizes may recrystallize at significantly different temperatures. This is illustrated in Figure 12 where three a-zones, all just over 2 nm in radius, were observed to recrystallize at temperatures of approximately 100°C, 200°C and 300°C respectively. A further indication of the diversity of behaviour observed in these experiments is presented in Figure 13 in which an area of a specimen irradiated to a fluence of 1.25×10^{12} ions cm^{-2} with 200 keV Xe ions at room temperature is shown. The top panel shows a number of a-zones following the irradiation. The bottom panel shows the same area after a 10 minute isochronal anneal at 115°C (with two prior 10 minute anneals at 75°C and 95°C; images following which are not shown).

The large zones, marked "A" and "B" and "C" on the figure not only shrink significantly, but also to tend towards a more spherical shape (a more circular

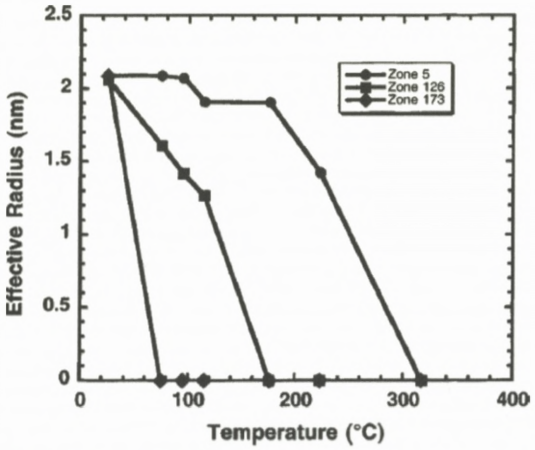

Figure 12. Change in effective radius of three individual amorphous zones with same starting radius following 10 minute anneals to successively higher temperatures. From Donnelly et al. (2003).

shape in projection), i.e. the regions of the a/c interface with small convex radii of curvature appear to recrystallize first. The smaller zones, indicated with an "x" in the figure appear to have completely recrystallized. Larger zones have thus shrunk and smaller zones have disappeared; however, a zone of intermediate size, "E" remains virtually unchanged. This diversity in behaviour is typical of the 500 zones whose individual lifecycles have been studied. The size of an a-zone does not uniquely determine the temperature at which it will recrystallize, and it is not possible to define a unique activation energy for the recrystallization process. Finally, the zone marked "D" in the bottom panel of Figure 13, despite being initially smaller than the zones marked "x" that have disappeared by 115°C, can be seen to grow following the annealing step. This type of "reverse annealing" process is seen in approximately 2% of the zones.

Questions to be resolved regarding the recrystallisation of amorphous zones thus include:

(i) Why is recrystallization, even for zones of similar starting size not characterized by a well-defined activation energy?
(ii) Why does recrystallization proceed in a small number of steps consisting of rapid reductions in size interspersed by longer plateau during which the size stays constant?
(iii) Why, in a small number of cases, do zones grow during an annealing step?

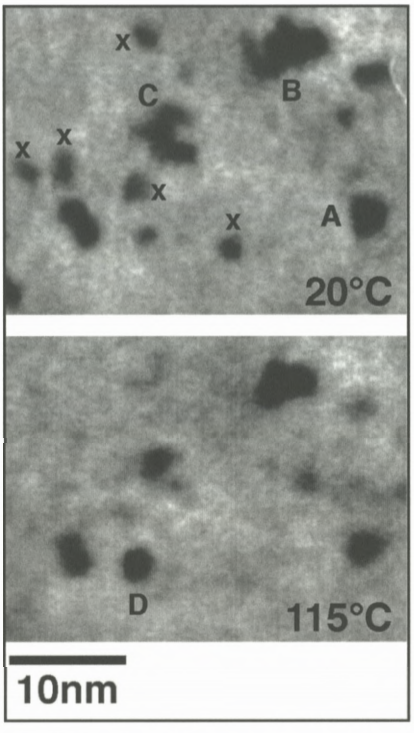

Figure 13. Amorphous zones produced by single impacts of 200 keV Xe ions in Si following creation at 20°C (top panel) and three 10 minute isochronal anneals at 75°C, 95°C and 110°C (bottom panel). See text for details.

In recent work involving both molecular dynamics (MD) and Monte-Carlo modelling of the amorphization and recrystallization of silicon, Pelaz et al. (2004) have investigated the atomistics of irradiation-induced amorphization of silicon. In this work they have focused on the so-called "bond defect" or I-V pair and its role in amorphization and recrystallization. This defect consists of a coupled interstitial and vacancy and contains 5 and 7 member rings characteristic of amorphous silicon. A volume of Si containing approximately 25% of I-V pairs has a radial pair distribution function essentially indistinguishable from amorphous silicon quenched from the melt. An isolated I-V pair has a recombination energy of only 0.43 eV and is thus not stable at room temperature. However, this recombination energy increases as the number of neighboring I-V pairs increases. For an I-V pair at the interface of an amorphous zone with crystal, this activation energy will depend on the local radius of curvature. This gives rise to variable recrystallization kinetics as seen in our experiments – with zone size, zone shape and interface

roughness all playing roles in determining the effective activation energy. For instance, the steplike behaviour seen experimentally in the recrystallization of individual zones is easily explained by this model: for a spherical zone, I-V pairs lying on the a/c interface will have the same co-ordination (i.e. the same number of neighbouring I-V pairs). The zone will remain stable until one of these IV pairs recombines, leaving a crystalline "hole" at the a/c interface. The I-V pairs around this hole now each have one fewer neighbour and therefore will recombine faster. The initial I-V pair recombination thus acts as a trigger for the recombination of the surrounding I-V pairs (Pelaz et al., 2004).

In addition, Lopez et al. (2004) have recently reported a kinetic Monte-Carlo simulation of an anneal at 400°C of two zones each containing approximately 500 atoms but with different shapes (approximately cubic and spherical respectively). The simulation exhibited significantly different average recrystallization rates (approximately a factor of two) and also exhibited plateaux and rapid steps exactly as observed experimentally.

The reverse annealing effect in which an amorphous zone *grows* rather than shrinks, following an increase in temperature, has not yet specifically been modelled. However, we speculate that, given the Gaussian nature of the energy deposition density radially outwards from the centre of the energy spike resulting from a single heavy ion impact, the zone morphology may consist of an amorphous core surrounded by a crystalline region in which a high density of point defects has been quenched in during the rapid decay of the thermal spike. This type of configuration has been seen in MD simulations (Caturla et al., 1996). Energetically, it may be favourable for this entire volume to become amorphous, rendering the growth of the zone possible when the temperature is raised.

Although, Pelaz's I-V pair model of silicon amorphization is not universally accepted, it does provide a consistent explanation of almost all aspects of the complex recrystallization behaviour of nanometre-sized amorphous zones. As such, it could be argued that the formation of amorphous zones by single-ion impacts in silicon and their thermal recrystallization is at least a tentatively solved problem. The remaining unsolved problem is the surprising observed growth of some amorphous zones on annealing. It is to be hoped that additional simulation work may serve to explain this phenomenon also in the light of the I-V model of silicon amorphization.

5. Conclusions

In summary, the *in-situ* TEM work carried out over the last decade or so on radiation damage processes in solids has had a good track record in providing

solutions to problems in ion beam physics; however, one or two puzzles remain. Specifically, the *in-situ* work has facilitated a fairly complete understanding of effects resulting from single heavy ion impacts on metal surfaces and, in particular, the importance of localised melting and flow processes have been highlighted.

For the work on single ion impacts on silicon, although arguments have been presented here that an explanation of Si amorphization in terms of I-V pairs would appear to be consistent with most experimental observations, this model is not accepted, at this juncture, by all researchers with an interest in the topic. And even in the context of the I-V pair model, the phenomenon of amorphous zone growth on annealing ("reverse annealing") is not fully understood.

Finally, although most of the behaviour of nanoscale Xe precipitates in Al under displacing electron irradiation can be understood in terms of stochastic changes to the Al cavity brought about by interactions with fluxes of vacancies and interstitials, the observed reversible melting of solid Xe precipitates remains an unsolved mystery.

Acknowledgements

I should like to acknowledge the major contribution of many colleagues in the work reported in this paper: in particular, Bob Birtcher and Charlie Allen of Argonne National Laboratory (both of whom have recently retired); Kazuo Furuya, Kazutaka Mitsuishi and Minghui Song of the National Institute for Materials Science; Vladimir Vishnyakov of Manchester Metropolitan University and finally, from my own institution, my career-long colleague and mentor, George Carter.

References

Allen C.W., Funk L.L., Ryan E.A. and Ockers S.T. (1989): In situ ion irradiation/implantation studies in the HVEM-tandem facility at Argonne National Laboratory. Nucl Inst Meth B **40–41**, 553–556

Allen C.W., Birtcher R.C., Donnelly S.E., Furuya K., Ishikawa N. and Song M. (1999): Migration and coalescence of Xe nanoprecipitates in Al induced by electron irradiation. Appl Phys Lett **74**, 2611–2613

Ashby M.F. and Brown L.M. (1963): On diffraction contrast from inclusions. Phil Mag **8**, 1649–1676

Averback R.S. and Ghaly M. (1994): A model for surface damage in ion-irradiated solids. J Appl Phys **76**, 3908–3910

Birtcher R.C., Donnelly S.E., Song M., Furuya K., Mitsuishi K. and Allen C.W. (1999): Behavior of crystalline Xe nanoprecipitates during coalescence. Phys Rev Lett **83**, 1617–1620

Bracht H., Haller E.E. and Clark-Phelps R. (1998): Silicon self-diffusion in isotope heterostructures. Phys Rev Lett **81**, 393–396

Brinkman J.A. (1954): On the nature of radiation damage in metals. J Appl Phys **25**, 961–970

Caturla M.J., Diaz de la Rubia T., Marque L.A. and Gilmer G.H. (1996): Ion-beam processing of silicon at keV energies: A molecular-dynamics study. Phys Rev B **54**, 16683–16695

Donnelly S.E. (2006): Video-clips available at: `http://www.imr.salford.ac.uk/fm/sed/media.php`

Donnelly S.E. and Birtcher R.C. (1999): Ion-induced spike effects on metal surfaces. Phil Mag **79**, 133–145

Donnelly S.E. and Rossouw C.J. (1985): High resolution electron microscopy of solid xenon bubbles in ion implanted aluminium. Science **230**, 1272–1273

Donnelly S.E., Furuya K., Song M., Birtcher R.C. and Allen C.W. (1998): 1 MeV electron irradiation of solid Xe nanoclusters in Al – An in-situ HRTEM study. In: Kirkland A. and Brown P.D. (Eds), Proceedings of the International Centennial Conference on the Electron. IOM Communications, Book 687, pp 306–312

Donnelly S.E., Vishnyakov V.M., Birtcher R.C. and Carter G. (2001): The effects of radiation damage and impurities on void dynamics in silicon. Nucl Instrum & Meth in Phys Res B **175–177**, 132–139

Donnelly S.E., Birtcher R.C., Vishnyakov V.M. and Carter G. (2003): Annealing of isolated amorphous zones in silicon. Appl Phys Lett **82**, 1860–1862

Donnelly S.E., Birtcher R.C. and Nordlund K. (2005): Single ion induced spike effects on thin metal films: Observation and simulation. In: Knystautas E.J. (Ed.), Engineering Thin Films and Nanostructures with Ion Beams. Marcel Dekker, New York, pp 7–78

Evans, J.H. (2002): Mechanisms of void coarsening in helium implanted silicon. Nucl Instrum & Meth in Phys Res B **196**, 125–134

Evans J.H. and Mazey D.J. (1986): Solid bubble formation in titanium injected with krypton ions. J Nucl Mat **138**, 176–184

Furuya K., Song M., Birtcher R.C., Allen C.W. and Donnelly S.E. (1998): Direct imaging of the atomic structure of Xe nanocrystals embedded in aluminium. In: Kirkland A. and Brown P.D. (Eds), Proceedings of the International Centennial Conference on the Electron. IOM Communications, Book 687, pp 341–347

Greenwood G.W., Foreman A.J.E. and Rimmer D.E. (1959): The role of vacancies and dislocations in the nucleation and growth of gas and bubbles in irradiated fissile material. J Nucl Mat **4**, 305–324

Ichimiya A., Tanaka Y., et al. (1997): Thermal relaxation of silicon islands and craters on silicon surfaces. Surf Sci **386**, 182–194

Jackson K.A. (1986): A defect model for ion-induced crystallization and amorphization. J Mater Res **3**, 1218–1226

Jencic I. and Robertson I.M. (1996): Low-energy electron beam induced regrowth of isolated amorphous zones in Si and Ge. J Mater Res **11**, 2152–2157

Kitamura N., Lagally M.G. and Webb M.B. (1993): Real-time observations of vacancy diffusion on Si(001)-(2x1) by scanning tunnelling microscopy. Phys Rev Lett **71**, 2082–2085

Lopez P., Pelaz L., Marquéz L.A., Santos I., Aboy M. and Barbolla J. (2004): Atomistic modeling of defect evolution in Si for amorphizing and subamorphizing implants. Mat Sci & Eng B **114–115**, 82–87

Merkle K.L. and Jäger W. (1981): Direct observation of spike effects in heavy-ion sputtering. Phil Mag A **44** 741–762

Pelaz L., Marqués L.A. and Barbolla J. (2004): Ion-beam-induced amorphization and recrystallization in silicon. J Appl Phys **96**, 5947–5976

Petersen G.A., Myers S.M. and Follstaedt D.M. (1997): Gettering of transition metals by cavities in silicon formed by helium ion implantation. Nucl Instrum & Meth in Phys Res B **127–128**, 301–306

Ronchi, C. (1980): Extrapolated equation of state for rare gases at high temperatures and densities. J Nucl Mat **96**, 314–328

Templier C. (1991): Inert gas bubbles in metals: A review. In: Donnelly S.E. and Evans J.H. (Eds), Fundamental Aspects of Inert Gases in Solids, Plenum, New York, pp 117–132

Templier C. et al. (1986): Transmission electron miscroscope study of xenon implanted into metals. Philos Mag A **53**, 667–675

Thompson D.A. (1981): High density cascade effects. Rad Eff **56**, 105–150

Trinkaus H. (1983): Conditions for dislocation-loop punching by helium bubbles. Rad Eff **78**, 189–212

Weber, B., Stock D.M. and Gärtner K. (2000): Defect-related growth processes at an amorphous/crystalline interface: A molecular dynamics study. Mat Sci & Eng B **71**, 213–218

Williams J.S. and Elliman R.G. (1983): Role of electronic processes in recrystallisation of amorphous semiconductors. Phys Rev Lett **51**, 1069–1072

Wulff G. (1901): Frage der Geschwindigkeit des Wachstums und der Anflösung der Krystallflachen. Z Krystall Min **34**, 449–530

Ziegler J.F., Biersack J.P. and Littmark U. (1985): The Stopping and Ranges of Ions in Solids. Pergamon Press, New York (see `http://www.srim.org`)

Radiation Damage in Carbon Nanotubes: What Is the Role of Electronic Effects?

K. Nordlund*

Accelerator Laboratory, P.O. Box 43
FIN-00014 University of Helsinki, Finland

Abstract

Since carbon nanotubes are unique materials with respect to a wide range of properties, it is of interest to pose the question whether radiation damage in this system can be well understood based on traditional defect production models. A review of recent experimental and theoretical work in the field indicates that while at least heavy ion and high-energy electron damage can be well described with established approaches, considerable uncertainty remains regarding at least the effects of low-energy electrons on the damage production.

Contents

1 Introduction **358**

2 Electron Irradiation Effects **360**

3 Nuclear Collision Effects **362**

4 Damage by Electronic Effects? **364**

5 Discussion and Conclusions **366**

Acknowledgements **367**

References **367**

* E-mail: kai.nordlund@helsinki.fi

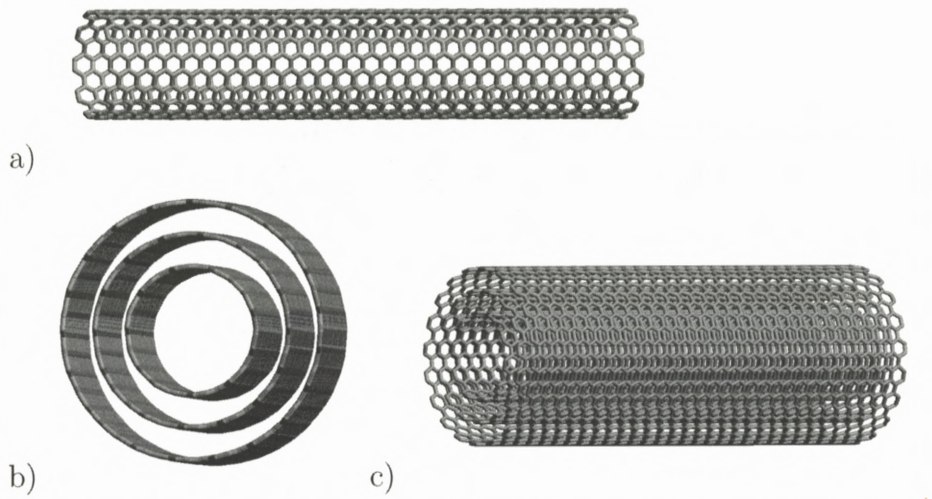

Figure 1. Atomic structure of carbon nanotubes, illustrated by plotting the chemical bonds joining the carbon atoms. (a) A single-wall carbon nanotube. (b) A triple-wall carbon nanotubes, almost axial view. (c) The same triple-wall carbon nanotube, viewed almost perpendicular to the axis.

1. Introduction

Notwithstanding the significant recent progress made in studies of radiation effects in carbon nanotubes, it remains unclear whether traditional radiation damage theories are fully applicable to describe irradiation effects in this prototypical nanosystem.

Carbon nanotubes are long, hollow cylinders of pure carbon consisting of either a single carbon cylinder or several concentric ones (Iijima, 1991; Ajayan and Iijima, 1992) (see Figure 1). The former kind are called single-walled nanotubes and the latter multi-walled ones. Their structure can conceptually be understood by imagining rolling up a single sheet of graphite ("graphene") into a cylinder with perfectly matching chemical bonds at the joining line (Dresselhaus et al., 2001), although it is noteworthy that the actual growth mechanism is very different (Raty et al., 2005). Despite being found already in the 1970s (Oberlin et al., 1976; Wiles and Abrahamson, 1978), large-scale interest in these systems emerged only in the 1990s (Iijima, 1991; Ajayan and Iijima, 1992; Iijima and Ichihashi, 1993). It quickly became clear that individual nanotubes have very interesting mechanical and electronic properties (Collins and Avouris, 2000; McEuen, 2000), giving rise to enormous basic and applied research interest (Baughman et al., 2002).

Studying irradiation effects in carbon nanotubes is well motivated both from a basic science and application point of view. On the basic science side, it is clear that the special geometry allows one to pose many interesting irradiation physics questions. From an applied science point of view, studies of radiation effects can be motivated in two ways. One can use irradiation as a way to introduce known controlled amounts of defects into a material, to understand damage effects on materials properties. This is quite important as even the best nanotubes manufactured to date do contain defects, and for instance electrical properties of nanotubes are highly sensitive to them (Fan et al., 2005; Gomez-Navarro et al., 2005). On the other hand, one can also look for ways in which irradiation can be used to modify nanotubes to obtain beneficial effects, such as tuning the electrical conductance of the tubes (Gomez-Navarro et al., 2005), using nanotubes as masks against ion irradiation (Yun et al., 2000; Krasheninnikov et al., 2002b), welding nanotubes together (Krasheninnikov et al., 2002a; Raghuveer et al., 2004) or introducing dopants into them (Kotakoski et al., 2005).

Central to both basic and applied science studies of irradiated carbon nanotubes is the understanding of the basic physics of damage production. This is a very interesting line of study for two reasons. First, the unique 1-dimensional nature and properties of nanotubes makes it questionable whether the traditional models of radiation effects are directly applicable to this system. Second, the nanotubes can be – and frequently are – studied one object at a time directly at the nanoscale. This makes it sometimes possible to study radiation effects experimentally down to the individual point defect level (Kimura-Hashimoto et al., 2004; Gomez-Navarro et al., 2005), something which has rarely been possible in any material. Thus studies of radiation effects in nanotubes might eventually lead to insights giving better understanding of radiation effects in other materials.

Since carbon nanotubes are either metallic or semiconductors with a relatively small band gap, the natural approach for attempting to understand radiation damage in them is using models developed for crystalline metals, semiconductors, and, of course, graphite. For these materials, the damage production can be understood in terms of three main classes of effects. For keV energy heavy ion irradiation, damage is dominated by nuclear collisions and cascades produced by them (Averback and Diaz de la Rubia, 1998; Smith, 1997). Electron irradiation can produce bulk damage only when the electron energy is high enough to produce atomic recoils with energies above the threshold displacement energy (Lucasson, 1975; Banhart, 1999). For MeV ions, when the electronic energy loss is of the order of 10 keV/nm or more, electronic effects can produce damage in some metals and semiconductors due to the high local heating around the ion track (Trautmann et al., 2000; Kanjijal, 2001; Bringa and Johnson, 2002).

During the last about eight years, a few groups have carried out systematic studies of electron and ion irradiation effects in nanotubes (for reviews, see Banhart, 1999; Krasheninnikov and Nordlund, 2004), and a great deal of understanding has been obtained. In this article, in the spirit of the Ion'06 workshop, the current understanding is summarized with an aim to explore where the damage production can clearly be treated with the conventional approaches, and where major open questions remain.

2. Electron Irradiation Effects

Electron irradiation of carbon nanosystems has been studied extensively by Banhart and co-workers with *in situ* experiments in electron microscopes. In these experiments, the electron beam of the microscope can be used to both irradiate and image the carbon nanosystems. These studies have shown that nanotubes can be damaged by electron irradiation. The irradiation has been shown to induce major structural rearrangements of the tubes, welding, and even phase transitions to the diamond phase (Wesolowski et al., 1997; Banhart, 1999, 2001; Terrones et al., 2000, 2002). As an example, the welding of two nanotubes is illustrated in Figure 2.

To establish how such effects have been understood, we first note that experiments have indicated that a threshold of damage production exists at an electron energy of about 86 keV (Smith and Luzzi, 2001). Assuming a direct knock-on between an electron and a carbon atom, this translates into a minimum threshold kinetic energy for damage production of 17 eV. This value is similar in magnitude to threshold energies found in conventional materials, including graphite (Nastasi et al., 1996; Andersen, 1979). Recoils produced by electron knock-ons above 86 keV will naturally lead to vacancy production, and indeed effects such as welding have been explained to be due to a high concentration of vacancies leading to coalescence of tubes (Terrones et al., 2000, 2002; Lopez et al., 2002; Jang et al., 2004) (cf. Figure 2).

One of the most dramatic irradiation effects known to occur in nanocarbon is the phase transition from graphene shells to diamond within carbon onions (concentric shells of fullerenes) (Wesolowski et al., 1997). This effect can also be understood based on vacancy and interstitial production: the irradiation-created vacancies in fullerenes and nanotubes have a special ability to recombine dangling bonds, leading to a shrinkage of the whole fullerene or nanotube (Sun et al., 2006). In the case of carbon onions, this leads to shrinkage of the concentric carbon spheres, with interstitials tending to migrate outwards due to the pressure gradient (Wesolowski et al., 1997; Banhart, 1999). This can

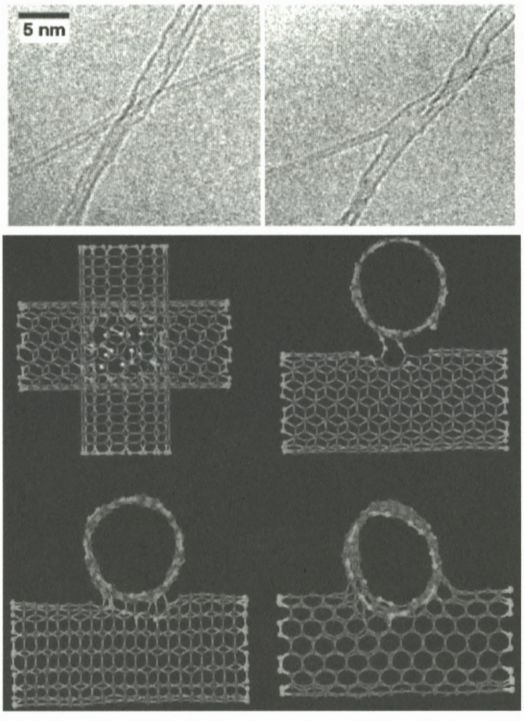

Figure 2. Welding of carbon nanotubes. The upper part shows an experimental TEM image of two crossed carbon nanotubes before and after electron irradiation. The two tubes were initially disjoint but then became welded by ion irradiation. The lower part shows a computer simulations of the welding process, based on creating vacancies in the near-junction region and allowing them to relax. Both figures are reprinted with permission from Terrones et al., 2002. Copyright (2002) by the American Physical Society.

lead to a high enough pressure to create diamond (Zaiser and Banhart, 1999; Astala et al., 2001).

Also the cross sections for recoil production by electrons have been considered in detail and found to be consistent with the observed damaging rates (Banhart, 1999). Thus it appears that the damage production in nanotubes by high-energy ($\gtrsim$ 100 keV) electron-irradiation can be understood well based on the traditional picture of knock-on displacements of atoms and subsequent defect migration.

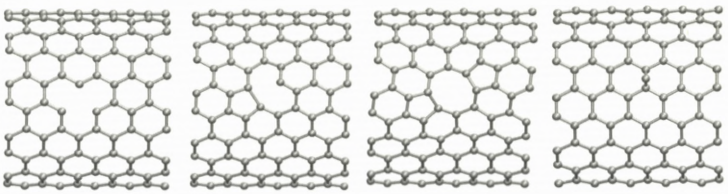

Figure 3. Some point defect structures in a carbon nanotube. (a) unreconstructed vacancy, (b) reconstructed "5-1db" vacancy, (c) divacancy, and (d) adatom on the outside of the tube.

3. Nuclear Collision Effects

The production of damage by low-energy ($\lesssim$100 keV) ion irradiation has been examined systematically with molecular dynamics (MD) simulations by Krasheninnikov and co-workers. These studies have shown that in single free-standing nanotubes ion irradiation produces predominantly single vacancies and small vacancy clusters (Krasheninnikov et al., 2001, 2002c). Some of these basic defects are illustrated in Figure 3. The initial vacancy structures produced during the irradiation by knocking out atoms are metastable: they contain dangling bonds, some of which tend to recombine to form more stable structures (Krasheninnikov and Nordlund, 2001; El-Barbary et al., 2003). Instead of becoming conventional interstitials (which would be atoms in the middle of a carbon hexagon in the tube) recoiled atoms either leave the tube or obtain an adatom-like structure. In this adatom-like structure a carbon atom is situated on a bond-centred site above or below the nanotube network (Nordlund et al., 1996). In a single tube this structure can be considered in many ways analogous to an interstitial.

In multi-walled tubes or a bundle of single-walled ones, also interstitials of a more conventional character exist in the form of carbon atoms lying between the individual carbon cylinders (Salonen et al., 2002; Pomoell et al., 2004). Sinnott and co-workers have shown that both low-energy electron and ion irradiation can be used to introduce such defects and thus cross-linking between the shells of multi-wall nanotubes (Pregler and Sinnott, 2006). For carbon peapods (fullerenes inside nanotubes) ion irradiation has somewhat similarly been shown to be able to cause cross-linking of the fullerenes (Hu et al., 2006).

The migration of the point defects has been examined with tight-binding and density-functional theory quantum mechanical simulations (Lehtinen et al., 2003; Krasheninnikov et al., 2004; Krasheninnikov et al., 2006). These studies show that the "adatom-interstitial" and vacancy exhibit rather special mobility properties: their mobility depends strongly on how the nanotube has been rolled up,

Figure 4. Example of a strongly damaged multi-wall carbon nanotube. The tube in the picture was irradiated by Ar ions with a range approximately half-way across the multi-wall tube, thus damaging the upper part strongly (Krasheninnikov et al., 2002b).

and on whether it is metallic or semiconducting. The interstitial is highly mobile, while the vacancy is less so. Once the vacancies have joined together to form di- or larger vacancy agglomerates, the mobility decreases strongly.

These theoretical results on migration are supported by recent transmission electron microscopy experiments (Kimura-Hashimoto et al., 2004) in which individual small immobile vacancy clusters produced by the electron irradiation were observed at room temperature. Since the irradiation was carried out just above the displacement threshold, the vacancy clusters must have formed by coalescence of single vacancies. Thus the experiment supports both the mobility of vacancies and immobility of larger clusters at room temperature.

The quantitative values of interstitial and vacancy mobility for the largest tubes studied are also in line with mobility values obtained in graphite (Thrower and Mayer, 1978), although some uncertainty exists in how these should be interpreted (El-Barbary et al., 2003).

We also consider whether the damage levels obtained are reasonable. In the MD simulations the damage builds up linearly with dose as no recombination occurs on the MD time scale, and amorphization occurs when most of the atoms have been displaced at least once. An example of a strongly damaged nanotube is shown in Figure 4. Even though some recombination does of course in reality always occurs due to long-time scale defect migration, recent kinetic Monte Carlo (KMC) simulations (Kotakoski et al., 2007) indicate that this effect becomes more important only at temperatures significantly above room temperature. At lower temperatures the formation of amorphous structures is not much slowed down by migration and recombination. Thus under the assumption that these MD and

KMC studies are correct, one may use simple displacement-per-atom (dpa) values obtained from binary collision approximation codes like TRIM/SRIM to examine whether reported amorphization fluences are reasonable.

Using the "vacancy" production numbers from SRIM-2003 (Ziegler, 2003), the dpa values of certain experiments on nanotube irradiation were estimated by the author of this Article. Unless the experimental papers reported a density of their material, a density of 0.5 g/cm^3 (typical of macroscopic nanotube materials like nanotube paper) was assumed. The threshold displacement energy was allowed to be at its default value for carbon. Since our aim is to make only order-of-magnitude estimates, such rough estimates are acceptable.

Raghuveer et al. (2004) reported major modifications of nanotubes by 10 keV Ga at a fluence of 10^{16} ions/cm^2. Using the SRIM calculations described in the previous paragraph, we obtained that this corresponds to a damage level of 8 dpa. Wang et al. (2004) showed clear transmission electron microscopy (TEM) images of nanotube amorphization after irradiation with 10^{17} ions/cm^2 50 keV C. This corresponds to a damage level of 6 dpa. Both values are quite reasonable, as at such high dpa values amorphization indeed would be expected, even accounting for some possible defect recombination.

4. Damage by Electronic Effects?

Summarising the discussion in the two previous sections, the basics of damage production by both electrons and ions in carbon nanotubes would appear to be well understood. However, considering some additional experiments makes this picture considerably less certain.

We first discuss proton irradiation of carbon nanotubes. Basiuk et al. (2002) irradiated carbon nanotubes with 3 MeV protons in air at room temperature, and subsequently analysed them in a TEM. They reported that at a fluence of 3×10^{16} ions/cm^2 this irradiation amorphized the tubes. Using a similar calculation as described in the previous section, this corresponds to a damage level of 0.0001 dpa. We checked that even accounting for Xe recoils or possible inaccuracies in the Xe or nanotube film thickness does not change this number by the several orders of magnitude needed to explain the amorphization by nuclear energy deposition.

Khare et al. (2003) irradiated a 0.5 μm single-wall nanotube film placed below a 16.75 μm Xe film at 15 K by 1 MeV protons. These samples were studied by Fourier transform infrared spectroscopy, Raman and TEM methods. The authors reported obtaining CH bonds and defects and changes in nanotube diameters, although quantitative damage levels were not reported. This irradiation, considering the Xe layer on top, corresponds to some 0.0001 dpa in the nanotube layer.

By contrast, Weaver and co-workers have carried out 2 MeV proton irradiation of nanotube paper and nanotubes in a polymer matrix (Weaver et al., 2004; Neupane et al., 2005) up to doses of 7×10^{16} ions/cm^2. They report on the one hand measurable resistivity and Raman spectroscopy effects already at a dose of 10^{12} ions/cm^2, but on the other hand interpret the results to mean that the tubes have a high radiation tolerance. Unfortunately the atomic structure of the samples after the irradiations is not characterised in these experiments.

The interpretation of these results is not straightforward. Since Khare does not report an overall damage level, it is of course possible that the damage level they observe is quite small, but it is not obvious how a damage level of only 0.0001 dpa could result in measurable changes in tube diameters. The amorphization reported by Basiuk et al. clearly cannot be explained by a damage level of 0.0001 dpa: this would be in contrast with the heavy ion dpa values discussed in the previous section by at least 4 orders of magnitude. This experiment was carried out in air, suggesting that oxidation or interaction with water may play a role on the results. However, even then it is difficult to understand why the tubes would amorphize: even though point defects created by the irradiation are likely to be oxygenated or hydrogen-stabilised, such defects have been observed at ambient conditions in other experiments without any reported runoff structural changes (Gomez-Navarro et al., 2005). If the effect is not explained by the presence of air, the only alternative explanation would be damage caused by electronic excitations. The electronic stopping by 1 MeV protons is some 2–3 orders of magnitude higher than the nuclear one, so plenty of electronic deposited energy would be available. It is again not obvious, however, what the mechanism could be. The nanotubes are metallic or semiconducting with a small band gap, and the electronic stopping is only some 0.05 keV/nm. Hence damage by electronic excitations of the kind associated with swift heavy ions would seem unlikely both by materials property and low stopping value (Kanjijal, 2001).

Although the effects of the TEM electrons with energies of $\sim$100 keV or more, can be well described by traditional ballistic knock-on mechanisms (cf. Section 2), there are some experimental indications that particles which can not possibly produce recoils above the 17 eV threshold can damage nanotubes. Yuzvinsky et al. (2005) reported that 5 keV electrons would cause major damage in nanotubes, and Miko et al. (2006) reported that ultraviolet light can affect electrical and mechanical properties of nanotubes. However, in both cases the effect was attributed to the presence of chemically active radicals from the environment. Skakalova et al. have shown that 1.3 MeV γ ion irradiation can be used to strengthen macroscopic nanotube materials. This effect could in principle be related to knock-on displacements of atoms by the highest-energy particles in an electron-gamma radiation

cascade, or to low-energy recoils produced by γ ray-nucleus collisions. It might also be related to production of radicals either in the surrounding atmosphere or impurities in the films.

5. Discussion and Conclusions

The literature overview presented in the previous sections has illustrated that the basic physics of keV heavy ion and hundreds-of-keV's electron irradiation damage in nanotubes appears to be fairly well understood. Although some unique features of the damage behaviour are observed in nanotubes, such as the chirality-dependent migration rates of point defects, the conventional theory frameworks appear to be well suited to understand the effects. However, considerable uncertainty exists on whether low-energy electronic excitations can cause damage in nanotubes.

The basic reason why it is natural to assume electronic excitations would not cause damage in nanotubes is that they are either metals or semiconductors with a small band gap. In bulk metals and semiconductors electronic stopping does not produce damage, except in the swift heavy ion regime where the electronic energy deposition is very large. Swift heavy ions are indeed known to produce damage and sputtering in graphite, but the energy depositions at which this is observed are much higher, of the order of 10 keV/nm (Liu et al., 1998; Tripathi et al., 2006), while for MeV protons it is of the order of 0.1 keV/nm, i.e. 2 orders of magnitude less.

Highly charged slow ions have been observed to produce electronic sputtering of carbon, but only for charge states larger than about +7 (Schulte and Holzapfel, 1997), which of course is not relevant for protons.

Although it is thus hard to understand how low-energy electron excitations could cause damage in nanotubes, there are several independent sets of experiments where nanotubes are damaged when the probability of producing knock-on recoils above the threshold must be very small or zero (cf. Section 4). All of these are, however, performed under conditions where the irradiated material is subject to the presence of air or other chemical compounds than nanotubes. Thus it is possible that the electronic excitations produce chemically active radical species around the nanotubes, which then react with the nanotubes. Hence at this stage it appears most likely that the low-energy electronic effects are not due to any unknown radiation physics, but rather to some interesting – and not well understood – radiation chemistry effects. Additional experimental and theoretical work will clearly be required to resolve the mechanisms involved.

Acknowledgements

The work giving the basis for the current discussion was funded by the Academy of Finland under the ELENA research project, and benefited from generous grants of computer time from CSC, the Finnish IT Center for Science.

References

Ajayan P.M. and Iijima S. (1992): Smallest carbon nanotube. Nature **358**, 23

Andersen H.H. (1979): The depth resolution of sputter profiling. Appl Phys **18**, 131

Astala R., Kaukonen M., Nieminen R.M., Jungnickel G. and Frauenheim T. (2001): Simulations of diamond nucleation in carbon-onion cores. Phys Rev B Rapid Commun **63**, 081402

Averback R.S. and Diaz de la Rubia T. (1998): Displacement damage in irradiated metals and semiconductors. In: Ehrenfest H. and Spaepen, F. (Eds), Solid State Physics, Vol. 51. Academic Press, New York, pp 281–402

Banhart F. (1999): Irradiation effects in carbon nanostructures. Rep Prog Phys **62**, 1181–1221

Banhart F. (2001): The formation of a connection between carbon nanotubes in an electron beam. Nano Letters **1**, 329–332

Basiuk V.A., Kobayashi K., Kaneko T., Negishi Y., Basiuk E.V. and Saniger-Blesa J.M. (2002): Irradiation of single-walled carbon nanotubes with high-energy protons. Nano Letters **2**, 789–791

Baughman R.H., Zakhidov A.A. and de Heer W.A. (2002): Carbon nanotubes – The route toward applications. Science **297**, 787

Bringa E.M. and Johnson R.E. (2002): Coulomb explosion and thermal spikes. Phys Rev Lett **88**, 165501

Collins P.G. and Avouris P. (2000): Nanotubes for electronics. Scientific American **283**, 62–69

Dresselhaus M.S., Dresselhaus G. and Avouris P. (Eds) (2001): Carbon Nanotubes, Synthesis, Structure, Properties and Applications. Springer, Berlin

El-Barbary A.A., Telling R.H., Ewels C.P., Heggie M.I. and Briddon P.R. (2003): Structure and energetics of the vacancy in graphite. Phys Rev B **68**, 144107

Fan Y., Goldsmith B.R. and Collins P.G. (2005): Identifying and counting point defects in carbon nanotubes. Nature Materials **4**, 906

Gomez-Navarro C., de Pablo P.J., J. Gomez-Herrero B.B., Garcia-Vidal F.J., Rubio A. and Flores F. (2005): Tuning the conductance of single-walled carbon nanotubes by ion irradiation in the Anderson localization regime. Nature Materials **4**, 534–539

Hu Y., Irving D.L. and Sinnott S.B. (2006): Ion deposition induced modification of carbon nanopeapods: A computational study. Chem Phys Lett **422**, 137

Iijima S. (1991): Helical microtubules of graphitic carbon. Nature **354**, 56–58

Iijima S. and Ichihashi T. (1993): Single-shell carbon nanotubes of 1-nm diameter. Nature **363**, 603

Jang I., Sinnott S.B., Danailov D. and Keblinski P. (2004): Molecular dynamics simulation study of carbon nanotube welding under electron beam irradiation. Nano Letters **4**, 109–114

Kanjijal D. (2001): Swift heavy ion-induced modification and track formation in materials. Current Science **80**, 1560

Khare B., Meyappan M., Moore M.H., Wilhite P., Imanaka H. and Chen B. (2003): Proton irradiation of carbon nanotubes. NanoLetters **3**, 643–646

Kimura-Hashimoto A., Suenaga K., Gloter A., Urita K. and Iijima S. (2004): Direct evidence for atomic defects in graphene layers. Nature **430**, 870–873

Kotakoski J., Krasheninnikov A.V., Ma Y., Foster A.S., Nordlund K. and Nieminen R.M. (2005): B and N implantation onto carbon nanotubes: Insight from atomistic simulations. Phys Rev B **71**, 205408

Kotakoski J., Krasheninnikov A.V. and Nordlund K. (2007): Kinetic Monte Carlo studies of defect mobility in carbon nanotubes. To be published

Krasheninnikov A.V. and Nordlund K. (2001): Stability of irradiation-induced point defects on walls of carbon nanotubes. J Vac Sci Techn B **20**, 728

Krasheninnikov A.V. and Nordlund K. (2004): Irradiation effects in carbon nanotubes. Nucl Instr Meth Phys Res B **216**, 355

Krasheninnikov A.V., Nordlund K., Sirviö M., Salonen E. and Keinonen J. (2001): Formation of ion-irradiation-induced atomic-scale defects on walls of carbon nanotubes. Phys Rev B **63**, 245405

Krasheninnikov A.V., Nordlund K., J.Keinonen and Banhart F. (2002a): Ion-irradiation induced welding of carbon nanotubes. Phys Rev B **66**, 245503

Krasheninnikov A.V., Nordlund K. and Keinonen J. (2002b): Carbon nanotubes as masks against ion irradiation: an insight from atomistic simulations. Appl Phys Lett **81**, 1101. Also selected to Virtual Journal of Nanoscale Science & Technology Vol. 6 Issue 7 (2002).

Krasheninnikov A.V., Nordlund K. and Keinonen J. (2002c): Production of defects in supported carbon nanotubes under ion irradiation. Phys Rev B **65**, 165423. Also selected to Virtual Journal of Nanoscale Science & Technology Vol. 5 Issue 16 (2002).

Krasheninnikov A.V., Nordlund K., Lehtinen P.O., Foster A.S., Ayuela A. and Nieminen R.M. (2004): Adsorption and migration of carbon adatoms on carbon nanotubes. Phys Rev B **69**, 073402

Krasheninnikov A.V., Lehtinen P.O., Foster A.S. and Nieminen R.M. (2006): Bending the rules: Contrasting vacancy energetics and migration in graphite and carbon nanotubes. Chem Phys Lett **418**, 132

Lehtinen P.O., Foster A.S., Ayuela A., Krasheninnikov A., Nordlund K. and Nieminen R.M. (2003): Magnetic properties and diffusion of adatoms on a graphene sheet. Phys Rev Lett **91**, 017202

Liu J., Hou M.D., Liu C.L., Wang Z.G., Jin Y.F., Zhai P.J., Feng S.L. and Zhang Y. (1998): Tracks of high energy heavy ions in HOPG studied with scanning tunneling microscopy. Nucl Instr Meth Phys Res B **146**, 356

Lopez M.J., Rubio A., Alonso J.A., Lefrant S., Metenier K. and Bonnamy S. (2002): Patching and tearing single-wall carbon nanotube ropes into multiwall carbon nanotubes. Phys Rev Lett **89**, 255501

Lucasson P. (1975): The production of Frenkel defects in metals. In: Robinson M.T. and Young Jr. F.N. (Eds), Fundamental Aspects of Radiation Damage in Metals. ORNL, Springfield, pp 42–65

McEuen P.L. (2000): Single-wall carbon nanotubes. Physics World **31**

Miko C., Milas M., Seo J.W., Gaal R., Kulik A. and Forro L. (2006): Effect of ultraviolet light irradiation on macroscopic single-walled carbon nanotube bundles. Appl Phys Lett **88**, 151905

Nastasi M., Mayer J. and Hirvonen J. (1996): Ion-Solid Interactions – Fundamentals and Applications. Cambridge University Press, Cambridge, Great Britain

Neupane P.P., Manasreh M.O., Weaver B.D., Landi B.J. and Raffaelle R.P. (2005): Proton irradiation effect on single-wall carbon nanotubes in a poly(3-octylthiophene) matrix. Appl Phys Lett **86**, 221908

Nordlund K., Keinonen J. and Mattila T. (1996): Formation of ion irradiation-induced small-scale defects on graphite surfaces. Phys Rev Lett **77**, 699

Oberlin A., Endo M. and Koyama T. (1976): Filamentous growth of carbon through benzene decomposition. J Cryst Growth **32**, 335

Pomoell J.A.V., Krasheninnikov A.V., Nordlund K. and Keinonen J. (2004): Ion ranges and irradiation-induced defects in multi-walled carbon nanotubes. J Appl Phys **96**, 2864

Pregler S.K. and Sinnott S.B. (2006): Molecular dynamics simulations of electron and ion beam irradiation of multiwalled carbon nanotubes: The effects on failure by inner tube sliding. Phys Rev B **73**, 224106

Raghuveer M.S., Ganesan P.G., D'Arcy-Gall J., Ramanath G., Marshall M. and Petrov I. (2004): Nanomachining carbon nanotubes with ion beams. Appl Phys Lett **84**, 4484

Raty J.Y., Gygi F. and Galli G. (2005): Growth of carbon nanotubes on metal nanoparticles: A microscopic mechanism from ab initio molecular dynamics simulations. Phys Rev Lett **95**, 096103

Salonen E., Krasheninnikov A. and Nordlund K. (2002): Ion-irradiation-induced defects in bundles of carbon nanotubes. Nucl Instr Meth Phys Res B **193**, 608–613

Schulte O. and Holzapfel W.B. (1997): Effect of pressure on atomic volume of Ga and Tl up to 68 Gpa. Phys Rev B **55**, 8122–8128

Smith B.W. and Luzzi D.E. (2001): Electron irradiation effects in single wall carbon nanotubes. J Appl Phys **90**, 3509

Smith R. (Ed.) (1997): Atomic & Ion Collisions in Solids and at Surfaces: Theory, Simulation and Applications. Cambridge University Prss, Cambridge, UK

Sun L., Banhart F., Krasheninnikov A.V., Rodriguez-Manzo J.A., Terrones M. and Ajayan P.M. (2006): Carbon nanotubes as high-pressure cylinders and nanoextruders. Science **312**, 1199

Terrones M., Terrones H., Banhart F., Charlier J.C. and Ajayan P.M. (2000): Coalescence of single-walled carbon nanotubes. Science **288**, 1226–1229

Terrones M., Banhart F., Grobert N., Charlier J.C., Terrones H. and Ajayan P.M. (2002): Molecular junctions by joining single-walled carbon nanotubes. Phys Rev Lett **89**, 075505

Thrower P.A. and Mayer R.M. (1978): Point defects and self-diffusion in graphite. Phys Stat Sol (a) **47**, 11

Trautmann C., Klaumünzer S. and Trinkaus H. (2000): Effect of stress on track formation in amorphous iron boron alloy: Ion tracks as elastic inclusion. Phys Rev Lett **85**, 3648

Tripathi A., Khan S.A., Kumar M., Baranwal V., Krishna R. and Pandey A.C. (2006): SHI induced surface modification studies of HOPG using STM. Nucl Instr Meth Phys Res B **244**, 225–229

Wang Z. et al. (2004): Amorphous molecular junctions produced by ion irradiation on carbon nanotubes. Phys Lett A **324**, 321–325

Weaver B.D., Landi B.J. and Raffaelle R. (2004): High radiation tolerance of carbon nanotube matrices for space power applications. In: Proceedings of the 2nd International Energy Conversion Engineering Conference, 16–19 August 2004, Providence, RI

Wesolowski P., Lyutovich Y., Banhart F., Carstanjen H.D. and Kronmüller H. (1997): Formation of diamond in carbon onions under MeV ion irradiation. Appl Phys Lett **71**, 1948–1950

Wiles P.G. and Abrahamson J. (1978): Carbon fibre layers on arc electrodes – I: Their properties and cool-down behaviour. Carbon **16**, 341

Yun W.S. et al. (2000): Fabrication of metal nanowire using carbon nanotube as a mask. J Vac Sci Technol A **18**, 1329

Yuzvinsky T.D., Fennimore A.M., Mickelson W., Esquivias C. and Zettl A. (2005): Precision cutting of nanotubes with a low-energy electron beam. Appl Phys Lett **86**, 053109. See also Erratum, Appl Phys Lett **87**, 069902 (E)

Zaiser M. and Banhart F. (1999): Radiation-induced transformation of graphite to diamond. Phys Rev B **79**, 3680

Ziegler J.F. (2003): SRIM-2003 software package, available online at `http://www.srim.org`

Index

This index has been compiled on the basis of keywords provided by the authors of individual contributions. Each entry refers to the start page(s) of the respective contribution(s).

adatoms 357
affinity level 465
affinity, electron 465
alkali layer 465
amorphisation 13, 227
amorphous materials 383
amorphous zones 329
amorphous-crystalline interfaces 227
amorphous-crystalline multilayers 227
analysis, ion beam 133
angular distribution 405
annealing, dynamic 227
approximation, Gaussian 151
athermal melting 293
atmospheres, generation of 13
atomic displacements 227
Auger electron spectroscopy 497
Auger electron spectroscopy, electronic temperatures 497
Auger electron spectroscopy, inner shell ionisation 497
Auger electron spectroscopy, track potential 497
band gaps, surface projected 625
Barkas correction 557
beam diagnostics 37
Bethe stopping theory 557
Betz–Grodzins models 595
binary encounter collisions 497
biological effectiveness 37
Bloch stopping theory 557
blocking 655
Bohr stopping theory 557
Bohr–Lindhard models 595
Bradley–Harper theory 207
bubbles 329
buried interfaces 133
carbon ions 357
carbon nanotubes 357
cells, ion tracks in 59
channeled particles, radiation from 655
channeling 731
channeling, energy loss in 655
charge exchange 557
charge state 109
charge transfer 625
charge transfer, multi-electron 625
charge transfer, resonant 625
chemical effects 357
Chudakov effect 699
classical *versus* quantal description 655
cluster emission 405, 433
cluster emission, fragmentation 405
cluster formation 405
cluster impact 433
collective excitations 497
configurational energy states 383
correction, Barkas 557
correction, shell 557
correlated emission 497
cosmic rays 13
Coulomb explosion 293
coupling, surface 497
craters 329, 433
crystal-glass transition 383

crystal-glass transition, amorphization 383
crystal-glass transition, ergodicity 383
crystal-glass transition, percolution transition 383
crystallisation, epitaxial 227
damage, electron irradiation 357
damage, ion 227
damage, lower-energy electron 357
damage, nuclear collision 357
damage, radiation 357, 731
dechanneling 655
defects, extended 329
defects, ion-induced 207
defects, point 357
density correction in stopping 557
deposition 87
deposition, radial energy 59
depth resolution, ultimate 133
detector, solid state 731
diagnostics, beam 37
diffusion, radiation enhanced 13
diffusion, surface 207
displacements, atomic 227
distribution, angular 405
distribution, energy 405
divertor 87
dosimetry 37
double strand breaks 59
dynamic annealing 227
dynamic screening 151
effects, chemical 357
effects, finite size 625
effects, relativistic 655
effects, single ion 329
effects, strong field 699
electron affinity 465
electron emission 525
electron emission, kinetic electron emission 525
electron emission, potential electron emission 525
electron irradiation damage 357
electron number statistics, coincident measurement 525
electron number statistics, surface-scattered projectiles 525
electron spectra 557
electron sputtering 357
electron yield, total 525
electronic desorption 13
electronic excitations 13
electron-photon coupling 263
emission, cluster 433
encounter collisions, binary 497
energy distribution 405
energy loss in channeling 655
energy states, configurational 383
energy, fusion 87
energy-loss profile, width of 151
energy-loss spectra 557
enhanced FIBs, need for 133
epitaxial crystallisation 227
epitaxy, solid phase 227
equilibrium charge states of ions in solids 595
erosion 87
evolution, morphology 187
evolution, nanophore 187
excitations, collective 497
excitations, electronic 13
experimental distinction between kinetic and potential electron emission 525
extended defects 329
FAIR project 109
fast melting 109
fast neutron recoil atoms 731
Fermi shuttle 497
finite size effects 625
formation length 699
fragmentation 699
free-electron metals *versus* band structure 625
fullerenes 357
fusion energy 87
fusion, inertial 109
gas release 731
gas trapping 731
Gaussian approximation 151
generation of atmospheres 13
grain sputtering 13
graphene 357
graphite 357
grazing incidence 525
guided self-organization, nanoscale morphology control 187

heating and cooling 655
heavy ions 595
high charges, primary ionisation 497
high-resolution 329
history 731
image potential 465
impact parameter dependence 151
impact, cluster 433
impurities and defects 655
inertial fusion 109
infinite velocity 465
instability 207
instability, morphological 187
insulator surfaces 525
insulators 595
insulators, amorphisable 263
insulators, non-amorphisable 263
interaction, plasma-surface 87
interfaces, amorphous-crystalline 227
interfaces, buried 133
internal and exit charge states 595
interstellar medium 13
interstitials 357
ion beam analysis 133
ion channeling 227
ion damage 227
ion emission, secondary 465
ion range in tissue 37
ion ranges 731
ion scattering limits 133
ion tracks 13
ion tracks, in cells 59
ionic crystals 263
ion-induced defects 207
ionisation potential 465
ionisation probability 465
ionization and excitation probability 405
ionization energy loss 699
ionization, multiple 151
ions carbon 357
ions, w-values for 37
irradiation, single cell 59
isotope separator 731
kinetic Monte Carlo 207
kinetics, relaxation 187
layer, alkali 465
level width 465
light ions 595
Lindhard theory 655
linear cascade sputtering 405
localised *versus* delocalised capture 625
low-energy electron damage 357
LPM effect 699
magnetospheric ions 13
materials, amorphous 11
measurements, stopping 557
melting, athermal 293
metal *versus* insulator surfaces 625
metal surfaces 525
metals 329, 595
micro beam 59
micrometeorite impact 13
microscopy, transmission electron 329
minimum yields and widths 655
monolayer resolution 151
morphological instability 187
morphology evolution 187
morphology, surface 207
multi-electron charge transfer 625
multilayers, amorphous-crystalline 227
multiple ionization 151
nanophore evolution 187
nano-structures 133
nanotubes, carbon, 357
need for enhanced FIBs 133
non-adiabatic transitions 625
non-proportionality effects, slow molecular projectiles 525
nuclear collision damage 357
nuclear lifetimes 655
nuclear spectroscopy 731
organic and molecular solids, desorption mechanism 405
organic and molecular solids, secondary ion formation 405
organic and molecular solids, sputter depth profile 405
parallel velocity effect 625
pattern formation 207
perturbation, strong 497
phase transition 109, 357
planetary regolith 13

planning, treatment 37
plasma-surface interaction 87
point defects 357
polyatomic projectile impact, emission mechanism 405
polyatomic projectile impact, excitation and ionization phenomena 405
polyatomic projectile impact, linear cascade and spike regime 405
probability, ionisation 465
proton pick-up 699
quantum dots 133
radial energy deposition 59
radiation chemistry 13
radiation damage 357, 731
radiation enhanced diffusion 13
radiation from channeled particles 655
radiation synthesis 13
radiological weight factor 59
radiolysis 13
radiotherapy 37
rate equation 625
recoil atoms, fast neutron 731
relativistic effects 655
relativistic effects, in stopping 557
relaxation kinetics 187
release, gas 731
resolution, monolayer 151
resonant charge transfer 625
ripples, 207
saturation effects 595
scattering 557
scattering limits, ion 133
screening 557
screening, dynamic 151
secondary ion emission 465
segregation 13
semiconductors 329, 595
sensitivity, ultimate 133
shell correction 557
shock wave 293
single cell irradiation 59
single collision 151
single ion effects 329
single strand breaks 59
slow hydrogen in solids, bound states 595
slow hydrogen in solids, pions 595
slow hydrogen in solids, positive muons 595
slow hydrogen in solids, positrons 595
solid phase epitaxy 227
solid state detector 731
spatial resolution, ultimate 133
spectra, electron 557
spectra, energy-loss 557
spectroscopy, Auger electron 497
spectroscopy, nuclear 731
spikes 433
sputter yield 207
sputtering 13, 207, 433
sputtering, angular distribution 433
sputtering, depth of origin 433
sputtering, electron 357
sputtering, energy distribution 433
sputtering, grain
sputtering, linear cascade 405
sputtering, molecular and organic solids 433
sputtering, preferential sputtering 433
sputtering, yield 433
stellar shocks 13
stellar winds 13
stoichiometry determination, ultimate 133
stopping 557
stopping, density correlation in 557
stopping, relativistic effects in 557
stopping measurements 557
stopping power 109
stopping power, ratios 37
stopping power, threshold 293
stopping theory, Bethe 557
stopping theory, Bloch 557
stopping theory, Bohr 557
straggling 557
strand breaks, double 59
strand breaks, single 59
strong field effects 699
strong perturbation 497
structure, track 59
supertail 731
surface coupling 497
surface diffusion 207
surface morphology 207
surface perturbation 465

surface projected band gaps 625
surface ripples 207
surface structure triangulation 525
surface topography 433
surfaces, insulator 525
surfaces, metal 525
swift-ion tracks 433
thermal spike 293
thermal vibrations 655
thermodynamics 293
thermodynamics, supercooling 293
thermodynamics, superheating 293
threshold behaviour 525
threshold, stopping power 293
tissue, ion range in 37
total electron yield 525
track description 263
track description, Poisson law 263
track description, threshold of track formation 263
track description, track morphology 263
track description, velocity effect 263
track mechanics 293
track mechanics, hillock formation 293
track mechanics, ion hammering 293
track model 263
track model, electron-photon coupling 263
track model, energy deposition 263
track model, linear energy loss 263
track model, radial energy distribution 263
track model, sputtering 263
track model, transient thermal process 263
track structure 59
tracks, swift-ion 433
transitions, non-adiabatic 625
transitions, phase 109
transmission electron microscopy 329
transport theory 433, 497
trapping, gas 731
treatment planning 37
triangulation, surface structure 525
tunnelling 625
tunnelling model 465
ultimate depth resolution 133
ultimate sensitivity 133
ultimate spatial resolution 133
ultimate stoichiometry determination 133
vacancies 357
velocity effect 557
velocity effect, parallel 625
viscoleastic properties 383
voids 329
warm dense matter 109
weight factor, radiological 59
width of energy-loss profile 151
work function 465
w-values for ions 37
yields and widths, minimum 655
zones, amorphous 329

Manuscript

General. – Manuscripts and illustrations must comply with the details given below. The original manuscript and illustrations plus one clear copy of both should be sent to the editor of the series. Manuscripts on digital media are accepted; contact the editor in advance, giving technical specifications.

A manuscript should contain no less than 48 printed pages. This also applies to the Mat.fys. Medd. where contributions to the history of science are welcome.

Language. – Manuscripts in Danish, English, German and French are accepted; in special cases other languages too. Linguistic revision may be made a condition of final acceptance.

Title. – Titles should be kept as short as possible, preferring words useful for indexing and information retrieval.

Abstract, Summary. – An abstract in English is required. It should be of 10-15 lines, outline main features, stress novel information and conclusions, and end with the author's name, title, and institutional and/or private postal address. – Papers in Danish must be provided with a summary in another language as agreed between author and editor.

Manuscript. – Page 1 should contain title, author's name and the name of the Academy. Page 2: Abstract, author's name and address. Page 3: Table of contents if necessary. Consult a *recent* issue of the series for general layout. Indicate the position of illustrations and tables. A printout must accompany manuscripts submitted electronically.

Figures. – All illustrations submitted must be marked with the author's name. It is important that the illustrations are of the highest possible quality. Foldout figures and tables should be avoided.

References. – In general, the editor expects all references to be formally consistent and in accordance with accepted practice within the particular field of research. Bibliographical references should be given in a way that avoids ambiguity.

Correspondence

Manuscripts are to be sent to

The Editor
Det Kongelige Danske Videnskabernes Selskab
H.C. Andersens Boulevard 35
DK-1553 Copenhagen V, Denmark.
Tel: +45 33 43 53 00
Fax: +45 33 43 53 01.
E-mail: e-mail@royalacademy.dk.
www.royalacademy.dk

Questions concerning subscription to the series should be directed to the Academy

Editor Flemming Lundgreen-Nielsen

Det Kongelige Danske Videnskabernes Selskab
The Royal Danish Academy of Sciences and Letters

Matematisk-fysiske Meddelelser

Priser ekskl. moms / Prices excl. VAT

45	*Magnetism in Metals.* A symposium in Memory of Allan Mackintosh, Copenhagen, 26-29 August 1996. Invited Review Papers. 1997. Edited by *D.F. McMorrow, J. Jensen* and *H.M. Rønnow.*	500, -
46:1	Caspar Wessel: *On the Analytical Representation of Direction. An Attempt Applied Chiefly to Solving Plane and Spherical Polygons.* Translated by *Flemming Damhus.* With introductory chapters by *Bodil Branner, Nils Voje Johansen, Kirsti Andersen.* Edited by *Bodil Branner* and *Jesper Lützen.* 1999. 150 pp. Fig.	500, -
46:2	*Around Caspar Wessel and the Geometric Representation of Complex Numbers.* Invited papers. Edited by *Jesper Lützen.* 2001. 304 pp.	300, -
47	Aksel Wiin-Nielsen: *On Limited Predictability.* 1999. 40 pp.	50, -
48	Aksel Wiin-Nielsen: *On Atmospheric Waves.* 2000. 53 pp.	80, -
49	Anders Hald: *On the History of Series Expansions.* 2002. 88 pp.	140, -
50	U. Bernth, R. Brousse, R. Frei & H. Sørensen: *The Origin of Phonolites and Thachytes from the Col de Guéry Area.* Le Mont-Dore, Massif Central, France. 2002. 61 pp.	100, -
51	Anders Hald: *Nogle danske statistikeres liv og deres værker.* 2005. 36 pp.	40, -
52:1	*Ion Beam Science: Solved and Unsolved problems.* Invited lectures presented at a symposium arranged by the Royal Danish Academy of Sciences and Letters, Copenhagen, 1-5 May 2006. Part I. Edited by *Peter Sigmund.* 2006. 376 pp.	350, -
52:2	*Ion Beam Science: Solved and Unsolved problems.* Invited lectures presented at a symposium arranged by the Royal Danish Academy of Sciences and Letters, Copenhagen, 1-5 May 2006. Part II. Edited by *Peter Sigmund.* 2006. 384 pp.	350, -

Printed in Denmark by Special-Trykkeriet Viborg a-s.
ISSN 0023-3323. ISBN10 87-7304-330-3; ISBN13 978-7304-330-1